U.PORTO

FEUP FACULDADE DE ENGENHARIA
UNIVERSIDADE DO PORTO

ANALYSIS AND MITIGATION OF VIBRATIONS INDUCED BY THE PASSAGE OF HIGH-SPEED TRAINS IN NEARBY BUILDINGS

JOÃO MANUEL DE OLIVEIRA BARBOSA
2013

Supervisors: *Prof. Álvaro Azevedo (FEUP)*
Prof. Rui Calçada (FEUP
Prof. Eduardo Kausel (MIT)

Thesis presented to the Faculty of Engineering of the University of Porto for the Doctor Degree in Civil Engineering

POPH QUALIFICAR É CRESCER.
QREN QUADRO DE REFERÊNCIA ESTRATÉGICO NACIONAL PORTUGAL 2007.2013
Governo da República Portuguesa
UNIÃO EUROPEIA Fundo Social Europeu

Ao titio e à titia

Aos meus pais

Aos meus irmãos

Abstract

The present dissertation addresses the subject of vibrations induced by the passage of high-speed trains. The main objective of the study is the development of numerical tools that allow investigating distinct geometries of train and track, considering buildings in the proximity of the track, and also assessing the behavior of mitigation solutions.

The problem of vibrations induced by moving vehicles is divided into three stages: a generation stage, in which the vehicle interacts with the track; a propagation stage, in which the forces that the train transmits to the track originate waves that propagate through track and ground; and a reception stage, in which the waves reach a nearby building, causing it to respond dynamically. Since the geometric specifications of the problem vary within the three stages, different strategies are chosen for each stage:

1. The generation stage involves a discrete structure (the vehicle) moving on top of a structure whose longitudinal dimension is infinite (track-ground system). In this way, the problem is formulated in a moving frame of reference, being the equations solved in the frequency domain;
2. For the propagation stage, since it is assumed that track and soil are invariant in the longitudinal direction, then the problem is formulated in the wavenumber-frequency domain (2.5D). In this way, the three-dimensional problem is reduced to a series of two-dimensional problems of smaller dimensions that are faster to solve. The track is simulated with finite elements while the surface of the soil interacting with the track is simulated with boundary elements. Mitigation measures in the soil must be included in this stage;
3. In the reception stage, the three-dimensional structure to be analyzed is irregular in all directions and therefore the 2.5D procedure cannot be applied. For this reason, a 3D frequency domain formulation is used, in which the structure is simulated with finite elements and the soil is simulated with boundary elements. The exterior loads considered in this stage are calculated based on the results of the propagation stage.

The response of the soil, which is of great relevance for the problem, is accounted for through the boundary element method (BEM). The fundamental solutions used to nurture the BEM are obtained with the thin-layer method, being this the main difference between the strategy adopted herein and the procedures followed by other authors that also use the BEM.

The numerical procedures mentioned above are described in chapters 2-4. Additionally, in chapter 4, the link between the three stages and the distinct procedures is established. In chapter 5, the methodology is applied to the study of trenches as mitigation solutions.

Resumo

Esta dissertação debruça-se sobre o tema de vibrações induzidas por tráfego ferroviário de alta velocidade. O principal objetivo do estudo reside no desenvolvimento de ferramentas numéricas capazes de simular o fenómeno e que permitam investigar vias e comboios com geometrias variadas, considerar edifícios na proximidade da via, e ainda avaliar o comportamento de diversas medidas mitigadoras.

O problema de vibrações induzidas por veículos pode ser dividido em 3 fases: uma fase de geração, em que o veículo interage com a via; uma fase de propagação, em que a ação que o veículo transmite à via-férrea origina ondas que se propagam através desta e através do solo; e uma fase de receção, em que as ondas chegam a um edifício próximo da via, induzindo a resposta dinâmica da estrutura. As especificidades geométricas variam de fase para fase, pelo que são tomadas diferentes estratégias para cada fase:

1. A fase de geração envolve a interação entre uma estrutura móvel de caráter discreto (o veículo) e uma estrutura de dimensão longitudinal infinita (sistema solo-via). Desta forma, formula-se o problema com base num referencial móvel, sendo as equações posteriormente resolvidas no domínio da frequência;
2. Para a fase de propagação, uma vez que se assume que tanto a via como o solo apresentam invariância longitudinal, as equações são formuladas no domínio do número de onda e da frequência (2.5D). Desta forma, reduz-se o problema tridimensional a um somatório de problemas bidimensionais de menor dimensão e de mais rápida resolução. A via-férrea é modelada com recurso a elementos finitos e a superfície do solo em contacto com a via é modelada com elementos de contorno. De salientar que medidas mitigadoras no solo, como por exemplo, trincheiras, devem ser incluídas nesta fase;
3. Na fase de receção, a estrutura a analisar apresenta um caracter tridimensional e irregular em todas as direções, pelo que a formulação 2.5D deixa de ser válida. Assim, opta-se por uma formulação tridimensional, no domínio da frequência, em que a estrutura é modelada com elementos finitos e a superfície do solo em contacto com a estrutura é modelada com elementos de contorno. Convém ainda referir que a ação considerada nesta fase é calculada com base nos resultados da fase de propagação.

Relativamente ao solo, elemento preponderante em todo o problema, o seu comportamento é tido em conta por intermédio do método dos elementos de contorno (MEC). As soluções fundamentais usadas para alimentar o MEC são obtidas pelo *thin-layer method*, sendo esta a principal diferença entre a estratégia aqui adotada e a estratégia seguida por outros autores que também usam o MEC.

A formulação das ferramentas acima mencionadas é descrita nos capítulos 2 a 4, sendo ainda no quarto capítulo exemplificada a ligação entre os diferentes procedimentos. No capítulo 5, a metodologia é aplicada ao estudo de medidas mitigadoras sob a forma de trincheiras.

Acknowledgments

It took me five years to conclude this Doctoral work, and such would not have been possible without the contribution and support of the people that one way or the other accompanied me throughout this process. To them, I want to demonstrate my appreciation.

- To my supervisors, Professors Álvaro Azevedo, Rui Calçada and Eduardo Kausel, for having accepted the responsibility of guiding. I would like to stress the role of Professor Eduardo Kausel, who received me in the United States and who was essential for the success of my stay at MIT.
- To Professor Pedro Costa, for his comments and opinions given during the development of the thesis, but mostly during the last year of work, which relates to Chapter 5 herein presented.
- To the colleagues developers of FEMIX, Prof. Álvaro Azevedo and Sérgio Neves, for making the software available, and for their effort in making FEMIX an attractive choice for people who want or need to develop their own calculation routines.
- To colleague Ricardo Nobre, PhD student in the field of computer science at FEUP, to the research group SPECS, to Professor Pedro Sobral from University Fernando Pessoa, to Professors João Cardoso, Rui Rodrigues and Jorge Barbosa from the Department of Computer Science of FEUP, and to Nuno Subtil from NVIDIA, for their support regarding GPU programming.
- To all colleagues from the High-Speed research group, headed by Professor Rui Calçada, for all help provided during these five years.
- To all colleagues and friends that have worked in office H301 and that made the working environment very friendly — Alés de Miguel, Cristina Ribeiro, Fernando Bastos, Luís Martins, Mário Marques, Miguel Araújo, Nuno Santos, Ricardo Monteiro, Sérgio Neves.
- To the MIT office mates, for the same reason — Dilip Thk, Swapnil Rajiwade, Rositta Jünemann, Anthoula Agn, Zeid Alghareeb, Inez Azaiez.
- To Fundação para a Ciência e Tecnologia (FCT – Portuguese Foundation for Science and Technology), that provided me financial support through PhD grant SFRH/BD/47724/2008 and through the research project PTDC/ECM/ 114505/2009 — Ground Vibration and Noise Induced by High-Speed Trains: Prediction and Mitigation.
- To MIT-Portugal program, for facilitating my research periods at MIT.

At last, the most special acknowledgment goes to those who have followed me on a daily basis, ever since my birth. An immeasurable thank you to my parents, Jorge Barbosa and Maria José Barbosa, my brothers, Ricardo Jorge and Rui Vasco, to may granduncle and grand aunt, Manuel Sala (*titio*) and Maria Elisa (*titia*). Without their absolute support, I would not have started the PhD.

Contents

1. Introduction

1.1 Motivation

High-speed railway networks have been under construction all over Europe and Asia during the last decades. Currently, in Europe, high-speed lines are being explored in Spain, France, Germany, Belgium, Netherlands, Luxemburg, Switzerland, Italy and Britain. In Asia, China holds the record for the largest high-speed network, with an extension of 7500 km. It is expected that by 2020 the Chinese network will be expanded to a total of 25000 km. In other countries, for example Sweden, even though there is no high-speed network, trains can travel at speeds up to around 200 km/h. In Portugal, in some sections of the Northern Line, the "Alfa Pendular" train can travel at speeds up to 220 km/h and, until a few years ago, there were plans to build high-speed railway lines that would connect Portugal with Spain.

Problems related to the increase of the travel speed of trains have been reported in the last years. Shortly after the opening of the Swedish line between Göteborg and Malmö in 1997, excessive vibration levels were detected both in the railway embankment and surrounding soil when the X-2000 train travelled at speeds around 200 km/h (Madshus and Kaynia, 2000). The high vibration levels were explained by the increase of the train speed, which approached the Rayleigh wave velocity of the soil, causing the resonance of the track-soil system and resulting in the potential instability of the train. Another problem that may arise from the circulation of trains is the excessive vibration level on nearby buildings originated by waves that propagate through the ground. The induced vibrations may cause annoyance to the occupants of the building, malfunction of sensitive equipment and, eventually, structural and non-structural damage.

Since during the planning stage of a high-speed railway network it is not possible to avoid sensitive areas in which vibrations may be problematic, such as zones of poor soil characteristics (soft soils with low wave velocities) or zones more or less urbanized (train-stations, for example), prediction tools for the assessment of vibrations induced by the passage of trains reveal themselves very valuable. This is the motivation for the present work. The main objective of the work is to develop numerical tools capable of predicting the vibration levels induced by trains in buildings and to study the efficiency of countermeasures to mitigate those vibrations.

In the next section, the state of the art on vibrations induced by vehicles is presented.

1.2 State of the art

Vibrations induced by moving sources are not a problem that emerged with high-speed trains. Long before the appearance of the first high-speed trains in Japan, in the mid-sixties, reports had been made regarding the impact that the circulation of vehicles could have on surrounding buildings. For example, in the XIX century, people were concerned with the effects that the passage of freight trains in a line yet to be constructed in the proximity of the Royal Observatory, in Greenwich, England, would have on its equipment (South, 1863). This concern led to experimental investigations on the subject. In another example, in the middle of the XX century, the National Research Council of Canada promoted experimental campaigns to evaluate the vibrations induced by the passage of trolley buses in nearby buildings (Sutherland, 1950). The campaigns were organized in response to the increasing

number of complaints received from inhabitants who sensed the vibrations and feared damage on their properties.

The construction of the subway systems inside the cities (excessively close to residences), together with the increase of train capacities and comfort standards, gave more importance to the problem of vibrations induced by moving vehicles and led to several experimental campaigns (Wilson et al., 1983; Dawn and Stanworth, 1979; Melke and Kramer, 1983). The experimental campaigns were carried out to assess if the vibrations induced by the circulation of trains could damage buildings, cause discomfort to inhabitants or cause the malfunction of sensitive equipment and, at the same time, to understand the mechanisms of generation of vibrations and to study possible mitigation measures.

In more recent years, in part due to the continuous increase of the weight and speed of trains and in part due to the higher standards for comfort, the problem became even more important and, in addition to the problem of vibrations induced on buildings, a new problem emerged: at some lines resting on soft soils the train speed approached the propagating velocity of the waves and, as a consequence, large displacements in the embankment were observed, causing the risk of derailment of the train. This happened, for example, in the very well documented case of Ledsgard, Sweden (Hall, 2000), and in a line of the Northwest of France (Picoux and Le Houedec, 2005). In those lines, the circulation speed was reduced and, in several other lines around the world, new experimental campaigns were conducted to assess the vibration levels. In addition, studies were performed on countermeasures to mitigate the vibrations and prediction models were developed or improved.

Two strategies for the study of the phenomenon of vehicle induced vibrations can be adopted: field measurements and numerical/analytical predictions. Field measurements are performed under real conditions and provide an enriched set of results, which account for all the factors that influence the phenomenon. The results of the experimental campaigns indicate which aspects most influence the level of induced vibrations, thus showing which factors must be taken into account when developing numerical models. When large databases collecting experimental data are available, it is possible to perform extrapolations in order to predict the vibration levels for scenarios with similar conditions (soil, track, vehicle, structure), and, consequently, it is possible to develop empirical models. The drawback of field experiments is their high cost and so it is desirable that they are employed as less as possible. Nevertheless, experiments are always needed to obtain inputs for numerical models and also to validate these models.

On the other hand, to use prediction models is not as expensive as performing in situ experiments but, contrarily to experiments, these models cannot reproduce the whole reality since they are based on assumptions and simplifications. On one side, empirical models that are developed based on experimental data provide good estimates but their range of applicability is limited to scenarios with conditions similar to the experiments. On the other side, numerical models are versatile and allow studying the influence of certain parameters on the vibration levels, but their accuracy depends on the simplifications made and on the assumptions on which the models lie. Numerical models can usually be adapted in order to account for countermeasures and study their performance.

In the following sub-sections, a historical overview of experimental campaigns, prediction models and countermeasures for vibrations is presented.

1.2.1 Experimental campaigns

As mentioned earlier, the problem of vibrations induced by moving vehicles harks back to the XIX century, when South (1863) performed experimental investigations in a tunnel located in Watford, England. These experiments were carried out to sustain the idea that the passage of freight trains in Greenwich Park, near the Royal Observatory, could be harmful to its equipment. The Watford tunnel was selected for the experiments because the geotechnical conditions at that place were similar to the ones observed in Greenwich.

Vibrations induced by road traffic have also been subjected to investigations since the mid twentieth century, as reported by Sutherland (1950), who refers to experiments made in Canada. There, the inhabitants of the city of Winnipeg sensed the vibrations and feared damage on their properties, and therefore presented their complaints to the City Hall. As a consequence of the multiple complaints, the National Research Council of Canada promoted experiments to investigate the problem. The results of the experiments suggested that the induced vibrations, even if felt, were not strong enough to cause damage in the structures. In addition, it was concluded that the irregularities of the surface of the road (such as bumps) were the factor that contributed most to the vibration levels.

Also concerning road traffic induced vibrations and still in Canada, more experimental campaigns were carried out to understand the phenomenon. As a consequence of complaints lodged by residents in Quebec, Al-Hunaidi and Rainer (1991a) performed field experiments in two different sites in order to study the factors that influence the level of vibrations. They studied the influence of speed, weight and type of vehicle and road roughness, and concluded that while the vehicle speed and the road irregularities influenced considerably the vibrations, the mass of the vehicle had little influence. Later, Al-Hunaidi and collaborators performed more tests in nine different sites of the city of Montreal to study the influence of the suspension system of the vehicles (Al-Hunaidi et al., 1996) and concluded that the vibrations could be greatly reduced by imposing an axle hop frequency lower than the cutoff frequency of the soil. The influence of the road surface condition and seasonal variation of soil conditions has also been taken into account in another study (Al-Hunaidi and Tremblay, 1997).

To study the efficiency of soil improvement as a countermeasure for road traffic induced vibrations, Taniguchi and Okada (1981) measured the acceleration before and after the improvement of the soil using the lime pile technique. When they compared the spectrum of the vibration reduction with the acceleration spectrum of a point situated 8m away from a national road, they observed that the frequency range over which the vibrations were reduced due to the soil improvement was approximately the same range that was excited by the road traffic, thus concluding that the method was efficient.

To validate their numerical model for the prediction of road traffic induced vibrations, Lombaert and Degrande organized two campaigns where a truck moving with variable speed was submitted to an artificial unevenness (Lombaert and Degrande, 2001; Lombaert and Degrande, 2003). Free field vibrations and acceleration of the axles were measured and the dynamic properties of the road and soil were determined experimentally. The results suggested that the vibration levels were dependent on the vehicle speed, the shape of the unevenness, and the vehicle and soil characteristics. The comparison between experimental and predicted results showed some differences that were explained by the loss of contact between the rear axle and the road.

With respect to rail traffic induced vibrations, Wilson et al. (1983) reported experiments made during the seventies to study the use of floating slabs as a countermeasure to mitigate ground-borne vibrations and to study the influence of the properties of the bogies on the induced vibrations. Measurements were made in tunnels, on the free surface, and inside buildings. Later, in the late seventies, Dawn and Stanworth (1979) measured the vibration levels on a wall of a single storey building situated about 42m away from a track during the passage of trains at speeds up to 100 km/h. They noticed that the vibrations increased with the speed of the train and observed that the frequency content of the response presented a peak on the passage frequency of the sleepers. Dawn (1983) performed further experimental studies and confirmed that the passage frequency of the sleepers is indeed a mechanism of excitation. He also recognized that the critical velocity (to which corresponds the maximum ground response) occurred when the sleeper passage frequency coincided with the resonance frequency of the vehicle-track system. Melke and Kramer (1983) reached the same conclusions in their experimental studies.

In more recent years, with the increase of the train speed, the problem of induced vibrations has been given even more importance and new experimental studies have been performed. In addition, with the construction of new railway lines, their homologation tests enabled the execution of new field experiments.

In Germany, Auersch (1994; 2005) performed measurements at three different sites near Würzburg during test runs of the ICE train with different configurations and at speeds between 100 and 300 km/h. During the tests, which considered three different track conditions (surface line, bridge and tunnel), the vibrations of the vehicle, track and soil were recorded. The results showed that the quasi-static component of the axle load was important for the response of the track and the surrounding soil, and that its importance vanished rapidly with the distance. The results also suggested that the sleepers act as harmonic forces, whose intensity increases with the train speed, but remains constant when the sleeper passage frequency exceeds the vehicle-track resonance frequency.

In Sweden, as a consequence of the high vibration levels observed shortly after the opening of the line between Göteborg and Malmö, in 1997, the train speed was reduced at some locations and investigations were conducted during the Autumn of 1997 and Spring of 1998 to diagnose the problem and to find solutions (Madshus and Kaynia, 2000; Hall, 2000). A X-2000 passenger train was used in a total of 20 runs at speeds ranging from 10 to 202 km/h and the responses of rail, sleepers, embankment and ground (at the surface and its interior) were measured. It was observed that for speeds below 70 km/h the displacements of the ground were similar to those obtained considering static loading and therefore were independent from the speed. At speeds around 200 km/h, the amplitude of the displacements increased drastically, causing the risk of derailment of the train.

In Belgium, the expansion of the railway network allowed to experimentally investigate the phenomenon in newly built high-speed lines. In December of 1997, six weeks before the inauguration of the high-speed line between Brussels and Paris, an extensive experimental campaign was organized by the Belgian railway company during the homologation phase of the line. Track response and free field vibrations up to 72 meters away from the track were measured during the passage of a Thalys train at speeds varying between 223 and 314 km/h (Degrande and Schillemans, 2001). Five years later, in August and September of 2002, the high-speed line between Brussels and Köln was also submitted to homologation tests (Kogut et al., 2003). The tests were performed at two different sites, Lincent and Waremme, and

included the measurement of vibration levels at the track, in the free field and in a single family dwelling located 50m away from the track during the passage of Thalys trains and IC trains at variable speed. The tests were complemented with the experimental determination of some dynamic properties of the track and soil. The two sets of experiments showed that the passage frequencies of bogies and sleepers and their higher harmonics could be noticed on the spectrum of the responses, namely in the near field. Also, differences in the registered responses for the different trains suggested that the induced vibrations depend on the train properties. In both cases, attenuation of vibrations with the distance to the track was detected.

In Italy, Lai et al. (2005) measured the transfer functions in two sections of a tunnel in the city of Rome. The aim of the study was to assess if the level of vibrations would affect the surrounding buildings. Since the line was not yet operational, it was not possible to perform a direct measurement of vibrations induced by the railway traffic. Hence, the transfer functions from the tunnel to the free field and to the interior of buildings were determined experimentally using a mechanical hammer. The transfer functions would serve as inputs in a simple numerical model to predict the level of vibrations induced by future passing trains.

In the Northwest of France, after it was observed that the ground presented excessive displacements, Picoux and Le Houedec (2005) measured the vibrations on rails, sleepers and free-field during the passage of different trains. The results showed the influence of the train speed and of the type of train on the induced vibrations.

In England, within the framework of the CONVURT project, vibrations were measured at a site in Regent's Park, London, during 35 passages of a test train in a tunnel at speeds between 20 and 50 km/h (Degrande et al., 2006). Accelerations of the axle boxes, of the tunnel, of the free field (both at surface and inside the soil) and on several floors of two buildings situated 70m away from the tunnel were measured. Rail and wheel roughness have also been measured and track characteristics were determined by receptance tests. Analysis of the measured fields allowed concluding that the peak velocities on the axle boxes and track increased with the train speed, a tendency that was less pronounced in the free-field and in the buildings.

In Beijing, China, a subway line was planned to pass close to the Physics Laboratory of the Beijing University and so there was concern about the vibrations that would be induced by the rail traffic (Gupta et al., 2008). To study if certain equipments would need to change place, measurements were performed in the free-field near the lab and inside the building to evaluate the existing vibration levels (induced by road traffic and people). In addition, measurements were made in a different line of the Beijing subway system with similar characteristics. The superposition of the existing background and the predicted vibration levels would provide the vibration level expected in the labs.

In Northeast China, Xia analyzed experimentally the problem of vibrations in buildings induced by trains running on bridges. Trains running at speeds varying between 60 and 80 km/h (Xia et al., 2005a) and between 160 and 307 km/h (Xia et al., 2005b) were considered. It was observed that the vibration levels would increase with the weight and speed of the train and would attenuate with the distance to the railway line. It was also observed that the vibrations were stronger at higher floors, exceeding in some places the levels allowed by the Chinese code.

To finalize the field measurements, some experimental campaigns have also been organized at the Portuguese Northern line by researchers from FEUP, whose objective was to characterize the site conditions and measure the vibrations induced by real traffic (Alves Costa et al.,

2012a; dos Santos, 2013). At the same site, further investigations have been conducted in order to evaluate the dispersion of the responses along the longitudinal directions. The results obtained from these campaigns are expected to be published in the near future.

1.2.2 Prediction models

Two types of prediction models can be considered: empirical and analytical/numerical. Empirical models are based on results from experimental campaigns and usually provide good predictions, but their range of applicability is limited to scenarios that are similar to the conditions under which the experiments were performed, thus lacking versatility. Description of empirical models can be found in works by Kurzweil (1979), Melke (1988) and Madshus et al. (1996). These models use chains of transmission losses for the source-path-receiver system and consider parameters such as train speed, axle loads, suspension systems, weight of the train, wheels and rail conditions, rail fastening systems, type of track, type of tunnel and type of buildings. The model described by Madshus et al. (1996) was developed based on a large number of vibration measurements made in Norway and Sweden and was used for the planning of a high-speed railway line in Norway. In another empirical work, to evaluate problems of excessive vibrations in preliminary stages, Bahrekazemi (2004) presented a model that is based on measurements performed in several sites of Sweden.

On the other hand, numerical and analytical methods are more versatile and can be efficiently used to study the effect of train speed or weight, track type, material resiliency, ground conditions, etc. The drawback is that these methods rely on idealizations and simplifications, then failing to reproduce reality as accurately as it would be possible with field experiments. Nonetheless, depending on the degree of detail of the model, the obtained prediction can be acceptable and useful.

To correctly model vibrations induced by vehicles, three stages must be accounted for in a numerical/analytical model: the generation stage, the propagation stage and the reception stage (Figure 1.1). In the generation stage, the vehicle interacts with the track and induces a moving stress field on it. The stresses are transmitted from the vehicle to the track through contact surfaces (wheels or tyres) that move in space. Due to the dynamic behavior of the vehicle and its interaction with the track, the vehicle is subjected to accelerations and so the contact stresses, besides moving with the vehicle, also change their value with time. The non varying component of the contact stresses is called quasi-static excitation (forces per wheel or tyre) while the component varying with time is termed dynamic excitation. In the propagation stage, the stress fields (or the vibrations) propagate through the track and part of them is transmitted to the soil. These stresses continue to propagate in the soil, being reflected or refracted whenever a different material or a barrier is encountered, and finally reach the building. In the reception stage, the vibrations that reach the building induce a dynamic response on it.

The problem of vibrations induced by moving vehicles is three dimensional: the vehicle moves in one direction while the waves propagate in the soil in three directions. Modeling a three dimensional problem can become very complicated and time consuming, even for the current computers. For this reason, the first works assumed that the phenomenon could be described by 2D models. For example, in their review paper, Gutowski and Dym (1976) mentioned that the vibrations generated along a road or a railway track could be modeled as a line source as long as the roadway was relatively uniform and the receiver was in the far field, but close enough to the source (less than $1/\pi$ times the length of the roadway or the train). The authors supplemented that if the ground motions were dominated by the surface (Rayleigh)

waves, then there would be no geometric damping and so the vibrations would attenuate only due to material damping. Later, Verhas (1979) compared the results of line source models with the results of point source models and concluded that by neglecting the geometric damping of waves inaccurate predictions would be obtained. This author suggested that the combination of the two models would yield better predictions, but no guidelines on how to combine the results from each model were indicated. In another 2D work where a finite element (FE) model was used, in order to account for the geometric damping of surface waves, the accelerations were corrected by a factor $1/\sqrt{r}$, being r the distance to the source (Taniguchi and Okada, 1981). This methodology was used to study the efficiency of soil improvement via the lime pile technique as a countermeasure. Also using a 2D FE procedure, Chua et al. (1995) determined the vibration levels in a four-storey podium block due to the passage of trains in a double-box tunnel, accounting both for the quasi-static and for the dynamic excitation. The authors used an iterative nodal condensation procedure to avoid extremely large meshes.

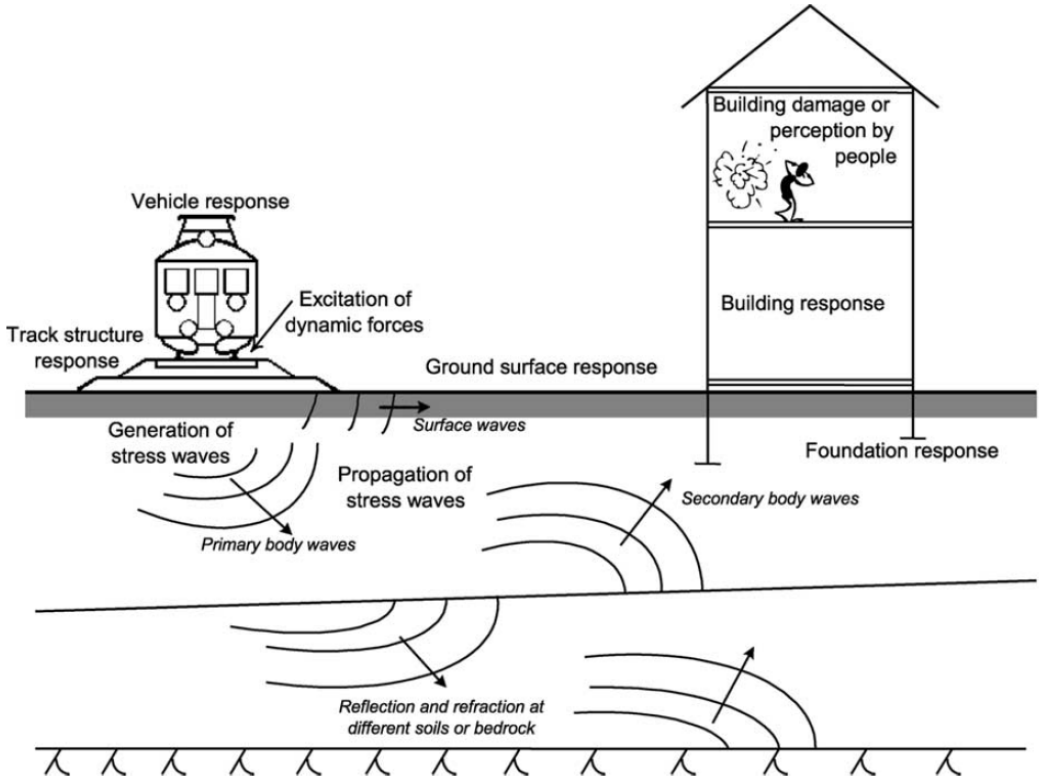

Figure 1.1: Generation, propagation and reception of vibrations (Hall, 2003)

With the improvement of computational performance, both in terms of memory and speed, the use of 3D models became possible. One of the first works that considered the three-dimensionality of the problem was performed by Krylov (Krylov and Ferguson, 1994; Krylov, 1994; Krylov, 1995). In their work, Krylov and his collaborators developed a model for surface trains where the forces transmitted to the ground through each sleeper are calculated analytically, and then, considering the sleepers as point sources, the field induced by each sleeper is combined, thus obtaining the response of the soil due to the passage of the train. Only the quasi-static component of the excitation is considered. The method for the calculation of the forces transmitted to the soil has been used by other researchers.

Conventional methods used for the analysis of three-dimensional problems, such as the FE method and the boundary element (BE) method, have also been employed to analyze the problem of induced vibrations. The FE method requires the discretization of the domain, which for 3D problems results in a large number of degrees of freedom and in sparse symmetric matrices. This method can be used to model irregular domains and, when applied in the time domain, can account for the non-linear behavior of materials. By itself, the classical FE method cannot simulate infinite domains, so special procedures need to be considered at the boundaries of the truncated domains in order to avoid fictitious reflections. Contrarily, the BE approach only requires the discretization of the boundary of the domain, thus resulting in less degrees of freedom, but, unlike the FE method, leads to full non-symmetric systems of equations. The BE method takes into account the radiation of waves towards infinity, but cannot account for non-linearities and requires the knowledge of the so called Green's functions (GF) or fundamental solutions. The hybrid FE-BE method combines the advantages of both approaches, being its use very attractive when the coupling between irregular domains and unbounded domains is required.

Regarding the FE approach, Hall (2003) used a time domain methodology and treated the reflections at the boundaries using dashpots. The considered mesh led to reasonable results only up to the frequency 10Hz and in the calculations only the quasi-static component of the excitation was considered. The results of the model showed a transient phenomenon that was not observed in real measurements and that was originated by the entrance of the loads in the model. However, this numerical phenomenon would have dissipated due to damping by the time that the waves reached the other extreme of the model, and so the results at that extreme were better. Using a model with 65 meters in the longitudinal direction, good results were limited to the near field. To obtain better results farther from the track, longer models would be needed, which would render the mesh impractical for calculation. The same author compared the results obtained with 3D models with those obtained with simpler 2D models and concluded that the 2D models could be used to study certain effects of traffic induced vibrations but not to obtain good predictions of the induced levels of vibrations (Hall, 2000).

In another work using the FE approach, Ekevid and Wiberg (2002) followed a similar approach but instead of treating the boundaries of the mesh with dashpots, these authors used the scaled boundary finite element method (Wolf, 2003). Even though the proposed methodology accounted for the radiation of waves to infinity, the fact of using a 3D mesh required a very large computational effort.

Also following the FE approach, Ju used a 3D formulation to simulate soil vibrations due to a high-speed train crossing a bridge and to study the efficiency of trenches (Ju, 2002) and of soil improvement (Ju, 2004) as countermeasures. The boundaries were treated with first-order absorbing boundaries and the systems of equations were solved using the preconditioned conjugate gradients method, i.e., an iterative method. The calculation time of the problem was over one week.

As for the BE and hybrid FE-BE approaches, Bode et al. (2002) used the BE method to model the soil and the FE method to model the sleepers and the rails (dos Santos, 2013). The methodology was formulated in the time domain and was used to determine the vibrations in the free-field and to study the influence of the soil-sleeper coupling scheme. The GF considered for the soil were the half-space Green's functions, thus limiting its discretization to the regions interacting with the sleepers. A similar strategy was followed by O'Brien and Rizos (2005), but instead of using half-space GF, they used full-space GF, which demanded

the additional discretization of the free surface of the soil and, consequently, increased the number of degrees of freedom.

In his PhD thesis, Galvín used an iterative scheme to couple the FE and BE methods and evaluated the response of structures near the railway track (Galvín, 2007). To account for the train excitation, he considered the forces transmitted by the sleepers to the soil or ballast as given by Krylov, and so only the quasi-static component of the excitation is included.

Auersch (1994) presented a model for surface trains based on transfer functions of point loads that could be either determined experimentally or calculated numerically. The train was simulated by a chain of point loads representing the axles, and for each axle a force function was assumed with the intent of simulating the dynamic forces of the train. Later, the work was extended and the FE method was combined with the BE method in order to include the train-track-soil interaction and to consider the irregularities of the vehicle/track system and the discrete sleeper support (Auersch, 2005).

In more recent years, approaches that take advantage of the invariance or periodicity of the geometry in the longitudinal direction were developed. Some authors consider that the geometry is invariant in the longitudinal direction, and after performing a Fourier transform of the field of variables in that direction, they reduce the three-dimensional problem to a series of two-dimensional problems. The transformed problems are solved in the wavenumber-frequency domain, which is termed 2.5D domain. Other authors consider that the problem is periodic in the longitudinal direction and after performing a Floquet transform of the field of variables in that direction, they reduce the geometry of the problem to a reference cell. Even though these two approaches, by themselves, cannot be used to predict the vibrations inside buildings (buildings are not invariant nor repeat themselves till infinite), they can be used to determine the wave fields that reach the buildings. Those wave fields can later be employed in the calculation of the response of the buildings. This is the approach followed by François, who obtains the response of buildings submitted to an incoming wave field using a FE-BE method in the time domain and considering the non-linear behavior of materials (François et al., 2006; François, 2008), and by Fiala et al. (2007), who use instead a frequency domain approach.

The following group of works assumed invariant geometries and used the 2.5D approach.

Dieterman and Metrikine (1996) coupled a beam and a half-space to model the track-soil interaction problem. They assumed smooth contact between the beam and the soil (no transmission of shear stresses) and assumed a uniform distribution of normal stresses between the beam and the half-space over the width of the beam. The model was used to determine the critical velocities of moving loads on the track-soil system. The authors concluded that there were two critical velocities: one that corresponds to the Rayleigh wave velocity and the other being slightly smaller. Both velocities resulted in severe amplifications of the beam displacements. Metrikine and Popp (2000) solved the same problem considering a visco-elastic layer instead of a half-space. They concluded that the critical speed of the moving load was close to the Rayleigh velocity of the layer and that it decreased slightly with the depth of the layer. The critical velocity of harmonic loads was treated by Dieterman and Metrikine (1997). These authors simulated the ballast using an elastic layer and determined the speed of the harmonic load that caused resonance of the system as a function of the thickness of the layer and of the frequency of the load. They concluded that resonance occurred when the velocity of the load was equal to the group velocity of the waves generated by the load. In the work by Steenbergen and Metrikine (2007), the validity of the assumptions concerning the

contact between the beam and the soil is studied and the authors concluded that in general, as long as the wavelength is large compared with the width of the beam and as long as the moving load spectrum does not present high frequency components, the simplified assumptions succeed in obtaining the track response. However, in order to obtain the near field response to constant moving loads and the far field response to moving harmonic loads with high oscillating frequencies, the interface between the soil and the track must be adequately modeled.

In a similar line of investigation, Jones, Sheng and Petyt modeled the track as a layered beam (accounting for rail, railpads, sleepers and ballast) and the ground as a layered half-space, for which they used the transfer matrices derived by Haskell (1953) and Thomson (1950). The contact between the layered beam and the layered half-space follows the same assumptions as the work of Metrikine and collaborators. The model can account for fixed harmonic loads (Sheng et al., 1999a) and moving loads with constant or oscillating amplitude (Sheng et al., 1999b; Jones et al., 2000). Together with the forces transmitted by the train to the track (Jones and Block, 1996; Sheng et al., 2004) these models can be efficiently used to simulate the vibrations induced by the circulation of surface trains at variable speed, accounting both for the quasi-static and the dynamic components of the excitation. In the work by Sheng et al. (2003) this model is validated against the results of experimental measurements, and later it is used to study the influence of the track stiffness and the layered soil properties (Sheng et al., 2004).

Still considering a beam resting on a layered half-space, Lombaert et al. (2000) developed a numerical model for road traffic induced vibrations. The road is modeled with a beam, the ground is modeled using the boundary element method, and the contact between the two sub-structures is assumed to be smooth. Since the tyres are much more flexible than the track-soil system, the vehicle-track interaction is uncoupled from the rest of the problem and the dynamic component of the excitation is calculated by simply submitting the vehicle to an irregular profile. The methodology is validated by means of field tests in the works of Lombaert and Degrande (2001, 2003) and used by Lombaert et al. (2001) to study the influence of the soil stratification. Clouteau et al. (2001) extended the methodology to the case of rail traffic and used it to exemplify the dynamic behavior of concrete slab tracks, to study resilient materials under the rail and slab, and to study the influence of the soil stratification. This last model was validated against experimental results (Lombaert et al., 2006a) and used to study the behavior of floating slabs as control measure for ground borne vibrations (Lombaert et al., 2006b). The model was also used to study the influence of the quasi-static and dynamic components of the excitation (Lombaert and Degrande, 2009).

Also with respect to surface trains, Karlstrom and Bostrom (2006) developed a semi-analytical model in which the ground is modeled as a visco-elastic layered half-space, the embankment and ballast with a rectangular layer, the sleepers by means of an anisotropic Kirchhoff plate, and the rails with Euler-Bernoulli beams. A simplification is considered at the lateral surfaces of the embankment, where it is assumed that the tangential stresses and the normal displacements are null. The results obtained with the model proposed by the authors were compared with the results obtained with finite element models, and it was concluded that the simplification provided good results as long as the load was vertical. The model was used to study the effect of the acceleration and deceleration of trains (Karlstrom, 2006), and it was concluded that the differences in terms of the vertical displacements between a train moving at constant speed and a train accelerating or decelerating were very small. In the longitudinal direction, however, large differences could be observed. These works were further extended

in order to account for the presence of water in the ground (poroelasticity) and to study the effect of trenches in the isolation of vibrations (Cao et al., 2012).

As final example concerning surface trains, Alves Costa (2011) used 2.5D finite/infinite elements to simulate the Leedsgard case taking into account the large deformations that may exist due to the poor quality of the soil. With that purpose, he simulated the non-linear behavior of the soil under the track by considering equivalent elastic parameters that depended on the deformation level of the finite elements (Alves Costa et al., 2010). Additionally, he also used a 2.5D coupled FE-BE model to simulate the vibrations induced by the passage of trains in the Portuguese railway system (Alves Costa et al., 2012a). This last model was also used to study the strategy for modeling the train (Alves Costa et al., 2012b), and to study ballast mats as mitigation measures (Alves Costa et al., 2012c). From these two works it is concluded that train models can be reduced to axles, bogies and primary suspension systems, and that ballast mats perform better when placed beneath the subballast layer, and not as well when placed between ballast and subballast layers.

Regarding tunnels, Forrest and Hunt (2006b) developed a model that assumes a tunnel with a cylindrical shape surrounded by a soil of infinite extent. Since the soil is treated by means of wave equations of an elastic continuum, no free surface is considered and consequently no surface waves are excited. In the far field, it is likely that buildings receive more energy from such waves than from body waves. Nonetheless, the model can be very effective in the evaluation of the response near the tunnel, where surface waves have much less influence. The model was also extended to account for tracks and then was used to assess the behavior of floating slab tracks (Forrest and Hunt, 2006a). The authors concluded that floating slabs yielded modest insertion losses and that under certain conditions they could even increase the transmission of vibrations. In the work by Hussein and Hunt (2007), the model was further extended to account for tangential forces at the tunnel walls, and in the work by Hussein et al. (2008) it was improved in order to permit the analysis of tunnels embedded in layered half-spaces. For that purpose, the authors assume that at a first step, the near field displacements are controlled by the dynamics of the tunnel and of the surrounding layer, i.e., they neglect the contribution of the other layers. At a second step, the response of the far field is calculated using the tractions calculated during the first step and assuming the proper stratification of the soil.

Yang et al. (2003) approached the problem using finite/infinite elements formulated in the wavenumber-frequency domain (Yang and Hung, 2001). When compared with the 2.5D models mentioned so far, this approach has the advantage of considering the transverse stiffness of the track and of allowing more complex geometries both for track and soil. However, it may become less attractive because the number of dofs increases significantly. The authors used the developed methodology to study the stiffness, damping and stratification of the underlying soil, and concluded that increasing the stiffness results in the decrease of vibration levels, that increasing the damping results in a decrease of vibration levels only if the loads move faster than the Rayleigh wave velocity of the soil, and that the soil stratification is extremely relevant owing to the fact that the cut-off frequencies depend on the layers depths and because no waves can propagate below the first cut-off frequency.

Also regarding tunnels, Rieckh et al. (2012) developed an invariant model in which the anisotropy of the soil is considered. The model is based on a boundary element formulation, and uses the 2.5D fundamental solutions of layered and anisotropic media, which are calculated with the method of potentials.

To conclude the discussion on invariant models, it must be mentioned that hybrid FE-BE methods formulated in the 2.5D domain can also be used (Sheng et al., 2006; Galvín et al., 2010; Galvín et al., 2010). These hybrid approaches are more efficient and more versatile than the predictions that simply rely on one of these methods.

In what concerns periodic models, they differ from the invariant models inasmuch as they can account for geometric features that repeat themselves through the longitudinal direction. For the case of railway tracks, the periodicity can account for the discrete sleeper support or for discontinuous slab tracks (Clouteau et al., 2005; Chebli et al., 2006; Sheng et al., 2005; Gupta et al., 2007; Gupta et al., 2008). Vostroukhov and Metrikine (2003) compared the results from periodic models with results from equivalent invariant models and concluded that the results were very similar. In this last study, only the quasi-static component of the excitation was considered.

To complete the discussion on prediction models, one must add that in recent years new approaches denominated by meshless methods (or mesh-free methods) were proposed and shown to be a promising alternative to the boundary element and finite element methods. The name meshless is given because these methods do not require the discretization neither of the interior nor of the boundary of the domain of interest. Within this family of methods, a popular approach is the Method of Fundamental Solutions (MFS), which resembles the BE method in the sense that it requires the availability of the fundamental solutions, but overcomes the need for evaluating the boundary integral, thus avoiding complications associated with the singularities of the fundamental solutions. Researchers from University of Coimbra have successfully applied the MFS in acoustic problems (Godinho et al., 2012; Soares et al., 2012) and in some elastodynamic problems (Godinho et al., 2013; Godinho et al., 2009), reporting encouraging results. The main drawbacks of these methods are their high computational cost (mostly when weak form formulations are considered) and, in some cases, their lack of stability (mostly when strong form formulations are considered) (Godinho and Soares Jr, 2013).

1.2.3 Countermeasures

The control of vibrations induced by moving vehicles can accompany all three stages of the phenomenon: the generation stage, the propagation stage and the reception stage. Hemsworth (2000) considers that the most effective and economical measures are those performed on the track, i.e., during the generation stage. For the rail traffic case, in order to control vibrations at the source, the following techniques are available: precision straightened rail, rail grinding, wheel truing, continuous welded rail, soft direct fixation fasteners, resilient materials under rails and sleepers, ballast, mats and floating slabs (Nelson, 1996; Hemsworth, 2000; Thompson, 2008). Rail straightening, rail grinding and wheel truing are maintenance works that improve the quality of circulation of the vehicle and consequently reduce the dynamic component of the excitation. It is evident that the weight, speed and damping systems of the vehicle also influence its dynamic behavior, so controlling these parameters also controls the induced vibration levels. The use of continuous welded rails avoids the impact forces that occur when a wheel passes a joint, thus reducing the vibrations. Regarding the use of soft fasteners, resilient materials, ballast mats and floating slabs, the objective is to absorb and attenuate the vibrations within the track, before they are transmitted to the ground. The softer the material, the more efficient is the isolation. However, the resiliency of the materials is limited by restrictions related to the safe operation of the vehicle. For this reason, the materials must be stiff enough so that large deflections do not occur. Floating slab tracks are

widely used, namely in subway lines that pass under urban areas. Several studies and measurements confirm that when compared with fixed slab tracks, the use of floating slab tracks is successful in reducing the vibrations at frequencies above the resonance of the track system (around 20Hz) (Grootenhuis, 1977; Wilson et al., 1983; Cui and Chew, 2000).

For the control of vibrations during the propagation stage, the most commonly used measures are soil improvement and wave barriers, such as trenches and wave impeding blocks (WIB). The objective of soil improvement is to make it stiffer and consequently to reduce its level of vibration. This technique was studied both experimentally and numerically by Taniguchi and Okada (1981) and Al-Hunaidi and Rainer (1991a; 1991b). Hildebrand (2004) confirms that this technique is successful for low frequencies, though the author warns that it produces amplifications in some audible bands and can give rise to perceptible sound in buildings near the track.

On the other hand, the objective of wave barriers is to reflect part of the waves that impinge on them. As a result, the part of the wave that is transmitted through the barrier carries less energy and consequently the vibration levels behind the barrier are reduced. Trenches are efficient in reducing the vibrations originated by surface waves. According to Hubert et al. (2001), trenches close to the track can provide a considerable reduction in the vibration levels, namely in urban areas, where distances between buildings and tracks are too short to provide sufficient radiation damping. Several authors compared the efficiency of open trenches and in-filled trenches and concluded that the former are more effective than the latter (Beskos et al., 1986; Dasgupta et al., 1990; Yang and Hung, 1997). However, the execution of open trenches is more complicated than the execution of in-filled trenches. With respect to the dimension of the trenches, for the case of open trenches only the depth is relevant, while for the case of in-filled trenches both the depth and width are relevant. Ahmad and Al-Hussaini (1991) derived expressions that can be used as guide lines to design trenches. In order for the trench to be effective its dimensions must be in the order of the length of the Rayleigh wave, and so trenches are only efficient in the isolation of high frequency vibrations (Hung et al., 2004).

WIBs are intended to simulate rigid frontiers, so that waves are reflected. WIBs can be constructed under the buildings, in order to shield them from vibrations coming from below, or under the railway track, simulating the presence of a bedrock (Hung and Yang, 2001). Takemiya (2003) studied numerically the reduction of vibrations due to the use of WIBs and concluded that the stiffening effects obtained by the installation of WIBs in soft layers could lead to a shift of the response from large and dynamic to small and quasi-static.

Finally, at the reception stage, countermeasures are applied in the building. The measures can be applied at the foundation level, isolating the whole building from the soil, or at certain parts of the building. Both approaches were studied by Fiala et al. (2007), who considered three different options to mitigate the vibrations induced by the passage of high-speed trains in a room: base-isolation (at the foundation), floating-floor and room-in-room (compartiment measures).

As last comment concerning countermeasures, at the moment there is an undergoing European Project named RIVAS (Railway Induced Vibration Abatement Solutions - http://www.rivas-project.eu) whose objective is to reduce the environmental impact of ground-borne vibrations while safeguarding the commercial competitiveness of the railway sector. The areas of research of this project include the mitigation at the source, at the track and at the propagation path.

1.3 Objectives and original contributions of the present work

The main objective of this thesis is to develop a numerical tool capable of predicting the vibrations induced by moving vehicles in nearby buildings. The tool must account for all stages of the problem, i.e., generation, propagation and reception stages, and must consider possible countermeasures, whether they are applied at the source, at the receiver, or at the propagation path. The purpose of the numerical tool is to provide the research group with a framework for investigations, which at the beginning of the PhD activities was not available. It is a fact that there is extensive knowledge in the scientific community addressing numerical models for the current problem, but it is also a fact that most of the advances and approaches reported in the previous section are not readily available to other researchers. Furthermore, their use is so complex that, by itself, a new implementation justifies a doctoral work.

In addition to the lack of a numerical tool within the research group, the existing tools that are based on 2.5D BEM formulations require the calculation of the fundamental solutions and their integration on the boundary elements, which represents a highly difficult task, namely if layered domains are considered. Thus, another objective of the present work is to make the developed tools more attractive in the user's perspective, which is accomplished by using the thin-layer method (TLM). With this approach, it is not needed to define wavenumber samples, which for an inexperienced user may be problematic. Instead, the layered domain is discretized into thinner layers, a task that is far simpler, especially if the user is familiar with any finite element software. The TLM is in fact the subject where the major original contributions of the work are included. The original contributions are:

- Development of the expressions for the calculation of the fundamental solutions in the 2.5D domain with the thin-layer method;
- The coupling between the TLM and perfectly matched layers (PML), with the intention of simulating half-spaces (this new procedure outperforms largely the previous strategy, the paraxial boundaries);
- Development of a 2.5D BEM procedure fully based on the TLM fundamental solutions and that avoids the numerical evaluation of boundary integrals.

Of course, the developed tool must also be regarded as a contribution, as it corresponds to a collection of several mathematical procedures of considerable complexity that is made available and ready to use: the 2.5D BEM-FEM procedure is implemented in the finite element software FEMIX, while the 3D BEM-FEM procedure is implemented in MATLAB.

The last objective of the thesis is the application of the developed numerical tool in the analysis of countermeasures for the abatement of vibrations induced by rail traffic. That is accomplished through the study of trench solutions, thus contributing to a better comprehension of the behavior of this type of measure.

1.4 Organization of the document

The thesis is divided into 6 chapters. The first and present chapter describes the problem to be studied, makes reference to previous works on the subject, and defines the main objectives of the work.

Chapter 2 addresses the propagation of waves through the soil. The thin-layer method is described and extended to the 2.5D domain, and perfectly matched layers are combined with thin-layers in order to simulate half-spaces.

In chapter 3, the numerical tools to solve soil-structure interaction problems are discussed. The 3D BEM-FEM algorithm is used to simulate the reception stage, in which an incoming wave field reaches a nearby building causing it to respond dynamically. The 2.5D BEM-FEM procedure is used to simulate the propagation stage (and part of the reception stage). The 3D formulation is described first because the common reader is more likely to be familiar with this type of problems. The less intuitive 2.5D formulation is presented afterwards. The fundamental solutions used to nurture the BEM in both 3D and 2.5D domains are obtained with the TLM, and therefore the connection between the BEM and TLM procedures is also established in this chapter.

Chapter 4 deals with the response of structures subjected to moving loads and moving vehicles. The solution of the train-track interaction problem is presented, which corresponds to the missing stage of the problem, i.e., the reception stage. By now, the reader must be wondering why the propagation stage is being addressed before the generation stage, which is in opposition to the natural order of events. This switch in the explanation of events is chosen because the train-track interaction solution procedure requires the knowledge of the 2.5D transfer functions of the track-ground system, which are calculated with the 2.5D BEM-FEM procedure (i.e., the propagation stage). An example is shown in which the link between all stages of the problem is carefully explained.

As an application of the tools described in chapters 2-4, in chapter 5 trenches are studied as a mitigation solution. The chapter is subdivided into 4 sections: in the first section, a parametric study of trenches is performed; in the second section, the case of study is described; in the third section, the reduction of vibrations on the soil surface is investigated; and in the last section, the effect of trenches on nearby buildings is addressed.

In chapter 6, conclusions and recommendations for further research are presented.

2. Wave propagation in the soil: fundamental solutions

2.1 Introduction

Soil is a discontinuous medium, whose porous may be partially filled with water. When loaded, it generally presents non-linear and anisotropic behavior. Nevertheless, for the case of traffic induced vibrations, the level of distortion induced in the ground is small and thus its behavior can be idealized as linear and elastic (Galvín, 2007). Moreover, according to Biot (Biot, 1956a; Biot, 1956b), when the frequencies of excitation are smaller than a characteristic frequency (inversely proportional to the permeability of the poroelastic medium), the relative movements between the liquid phase and the solid phase of the soil can be neglected, and so the soil can be idealized as a single-phased medium. For that reason, in this work the soil is handled as a linear viscoelastic solid, assumption that is also followed in several other works (Galvín, 2007; Lombaert, 2001).

Soil connects the track or the road to the nearby buildings and consequently its dynamic behavior plays an important role in the phenomenon of traffic induced vibrations. In that sense, to know the response of any point in the soil elicited by a dynamic source at some arbitrary location is a powerful tool. These expressions that relate the response of a receiver with a source located anywhere in a solid are called Fundamental Solutions (Kausel, 2010). These solutions have been subject of study during the XXth century and are the essential key to the Boundary Element Method (BEM), which is described in chapter 3.

Closed form expressions for the fundamental solutions of some particular cases, namely the homogeneous isotropic full-space and the homogeneous isotropic half-space, have been derived by some researchers. Concerning the full-space, expressions for both point (3D) and line (2D) sources were derived in the mid XIXth century by Sir William Thomson (Lord Kelvin) and by Sir George Gabriel Stokes for static and dynamic loads, respectively (Kausel, 2010). More recently, Tadeu and Kausel (2000) derived the fundamental solutions for line sources with sinusoidal variation in space and time (i.e., 2.5D solutions). Regarding the dynamic response of half-spaces, one of the leading works was performed by Lamb (1904). In his work, Lamb fails to obtain closed form expressions for the displacements of the half-space, but obtains an approximation of the displacements in the far field by considering only the contribution of the Rayleigh waves, whose discovery is due to Lord Rayleigh two decades earlier (Rayleigh, 1885). Closed form expressions for the surface displacements of half-spaces (limited to the Poisson's ratio $\nu = 0.25$) were obtained a half century after the work of Lamb by Pekeris (1955) and Chao (1960), for vertical and horizontal point loads, respectively. Mooney (1974) extended the work of Pekeris to account for arbitrary Poisson's ratios, but for the horizontal displacements the author only succeeded in obtaining closed form expressions for Poisson's ratios smaller than $\nu = 0.263$. All the previously referred to closed form expressions are compiled in the book by Kausel (2006). More recently, Kausel (2012) continued the work of the previous authors and generalized the analytical solutions for arbitrary Poisson's ratios and for any direction of load and displacements, thus concluding the work started by Lamb more than one century ago.

The four works referred to above were developed based on the Cargniard-de Hoop technique (De Hoop, 1960), which allows the direct evaluation of the double integral needed to transform the displacements from the wavenumber-frequency domain to the space-time domain. Interestingly, the direct evaluation of only one of these integrals is not possible and so closed form expressions of the fundamental solutions of half-spaces exist only in the space-time domain. Such is so because when using contour integration to evaluate the improper integrals to transform the displacements from the wavenumber to the space domain (Erigen and Suhubi, 1975) or from the frequency to the time domain (Park and Kausel, 2004a), some branch integrals are obtained and these cannot be solved analytically.

For the case of layered domains or sources/receivers inside homogeneous half-spaces, no closed form expressions are available and therefore it is needed to resort to numerical tools to determine the corresponding fundamental solutions. The most commonly used tools are based on integral transformation techniques, in which the fields of displacements are transformed to the wavenumber-frequency domain and consequently the wave equations are solved in that transformed domain. When necessary, the displacements can subsequently be transformed back to the space domain and/or time domain through the numerical evaluation of the integrals that result from the inverse transformations.

In the transformed domain, the solutions can be found using the transfer matrices derived by Thomson (1950) and corrected by Haskell (1953), using the stiffness matrices derived by Kausel and Roesset (1981), using the method of Potentials (Tadeu et al., 2001; Tadeu and Antonio, 2001; Tadeu and António, 2002) or using the Thin-Layer Method (TLM) (Kausel and Peek, 1982). The first three approaches handle the propagation of waves within each layer without any approximation. In opposition, the TLM approach is based on discretizations of the domain in the vertical direction and in approximations of displacements within the layers by means of the interpolation functions. Its advantage over the other three approaches is that it enables the analytical evaluation of at least one inverse transformation. As a drawback, it requires the solution of two eigenvalue problems. In this work, the TLM is adopted for the calculation of the fundamental solutions of layered soils, being the procedure and its 2.5D formulation presented in this chapter.

2.2 Thin-Layer Method in Cartesian coordinates

The TLM was introduced in the seventies (Lysmer, 1970; Lysmer and Waas, 1972; Waas, 1972) and since then it has found use in several areas related to wave propagation in layered media and in soil-structure interaction problems. The TLM is a semi-discrete numerical technique used for the analysis of wave motion in layered media, and consists in a finite element discretization in the direction of layering (for the case of soil, the vertical direction) combined with analytical solutions for the remaining directions, along which the material properties are assumed to be constant. A brief historical description of the method can be found in Park (2002). With respect to wave fields induced by moving loads or vehicles, the TLM is used in the works by Hanazato et al. (1991), Jones and Hunt (2011, 2012) and Celebi and Schmid (2005). In the first three references, the TLM is used in the context of transmitting boundaries (Kausel, 1988) or super-elements (Tassoulas and Kausel, 1981).

For the presentation of the TLM, the wave equation is first expressed in matrix notation and is then discretized in the vertical direction. These steps follow the works from Park (2002) and Barbosa and Kausel (2012).

One note before starting: cross-anisotropic materials are more general than isotropic materials since they can reproduce different behaviors of the medium when loaded in different directions. For the case of the soil response, this is an important aspect because the layers are formed by vertical sedimentation of particles and therefore they present different mechanical characteristics in the vertical and horizontal directions. The drawback of considering cross-anisotropic materials is that they require the quantification of more elastic constants, thus requiring more experiments in order to obtain the corresponding parameters. The constitutive matrix $\mathbf{D}$ of a cross-anisotropic material is the positive definite matrix defined by

$$\mathbf{D}=\begin{bmatrix} \lambda+2G & \lambda & \lambda_t & 0 & 0 & 0 \\ \lambda & \lambda+2G & \lambda_t & 0 & 0 & 0 \\ \lambda_t & \lambda_t & D_t & 0 & 0 & 0 \\ 0 & 0 & 0 & G_t & 0 & 0 \\ 0 & 0 & 0 & 0 & G_t & 0 \\ 0 & 0 & 0 & 0 & 0 & G \end{bmatrix} \qquad \begin{matrix} G>0 \\ G_t>0 \\ \lambda+G>0 \\ (\lambda+G)D_t>\lambda_t^2 \end{matrix} \tag{2.1}$$

where λ and G are the Lamé constants in the isotropic plane (horizontal planes) and λ_t, G_t, D_t are the Lamé constants and the constrained modulus in the transverse direction (vertical direction). When $\lambda_t=\lambda$, $G_t=G$ and $D_t=\lambda+2G$, the material reduces to an isotropic one. With the intention of being more general, the following formulation considers cross-anisotropic materials.

Consider a horizontally homogeneous and vertically stratified cross-anisotropic elastic medium of infinite lateral extent and characterized by the depth dependent mass density ρ and the depth dependent constitutive matrix $\mathbf{D}=\{d_{ij}\}$ $(i,j=1,...,6)$ as defined in equation (2.1). Assume that the medium is subjected to an arbitrary dynamic load $\mathbf{b}$ placed at some location. With dots denoting partial derivatives with respect to time, the dynamic equilibrium equation at any point can be written compactly in matrix format as

$$\rho\ddot{\mathbf{u}}-\mathbf{L}^{\mathrm{T}}\boldsymbol{\sigma}=\mathbf{b} \tag{2.2}$$

where the displacement vector $\mathbf{u}$, the stress vector $\boldsymbol{\sigma}$ and the differential operator $\mathbf{L}$ are defined as

$$\mathbf{u}^{\mathrm{T}}=\begin{bmatrix} u_x & u_y & u_z \end{bmatrix} \tag{2.3}$$

$$\boldsymbol{\sigma}^{\mathrm{T}}=\begin{bmatrix} \sigma_{xx} & \sigma_{yy} & \sigma_{zz} & \sigma_{yz} & \sigma_{xz} & \sigma_{xy} \end{bmatrix} \tag{2.4}$$

$$\mathbf{L}^{\mathrm{T}}=\begin{bmatrix} \dfrac{\partial}{\partial x} & 0 & 0 & 0 & \dfrac{\partial}{\partial z} & \dfrac{\partial}{\partial y} \\ 0 & \dfrac{\partial}{\partial y} & 0 & \dfrac{\partial}{\partial z} & 0 & \dfrac{\partial}{\partial x} \\ 0 & 0 & \dfrac{\partial}{\partial z} & \dfrac{\partial}{\partial y} & \dfrac{\partial}{\partial x} & 0 \end{bmatrix} \tag{2.5}$$

Additionally, consider the stress-strain and strain-displacement relations

$$\boldsymbol{\sigma}=\mathbf{D}\boldsymbol{\varepsilon} \tag{2.6}$$

$$\boldsymbol{\varepsilon} = \mathbf{L}\mathbf{u} \tag{2.7}$$

$$\boldsymbol{\varepsilon}^{\mathrm{T}} = \begin{bmatrix} \varepsilon_{xx} & \varepsilon_{yy} & \varepsilon_{zz} & \varepsilon_{yz} & \varepsilon_{xz} & \varepsilon_{xy} \end{bmatrix} \tag{2.8}$$

The substitution of equations (2.6) and (2.7) in equation (2.2) results in the elastic wave equation (in the 3-D space)

$$\rho\ddot{\mathbf{u}} - \mathbf{L}^{\mathrm{T}}\mathbf{D}\mathbf{L}\mathbf{u} = \mathbf{b} \tag{2.9}$$

The differential operator $\mathbf{L}$ can be expressed as

$$\mathbf{L} = \mathbf{L}_x \frac{\partial}{\partial x} + \mathbf{L}_y \frac{\partial}{\partial y} + \mathbf{L}_z \frac{\partial}{\partial z} \tag{2.10}$$

where the matrices $\mathbf{L}_x$, $\mathbf{L}_y$ and $\mathbf{L}_z$ are

$$\mathbf{L}_x = \begin{bmatrix} 1 & 0 & 0 \\ 0 & 0 & 0 \\ 0 & 0 & 0 \\ 0 & 0 & 0 \\ 0 & 0 & 1 \\ 0 & 1 & 0 \end{bmatrix} \qquad \mathbf{L}_y = \begin{bmatrix} 0 & 0 & 0 \\ 0 & 1 & 0 \\ 0 & 0 & 0 \\ 0 & 0 & 1 \\ 0 & 0 & 0 \\ 1 & 0 & 0 \end{bmatrix} \qquad \mathbf{L}_z = \begin{bmatrix} 0 & 0 & 0 \\ 0 & 0 & 0 \\ 0 & 0 & 1 \\ 0 & 1 & 0 \\ 1 & 0 & 0 \\ 0 & 0 & 0 \end{bmatrix} \tag{2.11}$$

Since the domain under study consists of homogeneous horizontal layers, the material properties are piecewise constant with depth and invariant in the horizontal directions leading to $\partial\mathbf{D}/\partial_\alpha = 0$ $(\alpha = x, y, z)$. Thus, the term $\mathbf{L}^{\mathrm{T}}\mathbf{D}\mathbf{L}$ in equation (2.9) can be expanded to

$$\begin{aligned} \mathbf{L}^{\mathrm{T}}\mathbf{D}\mathbf{L} = \mathbf{D}_{xx}\frac{\partial^2}{\partial x^2} + \left(\mathbf{D}_{xy} + \mathbf{D}_{yx}\right)\frac{\partial^2}{\partial x \partial y} + \left(\mathbf{D}_{xz} + \mathbf{D}_{zx}\right)\frac{\partial^2}{\partial x \partial z} + \\ + \mathbf{D}_{yy}\frac{\partial^2}{\partial y^2} + \left(\mathbf{D}_{yz} + \mathbf{D}_{zy}\right)\frac{\partial^2}{\partial y \partial z} + \mathbf{D}_{zz}\frac{\partial^2}{\partial z^2} \end{aligned} \tag{2.12}$$

being the material matrices $\mathbf{D}_{\alpha\beta}$ defined by

$$\mathbf{D}_{\alpha\beta} = \mathbf{L}_\alpha^{\mathrm{T}}\,\mathbf{D}\,\mathbf{L}_\beta, \quad \alpha, \beta = x, y, z \tag{2.13}$$

and given in Appendix I.

Now, consider the internal stresses in horizontal planes, which are calculated by

$$\mathbf{s} = \begin{bmatrix} \sigma_{zx} & \sigma_{zy} & \sigma_{zz} \end{bmatrix}^{\mathrm{T}} = \mathbf{L}_z^{\mathrm{T}}\boldsymbol{\sigma} = \mathbf{L}_z^{\mathrm{T}}\mathbf{D}\mathbf{L}\mathbf{u} \tag{2.14}$$

If one removes any horizontal slice of the medium and treats it as a free body in space, the dynamic equilibrium dictates the need to balance the internal stresses at the now exposed upper and lower surfaces with the external tractions $\mathbf{t}$, i.e.,

$$\mathbf{t} = \begin{bmatrix} \mathbf{t}_u \\ \mathbf{t}_l \end{bmatrix} = \begin{bmatrix} \mathbf{s}_u \\ -\mathbf{s}_l \end{bmatrix} \tag{2.15}$$

where $\mathbf{t}_u$ and $\mathbf{t}_l$ are the external tractions applied at the upper and lower boundaries of the removed domain and $\mathbf{s}_u$ and $\mathbf{s}_l$ are the internal stresses at the same locations.

The first step for the formulation of the TLM is to discretize the domain in the vertical direction, i.e., to subdivide the medium into horizontal layers which are thin in the finite element sense, or in other words, which are small in comparison with the expected wavelengths and strain gradients. Thereafter, considering an arbitrary thin-layer as a free body in space (Figure 2.1), the displacements field inside the layer is approximated by means of interpolation functions, i.e.

$$\mathbf{u} = \mathbf{N}\mathbf{U} \tag{2.16}$$

where $\mathbf{U} = \mathbf{U}(x, y)$ is a vector containing the nodal displacements (the nodes represent horizontal surfaces)

$$\mathbf{U}^{\mathrm{T}} = \left[\mathbf{u}_1^{\mathrm{T}} \ \ldots \ \mathbf{u}_m^{\mathrm{T}}\right], \quad \mathbf{u}_j^{\mathrm{T}} = \left[u_{xj} \ u_{yj} \ u_{zj}\right], \quad j = 1, 2, \cdots, m \tag{2.17}$$

and $\mathbf{N} = \mathbf{N}(z)$ is an interpolation matrix of the form

$$\mathbf{N} = \left[N_1\mathbf{I} \ \ldots \ N_m\mathbf{I}\right] \tag{2.18}$$

with N_j being the interpolation functions, which depend on the vertical coordinate z, and with $\mathbf{I}$ being a 3×3 identity matrix. (The subscript m is the number of nodal surfaces in each thin-layer, and $m-1$ is the interpolation order. When $m > 2$, there exist inner surfaces that are equidistant from each other. For example, $m = 3$ corresponds to a quadratic interpolation with one internal nodal surface, as shown in Figure 2.1, which depicts one thin-layer as a free body in space, acted upon and dynamically equilibrated by appropriate tractions applied onto the nodal surfaces.)

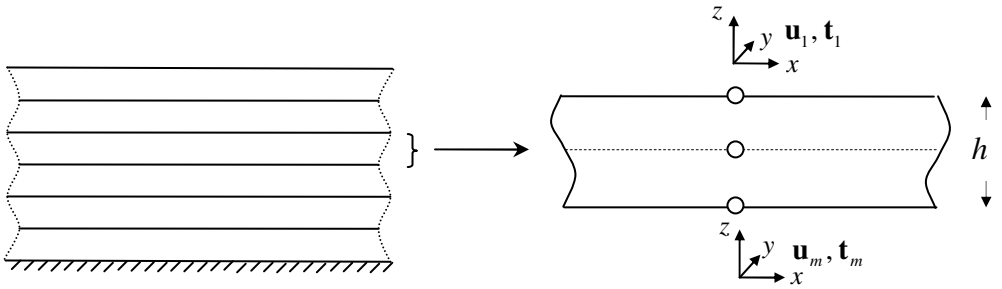

Figure 2.1: Discretization into thin-layers and thin-layer as a free body in space ($m = 3$).

When substituting the interpolation (2.16) into the wave equation (2.9) and boundary conditions (2.15), it can be verified that these equations are not satisfied exactly because the interpolation is only an approximation of the actual field. As a result, one finds unbalanced body forces $\mathbf{r}$ and boundary tractions $\mathbf{q}$ of the form

$$\mathbf{b} - \rho\ddot{\mathbf{u}} + \mathbf{L}^{\mathrm{T}}\mathbf{D}\mathbf{L}\mathbf{u} = \mathbf{r} \tag{2.19}$$

$$\begin{bmatrix}\mathbf{t}_1 \\ \mathbf{t}_m\end{bmatrix} - \begin{bmatrix}\mathbf{s}_1 \\ -\mathbf{s}_m\end{bmatrix} = \begin{bmatrix}\mathbf{q}_1 \\ \mathbf{q}_m\end{bmatrix} = \mathbf{q} \tag{2.20}$$

The discrete wave equation is obtained by applying the method of the weighted residuals and by requiring the virtual work done by the unbalanced forces within the thin-layer and on its bounding surfaces to be zero. This results in the discrete thin-layer equation

$$\mathbf{P} = \mathbf{M}\ddot{\mathbf{U}} - \mathbf{A}_{xx}\frac{\partial^2 \mathbf{U}}{\partial x^2} - \mathbf{A}_{xy}\frac{\partial^2 \mathbf{U}}{\partial x \partial y} - \mathbf{A}_{yy}\frac{\partial^2 \mathbf{U}}{\partial y^2} - \mathbf{B}_x\frac{\partial \mathbf{U}}{\partial x} - \mathbf{B}_y\frac{\partial \mathbf{U}}{\partial y} + \mathbf{G}\mathbf{U} \tag{2.21}$$

where the vector $\mathbf{P}$ contains the consistent external tractions at the interfaces of the thin-layer (which result from the external tractions $\mathbf{t}$ and the body loads $\mathbf{b}$). The thin-layer matrices $\mathbf{M}$, $\mathbf{A}_{\alpha\beta}$, $\mathbf{B}_\alpha$ and $\mathbf{G}$ are given by

$$\mathbf{M} = \int_0^h \rho\, \mathbf{N}^{\mathrm{T}}\mathbf{N}\, \mathrm{d}z \tag{2.22}$$

$$\mathbf{A}_{\alpha\alpha} = \int_0^h \mathbf{N}^{\mathrm{T}}\mathbf{D}_{\alpha\alpha}\mathbf{N}\mathrm{d}z, \qquad \alpha = x, y \tag{2.23}$$

$$\mathbf{A}_{xy} = \int_0^h \mathbf{N}^{\mathrm{T}}\left(\mathbf{D}_{xy} + \mathbf{D}_{yx}\right)\mathbf{N}\, \mathrm{d}z \tag{2.24}$$

$$\mathbf{B}_\alpha = \int_0^h \mathbf{N}^{\mathrm{T}}\mathbf{D}_{\alpha z}\mathbf{N}'\mathrm{d}z - \int_0^h \mathbf{N}'^{\mathrm{T}}\mathbf{D}_{z\alpha}\mathbf{N}\, \mathrm{d}z, \quad \alpha = x, y \tag{2.25}$$

$$\mathbf{G} = \int_0^h \mathbf{N}'^{\mathrm{T}}\mathbf{D}_{zz}\mathbf{N}'\, \mathrm{d}z \tag{2.26}$$

in which h is the thickness of the thin-layer and $\mathbf{N}' = \frac{\mathrm{d}}{\mathrm{d}z}\mathbf{N}$. Appendix I tabulates the above matrices for an individual thin-layer consisting of a cross-anisotropic material and considering both a linear and quadratic interpolation, i.e., $m = 2,3$, respectively.

After the individual matrices are overlapped in the usual finite element sense (i.e. layer by layer and in the natural top down order of the interfaces), one obtains a narrowly banded set of global system matrices and vectors which characterizes the complete stack of thin-layers. The resulting system of partial differential equations has the same form as equation (2.21), but its shape is now block-tridiagonal and has a correspondingly larger number of equations. In the remaining part of the present chapter, equation (2.21) refers to the complete assembly of thin-layers.

2.3 Displacements in the wavenumber-frequency domain

To solve the system of linear partial differential equations (2.21), the displacements $\mathbf{U}$ and tractions $\mathbf{P}$ are transformed from the space-time domain to the wavenumber-frequency domain by means of the triple Fourier transformations

$$\bar{\mathbf{U}}\left(k_x, k_y, \omega\right) = \int_{-\infty}^{+\infty}\int_{-\infty}^{+\infty}\int_{-\infty}^{+\infty} \mathbf{U}\left(x, y, t\right) \mathrm{e}^{-\mathrm{i}\left(\omega t - k_x x - k_y y\right)} \mathrm{d}x\, \mathrm{d}y\, \mathrm{d}t \tag{2.27}$$

$$\bar{\mathbf{P}}\left(k_x, k_y, \omega\right) = \int_{-\infty}^{\infty}\int_{-\infty}^{\infty}\int_{-\infty}^{\infty} \mathbf{P}\left(x, y, t\right) \mathrm{e}^{-\mathrm{i}\left(\omega t - k_x x - k_y y\right)} \mathrm{d}x\, \mathrm{d}y\, \mathrm{d}t \tag{2.28}$$

In the new domain, system (2.21) becomes

$$\bar{\mathbf{P}} = \left[k_x^2\mathbf{A}_{xx} + k_x k_y \mathbf{A}_{xy} + k_y^2\mathbf{A}_{yy} + \mathrm{i}\left(k_x\mathbf{B}_x + k_y\mathbf{B}_y\right) + \left(\mathbf{G} - \omega^2\mathbf{M}\right)\right]\bar{\mathbf{U}} \tag{2.29}$$

where $\mathrm{i}=\sqrt{-1}$. All matrices in this expression are symmetric, except for $\mathbf{B}_x$ and $\mathbf{B}_y$ which are skew-symmetric. Although this system could be easily solved for $\bar{\mathbf{U}}$, it is both possible and convenient to first change the system of equations into a fully symmetric form by means of a similarity transformation. This is accomplished by multiplying every third row of the system (2.29) by $-\mathrm{i}$ and every third column by i. This operation solely affects the vectors $\bar{\mathbf{P}}$ and $\bar{\mathbf{U}}$ and the matrices $\mathbf{B}_x$ and $\mathbf{B}_y$, leaving the other matrices unchanged. As a result of this transformation, the system of equations is now

$$\tilde{\mathbf{p}}=\left[k_x^2\mathbf{A}_{xx}+k_xk_y\mathbf{A}_{xy}+k_y^2\mathbf{A}_{yy}+k_x\tilde{\mathbf{B}}_x+k_y\tilde{\mathbf{B}}_y+\left(\mathbf{G}-\omega^2\mathbf{M}\right)\right]\tilde{\mathbf{u}} \tag{2.30}$$

where $\tilde{\mathbf{p}}$ and $\tilde{\mathbf{u}}$ are obtained from $\bar{\mathbf{P}}$ and $\bar{\mathbf{U}}$ by multiplying every third row by $-\mathrm{i}$. Also, $\tilde{\mathbf{B}}_x$ and $\tilde{\mathbf{B}}_y$ are obtained from $\mathbf{B}_x$ and $\mathbf{B}_y$ by reversing the sign of every third column [Note: in comparison with previous studies on the TLM (e.g. Kausel, 1986), in this work a reversed sign for the i factor is used for reasons of convenience]. After solving the system of equations (2.30), $\bar{\mathbf{U}}$ is recovered by multiplying every third row of $\tilde{\mathbf{u}}$ by i and the displacements in the space-time domain can be obtained —at least formally— from the triple inverse Fourier transform

$$\mathbf{U}(x,y,t)=\frac{1}{(2\pi)^3}\int_{-\infty}^{\infty}\int_{-\infty}^{\infty}\int_{-\infty}^{\infty}\bar{\mathbf{U}}(k_x,k_y,\omega)\,\mathrm{e}^{\mathrm{i}(\omega t-k_xx-k_yy)}\mathrm{d}k_x\,\mathrm{d}k_y\,\mathrm{d}\omega \tag{2.31}$$

The integrals in equation (2.31) can be evaluated numerically. However, by doing so the TLM loses its advantage over the integral transform techniques based on the transfer matrices or on the stiffness matrices, since these approaches, that also require the numerical evaluation of the inverse transformations, originate systems of equations of smaller size (usually, only the interfaces between the layers need to be discretized). In this way, a different procedure is followed, in which the displacement field is decomposed into a modal basis, similar to what is done in the modal superposition for linear dynamic analyses. As a result of this decomposition, the system of equations (2.30) can be diagonalized and that enables the evaluation in closed form expressions of at least one of the integrals of equation (2.31). If the integral to be evaluated is the outer integral, the fundamental solutions are obtained in the wavenumber-time domain (Kausel, 1994). If instead one changes the coordinates from Cartesian to cylindrical and evaluates the integral in the radial wavenumber, then the fundamental solutions are obtained in the space-frequency domain (Kausel and Peek, 1982; Kausel, 1981). Alternatively, if the inner integral of (2.31) is evaluated, then the fundamental solutions are obtained in a mixed space-wavenumber-frequency domain (2.5D domain), in which the plane-strain is the particular case $k_y=0$ (Barbosa and Kausel, 2012). In this work, in the propagation stage the geometry is assumed to be invariant and so the 2.5D fundamental solutions are of interest. On the other hand, in the reception stage the three-dimensionality of the problem has to be considered and so the cylindrical space-frequency domain solutions must be used.

In the ensuing, the system of equations (2.30) is transformed in order to obtain the displacements $\bar{\mathbf{U}}$ in the wavenumber-frequency domain through modal superposition. As a first step in that direction, the order of the degrees of freedom is rearranged, grouping first all horizontal-x, then all horizontal-y and finally all vertical-z degrees of freedom. This rearrangement is suggested solely to reveal the special structure possessed by the matrices in the system of equations (2.30) and the implications that the referred structures have on the

eigenvalue problems that are solved to find the modal basis. In practice, the degrees of freedom are ordered by interface and not by direction, which results in a reduction of the bandwidth of the matrices. Hence, after rearranging the degrees of freedom, the matrices ad vectors in system (2.30) attain the following structures

$$\mathbf{A}_{xx}=\begin{bmatrix}\mathbf{A}_x & \mathbf{O} & \mathbf{O}\\ \mathbf{O} & \mathbf{A}_y & \mathbf{O}\\ \mathbf{O} & \mathbf{O} & \mathbf{A}_z\end{bmatrix} \qquad \mathbf{A}_{yy}=\begin{bmatrix}\mathbf{A}_y & \mathbf{O} & \mathbf{O}\\ \mathbf{O} & \mathbf{A}_x & \mathbf{O}\\ \mathbf{O} & \mathbf{O} & \mathbf{A}_z\end{bmatrix}$$

$$\mathbf{A}_{xy}=\begin{bmatrix}\mathbf{O} & \mathbf{A}_x-\mathbf{A}_y & \mathbf{O}\\ \mathbf{A}_x-\mathbf{A}_y & \mathbf{O} & \mathbf{O}\\ \mathbf{O} & \mathbf{O} & \mathbf{O}\end{bmatrix} \qquad \tilde{\mathbf{B}}_x=\begin{bmatrix}\mathbf{O} & \mathbf{O} & \mathbf{B}_{xz}\\ \mathbf{O} & \mathbf{O} & \mathbf{O}\\ \mathbf{B}_{xz}^T & \mathbf{O} & \mathbf{O}\end{bmatrix}$$

$$\tilde{\mathbf{B}}_y=\begin{bmatrix}\mathbf{O} & \mathbf{O} & \mathbf{O}\\ \mathbf{O} & \mathbf{O} & \mathbf{B}_{yz}\\ \mathbf{O} & \mathbf{B}_{yz}^T & \mathbf{O}\end{bmatrix} \qquad \mathbf{G}=\begin{bmatrix}\mathbf{G}_x & \mathbf{O} & \mathbf{O}\\ \mathbf{O} & \mathbf{G}_y & \mathbf{O}\\ \mathbf{O} & \mathbf{O} & \mathbf{G}_z\end{bmatrix} \tag{2.32}$$

$$\mathbf{M}=\begin{bmatrix}\mathbf{M}_x & \mathbf{O} & \mathbf{O}\\ \mathbf{O} & \mathbf{M}_y & \mathbf{O}\\ \mathbf{O} & \mathbf{O} & \mathbf{M}_z\end{bmatrix} \qquad \tilde{\mathbf{u}}=\begin{bmatrix}\mathbf{u}_x\\ \mathbf{u}_y\\ -\mathrm{i}\,\mathbf{u}_z\end{bmatrix} \qquad \tilde{\mathbf{p}}=\begin{bmatrix}\mathbf{p}_x\\ \mathbf{p}_y\\ -\mathrm{i}\,\mathbf{p}_z\end{bmatrix}$$

where $\mathbf{O}$ is the null matrix, $\mathbf{G}_x \equiv \mathbf{G}_y$, $\mathbf{M}_x \equiv \mathbf{M}_y \equiv \mathbf{M}_z$, and $\mathbf{B}_{xz} \equiv \mathbf{B}_{yz}$. In addition, and except for the matrices $\mathbf{B}_{xz}$ and $\mathbf{B}_{yz}$, all sub-matrices are symmetric and block-tridiagonal.

Having rearranged the order of the degrees of freedom, it is now convenient to define the radial wavenumber k, the propagation angle ϑ, the transformation matrix $\mathbf{T}$, its inverse $\mathbf{T}^{-1}$ and the matrices $\mathbf{A}$ and $\mathbf{C}$ as

$$k=\sqrt{k_x^2+k_y^2} \qquad k_x=k\cos\vartheta \qquad k_y=k\sin\vartheta \tag{2.33}$$

$$\mathbf{T}=\begin{bmatrix}\mathbf{I}\cos\vartheta & \mathbf{I}\sin\vartheta & \mathbf{O}\\ -\mathbf{I}\sin\vartheta & \mathbf{I}\cos\vartheta & \mathbf{O}\\ \mathbf{O} & \mathbf{O} & k\mathbf{I}\end{bmatrix} \qquad \mathbf{T}^{-1}=\begin{bmatrix}\mathbf{I}\cos\vartheta & -\mathbf{I}\sin\vartheta & \mathbf{O}\\ \mathbf{I}\sin\vartheta & \mathbf{I}\cos\vartheta & \mathbf{O}\\ \mathbf{O} & \mathbf{O} & 1/k\mathbf{I}\end{bmatrix} \tag{2.34}$$

$$\mathbf{A}=\begin{bmatrix}\mathbf{A}_x & \mathbf{O} & \mathbf{O}\\ \mathbf{O} & \mathbf{A}_y & \mathbf{O}\\ \mathbf{B}_{xz}^{\mathrm{T}} & \mathbf{O} & \mathbf{A}_z\end{bmatrix} \qquad \mathbf{C}=\begin{bmatrix}\mathbf{G}_x-\omega^2\mathbf{M}_x & \mathbf{O} & \mathbf{B}_{xz}\\ \mathbf{O} & \mathbf{G}_y-\omega^2\mathbf{M}_y & \mathbf{O}\\ \mathbf{O} & \mathbf{O} & \mathbf{G}_z-\omega^2\mathbf{M}_z\end{bmatrix} \tag{2.35}$$

in which $\mathbf{I}$ is the identity matrix and $\mathbf{O}$ is a null matrix, both with the dimensions compatible with the submatrices in equation (2.32). By substituting each variable defined in equations (2.33)-(2.35) in the following equation, it can be shown that the system (2.30) is the same as

$$\tilde{\mathbf{p}}=\mathbf{T}^{-1}\left(k^2\mathbf{A}+\mathbf{C}\right)\mathbf{T}\tilde{\mathbf{u}} \tag{2.36}$$

or equivalently

$$\mathbf{T}\tilde{\mathbf{p}}=\left(k^2\mathbf{A}+\mathbf{C}\right)\mathbf{T}\tilde{\mathbf{u}} \tag{2.37}$$

The modal basis needed to decompose the displacements in a summation corresponds to the solution of the right eigenvalue problem in k_j and $\mathbf{r}_j$

$$\left(k_j^2\mathbf{A}+\mathbf{C}\right)\mathbf{r}_j=\mathbf{0} \tag{2.38}$$

Due to the structure of matrices $\mathbf{A}$ and $\mathbf{C}$, the eigenvalue problem (2.38) can be decoupled into two eigenvalue problems, one in the x and z directions (generalized Rayleigh problem) and the other in the y direction (generalized Love problem):

$$\begin{aligned}&\left\{k_{Rj}^2\begin{bmatrix}\mathbf{A}_x & \mathbf{O}\\ \mathbf{B}_{xz}^{\mathrm{T}} & \mathbf{A}_z\end{bmatrix}+\begin{bmatrix}\mathbf{G}_x-\omega^2\mathbf{M}_x & \mathbf{B}_{xz}\\ \mathbf{O} & \mathbf{G}_z-\omega^2\mathbf{M}_z\end{bmatrix}\right\}\begin{bmatrix}\boldsymbol{\phi}_{xj}\\ k_{Rj}\boldsymbol{\phi}_{zj}\end{bmatrix}=\mathbf{0}\\ &\left\{k_{Lj}^2\mathbf{A}_y+\left(\mathbf{G}_y-\omega^2\mathbf{M}_y\right)\right\}\boldsymbol{\phi}_{yj}=\mathbf{0}\end{aligned} \tag{2.39}$$

In this way, the right eigenvalue problem (2.38) has two sets of eigenpairs: one set associated with the eigenvalues k_{Rj} and right eigenvectors $\mathbf{r}_{Rj}^{\mathrm{T}}=\begin{bmatrix}\boldsymbol{\phi}_{xj}^{\mathrm{T}} & \mathbf{0} & k_{Rj}\boldsymbol{\phi}_{zj}^{\mathrm{T}}\end{bmatrix}$ and the other set associated with the eigenvalues k_{Lj} and right eigenvectors $\mathbf{r}_{Lj}^{\mathrm{T}}=\begin{bmatrix}\mathbf{0} & \boldsymbol{\phi}_{yj}^{\mathrm{T}} & \mathbf{0}\end{bmatrix}$.

Likewise, the left eigenvalue problem

$$\mathbf{l}_j^{\mathrm{T}}\left(k_j^2\mathbf{A}+\mathbf{C}\right)=\mathbf{0} \tag{2.40}$$

has two sets of eigenpairs: one set associated with the eigenvalues k_{Rj} and left eigenvectors $\mathbf{l}_{Rj}^{\mathrm{T}}=\begin{bmatrix}k_{Rj}\boldsymbol{\phi}_{xj}^{\mathrm{T}} & \mathbf{0} & \boldsymbol{\phi}_{zj}^{\mathrm{T}}\end{bmatrix}$ and the other set associated with the eigenvalues k_{Lj} and left eigenvectors $\mathbf{l}_{Lj}^{\mathrm{T}}=\begin{bmatrix}\mathbf{0} & \boldsymbol{\phi}_{yj}^{\mathrm{T}} & \mathbf{0}\end{bmatrix}$.

The left and right eigenvectors satisfy the orthogonal conditions (Barbosa and Kausel, 2012)

$$\begin{aligned}&\mathbf{l}_{Rj}^{\mathrm{T}}\mathbf{A}\mathbf{r}_{Rl}=\delta_{jl}k_{Rj}, && \mathbf{l}_{Rj}^{\mathrm{T}}\mathbf{C}\mathbf{r}_{Rl}=-\delta_{jl}k_{Rj}^3\\ &\mathbf{l}_{Lj}^{\mathrm{T}}\mathbf{A}\mathbf{r}_{Ll}=\delta_{jl}, && \mathbf{l}_{Lj}^{\mathrm{T}}\mathbf{C}\mathbf{r}_{Ll}=-\delta_{jl}k_{Lj}^2\\ &\mathbf{l}_{Rj}^{\mathrm{T}}\mathbf{A}\mathbf{r}_{Ll}=0, && \mathbf{l}_{Rj}^{\mathrm{T}}\mathbf{C}\mathbf{r}_{Ll}=0\end{aligned} \tag{2.41}$$

Having found the solutions of (2.38), the rotated displacements $\mathbf{T}\tilde{\mathbf{u}}$ are decomposed into a summation of the right eigenvectors, i.e.

$$\mathbf{T}\tilde{\mathbf{u}}=\sum_{j=1}^{N_R}\Gamma_{Rj}\mathbf{r}_{Rj}+\sum_{j=1}^{N_L}\Gamma_{Lj}\mathbf{r}_{Lj} \tag{2.42}$$

where Γ_{Rj} and Γ_{Lj} are participation factors yet to be determined and N_R and N_L are the number of degrees of freedom in the Rayleigh and Love eigenvalue problems, respectively. After replacing the identity (2.42) in equation (2.37) and after pre-multiplying it by $\mathbf{l}_{Rl}^{\mathrm{T}}$, the latter becomes

$$\mathbf{l}_{Rl}^{\mathrm{T}}\mathbf{T}\tilde{\mathbf{p}}=\mathbf{l}_{Rl}^{\mathrm{T}}\left[k^2\mathbf{A}+\mathbf{C}\right]\left(\sum_{j=1}^{N_R}\Gamma_{Rj}\mathbf{r}_{Rj}+\sum_{j=1}^{N_L}\Gamma_{Lj}\mathbf{r}_{Lj}\right) \tag{2.43}$$

Due to the orthogonal conditions expressed in (2.41), equation (2.43) is equivalent to

$$\mathbf{l}_{Rl}^{\mathrm{T}}\mathbf{T}\tilde{\mathbf{p}}=\left[k^2k_{Rl}-k_{Rl}^3\right]\Gamma_{Rl} \qquad \Leftrightarrow \qquad \Gamma_{Rl}=\frac{\mathbf{l}_{Rl}^{\mathrm{T}}\mathbf{T}\tilde{\mathbf{p}}}{k_{Rl}\left(k^2-k_{Rl}^2\right)} \tag{2.44}$$

If (2.37) is pre-multiplied instead by $\mathbf{l}_{Ll}^{\mathrm{T}}$, then

$$\mathbf{l}_{Ll}^{\mathrm{T}}\mathbf{T}\tilde{\mathbf{p}} = \left[k^2 - k_{Ll}^2\right]\Gamma_{Rl} \qquad \Leftrightarrow \qquad \Gamma_{Ll} = \frac{\mathbf{l}_{Ll}^{\mathrm{T}}\mathbf{T}\tilde{\mathbf{p}}}{k^2 - k_{Ll}^2} \tag{2.45}$$

The combination of (2.44), (2.45) and (2.42) yields

$$\mathbf{T}\tilde{\mathbf{u}} = \sum_{j=1}^{N_R}\left(\frac{\mathbf{l}_{Rj}^{\mathrm{T}}\mathbf{T}\tilde{\mathbf{p}}}{k_{Rj}\left(k^2 - k_{Rj}^2\right)}\mathbf{r}_{Rj}\right) + \sum_{j=1}^{N_L}\left(\frac{\mathbf{l}_{Lj}^{\mathrm{T}}\mathbf{T}\tilde{\mathbf{p}}}{k^2 - k_{Lj}^2}\mathbf{r}_{Lj}\right) \tag{2.46}$$

or equivalently

$$\tilde{\mathbf{u}} = \sum_{j=1}^{N_R}\left(\mathbf{T}^{-1}\frac{\mathbf{l}_{Rj}^{\mathrm{T}}\mathbf{T}\tilde{\mathbf{p}}}{k_{Rj}\left(k^2 - k_{Rj}^2\right)}\mathbf{r}_{Rj}\right) + \sum_{j=1}^{N_L}\left(\mathbf{T}^{-1}\frac{\mathbf{l}_{Lj}^{\mathrm{T}}\mathbf{T}\tilde{\mathbf{p}}}{k^2 - k_{Lj}^2}\mathbf{r}_{Lj}\right) \tag{2.47}$$

Equation (2.47) can be further simplified into

$$\begin{bmatrix}\mathbf{u}_x\\ \mathbf{u}_y\\ \mathbf{u}_z\end{bmatrix} = \sum_{j=1}^{N_R}\begin{bmatrix}\dfrac{\cos^2\vartheta}{k^2 - k_{Rj}^2}\boldsymbol{\phi}_{xj}\boldsymbol{\phi}_{xj}^{\mathrm{T}}\mathbf{p}_x + \dfrac{\sin\vartheta\cos\vartheta}{k^2 - k_{Rj}^2}\boldsymbol{\phi}_{xj}\boldsymbol{\phi}_{xj}^{\mathrm{T}}\mathbf{p}_y - \mathrm{i}\dfrac{k\cos\vartheta}{k_{Rj}\left(k^2 - k_{Rj}^2\right)}\boldsymbol{\phi}_{xj}\boldsymbol{\phi}_{zj}^{\mathrm{T}}\mathbf{p}_z\\ \dfrac{\sin\vartheta\cos\vartheta}{k^2 - k_{Rj}^2}\boldsymbol{\phi}_{xj}\boldsymbol{\phi}_{xj}^{\mathrm{T}}\mathbf{p}_x + \dfrac{\sin^2\vartheta}{k^2 - k_{Rj}^2}\boldsymbol{\phi}_{xj}\boldsymbol{\phi}_{xj}^{\mathrm{T}}\mathbf{p}_y - \mathrm{i}\dfrac{k\sin\vartheta}{k_{Rj}\left(k^2 - k_{Rj}^2\right)}\boldsymbol{\phi}_{xj}\boldsymbol{\phi}_{zj}^{\mathrm{T}}\mathbf{p}_z\\ \mathrm{i}\dfrac{k_{Rj}\cos\vartheta}{k\left(k^2 - k_{Rj}^2\right)}\boldsymbol{\phi}_{zj}\boldsymbol{\phi}_{xj}^{\mathrm{T}}\mathbf{p}_x + \mathrm{i}\dfrac{k_{Rj}\sin\vartheta}{k\left(k^2 - k_{Rj}^2\right)}\boldsymbol{\phi}_{zj}\boldsymbol{\phi}_{xj}^{\mathrm{T}}\mathbf{p}_y + \dfrac{1}{k^2 - k_{Rj}^2}\boldsymbol{\phi}_{zj}\boldsymbol{\phi}_{zj}^{\mathrm{T}}\mathbf{p}_z\end{bmatrix} + \sum_{j=1}^{N_L}\begin{bmatrix}\dfrac{\sin^2\vartheta}{k^2 - k_{Lj}^2}\boldsymbol{\phi}_{yj}\boldsymbol{\phi}_{yj}^{\mathrm{T}}\mathbf{p}_x - \dfrac{\sin\vartheta\cos\vartheta}{k^2 - k_{Lj}^2}\boldsymbol{\phi}_{yj}\boldsymbol{\phi}_{yj}^{\mathrm{T}}\mathbf{p}_y\\ -\dfrac{\sin\vartheta\cos\vartheta}{k^2 - k_{Lj}^2}\boldsymbol{\phi}_{yj}\boldsymbol{\phi}_{yj}^{\mathrm{T}}\mathbf{p}_x + \dfrac{\cos^2\vartheta}{k^2 - k_{Lj}^2}\boldsymbol{\phi}_{yj}\boldsymbol{\phi}_{yj}^{\mathrm{T}}\mathbf{p}_y\\ \mathbf{0}\end{bmatrix} \tag{2.48}$$

As a final step, taking into account the equality (Barbosa and Kausel, 2012)

$$\boldsymbol{\phi}_{zj}\boldsymbol{\phi}_{xj}^{\mathrm{T}}\frac{k_{Rj}}{k\left(k - k_{Rj}\right)} = \boldsymbol{\phi}_{zj}\boldsymbol{\phi}_{xj}^{\mathrm{T}}\frac{k}{k_{Rj}\left(k - k_{Rj}\right)} \tag{2.49}$$

equation (2.48) can be written in the more convenient form

$$\begin{bmatrix}\mathbf{u}_x\\ \mathbf{u}_y\\ \mathbf{u}_z\end{bmatrix}=\sum_{j=1}^{N_R}\begin{bmatrix}\dfrac{\cos^2\vartheta}{k^2-k_{Rj}^2}\boldsymbol{\phi}_{xj}\boldsymbol{\phi}_{xj}^{\mathrm{T}}\mathbf{p}_x+\dfrac{\sin\vartheta\cos\vartheta}{k^2-k_{Rj}^2}\boldsymbol{\phi}_{xj}\boldsymbol{\phi}_{xj}^{\mathrm{T}}\mathbf{p}_y-\mathrm{i}\dfrac{k\cos\vartheta}{k_{Rj}\left(k^2-k_{Rj}^2\right)}\boldsymbol{\phi}_{xj}\boldsymbol{\phi}_{zj}^{\mathrm{T}}\mathbf{p}_z\\ \dfrac{\sin\vartheta\cos\vartheta}{k^2-k_{Rj}^2}\boldsymbol{\phi}_{xj}\boldsymbol{\phi}_{xj}^{\mathrm{T}}\mathbf{p}_x+\dfrac{\sin^2\vartheta}{k^2-k_{Rj}^2}\boldsymbol{\phi}_{xj}\boldsymbol{\phi}_{xj}^{\mathrm{T}}\mathbf{p}_y-\mathrm{i}\dfrac{k\sin\vartheta}{k_{Rj}\left(k^2-k_{Rj}^2\right)}\boldsymbol{\phi}_{xj}\boldsymbol{\phi}_{zj}^{\mathrm{T}}\mathbf{p}_z\\ \mathrm{i}\dfrac{k\cos\vartheta}{k_{Rj}\left(k^2-k_{Rj}^2\right)}\boldsymbol{\phi}_{zj}\boldsymbol{\phi}_{xj}^{\mathrm{T}}\mathbf{p}_x+\mathrm{i}\dfrac{k\sin\vartheta}{k_{Rj}\left(k^2-k_{Rj}^2\right)}\boldsymbol{\phi}_{zj}\boldsymbol{\phi}_{xj}^{\mathrm{T}}\mathbf{p}_y+\dfrac{1}{k^2-k_{Rj}^2}\boldsymbol{\phi}_{zj}\boldsymbol{\phi}_{zj}^{\mathrm{T}}\mathbf{p}_z\end{bmatrix}+\sum_{j=1}^{N_L}\begin{bmatrix}\dfrac{\sin^2\vartheta}{k^2-k_{Lj}^2}\boldsymbol{\phi}_{yj}\boldsymbol{\phi}_{yj}^{\mathrm{T}}\mathbf{p}_x-\dfrac{\sin\vartheta\cos\vartheta}{k^2-k_{Lj}^2}\boldsymbol{\phi}_{yj}\boldsymbol{\phi}_{yj}^{\mathrm{T}}\mathbf{p}_y\\ -\dfrac{\sin\vartheta\cos\vartheta}{k^2-k_{Lj}^2}\boldsymbol{\phi}_{yj}\boldsymbol{\phi}_{yj}^{\mathrm{T}}\mathbf{p}_x+\dfrac{\cos^2\vartheta}{k^2-k_{Lj}^2}\boldsymbol{\phi}_{yj}\boldsymbol{\phi}_{yj}^{\mathrm{T}}\mathbf{p}_y\\ \mathbf{0}\end{bmatrix} \tag{2.50}$$

In the following, it will be implicitly understood that the eigenvalue problem for Rayleigh (shear vertical – pressure, SVP) waves will result in eigenvectors $\boldsymbol{\phi}_{xj}$, $\boldsymbol{\phi}_{zj}$ whose components at the m^{th} elevation and j^{th} mode are written as $\phi_{xj}^{(m)},\phi_{zj}^{(m)}$ and their eigenvalues are $k_j=k_{Rj}$, while the eigenvectors $\boldsymbol{\phi}_{yj}$ for Love (shear horizontal, SH) waves will have components written as $\phi_{yj}^{(m)}$ with eigenvalues $k_j=k_{Lj}$. In the light of equation (2.48), it is now convenient to define the set of kernels K_{nj} given in Table 2.1.

Table 2.1**:** Kernels of fundamental solutions

$K_{1j}=\dfrac{1}{k^2-k_j^2}$,	$K_{2j}=\dfrac{\sin\vartheta\cos\vartheta}{k^2-k_j^2}=\dfrac{k_xk_y}{k^2\left(k^2-k_j^2\right)}$
$K_{3j}=\dfrac{\cos^2\vartheta}{k^2-k_j^2}=\dfrac{k_x^2}{k^2\left(k^2-k_j^2\right)}$,	$K_{4j}=\dfrac{\sin^2\vartheta}{k^2-k_j^2}=\dfrac{k_y^2}{k^2\left(k^2-k_j^2\right)}$
$K_{5j}=\dfrac{k\cos\vartheta}{k_j\left(k^2-k_j^2\right)}=\dfrac{k_x}{k_j\left(k^2-k_j^2\right)}$,	$K_{6j}=\dfrac{k\sin\vartheta}{k_j\left(k^2-k_j^2\right)}=\dfrac{k_y}{k_j\left(k^2-k_j^2\right)}$

From equation (2.50) and in terms of the kernels in Table 2.1, the fundamental displacements $U_{\alpha\beta}^{(mn)}\left(k_x,k_y,\omega\right)$ at the m^{th} elevation in direction α due to a unit load applied at the n^{th} elevation in direction β can be expressed as listed in Table 2.2.

Table 2.2**:** Fundamental solutions in the wavenumber-frequency domain

$$U_{xx}^{(mn)} = \sum_{j}^{N_R} K_{3j}\,\phi_{xj}^{(m)}\phi_{xj}^{(n)} + \sum_{j}^{N_L} K_{4j}\phi_{yj}^{(m)}\phi_{yj}^{(n)}$$

$$U_{yy}^{(mn)} = \sum_{j}^{N_R} K_{4j}\,\phi_{xj}^{(m)}\phi_{xj}^{(n)} + \sum_{j}^{N_L} K_{3j}\,\phi_{yj}^{(m)}\phi_{yj}^{(n)}$$

$$U_{xy}^{(mn)} = \sum_{j}^{N_R} K_{2j}\,\phi_{xj}^{(m)}\phi_{xj}^{(n)} - \sum_{j}^{N_L} K_{2j}\,\phi_{yj}^{(m)}\phi_{yj}^{(n)} = G_{yx}^{(mn)}$$

$$U_{xz}^{(mn)} = -\mathrm{i}\sum_{j}^{N_R} K_{5j}\,\phi_{xj}^{(m)}\phi_{zj}^{(n)}\,, \qquad U_{zx}^{(mn)} = \mathrm{i}\sum_{j}^{N_R} K_{5j}\,\phi_{zj}^{(m)}\phi_{xj}^{(n)} = -U_{xz}^{(nm)}$$

$$U_{yz}^{(mn)} = -\mathrm{i}\sum_{j}^{N_R} K_{6j}\,\phi_{xj}^{(m)}\phi_{zj}^{(n)}\,, \qquad U_{zy}^{(mn)} = \mathrm{i}\sum_{j=1}^{N_R} K_{6j}\,\phi_{zj}^{(m)}\phi_{xj}^{(n)} = -U_{yz}^{(nm)}$$

2.4 Horizontal derivatives and tractions in the wavenumber domain

After the displacements are known, the horizontal derivatives in the wavenumber domain are easily obtained by multiplying the displacements by $-\mathrm{i}k_x$, for the case of the x-derivative, or by $-\mathrm{i}k_y$, for the case of the y-derivative. Similarly, the second derivatives are obtained by multiplying the first derivatives by $-\mathrm{i}k_x$ or $-\mathrm{i}k_y$. In this way, for the derivative $\partial^2/\partial x^2$ the displacements are multiplied by $-k_x^2$, for the derivative $\partial^2/\partial x\partial y$ the displacements are multiplied by $-k_x k_y$, and for the derivative $\partial^2/\partial y^2$ the displacements are multiplied by $-k_y^2$.

As for the consistent nodal tractions acting on one isolated thin-layer (say the i^{th} thin-layer delimited by the global TLM interfaces l and m), they can be calculated using eq. (2.30) once the nodal displacements of that thin-layer are known. In this case, eq. (2.30) refers to a single thin-layer and the vectors $\tilde{\mathbf{p}}$ and $\tilde{\mathbf{u}}$ contain the nodal values at the $nn+1$ nodes of the thin-layer ($nn+1$ is used instead of m to avoid confusion between global TLM interface and number of nodal interfaces of the thin-layer):

$$\tilde{\mathbf{p}} \to \tilde{\mathbf{p}}^{(i)} = \begin{bmatrix} \tilde{\mathbf{t}}_{(1)}^{(i)} \\ \vdots \\ \tilde{\mathbf{t}}_{(nn+1)}^{(i)} \end{bmatrix} \qquad \tilde{\mathbf{u}} \to \tilde{\mathbf{u}}^{(i)} = \begin{bmatrix} \tilde{\mathbf{u}}_{(1)}^{(i)} \\ \vdots \\ \tilde{\mathbf{u}}_{(nn+1)}^{(i)} \end{bmatrix}$$

For a load in direction β, the modified nodal tractions are $\tilde{\mathbf{t}}_{(k)}^{(i)} = \begin{bmatrix} \overline{t}_{x\beta(k)}^{(i)} & \overline{t}_{y\beta(k)}^{(i)} & -\mathrm{i}\overline{t}_{z\beta(k)}^{(i)} \end{bmatrix}^{\mathrm{T}}$ and the modified nodal displacements are $\tilde{\mathbf{u}}_{(k)}^{(i)} = \begin{bmatrix} \overline{u}_{x\beta(k)}^{(i)} & \overline{u}_{y\beta(k)}^{(i)} & -\mathrm{i}\overline{u}_{z\beta(k)}^{(i)} \end{bmatrix}^{\mathrm{T}}$ (the word modified is used to take into account the multiplication by the factor $-\mathrm{i}$; the first lower index represents the direction of the traction or displacement, the second index represents the direction of the source and the third index, in parentheses, represents the nodal number).

When there is no source acting in the interior of the considered thin-layer, the tractions $\overline{t}_{\alpha\beta(k)}^{(i)}$ for $k = 2,...,nn$ are null and only the tractions $\overline{t}_{\alpha\beta(1)}^{(i)}$ and $\overline{t}_{\alpha\beta(nn+1)}^{(i)}$ remain non-zero. These non-

zero values correspond to the tractions that the rest of the domain transmits to the thin-layer through the upper and lower interfaces. By replacing in eq. (2.30) the displacements by their modal expansion as given in Table 2.2, the fundamental tractions are obtained also in terms of modal superposition. Hence, considering first a force applied at the global interface n and in the direction $\beta = x$, the nodal tractions at the i^{th} thin-layer are obtained by

$$\begin{aligned}
\tilde{\mathbf{p}}^{(i)} = \mathbf{A}_{xx} & \left(\sum_{j=1}^{N_R} \phi_{xj}^{(n)} \begin{bmatrix} \Gamma_{jR}^{x(2)} & & \\ & \ddots & \\ & & \Gamma_{jR}^{x(2)} \end{bmatrix} \begin{bmatrix} \boldsymbol{\Phi}_{Rj}^{(l)} \\ \vdots \\ \boldsymbol{\Phi}_{Rj}^{(m)} \end{bmatrix} + \sum_{j=1}^{N_L} \phi_{yj}^{(n)} \begin{bmatrix} \Gamma_{jL}^{x(2)} & & \\ & \ddots & \\ & & \Gamma_{jL}^{x(2)} \end{bmatrix} \begin{bmatrix} \boldsymbol{\Phi}_{Lj}^{(l)} \\ \vdots \\ \boldsymbol{\Phi}_{Lj}^{(m)} \end{bmatrix} \right) + \\
\left(k_y \mathbf{A}_{xy} + \mathbf{B}_x \right) & \left(\sum_{j=1}^{N_R} \phi_{xj}^{(n)} \begin{bmatrix} \Gamma_{jR}^{x(1)} & & \\ & \ddots & \\ & & \Gamma_{jR}^{x(1)} \end{bmatrix} \begin{bmatrix} \boldsymbol{\Phi}_{Rj}^{(l)} \\ \vdots \\ \boldsymbol{\Phi}_{Rj}^{(m)} \end{bmatrix} + \sum_{j=1}^{N_L} \phi_{yj}^{(n)} \begin{bmatrix} \Gamma_{jL}^{x(1)} & & \\ & \ddots & \\ & & \Gamma_{jL}^{x(1)} \end{bmatrix} \begin{bmatrix} \boldsymbol{\Phi}_{Lj}^{(l)} \\ \vdots \\ \boldsymbol{\Phi}_{Lj}^{(m)} \end{bmatrix} \right) + \\
\left(k_y^2 \mathbf{A}_{yy} + k_y \mathbf{B}_y + \mathbf{G} - \omega^2 \mathbf{M} \right) & \left(\sum_{j=1}^{N_R} \phi_{xj}^{n} \begin{bmatrix} \Gamma_{jR}^{x(0)} & & \\ & \ddots & \\ & & \Gamma_{jR}^{x(0)} \end{bmatrix} \begin{bmatrix} \boldsymbol{\Phi}_{Rj}^{(l)} \\ \vdots \\ \boldsymbol{\Phi}_{Rj}^{(m)} \end{bmatrix} + \sum_{j=1}^{N_L} \phi_{yj}^{(n)} \begin{bmatrix} \Gamma_{jL}^{x(0)} & & \\ & \ddots & \\ & & \Gamma_{jL}^{x(0)} \end{bmatrix} \begin{bmatrix} \boldsymbol{\Phi}_{Lj}^{(l)} \\ \vdots \\ \boldsymbol{\Phi}_{Lj}^{(m)} \end{bmatrix} \right)
\end{aligned} \tag{2.51}$$

where

$$\Gamma_{jR}^{x(p)} = \begin{bmatrix} k_x^p K_{3j}\left(k_x, k_y\right) & 0 & 0 \\ 0 & k_x^p K_{2j}\left(k_x, k_y\right) & 0 \\ 0 & 0 & k_x^p K_{5j}\left(k_x, k_y\right) \end{bmatrix} \tag{2.52}$$

$$\Gamma_{jL}^{x(p)} = \begin{bmatrix} k_x^p K_{4j}\left(k_x, k_y\right) & 0 & 0 \\ 0 & -k_x^p K_{2j}\left(k_x, k_y\right) & 0 \\ 0 & 0 & 0 \end{bmatrix} \tag{2.53}$$

$$\boldsymbol{\Phi}_{Rj}^{(k)} = \begin{bmatrix} \phi_{xj}^{(k)} & \phi_{xj}^{(k)} & \phi_{zj}^{(k)} \end{bmatrix}^{\mathrm{T}}, \qquad \boldsymbol{\Phi}_{Lj}^{(k)} = \begin{bmatrix} \phi_{yj}^{(k)} & \phi_{yj}^{(k)} & 0 \end{bmatrix}^{\mathrm{T}}, \qquad k = l, ..., m \tag{2.54}$$

Similarly, for a load in the y direction the consistent nodal tractions are calculated by

$$\begin{aligned}
\tilde{\mathbf{p}}^{(i)} = \mathbf{A}_{xx} & \left(\sum_{j=1}^{N_R} \phi_{xj}^{(n)} \begin{bmatrix} \Gamma_{jR}^{y(2)} & & \\ & \ddots & \\ & & \Gamma_{jR}^{y(2)} \end{bmatrix} \begin{bmatrix} \boldsymbol{\Phi}_{Rj}^{(l)} \\ \vdots \\ \boldsymbol{\Phi}_{Rj}^{(m)} \end{bmatrix} + \sum_{j=1}^{NL} \phi_{yj}^{(n)} \begin{bmatrix} \Gamma_{jL}^{y(2)} & & \\ & \ddots & \\ & & \Gamma_{jL}^{y(2)} \end{bmatrix} \begin{bmatrix} \boldsymbol{\Phi}_{Lj}^{(l)} \\ \vdots \\ \boldsymbol{\Phi}_{Lj}^{(m)} \end{bmatrix} \right) + \\
\left(k_y \mathbf{A}_{xy} + \mathbf{B}_x \right) & \left(\sum_{j=1}^{N_R} \phi_{xj}^{(n)} \begin{bmatrix} \Gamma_{jR}^{y(1)} & & \\ & \ddots & \\ & & \Gamma_{jR}^{y(1)} \end{bmatrix} \begin{bmatrix} \boldsymbol{\Phi}_{Rj}^{(l)} \\ \vdots \\ \boldsymbol{\Phi}_{Rj}^{(m)} \end{bmatrix} + \sum_{j=1}^{N_L} \phi_{yj}^{(n)} \begin{bmatrix} \Gamma_{jL}^{y(1)} & & \\ & \ddots & \\ & & \Gamma_{jL}^{y(1)} \end{bmatrix} \begin{bmatrix} \boldsymbol{\Phi}_{Lj}^{(l)} \\ \vdots \\ \boldsymbol{\Phi}_{Lj}^{(m)} \end{bmatrix} \right) + \\
\left(k_y^2 \mathbf{A}_{yy} + k_y \mathbf{B}_y + \mathbf{G} - \omega^2 \mathbf{M} \right) & \left(\sum_{j=1}^{N_R} \phi_{xj}^{(n)} \begin{bmatrix} \Gamma_{jR}^{y(0)} & & \\ & \ddots & \\ & & \Gamma_{jR}^{y(0)} \end{bmatrix} \begin{bmatrix} \boldsymbol{\Phi}_{Rj}^{(l)} \\ \vdots \\ \boldsymbol{\Phi}_{Rj}^{(m)} \end{bmatrix} + \sum_{j=1}^{N_L} \phi_{yj}^{(n)} \begin{bmatrix} \Gamma_{jL}^{y(0)} & & \\ & \ddots & \\ & & \Gamma_{jL}^{y(0)} \end{bmatrix} \begin{bmatrix} \boldsymbol{\Phi}_{Lj}^{(l)} \\ \vdots \\ \boldsymbol{\Phi}_{Lj}^{(m)} \end{bmatrix} \right)
\end{aligned} \tag{2.55}$$

with

$$\Gamma_{jR}^{y(p)} = \begin{bmatrix} k_x^p K_{2j}\left(k_x,k_y\right) & 0 & 0 \\ 0 & k_x^p K_{4j}\left(k_x,k_y\right) & 0 \\ 0 & 0 & k_x^p K_{6j}\left(k_x,k_y\right) \end{bmatrix} \tag{2.56}$$

$$\Gamma_{jL}^{y(p)} = \begin{bmatrix} -k_x^p K_{2j}\left(k_x,k_y\right) & 0 & 0 \\ 0 & k_x^p K_{3j}\left(k_x,k_y\right) & 0 \\ 0 & 0 & 0 \end{bmatrix} \tag{2.57}$$

and for a load in the z direction, the tractions are calculated by

$$\begin{aligned} \tilde{\mathbf{p}}^{(i)} = \mathbf{A}_{xx} & \left(\sum_{j=1}^{N_R} \phi_{zj}^{(n)} \begin{bmatrix} \Gamma_{jR}^{z(2)} & & \\ & \ddots & \\ & & \Gamma_{jR}^{z(2)} \end{bmatrix} \begin{bmatrix} \mathbf{\Phi}_{Rj}^{(l)} \\ \vdots \\ \mathbf{\Phi}_{Rj}^{(m)} \end{bmatrix} \right) + \\ & \left(k_y \mathbf{A}_{xy} + \mathbf{B}_x\right) \left(\sum_{j=1}^{N_R} \phi_{zj}^{(n)} \begin{bmatrix} \Gamma_{jR}^{z(1)} & & \\ & \ddots & \\ & & \Gamma_{jR}^{z(1)} \end{bmatrix} \begin{bmatrix} \mathbf{\Phi}_{Rj}^{(l)} \\ \vdots \\ \mathbf{\Phi}_{Rj}^{(m)} \end{bmatrix} \right) + \\ & \left(k_y^2 \mathbf{A}_{yy} + k_y \mathbf{B}_y + \mathbf{G} - \omega^2 \mathbf{M}\right) \left(\sum_{j=1}^{N_R} \phi_{zj}^{(n)} \begin{bmatrix} \Gamma_{jR}^{z(0)} & & \\ & \ddots & \\ & & \Gamma_{jR}^{z(0)} \end{bmatrix} \begin{bmatrix} \mathbf{\Phi}_{Rj}^{(l)} \\ \vdots \\ \mathbf{\Phi}_{Rj}^{(m)} \end{bmatrix} \right) \end{aligned} \tag{2.58}$$

with

$$\Gamma_{jR}^{z(p)} = -\mathrm{i} \begin{bmatrix} k_x^p K_{5j}\left(k_x,k_y\right) & 0 & 0 \\ 0 & k_x^p K_{6j}\left(k_x,k_y\right) & 0 \\ 0 & 0 & k_x^p K_{1j}\left(k_x,k_y\right) \end{bmatrix} \tag{2.59}$$

2.5 Transformation of fundamental solutions to the 2.5D domain

Having obtained the fundamental solutions explicitly in terms of the two horizontal wavenumbers k_x and k_y, one can now proceed to carry out the inverse Fourier transform in k_x. In this work only the case of space harmonic line loads is considered, being different load distributions treated in Barbosa and Kausel (2012).

2.5.1 Fundamental displacements

Taking as example the displacements in the x direction induced by source in the same direction, it is seen in section 2.3 that the displacements $U_{xx}^{(mn)}$ in the wavenumber-frequency domain are given by (Table 2.2)

$$U_{xx}^{(mn)} = \sum_{j}^{N_R} K_{3j} \phi_{xj}^{(m)} \phi_{xj}^{(n)} + \sum_{j}^{N_L} K_{4j} \phi_{yj}^{(m)} \phi_{yj}^{(n)} \tag{2.60}$$

The corresponding fundamental displacement in the mixed space-wavenumber-frequency domain (2.5D) is obtained with

$$u_{xx}^{(mn)}\left(x,k_y,\omega\right)=\frac{1}{2\pi}\int_{-\infty}^{+\infty}U_{xx}^{(mn)}\mathrm{e}^{-\mathrm{i}k_x x}\mathrm{d}k_x=\frac{1}{2\pi}\int_{-\infty}^{+\infty}\left(\sum_j^{N_R}K_{3j}\phi_{xj}^{(m)}\phi_{xj}^{(n)}+\sum_j^{N_L}K_{4j}\phi_{yj}^{(m)}\phi_{yj}^{(n)}\right)\mathrm{e}^{-\mathrm{i}k_x x}\mathrm{d}k_x \tag{2.61}$$

Since the eigenvectors do not depend on the horizontal wavenumbers but instead on the frequency ω, equation (2.61) is equivalent to

$$u_{xx}^{(mn)}\left(x,k_y,\omega\right)=\frac{1}{2\pi}\sum_j^{N_R}\left(\phi_{xj}^{(m)}\phi_{xj}^{(n)}\int_{-\infty}^{+\infty}K_{3j}\mathrm{e}^{-\mathrm{i}k_x x}\mathrm{d}k_x\right)+\frac{1}{2\pi}\sum_j^{N_L}\left(\phi_{yj}^{(m)}\phi_{yj}^{(n)}\int_{-\infty}^{+\infty}K_{4j}\mathrm{e}^{-\mathrm{i}k_x x}\mathrm{d}k_x\right) \tag{2.62}$$

Similar conclusions are derived for the other components and thus, in order to obtain the fundamental displacements in the 2.5D domain, one simply needs to evaluate the integrals

$$I_{nj}^{(0)}\left(x\right)=\tfrac{1}{2\pi}\int_{-\infty}^{+\infty}K_{nj}\,\mathrm{e}^{-\mathrm{i}k_x x}\mathrm{d}k_x,\qquad n=1,...,6 \tag{2.63}$$

and then combine them in the same fashion as done with K_{nj} in Table 2.2. For example, the fundamental displacement $u_{xx}^{(mn)}$ is obtained with

$$u_{xx}^{(mn)}=\sum_j^{N_R}I_{3j}^{(0)}\phi_{xj}^{(m)}\phi_{xj}^{(n)}+\sum_j^{N_L}I_{4j}^{(0)}\phi_{yj}^{(m)}\phi_{yj}^{(n)} \tag{2.64}$$

The integrals $I_{nj}^{(0)}$ can be evaluated in closed form expressions by means of contour integration (Boas, 1983). These expressions are summarized in Table 2.3, where k_j stands for either the Rayleigh or the Love poles, as appropriate. The evaluation of the integral $I_{4j}^{(0)}$ with the contour integration technique is described in Appendix II. The evaluation of the remaining integrals follows similar steps.

Table 2.3: Closed form expressions for $I_{nj}^{(0)}$ ($\mathrm{Im}\sqrt{k_j^2-k_y^2}<0$)

$I_{1j}^{(0)}=\frac{1}{2\pi}\int_{-\infty}^{+\infty}K_{1j}\,\mathrm{e}^{-\mathrm{i}k_x x}\,\mathrm{d}k_x$	$=\dfrac{1}{2\mathrm{i}\sqrt{k_j^2-k_y^2}}\mathrm{e}^{-\mathrm{i}\lvert x\rvert\sqrt{k_j^2-k_y^2}}$
$I_{2j}^{(0)}=\frac{1}{2\pi}\int_{-\infty}^{+\infty}K_{2j}\,\mathrm{e}^{-\mathrm{i}k_x x}\,\mathrm{d}k_x$	$=\dfrac{k_y}{k_j^2}\dfrac{\mathrm{sign}\left(x\right)}{2\mathrm{i}}\left(\mathrm{e}^{-\mathrm{i}\lvert x\rvert\sqrt{k_j^2-k_y^2}}-\mathrm{e}^{-\lvert k_y x\rvert}\right)$
$I_{3j}^{(0)}=\frac{1}{2\pi}\int_{-\infty}^{+\infty}K_{3j}\,\mathrm{e}^{-\mathrm{i}k_x x}\,\mathrm{d}k_x$	$=\dfrac{1}{2\mathrm{i}k_j^2}\left\{\sqrt{k_j^2-k_y^2}\,\mathrm{e}^{-\mathrm{i}\lvert x\rvert\sqrt{k_j^2-k_y^2}}+\mathrm{i}\lvert k_y\rvert\mathrm{e}^{-\lvert k_y x\rvert}\right\}$
$I_{4j}^{(0)}=\frac{1}{2\pi}\int_{-\infty}^{+\infty}K_{4j}\,\mathrm{e}^{-\mathrm{i}k_x x}\,\mathrm{d}k_x$	$=\dfrac{1}{2\mathrm{i}k_j^2}\left\{\dfrac{k_y^2}{\sqrt{k_j^2-k_y^2}}\mathrm{e}^{-\mathrm{i}\lvert x\rvert\sqrt{k_j^2-k_y^2}}-\mathrm{i}\lvert k_y\rvert\mathrm{e}^{-\lvert k_y x\rvert}\right\}$
$I_{5j}^{(0)}=\frac{1}{2\pi}\int_{-\infty}^{+\infty}K_{5j}\,\mathrm{e}^{-\mathrm{i}k_x x}\,\mathrm{d}k_x$	$=\dfrac{\mathrm{sign}\left(x\right)}{2\mathrm{i}k_j}\mathrm{e}^{-\mathrm{i}\lvert x\rvert\sqrt{k_j^2-k_y^2}}$
$I_{6j}^{(0)}=\frac{1}{2\pi}\int_{-\infty}^{+\infty}K_{6j}\,\mathrm{e}^{-\mathrm{i}k_x x}\,\mathrm{d}k_x$	$=\dfrac{k_y}{2\mathrm{i}k_j\sqrt{k_j^2-k_y^2}}\mathrm{e}^{-\mathrm{i}\lvert x\rvert\sqrt{k_j^2-k_y^2}}$

2.5.2 Horizontal derivatives

One now proceeds to transform the horizontal derivatives to the 2.5D domain. Starting with y direction, the first y-derivative is obtained with $u_{\alpha\beta,y} = -\mathrm{i}k_y\, u_{\alpha\beta}$ while the second y-derivative is obtained with $u_{\alpha\beta,yy} = -k_y^2\, u_{\alpha\beta}$. Regarding the derivatives in the x direction, taking as example the component xx and following the procedure explained in subsection 2.5.1 for both first and second derivatives, the following two expressions are obtained (see section 2.4):

$$u_{xx,x}^{mn}\left(x,k_y,\omega\right) = \frac{1}{2\pi}\sum_{j}^{N_R}\left(-\mathrm{i}\phi_{xj}^{m}\phi_{xj}^{n}\int_{-\infty}^{+\infty} k_x K_{3j}\mathrm{e}^{-\mathrm{i}k_x x}\mathrm{d}k_x\right) + \frac{1}{2\pi}\sum_{j}^{N_L}\left(-\mathrm{i}\phi_{yj}^{m}\phi_{yj}^{n}\int_{-\infty}^{+\infty} k_x K_{4j}\mathrm{e}^{-\mathrm{i}k_x x}\mathrm{d}k_x\right) \tag{2.65}$$

$$u_{xx,xx}^{mn}\left(x,k_y,\omega\right) = \frac{1}{2\pi}\sum_{j}^{N_R}\left(-\phi_{xj}^{m}\phi_{xj}^{n}\int_{-\infty}^{+\infty} k_x^2 K_{3j}\mathrm{e}^{-\mathrm{i}k_x x}\mathrm{d}k_x\right) + \frac{1}{2\pi}\sum_{j}^{N_L}\left(-\phi_{yj}^{m}\phi_{yj}^{n}\int_{-\infty}^{+\infty} k_x^2 K_{4j}\mathrm{e}^{-\mathrm{i}k_x x}\mathrm{d}k_x\right) \tag{2.66}$$

Hence, to obtain the first and second x-derivatives, the integrals

$$I_{nj}^{(1)}\left(x\right) = \tfrac{1}{2\pi}\int_{-\infty}^{+\infty} k_x K_{nj}\,\mathrm{e}^{-\mathrm{i}k_x x}\mathrm{d}k_x, \quad n = 1,...,6 \tag{2.67}$$

and

$$I_{nj}^{(2)}\left(x\right) = \tfrac{1}{2\pi}\int_{-\infty}^{+\infty} k_x^2 K_{nj}\,\mathrm{e}^{-\mathrm{i}k_x x}\mathrm{d}k_x, \quad n = 1,...,6 \tag{2.68}$$

must be evaluated and multiplied by $-\mathrm{i}$ and -1, respectively, and then used in Table 2.2 in place of K_{nj}. For instance, the expressions for $u_{xx,x}^{(mn)}$ and $u_{xx,xx}^{(mn)}$ are

$$u_{xx,x}^{(mn)}\left(x,k_y,\omega\right) = -\frac{\mathrm{i}}{2\pi}\sum_{j}^{N_R} I_{3j}^{(1)}\phi_{xj}^{(m)}\phi_{xj}^{(n)} - \frac{\mathrm{i}}{2\pi}\sum_{j}^{N_L} I_{4j}^{(1)}\phi_{yj}^{(m)}\phi_{yj}^{(n)} \tag{2.69}$$

$$u_{xx,xx}^{(mn)}\left(x,k_y,\omega\right) = -\frac{1}{2\pi}\sum_{j}^{N_R} I_{3j}^{(2)}\phi_{xj}^{(m)}\phi_{xj}^{(n)} - \frac{1}{2\pi}\sum_{j}^{N_L} I_{4j}^{(2)}\phi_{yj}^{(m)}\phi_{yj}^{(n)} \tag{2.70}$$

For the remaining components similar expressions can be obtained. Closed form expressions for integrals $I_{nj}^{(1)}$ and $I_{nj}^{(2)}$ are given in Table 2.4 and Table 2.5, respectively.

After the first x-derivatives are known, the cross derivatives $u_{\alpha\beta,xy}$ can be obtained through the multiplication $u_{\alpha\beta,xy} = -\mathrm{i}k_y\, u_{\alpha\beta,x}$.

2.5.3 Fundamental tractions

Such as described in the previous subsections, the fundamental tractions $t_{\alpha\beta}$ in horizontal planes result from the inverse Fourier transform in k_x of equations (2.51), (2.55) and (2.58). Since the eigenvectors do not depend on the wavenumber k_x, the inverse Fourier transform is accomplished by replacing in the equations (2.51), (2.55) and (2.58) the matrices $\Gamma_{jR}^{\beta(p)}$ and $\Gamma_{jL}^{\beta(p)}$ by the matrices $\Lambda_{jR}^{\beta(p)}$ and $\Lambda_{jL}^{\beta(p)}$, whose general expressions are

$$\Lambda_{jR}^{\beta(p)} = \frac{1}{2\pi}\int_{-\infty}^{+\infty}\Gamma_{jR}^{\beta(p)}\,\mathrm{e}^{-\mathrm{i}k_x x}\,\mathrm{d}k_x \qquad \Lambda_{jL}^{\beta(p)} = \frac{1}{2\pi}\int_{-\infty}^{+\infty}\Gamma_{jL}^{\beta(p)}\,\mathrm{e}^{-\mathrm{i}k_x x}\,\mathrm{d}k_x \tag{2.71}$$

Table 2.4: Closed form expressions for $I_{nj}^{(1)}$ ($\mathrm{Im}\sqrt{k_j^2-k_y^2}<0$)

$$
\begin{aligned}
I_{1j}^{(1)} &= \frac{1}{2\pi}\int_{-\infty}^{+\infty} k_x K_{1j}\, \mathrm{e}^{-\mathrm{i}k_x x}\,\mathrm{d}k_x &&= \frac{\mathrm{sgn}(x)}{2\mathrm{i}}\mathrm{e}^{-\mathrm{i}|x|\sqrt{k_j^2-k_y^2}} \\
I_{2j}^{(1)} &= \frac{1}{2\pi}\int_{-\infty}^{+\infty} k_x K_{2j}\, \mathrm{e}^{-\mathrm{i}k_x x}\,\mathrm{d}k_x &&= \frac{k_y}{2\mathrm{i}k_j^2}\left(\sqrt{k_j^2-k_y^2}\,\mathrm{e}^{-\mathrm{i}|x|\sqrt{k_j^2-k_y^2}} + \mathrm{i}\left|k_y\right|\mathrm{e}^{-|k_y x|}\right) \\
I_{3j}^{(1)} &= \frac{1}{2\pi}\int_{-\infty}^{+\infty} k_x K_{3j}\, \mathrm{e}^{-\mathrm{i}k_x x}\,\mathrm{d}k_x &&= \frac{\mathrm{sgn}(x)}{2\mathrm{i}\,k_j^2}\left\{\left(k_j^2-k_y^2\right)\mathrm{e}^{-\mathrm{i}|x|\sqrt{k_j^2-k_y^2}} + k_y^2\,\mathrm{e}^{-|k_y x|}\right\} \\
I_{4j}^{(1)} &= \frac{1}{2\pi}\int_{-\infty}^{+\infty} k_x K_{4j}\, \mathrm{e}^{-\mathrm{i}k_x x}\,\mathrm{d}k_x &&= \frac{\mathrm{sgn}(x)}{2\mathrm{i}\,k_j^2}\left\{k_y^2\,\mathrm{e}^{-\mathrm{i}|x|\sqrt{k_j^2-k_y^2}} - k_y^2\,\mathrm{e}^{-|k_y x|}\right\} \\
I_{5j}^{(1)} &= \frac{1}{2\pi}\int_{-\infty}^{+\infty} k_x K_{5j}\, \mathrm{e}^{-\mathrm{i}k_x x}\,\mathrm{d}k_x &&= \frac{\sqrt{k_j^2-k_y^2}}{2\mathrm{i}\,k_j}\mathrm{e}^{-\mathrm{i}|x|\sqrt{k_j^2-k_y^2}} \\
I_{6j}^{(1)} &= \frac{1}{2\pi}\int_{-\infty}^{+\infty} k_x K_{6j}\, \mathrm{e}^{-\mathrm{i}k_x x}\,\mathrm{d}k_x &&= \frac{\mathrm{sgn}(x)\,k_y}{2\mathrm{i}\,k_j}\mathrm{e}^{-\mathrm{i}|x|\sqrt{k_j^2-k_y^2}}
\end{aligned}
$$

Table 2.5: Closed form expressions for $I_{nj}^{(2)}$ ($\mathrm{Im}\sqrt{k_j^2-k_y^2}<0$)

$$
\begin{aligned}
I_{1j}^{(2)} &= \frac{1}{2\pi}\int_{-\infty}^{+\infty} k_x^2 K_{1j}\, \mathrm{e}^{-\mathrm{i}k_x x}\,\mathrm{d}k_x &&= \frac{\sqrt{k_j^2-k_y^2}}{2\mathrm{i}}\mathrm{e}^{-\mathrm{i}|x|\sqrt{k_j^2-k_y^2}} \\
I_{2j}^{(2)} &= \frac{1}{2\pi}\int_{-\infty}^{+\infty} k_x^2 K_{2j}\, \mathrm{e}^{-\mathrm{i}k_x x}\,\mathrm{d}k_x &&= \frac{k_y}{k_j^2}\frac{\mathrm{sgn}(x)}{2\mathrm{i}}\left\{\left(k_j^2-k_y^2\right)\mathrm{e}^{-\mathrm{i}|x|\sqrt{k_j^2-k_y^2}} + k_y^2\,\mathrm{e}^{-|k_y x|}\right\} \\
I_{3j}^{(2)} &= \frac{1}{2\pi}\int_{-\infty}^{+\infty} k_x^2 K_{3j}\, \mathrm{e}^{-\mathrm{i}k_x x}\,\mathrm{d}k_x &&= \frac{1}{2\mathrm{i}\,k_j^2}\left\{\left(k_j^2-k_y^2\right)^{3/2}\mathrm{e}^{-\mathrm{i}|x|\sqrt{k_j^2-k_y^2}} - \mathrm{i}\left|k_y\right|^3\mathrm{e}^{-|k_y x|}\right\} \\
I_{4j}^{(2)} &= \frac{1}{2\pi}\int_{-\infty}^{+\infty} k_x^2 K_{4j}\, \mathrm{e}^{-\mathrm{i}k_x x}\,\mathrm{d}k_x &&= \frac{1}{2\mathrm{i}\,k_j^2}\left\{k_y^2\sqrt{k_j^2-k_y^2}\,\mathrm{e}^{-\mathrm{i}|x|\sqrt{k_j^2-k_y^2}} + \mathrm{i}\left|k_y\right|^3\mathrm{e}^{-|k_y x|}\right\} \\
I_{5j}^{(2)} &= \frac{1}{2\pi}\int_{-\infty}^{+\infty} k_x^2 K_{5j}\, \mathrm{e}^{-\mathrm{i}k_x x}\,\mathrm{d}k_x &&= \frac{\mathrm{sgn}(x)\left(k_j^2-k_y^2\right)}{2\mathrm{i}\,k_j}\mathrm{e}^{-\mathrm{i}|x|\sqrt{k_j^2-k_y^2}} \\
I_{6j}^{(2)} &= \frac{1}{2\pi}\int_{-\infty}^{+\infty} k_x^2 K_{6j}\, \mathrm{e}^{-\mathrm{i}k_x x}\,\mathrm{d}k_x &&= \frac{k_y\sqrt{k_j^2-k_y^2}}{2\mathrm{i}\,k_j}\mathrm{e}^{-\mathrm{i}|x|\sqrt{k_j^2-k_y^2}}
\end{aligned}
$$

Obtaining the matrices $\Lambda_{jR}^{\beta(p)}$ and $\Lambda_{jL}^{\beta(p)}$ is straightforward, as they results from the combination of the integrals $I_{nj}^{(p)}$ ($p=0,1,2$). For instance, the matrix $\Lambda_{jR}^{z(p)}$ is

$$
\Lambda_{jR}^{z(p)} = -\mathrm{i}\begin{bmatrix} I_{5j}^{(p)}\left(x,k_y\right) & 0 & 0 \\ 0 & I_{6j}^{(p)}\left(x,k_y\right) & 0 \\ 0 & 0 & I_{1j}^{(p)}\left(x,k_y\right) \end{bmatrix} \tag{2.72}
$$

2.5.4 Vertical derivatives and internal stresses

The z-derivatives can be obtained through the combination of the nodal displacements weighted by the derivatives of the associated shape functions. However, following that approach, the derivatives at the top and bottom interfaces of the thin-layers are not consistent with the tractions calculated in subsection 2.5.3, and so their accuracy is inferior. To compensate for the lack of precision of the vertical derivative, Kausel (2004) proposed an alternative strategy for their calculation. The procedure is based on the definition of secondary interpolation functions that are consistent with the tractions at the top and bottom interfaces of the thin-layer. In this work, that procedure is used to define the vertical derivatives and, subsequently, the internal stresses at the internal nodal interfaces.

Consider the i^{th} thin-layer (of expansion nn), from which the displacements $u^{(i)}_{\alpha\beta(j)}$ at the $nn+1$ nodal interfaces, the horizontal derivatives ($u^{(i)}_{\alpha\beta(j),x}$ and $u^{(i)}_{\alpha\beta(j),y}$), and the nodal tractions ($t^{(i)}_{\alpha\beta(j)}$) at the top and bottom interfaces are known for all directions $\alpha = x, y, z$ and for a source in the direction β. The tractions at the upper surface and the internal stresses at the same horizontal plane are related by

$$\mathbf{t}^{(i)}_{(1)} = \left[\sigma^{\text{top}}_{xz\beta} \quad \sigma^{\text{top}}_{yz\beta} \quad \sigma^{\text{top}}_{zz\beta}\right]^{\text{T}} \tag{2.73}$$

while the tractions at the lower surface and the internal stresses at the corresponding plane are related by

$$\mathbf{t}^{(i)}_{(nn+1)} = -\left[\sigma^{\text{bottom}}_{xz\beta} \quad \sigma^{\text{bottom}}_{yz\beta} \quad \sigma^{\text{bottom}}_{zz\beta}\right]^{\text{T}} \tag{2.74}$$

In their turn, the internal stresses and the derivatives of displacements are related by

$$\begin{aligned}
\sigma_{xz\beta} &= G_t\left(u_{x\beta,z} + u_{z\beta,x}\right) \\
\sigma_{yz\beta} &= G_t\left(u_{y\beta,z} + u_{z\beta,y}\right) \\
\sigma_{zz\beta} &= \lambda_t\left(u_{x\beta,x} + u_{y\beta,y}\right) + D_t u_{z\beta,z}
\end{aligned} \tag{2.75}$$

The previous equation can be solved for the vertical derivatives, yielding

$$\begin{aligned}
u_{x\beta,z} &= \frac{\left(\sigma_{xz\beta} - G u_{z\beta,x}\right)}{G_t} \\
u_{y\beta,z} &= \frac{\left(\sigma_{yz\beta} - G u_{z\beta,y}\right)}{G_t} \\
u_{z\beta,z} &= \frac{\sigma_{zz\beta} - \lambda_t\left(u_{x\beta,x} + u_{y\beta,y}\right)}{D_t}
\end{aligned} \tag{2.76}$$

For each response direction α and for each source direction β, the values of the displacements at the $nn+1$ nodal interfaces and of the vertical derivatives at the upper and lower interfaces are now known. In this way, it is possible to employ the $nn+3$ known quantities and use Hermitian interpolation to define a polynomial of degree $nn+2$ that approximates the vertical variation of the displacements. If the thin-layer is linear ($nn=1$) and its thickness is h, then

$$u_{\alpha\beta}(z) = A_{\alpha\beta} + B_{\alpha\beta} z + C_{\alpha\beta} z^2 + D_{\alpha\beta} z^3 \tag{2.77}$$

$$u_{\alpha\beta,z}(z) = B_{\alpha\beta} + 2C_{\alpha\beta} z + 3D_{\alpha\beta} z^2 \tag{2.78}$$

$$\begin{bmatrix} A_{\alpha\beta} \\ B_{\alpha\beta} \\ C_{\alpha\beta} \\ D_{\alpha\beta} \end{bmatrix} = \begin{bmatrix} 1 & 0 & 0 & 0 \\ 1 & h & h^2 & h^3 \\ 0 & 1 & 0 & 0 \\ 0 & 1 & 2h & 3h^2 \end{bmatrix}^{-1} \begin{bmatrix} u^{(i)}_{\alpha\beta(2)} \\ u^{(i)}_{\alpha\beta(1)} \\ u^{(i)}_{\alpha\beta(2),z} \\ u^{(i)}_{\alpha\beta(1),z} \end{bmatrix} = \begin{bmatrix} 0 & 1 & 0 & 0 \\ 0 & 0 & 0 & 1 \\ 3/h^2 & -3/h^2 & -1/h & -2/h \\ -2/h^3 & 2/h^3 & 1/h^2 & 1/h^2 \end{bmatrix} \begin{bmatrix} u^{(i)}_{\alpha\beta(2)} \\ u^{(i)}_{\alpha\beta(1)} \\ u^{(i)}_{\alpha\beta(2),z} \\ u^{(i)}_{\alpha\beta(1),z} \end{bmatrix} \tag{2.79}$$

If instead the thin-layer is quadratic ($nn = 2$), then

$$u_{\alpha\beta}(z) = A_{\alpha\beta} + B_{\alpha\beta} z + C_{\alpha\beta} z^2 + D_{\alpha\beta} z^3 + E_{\alpha\beta} z^4 \tag{2.80}$$

$$u_{\alpha\beta,z}(z) = B_{\alpha\beta} + 2C_{\alpha\beta} z + 3D_{\alpha\beta} z^2 + 4E_{\alpha\beta} z^3 \tag{2.81}$$

$$\begin{bmatrix} A_{\alpha\beta} \\ B_{\alpha\beta} \\ C_{\alpha\beta} \\ D_{\alpha\beta} \\ E_{\alpha\beta} \end{bmatrix} = \begin{bmatrix} 1 & 0 & 0 & 0 & 0 \\ 1 & h/2 & (h/2)^2 & (h/2)^3 & (h/2)^4 \\ 1 & h & h^2 & h^3 & h^4 \\ 0 & 1 & 0 & 0 & 0 \\ 0 & 1 & 2h & 3h^2 & 4h^3 \end{bmatrix}^{-1} \begin{bmatrix} u^{(i)}_{\alpha\beta(3)} \\ u^{(i)}_{\alpha\beta(2)} \\ u^{(i)}_{\alpha\beta(1)} \\ u^{(i)}_{\alpha\beta(3),z} \\ u^{(i)}_{\alpha\beta(1),z} \end{bmatrix} = \begin{bmatrix} 0 & 0 & 1 & 0 & 0 \\ 0 & 0 & 0 & 0 & 1 \\ -5/h^2 & 16/h^2 & -11/h^2 & 1/h & -4/h \\ 14/h^3 & -32/h^3 & 18/h^3 & -3/h^2 & 5/h^2 \\ -8/h^4 & 16/h^4 & -8/h^4 & 2/h^3 & -4/h^3 \end{bmatrix} \begin{bmatrix} u^{(i)}_{\alpha\beta(3)} \\ u^{(i)}_{\alpha\beta(2)} \\ u^{(i)}_{\alpha\beta(1)} \\ u^{(i)}_{\alpha\beta(3),z} \\ u^{(i)}_{\alpha\beta(1),z} \end{bmatrix} \tag{2.82}$$

After finding the left-hand side of equations (2.79) and (2.82), the vertical derivatives of the displacements at the nodal interfaces can be determined using eq. (2.78) or eq. (2.81). As for the vertical derivatives $u_{\alpha\beta,z}(z)$ of points in the interior of the thin-layer, though they can be calculated using the same two equations, one chooses to use instead the original interpolation functions to determine these variables, i.e.,

$$u_{\alpha\beta,z}(z) = \sum_{j=1}^{nn+1} N_j(z) u^{(i)}_{\alpha\beta(j),z} \tag{2.83}$$

With all the first derivatives known, eq. (2.6) can be used to calculate the internal stresses.

Regarding the calculation of the second derivatives involving the z direction ($\partial^2/\partial x \partial z$, $\partial^2/\partial y \partial z$ and $\partial^2/\partial z^2$), $u_{\alpha\beta,yz}$ is obtained by multiplying $u_{\alpha\beta,z}$ by $-\mathrm{i}k_y$, while $u_{\alpha\beta,xz}$ is obtained by differentiating equation (2.76) with respect to x, i.e.

$$
\begin{aligned}
u_{x\beta,xz} &= \frac{\left(\sigma_{xz\beta,x} - G u_{z\beta,xx}\right)}{G_t} \\
u_{y\beta,xz} &= \frac{\left(\sigma_{yz\beta,x} - G u_{z\beta,xy}\right)}{G_t} \\
u_{z\beta,xz} &= \frac{\sigma_{zz\beta,x} - \lambda_t \left(u_{x\beta,xx} + u_{y\beta,xy}\right)}{D_t}
\end{aligned}
\tag{2.84}
$$

The traction derivatives $\sigma_{\alpha z\beta,x}$ are calculated as explained in subsection 2.5.3, with the exception that matrices $\Lambda_{jR}^{\beta(p)}$ and $\Lambda_{jL}^{\beta(p)}$ must be replaced with matrices $-\mathrm{i}\Lambda_{jR}^{\beta(p+1)}$ and $-\mathrm{i}\Lambda_{jL}^{\beta(p+1)}$, respectively. For the calculation of the matrices $\Lambda_{jR}^{\beta(3)}$ and $\Lambda_{jL}^{\beta(3)}$ the integrals $I_{nj}^{(3)}$ of the form

$$
I_{nj}^{(3)}(x) = \tfrac{1}{2\pi}\int_{-\infty}^{+\infty} k_x^3 K_{nj}\, \mathrm{e}^{-\mathrm{i}k_x x}\mathrm{d}k_x, \quad n = 1,...,6 \tag{2.85}
$$

are needed. Closed form expressions for these integrals are given in Table 2.6.

Table 2.6: Closed form expressions for $I_{nj}^{(3)}$ ($\mathrm{Im}\sqrt{k_j^2 - k_y^2} < 0$)

$$
\begin{aligned}
I_{1j}^{(3)} &= \frac{1}{2\pi}\int_{-\infty}^{+\infty} k_x^3 K_{1j}\, \mathrm{e}^{-\mathrm{i}k_x x}\,\mathrm{d}k_x &&= \mathrm{sgn}(x)\frac{k_j^2 - k_y^2}{2\mathrm{i}}\mathrm{e}^{-\mathrm{i}|x|\sqrt{k_j^2 - k_y^2}} \\
I_{2j}^{(3)} &= \frac{1}{2\pi}\int_{-\infty}^{+\infty} k_x^3 K_{2j}\, \mathrm{e}^{-\mathrm{i}k_x x}\,\mathrm{d}k_x &&= \frac{k_y}{2\mathrm{i}k_j^2}\left\{\left(k_j^2 - k_y^2\right)^{3/2}\mathrm{e}^{-\mathrm{i}|x|\sqrt{k_j^2 - k_y^2}} - \mathrm{i}\left|k_y\right|^3 \mathrm{e}^{-|k_y x|}\right\} \\
I_{3j}^{(3)} &= \frac{1}{2\pi}\int_{-\infty}^{+\infty} k_x^3 K_{3j}\, \mathrm{e}^{-\mathrm{i}k_x x}\,\mathrm{d}k_x &&= \frac{\mathrm{sgn}(x)}{2\mathrm{i}k_j^2}\left\{\left(k_j^2 - k_y^2\right)^2 \mathrm{e}^{-\mathrm{i}|x|\sqrt{k_j^2 - k_y^2}} - k_y^4\,\mathrm{e}^{-|k_y x|}\right\} \\
I_{4j}^{(3)} &= \frac{1}{2\pi}\int_{-\infty}^{+\infty} k_x^3 K_{4j}\, \mathrm{e}^{-\mathrm{i}k_x x}\,\mathrm{d}k_x &&= \frac{\mathrm{sgn}(x)}{2\mathrm{i}k_j^2}\left\{k_y^2\left(k_j^2 - k_y^2\right)\mathrm{e}^{-\mathrm{i}|x|\sqrt{k_j^2 - k_y^2}} + k_y^4\,\mathrm{e}^{-|k_y x|}\right\} \\
I_{5j}^{(3)} &= \frac{1}{2\pi}\int_{-\infty}^{+\infty} k_x^3 K_{5j}\, \mathrm{e}^{-\mathrm{i}k_x x}\,\mathrm{d}k_x &&= \frac{\left(k_j^2 - k_y^2\right)^{3/2}}{2\mathrm{i}k_j}\mathrm{e}^{-\mathrm{i}|x|\sqrt{k_j^2 - k_y^2}} \\
I_{6j}^{(3)} &= \frac{1}{2\pi}\int_{-\infty}^{+\infty} k_x^3 K_{6j}\, \mathrm{e}^{-\mathrm{i}k_x x}\,\mathrm{d}k_x &&= \mathrm{sgn}(x)\frac{k_y\left(k_j^2 - k_y^2\right)}{2\mathrm{i}k_j}\mathrm{e}^{-\mathrm{i}|x|\sqrt{k_j^2 - k_y^2}}
\end{aligned}
$$

[Note about Table 2.5 and Table 2.6: $\left(k_j^2 - k_y^2\right)^{3/2}$ must be calculated as $\left(k_j^2 - k_y^2\right)\sqrt{k_j^2 - k_y^2}$, with $\mathrm{Im}\sqrt{k_j^2 - k_y^2} < 0$; a direct use of the expression $\left(k_j^2 - k_y^2\right)^{3/2}$ might possibly assign the wrong sign to the result.]

The remaining second derivative, $u_{\alpha\beta,zz}$, can be calculated resorting to the Navier equation (Achenbach, 1973)

$$
G\,u_{i,jj} + (G + \lambda)\,u_{j,ij} + F_i = -\rho\omega^2 u_i \tag{2.86}
$$

which after being solved for $u_{\alpha\beta,zz}$ yields (it is assumed that $F_i = 0$, i.e., no internal sources)

$$
\begin{aligned}
u_{x\beta,zz} &= \frac{-\rho\omega^2 u_{x\beta} - (\lambda+G)\left(u_{x\beta,xx} + u_{y\beta,xy} + u_{z\beta,xz}\right) - G\left(u_{x\beta,xx} + u_{x\beta,yy}\right)}{G} \\
u_{y\beta,zz} &= \frac{-\rho\omega^2 u_{y\beta} - (\lambda+G)\left(u_{x\beta,xy} + u_{y\beta,yy} + u_{z\beta,yz}\right) - G\left(u_{y\beta,xx} + u_{y\beta,yy}\right)}{G} \\
u_{z\beta,zz} &= \frac{-\rho\omega^2 u_{z\beta} - (\lambda+G)\left(u_{x\beta,xz} + u_{y\beta,yz}\right) - G\left(u_{z\beta,xx} + u_{z\beta,yy}\right)}{\lambda+2G}
\end{aligned}
\tag{2.87}
$$

2.5.5 Validation

To validate the equations derived in this and previous sections, the response of a homogeneous full-space obtained with the TLM is compared with the analytical solution derived by Tadeu and Kausel (2000). The isotropic full-space has mass density $\rho = 1$, shear modulus $G = 1$ and Poisson's ratio $\nu = 0.25$, and is subjected to a time harmonic line load of the form $\mathbf{b}(x, y, z, t) = \delta(x)\delta(z)\exp\left(\mathrm{i}\omega t - \mathrm{i}k_y y\right)$, being the excitation frequency $f = 1\,\mathrm{Hz}$ ($\omega = 2\pi$). The thin-layer model used to simulate the full-space consists of an elastic layer with thickness $20\lambda_s$ divided into 200 thin-layers of quadratic expansion — a discussion on discretization errors can be found in Park and Kausel (2004b) — and supplemented at its upper and lower horizons with paraxial boundaries (Seale and Kausel, 1989), which are used to simulate the infinite domain — in section 2.6 of this chapter, a more efficient strategy to model infinite domains is presented. The parameters λ_s is the wavelength of the shear wave, which is defined by

$$
\lambda_s = \frac{C_s}{f} \qquad C_s = \sqrt{\frac{G}{\rho}} \tag{2.88}
$$

The load is applied at the middle surface of the elastic layer. To avoid strong oscillations in the response, a small amount of damping is considered ($\xi_P = \xi_S = 0.005$), which renders the wave velocities complex.

In the first validation scenario, the displacements induced by a vertical load are computed as function of the wavenumber k_y at the horizontal plane $z = 0$ and horizontal distances $x = 0.01\lambda_s$, $x = \lambda_s$ and $x = 5\lambda_s$. Figure 2.2 depicts the comparison between the vertical displacements obtained with the TLM and those calculated with the analytical solution.

As can be observed in Figure 2.2b) and c), the match between the exact solution and the TLM solution is very good. Nonetheless, very close to the load (Figure 2.2a), one can observe a rather small difference in the real part, which is due to discretization effects. This is because the thickness of the thin-layers is only $0.1\lambda_s$ while the receiver is placed at one tenth of that distance from the source. Still, given the excellent quality of the comparison even at that short range, the results obtained clearly demonstrate the robustness of the TLM solution.

Observe that at large distances the response decays very fast with the wavenumber k_y beyond the threshold $k_s = \omega / C_s$ (the branch point), while below that value the response is highly wavy. Hence, when computing the inverse transform from k_y–space into *y*–space for remote points, one can truncate the integrals at the branch point, but then again because of the rapid oscillations one must consider a sufficiently dense number of points below that threshold. Conversely, for receivers at close range, the response functions are less wavy, but they also

decay more slowly with k_y. Hence, their Fourier inversion must include points beyond the branch point even if one can get away with coarser spacing.

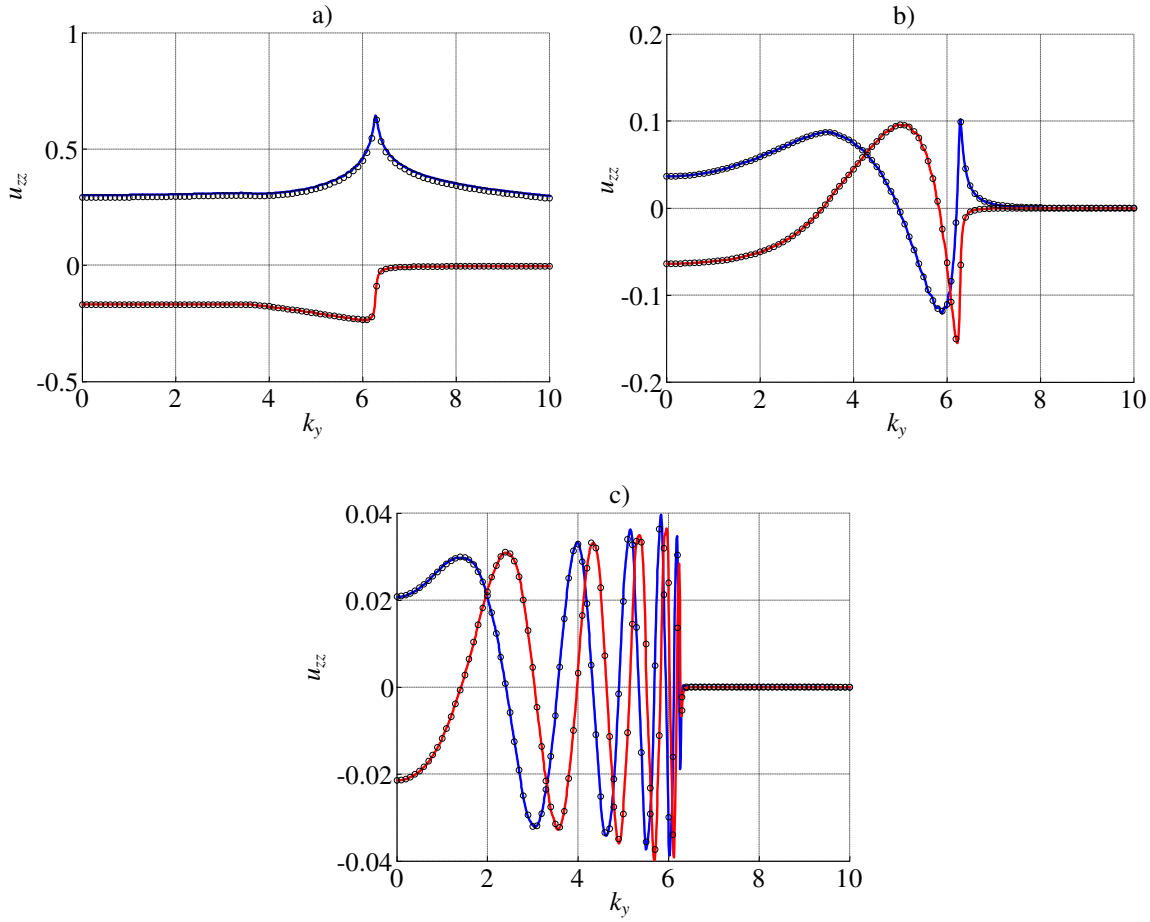

Figure 2.2: Vertical displacements at a) $x = 0.01\lambda_s$, b) $x = \lambda_s$, and c) $x = 5\lambda_s$. Solid lines = TLM solution (real part — blue; imaginary part — red). Circles = analytical solution

In the second validation example, both displacements and derivatives are computed as function of the horizontal distance x and considering all three directions for the load and for the response. The longitudinal wavenumber is $k_y = 0.4$ and the receivers are placed at the depth $z = 4\lambda_s$ and up to the horizontal distance $x_{\max} = 4\lambda_s$. The stresses are not compared because they can be calculated based on the derivatives of displacements, and if the latter are correct, then the former are also correct. Likewise, the y-derivatives are not represented because they result from the multiplication of other response fields (displacement or derivative) by $-ik_y$. Figures 2.3 to 2.8 depict the comparison between the theoretical solution and the responses obtained with the TLM. All figures suggest that the two approaches yield results that are virtually the same, thus confirming that the TLM is indeed capable of reproducing the wave motion with high accuracy. This validates the expressions derived in the previous sections of this work.

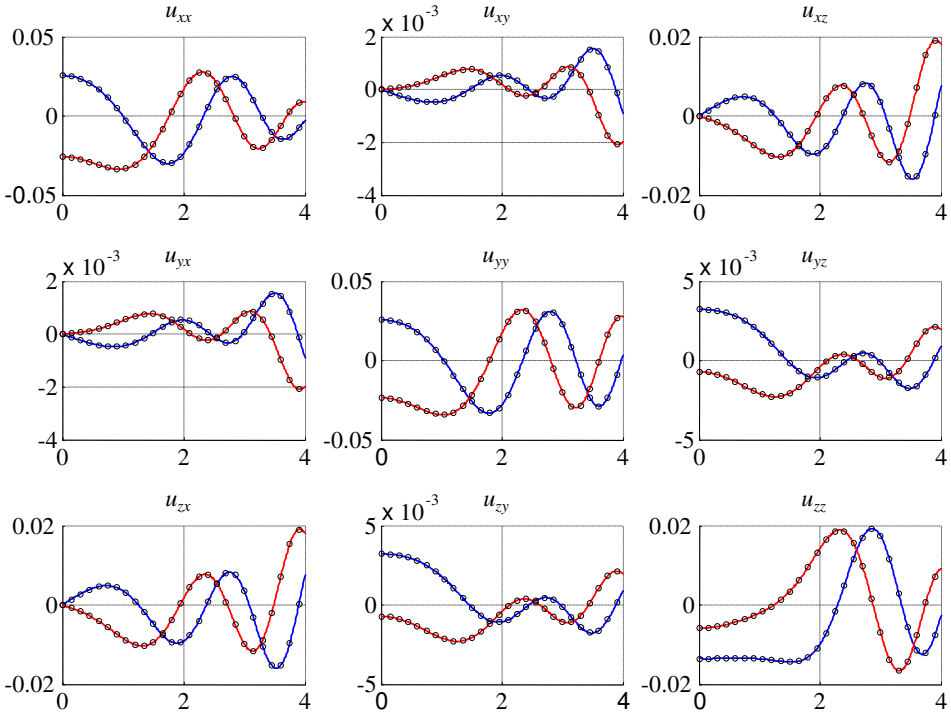

Figure 2.3: Displacements $u_{\alpha\beta}$. Solid lines = TLM solution (real part — blue; imaginary part — red). Circles = analytical solution

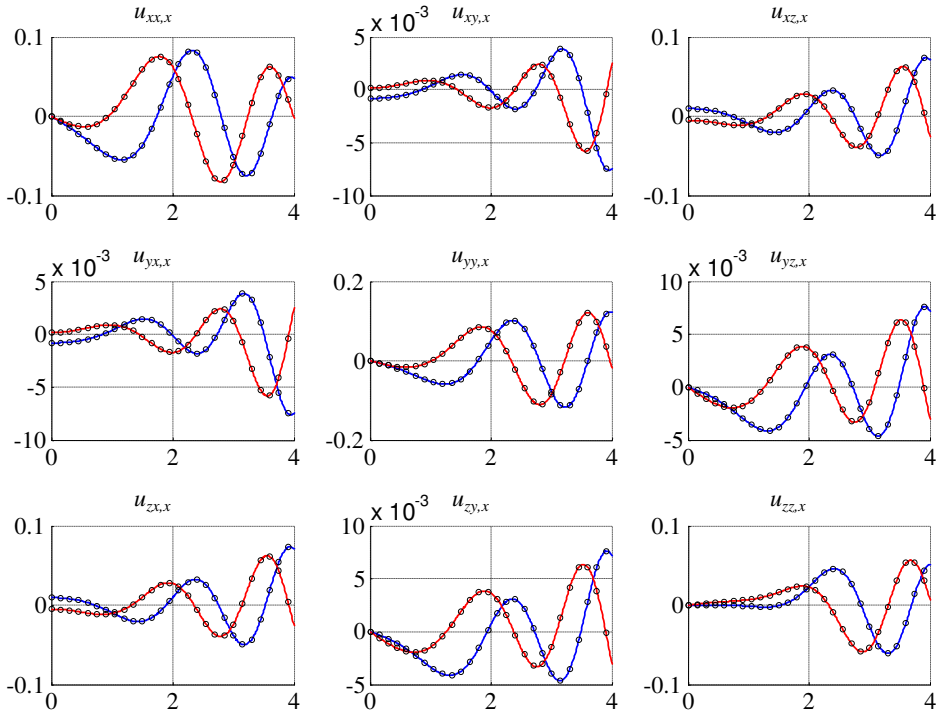

Figure 2.4: Displacement derivatives $u_{\alpha\beta,x}$. Solid lines = TLM solution (real part — blue; imaginary part — red). Circles = analytical solution

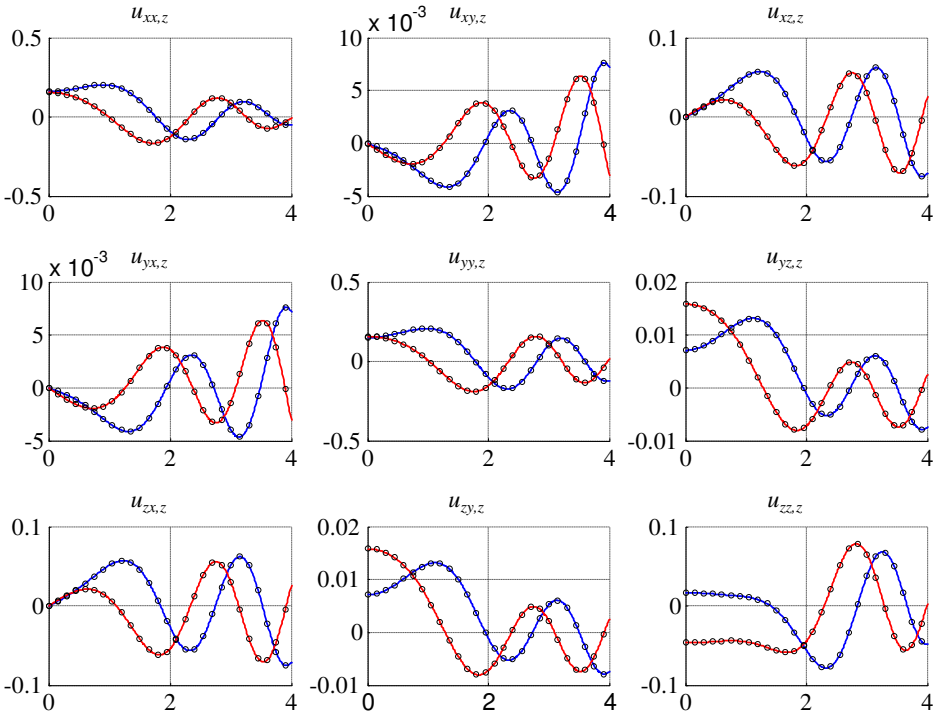

Figure 2.5: Displacement derivatives $u_{\alpha\beta,z}$. Solid lines = TLM solution (real part — blue; imaginary part — red). Circles = analytical solution

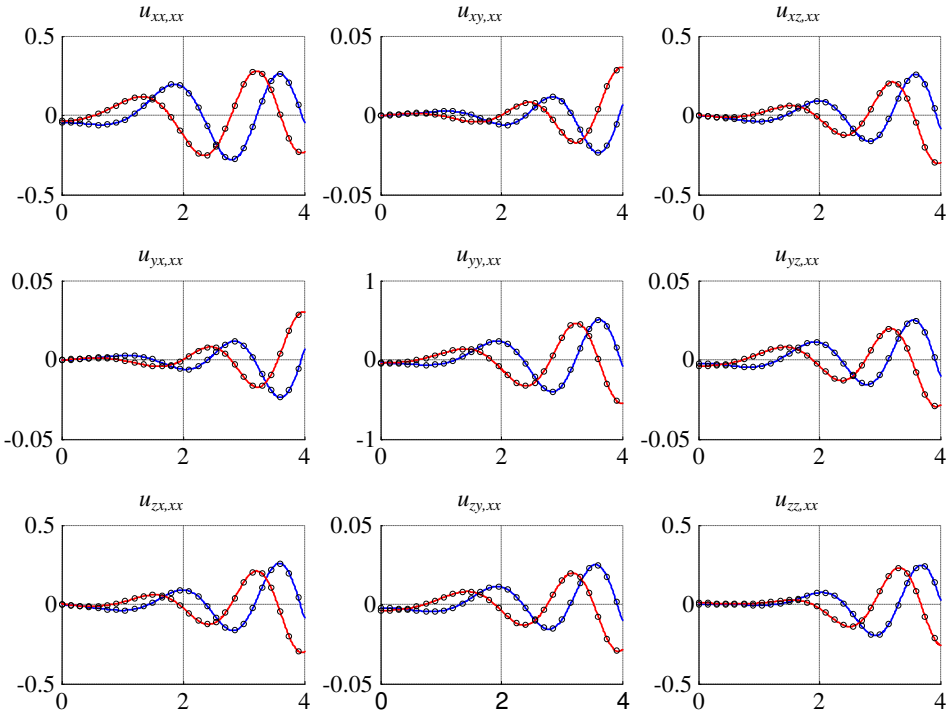

Figure 2.6: Displacement derivatives $u_{\alpha\beta,xx}$. Solid lines = TLM solution (real part — blue; imaginary part — red). Circles = analytical solution

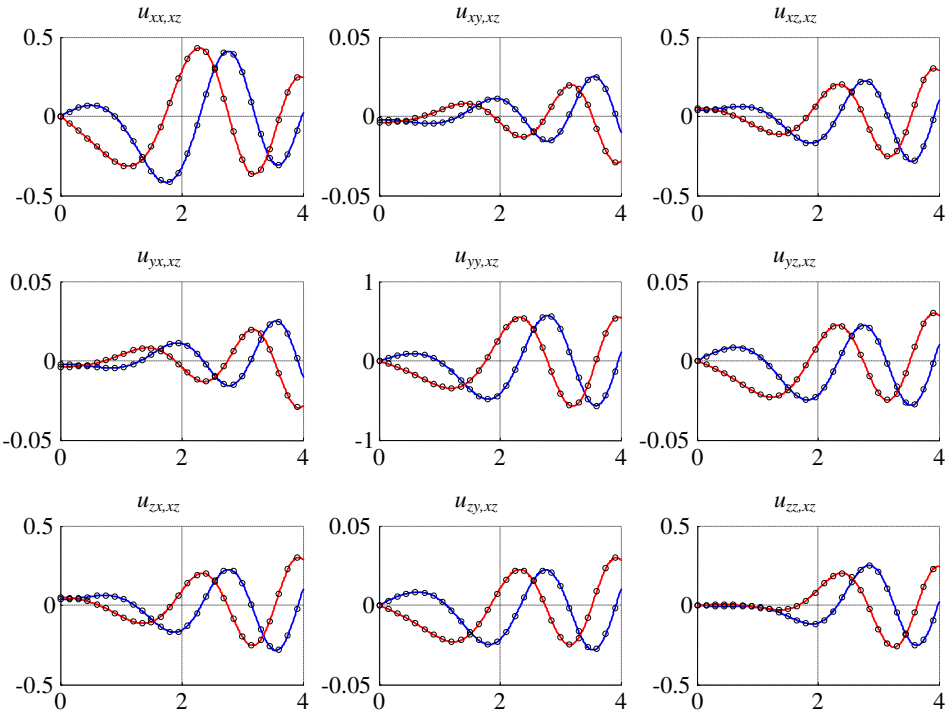

Figure 2.7: Displacement derivatives $u_{\alpha\beta,xz}$. Solid lines = TLM solution (real part — blue; imaginary part — red). Circles = analytical solution

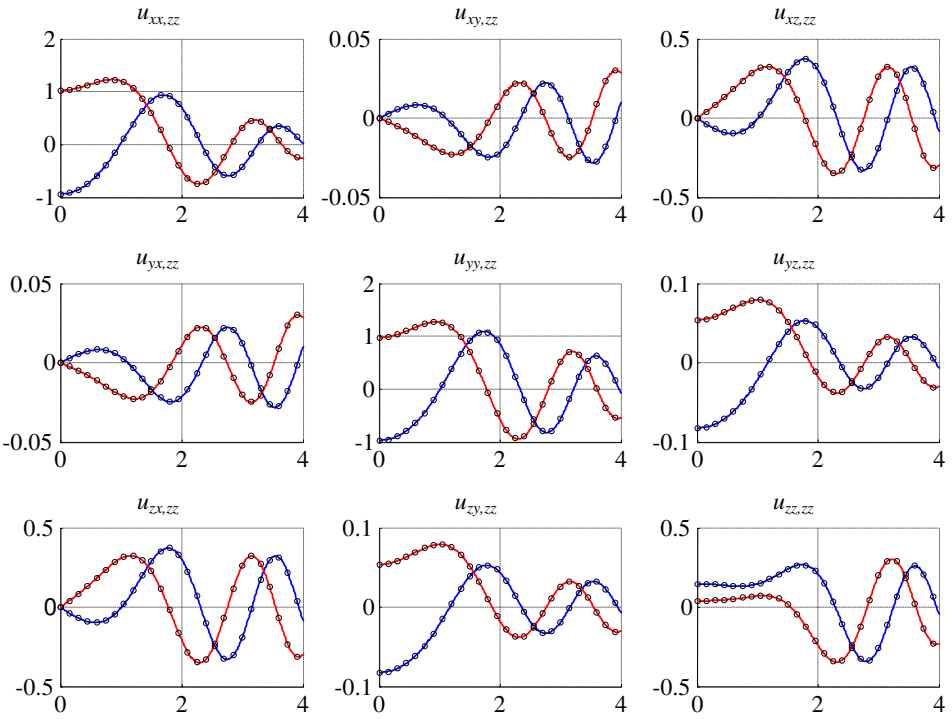

Figure 2.8: Displacement derivatives $u_{\alpha\beta,zz}$. Solid lines = TLM solution (real part — blue; imaginary part — red). Circles = analytical solution

2.6 Modeling unbounded domains

The TLM is a semi-discrete numerical technique for the analysis of wave motion in layered media and relies on a finite element discretization in the direction of layering. Due to the discrete character of the TLM, by itself the analyses are limited to bounded domains. Nevertheless, in the mid eighties, the *Paraxial Boundaries* (PB) were coupled to the TLM to allow the simulation of infinite domains (Seale and Kausel, 1989). Very briefly, the PB for the TLM can be obtained by expanding the stiffness matrices (Kausel and Roesset, 1981) in a Taylor series in the wavenumber and retaining only the first three terms. Hence, this technique works very well for small wavenumbers and not so well for higher wavenumbers. In other words, waves propagating vertically or almost vertically are mostly absorbed when they reach the paraxial boundary while waves propagating with a considerable horizontal component are mostly reflected. For this reason, the PBs are usually augmented with buffer (elastic) layers that are thick enough so that the component of waves that is reflected at the PB returns to the region of interest at a horizontal coordinate larger than the maximum distance of interest. Explicit expressions for the PB matrices can be found in the thesis of Park (Park, 2002, p. 284 for SH waves and p. 289 for the SVP waves) while comments and considerations about their stability can be found in the works by Kausel (1988, 1992).

More recently, Barbosa et al. (2012) successfully coupled the *Perfectly Matched Layer* (PML) to the TLM, resulting in a more efficient technique to model unbounded domains. The PML is a numerical technique used for purposes similar to those of absorbing or transmitting boundaries, namely to suppress undesirable echoes and reflections of waves in infinite media modeled with discrete finite systems. The technique was introduced in the nineties by Berenger (1994), who developed and coupled it to the time-domain finite differences method for the analysis of electromagnetic fields. Initially, the formulation of the PML followed the split-field approach, in which the systems of equations are solved both for displacements and stresses, but later new formulations for the PML were derived, namely by considering the PML as an equivalent anisotropic material (Gedney, 1996; Teixeira and Chew, 1998) or by stretching the coordinates to the complex space (Chew and Weedon, 1994; Hugonin and Lalanne, 2005). The PML has also been applied to elastodynamic problems, both in time and frequency domains (Basu and Chopra, 2003; Basu and Chopra, 2004; Basu, 2009; Harari and Albocher, 2006). A good literature review on the subject can be found in (Kucukcoban and Kallivokas, 2010).

In the work (Barbosa et al., 2012), the PML is formulated based on the coordinate stretching approach. This approach consists in stretching the real space to a complex space by means of position-dependent complex-valued scaling functions, which begin with unit values at the interface or horizon delimiting the elastic region and then attain progressively larger complex values with the distance from this horizon, which causes the waves within the PML to attenuate exponentially (Johnson, 2008). Since there is no impedance contrast at the PML boundary, no reflections take place no matter what the angle of propagation of the waves entering the PML is. In the following subsections, it is shown how the coordinate stretching allows the simulation of infinite domains and then the PML is coupled to the TLM.

2.6.1 Coordinate stretching

Consider a plane wave travelling at an angle θ with the vertical direction (z) in a medium whose wave speed is C. This wave has the form

$$u(x,z,t) = A\mathrm{e}^{\mathrm{i}\left(\omega t - x\frac{\omega}{C}\sin\theta - z\frac{\omega}{C}\cos\theta\right)} \tag{2.89}$$

No restriction is made regarding the vertical coordinate, and thus admit that this coordinate may assume the complex values, and denote it by $\overline{z}$. Equation (2.89) is still valid but now z must be replaced by $\overline{z}$. Assume also that the imaginary part of $\overline{z}$ depends on the depth (real part) and define $\overline{z}$ as

$$\overline{z} = z - \mathrm{i}\Psi(z) \tag{2.90}$$

where $\Psi(z)$ is a function yet to be determined. After replacing equation (2.90) into (2.89), the latter becomes

$$u(x,\overline{z},t) = A\mathrm{e}^{\mathrm{i}\left(\omega t - x\frac{\omega}{C}\sin\theta - z\frac{\omega}{C}\cos\theta\right)}\mathrm{e}^{-\Psi(z)\frac{\omega}{C}\cos\theta} \tag{2.91}$$

The aim is to attenuate the waves that enter a finite PML region defined by $H > z > 0$ (Figure 2.9). For waves that propagate in the positive z direction ($\cos\theta_{\mathrm{pos}} > 0$), for the amplitude of the waves to decay as z increases, the exponential term $\exp\left(-\omega\cos\theta\,\Psi(z)/C\right)$ must decrease and consequently $\Psi(z)$ must increase with z. Similarly, for waves that propagate in the negative z direction ($\cos\theta_{\mathrm{neg}} < 0$), for their amplitude to decay in the direction of propagation, $\Psi(z)$ must obey the same rule. A possible choice for $\Psi(z)$ that respects the established rule is

$$\Psi(z) = \int_0^z \psi(\zeta)\,d\zeta \tag{2.92}$$

where $\psi(z)$ is an always positive stretching function.

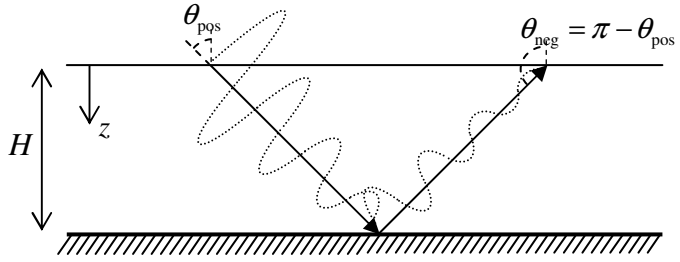

Figure 2.9: Propagation of a wave inside the PML region

In theory, $\psi(z)$ might assume any shape as long as $\Psi(0) < \Psi(H)$ (Bienstman and Baets, 2002). However, once the domain is discretized so that the differential equations can be solved, spurious reflections occur due to changes in $\psi(z)$ and therefore it is convenient that this function changes smoothly with z. A commonly used stretching function is (Basu and Chopra, 2003)

$$\psi(z) = \frac{\omega_0}{\omega}\left(\frac{z}{H}\right)^m \tag{2.93}$$

where ω_0 controls the level of absorption of the wave and $m > 0$ defines the rate of variation of the stretching function within the PML (Note: in section 2.2 the parameter m has a different meaning). This implies

$$\Psi(z) = \frac{\omega_0 H}{\omega(m+1)}\left(\frac{z}{H}\right)^{m+1} \tag{2.94}$$

which can be written compactly as

$$\Psi(z) = \Omega H \zeta^{m+1} \tag{2.95}$$

where

$$\Omega = \frac{\omega_0}{\omega(m+1)} \qquad \zeta = \frac{z}{H} \tag{2.96}$$

The stretched vertical coordinate then simplifies to

$$\bar{z} = z\left(1 - \mathrm{i}\,\Omega\zeta^m\right) \tag{2.97}$$

which implies a total complex depth $\bar{H} = H\left[1 - \mathrm{i}\,\Omega\right]$.

Consider now a plane wave traveling at an angle θ with respect to the vertical direction z (Figure 2.9). In the stretched space, this wave can be expressed as

$$\begin{aligned} u(x,\bar{z},t) &= A\,\mathrm{e}^{\mathrm{i}\left(\omega t - x\frac{\omega}{C}\sin\theta - \bar{z}\frac{\omega}{C}\cos\theta\right)} \\ &= A\,\mathrm{e}^{\mathrm{i}\left(\omega t - x\frac{\omega}{C}\sin\theta - z\frac{\omega}{C}\cos\theta\right)}\,\mathrm{e}^{-\frac{\omega}{C}\cos\theta\,\Psi(z)} \end{aligned} \tag{2.98}$$

When the wave reaches the bottom of the PML and is reflected, its amplitude is $A\exp\left(-\omega\cos\theta\,\Psi(H)/C\right) = A\exp\left(-\omega\cos\theta\,\Omega H/C\right)$. When the wave reaches again the free surface of the PML, its amplitude is $A\exp\left(-2\omega\cos\theta\,\Omega H/C\right)$. Hence, the total roundtrip decay Δ of the wave is

$$\Delta = \mathrm{e}^{-2\omega\Omega\frac{H}{C}\cos\theta} \tag{2.99}$$

Accounting for the relation between the wave velocity, frequency and wavelength ($\lambda = 2\pi C/\omega$) and defining the ratio $\eta = H/\lambda$, then equation (2.99) is equivalent to

$$\Delta = \mathrm{e}^{-4\pi\Omega\eta\cos\theta} \tag{2.100}$$

Clearly, as long as the thickness of the layer is made proportional to the wavelength (i.e. η is chosen as a constant), the effectiveness of the PML for a given angle of incidence depends solely on the dimensionless parameter Ω. On the other hand, a ray entering the PML at x_0 with an inclination θ returns to the surface at a distance $r = x - x_0 = 2H\tan\theta$ from the point of entrance, i.e.

$$\frac{r}{\lambda} = 2\eta\tan\theta \tag{2.101}$$

Equations (2.100) and (2.101) indicate that the higher the horizontal range of interest is, the higher the value needed for Ω, η, or both.

The suitability of PMLs for the simulation of a half-space is examined next. For that purpose, consider an elastic half-space with shear modulus $G=1$ and shear wave velocity $C_s=1$ excited by an in-plane (SH) line source acting at the depth z_s with frequency $\omega=2\pi$. For an elastic half-space, the exact solution for the displacement observed at a receiver at range x and depth z_r is (Kausel, 2006; p. 69)

$$u_{yy}=\frac{1}{2\mathrm{i}G}\left[H_0^{(2)}\left(k_s r_1\right)+H_0^{(2)}\left(k_s r_2\right)\right] \qquad k=\frac{\omega}{C_s}=\frac{2\pi}{\lambda}, \quad r_{1,2}=\sqrt{x^2+\left(z_s\mp z_r\right)^2} \tag{2.102}$$

By contrast, the PML admits an exact solution based on an expansion in terms of the normal modes of the stratum, as given in Kausel (2006; p. 130). Accounting for the fact that the vertical dimensions have been stretched, the solution is

$$u_{yy}\left(x,\omega\right)=\frac{1}{\mathrm{i}G}\sum_{j=1}^{\infty}\phi_j\left(\overline{z}_s\right)\phi_j\left(\overline{z}_r\right)\frac{\mathrm{e}^{-\mathrm{i}\,k_j|x|}}{k_j\overline{H}} \tag{2.103}$$

$$k_j=\sqrt{\left(\frac{\omega}{C_s}\right)^2-\left(\frac{\pi\left(2j-1\right)}{2\overline{H}}\right)^2} \qquad \mathrm{Im}\,k_j<0 \tag{2.104}$$

$$\phi_j\left(\overline{z}\right)=\cos\left(\frac{\pi\left(2j-1\right)}{2}\frac{\overline{z}}{\overline{H}}\right) \tag{2.105}$$

where $\overline{z}_s$ and $\overline{z}_r$ are the stretched depths of the source and of the receiver, respectively, and $\overline{H}$ is the total stretched depth. With $\lambda_s=C_s/f=1$, and choosing for the PML the parameters $\eta=H/\lambda_s=\frac{1}{2}$, a maximum range $r\le x_{\max}=5\lambda_s=5$, a roundtrip decay of two orders of magnitude, i.e., $\Delta=10^{-2}$, and $m=2$, the following can be inferred

$$\tan\theta_{\max}=\frac{x_{\max}}{2\eta\lambda_s}=\frac{5}{2\times\frac{1}{2}}=5 \qquad \Rightarrow \theta_{\max}=78.7^\circ \qquad \Rightarrow \qquad \cos\theta_{\max}=0.196$$

$$\Omega=\frac{\ln\Delta^{-1}}{4\pi\eta\cos\theta_{\max}}=\frac{\ln 100}{4\pi\frac{1}{2}\times 0.196}=3.74$$

$$\overline{H}=H-\mathrm{i}\,\Psi\left(H\right)=H\left[1-\mathrm{i}\,\Omega\right]=0.5\times\left[1-3.74\mathrm{i}\right]=0.5-1.87\mathrm{i}$$

This data is used to construct a PML that is subjected to a SH line source at its surface $\overline{z}_s=0$ and then equations (2.103) to (2.105) are used to compute the displacements for receivers at variable positions on the surface $\overline{z}_r=0$. Figure 2.10 compares the displacements thus computed against the displacements on the surface of the half-space predicted by equation (2.102). As can be seen, both the real and imaginary parts of the displacements agree perfectly until a range of about $x=8\lambda_s$ is exceeded. On the other hand, Figure 2.11 shows the ratio between the absolute values of the displacements obtained by the two approaches. This figure confirms that until the distance $x_{\max}=5\lambda_s$, the ratio of amplitudes is virtually one, with an error less than 1%. Then again, at the distance $x=8\lambda_s$ the error has grown to approximately 5%, and thereafter it increases substantially. This shows that with the chosen parameters and as seen from its surface, the PML behaves essentially as an elastic half-space, yet is a perfect absorber of waves only up to some maximum distance which depends on the parameters chosen.

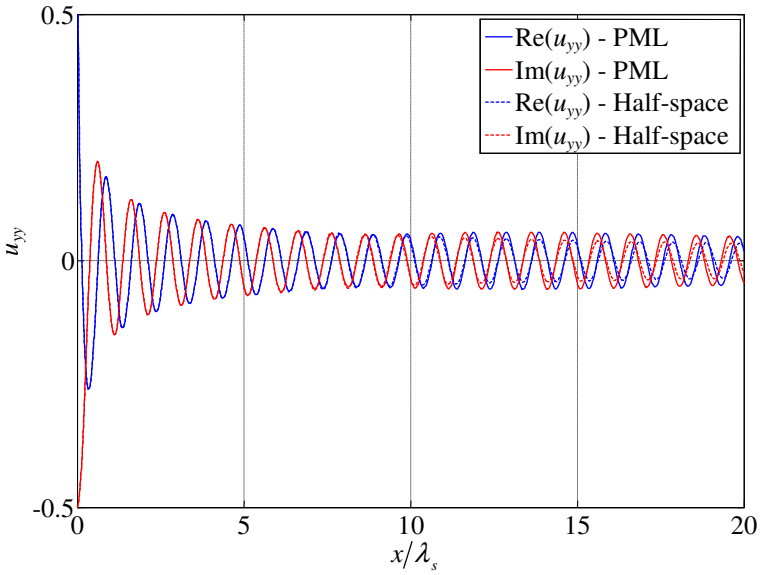

Figure 2.10: Displacements of the PML vs displacements of half-space

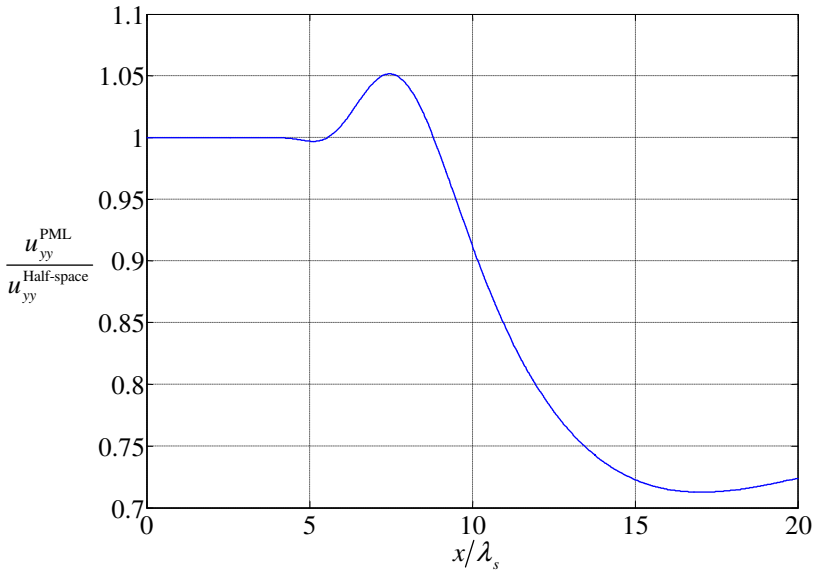

Figure 2.11: Ratio of displacements at surface of the PML and those of the half-space

2.6.2 PMLs for the TLM

In the context of elastodynamics, two different waves with different wave speeds must be accounted for: the shear wave with speed C_s and the dilatational wave with speed C_p. If the waves are considered separately, the concept of the PML as explained in the previous subsection is still valid, but now each wave has its own rate of attenuation inside the PML.

In the following, a PML is constructed by means of a stack of thin-layers in the context of the TLM. As shown in a previous work (Kausel and Barbosa, 2011), a very simple way to construct a PML with finite elements is to directly stretch the linear dimensions of the elements in accordance with their horizontal and vertical position within the PML. In the

TLM, this recipe translates into replacing the thicknesses of the thin-layers composing a PML by their complex counterparts, which depend on the location (i.e. depth) of the thin-layers within the PML. Thus, if it is assumed that the PML is divided into N equal thin-layers, then the stretched thickness $\overline{h}_j$ of the j^{th} thin-layer is

$$\overline{h}_j = \overline{z}_j - \overline{z}_{j-1} = H\left\{\frac{1}{N} - \mathrm{i}\,\Omega\left[\left(\frac{j}{N}\right)^{m+1} - \left(\frac{j-1}{N}\right)^{m+1}\right]\right\} \tag{2.106}$$

where $1 \le j \le N$, with j increasing downwards. On the other hand, in the TLM, each of the thin-layers is characterized by elementary layer matrices $\mathbf{A}_{\alpha j}, \mathbf{G}_{\alpha j}, \mathbf{M}_{\alpha j}, \mathbf{B}_{xzj}$ —see equations (2.32), (2.35) and (2.39)— two of which are proportional to the sub-layer thickness, while another one is inversely proportional to that thickness, i.e.

$$\mathbf{A}_{\alpha j} = h_j\left[\ddot{\cdot}\right]; \qquad \mathbf{G}_{\alpha j} = h_j^{-1}\left[\ddot{\cdot}\right]; \qquad \mathbf{M}_{\alpha j} = h_j\left[\ddot{\cdot}\right] \tag{2.107}$$

Thus, in order to obtain the layer matrices for the PML, it suffices to substitute $\overline{h}_j$ in lieu of h_j. Thereafter, the layer matrices are overlapped as usual, which leads to the block-tridiagonal system matrices and the eigenvalue problems (2.39).

The parameters for the PML (m, η and Ω) can be selected following the strategy explained in the previous subsection. However, since with the TLM the domain is discretized, the variation of the complex thicknesses of the sub-layers originates spurious reflections that influence the results. On one hand, these reflections become larger as Ω increases, and so thinner discretizations are needed for larger values of Ω. On the other hand, when Ω is not large enough, the waves are not attenuated sufficiently as they travel through the PML. This can be compensated with thicker PMLs, which also causes the increase of the number of degrees of freedom. In this way, it is important to find a good compromise between the different parameters of the PML so that they minimize the number of degrees of freedom as much as possible. The following values are suggested as optimal parameters for the PMLs (Barbosa et al., 2012)

$$m = 2 \qquad \eta = \frac{H}{\lambda_s} = \sqrt[3]{\tfrac{1}{12}\, x_{\max} / \lambda_s} \ge 1 \qquad nN = 10\eta \qquad \Omega = 4\eta \tag{2.108}$$

In this equation, N is the number of thin-layers in the PML, n is the expansion order used in the discretization (the same as $m-1$ in section 2.2) and $x_{\max}$ is the maximum horizontal distance of interest.

Next, the PML technique is compared with Paraxial Boundaries, which have already been used to solve some examples in the previous sections. For that purpose, consider a full-space ($\rho = 1$, $G = 1$, $\nu = 0.25$ and $\xi_s = \xi_p = 0$) and submit it to a vertical 2D line load ($k_y = 0$) with frequency $\omega = 2\pi$. For the PML approach the full-space is modeled using two PMLs (one upper and one lower), while for the PB approach the full-space is modeled considering two buffer layers plus paraxial boundaries, having the buffer layers the same depths and discretizations as the PMLs. The parameters chosen for the PML are $m = 2$, $\eta = 2$, $\Omega = 8$ and $N = 10$, having the thin-layers quadratic expansion ($n = 2$). Figure 2.12 plots the relative errors of the two approaches, defined as the percent deviation of the absolute values of the vertical displacements at the depth of the source when compared to those of the exact solution. Clearly, the PML approach is substantially more accurate than the PB approach,

with errors below 1% up to distances $x = 20\lambda_s$, while the errors in the second approach exceed 10% even at a distance lower than $x = 4\lambda_s$, and it becomes intolerable at larger distances. It is then clear that the PML approach outperforms the PB approach by a vast margin.

The example shown in this subsection considers a 2D model. For 2.5D models, the PML technique has been used to solve the examples of the previous sections, having the PMLs only one tenth of the thickness of the buffer layers. The results obtained are similar to the results shown in Figures 2.2-2.8, which confirms that the PML is also applicable in the 2.5D case.

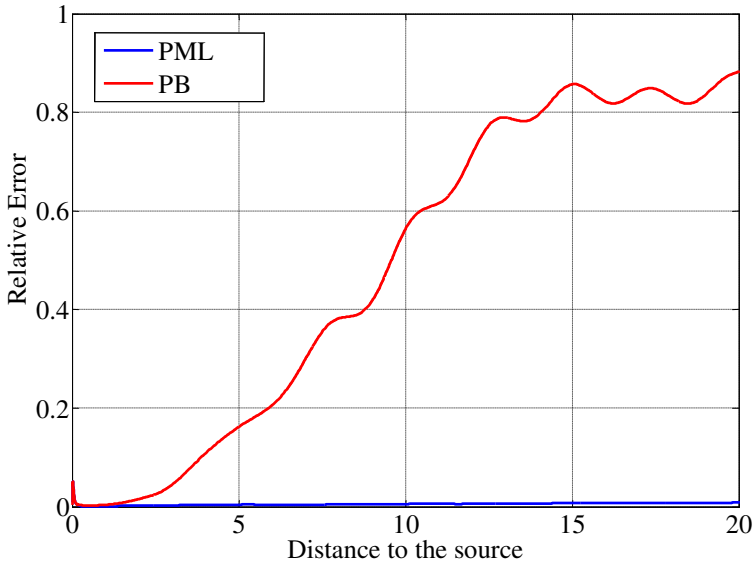

Figure 2.12: PML vs. Paraxial boundaries

2.6.3 Example of a layered domain

Up to this point all examples have been solved with the intent to validate the procedure and therefore only models for homogeneous full-spaces are considered, since only for these cases the fundamental solutions are available in closed form expressions. In this subsection, the example of a layered half-space is considered.

Layered half-spaces differ from homogeneous full-spaces due to the presence of surface waves, which result from the interaction between the body waves at the surface between two different materials. For the case of elastic half-spaces, only one surface wave exists, the Rayleigh wave, and that wave is not dispersive, i.e., its velocity of propagation does not depend on the frequency of excitation. For the case of layered domains, depending on the frequency considered, none or more than one surface waves may exist. Because they are frequency dependent, these waves are called dispersive waves. Theoretical works on propagation of waves in layered domains can be found in (Achenbach, 1973; Erigen and Suhubi, 1975; Ewing et al., 1957). As for numerical works, Luco and Apsel (1983) and Apsel and Luco (1983) treat fixed loads while De Barros and Luco (1994) treat moving loads.

The layered system considered in this subsection consists of a soft layer resting on a stiffer half-space. The material properties of the layer and half-space are

Layer: $C_s = 0.5,\ \rho = 1.0, \nu = 0.30,\ \xi_s = \xi_p = 0.005,\ H = 1$

Half-space: $C_s = 1.0,\ \rho = 1.0,\ \nu = 0.25,\ \xi_s = \xi_p = 0.005$

The layer is modeled by means of 100 thin-layers of quadratic expansion, while the half-space is modeled using a PML whose parameters are $\eta = 2$, $\Omega = 6.67$ and $m = 2$. The PML is divided into 10 thin-layers of quadratic expansion.

Eigenvalues of the layered system

First, the solutions of the Rayleigh eigenvalue problem (2.39) for the frequencies $f = 0.1\,\text{Hz}$, $f = 0.2\,\text{Hz}$, $f = 1\,\text{Hz}$ and $f = 10\,\text{Hz}$ are shown. Figure 2.13 plots the eigenvalues obtained with the TLM and the eigenvalues of the exact formulation (stiffness matrices) obtained via search techniques.

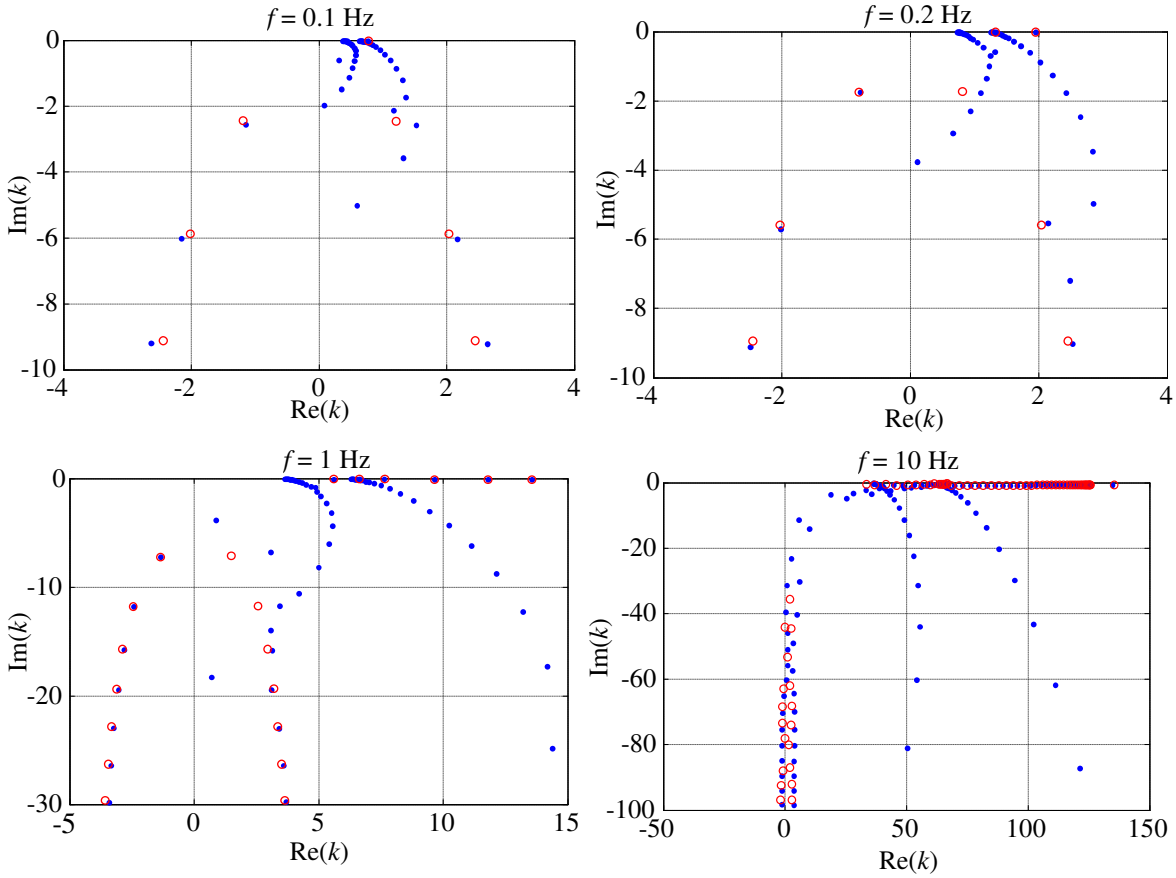

Figure 2.13: Eigenvalues of the layered system obtain with the TLM (blue dots) and via search techniques (red circles)

Even though the agreement between the eigenvalues obtained with the two distinct approaches does not look very good, when the displacements are calculated by means of modal combination, the obtained results are quite good (as seen next). In Figure 2.13, it can be observed that the number of propagating modes (to which correspond real, or nearly real, eigenvalues) increases with the frequency. Also, one can distinguish the existence of two branches in the TLM modes that do not exist in the exact formulation. These modes are named Berenger modes and they are mathematical artifacts that are a consequence of the stretching of coordinates. They have been detected in some works related to electromagnetic waves (Bienstman and Baets, 2002; Derudder et al., 2001; Rogier and De Zutter, 2001;

Bienstman et al., 2001), but in these works, only one branch exists. In the present work, the two branches are justified by the existence of two different body waves. The branches start at the wavenumbers $k_s = \omega/C_s$ and $k_p = \omega/C_p$ and the number of modes contained in each branch equals the number of degrees of freedom associated with the PML layer.

Vertical displacements due to a vertical line load ($k_y = 0$)

The modes obtained in subsection 2.6.3.1 are now combined in order to obtain the displacements in the interface between the layer and the half-space due to loads at the same elevation. Figures 2.14 and 2.15 plot the displacements for the frequencies $f = 0.2\,\text{Hz}$ and $f = 1\,\text{Hz}$ obtained both with the TLM and with numerical integration on the wavenumbers of the displacements given by the stiffness matrices.

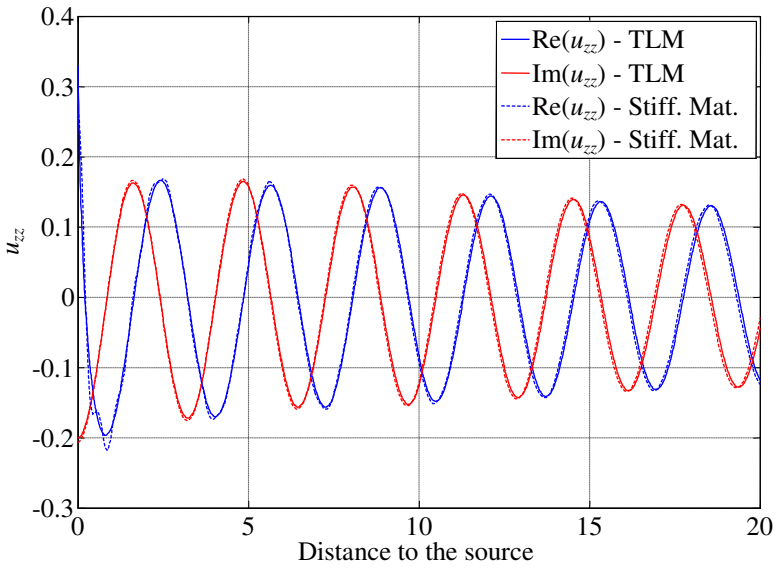

Figure 2.14: Displacements of the layered half-space: TLM vs Stiffness matrices ($f = 0.2\,\text{Hz}$)

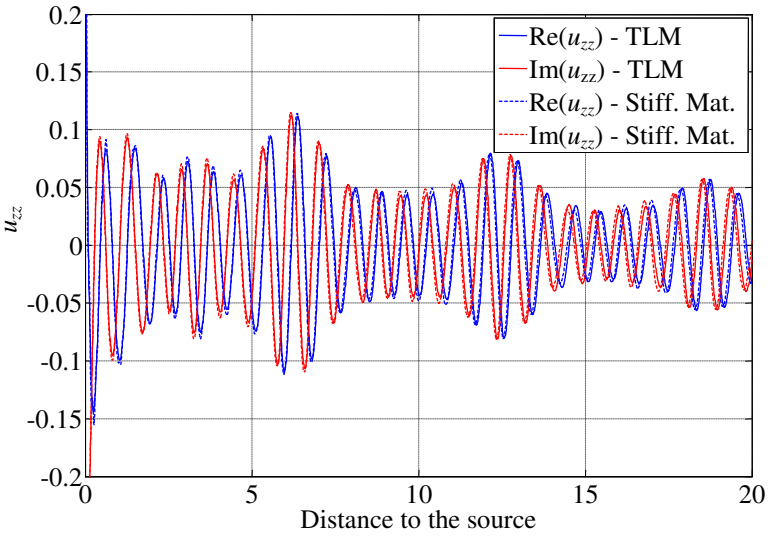

Figure 2.15: Displacements of the layered half-space: TLM vs Stiffness matrices ($f = 1\,\text{Hz}$)

The comparison of the results obtained with the two approaches shows that except for very small shifts, the displacements agree very well. Hence, it is concluded that the PML is accurate in reproducing the behavior of infinitely deep stratified domains.

2.7 Solution of the eigenvalue problems

One of the more time consuming and complex steps in the TLM process is the solution of the eigenvalue problems (2.39). Even though commercial software, like Matlab, contain functions capable of solving both the linear and the quadratic eigenvalue problems with complex matrices (for example, eig and polyeig), these functions do not take advantage of the banded structure of the matrices and therefore become inefficient for the solution of eigenproblems with dimension of just a few hundred. Also, these routines, which are based on the QZ algorithm (Kressner, 2005) and thus based on iterative rotations of the modal basis until convergence, may yield eigenvectors that do not respect entirely the orthogonal conditions (2.41) due to accumulation of round-of errors, hence introducing errors in the remaining steps of the modal combinations: though rare, this case has been observed when a large number of thin-layers and PMLs are used.

Alternative approaches to the QZ algorithm are the methods based on the Power Method. This family of methods is based on successive matrix-vector multiplication until the direction of the resulting vector has converged to the eigen direction. Several variations exist, namely the Power Method itself, the Inverse Iteration method, in which instead of the matrix-vector multiplication, a system of equations is solved, and the Inverse Iteration with Rayleigh Shift method (Shit and Invert method), in which the eigenvalues are shifted in order to speed up convergence (Saad, 1992). In this family of methods, the eigenvectors are found one by one, being then deflated from the eigen base (remove them from the modal spectrum) in order to avoid convergence to the same pair.

Projection methods can also be employed: the most common ones are the Lanczos method (or Arnoldi method, for non-hermitian matrices) and the Locally Optimal Preconditionated Conjugated Gradients method. These projection methods iterate with a group of vectors instead of a single vector and are used to extract a small spectrum range, not the full spectrum of eigenpairs (Saad, 1992).

Because the complete spectrum of the system of matrices is needed, the Inverse Iteration with Rayleigh Shift is chosen for the solution of the eigenvalue problems (2.39). In the next subsections, it is explained how to apply this method taking into account the special structure of the TLM matrices.

2.7.1 Eigenvalue problem for SH waves

The linear eigenvalue problem to be solved has the form

$$\left(k_j^2\mathbf{A}+\mathbf{C}\right)\mathbf{v}_j=\mathbf{0} \tag{2.109}$$

where matrices $\mathbf{A}$ and $\mathbf{C}$ are complex, symmetric and banded. The eigenvalues k_j and eigenvector $\mathbf{v}_j$ are also complex. The bandwidth of the matrices is 2 if the thin-layers are of linear expansion and is 3 if the thin-layers are of quadratic expansion. The eigenvalue problem admits $2N$ solutions, being N the dimension of the matrices, and if the pair $\left(k_j,\mathbf{v}_j\right)$ is a solution of (2.109), then the pair $\left(-k_j,\mathbf{v}_j\right)$ is also a solution of (2.109). In this way, only

half of the spectrum of the system needs to be computed. Taking into account the orthogonal conditions expressed in the second row of eq. (2.41), the Inverse Iteration with Rayleigh Shift method applied to the linear pencil (2.109) results in the algorithm described in Table 2.7.

Table 2.7: Algorithm for the solution of the linear eigenvalue problem

$\mathbf{v}_j = \text{rand}(N)$	Initial guess
$\mathbf{v}_j = \mathbf{v}_j - \mathbf{v}_j^{\mathrm{T}}\mathbf{A}\mathbf{v}_i$	Normalize the initial guess against previously found eigenvectors ($i = 1,2,\ldots j-1$)
$\mathbf{w}_j = \mathbf{A}\mathbf{v}_j$	Auxiliary vector
$k_j = \sqrt{-\dfrac{\mathbf{v}_j^{\mathrm{T}}\mathbf{C}\mathbf{v}_j}{\mathbf{v}_j^{\mathrm{T}}\mathbf{w}_j}}$	Rayleigh quotient
Iterate (until Rayleigh quotient has converged)	
$\mathbf{E} = \mathbf{A}k_j^2 + \mathbf{C}$	From shifted matrix
$\mathbf{v}_j = -\mathbf{E}^{-1}\mathbf{w}_j$	New approximation of eigenvector
$\mathbf{v}_j = \mathbf{v}_j - \mathbf{v}_j^{\mathrm{T}}\mathbf{A}\mathbf{v}_i$	Normalize against previously found eigenvectors (if $k_j \approx k_i$, $i = 1,2,\ldots j-1$)
$k_j = \sqrt{k_j^2 + \dfrac{\mathbf{v}_j^{\mathrm{T}}\mathbf{w}_j}{\mathbf{v}_j^{\mathrm{T}}\mathbf{A}\mathbf{v}_j}}$	Update the Rayleigh quotient
$\mathbf{w}_j = \mathbf{A}\mathbf{v}_j$	Auxiliary vector
$\begin{cases} \delta = \sqrt{\mathbf{v}_j^{\mathrm{T}}\mathbf{w}_j} \\ \mathbf{v}_j = \mathbf{v}_j / \delta \\ \mathbf{w}_j = \mathbf{w}_j / \delta \end{cases}$	Normalize the approximation

The normalization step (against previously found eigenpairs) is forced at the beginning of the procedure and during the iterative procedure in order to avoid finding the same solution twice. Notice however that at the iteration loop, the normalization is only performed against the eigenvectors whose associated eigenvalue approximates the current Rayleigh quotient.

Another important aspect of the algorithm is the solution of the system of equations $\mathbf{v}_j = -\mathbf{E}^{-1}\mathbf{w}_j$. Because matrices $\mathbf{A}$ and $\mathbf{C}$ are symmetric and banded, matrix $\mathbf{E}$ contains similar structure. Hence, the application of Gaussian elimination to this system of equations is very efficient.

In opposition to the Power method or the Inverse Iteration method, the chosen approach requires the calculation and factorization of matrix $\mathbf{E}$ at every iteration. Nevertheless, because the cost of factorization of the matrix is very low (due to its slim banded structure), because the convergence is greatly improved (due to the application of the Rayleigh shift), and

because the normalization (deflation) is imposed only against the pairs that are in close proximity, then the Inverse Iteration with Rayleigh Shift method turns out to be the most efficient tool among the three mentioned methods.

One last comment: the speed of convergence depends on the quality of the initial guess of $\mathbf{v}_j$. In this work, the initial guess is a random value. However, because the eigenvalue problem needs to be solved for different values of ω ($\mathbf{C}=\mathbf{G}-\omega^2\mathbf{M}$), if two successive frequencies are close enough to each other ($\omega_2=\omega_1+\mathrm{d}\omega$), one can use the eigenvectors computed for ω_1 as initial guesses for the eigenvectors of ω_2. This strategy shall improve the convergence of the procedure (examples have shown that the average number of iteration per eigenpair reduces from 7-8 to 2-3; this strategy has not been used in this work due to complications that occur when two eigenvalues are too close from each other, and as a consequence the solutions jump from one branch to another).

2.7.2 Eigenvalue problem for SVP waves

The first eigenvalue problem of eq. (2.39) is equivalent to

$$\left(k_j^2\mathbf{A}+k_j\mathbf{B}+\mathbf{C}\right)\mathbf{v}_j=\mathbf{0} \tag{2.110}$$

where

$$\mathbf{A}=\begin{bmatrix}\mathbf{A}_x & \mathbf{O}\\ \mathbf{O} & \mathbf{A}_z\end{bmatrix} \qquad \mathbf{B}=\begin{bmatrix}\mathbf{O} & \mathbf{B}_{xz}\\ \mathbf{B}_{xz}^T & \mathbf{O}\end{bmatrix} \qquad \mathbf{C}=\begin{bmatrix}\mathbf{G}_x-\omega^2\mathbf{M}_x & \mathbf{O}\\ \mathbf{O} & \mathbf{G}_z-\omega^2\mathbf{M}_z\end{bmatrix}$$

$$v_v=\begin{bmatrix}\boldsymbol{\phi}_{xj}\\ \boldsymbol{\phi}_{zj}\end{bmatrix} \qquad k_{Rj}=k_j$$

Taking into consideration the original order of the degrees of freedom instead of the order organized by direction (see section 2.3), matrices $\mathbf{A}$, $\mathbf{B}$ and $\mathbf{C}$ result symmetric and banded, being the bandwidth 4 if the thin-layers are of linear expansion or 6 if the thin-layers are of quadratic expansion.

System (2.110) can be further expanded and written as

$$\begin{bmatrix}\mathbf{B} & \mathbf{C}\\ \mathbf{C} & \mathbf{O}\end{bmatrix}\begin{bmatrix}k_j\mathbf{v}_j\\ \mathbf{v}_j\end{bmatrix}=k_j\begin{bmatrix}-\mathbf{A} & \mathbf{O}\\ \mathbf{O} & \mathbf{C}\end{bmatrix}\begin{bmatrix}k_j\mathbf{v}_j\\ \mathbf{v}_j\end{bmatrix} \tag{2.111}$$

and so it can be easily concluded that the eigenvalue problem has $2N$ solutions, being N the dimension of matrices $\mathbf{A}$, $\mathbf{B}$ and $\mathbf{C}$. Also, due to the symmetric properties of these matrices and due to the special structure of matrix $\mathbf{B}$, if the pair $\left(k_j,\mathbf{v}_j\right)$ is a solution of (2.110), then the pair $\left(-k_j,\bar{\mathbf{v}}_j\right)$ is also a solution. The modified eigenvector $\bar{\mathbf{v}}_j$ coincides with $\mathbf{v}_j$, except for the components associated with the z direction, which have their sign reversed.

Because the quadratic eigenvalue problem is slightly more complex than the linear one, some explanations are needed before presenting the solution procedure. Of equation (2.111), drop the modal index j and consider a general iteration (say, the l^{th} iteration) of the Inverse Iteration with Rayleigh Shift:

$$\begin{bmatrix} k_l\mathbf{A}+\mathbf{B} & \mathbf{C} \\ \mathbf{C} & -k_l\mathbf{C} \end{bmatrix}\begin{bmatrix} \mathbf{u}_{l+1} \\ \mathbf{v}_{l+1} \end{bmatrix}=\begin{bmatrix} -\mathbf{A} & \mathbf{O} \\ \mathbf{O} & \mathbf{C} \end{bmatrix}\begin{bmatrix} \mathbf{u}_l \\ \mathbf{v}_l \end{bmatrix} \tag{2.112}$$

Handling simultaneously both rows of the system (2.112), it is possible to obtain

$$\begin{cases} \mathbf{v}_{l+1}=\dfrac{\mathbf{u}_{l+1}-\mathbf{v}_l}{k_l} \\ \left(k_l^2\mathbf{A}+k_l\mathbf{B}+\mathbf{C}\right)\mathbf{u}_{l+1}=\mathbf{C}\mathbf{v}_l-k_l\mathbf{A}\mathbf{u}_l \end{cases} \tag{2.113}$$

Notice that at each iteration, it is needed to solve a system of equations with dimension N and not $2N$, as could be suggested by equation (2.112).

As for the Rayleigh quotient, its value is given by

$$k_l=\frac{\begin{bmatrix} \mathbf{u}_l^{\mathrm{T}} & \mathbf{v}_l^{\mathrm{T}} \end{bmatrix}\begin{bmatrix} \mathbf{B} & \mathbf{C} \\ \mathbf{C} & \mathbf{O} \end{bmatrix}\begin{bmatrix} \mathbf{u}_l \\ \mathbf{v}_l \end{bmatrix}}{\begin{bmatrix} \mathbf{u}_l^{\mathrm{T}} & \mathbf{v}_l^{\mathrm{T}} \end{bmatrix}\begin{bmatrix} -\mathbf{A} & \mathbf{O} \\ \mathbf{O} & \mathbf{C} \end{bmatrix}\begin{bmatrix} \mathbf{u}_l \\ \mathbf{v}_l \end{bmatrix}}=\frac{\mathbf{u}_l^{\mathrm{T}}\mathbf{B}\mathbf{u}_l+2\mathbf{u}_l^{\mathrm{T}}\mathbf{C}\mathbf{v}_l}{\mathbf{v}_l^{\mathrm{T}}\mathbf{C}\mathbf{v}_l-\mathbf{u}_l^{\mathrm{T}}\mathbf{A}\mathbf{u}_l} \tag{2.114}$$

However, in this work, instead of calculating the Rayleigh quotient according to (2.114), the quotient is updated in every iteration according to the recursive formula (Waas, 1972)

$$k_{l+1}=k_l+\frac{\mathbf{u}_{l+1}^{\mathrm{T}}\mathbf{A}\mathbf{u}_l-\mathbf{v}_{l+1}^{\mathrm{T}}\mathbf{C}\mathbf{v}_l}{\mathbf{u}_{l+1}^{\mathrm{T}}\mathbf{A}\mathbf{u}_{l+1}-\mathbf{v}_{l+1}^{\mathrm{T}}\mathbf{C}\mathbf{v}_{l+1}} \tag{2.115}$$

Equation (2.115) works as well as eq. (2.114), but is more convenient in terms of computational resources.

The orthogonality between a iteration of the j^{th} eigenvector and an eigenvector already converged (the i^{th} eigenvector) is imposed through

$$\begin{bmatrix} \mathbf{u}_j \\ \mathbf{v}_j \end{bmatrix}=\begin{bmatrix} \mathbf{u}_j \\ \mathbf{v}_j \end{bmatrix}-\left(\mathbf{v}_j^{\mathrm{T}}\mathbf{C}\mathbf{v}_i-k_i\mathbf{u}_j^{\mathrm{T}}\mathbf{A}\mathbf{v}_i\right)\begin{bmatrix} k_i\mathbf{v}_i \\ \mathbf{v}_i \end{bmatrix}-\left(\mathbf{v}_j^{\mathrm{T}}\mathbf{C}\overline{\mathbf{v}}_i+k_i\mathbf{u}_j^{\mathrm{T}}\mathbf{A}\overline{\mathbf{v}}_i\right)\begin{bmatrix} -k_i\overline{\mathbf{v}}_i \\ \overline{\mathbf{v}}_i \end{bmatrix} \tag{2.116}$$

As can be seen in eq. (2.116), both the eigenvector associated with k_i and the eigenvector associated with $-k_i$ are being deflated.

The algorithm used for the solution of the eigenvalue problem takes into account the major steps described above and is listed in Table 2.8.

Table 2.8: Algorithm for the solution of the quadratic eigenvalue problem

$\mathbf{v}_j = \text{rand}(N)$	Initial guess
$\mathbf{u}_j = \text{rand}(N)$	Initial guess (auxiliary)
Equation (2.116)	Normalize the initial guess against previously found eigenvectors ($i = 1,2,...j-1$)
$\mathbf{w}_j = \mathbf{A}\mathbf{u}_j$	Auxiliary vector
$\mathbf{y}_j = \mathbf{C}\mathbf{v}_j$	Auxiliary vector
$k_j = \dfrac{\mathbf{u}_j^{\mathrm{T}}\mathbf{B}\mathbf{u}_j + 2\mathbf{u}_j^{\mathrm{T}}\mathbf{y}_j}{\mathbf{v}_j^{\mathrm{T}}\mathbf{y}_j - \mathbf{u}_j^{\mathrm{T}}\mathbf{w}_l}$	Rayleigh quotient
Iterate (until Rayleigh quotient has converged)	
$\mathbf{E} = \mathbf{A}k_j^2 + \mathbf{B}k_j + \mathbf{C}$	From shifted matrix
$\mathbf{u}_j = \mathbf{E}^{-1}\left(\mathbf{y}_j - k_j\mathbf{w}_j\right)$	
$\mathbf{v}_j = \left(\mathbf{u}_j - \mathbf{v}_j\right)/k_j$	New approximation of eigenvector
Equation (2.116)	Normalize against previously found eigenvectors (if $k_j \approx k_i$ or $k_j \approx -k_i$, $i = 1,2,..., j-1$)
$k_j = k_j + \dfrac{\mathbf{u}_j^{\mathrm{T}}\mathbf{w}_j - \mathbf{v}_j^{\mathrm{T}}\mathbf{y}_j}{\mathbf{u}_j^{\mathrm{T}}\mathbf{A}\mathbf{u}_j - \mathbf{v}_j^{\mathrm{T}}\mathbf{C}\mathbf{v}_j}$	Update the Rayleigh quotient
$\mathbf{w}_j = \mathbf{A}\mathbf{u}_j$	Auxiliary vector
$\mathbf{y}_j = \mathbf{C}\mathbf{v}_j$	Auxiliary vector
$\begin{cases} \delta = \sqrt{\dfrac{\mathbf{u}_j^{\mathrm{T}}\mathbf{w}_j - \left(\mathbf{u}_j^{T}\mathbf{C}\mathbf{u}_j\right)/k_j^2}{2}} \\ \mathbf{v}_j = \mathbf{v}_j/\delta \\ \mathbf{w}_j = \mathbf{w}_j/\delta \\ \mathbf{y}_j = \mathbf{y}_j/\delta \end{cases}$	Normalize the approximations

2.8 Conclusions

In this chapter, the Thin-Layer Method is introduced as a tool to calculate the response of layered domains (for example, soil) to dynamic loads. The TLM is extended to the 2.5D domain and closed form expressions for the fundamental displacements, derivatives, tractions and stresses are given and validated. It is worth noting that the proposed methodology relies on the solution of two eigenvalue problems that in no way depend on the horizontal wavenumbers k_x and k_y, hence they need to be solved only once for each frequency. The 3D

fundamental solutions obtained with the TLM can be found in other works on the subject (Kausel, 1981).

A new and more efficient procedure, the Perfectly Matched Layer, is proposed for the simulation of infinite domains. The PML is used to solve examples of full-spaces and layered half-spaces and is validated by means of the same examples. This new procedure is much more efficient than the previous one (the paraxial boundaries), and from now on it is recommended that the PB be replaced by the PML.

In the last section of this chapter, efficient algorithms for the solution of the two eigenvalue problems are described.

3. Numerical tools for soil-structure interaction

3.1 Introduction

Soil-structure interaction received a lot of attention during the XXth century. It is an interesting and complex problem, and many works covering a wide range of fields can be found in the literature. The interested reader is referred to the work (Kausel, 2010) for a historical overview on the subject.

For the case of traffic induced vibrations, track and building are coupled through the ground, and so, both in the propagation stage and in the reception stage, the interaction between the soil and the track or the building must be considered. Due to the differences in the typology, the ideal numerical tool to model each of the sub-domains may vary. For example, to model the soil, which is an infinite domain, the Boundary Element Method (BEM) is preferred because it can account for the radiation of waves to the infinity (Dominguez, 1993). On the other hand, the use of the Finite Element Method (FEM) reveals to be more appropriate to model the behavior of buildings and tracks, since these structures are circumscribed and generally irregular. Additionally, in the propagation stage the geometry of the problem can be assumed invariant in the longitudinal direction, and thus a 2.5D formulation is advantageous, while in the reception stage the problem is limited to the structure under analysis and the surrounding environment, and therefore a 3D formulation is more appropriate.

In this work, the propagation stage and the reception stage are decoupled. Hence, the wave field that the track induces in the soil is calculated disregarding the presence of the building in the far field. This simplification has been used by other authors (François, 2008; Fiala et al., 2007) and is valid when the distance between the building and the track is larger than the characteristic wavelengths of the soil, i.e., the simplification is valid for the medium and the high frequency range. Nevertheless, in this work this assumption is also used for the low frequencies.

In the present chapter, the 3D BEM, the 2.5D BEM and the 2.5 D FEM are described.

3.2 3D Boundary Element Method

3.2.1 Introduction

The Boundary Element Method is a discrete numerical procedure that can be used to solve partial differential equations. This procedure relies on the discretization of the boundary of the domain, as opposed to the Finite Element Method, for which the whole domain must be modeled. For this reason, for problems involving very large domains (such as the soil) the BEM becomes advantageous over the FEM as it avoids the discretization of the interior of the domain, which results in a reduced number of degrees of freedom. Another advantage of the BEM is that it deals with the radiation of waves to infinity exactly, contrarily to the FEM, in which special procedures need to be applied at the boundaries of the truncated domain in order to model unbounded domains. As drawbacks, the BEM renders systems of equations which involve fully populated and non-symmetric matrices and requires the knowledge of the

Fundamental Solutions of auxiliary domains, which can be homogeneous full-spaces, half-spaces or layered spaces.

In this work the soil is assumed to be horizontally stratified — in the work of Jones (2010), the importance of the inclination of layers is assessed. For this reason, the more appropriate auxiliary domain is the layered half-space. Using the fundamental solutions of such auxiliary domain, the BEM requires solely the discretization of the surfaces of the soil interacting with the structures. Unfortunately, such fundamental solutions are not known in closed form expressions. An alternative would be to use the full-space fundamental solutions, for which analytical expressions are known. However, when considering such auxiliary domain, the free-surface of the soil and of the interfaces between the different layers that characterize the soil must also be discretized, and that results in a substantial increase of the number of degrees of freedom, which renders the approach less attractive.

Three-dimensional formulations of the BEM can be found in the works of Brebbia and Dominguez (1992) for elastostatic problems and of Dominguez (1993) for elastodynamic problems. For train induced vibration problems, the time domain 3D BEM has been used by Galvín (2007) and O'Brien and Rizos (2005), who considered the fundamental solutions of homogeneous full-spaces, by François (2008), who considered the fundamental solutions of layered half-spaces, and by Bode et al. (2002), who considered the fundamental solutions of homogeneous half-spaces. The frequency domain 3D BEM has been used by Hubert et al. (2001), who considered full-space fundamental solutions, and by Fiala et al. (2007), who considered the layered half-space fundamental solutions. In this work, a frequency domain 3D BEM procedure is coupled to the 3D FEM in order to obtain the response of a structure due to an incoming wave field. In the following section, the 3D BEM is presented.

3.2.2 Integral representation

Consider an elastic body Ω with boundary Γ and two elastodynamic states described by the displacement fields $u_k(\mathbf{x},t)$ and $u_k^*(\mathbf{x},t)$, the initial displacements $u_{0k}(\mathbf{x})$ and $u_{0k}^*(\mathbf{x})$, the initial velocities $v_{0k}(\mathbf{x})$ and $v_{0k}^*(\mathbf{x})$, the body forces $\rho b_k(\mathbf{x},t)$ and $\rho b_k^*(\mathbf{x},t)$ and the boundary tractions $p_k(\mathbf{x},t)$ and $p_k^*(\mathbf{x},t)$, where $k=1,2,3$ corresponds to the x, y and z directions and where $\mathbf{x}$ is a point with coordinates $\mathbf{x}=(x,y,z)$. The two elastodynamic states are interrelated by the *Reciprocal Theorem*, which states (Achenbach, 1973)

$$\begin{aligned}&\int_\Gamma p_k(\mathbf{x},t)*u_k^*(\mathbf{x},t)\,\mathrm{d}\Gamma+\int_\Omega \rho\left\{b_k(\mathbf{x},t)*u_k^*(\mathbf{x},t)+u_{0k}(\mathbf{x})\dot{u}_k^*(\mathbf{x},t)+v_{0k}(\mathbf{x})u_k^*(\mathbf{x},t)\right\}\mathrm{d}\Omega=\\&=\int_\Gamma p_k^*(\mathbf{x},t)*u_k(\mathbf{x},t)\,\mathrm{d}\Gamma+\int_\Omega \rho\left\{b_k^*(\mathbf{x},t)*u_k(\mathbf{x},t)+u_{0k}^*(\mathbf{x})\dot{u}_k(\mathbf{x},t)+v_{0k}^*(\mathbf{x})u_k(\mathbf{x},t)\right\}\mathrm{d}\Omega\end{aligned}\tag{3.1}$$

In equation (3.1), a dot over a variable represents the derivative with respect to time and the operator "$*$" represents the time convolution, defined by

$$f(t)*g(t)=\int_0^t f(t-\tau)\,g(\tau)\,\mathrm{d}\tau=\int_0^t g(t-\tau)\,f(\tau)\,\mathrm{d}\tau\tag{3.2}$$

Also, the Einstein notation is used, i.e., a repeated index in a term implies the summation over that index. For example,

$$p_k^**u_k=\sum_{k=1}^{3}p_k^**u_k=p_1^**u_1+p_2^**u_2+p_3^**u_3\tag{3.3}$$

Now, assume that the second elastodynamic state (the one associated with the supperscript *) is elicited by a body force of the form

$$\rho b_k^* (\mathbf{x},t) = \delta_{kl}\delta(\xi,0) \tag{3.4}$$

where $l = 1, 2, 3$ is the direction of the body force, δ_{kl} is the Kronecker delta, $\delta(\ldots)$ is the Dirac delta function and $\xi = (x_\xi, y_\xi, z_\xi)$ is the point where the body force is applied, which can be inside or outside the domain Ω. In this case, the displacements induced by such load correspond to the fundamental displacements in the time domain and, in the ensuing, are denoted by $u_{kl}^*(\mathbf{x},\xi,t)$, in which the first index represents the direction of the displacement and the second index represents the direction of the body load as given in equation (3.4). Analogously, the fundamental tractions at the boundary Γ are denoted by $p_{kl}^*(\mathbf{x},\xi,t)$ and are calculated with

$$p_{kl}^*(\mathbf{x},\xi,t) = \sum_{j=1}^{3} \sigma_{kjl}^*(\mathbf{x},\xi,t) n_j \tag{3.5}$$

where n_j are the components of the vector $\mathbf{n}$ that is normal to the boundary Γ at the point $\mathbf{x}$ (pointing outwards) and where $\sigma_{kjl}^*(\mathbf{x},\xi,t)$ are the fundamental stresses in the time domain induced at the point $\mathbf{x}$ by a point load at ξ. Assume also that the first elastodynamic state presents no body forces and that it is initially at rest, i.e., $\rho b_k(x,y,z,t) = 0$, $u_{0k}(x,y,z) = 0$ and $v_{0k}(x,y,z) = 0$. Under these two assumptions, equation (3.1) becomes

$$\int_\Gamma p_k(\mathbf{x},t) * u_{kl}^*(\mathbf{x},\xi,t)\,\mathrm{d}\Gamma = \int_\Gamma p_{kl}^*(\mathbf{x},\xi,t) * u_k(\mathbf{x},t)\,\mathrm{d}\Gamma + \kappa_{kl} u_k(\xi,t) \tag{3.6}$$

where $\kappa_{kl} = \delta_{kl}$ if $\xi \in \Omega$ and $\kappa_{kl} = 0$ if $\xi \notin \Omega$. The integral equation (3.6) relates the displacements of a point ξ of the domain Ω with the displacements and tractions at the boundary Γ. In the frequency domain, equation (3.6) becomes

$$\int_\Gamma \tilde{p}_k(\mathbf{x},\omega)\tilde{u}_{kl}^*(\mathbf{x},\xi,\omega)\,\mathrm{d}\Gamma = \int_\Gamma \tilde{p}_{kl}^*(\mathbf{x},\xi,\omega)\tilde{u}_k(\mathbf{x},\omega)\,\mathrm{d}\Gamma + \kappa_{kl}\tilde{u}_k(\xi,\omega) \tag{3.7}$$

where a tilde over the variables denotes their Fourier transform with respect to time. Hence, $\tilde{u}_{kl}^*(\mathbf{x},\xi,\omega)$ and $\tilde{p}_{kl}^*(\mathbf{x},\xi,\omega)$ represent the three-dimensional fundamental displacements and tractions in the frequency domain, which can be calculated using the Thin Layer Method (TLM) (Kausel, 1981).

3.2.3 Regularization of the integral equation

The fundamental displacements and fundamental traction are singular at the collocation point ξ and consequently equations (3.6) and (3.7) are not valid if ξ belongs to the boundary Γ. Two approaches can be followed to deal with this problem: a limiting process in which a spherical portion of the domain with radius tending to zero is excluded (or included) around the collocation ξ (Figure 3.1) (Dominguez, 1993); and a regularization procedure in which the singularities of the fundamental solutions are removed (François, 2008).

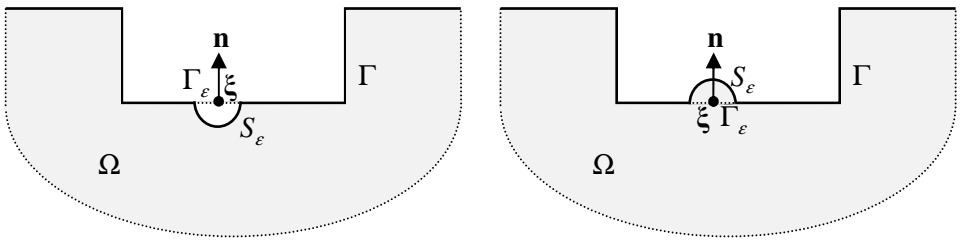

Figure 3.1: Exclusion (left) and inclusion (right) at point ξ (Γ_ε is the projection of S_ε on Γ)

Following the first approach, equation (3.7) becomes

$$\int_{\Gamma-\Gamma_\varepsilon} \tilde{p}_k(\mathbf{x},\omega)\tilde{u}^*_{kl}(\mathbf{x},\xi,\omega)\,\mathrm{d}\Gamma + \tilde{p}_k(\xi,\omega)\int_{S_\varepsilon} \tilde{u}^*_{kl}(\mathbf{x},\xi,\omega)\,\mathrm{d}S = \\ = \int_{\Gamma-\Gamma_\varepsilon} \tilde{p}^*_{kl}(\mathbf{x},\xi,\omega)\tilde{u}_k(\mathbf{x},\omega)\,\mathrm{d}\Gamma + \left(\kappa_{kl} + \int_{S_\varepsilon} \tilde{p}^*_{kl}(\mathbf{x},\xi,\omega)\,\mathrm{d}S\right)\tilde{u}_k(\xi,\omega) \tag{3.8}$$

The integral $\int_{S_\varepsilon} \tilde{u}^*_{kl}(\mathbf{x},\xi,\omega)\,\mathrm{d}S$ vanishes for ε tending to zero (Dominguez, 1993) and so equation (3.8) is condensed to

$$c_{kl}\tilde{u}_k(\xi,\omega) = \int_{\Gamma-\Gamma_\varepsilon} \tilde{p}_k(\mathbf{x},\omega)\tilde{u}^*_{kl}(\mathbf{x},\xi,\omega)\,\mathrm{d}\Gamma - \int_{\Gamma-\Gamma_\varepsilon} \tilde{p}^*_{kl}(\mathbf{x},\xi,\omega)\tilde{u}_k(\mathbf{x},\omega)\,\mathrm{d}\Gamma \tag{3.9}$$

where

$$c_{kl} = \kappa_{kl} + \int_{S_\varepsilon} \tilde{p}^*_{kl}(\mathbf{x},\xi,\omega)\,\mathrm{d}S = \begin{cases} \delta_{kl} + \int_{S_\varepsilon} \tilde{p}^*_{kl}(\mathbf{x},\xi,\omega)\,\mathrm{d}S, & \text{if inclusion} \\ \int_{S_\varepsilon} \tilde{p}^*_{kl}(\mathbf{x},\xi,\omega)\,\mathrm{d}S, & \text{if exclusion} \end{cases} \tag{3.10}$$

When the boundary is smooth at ξ and the full-space fundamental solutions are being used, $c_{kl} = 0.5\delta_{kl}$. For different geometries at the node ξ, Guiggiani and Gigante (1990) and Mantic (1993) indicate procedures to obtain the coefficient c_{kl}, also considering the full-space fundamental solutions. For different fundamental solutions (such as the layered half-space fundamental solutions), no work addressing the calculation of the coefficients c_{kl} was found in the literature.

The remaining integrals in equation (3.9) must be evaluated in the Cauchy principal value sense. The fundamental displacements $\tilde{u}^*_{kl}$ present a weak singularity at ξ and so the integral involving $\tilde{u}^*_{kl}$ can be evaluated easily. The fundamental tractions $\tilde{p}^*_{kl}$ present a strong singularity at ξ and for that reason the evaluation of the integral involving $\tilde{p}^*_{kl}$ is not straightforward. Cerrolaza and Alarcon (1989) present a procedure based on a polynomial coordinate transformation that can be used to evaluate this type of integrals.

Following the regularization procedure mentioned in the beginning of this subsection, the strong singularity that is contained in the fundamental tractions $\tilde{p}^*_{kl}$ is removed by employing the "rigid body motion technique". The details of this technique can be found in (François, 2008). For unbounded domains, the regularized integral equation that is obtained using this technique is

$$\tilde{u}_l(\boldsymbol{\xi},\omega) = \int_{\Gamma} \tilde{p}_k(\mathbf{x},\omega)\tilde{u}^*_{kl}(\mathbf{x},\boldsymbol{\xi},\omega)\,\mathrm{d}\Gamma - \int_{\Gamma}\left[\tilde{p}^*_{kl}(\mathbf{x},\boldsymbol{\xi},\omega)\tilde{u}_k(\mathbf{x},\omega) - \tilde{p}^*_{kl}(\mathbf{x},\boldsymbol{\xi},0)\tilde{u}_k(\boldsymbol{\xi},\omega)\right]\mathrm{d}\Gamma \tag{3.11}$$

in which $\tilde{p}^*_{kl}(\mathbf{x},\boldsymbol{\xi},0)$ are the fundamental static tractions.

In this work, for the 3D BEM, equation (3.11) is used. The reason why equation (3.11) is chosen instead of (3.9) is because with that equation the calculation of c_{kl} is avoided. Furthermore, because the layered half-space fundamental solutions are used and since only structures resting on the surface of half-spaces are considered, the calculation of the fundamental tractions is not necessary as they are zero (free traction boundary condition).

[Note: For buried structures, a more convenient strategy can be used: if the collocation points are placed inside the part of domain to be excluded instead of in the boundary, equation (3.7) can be used directly without the need for regularization because the collocation points are not contained in the integration path; hence, if one defines as many collocation points as nodes of the discretized boundary Γ, a system of equations that relates the boundary tractions and the boundary displacements is obtained, and from that system, a stiffness (or flexibility matrix) can be easily obtained. Nevertheless, the integration of the fundamental solutions over vertical boundaries is still needed and that can become troublesome.]

3.2.4 Discretization of the boundary

To solve the integral equation (3.11), the boundary Γ is divided into N_e boundary elements and N_n boundary nodes. Within each boundary element, the displacement and traction fields are approximated by means of interpolation functions and nodal values, i.e.,

$$\tilde{u}_k(\mathbf{x},\omega) = \sum_{j=1}^{N_n^{(e)}} \tilde{u}_k^{(ej)}(\omega) S_{(j)}^{(e)}(\mathbf{x}) \tag{3.12}$$

$$\tilde{p}_k(\mathbf{x},\omega) = \sum_{j=1}^{N_n^{(e)}} \tilde{p}_k^{(ej)}(\omega) S_{(j)}^{(e)}(\mathbf{x}) \tag{3.13}$$

in which $\tilde{u}_k(\mathbf{x},\omega)$ and $\tilde{p}_k(\mathbf{x},\omega)$ are the interpolated displacements and tractions (in this case, $\mathbf{x}$ belongs to the e^{th} boundary element), $\tilde{u}_k^{(ej)}(\omega)$ and $\tilde{p}_k^{(ej)}(\omega)$ are the nodal values of the j^{th} node of the e^{th} element, $S_{(j)}^{(e)}(\mathbf{x})$ are the associated interpolation (shape) functions evaluated at $\mathbf{x}$ and $N_n^{(e)}$ is the number of nodes contained in the e^{th} element. The type of boundary elements and respective shape functions that are commonly used can be found in (Dominguez, 1993).

Now, assume that the collocation point $\boldsymbol{\xi}$ corresponds to one of the N_n nodes of the boundary (say, the i^{th} node, with coordinates $\mathbf{x}_i$). In this case, after accounting for the approximations in equations (3.12) and (3.13), equation (3.11) becomes

$$\tilde{u}_l^{(i)}(\omega)=\sum_{e=1}^{N_e}\left\{\sum_{j=1}^{N_n^e}\left(\tilde{p}_k^{(ej)}(\omega)\overbrace{\int_{\Gamma_e}\tilde{u}_{kl}^*(\mathbf{x},\mathbf{x}_i,\omega)S_{(j)}^{(e)}(\mathbf{x})\mathrm{d}\Gamma_e}^{\tilde{U}_{kl}^{(ej)}(\mathbf{x}_i,\omega)}\right)\right\}$$
$$-\sum_{e=1}^{N_e}\left\{\sum_{j=1}^{N_n^{(e)}}\left(\tilde{u}_k^{(ej)}(\omega)\overbrace{\int_{\Gamma_e}\tilde{p}_{kl}^*(\mathbf{x},\mathbf{x}_i,\omega)S_{(j)}^{(e)}(\mathbf{x})\mathrm{d}\Gamma_e}^{\tilde{P}_{kl}^{(ej)}(\mathbf{x}_i,\omega)}\right)\right\} \tag{3.14}$$
$$+\tilde{u}_k^{(i)}(\omega)\sum_{e=1}^{N_e}\left(\overbrace{\int_{\Gamma_e}\tilde{p}_{kl}^*(\mathbf{x},\mathbf{x}_i,0)\mathrm{d}\Gamma_e}^{\tilde{P}_{kl}^{(e,3\mathrm{Dstat})}(\mathbf{x}_i)}\right)$$

or in compact form,

$$\tilde{u}_l^{(i)}(\omega)=\sum_{e=1}^{N_e}\sum_{j=1}^{N_n^{(e)}}\tilde{p}_k^{(ej)}(\omega)\tilde{U}_{kl}^{(ej)}(\mathbf{x}_i,\omega)-\sum_{e=1}^{N_e}\sum_{j=1}^{N_n^{(e)}}\tilde{u}_k^{(ej)}(\omega)\tilde{P}_{kl}^{(ej)}(\mathbf{x}_i,\omega)+$$
$$\tilde{u}_k^{(i)}(\omega)\sum_{e=1}^{N_e}\tilde{P}_{kl}^{(e,3\mathrm{Dstat})}(\mathbf{x}_i) \tag{3.15}$$

By making l assume all the three directions, equation (3.15) assumes the vector form

$$\tilde{\mathbf{u}}^{(i)}(\omega)=\sum_{e=1}^{N_e}\sum_{j=1}^{N_n^{(e)}}\tilde{\mathbf{U}}^{(ej)}(\mathbf{x}_i,\omega)\tilde{\mathbf{p}}^{(ej)}(\omega)-\sum_{e=1}^{N_e}\sum_{j=1}^{N_n^{(e)}}\tilde{\mathbf{P}}^{(ej)}(\mathbf{x}_i,\omega)\tilde{\mathbf{u}}^{(ej)}(\omega)$$
$$+\left(\sum_{e=1}^{N_e}\tilde{\mathbf{P}}^{(e,3\mathrm{Dstat})}(\mathbf{x}_i)\right)\tilde{\mathbf{u}}^{(i)}(\omega) \tag{3.16}$$

where the bold variables have the following meanings (the arguments $\mathbf{x}_i$ and ω were dropped)

$$\tilde{\mathbf{u}}^{(i)}=\begin{bmatrix}\tilde{u}_x^{(i)}\\ \tilde{u}_y^{(i)}\\ \tilde{u}_z^{(i)}\end{bmatrix}\qquad \tilde{\mathbf{u}}^{(ej)}=\begin{bmatrix}\tilde{u}_x^{(ej)}\\ \tilde{u}_y^{(ej)}\\ \tilde{u}_z^{(ej)}\end{bmatrix}\qquad \tilde{\mathbf{p}}^{(ej)}=\begin{bmatrix}\tilde{p}_x^{(ej)}\\ \tilde{p}_y^{(ej)}\\ \tilde{p}_z^{(ej)}\end{bmatrix}$$
$$\tilde{\mathbf{U}}^{(ej)}=\begin{bmatrix}\tilde{U}_{xx}^{(ej)} & \tilde{U}_{yx}^{(ej)} & \tilde{U}_{zx}^{(ej)}\\ \tilde{U}_{xy}^{(ej)} & \tilde{U}_{yy}^{(ej)} & \tilde{U}_{zy}^{(ej)}\\ \tilde{U}_{xz}^{(ej)} & \tilde{U}_{yz}^{(ej)} & \tilde{U}_{zz}^{(ej)}\end{bmatrix}\qquad \tilde{\mathbf{P}}^{(ej)}=\begin{bmatrix}\tilde{P}_{xx}^{(ej)} & \tilde{P}_{yx}^{(ej)} & \tilde{P}_{zx}^{(ej)}\\ \tilde{P}_{xy}^{(ej)} & \tilde{P}_{yy}^{(ej)} & \tilde{P}_{zy}^{(ej)}\\ \tilde{P}_{xz}^{(ej)} & \tilde{P}_{yz}^{(ej)} & \tilde{P}_{zz}^{(ej)}\end{bmatrix} \tag{3.17}$$
$$\tilde{\mathbf{P}}^{(e,3\mathrm{Dstat})}=\begin{bmatrix}\tilde{P}_{xx}^{(e,3\mathrm{Dstat})} & \tilde{P}_{yx}^{(e,3\mathrm{Dstat})} & \tilde{P}_{zx}^{(e,3\mathrm{Dstat})}\\ \tilde{P}_{xy}^{(e,3\mathrm{Dstat})} & \tilde{P}_{yy}^{(e,3\mathrm{Dstat})} & \tilde{P}_{zy}^{(e,3\mathrm{Dstat})}\\ \tilde{P}_{xz}^{(e,3\mathrm{Dstat})} & \tilde{P}_{yz}^{(e,3\mathrm{Dstat})} & \tilde{P}_{zz}^{(e,3\mathrm{Dstat})}\end{bmatrix}$$

After making the collocation point ξ correspond to all the N_n nodes and after assembling the matrices $\tilde{\mathbf{U}}^{(ej)}$ into a square matrix $\mathbf{U}$ and the matrices $\tilde{\mathbf{P}}^{(ej)}$ and $\tilde{\mathbf{P}}^{(e,3\mathrm{Dstat})}$ into a square matrix $\mathbf{P}$, the final system of equations is obtained

$$\{\mathbf{P}(\omega)+\mathbf{I}\}\tilde{\mathbf{u}}(\omega)=\mathbf{U}(\omega)\tilde{\mathbf{p}}(\omega) \tag{3.18}$$

in which $\tilde{\mathbf{u}}(\omega)$ is a vector that collects all the nodal displacements and $\tilde{\mathbf{p}}(\omega)$ is a vector that collects all the nodal tractions. Equation (3.18) can be solved for $\tilde{\mathbf{u}}$, $\tilde{\mathbf{p}}$ or a combination of the two vectors, depending on the unknowns of the problem.

3.2.5 Coupling BEM-FEM

To model the behavior of structures composed of irregular and finite domains, the FEM is more adequate than the BEM. Hence, when such structures interact with the soil, the coupled BEM-FEM strategy may be the most attractive option.

In the frequency domain, the FEM sub-domain is governed by the system of equations (neglecting the damping)

$$\underbrace{\left(\mathbf{K}-\omega^2\mathbf{M}\right)}_{\tilde{\mathbf{K}}}\tilde{\mathbf{u}}=\tilde{\mathbf{F}} \tag{3.19}$$

in which $\mathbf{M}$ represents the mass matrix

$$\mathbf{M}=\int_{\Omega^{\mathrm{FEM}}}\rho\mathbf{N}^{\mathrm{T}}\mathbf{N}\,\mathrm{d}\Omega \tag{3.20}$$

and $\mathbf{K}$ represents the stiffness matrix

$$\mathbf{K}=\int_{\Omega^{\mathrm{FEM}}}\mathbf{B}^{\mathrm{T}}\mathbf{D}\mathbf{B}\,\mathrm{d}\Omega \tag{3.21}$$

and where the vectors $\tilde{\mathbf{u}}$ and $\tilde{\mathbf{F}}$ represent the frequency domain displacements and external forces, respectively, and the variables ρ, $\mathbf{D}$, $\mathbf{N}$ and $\mathbf{B}$ correspond to the density, the constitutive matrix, the shape function matrix and the linear operator containing the derivatives of the shape functions. On the other hand, the behavior of the BEM sub-domain is described by equation (3.18). In the following, the superscripts F and B are used to distinguish the response fields of the FEM and BEM sub-domains, respectively.

Consider a sub-domain Ω^{FEM} modeled by means of the FEM, which interacts along the surface Γ^{FEM} with a sub-domain modeled with the BEM and whose boundary is Γ^{BEM} (Figure 3.2). To couple the two sub-domains, first it is convenient to separate the degrees of freedom of both sub-domains into two groups: one that contains the degrees of freedom belonging to Γ^{FEM} (represented here by the index I); and another that contains the remaining degrees of freedom (represented by the index II). Taking into account the defined groups, systems of equations (3.18) and (3.19) are written as (the argument ω is dropped)

$$\begin{bmatrix}\mathbf{P}_{\mathrm{I,I}}+\mathbf{I} & \mathbf{P}_{\mathrm{I,II}}\\ \mathbf{P}_{\mathrm{II,I}} & \mathbf{P}_{\mathrm{II,II}}+\mathbf{I}\end{bmatrix}\begin{bmatrix}\tilde{\mathbf{u}}_{\mathrm{I}}^{\mathrm{B}}\\ \tilde{\mathbf{u}}_{\mathrm{II}}^{\mathrm{B}}\end{bmatrix}=\begin{bmatrix}\mathbf{U}_{\mathrm{I,I}} & \mathbf{U}_{\mathrm{I,II}}\\ \mathbf{U}_{\mathrm{II,I}} & \mathbf{U}_{\mathrm{II,II}}\end{bmatrix}\begin{bmatrix}\tilde{\mathbf{p}}_{\mathrm{I}}\\ \tilde{\mathbf{p}}_{\mathrm{II}}\end{bmatrix} \tag{3.22}$$

and

$$\begin{bmatrix}\tilde{\mathbf{K}}_{\mathrm{I,I}} & \tilde{\mathbf{K}}_{\mathrm{I,II}}\\ \tilde{\mathbf{K}}_{\mathrm{II,I}} & \tilde{\mathbf{K}}_{\mathrm{II,II}}\end{bmatrix}\begin{bmatrix}\tilde{\mathbf{u}}_{\mathrm{I}}^{\mathrm{F}}\\ \tilde{\mathbf{u}}_{\mathrm{II}}^{\mathrm{F}}\end{bmatrix}=\begin{bmatrix}\tilde{\mathbf{F}}_{\mathrm{I}}\\ \tilde{\mathbf{F}}_{\mathrm{II}}\end{bmatrix} \tag{3.23}$$

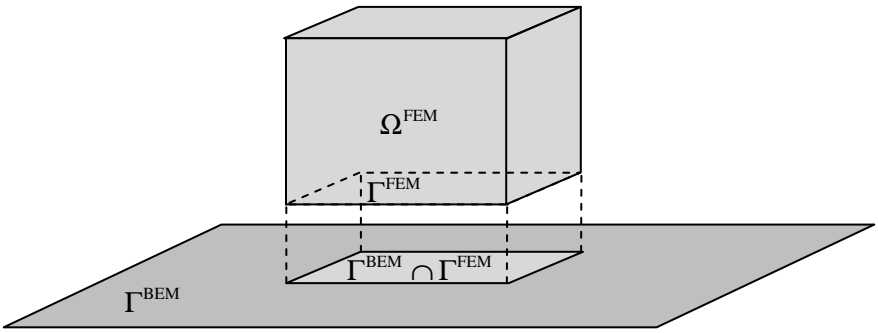

Figure 3.2: FEM sub-domain Ω^{FEM} interacting with BEM sub-domain with boundary Γ^{BEM}

The two sub-domains are now coupled by enforcing the compatibility of displacements and the equilibrium of forces at the interface Γ^{FEM}. Since the interpolation functions may differ from one sub-domain to the other, the compatibility of displacements cannot be imposed at all points of Γ^{FEM}. Hence, the compatibility is enforced only at the nodes of the BEM model interacting with the FEM domain, condition that is accomplished through the identity

$$\mathbf{N}_{\mathrm{I}}\tilde{\mathbf{u}}_{\mathrm{I}}^{\mathrm{F}} = \tilde{\mathbf{u}}_{\mathrm{I}}^{\mathrm{B}} \tag{3.24}$$

where the matrix $\mathbf{N}_{\mathrm{I}}$ contains the FEM shape functions associated with the degrees of freedom I and evaluated at the nodes of the boundary element model that belong to Γ^{FEM}.

Regarding the equilibrium of forces at Γ^{FEM}, the FEM formulation relates displacements with nodal forces while the BEM relates displacements with nodal tractions, and for this reason the equilibrium can only be respected in an approximate manner. The equilibrium is therefore established by enforcing that the resultant of the boundary tractions equals the nodal forces, i.e.,

$$\overbrace{\left(\int_{\Gamma^{FEM}} \mathbf{N}_{\mathrm{I}}^{\mathrm{T}}(\mathbf{x})\mathbf{S}_{\mathrm{I}}(\mathbf{x})\,\mathrm{d}\Gamma\right)}^{\mathbf{T}}\tilde{\mathbf{p}}_{\mathrm{I}} + \tilde{\mathbf{F}}_{\mathrm{I}} = 0 \tag{3.25}$$

Matrix $\mathbf{T}$, defined by the integral in (3.25), transforms the nodal tractions into equivalent nodal forces. Matrix $\mathbf{N}_{\mathrm{I}}(\mathbf{x})$ collects the FEM shape functions associated with the FEM nodes I and evaluated at $\mathbf{x}$ while $\mathbf{S}_{\mathrm{I}}(\mathbf{x})$ collects the BEM shape functions associated with the BEM nodes I and evaluated at $\mathbf{x}$.

The system of equations (3.22) can be solved for $\tilde{\mathbf{p}}_{\mathrm{I}}$ and the following identity can be reached (see Appendix III)

$$\tilde{\mathbf{p}}_{\mathrm{I}} = \mathbf{A}^{-1}\mathbf{B}\tilde{\mathbf{u}}_{\mathrm{I}}^{\mathrm{B}} + \mathbf{A}^{-1}\mathbf{C}\tilde{\mathbf{p}}_{\mathrm{II}} \tag{3.26}$$

in which the matrices $\mathbf{A}$, $\mathbf{B}$ and $\mathbf{C}$ are defined by

$$\mathbf{A} = \mathbf{U}_{\mathrm{I,I}} - \mathbf{P}_{\mathrm{I,II}}\left(\mathbf{P}_{\mathrm{II,II}} + \mathbf{I}\right)^{-1}\mathbf{U}_{\mathrm{II,I}} \tag{3.27}$$

$$\mathbf{B} = \mathbf{P}_{\mathrm{I,I}} + \mathbf{I} - \mathbf{P}_{\mathrm{I,II}}\left(\mathbf{P}_{\mathrm{II,II}} + \mathbf{I}\right)^{-1}\mathbf{P}_{\mathrm{II,I}} \tag{3.28}$$

$$\mathbf{C} = \mathbf{P}_{\mathrm{I,II}}\left(\mathbf{P}_{\mathrm{II,II}} + \mathbf{I}\right)^{-1}\mathbf{U}_{\mathrm{II,II}} - \mathbf{U}_{\mathrm{I,II}} \tag{3.29}$$

The combination of equations (3.24), (3.25) and (3.26) yields

$$\tilde{\mathbf{F}}_{\mathrm{I}} = -\mathbf{T}\mathbf{A}^{-1}\mathbf{B}\,\mathbf{N}_{\mathrm{I}}\tilde{\mathbf{u}}_{\mathrm{I}}^{\mathrm{F}} - \mathbf{T}\mathbf{A}^{-1}\mathbf{C}\tilde{\mathbf{p}}_{\mathrm{II}} \tag{3.30}$$

and the use of eq. (3.30) in (3.23) renders the final system of equations

$$\begin{bmatrix} \tilde{\mathbf{K}}_{\mathrm{I,I}} + \mathbf{K}_{\mathrm{BEM}} & \tilde{\mathbf{K}}_{\mathrm{I,II}} \\ \tilde{\mathbf{K}}_{\mathrm{II,I}} & \tilde{\mathbf{K}}_{\mathrm{II,II}} \end{bmatrix} \begin{bmatrix} \tilde{\mathbf{u}}_{\mathrm{I}}^{\mathrm{F}} \\ \tilde{\mathbf{u}}_{\mathrm{II}}^{\mathrm{F}} \end{bmatrix} = \begin{bmatrix} \mathbf{0} \\ \tilde{\mathbf{F}}_{\mathrm{II}} \end{bmatrix} - \begin{bmatrix} \mathbf{F}_{\mathrm{BEM}} \\ \mathbf{0} \end{bmatrix} \tag{3.31}$$

in which

$$\mathbf{K}_{\mathrm{BEM}} = \mathbf{T}\mathbf{A}^{-1}\mathbf{B}\,\mathbf{N}_{\mathrm{I}} \tag{3.32}$$

and

$$\mathbf{F}_{\mathrm{BEM}} = \mathbf{T}\mathbf{A}^{-1}\mathbf{C}\,\tilde{\mathbf{p}}_{\mathrm{II}} \tag{3.33}$$

The system of equations (3.31) is solved for $\tilde{\mathbf{u}}_{\mathrm{I}}^{\mathrm{F}}$ and $\tilde{\mathbf{u}}_{\mathrm{II}}^{\mathrm{F}}$ and as a result the displacements in Ω^{FEM} are obtained. The displacements $\tilde{\mathbf{u}}_{\mathrm{I}}^{\mathrm{B}}$ of the BEM model are then obtained by employing equation (3.24). The boundary tractions $\tilde{\mathbf{p}}_{\mathrm{I}}$ and displacements $\tilde{\mathbf{u}}_{\mathrm{II}}^{\mathrm{B}}$ are obtained by solving the system of equations (3.22) for these variables.

Example: massless rigid footing resting on a half-space

For the case of a rigid footing, its behavior is described by the displacements and rotations at some reference point. Assuming that the reference point coincides with the origin of the Cartesian coordinate system, which in turn is placed at the center of the footing (Figure 3.3), the displacements at any point $\mathbf{x} = \{x \quad y \quad 0\}$ that belongs to the footing can be calculated with

$$\mathbf{u}(\mathbf{x}) = \overbrace{\begin{bmatrix} 1 & 0 & 0 & 0 & 0 & -y \\ 0 & 1 & 0 & 0 & 0 & x \\ 0 & 0 & 1 & y & -x & 0 \end{bmatrix}}^{\mathbf{N}=\mathbf{N}_{\mathrm{I}}} \overbrace{\begin{bmatrix} u_x \\ u_y \\ u_z \\ \theta_x \\ \theta_y \\ \theta_z \end{bmatrix}}^{\mathbf{U}_{\mathrm{Foot}}} \tag{3.34}$$

where u_α is the translation of the footing in the α direction and θ_α is the rotation of the footing about the α axis, with $\alpha = x, y, z$.

To account for the soil reaction, the soil-structure interface is divided into N_e boundary elements and N_n nodes, all belonging to the group I of degrees of freedom. In addition, since the half-space fundamental solutions are used, the fundamental tractions are null. Hence, in equation (3.22) only the sub matrices $\mathbf{U}_{\mathrm{I,I}}$ and $\mathbf{I}$ are not null, and consequently the matrix $\mathbf{K}_{\mathrm{BEM}}$ simplifies to $\mathbf{K}_{\mathrm{BEM}} = \mathbf{T}\mathbf{U}_{\mathrm{I,I}}^{-1}\mathbf{N}_{\mathrm{I}}$, while the vector $\mathbf{F}_{\mathrm{BEM}}$ vanishes.

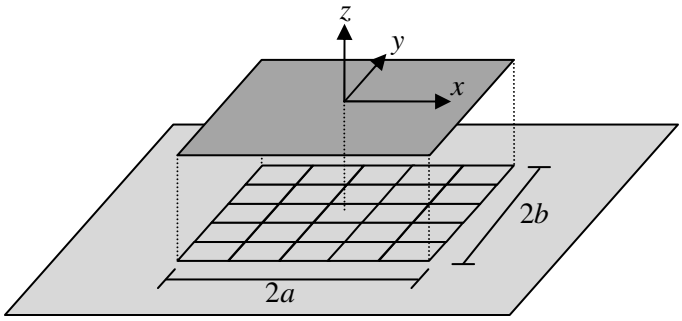

Figure 3.3: Rigid footing resting on a half-space: boundary element mesh

Next, to validate the procedure, the horizontal compliance ($C_{HH} = u_x Ga$, considering a unit horizontal load) and the vertical compliance ($C_{VV} = u_z Ga$, considering a unit vertical load) of a square footing ($a = b$) are compared with the compliances obtained by Wong and Luco (1978), for the dimensionless frequency $a_0 = \omega a / C_s$ ($C_s = \sqrt{G/\rho}$) varying from 0 to 4. The size of the square foundation is $2a = 60$ and the soil properties are $G = 3.315 \times 10^6$, $\rho = 2.82 \times 10^{-4}$ and $\nu = 1/3$ (consistent units). The soil-structure interface is divided into 100 equally sized squares, and within each square the displacement and traction fields are assumed to be constant (constant boundary elements). The fundamental solutions of the half-space are obtained via the TLM with a model consisting of a elastic layer with thickness $h = \pi C_s / 5\omega = 0.1\lambda_s$ (divided into 25 thin layers of quadratic expansion) that rests on a PML with parameters $m = 2$, $\eta = 3$, $n = 2$, $N = 15$ and $\Omega = 12$ (see Chapter 2, equation 2.108). The elastic layer is added to the TLM model to improve the quality of the fundamental solutions near the source (recall that the TLM is a discrete method and so, near a point source, where the displacement and stress fields vary rapidly, thinner meshes are required in order to obtain a good accuracy). Figures 3.4 and 3.5 plot the results herein obtained and the results reported by Wong and Luco. Though not perfect, the agreement is good, which validates the procedure.

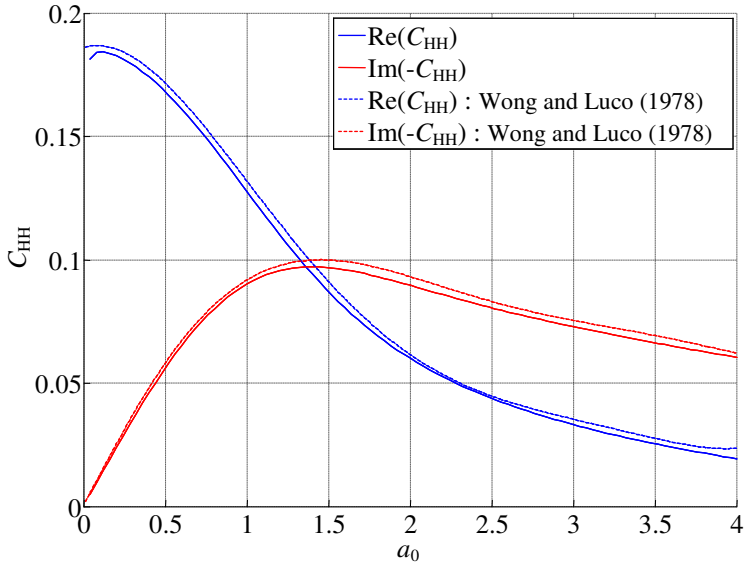

Figure 3.4: Horizontal compliance C_{HH}

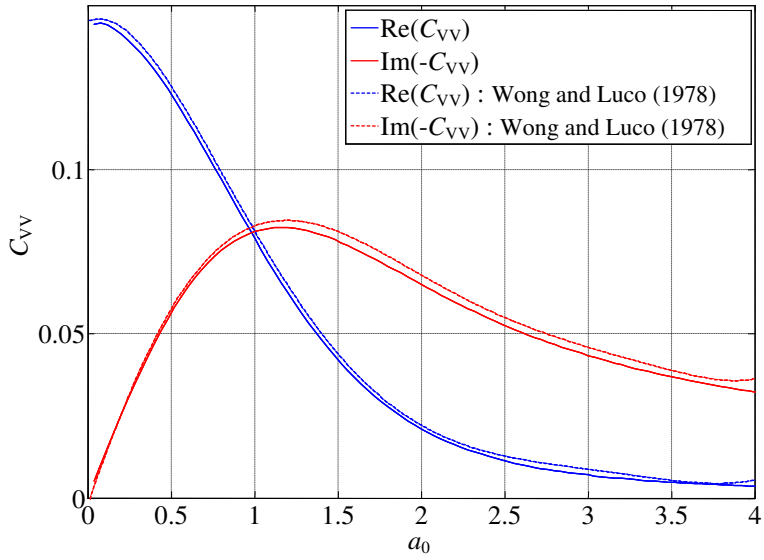

Figure 3.5: Vertical compliance C_{VV}

Note: In this example, because the boundary elements are constant, square shaped, and resting at the surface of the half-space, the calculation of the boundary element matrices $\mathbf{U}_{I(II),I(II)}$ of equation (3.22) can be accomplished with a simplified procedure: instead of integrating the displacements induced by a point load at the i^{th} boundary node on the surface of the j^{th} boundary element, the 3x3 sub-matrix associated with the i^{th} boundary node (rows) and j^{th} boundary element (columns) can be taken as the displacements (all nine components) at the i^{th} boundary node induced by a disk load applied at the j^{th} boundary element. The radius of the disk load must be such that the area of the disk is the same as the area of the boundary element. This simplified procedure yields very good approximations as long as the boundary elements are horizontal, fairly square and of constant expansion. If the elements are not at the surface, this procedure cannot be used because it is not valid for the traction integrals. The displacements induced by disk loads are given in the work (Kausel and Peek, 1982b) and transcribed in Appendix IV.

3.2.6 Weak coupling – response to incoming wave fields

As mentioned in the beginning of this chapter, in this work the propagation and the reception stages are decoupled, i.e., the wave-field that the track transmits to the soil is calculated disregarding the presence of the building in the far field. Hence, there is a weak coupling between the two sub-structures: the connection between the track and the structure is kept, while the connection between the structure and the track is not (Figure 3.6).

So, consider that the tractions $\mathbf{p}^t$ at the boundary Γ_t (that result from the interaction between the track and the soil, and that are calculated without accounting for the removal of the volume of soil Ω_s) induce at the boundary Γ_s the displacement field $\mathbf{u}^0$ and the traction field $\mathbf{p}^0$ (Figure 3.6). The displacements $\mathbf{u}^0$ are calculated by placing collocation points on the boundary Γ_s and then using equation (3.7) with $\Gamma = \Gamma_t$. The traction field $\mathbf{p}^0$ is obtained using the derivatives of $\mathbf{u}^0$ in the strain-stress relations (2.6). The derivatives of $\mathbf{u}^0$ are obtained by deriving equation (3.7) with respect to $\boldsymbol{\xi}$ — see (Dominguez, 1993) for details.

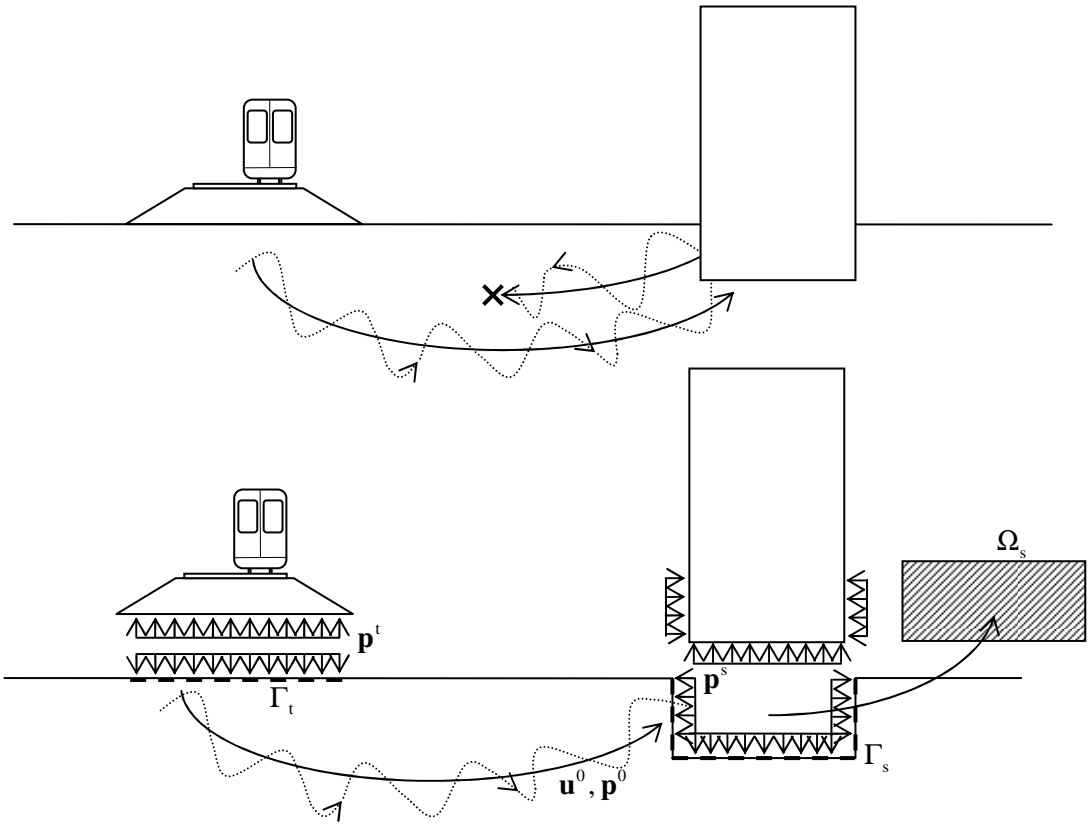

Figure 3.6: Weak coupling between track and structure

The first step to obtain the response of Γ_s is to make it traction free, a condition that is needed to account for the volume Ω_s of soil that is excavated. Such is accomplished by applying the tractions $-\mathbf{p}^0$ at Γ_s (same magnitude but opposite direction). These tractions induce an extra displacement field $\mathbf{u}^{\mathbf{p}}$ at Γ_s calculated with

$$\mathbf{u}^{\mathbf{p}} = -\left(\mathbf{P}_s + \mathbf{I}\right)^{-1} \mathbf{U}_s \, \mathbf{p}^0 \tag{3.35}$$

where $\mathbf{P}_s$ and $\mathbf{U}_s$ are the boundary element matrices of the discretized boundary Γ_s. The displacement field $\mathbf{u}^{\text{inc}}$ that $\mathbf{p}^t$ induces at Γ_s (and that accounts for the volume of excavated soil Ω_s) is then

$$\mathbf{u}^{\text{inc}} = \mathbf{u}^0 + \mathbf{u}^{\mathbf{p}} = \mathbf{u}^0 - \left(\mathbf{P}_s + \mathbf{I}\right)^{-1} \mathbf{U}_s \, \mathbf{p}^0 \tag{3.36}$$

(for Γ_s at the surface, $\mathbf{p}^0$ is null and so $\mathbf{u}^{\text{inc}} = \mathbf{u}^0$).

The second step to obtain the response of Γ_s is to establish the compatibility of displacements and equilibrium of forces between the soil and the structure. The incident displacement field $\mathbf{u}^{\text{inc}}$ needs to be taken into account in the compatibility equation (3.24), which becomes

$$\mathbf{N}_I \tilde{\mathbf{u}}_I^F = \tilde{\mathbf{u}}_I^B + \tilde{\mathbf{u}}^{\text{inc}} \tag{3.37}$$

The equilibrium equation does not change. After combining the compatibility equation (3.37) and the equilibrium equation (3.25), a system of equations with the same form as equation (3.31) is obtained, with $\mathbf{F}_{\text{BEM}}$ being calculated with

$$\mathbf{F}_{\mathrm{BEM}} = \mathbf{T}\mathbf{A}^{-1}\mathbf{C}\,\tilde{\mathbf{p}}_{\mathrm{II}} - \mathbf{T}\mathbf{A}^{-1}\mathbf{B}\,\mathbf{u}^{\mathrm{inc}} \tag{3.38}$$

and with the remaining matrices and vectors being calculated as explained in section 3.2.5 for $\Gamma = \Gamma_s$.

Example: two weakly coupled rigid footings resting on a half-space

Two square rigid footings ($2a = 2b = 60$) are placed at a distance $d = 4a = 120$ from each other (center to center). Both footings have concentrated masses placed at their center of gravity ($M = 500$), which results in inertial forces in the translational degrees of freedom. The footings rest on a half-space whose properties are the same of those of the previous example. One of the foundations (footing 1) is loaded vertically and the vertical response of both footings ($C_{\mathrm{VV},1} = u_{z,1}Ga$ and $C_{\mathrm{VV},2} = u_{z,2}Ga$) is calculated considering full coupling and weak coupling between the two foundations. Figures 3.7 and 3.8 compare the responses obtained considering the two coupling schemes for the dimensionless frequency a_0 varying between 0 and 1.

The presence of the concentrated masses in the footings significantly modifies the behavior of the footing-soil system, as can be concluded from the comparison between Figures 3.5 and 3.7: both the shape and the magnitude of the response are different. It is also observed that the two coupling schemes yield different results. Nevertheless, the response of the weak coupling scheme follows the main trends of the response of the full coupling scheme.

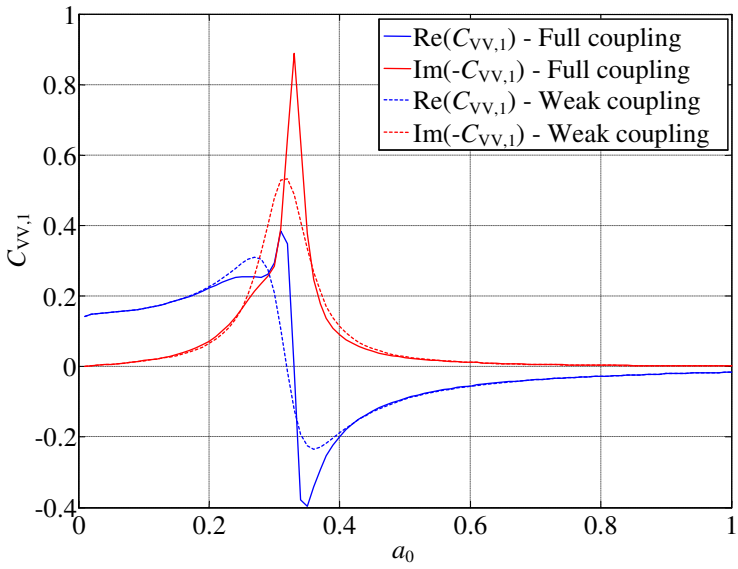

Figure 3.7: Vertical displacement of loaded footing: full coupling versus weak coupling

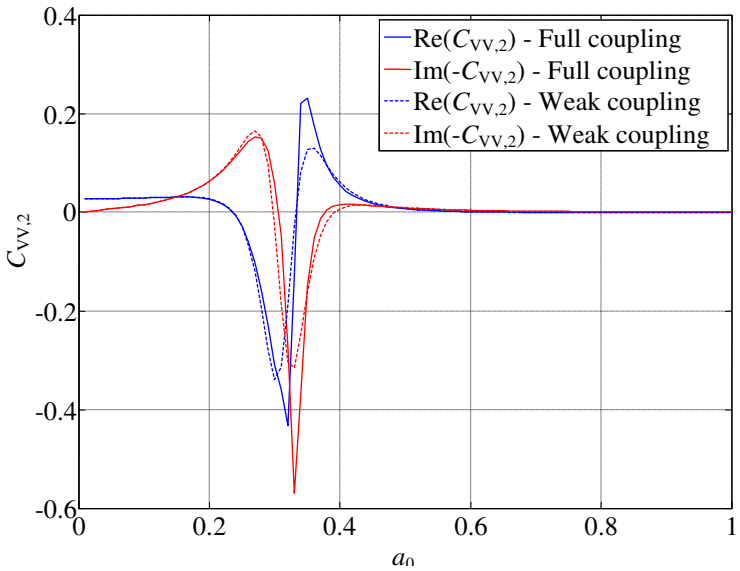

Figure 3.8: Vertical displacement of free footing: full coupling versus weak coupling

3.2.7 Final considerations

In this section of chapter 3, the 3D BEM was introduced and coupled to the 3D FEM in order to perform dynamic analyses of structures interacting with the soil. To validate the implemented methodology, the example of a rigid footing resting on a half-space was solved and the results were compared with results available in the literature. Then, the definition of weak coupling between two structures was introduced and an example was shown where the results obtained considering weak coupling and full coupling were compared. It was observed that the two coupling approaches yielded different results, but that the major trends of the responses were kept.

In this work, the 3D BEM-FEM methodology is used in the context of railway induced vibrations to analyze the response of structures to incoming wave-fields. The wave-fields are calculated using a 2.5D BEM-FEM procedure, which is explained in the following subsections. In the 2.5D BEM-FEM procedure, the presence of the building in the far field is disregarded, i.e., it is considered that the track and the buildings are weakly coupled.

The consideration of buried structures is not attempted in this work, but some comments are proffered next about this issue:

1. The calculation of the boundary matrices for non-horizontal boundaries using the TLM becomes much more complicated than to integrate the fundamental displacements on a horizontal surface or to use the simplified procedure explained at the end of section 3.2.5. The difficulties arise because the boundary integrals cannot be calculated directly (unlike in the 2.5D case, explained in a later section of this chapter), which leads to the necessity of using special integration schemes (Gaussian integration, for example) and consequently an increase in the time needed for the computation of these integrals. Nevertheless, in the work (Kausel and Peek, 1982a) the BEM is formulated both in 2D and 3D spaces using the TLM, and these formulation can be used for the analyses of buried structures.
2. Alternative approaches can also be used: in recent years, some authors suggested the use of the Perfectly Matched Layer together with finite elements to calculate

the stiffness matrix $\mathbf{K}_{\Gamma s}$ ($=\mathbf{K}_{\mathrm{BEM}}$) of the soil interface (Basu and Chopra, 2003; Harari and Albocher, 2006). However, there are reports of incorrect results of the FEM-PML when the domain is layered, and that occurs due to grazing incidence of waves (Komatitsch and Martin, 2007). In this work, during some tests with FEM-PML to simulate a single stratum, for certain frequencies, the response of the stratum diverged from the expected.

3. Another alternative for the calculation of the stiffness matrix of the soil is the "SASSI" approach (Lysmer et al., 1999). In this approach, a flexibility matrix $\mathbf{F}_{\Omega}$ that relates forces and displacements of a grid of nodes that delimit the volume of soil to be excavated is calculated using the TLM. The flexibility matrix is then inverted, being thus obtained a stiffness matrix ($\mathbf{K}_{\Omega}=\mathbf{F}_{\Omega}^{-1}$). The stiffness matrix $\mathbf{K}_{\Gamma s}$ of the soil is finally obtained by subtracting from $\mathbf{K}_{\Omega}$ the stiffness $\mathbf{K}_{\Omega s}$ of the volume to be excavated, which is calculated with the FEM ($\mathbf{K}_{\Gamma s}=\mathbf{K}_{\Omega}-\mathbf{K}_{\Omega s}$).

4. As a final comment, independently of the approach that is followed, there is always a huge computational cost that cannot be avoided because of the need for a 3D mesh.

3.3 2.5D Finite Element Method

3.3.1 Introduction

When the geometry of the structure is invariant in one of the directions, space-wavenumber-frequency domain (2.5D) analyses are usually more advantageous than space domain (3D) analyses. In essence, a 2.5D analysis consists in performing a Fourier transform of the longitudinal coordinate, which results in the reduction of the dimensionality of the problem by one, and consequently in the reduction of the 3D analysis to the summation of a set of 2D analyses.

In the context of railway induced vibrations, since in most cases it can be assumed that the geometry of the track and the profile of the soil are invariant in the longitudinal direction, 2.5D analyses can be used to calculate the wave-fields that propagate in the track and soil and reach the buildings. The 2.5D analyses have been used by several authors in this context, as mentioned in the literature review presented in chapter 1.

In this work, the track is modeled using 2.5D finite elements while the soil is modeled using 2.5D boundary elements. The two procedures are coupled in order to solve the track-soil system and to calculate the vibration field that propagates in the track and soil. Coupled 2.5D BEM-FEM schemes can be found in the literature, for example in Galvín et al. (2010) and in Sheng et al. (2005). The first work uses layered half-space fundamental solutions calculated with the stiffness matrices while the latter uses the analytical full-space fundamental solutions that are given in the same reference. The fundamental solutions used in the present work are the 2.5D fundamental solutions explained in chapter 2.

3.3.2 2.5D Finite Element Method

Consider an elastic body that extends to infinity in one direction (longitudinal direction y) and whose cross section Ω_S is constant (Figure 3.9). It is assumed that the material properties are invariant in the y direction while within the cross section the material properties may vary in a stepwise fashion.

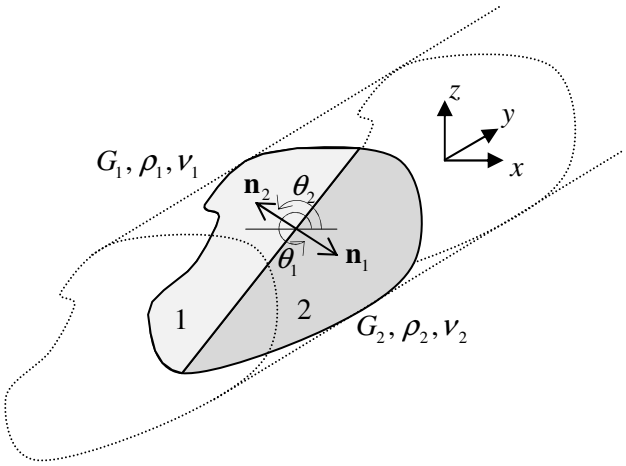

Figure 3.9: Elastic solid: definition of invariance and angles θ

Under the mentioned conditions, and following the same steps as for the TLM — see chapter 2, equations (2.2) to (2.13) — the wave equation in the elastic body can be written as (the following variables have the same meaning as in chapter 2)

$$\rho\ddot{\mathbf{u}} - \left(\mathbf{D}_{xx}\frac{\partial^2}{\partial x^2} + \left(\mathbf{D}_{xy}+\mathbf{D}_{yx}\right)\frac{\partial^2}{\partial x\partial y} + \left(\mathbf{D}_{xz}+\mathbf{D}_{zx}\right)\frac{\partial^2}{\partial x\partial z} + \mathbf{D}_{yy}\frac{\partial^2}{\partial y^2} + \left(\mathbf{D}_{yz}+\mathbf{D}_{zy}\right)\frac{\partial^2}{\partial y\partial z} + \mathbf{D}_{zz}\frac{\partial^2}{\partial z^2}\right)\mathbf{u} = \mathbf{b} \tag{3.39}$$

On the other hand, the internal stresses $\mathbf{s}$ at any plane parallel to y can be calculated with

$$\mathbf{s} = \left(\mathbf{L}_x^{\mathrm{T}}\cos\theta + \mathbf{L}_z^{\mathrm{T}}\sin\theta\right)\mathbf{D}\mathbf{L}\mathbf{u} \tag{3.40}$$

where θ is the angle of the outwards normal to the plane with respect to the x axis. At the interface between different materials, the internal stresses must be in equilibrium, i.e.,

$$\mathbf{s}_1 = \mathbf{s}_2, \qquad \theta_1 = \pi + \theta_2 \tag{3.41}$$

while at the boundary of the cross section Ω_{S} the internal stresses must balance the external tractions $\mathbf{t}$, i.e.,

$$\mathbf{s} = \mathbf{t} \tag{3.42}$$

As in the TLM case, one proceeds to discretize the domain to solve the wave equation. However, instead of discretizing only in the vertical direction z, in this case the domain is discretized in the xz plane. Hence, after dividing the cross section Ω_{S} into plane finite elements, the displacement field in the solid is approximated by

$$\mathbf{u}(x,y,z) = \mathbf{N}(x,z)\mathbf{U}(y) \tag{3.43}$$

where $\mathbf{N}$ is a matrix containing the interpolation functions and $\mathbf{U}$ is a vector containing the displacements of the associated nodes. The interpolation functions $\mathbf{N}$ used in the 2.5D case are the same functions that are commonly used in plane strain or plane stress problems.

After inserting the approximation (3.43) in the wave equation (3.39) and boundary conditions (3.41) and (3.42), it can be verified that these equations are not rigorously satisfied, due to the

presence of unbalanced body forces and tractions. The discrete wave equation is derived after the application of the method of the weighted residuals and by requiring the virtual work done by the unbalanced forces within each finite element to be null, which results in the single finite element equation

$$\mathbf{F} = \mathbf{M}\ddot{\mathbf{U}} + \mathbf{G}_{xx}\mathbf{U} - \mathbf{B}_{xy}\frac{\partial \mathbf{U}}{\partial y} + \mathbf{G}_{xz}\mathbf{U} - \mathbf{A}_{yy}\frac{\partial^2 \mathbf{U}}{\partial y^2} - \mathbf{B}_{zy}\frac{\partial \mathbf{U}}{\partial y} + \mathbf{G}_{zz}\mathbf{U} \tag{3.44}$$

The vector $\mathbf{F}$ contains the consistent external forces at the nodes of the finite elements (which result from the external tractions $\mathbf{t}$ and the body loads $\mathbf{b}$), while the finite element matrices $\mathbf{M}$, $\mathbf{A}_{yy}$, $\mathbf{B}_{\alpha y}$, $\mathbf{G}_{\alpha\alpha}$ and $\mathbf{G}_{xz}$ are given by ($\alpha = x, z$)

$$\mathbf{M} = \iint_{\Omega_S} \rho \mathbf{N}^{\mathrm{T}}\mathbf{N}\,\mathrm{d}x\mathrm{d}z \tag{3.45}$$

$$\mathbf{A}_{yy} = \iint_{\Omega_S} \mathbf{N}^{\mathrm{T}}\mathbf{D}_{yy}\mathbf{N}\,\mathrm{d}x\mathrm{d}z \tag{3.46}$$

$$\mathbf{B}_{\alpha y} = -\iint_{\Omega_S} \mathbf{N}_{\alpha}^{\mathrm{T}}\mathbf{D}_{\alpha y}\mathbf{N}\,\mathrm{d}x\mathrm{d}z + \iint_{\Omega_S} \mathbf{N}^{T}\mathbf{D}_{y\alpha}\mathbf{N}_{\alpha}\,\mathrm{d}x\mathrm{d}z \tag{3.47}$$

$$\mathbf{G}_{\alpha\alpha} = \iint_{\Omega_S} \mathbf{N}_{\alpha}^{\mathrm{T}}\mathbf{D}_{\alpha\alpha}\mathbf{N}_{\alpha}\,\mathrm{d}x\mathrm{d}z \tag{3.48}$$

$$\mathbf{G}_{xz} = \iint_{\Omega_S} \mathbf{N}_{x}^{\mathrm{T}}\mathbf{D}_{xz}\mathbf{N}_{z}\,\mathrm{d}x\mathrm{d}z + \iint_{\Omega_S} \mathbf{N}_{z}^{\mathrm{T}}\mathbf{D}_{zx}\mathbf{N}_{x}\,\mathrm{d}x\mathrm{d}z \tag{3.49}$$

being $\mathbf{N}_x = \frac{\partial}{\partial x}\mathbf{N}$ and $\mathbf{N}_z = \frac{\partial}{\partial z}\mathbf{N}$. After the assembly of the finite element matrices, one is left with a global system of differential equations with the same form as (3.44). To solve it, the displacements $\mathbf{U}$ and forces $\mathbf{F}$ are transformed to the wavenumber-frequency domain by means of the double Fourier transformations

$$\bar{\mathbf{U}}\left(k_y, \omega\right) = \int_{-\infty}^{+\infty}\int_{-\infty}^{+\infty} \mathbf{U}\left(y,t\right)\mathrm{e}^{-\mathrm{i}\left(\omega t - k_y y\right)}\mathrm{d}y\,\mathrm{d}t \tag{3.50}$$

$$\bar{\mathbf{F}}\left(k_y, \omega\right) = \int_{-\infty}^{+\infty}\int_{-\infty}^{+\infty} \mathbf{F}\left(y,t\right)\mathrm{e}^{-\mathrm{i}\left(\omega t - k_y y\right)}\mathrm{d}y\,\mathrm{d}t \tag{3.51}$$

In the transformed domain, the system (3.44) changes into

$$\bar{\mathbf{F}} = \left[\mathbf{A}_{yy}k_y^2 + \mathrm{i}k_y\left(\mathbf{B}_{xy} + \mathbf{B}_{zy}\right) + \left(\mathbf{G}_{xx} + \mathbf{G}_{xz} + \mathbf{G}_{zz} - \omega^2\mathbf{M}\right)\right]\bar{\mathbf{U}} \tag{3.52}$$

All matrices in (3.52) are symmetric, except for $\mathbf{B}_{xy}$ and $\mathbf{B}_{zy}$, which are skew-symmetric. However, for cross-anisotropic materials whose constitutive matrix is given in equation (2.1) of chapter 2, it is possible to transform these matrices into symmetric matrices by means of a *similarity* transformation that consists in multiplying the rows of (3.52) that are related to the y direction by $-\mathrm{i}$ and the columns related to the y direction by i. The referred to rows and columns have indexes $l = 2 + 3j$, with $j = 0,1,2,\ldots$. This transformation solely affects the matrices $\mathbf{B}_{xy}$ and $\mathbf{B}_{zy}$ and the vectors $\bar{\mathbf{F}}$ and $\bar{\mathbf{U}}$. After the transformation, the system (3.52) becomes

$$\overline{\mathbf{f}} = \left[\mathbf{A}_{yy} k_y^2 + k_y \left(\overline{\mathbf{B}}_{xy} + \overline{\mathbf{B}}_{zy} \right) + \left(\mathbf{G}_{xx} + \mathbf{G}_{xz} + \mathbf{G}_{zz} - \omega^2 \mathbf{M} \right) \right] \overline{\mathbf{u}} \tag{3.53}$$

where $\overline{\mathbf{f}}$ and $\overline{\mathbf{u}}$ are obtained from $\overline{\mathbf{F}}$ and $\overline{\mathbf{U}}$ after multiplying the rows l by $-\mathrm{i}$. Also, $\overline{\mathbf{B}}_{xy}$ and $\overline{\mathbf{B}}_{zy}$ are obtained from $\mathbf{B}_{xy}$ and $\mathbf{B}_{zy}$ by reversing the sign of the columns with index l. After solving the system of equations (3.53) for $\overline{\mathbf{u}}$, the displacements $\overline{\mathbf{U}}$ in the wavenumber-frequency domain are recovered by multiplying every row l of $\overline{\mathbf{u}}$ by $+\mathrm{i}$.

[Note1: the above description considered the cross-anisotropic material defined in eq. (2.1). In some cases, it is more convenient to define materials whose direction of anisotropy is the longitudinal direction instead of the vertical one. For example, it is common to model the sleepers (which are discontinuous) as a continuous anisotropic slab, where the in-plane behavior differs from the out-of-plane behavior (Alves Costa, 2011). In that case, the constitutive matrix

$$\mathbf{D} = \begin{bmatrix} \frac{1}{E_{xz}} & -\frac{\nu_{xyz}}{E_{xz}} & -\frac{\nu_{xz}}{E_{xz}} & 0 & 0 & 0 \\ -\frac{\nu_{xyz}}{E_{xz}} & \frac{1}{E_y} & -\frac{\nu_{xyz}}{E_{xz}} & 0 & 0 & 0 \\ -\frac{\nu_{xz}}{E_{xz}} & -\frac{\nu_{xyz}}{E_{xz}} & \frac{1}{E_{xz}} & 0 & 0 & 0 \\ 0 & 0 & 0 & \frac{2(1+\nu_y)}{E_y} & 0 & 0 \\ 0 & 0 & 0 & 0 & \frac{2(1+\nu_{xz})}{E_{xz}} & 0 \\ 0 & 0 & 0 & 0 & 0 & \frac{2(1+\nu_y)}{E_y} \end{bmatrix}^{-1} \tag{3.54}$$

is more appropriate. E_{xz} and E_y are the in-plane and out-of-plane elastic modulus, ν_{xz} and ν_y are the in-plane and out-of-plane Poisson's ratio, and ν_{xyz} is the cross Poisson's ratio. This last variable can assume negative values and must be such that matrix $\mathbf{D}$ is definite positive. The equations presented in this section are still valid for this constitutive matrix.]

[Note2: the above formulation considers only volume elements. In order to consider different elements, such as beams or shells, different differential equations and discretizations have to be used, resulting in a final system of equations that will contain terms in k_y^3 and k_y^4 (Galvín et al., 2010). For an Euler beam, the system of equations is

$$\begin{cases} f_x = \left(EI_x k_y^4 - \omega^2 \rho A \right) u_x \\ f_y = \left(EA k_y^2 - \omega^2 \rho A \right) u_y \\ f_z = \left(EI_z k_y^4 - \omega^2 \rho A \right) u_z \end{cases} \tag{3.55}$$

where E is the Young's modulus of the beam, ρ is the mass density, $I_{x,z}$ are the moments of intertia, A is the cross section area, $f_{x,y,z}$ represent the external forces and $u_{x,y,z}$ represent the displacements of the axis of the beam.]

3.3.3 Example - dispersion curves of a UCI861-3 rail

To validate the implementation of the procedure presented in this section, the dispersion curves of a UCI861-3 rail are calculated and compared with the curves obtained by Gavric (1995), who also used a 2.5D FEM procedure. Dispersion curves correspond to the pairs

(k_y, ω) that result in singular systems of equations (3.52) or (3.53). In other words, the dispersion curves plot the values k_y that are solutions of

$$\det\left[\mathbf{A}_{yy}k_y^2 + k_y\left(\overline{\mathbf{B}}_{xy} + \overline{\mathbf{B}}_{zy}\right) + \left(\mathbf{G}_{xx} + \mathbf{G}_{xz} + \mathbf{G}_{zz} - \omega^2\mathbf{M}\right)\right] = 0 \tag{3.56}$$

as function of the frequency ω. The solutions of (3.56) may be real or complex: the real solutions correspond to waves that propagate while the complex solutions correspond to waves that evanesce (i.e., attenuate) with the distance to the source.

The 2.5D FEM methodology presented in this section is employed to determine the dispersion curves of the propagating modes of the rail. With that intention, the rail section is divided into 166 quadrilateral elements and a total of 214 nodes, resulting in the mesh shown in Figure 3.10. For that mesh, the global matrices $\mathbf{A}_{yy}$, $\overline{\mathbf{B}}_{\alpha y}$, $\mathbf{G}_{\alpha\beta}$ and $\mathbf{M}$ are calculated and then used in equation (3.56).

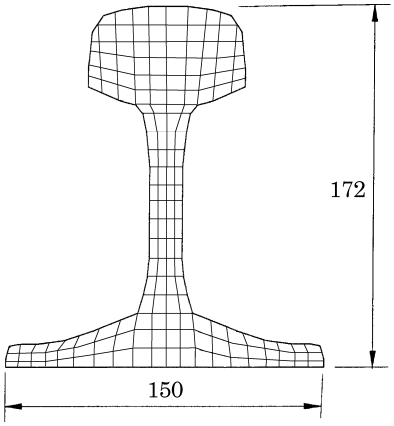

Figure 3.10: Used mesh for the rail section (dimensions in mm)

In Figure 3.11, the results obtained in this work (black) are compared with the curves obtained by Gavric (red). The agreement of the curves is good namely for the lower frequencies. For the higher frequencies (above 3000 Hz), even though the shapes of the curves are the same, there is a shift between the results obtained in this work and the results obtained by Gavric. The disagreement might be justified by discrepancies in the material parameters: while in this work the material properties are Young's Modulus $E = 200\,\text{GPa}$, mass density $\rho = 7859\,\text{kg/m}^3$, and Poisson's ratio $\nu = 0.28$, in (Gavric, 1995) the material properties are not specified.

[Note: equation (3.56) is solved for k_y by determining the eigenvalues and eigenvectors of

$$\left[\mathbf{A}_{yy}k_y^2 + k_y\left(\overline{\mathbf{B}}_{xy} + \overline{\mathbf{B}}_{zy}\right) + \left(\mathbf{G}_{xx} + \mathbf{G}_{xz} + \mathbf{G}_{zz} - \omega^2\mathbf{M}\right)\right]\boldsymbol{\phi} = \mathbf{0} \tag{3.57}$$

If the rows $l = 2 + 3j$ $(j = 0,1,2,...)$ of (3.57) are multiplied by k_y and the columns l are divided by k_y, the symmetric eigenvalue problem (3.57) can be reduced to a non-symmetric general eigenvalue problem of the form

$$\left(\mathbf{A}k_y^2 + \mathbf{C}\right)\boldsymbol{\phi} = \mathbf{0} \tag{3.58}$$

where $\mathbf{A}$ is obtained by adding to matrix $\mathbf{A}_{yy}$ the rows l of $\bar{\mathbf{B}}_{xy}+\bar{\mathbf{B}}_{zy}$ and $\mathbf{C}$ is obtained by adding to matrix $\mathbf{G}_{xx}+\mathbf{G}_{xz}+\mathbf{G}_{zz}-\omega^2\mathbf{M}$ the columns l of $\bar{\mathbf{B}}_{xy}+\bar{\mathbf{B}}_{zy}$.]

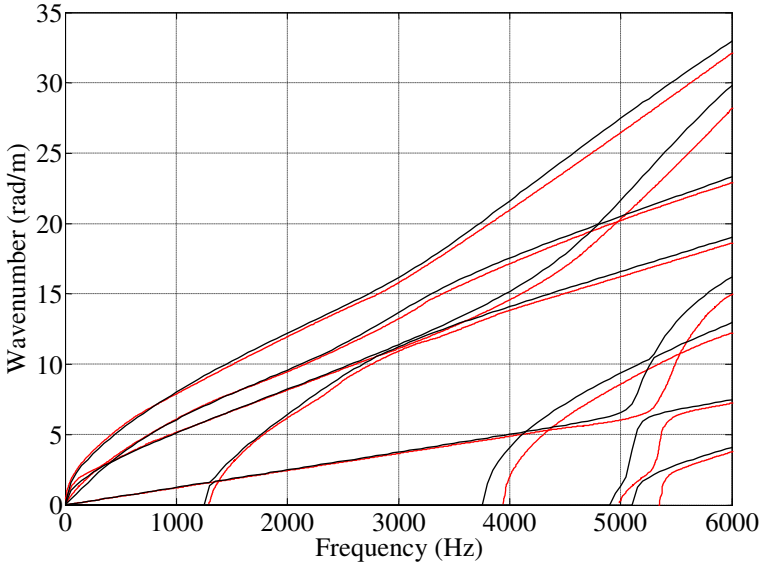

Figure 3.11: Dispersion curves for the UIC861-3 rail: present work (black); Gavric (1995) (red)

3.4 2.5D Boundary Element Method

3.4.1 Introduction

The formulation of the 2.5D BEM is very similar to the formulation of the 3D BEM. However, because in the 2.5D BEM the mesh is 2D, and because the TLM is used to calculate the fundamental solution, it is possible to evaluate the boundary integrals analytically via modal summation. This feature is not possible with methods such as the stiffness matrix method, and represents one of the advantages of the TLM. In this section, the 2.5D BEM is presented and it is explained how use the TLM to calculate the boundary integrals.

3.4.2 Formulation

Recall the boundary integral equation expressed in (3.7), which concerns a three-dimensional body. Since in the present case the body is assumed to be invariant in the longitudinal y direction, the boundary integral (3.7) is equivalent to

$$\kappa_{kl}\tilde{u}_k(\xi,\omega)=\int_{\Gamma_S}\int_{-\infty}^{+\infty}\tilde{p}_k(\mathbf{x},\omega)\tilde{u}^*_{kl}(\mathbf{x},\xi,\omega)\,dy\,d\Gamma-\int_{\Gamma_S}\int_{-\infty}^{+\infty}\tilde{p}^*_{kl}(\mathbf{x},\xi,\omega)\tilde{u}_k(\mathbf{x},\omega)\,dy\,d\Gamma \tag{3.59}$$

where Γ_S is the boundary of the cross section Ω_S. The Fourier transform of equation (3.59) with respect to the longitudinal coordinate results in the boundary integral equation in the 2.5D domain, which is (Galvín et al., 2010)

$$\kappa_{kl}\overline{u}_k\left(\boldsymbol{\xi},k_y,\omega\right)=\int_{\Gamma_S}\overline{p}_k\left(\mathbf{x},k_y,\omega\right)\overline{u}^*_{kl}\left(\mathbf{x},\boldsymbol{\xi},-k_y,\omega\right)d\Gamma-\int_{\Gamma_S}\overline{p}^*_{kl}\left(\mathbf{x},\boldsymbol{\xi},-k_y,\omega\right)\overline{u}_k\left(\mathbf{x},k_y,\omega\right)d\Gamma \tag{3.60}$$

In equation (3.60), $\overline{u}_k\left(\mathbf{x},k_y,\omega\right)$ and $\overline{p}_k\left(\mathbf{x},k_y,\omega\right)$ are the displacement and traction fields in the wavenumber-space-frequency domain, while $\overline{u}^*_{kl}\left(\mathbf{x},\boldsymbol{\xi},k_y,\omega\right)$ and $\overline{p}^*_{kl}\left(\mathbf{x},\boldsymbol{\xi},k_y,\omega\right)$ are the 2.5D fundamental displacements and tractions discussed in chapter 2 (Note: in chapter 2, these variables are written without the over bar). Also, the longitudinal coordinate y is dropped, i.e., $\mathbf{x}=(x,z)$ and $\boldsymbol{\xi}=(\xi_x,\xi_z)$. When $\boldsymbol{\xi}$ belongs to the cross section Ω_S then $\kappa_{kl}=\delta_{kl}$, and when $\boldsymbol{\xi}$ does not belong to the cross section Ω_S then $\kappa_{kl}=0$.

Similarly to the 3D case, the boundary equation (3.60) is not valid for collocation points $\boldsymbol{\xi}$ that belong to the boundary Γ_S. Hence, (3.60) must be regularized, and for that purpose the two approaches discussed in section 3.2.3 can be followed. However, as apposed to the option taken for the 3D case, for the 2.5D case the first approach is followed (i.e., the "limiting procedure"), which yields the regularized boundary integral equation

$$c^{\boldsymbol{\xi}}_{kl}\overline{u}_k\left(\boldsymbol{\xi},k_y,\omega\right)=\int_{\Gamma_S}\overline{p}_k\left(\mathbf{x},k_y,\omega\right)\overline{u}^*_{kl}\left(\mathbf{x},\boldsymbol{\xi},-k_y,\omega\right)d\Gamma-\int_{\Gamma_S}\overline{p}^*_{kl}\left(\mathbf{x},\boldsymbol{\xi},-k_y,\omega\right)\overline{u}_k\left(\mathbf{x},k_y,\omega\right)d\Gamma \tag{3.61}$$

The boundary coefficient $c^{\boldsymbol{\xi}}_{kl}$ depends on the geometry of the boundary at the collocation point $\boldsymbol{\xi}$. The calculation of this coefficient is addressed in a later section of this work.

To solve equation (3.61), the boundary Γ_S is divided into N_e boundary elements and N_n boundary nodes, similarly to the 3D case: the difference is that in the 2.5D case the boundary elements consist in one dimensional elements in the xz plane while in the 3D case the boundary elements consist in surface elements that can have any orientation in the xyz space. Within each boundary element the displacement and traction fields are approximated by means of interpolation functions and nodal values, i.e.,

$$\overline{u}_k\left(\mathbf{x},k_y,\omega\right)=\sum_{j=1}^{N_n^{(e)}}\overline{u}_k^{(ej)}\left(k_y,\omega\right)S^{(e)}_{(j)}\left(\mathbf{x}\right) \tag{3.62}$$

$$\overline{p}_k\left(\mathbf{x},k_y,\omega\right)=\sum_{j=1}^{N_n^{(e)}}\overline{p}_k^{(ej)}\left(k_y,\omega\right)S^{(e)}_{(j)}\left(\mathbf{x}\right) \tag{3.63}$$

where $\overline{u}_k^{(ej)}\left(k_y,\omega\right)$ and $\overline{p}_k^{(ej)}\left(k_y,\omega\right)$ are the nodal values of the j^{th} node of the e^{th} element, $S^{(e)}_{(j)}\left(\mathbf{x}\right)$ is the associated interpolation (shape) function evaluated at point $\mathbf{x}$ ($\mathbf{x}$ is contained in the e^{th} element) and $N_n^{(e)}$ is the number of nodes contained in the e^{th} element. The shape functions $S^{(e)}_{(j)}\left(\mathbf{x}\right)$ used for the 2.5D case are the same shape functions used for the 2D boundary elements and can be found in Dominguez (1993).

Now, assume that the collocation point $\boldsymbol{\xi}$ corresponds to one of the N_n nodes of the boundary (say, the i^{th} node, with coordinates $\mathbf{x}_i$). In this case, after accounting for the approximations in equations (3.62) and (3.63), equation (3.61) becomes

$$\begin{aligned} c_{kl}^{(i)}\overline{u}_l^{(i)}\left(k_y,\omega\right) = &\sum_{e=1}^{N_e}\left\{\sum_{j=1}^{N_n^{(e)}}\left(\overline{p}_k^{(ej)}\left(k_y,\omega\right)\overbrace{\int_{\Gamma_e}\overline{u}_{kl}^{*}\left(\mathbf{x},\mathbf{x}_i,-k_y,\omega\right)S_{(j)}^{(e)}\left(\mathbf{x}\right)d\Gamma_e}^{\overline{U}_{kl}^{(ej)}\left(\mathbf{x}_i,-k_y,\omega\right)}\right)\right\} \\ &-\sum_{e=1}^{N_e}\left\{\sum_{j=1}^{N_n^{(e)}}\left(\overline{u}_k^{(ej)}\left(k_y,\omega\right)\overbrace{\int_{\Gamma_e}\overline{p}_{kl}^{*}\left(\mathbf{x},\mathbf{x}_i,-k_y,\omega\right)S_{(j)}^{(e)}\left(\mathbf{x}\right)d\Gamma_e}^{\overline{P}_{kl}^{(ej)}\left(\mathbf{x}_i,-k_y,\omega\right)}\right)\right\} \end{aligned} \tag{3.64}$$

or in compact form,

$$\begin{aligned} c_{kl}^{(i)}\overline{u}_l^{(i)}\left(k_y,\omega\right) = &\sum_{e=1}^{N_e}\sum_{j=1}^{N_n^{(e)}}\overline{p}_k^{(ej)}\left(k_y,\omega\right)\overline{U}_{kl}^{(ej)}\left(\mathbf{x}_i,-k_y,\omega\right) \\ &-\sum_{e=1}^{N_e}\sum_{j=1}^{N_n^{(e)}}\overline{u}_k^{(ej)}\left(k_y,\omega\right)\overline{P}_{kl}^{(ej)}\left(\mathbf{x}_i,-k_y,\omega\right) \end{aligned} \tag{3.65}$$

Since the shape functions $S_{(j)}^{(e)}\left(\mathbf{x}\right)$ are polynomial functions (usually up to the second degree), for the case of horizontally or vertically oriented boundary elements, the terms $\overline{U}_{kl}^{(ej)}\left(\mathbf{x}_i,-k_y,\omega\right)$ and $\overline{P}_{kl}^{(ej)}\left(\mathbf{x}_i,-k_y,\omega\right)$ can be calculated in closed form expressions, as explained in the following sections.

Equation (3.65) is now expanded so that l assumes all the three different directions. Equation (3.65) can then be replaced with

$$\begin{aligned} \mathbf{C}^{(i)}\overline{\mathbf{u}}^{(i)}\left(k_y,\omega\right) = &\sum_{e=1}^{N_e}\sum_{j=1}^{N_n^{(e)}}\overline{\mathbf{U}}^{(ej)}\left(\mathbf{x}_i,-k_y,\omega\right)\overline{\mathbf{p}}^{(ej)}\left(k_y,\omega\right) \\ &-\sum_{e=1}^{N_e}\sum_{j=1}^{N_n^{e}}\overline{\mathbf{P}}^{(ej)}\left(\mathbf{x}_i,-k_y,\omega\right)\overline{\mathbf{u}}^{(ej)}\left(k_y,\omega\right) \end{aligned} \tag{3.66}$$

where the bold variables have the following meanings (the arguments $\mathbf{x}_i$, k_y and ω are dropped):

$$\overline{\mathbf{u}}^{(i)} = \begin{bmatrix} \overline{u}_x^{(i)} \\ \overline{u}_y^{(i)} \\ \overline{u}_z^{(i)} \end{bmatrix} \qquad \overline{\mathbf{u}}^{(ej)} = \begin{bmatrix} \overline{u}_x^{(ej)} \\ \overline{u}_y^{(ej)} \\ \overline{u}_z^{(ej)} \end{bmatrix} \qquad \overline{\mathbf{p}}^{(ej)} = \begin{bmatrix} \overline{p}_x^{(ej)} \\ \overline{p}_y^{(ej)} \\ \overline{p}_z^{(ej)} \end{bmatrix}$$

$$\overline{\mathbf{U}}^{(ej)} = \begin{bmatrix} \overline{U}_{xx}^{(ej)} & \overline{U}_{yx}^{(ej)} & \overline{U}_{zx}^{(ej)} \\ \overline{U}_{xy}^{(ej)} & \overline{U}_{yy}^{(ej)} & \overline{U}_{zy}^{(ej)} \\ \overline{U}_{xz}^{(ej)} & \overline{U}_{yz}^{(ej)} & \overline{U}_{zz}^{(ej)} \end{bmatrix} \qquad \overline{\mathbf{P}}^{(ej)} = \begin{bmatrix} \overline{P}_{xx}^{(ej)} & \overline{P}_{yx}^{(ej)} & \overline{P}_{zx}^{(ej)} \\ \overline{P}_{xy}^{(ej)} & \overline{P}_{yy}^{(ej)} & \overline{P}_{zy}^{(ej)} \\ \overline{P}_{xz}^{(ej)} & \overline{P}_{yz}^{(ej)} & \overline{P}_{zz}^{(ej)} \end{bmatrix} \qquad \mathbf{C}^{(i)} = \begin{bmatrix} c_{xx}^{(i)} & c_{xy}^{(i)} & c_{xz}^{(i)} \\ c_{yx}^{(i)} & c_{yy}^{(i)} & c_{yz}^{(i)} \\ c_{zx}^{(i)} & c_{zy}^{(i)} & c_{zz}^{(i)} \end{bmatrix}$$

Finally, after forcing the collocation point $\boldsymbol{\xi}$ to assume all the N_n nodes and assembling the matrices $\overline{\mathbf{U}}^{(ej)}$ into a square matrix $\mathbf{U}$, the matrices $\overline{\mathbf{P}}^{(ej)}$ into a square matrix $\mathbf{P}$ and the

matrices $\mathbf{C}^{(i)}$ into a square block diagonal matrix $\mathbf{C}$, one arrives at the final system of equations

$$\left\{\mathbf{P}\left(-k_y,\omega\right)+\mathbf{C}\right\}\bar{\mathbf{u}}\left(k_y,\omega\right)=\mathbf{U}\left(-k_y,\omega\right)\bar{\mathbf{p}}\left(k_y,\omega\right) \tag{3.67}$$

in which $\bar{\mathbf{u}}\left(k_y,\omega\right)$ is a vector that collects all the nodal displacements and $\bar{\mathbf{p}}\left(k_y,\omega\right)$ is a vector that collects all the nodal tractions. Equation (3.67) can be solved for $\bar{\mathbf{u}}$, $\bar{\mathbf{p}}$ or a combination of the two, depending on the unknowns of the problem.

When the boundary elements are horizontally or vertically oriented, it is possible to calculate the boundary integrals

$$\bar{U}_{kl}^{(ej)}=\int_{\Gamma_e}\bar{u}_{kl}^{*}\left(\mathbf{x},\mathbf{x}_i,-k_y,\omega\right)S_{(j)}^{(e)}\left(\mathbf{x}\right)d\Gamma_e \tag{3.68}$$

and

$$\bar{P}_{kl}^{(ej)}=\int_{\Gamma_e}\bar{p}_{kl}^{*}\left(\mathbf{x},\mathbf{x}_i,-k_y,\omega\right)S_{(j)}^{(e)}\left(\mathbf{x}\right)d\Gamma_e \tag{3.69}$$

in closed form expressions. The next sections address this issue.

3.4.3 Horizontal boundary elements

Horizontal boundaries are defined by a constant depth. If it is assumed that the collocation point ξ is placed at the depth z_n (n^{th} interface of the TLM model) and that the boundary element Γ_e is at the depth z_m (m^{th} interface of the TLM model) (Figure 3.12), then the integrals (3.68) and (3.69) can be replaced by integrals of the form (the variables k_y,ω are dropped)

$$\bar{U}_{kl}^{(ej)}=\int_{\Gamma_e}\bar{u}_{kl}^{(mn)}\left(x-x_\xi\right)S_j^{(e)}\left(x\right)\mathrm{d}x \tag{3.70}$$

$$\bar{P}_{kl}^{(ej)}=\int_{\Gamma_e}\bar{p}_{kl}^{(mn)}\left(x-x_\xi\right)S_{(j)}^{(e)}\left(x\right)\mathrm{d}x \tag{3.71}$$

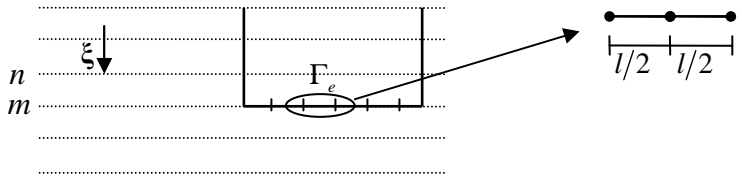

Figure 3.12: Horizontal boundary element

The variables $\bar{u}_{kl}^{(mn)}$ correspond to the fundamental displacements in the 2.5D domain described in chapter 2 (and referred to as $u_{\alpha\beta}^{(mn)}$), while $\bar{p}_{kl}^{(mn)}$ corresponds to the 2.5D fundamental stresses $\pm\sigma_{\alpha z\beta}^{(mn)}$, also described in chapter 2 (the positive sign is used when the outwards normal of the boundary faces the positive z direction, while the negative sign is used otherwise).

In order to complete the analytical evaluations of the integrals, equation (3.70) is first changed into a more convenient form. As seen in the previous chapter, the fundamental displacements are obtained through the inversion of the solutions in the wavenumber domain, i.e.,

$$\bar{u}_{kl}^{(mn)}(x)=\frac{1}{2\pi}\int_{-\infty}^{+\infty}U_{kl}^{(mn)}(k_x)\mathrm{e}^{-\mathrm{i}k_x x}\mathrm{d}k_x \tag{3.72}$$

In this equation, $U_{kl}^{(mn)}(k_x)$ are the wavenumber displacements defined in Table 2.2, having a different meaning than $\bar{U}_{kl}^{(ej)}$.

Assuming that the x axis is centered at the midpoint of the boundary element (of total width l), after substituting (3.72) into equation (3.70), the latter becomes

$$\begin{aligned}\bar{U}_{kl}^{(ej)} &= \int_{-l/2}^{l/2}\frac{1}{2\pi}\int_{-\infty}^{+\infty}U_{kl}^{(mn)}(k_x)\mathrm{e}^{-\mathrm{i}k_x\left(x-x_\xi\right)}\mathrm{d}k_x S_{(j)}^{(e)}(x)\mathrm{d}x \\ &= \frac{1}{2\pi}\int_{-\infty}^{+\infty}U_{kl}^{(mn)}(k_x)\int_{-l/2}^{l/2}S_{(j)}^{(e)}(x)\mathrm{e}^{-\mathrm{i}k_x x}\mathrm{d}x\,\mathrm{e}^{\mathrm{i}k_x x_\xi}\mathrm{d}k_x\end{aligned} \tag{3.73}$$

The Fourier transform of $S_{(j)}^{(e)}(x)$ is defined by

$$\tilde{S}_{(j)}^{(e)}(k_x)=\int_{-\infty}^{+\infty}S_{(j)}^{(e)}(x)\mathrm{e}^{-\mathrm{i}k_x x}\mathrm{d}x=\int_{-l/2}^{l/2}S_{(j)}^{(e)}(x)\mathrm{e}^{-\mathrm{i}k_x x}\mathrm{d}x \tag{3.74}$$

and after introducing this in equation (3.73) one obtains

$$\bar{U}_{kl}^{(ej)}=\frac{1}{2\pi}\int_{-\infty}^{+\infty}U_{kl}^{(mn)}(k_x)\tilde{S}_{(j)}^{(e)}(k_x)\,\mathrm{e}^{\mathrm{i}k_x x_\xi}\mathrm{d}k_x \tag{3.75}$$

The application of the same procedure to equation (3.71) yields

$$\bar{P}_{kl}^{(ej)}=\frac{1}{2\pi}\int_{-\infty}^{+\infty}\pm\bar{\sigma}_{kzl}^{(mn)}(k_x)\tilde{S}_{(j)}^{(e)}(k_x)\,\mathrm{e}^{\mathrm{i}k_x x_\xi}\mathrm{d}k_x \tag{3.76}$$

The variable $U_{kl}^{(mn)}(k_x)$ is calculated by modal superposition. If the horizontal boundary is placed at the interface between two thin-layers (a condition that is assumed to be true throughout the remainder of the formulation), then $\bar{\sigma}_{kzl}^{(mn)}$ corresponds to the consistent nodal tractions $\bar{t}_{kl}^{(mn)}$ at that interface and thus $\bar{\sigma}_{kzl}^{(mn)}(k_x)$ can also be obtained by modal superposition – eqs. (2.51)-(2.59). For these reasons, if $\tilde{S}_{(j)}^{(e)}(k_x)$ can be expressed analytically, then $\bar{U}_{kl}^{(ej)}$ and $\bar{P}_{kl}^{(ej)}$ can also be obtained analytically by modal superposition (in the BEM, the shape functions $S_{(j)}^{(e)}(x)$ are usually polynomial functions whose Fourier transforms can be easily calculated). This idea is explored next for $S_{(j)}^{(e)}(x)=S_n(x)=x^n, n=0,1,2$, but first observe that even though $u_{\alpha\beta}^{(mn)}(x)$ and $\sigma_{\alpha z\beta}^{(mn)}(x)$ become singular when $x\to 0$, the variables $U_{\alpha\beta}^{(mn)}(k_x)$ and $\bar{\sigma}_{\alpha z\beta}^{(mn)}(k_x)$ are finite, and therefore the values of $\bar{U}_{kl}^{(ej)}$ and $\bar{P}_{kl}^{(ej)}$ calculated with equations (3.75) and (3.76) are also finite. Hence, when the collocation point belongs to the horizontal boundary element, $\bar{P}_{kl}^{(ej)}$ already includes the factor c_{kl}. In other words, using the proposed procedure, eq. (3.60) can be used directly in place of the regularized equation (3.61), with the term c_{kl} being automatically accounted for.

Case 1: $S_{(j)}^{(e)}(x) = S_0(x) = 1$

The Fourier transform of $S_0(x)$, according to (3.74), is

$$\tilde{S}_0(k_x) = \int_{-l/2}^{l/2} \mathrm{e}^{-\mathrm{i}k_x x}\mathrm{d}x = -\frac{\mathrm{i}}{k_x}\left(\mathrm{e}^{\mathrm{i}\frac{k_x l}{2}} - \mathrm{e}^{-\mathrm{i}\frac{k_x l}{2}}\right) \tag{3.77}$$

The coefficients $\bar{U}_{kl}^{(ej)}$ are then obtained with

$$\bar{U}_{kl}^{(ej)} = \frac{1}{2\pi}\int_{-\infty}^{+\infty} -\frac{\mathrm{i}}{k_x} U_{kl}^{(mn)}(k_x)\left[\mathrm{e}^{\mathrm{i}k_x\left(x_\xi + \frac{l}{2}\right)} - \mathrm{e}^{\mathrm{i}k_x\left(x_\xi - \frac{l}{2}\right)}\right]\mathrm{d}k_x \tag{3.78}$$

and the coefficients $\bar{P}_{kl}^{(ej)}$ with

$$\bar{P}_{kl}^{(ej)} = \frac{1}{2\pi}\int_{-\infty}^{+\infty} -\frac{\mathrm{i}}{k_x} \bar{t}_{kl}^{(mn)}(k_x)\left[\mathrm{e}^{\mathrm{i}k_x\left(x_\xi + \frac{l}{2}\right)} - \mathrm{e}^{\mathrm{i}k_x\left(x_\xi - \frac{l}{2}\right)}\right]\mathrm{d}k_x \tag{3.79}$$

From equations (3.78) and (3.79) it can be concluded that the calculation of the coefficients $\bar{U}_{kl}^{(ej)}$ and $\bar{P}_{kl}^{(ej)}$ follow exactly the same steps as the calculation of $u_{kl}^{(mn)}(x)$ (section 2.5.1) and $t_{kl}^{(mn)}(x)$ (section 2.5.3), changing only the integrals $I_{nj}^{(p)}(x)$ by the integrals $J_{nj}^{(p)}$ of the form

$$J_{nj}^{(p)} = -\mathrm{i}\left[I_{nj}^{(p-1)}\left(-x_\xi - \frac{l}{2}\right) - I_{nj}^{(p-1)}\left(-x_\xi + \frac{l}{2}\right)\right] \tag{3.80}$$

The integrals $I_{nj}^{(-1)}(x)$ required to evaluate the coefficients $\bar{U}_{kl}^{(ej)}$ and $\bar{P}_{kl}^{(ej)}$ are given in Table 2.1.

Case 2: $S_j^e(x) = S_1(x) = x$

The Fourier transform of $S_1(x)$, according to (3.74), is

$$\tilde{S}_1(k_x) = \int_{-l/2}^{l/2} x\,\mathrm{e}^{-\mathrm{i}k_x x}\mathrm{d}x = \frac{l}{2}\frac{\mathrm{i}}{k_x}\left(\mathrm{e}^{\mathrm{i}\frac{k_x l}{2}} + \mathrm{e}^{-\mathrm{i}\frac{k_x l}{2}}\right) + \frac{1}{k_x^2}\left(\mathrm{e}^{-\mathrm{i}\frac{k_x l}{2}} - \mathrm{e}^{\mathrm{i}\frac{k_x l}{2}}\right) \tag{3.81}$$

The coefficients $\bar{U}_{kl}^{(ej)}$ are then obtained with

$$\bar{U}_{kl}^{(ej)} = \frac{1}{2\pi}\int_{-\infty}^{+\infty} U_{kl}^{(mn)}(k_x)\left[\frac{l}{2}\frac{\mathrm{i}}{k_x}\left(\mathrm{e}^{\mathrm{i}k_x\left(x_\xi + \frac{l}{2}\right)} + \mathrm{e}^{\mathrm{i}k_x\left(x_\xi - \frac{l}{2}\right)}\right) + \frac{1}{k_x^2}\left(\mathrm{e}^{\mathrm{i}k_x\left(x_\xi - \frac{l}{2}\right)} - \mathrm{e}^{\mathrm{i}k_x\left(x_\xi + \frac{l}{2}\right)}\right)\right]\mathrm{d}k_x \tag{3.82}$$

and the coefficients $\bar{P}_{kl}^{(ej)}$ with

$$\bar{P}_{kl}^{(ej)} = \frac{1}{2\pi}\int_{-\infty}^{+\infty} \bar{t}_{kl}^{(mn)}(k_x)\left[\frac{l}{2}\frac{\mathrm{i}}{k_x}\left(\mathrm{e}^{\mathrm{i}k_x\left(x_\xi + \frac{l}{2}\right)} + \mathrm{e}^{\mathrm{i}k_x\left(x_\xi - \frac{l}{2}\right)}\right) + \frac{1}{k_x^2}\left(\mathrm{e}^{\mathrm{i}k_x\left(x_\xi - \frac{l}{2}\right)} - \mathrm{e}^{\mathrm{i}k_x\left(x_\xi + \frac{l}{2}\right)}\right)\right]\mathrm{d}k_x \tag{3.83}$$

From equations (3.82) and (3.83) it can be concluded that the calculation of the coefficients $\bar{U}_{kl}^{(ej)}$ and $\bar{P}_{kl}^{(ej)}$ follow exactly the same steps as the calculation of $u_{kl}^{(mn)}(x)$ (section 2.5.1) and $t_{kl}^{(mn)}(x)$ (section 2.5.3), changing only the integrals $I_{nj}^{(p)}(x)$ by the integrals $J_{nj}^{(p)}$ of the form

$$J_{nj}^{(p)} = \mathrm{i}\frac{l}{2}\left[I_{nj}^{(p-1)}\left(-x_\xi - \frac{l}{2}\right) + I_{nj}^{(p-1)}\left(-x_\xi + \frac{l}{2}\right)\right] + \left[I_{nj}^{(p-2)}\left(-x_\xi - \frac{l}{2}\right) - I_{nj}^{(p-2)}\left(-x_\xi + \frac{l}{2}\right)\right] \tag{3.84}$$

The integrals $I_{nj}^{(-2)}(x)$ required to evaluate the coefficients $\bar{U}_{kl}^{(ej)}$ and $\bar{P}_{kl}^{(ej)}$ are given in Table 3.2.

Case 3: $S_j^e(x) = S_2(x) = x^2$

The Fourier transform of $S_2(x)$, according to (3.74), is

$$\tilde{S}_2(k_x) = \int_{-l/2}^{l/2} x^2 \mathrm{e}^{-\mathrm{i}k_x x}\mathrm{d}x = -\frac{l^2\mathrm{i}}{4k_x}\left(\mathrm{e}^{\mathrm{i}\frac{k_x l}{2}} - \mathrm{e}^{-\mathrm{i}\frac{k_x l}{2}}\right) + \frac{l}{k_x^2}\left(\mathrm{e}^{\mathrm{i}\frac{k_x l}{2}} + \mathrm{e}^{-\mathrm{i}\frac{k_x l}{2}}\right) + \frac{2\mathrm{i}}{k_x^3}\left(\mathrm{e}^{\mathrm{i}\frac{k_x l}{2}} - \mathrm{e}^{-\mathrm{i}\frac{k_x l}{2}}\right) \tag{3.85}$$

The coefficients $\bar{U}_{kl}^{(ej)}$ are then obtained with

$$\bar{U}_{kl}^{(ej)} = \frac{1}{2\pi}\int_{-\infty}^{+\infty} U_{kl}^{(mn)}(k_x)\left[-\frac{l^2\mathrm{i}}{4k_x}\left(\mathrm{e}^{\mathrm{i}k_x\left(x_\xi+\frac{l}{2}\right)} - \mathrm{e}^{\mathrm{i}k_x\left(x_\xi-\frac{l}{2}\right)}\right) + \frac{l}{k_x^2}\left(\mathrm{e}^{\mathrm{i}k_x\left(x_\xi+\frac{l}{2}\right)} + \mathrm{e}^{\mathrm{i}k_x\left(x_\xi-\frac{l}{2}\right)}\right) + \frac{2\mathrm{i}}{k_x^3}\left(\mathrm{e}^{\mathrm{i}k_x\left(x_\xi+\frac{l}{2}\right)} - \mathrm{e}^{\mathrm{i}k_x\left(x_\xi-\frac{l}{2}\right)}\right)\right]\mathrm{d}k_x \tag{3.86}$$

and the coefficients $\bar{P}_{kl}^{(ej)}$ with

$$\bar{P}_{kl}^{(ej)} = \frac{1}{2\pi}\int_{-\infty}^{+\infty} \bar{t}_{kl}^{mn}(k_x)\left[-\frac{l^2\mathrm{i}}{4k_x}\left(\mathrm{e}^{\mathrm{i}k_x\left(x_\xi+\frac{l}{2}\right)} - \mathrm{e}^{\mathrm{i}k_x\left(x_\xi-\frac{l}{2}\right)}\right) + \frac{l}{k_x^2}\left(\mathrm{e}^{\mathrm{i}k_x\left(x_\xi+\frac{l}{2}\right)} + \mathrm{e}^{\mathrm{i}k_x\left(x_\xi-\frac{l}{2}\right)}\right) + \frac{2\mathrm{i}}{k_x^3}\left(\mathrm{e}^{\mathrm{i}k_x\left(x_\xi+\frac{l}{2}\right)} - \mathrm{e}^{\mathrm{i}k_x\left(x_\xi-\frac{l}{2}\right)}\right)\right]\mathrm{d}k_x \tag{3.87}$$

From equations (3.86) and (3.87) it can be concluded that the calculation of the coefficients $\bar{U}_{kl}^{(ej)}$ and $\bar{P}_{kl}^{(ej)}$ follow exactly the same steps as the calculation of $u_{kl}^{(mn)}(x)$ (section 2.5.1) and $t_{kl}^{(mn)}(x)$ (section 2.5.3), changing only the integrals $I_{nj}^{(p)}(x)$ by the integrals $J_{nj}^{(p)}$ of the form

$$J_{nj}^{(p)} = -\mathrm{i}\frac{l^2}{4}\left[I_{nj}^{(p-1)}\left(-x_\xi - \frac{l}{2}\right) - I_{nj}^{(p-1)}\left(-x_\xi + \frac{l}{2}\right)\right] + l\left[I_{nj}^{(p-2)}\left(-x_\xi - \frac{l}{2}\right) + I_{nj}^{(p-2)}\left(-x_\xi + \frac{l}{2}\right)\right] + 2\mathrm{i}\left[I_{nj}^{(p-3)}\left(-x_\xi - \frac{l}{2}\right) - I_{nj}^{(p-3)}\left(-x_\xi + \frac{l}{2}\right)\right] \tag{3.88}$$

The integrals $I_{nj}^{(-3)}(x)$ required to evaluate the coefficients $\bar{U}_{kl}^{(ej)}$ and $\bar{P}_{kl}^{(ej)}$ are given in Table 3.3.

Table 3.1: Closed form expressions for $I_{nj}^{(-1)}$ ($\mathrm{Im}\sqrt{k_j^2-k_y^2}<0$)

$$I_{1j}^{(-1)}=\frac{1}{2\pi}\int_{-\infty}^{+\infty}k_x^{-1}K_{1j}\,\mathrm{e}^{-\mathrm{i}k_x x}\,\mathrm{d}k_x=\frac{\mathrm{sign}(x)}{2\mathrm{i}\left(k_y^2-k_j^2\right)}\left(1-\mathrm{e}^{-\mathrm{i}\sqrt{k_j^2-k_y^2}|x|}\right)$$

$$I_{2j}^{(-1)}=\frac{1}{2\pi}\int_{-\infty}^{+\infty}k_x^{-1}K_{2j}\,\mathrm{e}^{-\mathrm{i}k_x x}\,\mathrm{d}k_x=-\frac{1}{2k_j^2}\left(\mathrm{sign}\left(k_y\right)\mathrm{e}^{-|k_y x|}+\mathrm{i}\frac{k_y}{\sqrt{k_j^2-k_y^2}}\mathrm{e}^{-\mathrm{i}\sqrt{k_j^2-k_y^2}|x|}\right)$$

$$I_{3j}^{(-1)}=\frac{1}{2\pi}\int_{-\infty}^{+\infty}k_x^{-1}K_{3j}\,\mathrm{e}^{-\mathrm{i}k_x x}\,\mathrm{d}k_x=-\frac{\mathrm{sign}(x)}{2\mathrm{i}k_j^2}\left(\mathrm{e}^{-|k_y x|}-\mathrm{e}^{-\mathrm{i}\sqrt{k_j^2-k_y^2}|x|}\right)$$

$$I_{4j}^{(-1)}=\frac{1}{2\pi}\int_{-\infty}^{+\infty}k_x^{-1}K_{4j}\,\mathrm{e}^{-\mathrm{i}k_x x}\,\mathrm{d}k_x=\frac{\mathrm{sign}(x)}{2\mathrm{i}}\left\{\frac{1}{k_y^2-k_j^2}+\frac{\mathrm{e}^{-|k_y x|}}{k_j^2}-\frac{k_y^2}{k_j^2\left(k_y^2-k_j^2\right)}\mathrm{e}^{-\mathrm{i}\sqrt{k_j^2-k_y^2}|x|}\right\}$$

$$I_{5j}^{(-1)}=\frac{1}{2\pi}\int_{-\infty}^{+\infty}k_x^{-1}K_{5j}\,\mathrm{e}^{-\mathrm{i}k_x x}\,\mathrm{d}k_x=\frac{1}{2\,\mathrm{i}k_j\sqrt{k_j^2-k_y^2}}\mathrm{e}^{-\mathrm{i}\sqrt{k_j^2-k_y^2}|x|}$$

$$I_{6j}^{(-1)}=\frac{1}{2\pi}\int_{-\infty}^{+\infty}k_x^{-1}K_{6j}\,\mathrm{e}^{-\mathrm{i}k_x x}\,dk_x=\frac{\mathrm{sign}(x)k_y}{2\mathrm{i}k_j\left(k_y^2-k_j^2\right)}\left(1-\mathrm{e}^{-\mathrm{i}\sqrt{k_j^2-k_y^2}|x|}\right)$$

Table 3.2: Closed form expressions for $I_{nj}^{(-2)}$ ($\mathrm{Im}\sqrt{k_j^2-k_y^2}<0$)

$$I_{1j}^{(-2)}=\frac{1}{2\pi}\int_{-\infty}^{+\infty}k_x^{-2}K_{1j}\,\mathrm{e}^{-\mathrm{i}k_x x}\,\mathrm{d}k_x=-\frac{1}{2\left(k_y^2-k_j^2\right)}\left(|x|-\mathrm{i}\frac{\mathrm{e}^{-\mathrm{i}\sqrt{k_j^2-k_y^2}|x|}}{\sqrt{k_j^2-k_y^2}}\right)$$

$$I_{2j}^{(-2)}=\frac{1}{2\pi}\int_{-\infty}^{+\infty}k_x^{-2}K_{2j}\,\mathrm{e}^{-\mathrm{i}k_x x}\,\mathrm{d}k_x=\frac{k_y\mathrm{sign}(x)}{2\mathrm{i}}\left\{\frac{1}{k_y^2\left(k_y^2-k_j^2\right)}+\frac{\mathrm{e}^{-|k_y x|}}{k_y^2k_j^2}-\frac{\mathrm{e}^{-\mathrm{i}\sqrt{k_j^2-k_y^2}|x|}}{k_j^2\left(k_y^2-k_j^2\right)}\right\}$$

$$I_{3j}^{(-2)}=\frac{1}{2\pi}\int_{-\infty}^{+\infty}k_x^{-2}K_{3j}\,\mathrm{e}^{-\mathrm{i}k_x x}\,\mathrm{d}k_x=-\frac{1}{2k_j^2}\left(\frac{\mathrm{e}^{-|k_y x|}}{|k_y|}+\mathrm{i}\frac{\mathrm{e}^{-\mathrm{i}\sqrt{k_j^2-k_y^2}|x|}}{\sqrt{k_j^2-k_y^2}}\right)$$

$$I_{4j}^{(-2)}=\frac{1}{2\pi}\int_{-\infty}^{+\infty}k_x^{-2}K_{4j}\,\mathrm{e}^{-\mathrm{i}k_x x}\,\mathrm{d}k_x=\frac{1}{2}\left\{\frac{-|x|}{k_y^2-k_j^2}+\frac{\mathrm{e}^{-|k_y x|}}{|k_y|k_j^2}+\mathrm{i}\frac{k_y^2\mathrm{e}^{-\mathrm{i}\sqrt{k_j^2-k_y^2}|x|}}{k_j^2\left(k_y^2-k_j^2\right)\sqrt{k_j^2-k_y^2}}\right\}$$

$$I_{5j}^{(-2)}=\frac{1}{2\pi}\int_{-\infty}^{+\infty}k_x^{-2}K_{5j}\,\mathrm{e}^{-\mathrm{i}k_x x}\,\mathrm{d}k_x=\frac{\mathrm{sign}(x)}{2\mathrm{i}k_j\left(k_y^2-k_j^2\right)}\left(1-\mathrm{e}^{-\mathrm{i}\sqrt{k_j^2-k_y^2}|x|}\right)$$

$$I_{6j}^{-2}=\frac{1}{2\pi}\int_{-\infty}^{+\infty}k_x^{-2}K_{6j}\,\mathrm{e}^{-\mathrm{i}k_x x}\,\mathrm{d}k_x=-\frac{k_y}{2k_j\left(k_y^2-k_j^2\right)}\left(|x|-\mathrm{i}\frac{\mathrm{e}^{-\mathrm{i}\sqrt{k_j^2-k_y^2}|x|}}{\sqrt{k_j^2-k_y^2}}\right)$$

Table 3.3: Closed form expressions for $I_{nj}^{(-3)}$ ($\mathrm{Im}\sqrt{k_j^2-k_y^2}<0$)

$$I_{1j}^{(-3)}=\frac{1}{2\pi}\int_{-\infty}^{+\infty}k_x^{-3}K_{1j}\,\mathrm{e}^{-\mathrm{i}k_x x}\,\mathrm{d}k_x = -\frac{\mathrm{sign}(x)}{2\mathrm{i}\left(k_y^2-k_j^2\right)}\left(\frac{x^2}{2}+\frac{1}{k_y^2-k_j^2}-\frac{\mathrm{e}^{-\mathrm{i}\sqrt{k_j^2-k_y^2}|x|}}{k_y^2-k_j^2}\right)$$

$$I_{2j}^{(-3)}=\frac{1}{2\pi}\int_{-\infty}^{+\infty}k_x^{-3}K_{2j}\,\mathrm{e}^{-\mathrm{i}k_x x}\,\mathrm{d}k_x = \frac{1}{2k_y}\left\{\frac{-|x|}{k_y^2-k_j^2}+\frac{\mathrm{e}^{-|k_y x|}}{|k_y|k_j^2}+\mathrm{i}\frac{k_y^2\mathrm{e}^{-\mathrm{i}\sqrt{k_j^2-k_y^2}|x|}}{k_j^2\left(k_y^2-k_j^2\right)\sqrt{k_j^2-k_y^2}}\right\}$$

$$I_{3j}^{(-3)}=\frac{1}{2\pi}\int_{-\infty}^{+\infty}k_x^{-3}K_{3j}\,\mathrm{e}^{-\mathrm{i}k_x x}\,\mathrm{d}k_x = \frac{\mathrm{sign}(x)}{2\mathrm{i}k_y^2}\left\{\frac{1}{k_y^2-k_j^2}+\frac{\mathrm{e}^{-|k_y x|}}{k_j^2}-\frac{k_y^2\mathrm{e}^{-\mathrm{i}\sqrt{k_j^2-k_y^2}|x|}}{k_j^2\left(k_y^2-k_j^2\right)}\right\}$$

$$I_{4j}^{(-3)}=\frac{1}{2\pi}\int_{-\infty}^{+\infty}k_x^{-3}K_{4j}\,\mathrm{e}^{-\mathrm{i}k_x x}\,\mathrm{d}k_x = -\frac{\mathrm{sign}(x)}{2\mathrm{i}}\left\{\frac{x^2}{2\left(k_y^2-k_j^2\right)}+\frac{2k_y^2-k_j^2}{k_y^2\left(k_y^2-k_j^2\right)^2}+\frac{\mathrm{e}^{-|k_y x|}}{k_y^2k_j^2}-\frac{k_y^2\mathrm{e}^{-\mathrm{i}\sqrt{k_j^2-k_y^2}|x|}}{k_j^2\left(k_y^2-k_j^2\right)^2}\right\}$$

$$I_{5j}^{(-3)}=\frac{1}{2\pi}\int_{-\infty}^{+\infty}k_x^{-3}K_{5j}\,\mathrm{e}^{-\mathrm{i}k_x x}\,\mathrm{d}k_x = -\frac{1}{2k_j\left(k_y^2-k_j^2\right)}\left(|x|-\mathrm{i}\frac{\mathrm{e}^{-\mathrm{i}\sqrt{k_j^2-k_y^2}|x|}}{\sqrt{k_j^2-k_y^2}}\right)$$

$$I_{6j}^{(-3)}=\frac{1}{2\pi}\int_{-\infty}^{+\infty}k_x^{-3}K_{6j}\,\mathrm{e}^{-\mathrm{i}k_x x}\,\mathrm{d}k_x = -\frac{\mathrm{sign}(x)k_y}{2\mathrm{i}k_j\left(k_y^2-k_j^2\right)}\left(\frac{x^2}{2}+\frac{1}{k_y^2-k_j^2}-\frac{\mathrm{e}^{-\mathrm{i}\sqrt{k_j^2-k_y^2}|x|}}{k_y^2-k_j^2}\right)$$

Considerations concerning horizontal boundaries

The calculation of the coefficients $\bar{U}_{kl}^{(ej)}$ involves only the components of the modal shapes at the elevation of the collocation point and at the elevation of the boundary element. By contrast, the calculation of the coefficients $\bar{P}_{kl}^{(ej)}$ involves the components of all TLM nodes that compose the thin-layer delimiting the boundary element. Since the boundary elements are placed at the interface between two consecutive thin-layers, a decision is required as to whether to consider the upper or the lower thin-layer.

When the collocation point is not contained in the boundary element, it is immaterial which thin-layer is used. On the other hand, when the collocation point is contained in the boundary element, the value of $\bar{P}_{kl}^{(ej)}$ depends on the thin-layer selected for the evaluation. The rule used in this work is that if the outwards normal faces up, the thin-layer located below the boundary is employed in the calculation of $\bar{P}_{kl}^{(ej)}$, otherwise the thin-layer above is used. By following this procedure, collocation points on horizontal boundaries are circumvented as depicted in Figure 3.13.

It is important to note that according to this procedure, when the collocation point ξ is at an edge of a boundary element ($x_\xi=\pm l/2$), then the coefficient $\bar{P}_{kl}^{(ej)}$ is calculated considering that the boundary is distorted as shown in Figure 3.14. This aspect is important for the treatment of corners, i.e., points where horizontal boundaries meet vertical boundaries (Figure 3.13b-c).

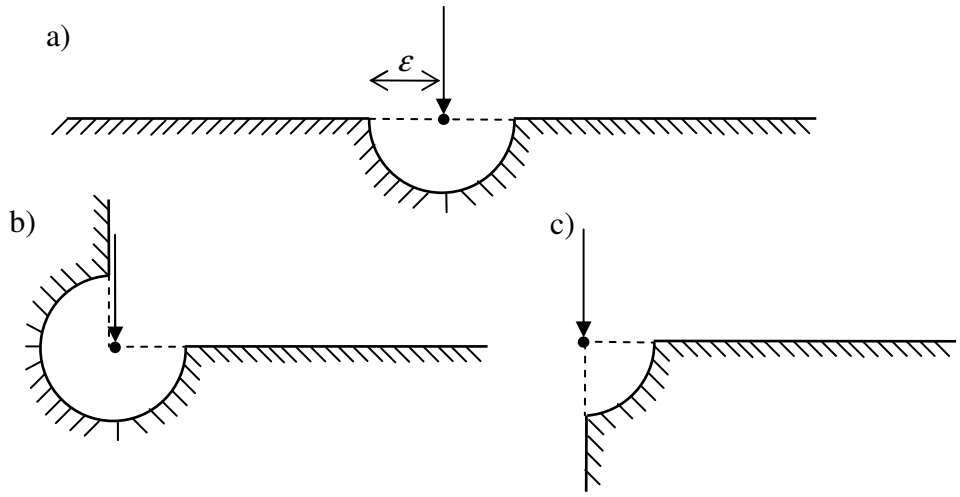

Figure 3.13: Exclusions in the domain at the collocation points. a) smooth horizontal boundary; b) concave corner; c) convex corner

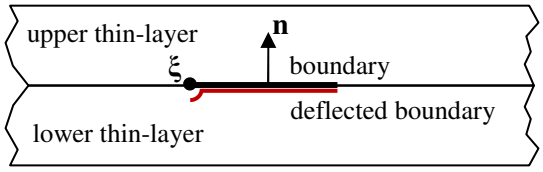

Figure 3.14: Deflection of the horizontal boundary when the collocation point is at one extreme

Due to the homogeneity of layered domains in the horizontal direction, the fundamental solutions depend on the horizontal distance between the source and the receiver, and not on their absolute horizontal coordinates. Hence, if the horizontal boundaries are dicretized in such a way that the boundary elements have the same length and expansion order, then the boundary coefficients $\bar{U}_{kl}^{(ej)}$ and $\bar{P}_{kl}^{(ej)}$ can be reused whenever the distance between the collocation points and the boundary elements is repeated. This fact can reduce significantly the cost of computation of matrices $\mathbf{U}$ and $\mathbf{P}$.

Validation

Consider a homogeneous full-space with mass density $\rho = 1$, shear modulus $G = 1$, Poisson's ratio $\nu = 0.25$ and hysteretic damping $\xi_p = \xi_s = 0.001$. The full-space is simulated with a TLM model consisting of an elastic layer with thickness $H = 2$ that is divided into 40 thin-layers of quadratic expansion and that is supplemented with two PMLs, one at the top and the other at the bottom, with parameters $m = 2$, $\eta = 2$, $\Omega = 8$ and $N = 10$ (see section 2.6). Consider also a horizontal boundary element (of quadratic expansion) whose width is $l_{BEM} = 0.1$ and place it at the depth $z_{BEM} = 0$ and horizontal coordinate $x_{BEM} = 0$. The shape functions associated with the nodes of the boundary elements are (from left to right)

$$\begin{cases} S_1(x) = -\dfrac{x}{l_{BEM}} + \dfrac{2x^2}{l_{BEM}^2} \\ S_2(x) = 1 - \dfrac{4x^2}{l_{BEM}^2} \\ S_3(x) = \dfrac{x}{l_{BEM}} + \dfrac{2x^2}{l_{BEM}^2} \end{cases} \tag{3.89}$$

In the following, the coefficients $\bar{U}_{kl}$ and $\bar{P}_{kl}$ associated with the middle node (node 2) are calculated with the procedure described in this section and compared with the results obtained through simple numerical integration (1000 integrating points) of the analytical solutions (Tadeu and Kausel, 2000). Three collocation points are considered: the first is placed at the position $\xi_1 = (0.5, 0.5)$ (outside the boundary element), the second at $\xi_2 = (0.05, 0)$ (right edge of the boundary element) and the third at $\xi_3 = (0, 0)$ (center of the boundary element). For the last collocation point and for the integration of the analytical solutions, the boundary contour is deflected as indicated in Figure 3.13a in order to avoid the singularities. The assumed frequency is $f = 1\,\text{Hz}$ ($\omega = 2\pi$ rad/s). Figure 3.15-3.17 plot the comparison between the results obtained with the two approaches.

As can be observed from Figure 3.15, the two approaches yield practically the same results, thus validating the procedure. Figure 3.16 provides exactly the same conclusions: discrepancies can be noticed for some components of $\bar{U}_{kl}$ and $\bar{P}_{kl}$ but these differences exist merely due to some residual values of the TLM results. In Figure 3.17, the agreement is also very good: also in this example, the differences are caused by residual values. Notice that the last two collocation points are placed inside the boundary element and that no special treatment is given to the fundamental solutions of the TLM and that the results are still correct. This confirms that using this procedure the coefficients c_{kl} are already accounted for during the calculation of the boundary integrals $\bar{P}_{kl}$: for the collocation point ξ_3, the components $\bar{P}_{xx}$, $\bar{P}_{yy}$ and $\bar{P}_{zz}$ correspond to $c_{kl} = 0.5\delta_{kl}$ (smooth boundary).

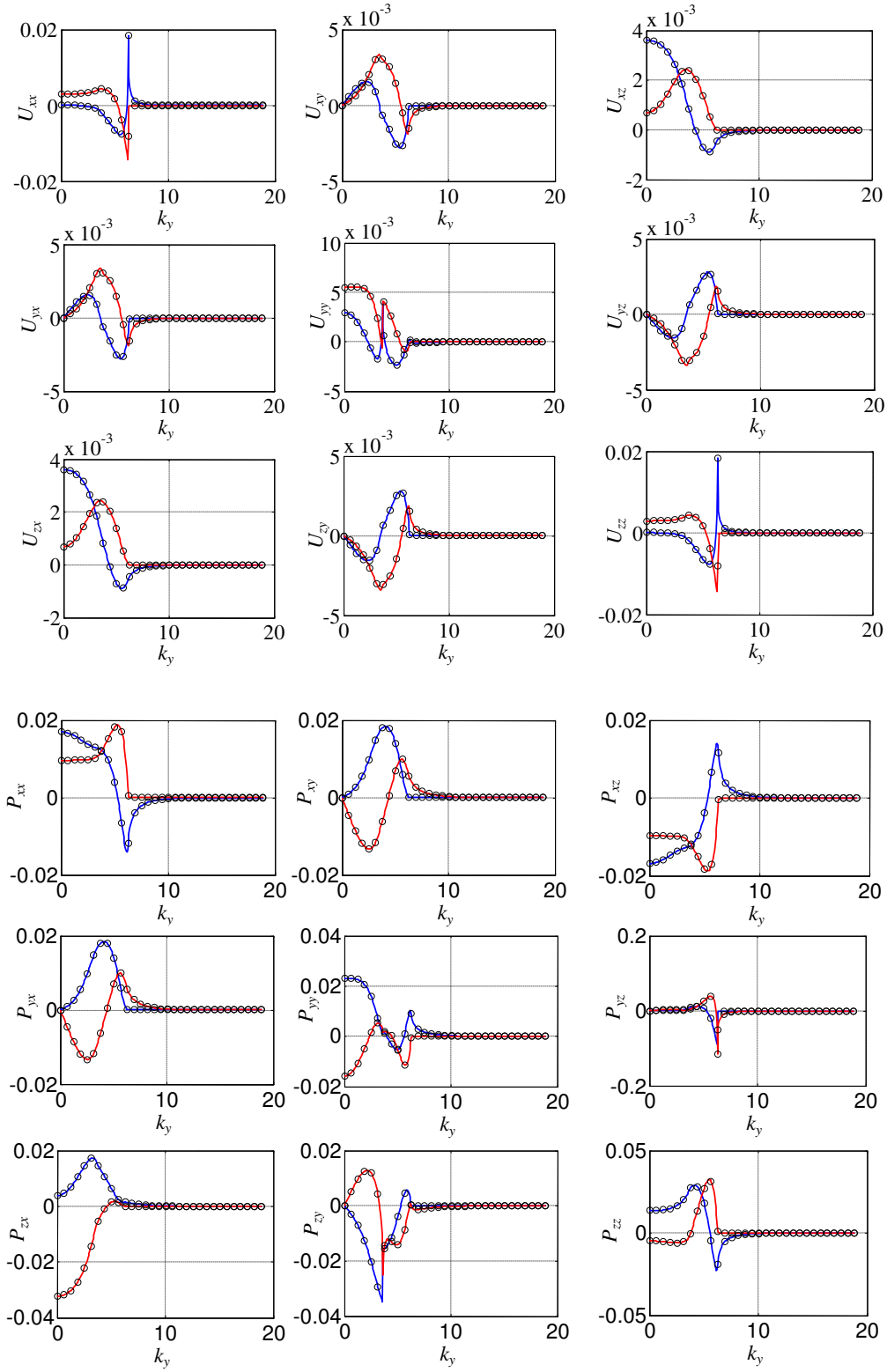

Figure 3.15: Boundary coefficients $\bar{U}_{kl}$ and $\bar{P}_{kl}$ for ξ_1. Solid lines – TLM solution; circles – analytical solutions. Blue – real component; red – imaginary component

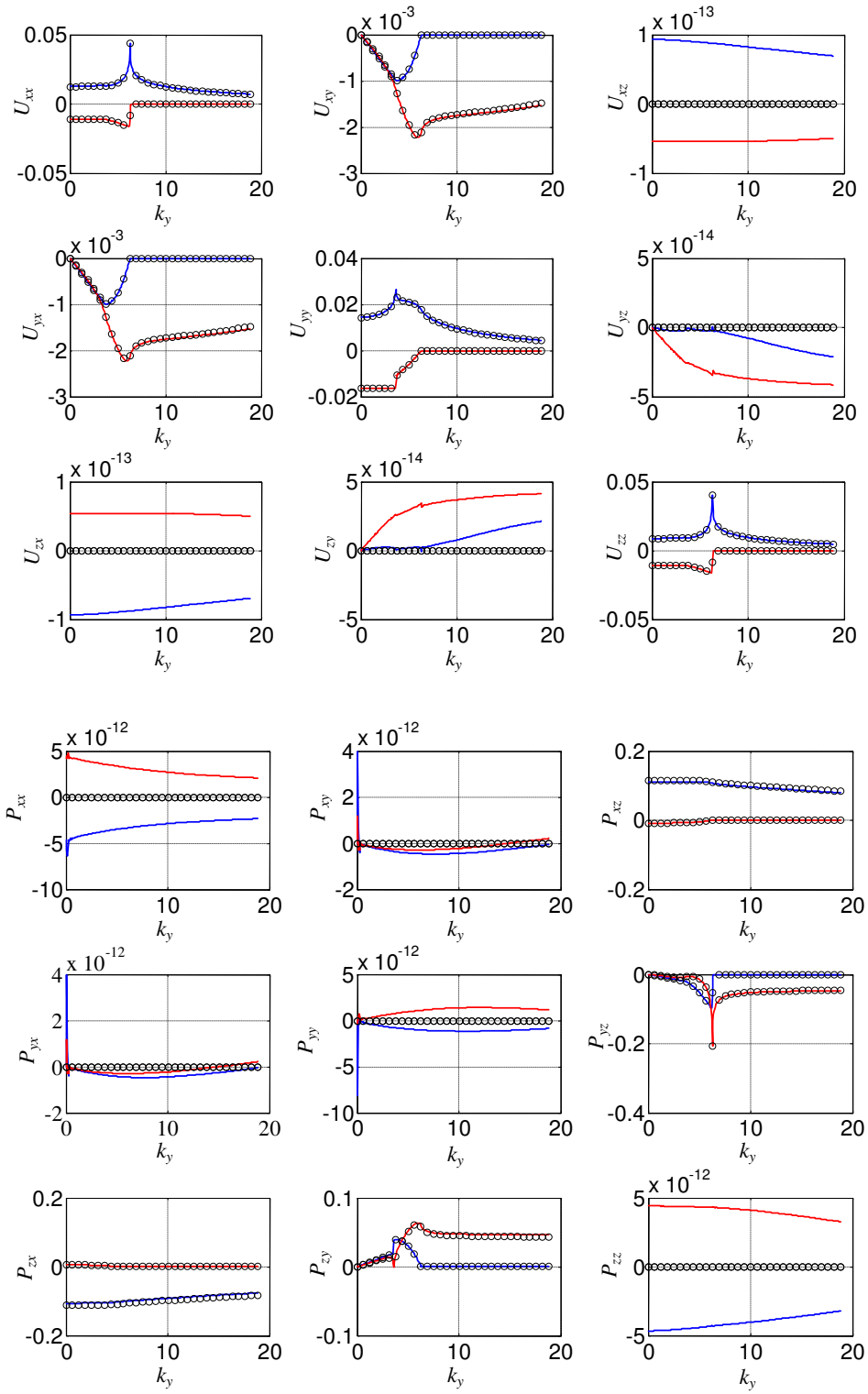

Figure 3.16: Boundary coefficients $\bar{U}_{kl}$ and $\bar{P}_{kl}$ for ξ_2. Solid lines – TLM solution; circles – analytical solutions. Blue – real component; red – imaginary component

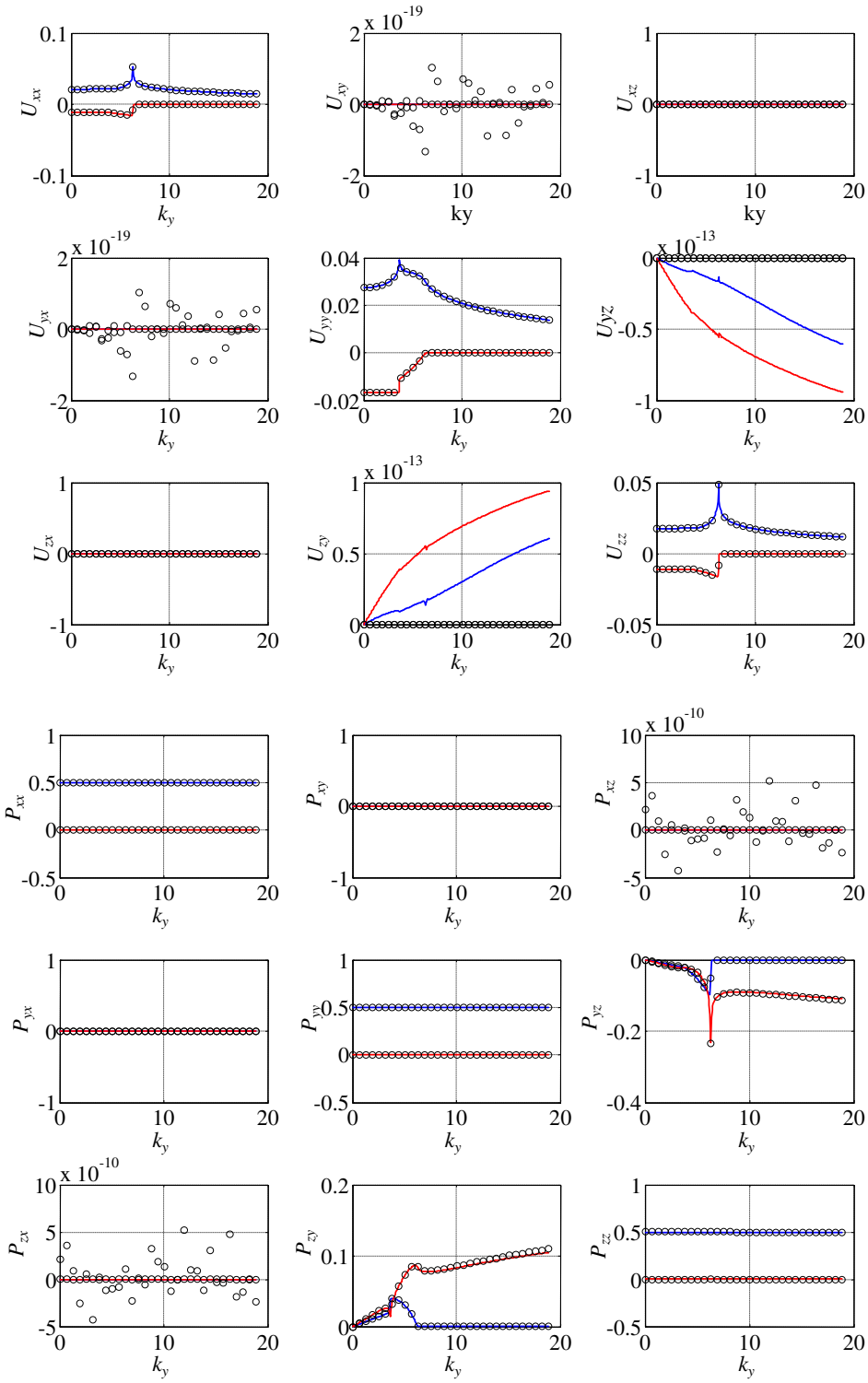

Figure 3.17: Boundary coefficients $\bar{U}_{kl}$ and $\bar{P}_{kl}$ for ξ_3. Solid lines – TLM solution; circles – analytical solutions. Blue – real component; red – imaginary component

3.4.4 Vertical boundary elements

Vertical boundaries are defined by a constant horizontal coordinate x_{BEM} (Figure 3.18). If it is assumed that the load is applied at the depth z_n (n^{th} interface of the TLM model) and that the boundary element is placed between depths z_{m1} and z_{m2} (m_1^{th} and m_2^{th} interfaces of the TLM model), then the integrals in equations (3.68) and (3.69) can be replaced by integrals of the form (for convenience, the variables k_y, ω are dropped)

$$\bar{U}_{kl}^{(ej)} = \sum_{m=m_1}^{m_2} \int u_{kl}^{(mn)} \left(x_{BEM} - x_\xi \right) N_{(m)}(z) S_{(e)}^{(j)}(z) \mathrm{d}z \tag{3.90}$$

$$\bar{P}_{kl}^{(ej)} = \sum_{m=m_1}^{m_2} \int \pm \sigma_{kxl}^{(mn)} \left(x_{BEM} - x_\xi \right) N_{(m)}(z) S_{(j)}^{(e)}(z) \mathrm{d}z \tag{3.91}$$

In these equations, the factors $u_{kl}^{(mn)} \left(x_{BEM} - x_\xi \right) N_{(m)}(z)$ and $\sigma_{kxl}^{(mn)} \left(x_{BEM} - x_\xi \right) N_{(m)}(z)$ represent the vertically interpolated displacements and tractions fields, with $N_{(m)}(z)$ being the TLM shape function associated with the m^{th} interface. In equation (3.91), the positive sign must be used if the outwards normal is in the positive x direction, while the negative sign must be used otherwise.

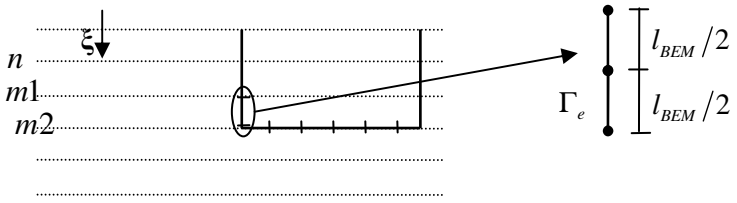

Figure 3.18: Vertical boundary element

Since $u_{kl}^{(mn)} \left(x_{BEM} - x_\xi \right)$ and $\sigma_{kxl}^{(mn)} \left(x_{BEM} - x_\xi \right)$ are nodal values and therefore do not depend on the depth z, the expressions (3.90) and (3.91) can be replaced by

$$\bar{U}_{kl}^{(ej)} = \sum_{m=m_1}^{m_2} u_{kl}^{(mn)} \left(x_{BEM} - x_\xi \right) \int N_{(m)}(z) S_{(e)}^{(j)}(z) \mathrm{d}z \tag{3.92}$$

$$\bar{P}_{kl}^{(ej)} = \sum_{m=m_1}^{m_2} \pm \sigma_{kxl}^{(mn)} \left(x_{BEM} - x_\xi \right) \int N_{(m)}(z) S_{(j)}^{(e)}(z) \mathrm{d}z \tag{3.93}$$

Thus, only the integrals of the form $\int N_{(m)}(z) S_{(j)}^{(e)}(z) \mathrm{d}z$ need to be evaluated. Since $N_{(m)}(z)$ and $S_{(j)}^{(e)}(z)$ are both polynomial functions, these integrals can be evaluated in closed form.

As final note, since the displacements are interpolated in the vertical direction using polynomial functions, the singular behavior of the fundamental solutions is not captured. Hence, when the collocation point lies within the vertical boundary element, in the calculation of $\bar{P}_{kl}^{(ej)}$ the term c_{kl} is not accounted for. Nonetheless, since the boundary elements are vertically oriented and the fundamental solutions are symmetric with respect to vertical planes, the resulting value for the missing term is $c_{kl} = 0.5\delta_{kl}$. In this way, for nodes that belong to vertical boundary elements and that do not correspond to corners, the term

$c_{kl} = 0.5\delta_{kl}$ must be added to the diagonal of **P** associated with the node. When the node corresponds to a corner, two situations occur:

1. Concave corner (Figure 3.13b): in this case, because the horizontal boundary element already accounts for the quarter of circle of the deflected boundary (Figure 3.14), then the factor c_{kl} must only account for the remaining semi-circle, and so $c_{kl} = 0.5\delta_{kl}$;
2. Convex corner (Figure 3.13c): the horizontal boundary element already accounts for the quarter circle of the deflected boundary (Figure 3.14), and so the factor c_{kl} is null.

Validation

Recall the homogeneous full-space used to validate the horizontal boundary elements, which is simulated with the same TLM model, and consider a vertical boundary element with width $l_{BEM} = 0.1$, centered at $(x_{BEM}, z_{BEM}) = (0,0)$ and of quadratic expansion (the boundary element is contained in two distinct thin-layers). The shape functions of the boundary element are the same as in equation (3.89), with the argument being replaced by z.

In the following, the boundary coefficients $\bar{U}_{kl}$ and $\bar{P}_{kl}$ associated with the middle node (node 2) are calculated with the procedure described in this section and compared with the results obtained through simple numerical integration (1000 integrating points) of the analytical fundamental solutions (Tadeu and Kausel, 2000). Three collocation points are considered: the first is placed at the position $\xi_1 = (0.5, 0.5)$ (outside the boundary element), the second at $\xi_2 = (0, 0.05)$ (upper edge of the boundary element) and the third at $\xi_3 = (0, 0)$ (center of the boundary element). The assumed frequency is again $f = 1$ Hz ($\omega = 2\pi$ rad/s). Figure 3.19-3.21 plot the comparison between the results obtained with the two approaches.

Such as in the case of the horizontal boundary element, a very good agreement is obtained between the two procedures. There is however a shift in the real components of the boundary coefficients $\bar{P}_{xz}$ and $\bar{P}_{zx}$ for $\xi = \xi_2$ and this difference does not vanish with the refinement of the TLM model. Nevertheless, as it is seen by the examples described in the next section, despite these differences, the results obtained with the TLM-BEM exhibit a good quality.

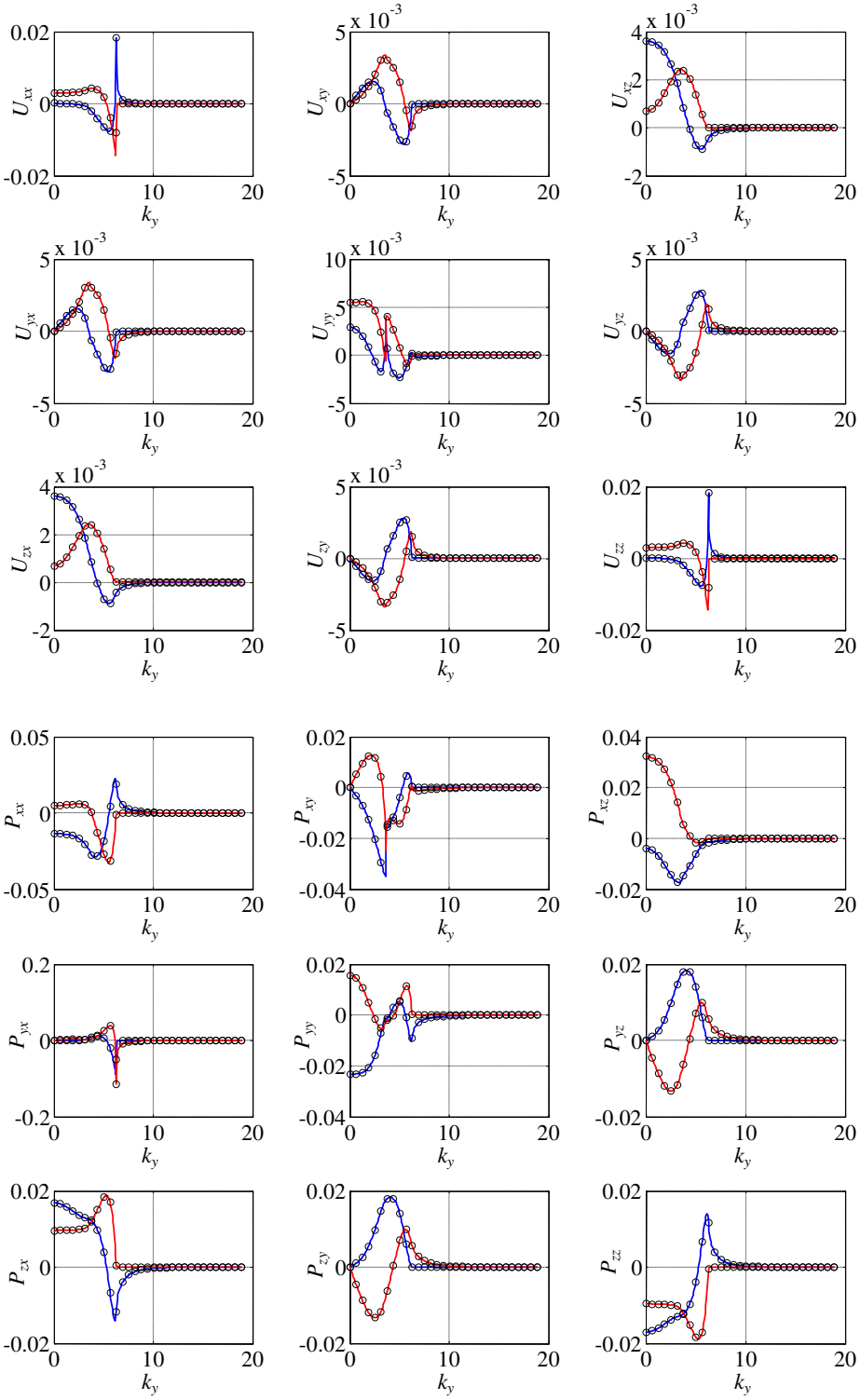

Figure 3.19: Boundary coefficients $\bar{U}_{kl}$ and $\bar{P}_{kl}$ for $\boldsymbol{\xi}_1$. Solid lines – TLM solution; circles – analytical solutions. Blue – real component; red – imaginary component

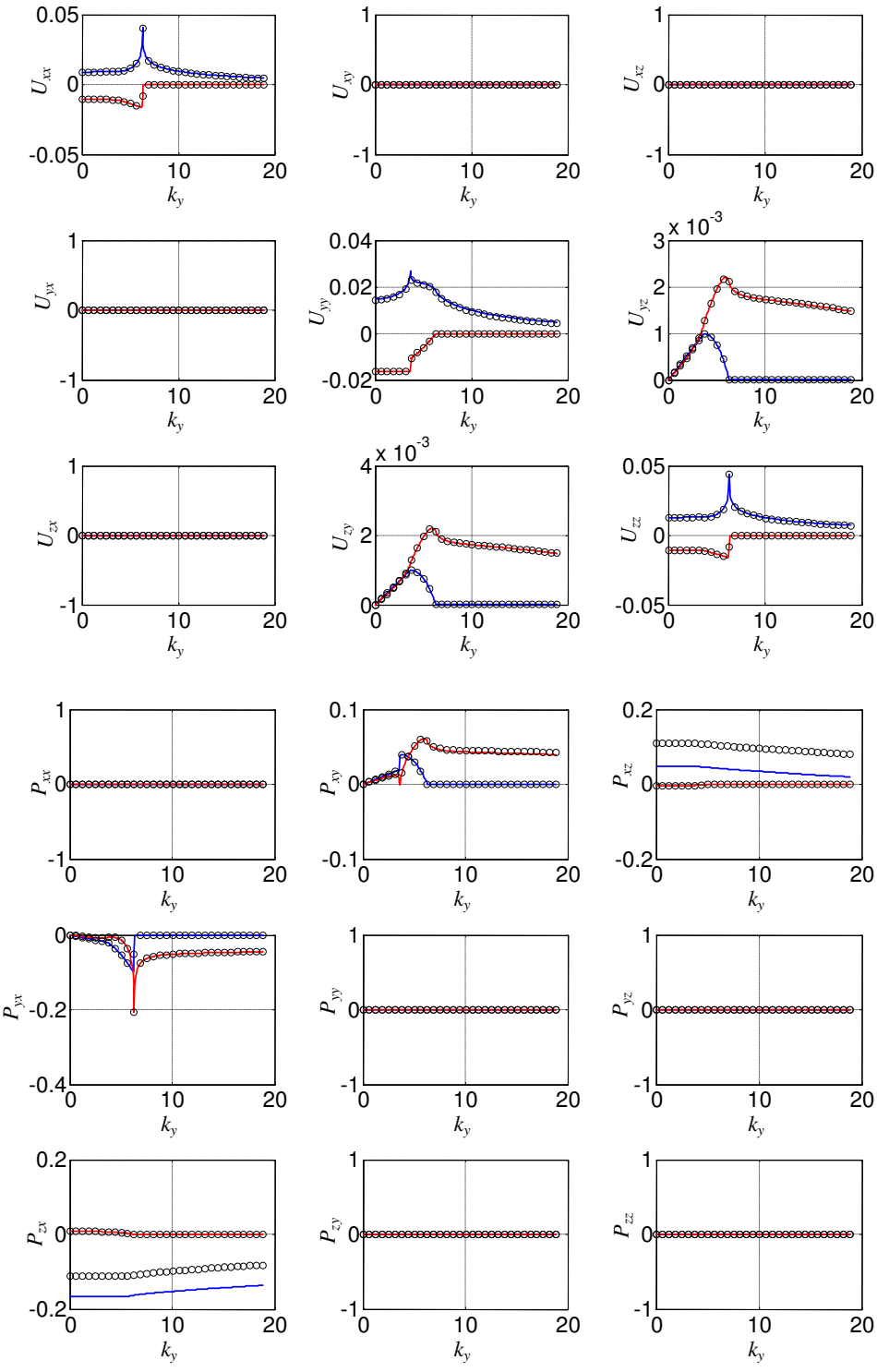

Figure 3.20: Boundary coefficients $\bar{U}_{kl}$ and $\bar{P}_{kl}$ for ξ_2. Solid lines – TLM solution; circles – analytical solutions. Blue – real component; red – imaginary component

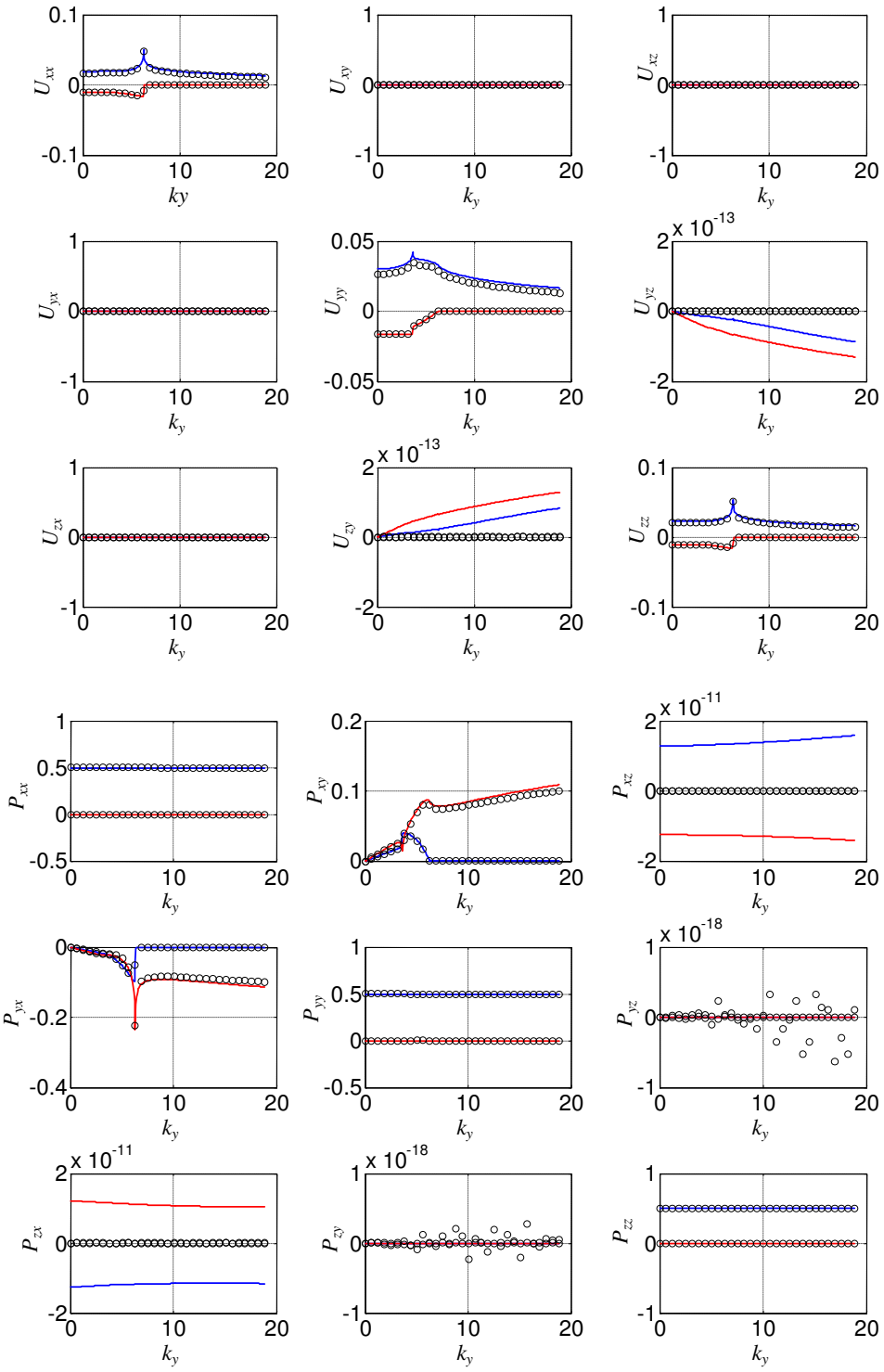

Figure 3.21: Boundary coefficients $\bar{U}_{kl}$ and $\bar{P}_{kl}$ for ξ_3. Solid lines – TLM solution; circles – analytical solutions. Blue – real component; red – imaginary component

3.4.5 Outgoing stress fields

To calculate the response of a close by structure due to wave-fields that are generated at the boundary Γ_S, both the outgoing displacement field and the outgoing stress field that reach the structure must be known. The outgoing displacement field is calculated using eq. (3.60), where $\boldsymbol{\xi}$ corresponds to a point of the layered domain but outside the boundary Γ_S, and so $\kappa_{kl} = \delta_{kl}$. Its calculation follows what is described in the two previous subsections. The calculation of the outgoing stress-field can be based on the derivatives of the displacements, which are obtained through the derivation of eq. (3.60) with respect to $\boldsymbol{\xi}$. For the generic direction $\delta = x, y, z$, the derivative of equation (3.60) is

$$\bar{u}_{l,\delta}\left(\boldsymbol{\xi}, k_y, \omega\right) = \int_{\Gamma_S} \bar{p}_k\left(\mathbf{x}, k_y, \omega\right) \bar{u}^*_{kl,\delta_{\boldsymbol{\xi}}}\left(\mathbf{x}, \boldsymbol{\xi}, -k_y, \omega\right) \mathrm{d}\Gamma - \int_{\Gamma_S} \bar{p}^*_{kl,\delta_{\boldsymbol{\xi}}}\left(\mathbf{x}, \boldsymbol{\xi}, -k_y, \omega\right) \bar{u}_k\left(\mathbf{x}, k_y, \omega\right) \mathrm{d}\Gamma \tag{3.94}$$

If $\delta = y$, the derivative can be easily calculated as $\bar{u}_{l,y}\left(\boldsymbol{\xi}, k_y, \omega\right) = -\mathrm{i} k_y \bar{u}_l\left(\boldsymbol{\xi}, k_y, \omega\right)$.

For the horizontal derivative x, since the domain is homogeneous in the horizontal direction, eq. (3.94) is equivalent to

$$\bar{u}_{l,x}\left(\boldsymbol{\xi}, k_y, \omega\right) = -\int_{\Gamma_S} \bar{p}_k\left(\mathbf{x}, k_y, \omega\right) \bar{u}^*_{kl,x_{\mathbf{x}}}\left(\mathbf{x}, \boldsymbol{\xi}, -k_y, \omega\right) \mathrm{d}\Gamma + \int_{\Gamma_S} \bar{p}^*_{kl,x_{\mathbf{x}}}\left(\mathbf{x}, \boldsymbol{\xi}, -k_y, \omega\right) \bar{u}_k\left(\mathbf{x}, k_y, \omega\right) \mathrm{d}\Gamma \tag{3.95}$$

Conversely, in the vertical direction the domain is not homogeneous, and so the previous equivalence is not valid. Hence, in order to calculate the vertical strains $\bar{u}_{l,z}$, a better approach is to compute the displacements at two consecutive nodal interfaces and then calculate the derivative with

$$\bar{u}_{l,z}\left(\boldsymbol{\xi}, k_y, \omega\right) = \frac{\bar{u}_l\left(\boldsymbol{\xi} + \Delta z, k_y, \omega\right) - \bar{u}_l\left(\boldsymbol{\xi}, k_y, \omega\right)}{\Delta z} \tag{3.96}$$

Returning to the horizontal direction x, after discretization of the boundary Γ_S, equation (3.95) gives rise to the matrix equation

$$\bar{\mathbf{u}}^{\boldsymbol{\xi}}_{,x} = -\mathbf{U}_{,x}\bar{\mathbf{p}} + \mathbf{P}_{,x}\bar{\mathbf{u}} \qquad \boldsymbol{\xi} \notin \Gamma_S \tag{3.97}$$

where $\mathbf{P}_{,x}$ is a matrix that collects the coefficients $\bar{P}^{(ej)}_{kl,x}$ of the form

$$\bar{P}^{(ej)}_{kl,x} = \int_{\Gamma_e} \bar{p}^*_{kl,x}\left(\mathbf{x}, \mathbf{x}_i, -k_y, \omega\right) S^{(e)}_{(j)}\left(\mathbf{x}\right) \mathrm{d}\Gamma_e \tag{3.98}$$

and $\mathbf{U}_{,x}$ is a matrix that collects the coefficients $\bar{U}^{(ej)}_{kl,x}$ of the form

$$\bar{U}^{(ej)}_{kl,x} = \int_{\Gamma_e} \bar{u}^*_{kl,x}\left(\mathbf{x}, \mathbf{x}_i, -k_y, \omega\right) S^{(e)}_{(j)}\left(\mathbf{x}\right) \mathrm{d}\Gamma_e \tag{3.99}$$

The vectors $\bar{\mathbf{u}}$ and $\bar{\mathbf{p}}$ collect the nodal displacements and tractions at the boundary Γ_S.

For vertical boundaries Γ_e, the quantities in equation (3.98) and (3.99) are calculated as described in section 3.4.4, i.e., after calculating the nodal values of the interested quantities in the space domain (see chapter 2), the integrals are calculated through polynomial integration. For horizontal boundaries, the quantities $\bar{U}_{kl,x}^{(ej)}$ and $\bar{P}_{kl,x}^{(ej)}$ are calculated as $\bar{U}_{kl}^{(ej)}$ and $\bar{P}_{kl}^{(ej)}$ in section 3.4.3, with the integrals of the form $I_{ij}^{(p)}$ replaced with $-\mathrm{i}I_{ij}^{(p+1)}$.

3.4.6 Coupling 2.5D BEM and 2.5D FEM

The coupling between the BEM and FEM sub-domains in the wavenumber domain follows the steps that are explained in section 3.2.5 for the case of BEM-FEM coupling in the space domain. The main differences consist in the matrix $\tilde{\mathbf{K}}$, that is now

$$\bar{\mathbf{K}} = \mathbf{A}_{yy} k_y^2 + k_y \left(\bar{\mathbf{B}}_{xy} + \bar{\mathbf{B}}_{zy} \right) + \left(\mathbf{G}_{xx} + \mathbf{G}_{xz} + \mathbf{G}_{zz} - \omega^2 \mathbf{M} \right) \tag{3.100}$$

and in the shape functions that are used in the calculation of $\mathbf{T}$ — equation (3.25) — that in this case must be the shape functions of 2D finite and boundary elements. The application of the steps expressed in equations (3.22) to (3.33) yield the final system of equations, which is of the form

$$\begin{bmatrix} \bar{\mathbf{K}}_{\mathrm{I,I}} + \mathbf{K}_{\mathrm{BEM}} & \bar{\mathbf{K}}_{\mathrm{I,II}} \\ \bar{\mathbf{K}}_{\mathrm{II,I}} & \bar{\mathbf{K}}_{\mathrm{II,II}} \end{bmatrix} \begin{bmatrix} \bar{\mathbf{u}}_{\mathrm{I}}^{\mathrm{F}} \\ \bar{\mathbf{u}}_{\mathrm{II}}^{\mathrm{F}} \end{bmatrix} = \begin{bmatrix} \mathbf{0} \\ \bar{\mathbf{f}}_{\mathrm{II}} \end{bmatrix} - \begin{bmatrix} \mathbf{F}_{\mathrm{BEM}} \\ \mathbf{0} \end{bmatrix} \tag{3.101}$$

This system is solved for $\bar{\mathbf{u}}_{\mathrm{I}}^{\mathrm{F}}$ and $\bar{\mathbf{u}}_{\mathrm{II}}^{\mathrm{F}}$ in order to obtain the 2.5D displacements of the FEM domain. The displacements $\bar{\mathbf{u}}_{\mathrm{I}}^{\mathrm{B}}$ of the BEM domain are obtained subsequently by application of equation (3.24) — the over tilde is replaced by a bar — and the boundary tractions $\bar{\mathbf{p}}_{\mathrm{I}}$ and displacements $\bar{\mathbf{u}}_{\mathrm{II}}^{\mathrm{B}}$ are obtained after solving the system of equations (3.22) for these variables — again, the over tildes are replaced by bars.

[Note: in order to add $\mathbf{K}_{\mathrm{BEM}}$ to the sub-matrix $\bar{\mathbf{K}}_{\mathrm{I,I}}$, after its calculation according to (3.32), the columns related to the y dofs must be multiplied by i while the rows related to the y dofs must be multiplied by $-\mathrm{i}$. For the same reasons, before subtracting the vector $\mathbf{F}_{\mathrm{BEM}}$ at the right-hand side of equation (3.101), after its calculation according to equation (3.33), the rows of $\mathbf{F}_{\mathrm{BEM}}$ related to the y dofs must be multiplied by $-\mathrm{i}$. After solving the system (3.101) for $\bar{\mathbf{u}}_{\mathrm{I}}^{\mathrm{F}}$ and $\bar{\mathbf{u}}_{\mathrm{II}}^{\mathrm{F}}$, the rows related to the y dofs of these vectors must also be multiplied by i.]

3.4.7 Conclusions

In this section, a 2.5D BEM procedure based on the TLM fundamental solutions is presented. For horizontal boundary elements, the BEM coefficients are calculated directly based on a modal superposition, rendering accurate results and accounting for the singularities of the fundamental solutions. For vertical boundary elements, the vertically interpolated fundamental solutions are integrated analytically but the singularities are not accounted for: to account for the singular behavior of the fundamental solutions, the term c_{kl} must be added *à posteriori*, being its value $0.5\delta_{kl}$ in smooth vertical boundaries or concave corners and being null in convex corners.

When compared with the BEM procedures based on the analytical fundamental solutions of full-spaces, the proposed procedure presents the advantage of simulating horizontally layered domains with the same ease as homogeneous domains, and of avoiding the discretization of

free surfaces and layer interfaces. When compared with the BEM procedures based on fundamental solutions obtained with wavenumber transfer or stiffness matrices, the proposed method has the advantage of evaluating the inverse Fourier transform in closed form expression, which yield more accurate results. In addition, the proposed methodology turn out to be more user friendly than other procedures based on the stiffness/transfer matrices since the definition of a proper wavenumber sample k_x is replaced by the subdivision of the layered domain into small thin-layers, a task that is far simpler. As major drawbacks, the proposed procedure requires the solution of two eigenvalue problems for each frequency, and since it is based on modal combinations, it might be inefficient for very deep structures that require soil models with a large number of thin-layers and interfaces.

The proposed methodology only considers horizontal and vertical boundary elements. If the actual boundary presents inclined surfaces, such geometry can be achieved by filling the irregular volume with finite elements.

As a final remark, the TLM model must be compatible with the BEM mesh in such a way that:

1. The horizontal boundaries are placed at the interface between two thin-layers and not inside a thin-layer;
2. The extremities of vertical boundaries correspond to interfaces between thin-layers and not to intermediate elevations within the thin-layers;
3. If there are boundary nodes inside vertical boundary elements (in constant and quadratic boundary elements, for example), these nodes must be located at the interface of thin-layers;
4. It is not recommended that the horizontal boundary elements be smaller than the thickness of the thin-layers. Likewise, it is not recommended that the distance between vertical boundary elements at the same elevation be smaller than the thickness of the thin-layers.

3.5 2.5D BEM-FEM validation examples

In sections 3.3 and 3.4, the 2.5D FEM and the 2.5D BEM are presented and validated: the 2.5D FEM is validated through the determination of the dispersion curves of a UIC861-3 rail, while the 2.5D BEM is validated through the calculation of the BEM coefficients $\bar{U}_{kl}^{(ej)}$ and $\bar{P}_{kl}^{(ej)}$ for horizontal and vertical boundary elements. In the present section, the coupled 2.5D BEM-FEM procedure is validated by means of two examples: the first example consists in the calculation of the response of a square tunnel inside a layered domain, while the second example consists in the calculation of the response of a homogeneous slab free in space. The results of the 2.5D BEM-FEM procedure are compared with the results of the 2.5D FEM procedure.

3.5.1 Example 1 – square tunnel in a layered medium

In the present subsection, the dynamic compliances of a tunnel are computed and compared with the corresponding values obtained with a 2.5D finite element approach. The tunnel is massless, has rigid cross section, and is placed inside a horizontally layered domain. The geometry and properties of the problem are illustrated in Figure 3.22.

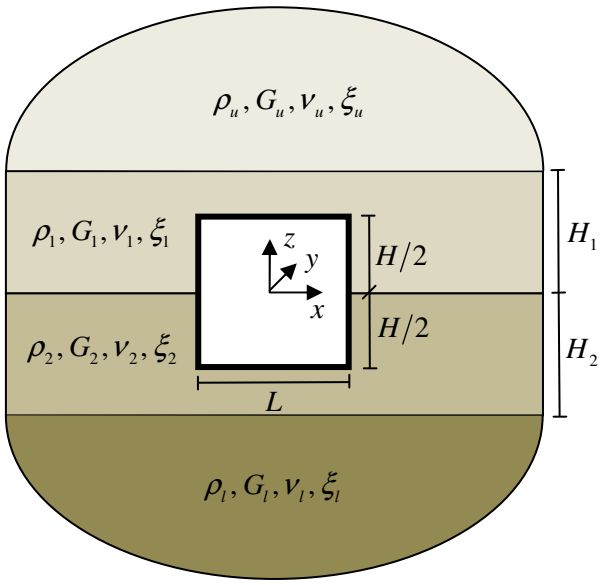

Figure 3.22: Square tunnel inside a horizontally layered domain

Since the cross section of the tunnel is rigid, the displacements of the walls of the tunnel can be described as function of the translation and rotation of the tunnel, i.e.,

$$\begin{bmatrix} u_x(x,z) \\ u_y(x,z) \\ u_z(x,z) \end{bmatrix} = \mathbf{N}\mathbf{u}^{\text{Tunnel}} \qquad \mathbf{N} = \begin{bmatrix} 1 & 0 & 0 & 0 & z & 0 \\ 0 & 1 & 0 & -z & 0 & x \\ 0 & 0 & 1 & 0 & -x & 0 \end{bmatrix} \qquad \mathbf{u}^{\text{Tunnel}} = \begin{bmatrix} u_x^{\text{Tunnel}} \\ u_y^{\text{Tunnel}} \\ u_z^{\text{Tunnel}} \\ \theta_x^{\text{Tunnel}} \\ \theta_y^{\text{Tunnel}} \\ \theta_z^{\text{Tunnel}} \end{bmatrix} \tag{3.102}$$

On the other hand, the pressures that the layered domain transmits to the walls of the tunnel induce at the center of the tunnel forces and moments that are calculated with

$$\mathbf{f}^{\text{Tunnel}} = \begin{bmatrix} f_x & f_y & f_z & m_x & m_y & m_z \end{bmatrix}^{\text{T}} = \int_{\Gamma} \mathbf{N}^{\text{T}} \begin{bmatrix} p_x(x,z) \\ p_y(x,z) \\ p_z(x,z) \end{bmatrix} \text{d}\Gamma \tag{3.103}$$

where Γ represents the boundary of the tunnel.

After discretizing the surface of the layered domain that is in contact with the tunnel into boundary elements and N boundary nodes, the nodal displacements $\mathbf{u}_j$ at the boundary are obtained with

$$\begin{bmatrix} \mathbf{u}_1 \\ \vdots \\ \mathbf{u}_N \end{bmatrix} = \mathbf{N}_{\text{U}}\mathbf{u}^{\text{Tunnel}} \qquad \mathbf{N}_{\text{U}} = \begin{bmatrix} \mathbf{N}(x_1, z_1) \\ \vdots \\ \mathbf{N}(x_N, z_N) \end{bmatrix} \tag{3.104}$$

The forces $\mathbf{f}^{\text{Tunnel}}$ are obtained from the boundary pressures $\mathbf{p}_j$ through

$$\mathbf{f}^{\text{Tunnel}} = \mathbf{N}_{\text{P}} \begin{bmatrix} \mathbf{p}_1 \\ \vdots \\ \mathbf{p}_N \end{bmatrix} \qquad \mathbf{N}_{\text{P}} = \begin{bmatrix} \int_\Gamma \mathbf{N}^{\text{T}}(x,z) S_1(x,z) \mathrm{d}\Gamma & \cdots & \int_\Gamma \mathbf{N}^{\text{T}}(x,z) S_N(x,z) \mathrm{d}\Gamma \end{bmatrix} \tag{3.105}$$

with $S_j(x,z)$ being the shape function associated to the j^{th} boundary node.

Replacing eqs. (3.104) and (3.105) in equation (3.67) yields

$$\left(\mathbf{N}_{\text{P}} \mathbf{U}^{-1} (\mathbf{P} + \mathbf{C}) \mathbf{N}_{\text{U}}\right) \mathbf{u}^{\text{Tunnel}} = \mathbf{f}^{\text{Tunnel}} \tag{3.106}$$

and so the compliance matrix corresponds to the 6 by 6 matrix $\mathbf{F}$ obtained with

$$\mathbf{F} = \left(\mathbf{N}_{\text{P}} \mathbf{U}^{-1} (\mathbf{P} + \mathbf{C}) \mathbf{N}_{\text{U}}\right)^{-1} \tag{3.107}$$

In the subsequent examples, the components of the compliance matrix $\mathbf{F}$ are evaluated using the 2.5D BEM methodology explained earlier. The tunnel is given the cross section $H = L = 1[\text{m}]$ and each edge of the tunnel is divided into 5 boundary elements of quadratic expansion (3 nodes per boundary element). The total number of nodes is then $N = 40$. To validate the results, the compliance matrices are also calculated using a finite element model coupled with PMLs, which are obtained as explained in (Kausel and Barbosa, 2011). The excitation frequency is $\omega = 2\pi[\text{rad/s}]$ and the wavenumbers k_y range from 0 to $6\pi[\text{rad/m}]$ (301 wavenumbers).

Homogeneous full-space

The material properties of the full-space are: mass density $\rho_u = \rho_1 = \rho_2 = \rho_l = 1\ \text{kg/m}^3$; shear modulus $G_u = G_1 = G_2 = G_l = 1\text{Pa}$; Poison's ratio $\nu_u = \nu_1 = \nu_2 = \nu_l = 0.25$; hysteretic damping $\xi_u = \xi_1 = \xi_2 = \xi_l = 0.01$. The TLM model consists of the 4 macro-layers identified in Figure 3.22, where the upper and the lower semi-infinite elements are modeled with PMLs (with parameters $\eta = 2$, $\Omega = 8$, $N = 10$, $m = 2$; see chapter 2 for definition of variables), and the middle layer satisfy $H_1 = H_2 = 2\,\text{m}$ and are divided into 40 thin-layers of quadratic expansion.

Due to symmetry conditions, only the components f_{xx}, f_{yy}, f_{zz}, $f_{\theta_x\theta_x}$, $f_{\theta_y\theta_y}$, $f_{\theta_z\theta_z}$, $f_{x\theta_z} = -f_{\theta_z x}$ and $f_{z\theta_x} = -f_{\theta_x z}$ are non-zero. Also, due to the geometry of the problem, $f_{xx} = f_{zz}$, $f_{\theta_x\theta_x} = f_{\theta_z\theta_z}$ and $f_{x\theta_z} = f_{z\theta_x}$. Hence, considering only the five compliance components f_{xx}, f_{yy}, $f_{\theta_x\theta_x}$, $f_{\theta_y\theta_y}$ and $f_{x\theta_z}$, it is possible to describe the entire system. In Figure 3.23, the 5 components of the compliance matrix obtained with the proposed procedure (solid lines) are compared with the results obtained with the FEM (black circles). Blue is used for the representation of the real part, while red is used for the imaginary part.

Figure 3.23 shows that the two approaches yield virtually identical results, leading to the conclusion that both procedures are correct. It can also be observed that the in-plane components (f_{xx}, $f_{\theta_x\theta_x}$ and $f_{x\theta_z}$) present singularities at $k_y = k_S = \omega / C_S = 2\pi$.

It should be noted that, because in this example the soil is a homogeneous, infinite space, it follows that the classical BEM that uses the fundamental solutions of a full-space has a clear advantage over the use of BEM-TLM. However, this problem of very simple geometry is used solely for validation purposes. In the next examples, the use of full-space fundamental solutions requires the discretization not only of the edges of the tunnel but also of the free-

surfaces and of the interface between different layers, and now the TLM offers clear advantages inasmuch as these interfaces need not to be discretized.

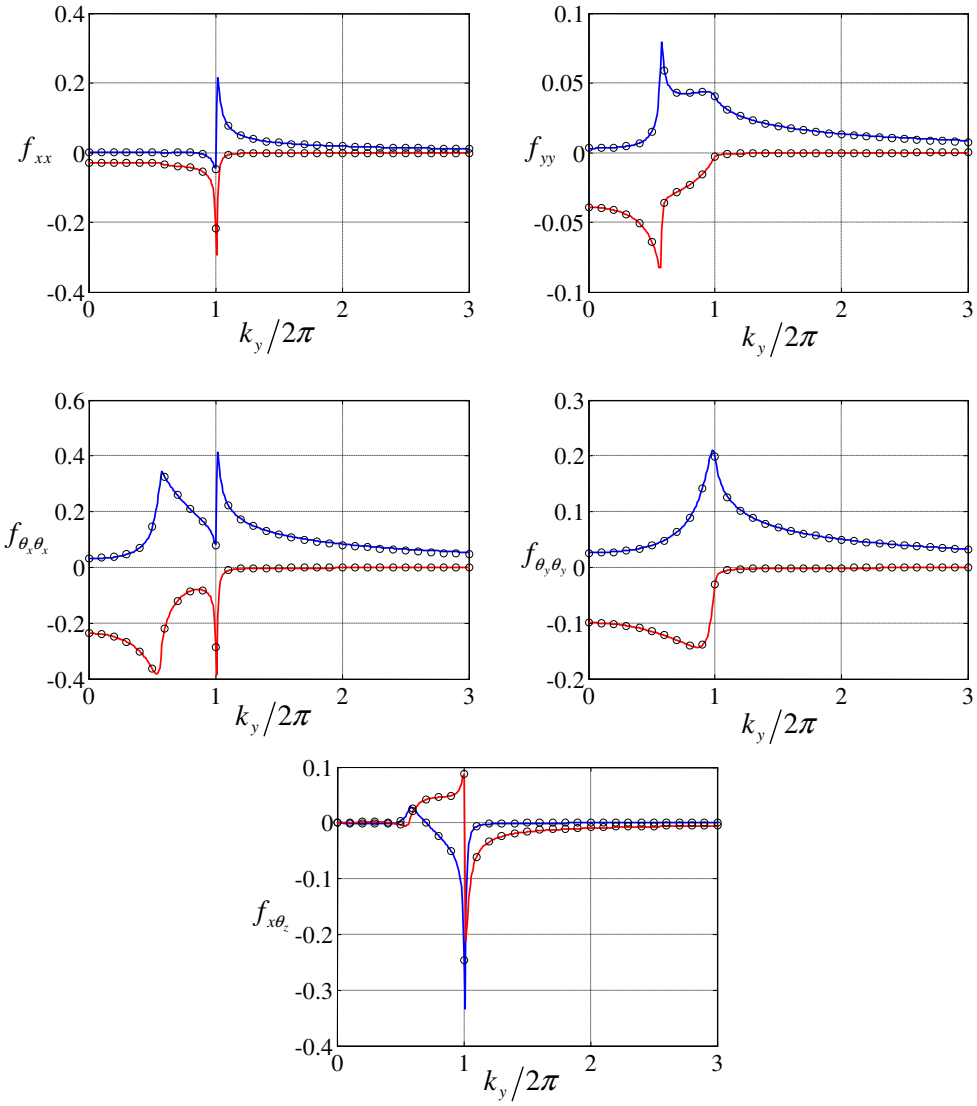

Figure 3.23: Tunnel compliances for the full-space case. Solid lines = 2.5D BEM (real part – blue; imaginary part – red). Black circles = FEM

Homogeneous layer free in space

The free layer consists of the two intermediate macro layers depicted in Figure 3.22 ($H_1 = H_2 = 2$ m). The material properties of the free layer are the same of the full- space considered in the previous example. The TLM model is similar to the one used therein, but with the upper and lower PMLs excluded. Again, due to symmetry conditions, only the components f_{xx}, f_{yy}, f_{zz}, $f_{\theta_x\theta_x}$, $f_{\theta_y\theta_y}$, $f_{\theta_z\theta_z}$, $f_{x\theta_z} = -f_{\theta_z x}$ and $f_{z\theta_x} = -f_{\theta_x z}$ do not vanish. However, the identities $f_{xx} = f_{zz}$, $f_{\theta_x\theta_x} = f_{\theta_z\theta_z}$ and $f_{x\theta_z} = f_{z\theta_x}$ do not hold, and so a total of eight components of the compliance matrix are needed to describe the system. Figure 3.24 shows the eight components obtained with the proposed methodology and with the FEM. Once again, the results obtained with the two procedures match perfectly.

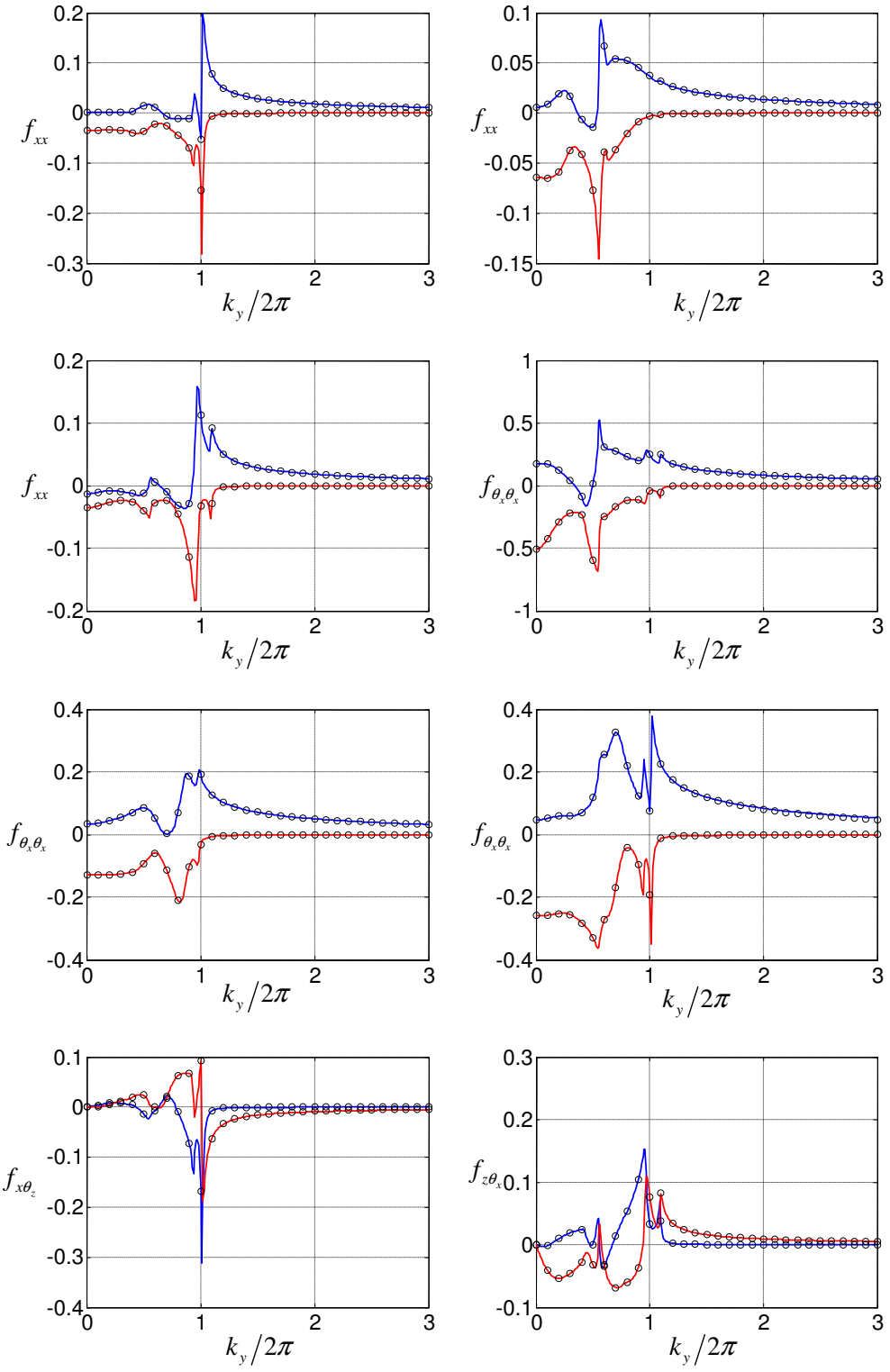

Figure 3.24: Tunnel compliances for the free layer in space. Solid lines = 2.5D BEM (real part – blue; imaginary part – red). Black circles = FEM

Homogeneous half-space

The material properties of the homogeneous half-space are the same as in the previous case. The TLM model differs from the model in the first example in that the upper PML is excluded. In this case, 12 distinct components are needed to define the compliance matrix, whose structure is

$$\mathbf{F}=\begin{bmatrix} f_{xx} & 0 & 0 & 0 & f_{x\theta_y} & f_{x\theta_z} \\ 0 & f_{yy} & f_{yz} & f_{y\theta_x} & 0 & 0 \\ 0 & -f_{yz} & f_{zz} & f_{z\theta_x} & 0 & 0 \\ 0 & f_{y\theta_x} & -f_{z\theta_x} & f_{\theta_x\theta_x} & 0 & 0 \\ f_{x\theta_y} & 0 & 0 & 0 & f_{\theta_y\theta_y} & f_{\theta_y\theta_z} \\ -f_{x\theta_z} & 0 & 0 & 0 & -f_{\theta_y\theta_z} & f_{\theta_z\theta_z} \end{bmatrix} \tag{3.108}$$

The 12 components of the compliance matrix are plotted in Figure 3.25. A good agreement is once again reached.

Layered half-space

The case of a non-homogeneous half-space is considered next. The properties of the layers, based on Figure 3.22, are the following:

$\rho_u = 0, G_u = 0$ (the upper half-space does not exist)

$\rho_1 = 1.2\,\mathrm{kg/m^3},\ G_1 = 1.0\,\mathrm{Pa},\ \nu_1 = 0.25,\ \xi_1 = 0.01,\ H_1 = 2\,\mathrm{m}$

$\rho_2 = 1.3\,\mathrm{kg/m^3},\ G_2 = 2.0\,\mathrm{Pa},\ \nu_2 = 0.3,\ \xi_2 = 0.01,\ H_2 = 2\,\mathrm{m}$

$\rho_l = \rho_2,\ G_l = G_2,\ \nu_l = \nu_2,\ \xi_l = \xi_2$

Each of the physical layers are modeled with 40 thin-layers based on a quadratic expansion. The lower half-space is modeled with PMLs with the same parameters used in the first example ($\eta = 2,\ \Omega = 8,\ N = 10,\ m = 2$).

As in the case of the half-space, the 12 components given by eq. (3.108) are needed to define the compliance matrix $\mathbf{F}$. These compliance components, obtained with the proposed procedure and with the FEM, are plotted in Figure 3.26. Again, the agreement between the proposed method and the FEM is very good. It can be concluded from this example that the BEM based on the TLM fundamental solutions can correctly simulate horizontally layered domains without the need to discretize the interfaces between layers, as is necessary in the standard BEM.

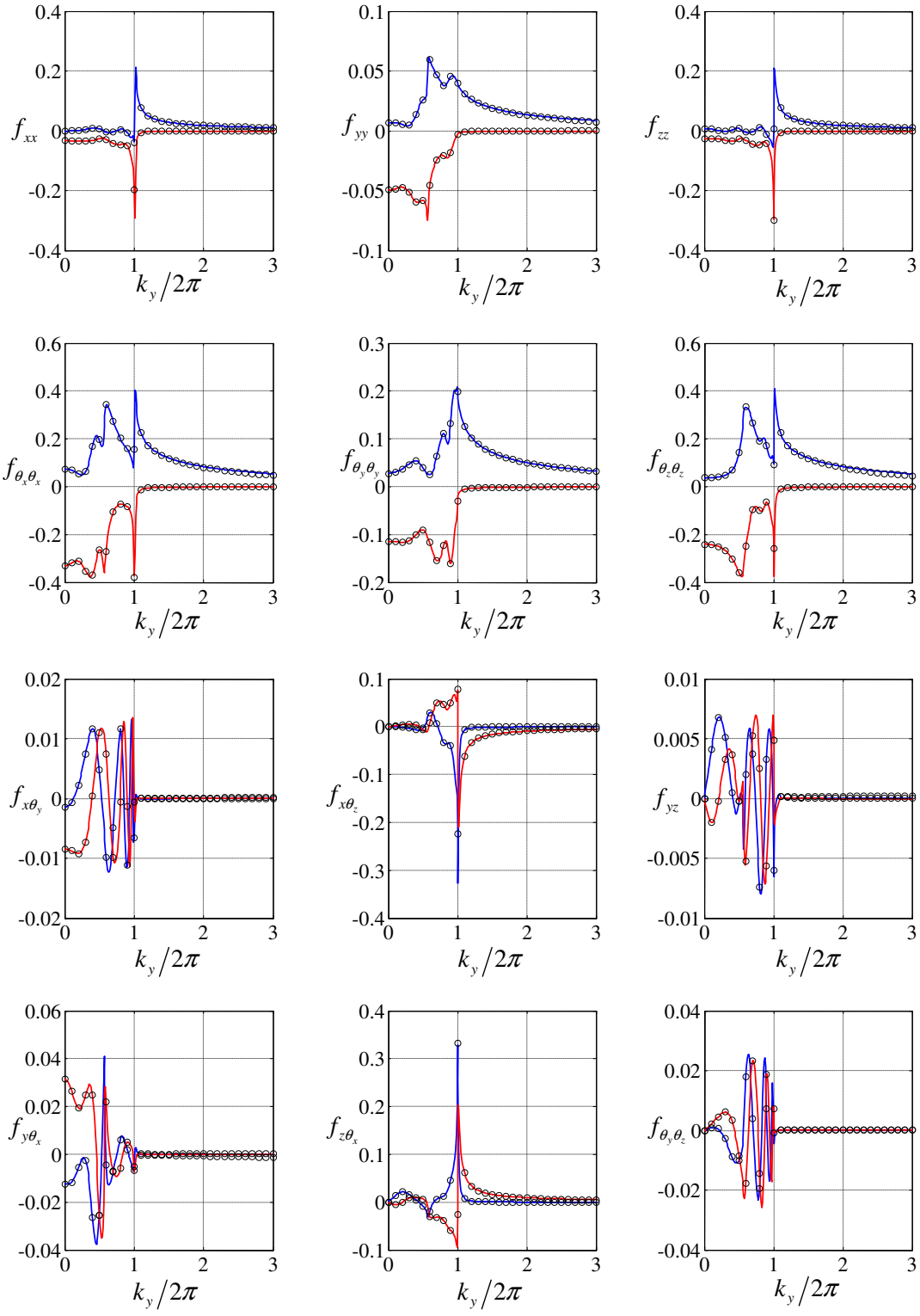

Figure 3.25: Tunnel compliances for the half-space. Solid lines = 2.5D BEM (real part – blue; imaginary part – red). Black circles = FEM

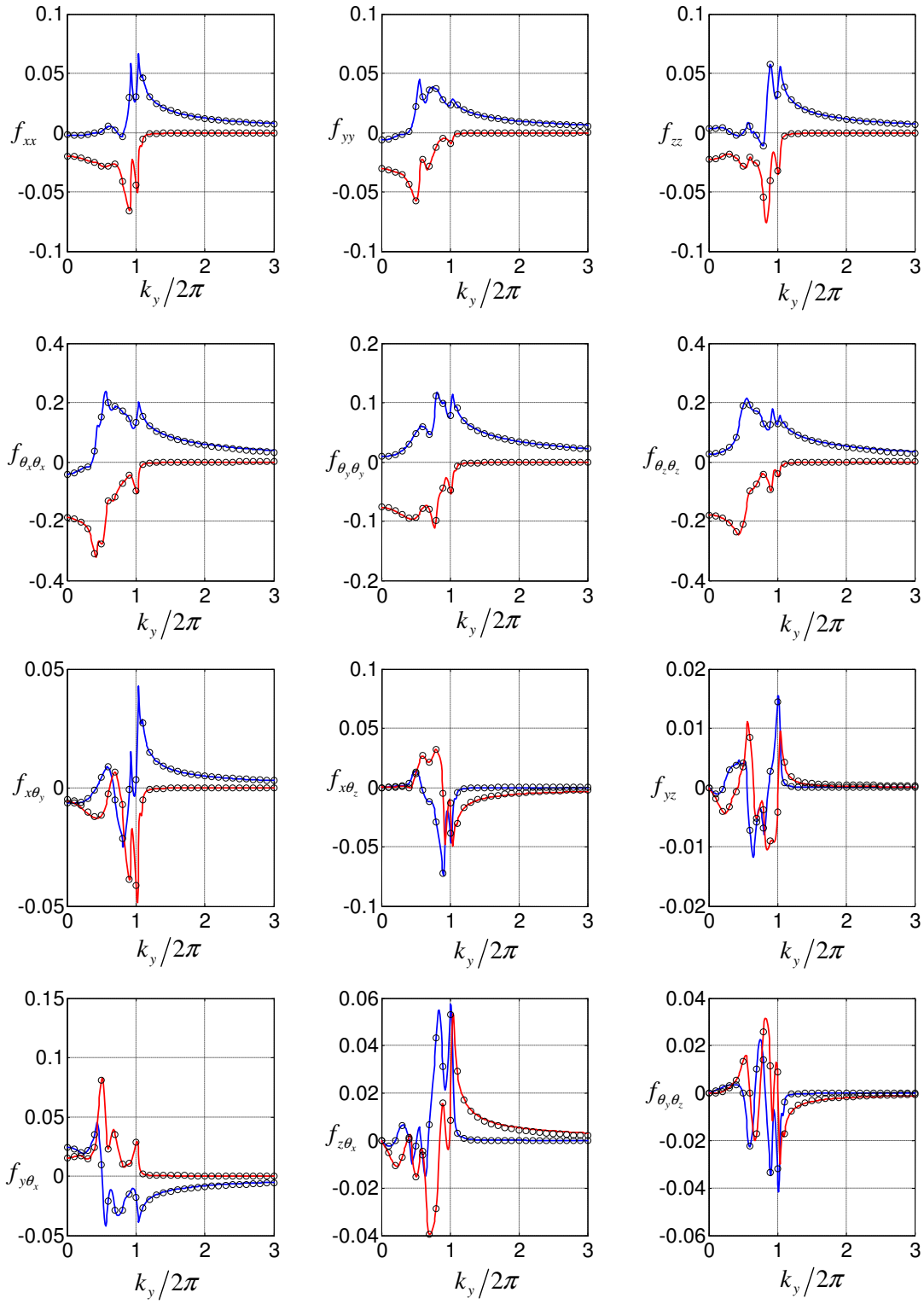

Figure 3.26: Tunnel compliances for the layered half-space. Solid lines = 2.5D BEM (real part – blue; imaginary part – red). Black circles = FEM

3.5.2 Example 2 – slab free in space

For the second example an infinitely long slab with width $L = 1\,\text{m}$ and thickness $H = 0.1\,\text{m}$ that is free in space is considered. The material properties of the slab are: mass density $\rho = 1\text{kg}/\text{m}^3$; shear modulus $G = 1\text{Pa}$; Poison's ratio $\nu = 0.25$; material damping $\xi = 0.01$. The slab is submitted to a vertical line load at its top (at the middle alignment) and the displacements of the top right corner, center right point and bottom right corner are calculated. The excitation frequency is $\omega = 2\pi$ rad/s and the range of wavenumbers of the line load is $k_y = [0, 6\pi]$ rad/m .

The displacements of the points referred to above are calculated using a 2.5D FEM procedure and using a coupled 2.5D BEM-FEM procedure, and then compared. For the first approach the cross section of the slab is divided into a regular mesh of 20×8 solid elements of quadratic expansion (8 nodes per element), while for the second approach the cross section of the slab is divided into two sub-domains: a FEM sub-domain, with dimensions $1\text{m} \times 0.05\text{m}$ and divided into a regular mesh of 20×4 solid elements of quadratic expansion; and a BEM sub-domain with the same dimensions, whose lateral boundaries are divided into 4 boundary elements each and whose interface between the BEM and the FEM sub-domains is divided into 20 boundary elements. The boundary elements are of quadratic expansion (3 nodes per element). The fundamental solutions of an elastic layer free in space, calculated with the TLM (the elastic layer is divided into 32 thin-layers of quadratic expansion), are used to nurture the boundary elements: this choice for the fundamental solutions avoids the discretization of the free lower surface of the slab, thus reducing the cost of computation of the BEM matrices. The results obtained with the two approaches are compared in Figure 3.27-3.29 for the 3 points considered. As can be observed, the agreement is very good even for the center right point, which belongs to the BEM-FEM interface, and for the bottom left corner, which belongs to the BEM domain. The good quality of the results validates the two procedures.

As a concluding remark regarding this example, it is important to be aware that the use of the 2.5D BEM-FEM is inefficient when compared to the 2.5D FEM. The structure under analysis is finite and of relatively small dimensions, which means that the reduction in the number of degrees of freedom achieved with the BEM does not compensate the computational cost associated with the calculation of the BEM matrices. This example is considered herein solely for validation purposes, and not to demonstrate the advantages of the 2.5D BEM.

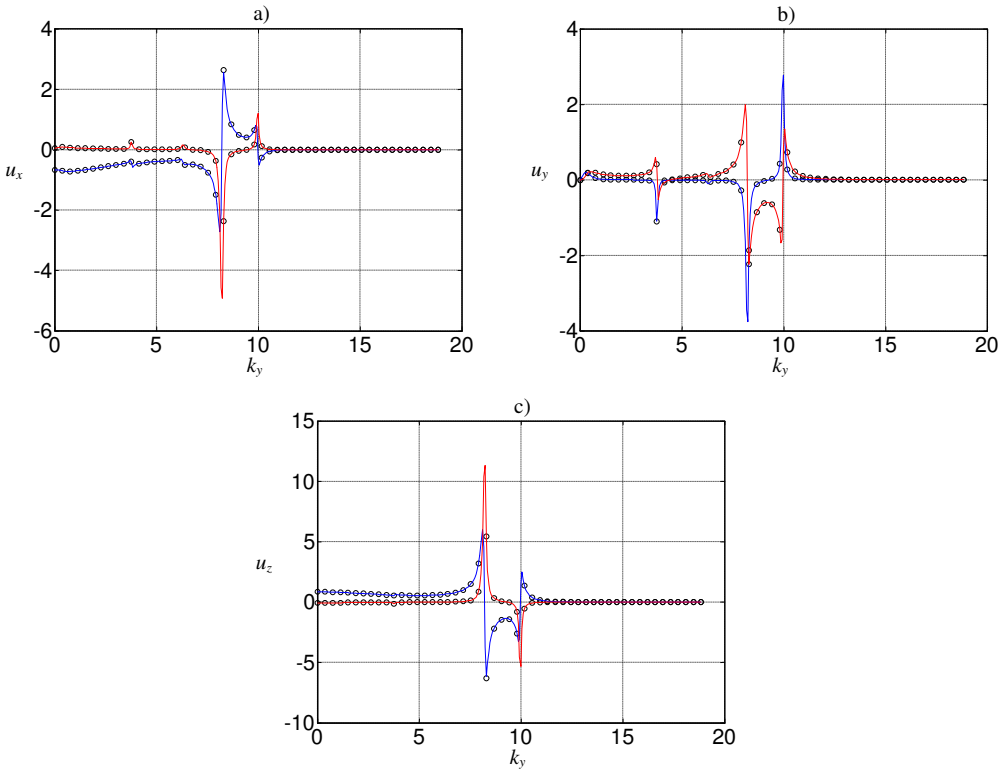

Figure 3.27: Displacements of the top right corner of the slab: a) u_x; b) u_y; c) u_z. Solid lines = 2.5D BEM (real part – blue; imaginary part – red). Black circles = FEM

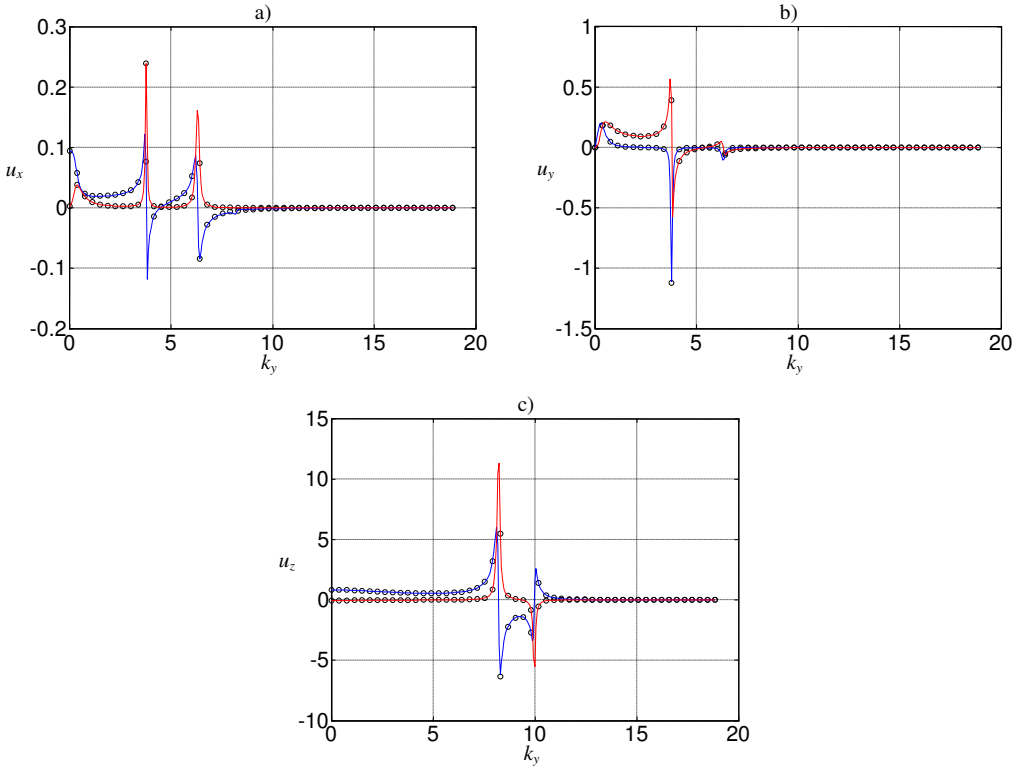

Figure 3.28: Displacements of the center right point of the slab: a) u_x; b) u_y; c) u_z. Solid lines = 2.5D BEM (real part – blue; imaginary part – red). Black circles = FEM

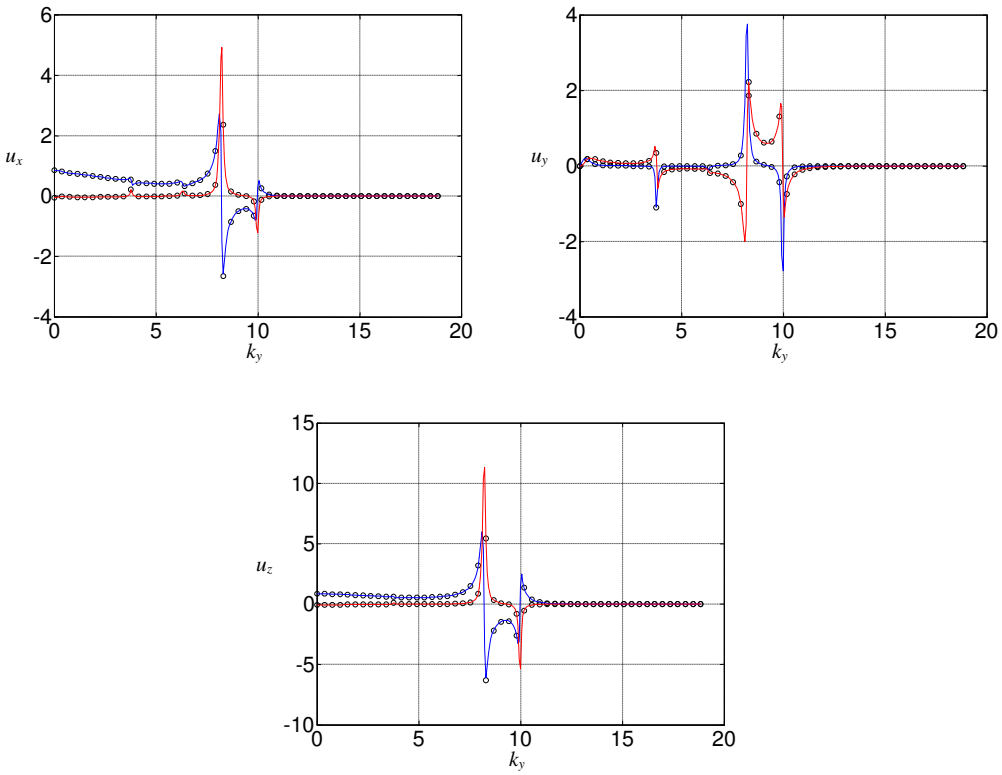

Figure 3.29: Displacements of the bottom right corner of the slab: a) u_x; b) u_y; c) u_z. Solid lines = 2.5D BEM (real part – blue; imaginary part – red). Black circles = FEM

3.6 Conclusions

In this chapter, the numerical tools used for the solution of soil-structure interaction problems are presented and validated. To solve the interaction between the track and the soil, a coupled 2.5D BEM-FEM procedure is used, and for the case of the interaction between the building and the soil, a coupled 3D BEM-FEM procedure is used. Both procedures are based on the fundamental solutions obtained with the TLM, which is described in chapter 2.

The 2.5D BEM-FEM procedures are developed in the space-wavenumber-frequency (k_y,ω) domain. In order to use the responses obtained with this methodology in a coupled 3D BEM-FEM procedure, the responses must first be transformed to the space-frequency (y,ω) domain, which is accomplished by an inverse Fourier transform. After having calculated the responses in the (k_y,ω) domain for a discrete sample of the wavenumber k_y, the inverse transform can be calculated numerically by means of a summation.

It is important to recall that when the proposed 2.5D BEM methodology is used, the coefficients for the BEM matrices can be calculated in closed form expressions. This fact leads to fast and precise calculations of such coefficients. The drawback of this approach is the time required to calculate the eigenmodes of the soil, which can become large when the fundamental solutions are needed at deep positions. Nevertheless, for each soil profile, the eigenmodes only have to be calculated once for each frequency. Then, they can be stored and reused to analyze different configurations of tracks, buildings and countermeasures.

Concerning the BEM procedures, the step that consumes more time is the calculation of the BEM matrices $\mathbf{P}$ and $\mathbf{U}$. The components of these matrices are obtained by applying a load

at one BEM node and by integrating the fundamental solutions over the surface of the BEM element, being this procedure repeated $N_n \times N_e$ times (N_n is the number of boundary nodes and N_e is the number of boundary elements). Since these $N_n \times N_e$ calculations can be performed simultaneously, parallel computing becomes of great advantage. Using CPU parallelization, the calculation of the matrices $\mathbf{P}$ and $\mathbf{U}$ can become up to N_{CPU} times faster than without parallelization, since the $N_n \times N_e$ calculation can be divided by N_{CPU} (number of CPUs). During the last two decades, the GPU boards, commonly used for image processing, have been used for scientific calculation and in some cases a reduction of two orders of magnitude in the time needed for the calculations has been achieved (Hwu and Kirk, 2009). The GPU processors allow a large number of processes to run simultaneously, at the expense of slower clock speeds. Also, the memory access of GPUs is more complicated than the RAM access by the CPUs, and so the algorithms must be properly adapted so that time needed to access the memory does not reduce the efficiency.

During the PhD works, a GPU implementation has been attempted for the calculation of matrices $\mathbf{P}$ and $\mathbf{U}$. The resulting program did work correctly, but an improvement in the calculation time could not be achieved, since at the end, the computational time needed to run a calculation with GPU parallelization was roughly the same computational time that was needed to run the same calculation parallelized with the CPU. The author believes that the reason for not achieving better performances is related to the GPU memory access.

The results contained in this chapter were obtained with MATLAB. No special attention was given in terms of the efficiency of the calculations or versatility of the subroutines, since the main purpose of these calculations was the validation of the procedures described throughout this chapter. For chapters 4 and 5, in order to obtain better computational costs, the 2.5D BEM-FEM and the TLM were implemented in FEMIX, which is a finite element code written in C programming language (http://www.alvaroazevedo.com/femix/).

4. Invariant structures subjected to moving loads and moving vehicles

4.1 Introduction

In problems of vibrations induced by moving vehicles, the vehicle transmits to its supporting structure a set of moving forces (as many as the number of contact points/surfaces). For the cases in which the dynamic behavior of the vehicle is considered, the interaction between the vehicle and the supporting structure causes the vehicle to respond dynamically, and consequently the contact forces between the two structures are not constant in time.

Even though in general the most significant contribution to the magnitude of the contact forces is attributable to the weight of the vehicle (quasi-static component), the oscillating (dynamic) component, whose contribution to the total force is smaller, has an important role in the response of the supporting structure, specially for points located at remote positions. Hence, it is of great importance to consider the dynamic component of the transmitted forces in order to obtain accurate predictions of the vibrations in the nearby buildings and in the far field.

The dynamic response of the vehicle is caused, among other aspects, by longitudinal variations of the stiffness of the supporting structure and by geometric irregularities observed at the contact surface between the vehicle and the structure. In this work, because it is assumed that the track-soil system is invariant in the longitudinal direction, the variations of stiffness cannot be considered, and therefore the excitation associated with the discrete sleeper support is not accounted for. Regarding the geometric irregularities at the contact surface between the vehicle and the supporting structure (in the railway case, wheel-rail contact), they are considered by means of position dependent gap/irregularity profiles. These irregularity profiles may account for both the unevenness of the track and the imperfections of the wheels.

In the present chapter, the 2.5D BEM-FEM procedure presented in the previous chapter is employed in the analysis of longitudinally invariant structures that are subjected to moving loads. The results obtained with the 2.5D BEM-FEM are in the (k_y,ω) domain, and in order for them to provide meaningful information, they must be transformed to the space-frequency domain, and in some cases also to the space-time domain. The transformation to these domains can be simplified due to the moving nature of the perturbation.

After describing the solution procedure for the case of moving loads, the vehicle-structure interaction problem is addressed. The solution of this interaction problem returns the forces that the vehicle induces in the structure. In the context of vibrations induced by railway traffic, this corresponds to the generation stage, the last stage to be described in this work (the propagation and the reception stages were explained in the previous chapter). Having characterized the forces that the train transmits to the track, the tools explained in chapter 3 and the expressions for moving loads described in this chapter can be used to determine the response of the track, soil and nearby buildings.

4.2 Moving loads

4.2.1 Introduction

The results obtained with the 2.5D BEM-FEM procedure are in the wavenumber-frequency domain (k_y,ω), and in order for them to be meaningful and be used as inputs in the 3D BEM-FEM procedure, the results have to be transformed to the space-frequency domain (y,ω), and in some cases, to the space-time domain (y,t). The transformation to the space-time domain requires the evaluation of the double inverse Fourier transform

$$h(y,t)=\frac{1}{2\pi}\int_{-\infty}^{+\infty}\overbrace{\frac{1}{2\pi}\int_{-\infty}^{+\infty}\tilde{H}\left(k_y,\omega\right)\mathrm{e}^{-\mathrm{i}k_y y}\mathrm{d}k_y}^{\bar{h}(y,\omega)}\,\mathrm{e}^{\mathrm{i}\omega t}\mathrm{d}\omega \tag{4.1}$$

in which $\tilde{H}\left(k_y,\omega\right)$ corresponds to some response field in the wavenumber-frequency domain (displacement, derivative, traction, etc) and in which $h(y,t)$ corresponds to the associated response field in the space-time domain. When the response is needed in the space-frequency domain, i.e., when $\bar{h}(y,\omega)$ is required, only the inner integral needs to be evaluated.

In some practical cases, the longitudinal and temporal variations of the load are independent of the variation within the cross section of the domain in such a way that at any given instant t and any given cross section y, the load vector $\mathbf{P}(y,t)$ can be factorized into the product

$$\mathbf{P}(y,t)=\mathbf{p}\;p(y,t) \tag{4.2}$$

where $\mathbf{p}$ is a vector containing the distribution of the load within the two dimensional cross section (this vector is to be used as right-hand side of equation (3.101)) and where $p(y,t)$ is a function representing the evolution of the load in time and with the longitudinal coordinate. Under this condition, the response fields $\tilde{H}\left(k_y,\omega\right)$ can be written as

$$\tilde{H}\left(k_y,\omega\right)=\tilde{h}\left(k_y,\omega\right)\tilde{p}\left(k_y,\omega\right) \tag{4.3}$$

being $\tilde{h}\left(k_y,\omega\right)$ the response function (usually called transfer function) obtained with the 2.5D BEM-FEM tool (and considering that the load vector corresponds to $\mathbf{p}$) and being $\tilde{p}\left(k_y,\omega\right)$ the wavenumber-frequency content of the load, calculated with

$$\tilde{p}\left(k_y,\omega\right)=\int_{-\infty}^{+\infty}\int_{-\infty}^{+\infty}p(y,t)\mathrm{e}^{\mathrm{i}k_y y}\mathrm{d}y\,\mathrm{e}^{-\mathrm{i}\omega t}\mathrm{d}t \tag{4.4}$$

For general structures in which the transfer functions $\tilde{h}\left(k_y,\omega\right)$ cannot be determined analytically and for general load variations $p(y,t)$, the inverse Fourier transforms (4.1) can only be calculated numerically based on the FFT technique or based on some numerical integration scheme, and so the values of $\tilde{h}\left(k_y,\omega\right)$ need to be evaluated for a large range of k_y and ω. For instance, an impulsive point load applied at the instant $t=0$ and at the longitudinal coordinate $y=0$ is defined by $p(y,t)=\delta(y)\delta(t)$ and its wavenumber-frequency content is $\tilde{p}\left(k_y,\omega\right)=1$. Hence, the integral (4.1) becomes

$$h(y,t)=\frac{1}{2\pi}\int_{-\infty}^{+\infty}\frac{1}{2\pi}\int_{-\infty}^{+\infty}\tilde{h}\left(k_y,\omega\right)\mathrm{e}^{-\mathrm{i}k_y y}\mathrm{d}k_y\mathrm{e}^{\mathrm{i}\omega t}\mathrm{d}\omega\approx\frac{1}{4\pi^2}\sum_i\sum_j\tilde{h}\left(k_i,\omega_j\right)\Delta k_i\Delta\omega_j \tag{4.5}$$

For loads moving with constant speed, the frequency-wavenumber content $\tilde{p}\left(k_y,\omega\right)$ contains a special structure that enables the calculation of one of the integrals in equation (4.1) directly. This issue is addressed in the following sub-sections, where constant loads and oscillating loads moving with constant speed are considered and exemplified for the case of a beam on a Kelvin foundation.

4.2.2 Constant moving loads

Consider that a load moving with constant speed V and constant amplitude A_0 crosses the longitudinal section $y=y_0$ at the instant $t=0$. The function $p(y,t)$ associated with such load is

$$p(y,t)=A_0\delta(y-Vt-y_0) \tag{4.6}$$

and its wavenumber-frequency content is

$$\begin{aligned}\tilde{p}\left(k_y,\omega\right)&=A_0\int_{-\infty}^{+\infty}\int_{-\infty}^{+\infty}\delta(y-Vt-y_0)\mathrm{e}^{\mathrm{i}k_y y}\mathrm{d}y\,\mathrm{e}^{-\mathrm{i}\omega t}\mathrm{d}t=\\&=A_0\mathrm{e}^{\mathrm{i}k_y y_0}\int_{-\infty}^{+\infty}\mathrm{e}^{-\mathrm{i}t\left(\omega-k_y V\right)}\mathrm{d}t=2\pi A_0\mathrm{e}^{\mathrm{i}k_y y_0}\delta\left(k_y V-\omega\right)\end{aligned} \tag{4.7}$$

The insertion of (4.7) and (4.3) in equation (4.1) yields

$$h(y,t)=\frac{1}{2\pi}\int_{-\infty}^{+\infty}\int_{-\infty}^{+\infty}A_0\tilde{h}\left(k_y,\omega\right)\mathrm{e}^{-\mathrm{i}k_y(y-y_0)}\delta\left(k_y V-\omega\right)\mathrm{d}k_y\,\mathrm{e}^{\mathrm{i}\omega t}\mathrm{d}\omega \tag{4.8}$$

and after solving equation (4.8) for the inner integral, the following result is obtained

$$h(y,t)=\frac{1}{2\pi}\int_{-\infty}^{+\infty}\overbrace{\frac{A_0}{V}\tilde{h}\left(\omega/V,\omega\right)\mathrm{e}^{-\mathrm{i}\omega\frac{y-y_0}{V}}}^{\bar{h}(y,\omega)}\mathrm{e}^{\mathrm{i}\omega t}\mathrm{d}\omega=\frac{A_0}{2\pi V}\int_{-\infty}^{+\infty}\tilde{h}\left(\omega/V,\omega\right)\mathrm{e}^{\mathrm{i}\omega\left(t-\frac{y-y_0}{V}\right)}\mathrm{d}\omega \tag{4.9}$$

The previous equation reveals that for the case of moving loads, the transformation of the response from the wavenumber-frequency domain to the space-frequency domain can be accomplished without solving any integral. Instead, such inverse transformation is obtained by evaluating the transfer function $\tilde{h}\left(k_y,\omega\right)$ at the wavenumber-frequency pair ($\omega/V,\omega$).

In the following example, $\tilde{h}\left(k_y,\omega\right)$ can be determined analytically and consequently so does $h(y,t)$. For more general structures in which the transfer function $\tilde{h}\left(k_y,\omega\right)$ cannot be evaluated in closed-form expressions, the remaining integral in eq. (4.9) can only be solved numerically using, for example, a discrete inverse Fourier transform (as in this work), an adaptive Filon method (De Barros and Luco, 1994), a classical FFT, or a logarithm FFT (Talman, 1978). This last technique is used in the works developed at Leuven (e.g., François et al., 2010).

Before the presentation of the example, it is important to note that the space-time domain response field is a function of $t-(y-y_0)/V$ and not of y and t separately. This aspect

indicates that for moving loads with constant amplitude, the response field moves with the load and is constant in time.

Beam on a Kelvin foundation subjected to a constant moving load

The example of a beam on a Kelvin foundation (Andersen and Nielsen, 2003) is used next to illustrate the procedure. This example is chosen because the displacements in the wavenumber-frequency domain of such structure are known in closed-form expressions and consequently the integral (4.9) can be evaluated analytically. In this context, consider an Euler beam with flexural stiffness EI and unit mass m resting on a Kelvin foundation with stiffness k and damping c, as represented in Figure 4.1.

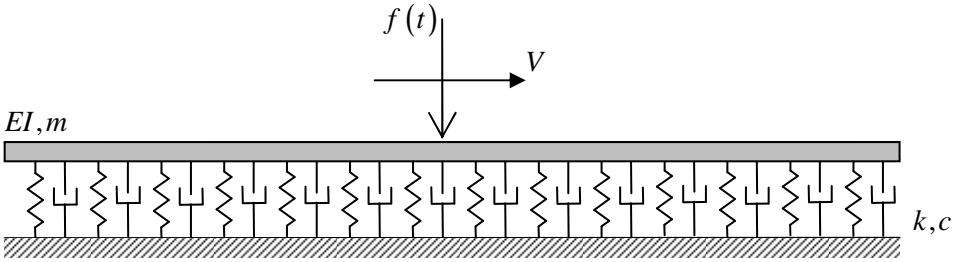

Figure 4.1: Beam on a Kelvin foundation subjected to a moving load

The wavenumber-frequency domain displacement $\tilde{u}$ of the beam is

$$\tilde{u}\left(k_y,\omega\right)=\frac{1}{EI\,k_y^4+k+\mathrm{i}\omega c-\omega^2 m} \tag{4.10}$$

and, according to (4.9), the space-time domain displacement induced by a constant moving load ($f\left(t\right)=A_0$) is

$$u\left(y,t\right)=\frac{A_0V^3}{2\pi}\int_{-\infty}^{+\infty}\frac{\mathrm{e}^{\mathrm{i}\omega\left(t-\frac{y-y_0}{V}\right)}}{EI\omega^4+kV^4+\mathrm{i}\omega cV^4-\omega^2mV^4}\,\mathrm{d}\omega \tag{4.11}$$

Since the integrand in (4.11) is a regular expression, and since it is bounded in the complex plane, the integral can be evaluated by means of contour integration, which results in

$$u\left(y,t\right)=\mathrm{i}\,\frac{A_0V^3}{EI}\mathrm{sign}\left(t-\frac{y-y_0}{V}\right)\sum_{\mathrm{imag}\left(\omega_j\right)\left(t-\frac{y-y_0}{V}\right)>0}^{4}\left(\mathrm{e}^{\mathrm{i}\omega_j\left(t-\frac{y-y_0}{V}\right)}\prod_{\substack{k=1\\k\neq j}}^{4}\frac{1}{\left(\omega_j-\omega_k\right)}\right) \tag{4.12}$$

where the values ω_j represent the roots of the polynomial

$$EI\omega_j^4+kV^4+\mathrm{i}\omega_j cV^4-\omega_j^2mV^4=0 \tag{4.13}$$

Furthermore, for cases in which the damping is null ($c=0$), there is a critical speed V_{cr} around which the response of the beam is greatly amplified. This critical speed equals the lowest bending velocity of the system (Hung and Yang, 2001) and corresponds to the lowest velocity that yields the roots of the polynomial (4.13) real, and so V_{cr} is given by

$$V_{cr} = \sqrt[4]{\frac{4EI\ k}{m^2}} \tag{4.14}$$

Next, the beam displacements are calculated with eq. (4.12) and with a time domain finite element procedure (FEMIX, www.alvaroazevedo.com\femix), and then compared. The mechanical and dynamic properties of the beam are $EI = 1.222\times10^6$ Pa and $m = 120.89$ kg/m, the stiffness and damping of the foundation are $k = 200\times10^6$ N/m and $c = 30\times10^3$ Ns/m, and the magnitude of the force is $A_0 = 195\times10^3$ N. The critical load speed of this system, according to (4.14), is $V_{cr} = 508.6$ m/s. The beam displacements are computed for the load speeds $V = 250$ m/s, $V = 500$ m/s, $V = 550$ m/s and $V = 700$ m/s and plotted in Figure 4.2.

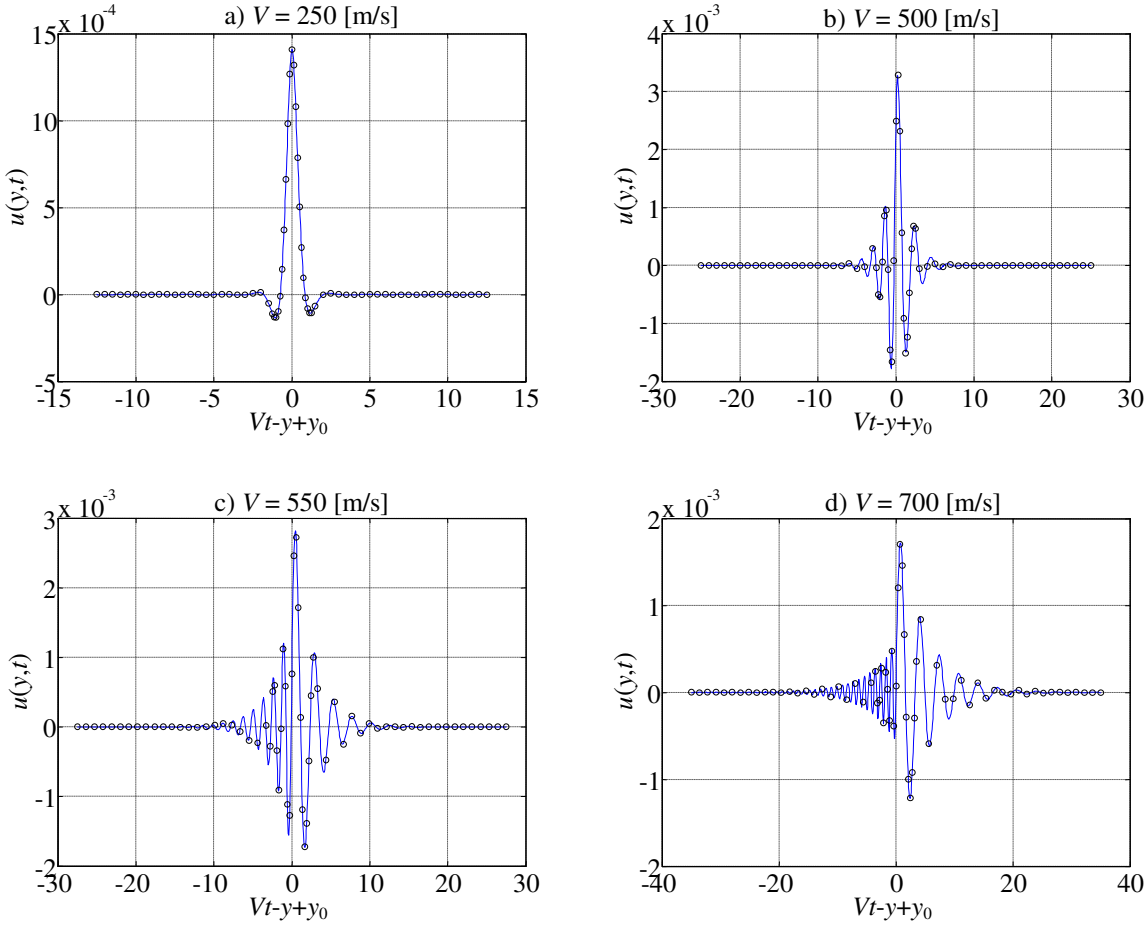

Figure 4.2: Beam displacements induced by a constant moving load. Blue line = eq. (4.12); black circles = time domain FEM (FEMIX)

The displacements represented in Figure 4.2a show that for speeds below V_{cr}, the behavior ahead of the load ($Vt - y + y_0 < 0$) and behind the load position ($Vt - y + y_0 > 0$) are identical. This fact is observed mostly because the roots ω_j are complex and characterized by a significant imaginary component, which causes the response to evanesce away from the load. As the load speed V increases, the roots ω_j come closer to the real axis and therefore the response decays slower with the distance to the position of the load.

When the load speed is near V_{cr} and the damping is neglected, the roots ω_j are very close to the real axis and have approximately the same value (apart from the sign) and so the response propagates both ahead and behind the load with roughly the same wavelength, which is approximately $2\pi V_{cr}/\omega_{re}$, being $\omega_{re} \approx V^2\sqrt{m/(2EI)}$. The presence of damping makes the wavelengths ahead and behind the load different, but their values are still close to each other, as can be inferred from Figure 4.2b-c.

Finally, for $V > V_{cr}$ and again for null damping, there are two distinct pairs of real roots: $\pm\omega_1$ and $\pm\omega_2$ ($|\omega_1| > |\omega_2|$), being ω_1 associated with the waves ahead of the load and ω_2 associated with the waves behind the load position, thus turning the wavelength ahead of the load smaller than the wavelength behind the load. As V increases, ω_1 increases and ω_2 decreases (tending to a minimum of $\sqrt{k/m}$) and consequently the wavelength ahead of the load shortens, while the wavelength behind the load increases. In the case under study, the presence of damping makes the roots ω_j complex, but the features explained in the last sentence are still present, as can be observed in Figure 4.2d.

Also observable in Figure 4.2a-d is the amplification of the displacements when the load speed approaches V_{cr}. That fact is confirmed in Figure 4.3, where the maximum beam displacement is plotted as a function of the load speed V for two distinct damping scenarios: $c = 30\times10^3$ Ns/m (blue line) and $c = 0$ Ns/m (red line). The effect of the damping is similar to the effect of a dashpot on one-degree-of-freedom systems, which reduces the amplification of the response at the resonance frequency of the systems.

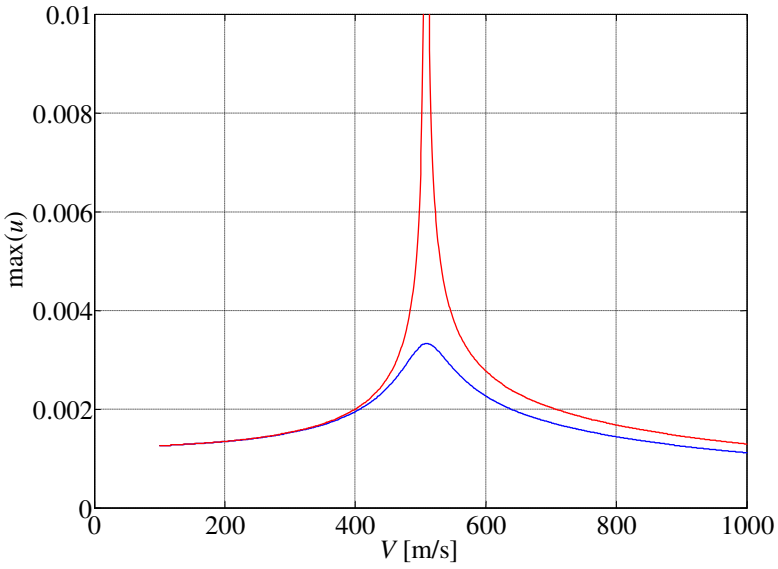

Figure 4.3: Beam maximum displacements as a function of the load speed. Blue line = with damping; red line = no damping

4.2.3 Oscillating moving loads

Consider now that a load moving with constant speed V and with time varying amplitude defined by $f(t,\omega_0) = A_0\exp(i\omega_0 t)$ crosses the longitudinal section $y = y_0$ at the instant $t = 0$

(the forcing frequency ω_0 is added as an argument for convenience). The function $p(y,t,\omega_0)$ associated with such load is

$$p(y,t,\omega_0) = A_0 \mathrm{e}^{\mathrm{i}\omega_0 t}\delta(y - Vt - y_0) \tag{4.15}$$

and its wavenumber-frequency content $\tilde{p}(k_y,\omega,\omega_0)$ is

$$\begin{aligned}\tilde{p}(k_y,\omega,\omega_0) &= \int_{-\infty}^{+\infty}\int_{-\infty}^{+\infty} A_0 \mathrm{e}^{\mathrm{i}\omega_0 t}\delta(y - Vt - y_0)\mathrm{e}^{\mathrm{i}k_y y}\mathrm{d}y\,\mathrm{e}^{-\mathrm{i}\omega t}\mathrm{d}t = \\ &= A_0 \mathrm{e}^{\mathrm{i}k_y y_0}\int_{-\infty}^{+\infty}\mathrm{e}^{-\mathrm{i}t(\omega-\omega_0-k_y V)}\mathrm{d}t = 2\pi A_0 \mathrm{e}^{\mathrm{i}k_y y_0}\delta(k_y V + \omega_0 - \omega)\end{aligned} \tag{4.16}$$

The insertion of (4.16) and (4.3) in equation (4.1) yields

$$h(y,t,\omega_0) = \frac{1}{2\pi}\int_{-\infty}^{+\infty}\int_{-\infty}^{+\infty} A_0 \tilde{h}(k_y,\omega)\mathrm{e}^{-\mathrm{i}k_y(y-y_0)}\delta(k_y V + \omega_0 - \omega)\mathrm{d}k_y\,\mathrm{e}^{\mathrm{i}\omega t}\mathrm{d}\omega \tag{4.17}$$

and after solving equation (4.17) for the inner integral, the following expression is obtained

$$\begin{aligned}h(y,t,\omega_0) &= \frac{1}{2\pi}\int_{-\infty}^{+\infty}\overbrace{\frac{A_0}{V}\mathrm{e}^{\mathrm{i}\omega_0\frac{y-y_0}{V}}\tilde{h}\left(\frac{\omega-\omega_0}{V},\omega\right)\mathrm{e}^{-\mathrm{i}\omega\frac{y-y_0}{V}}}^{\bar{h}(y,\omega,\omega_0)}\mathrm{e}^{\mathrm{i}\omega t}\mathrm{d}\omega = \\ &= \frac{A_0}{2\pi V}\mathrm{e}^{\mathrm{i}\omega_0\frac{y-y_0}{V}}\int_{-\infty}^{+\infty}\tilde{h}\left(\frac{\omega-\omega_0}{V},\omega\right)\mathrm{e}^{\mathrm{i}\omega\left(t-\frac{y-y_0}{V}\right)}\mathrm{d}\omega\end{aligned} \tag{4.18}$$

The force $f(t,\omega_0)$ described above has no physical meaning since it contains an imaginary component, which results from the exponential factor $\exp(\mathrm{i}\omega_0 t)$. However, this type of expression can be used to define real functions of the type cosine or sine, as stated in the next equations

$$\begin{aligned}f_{\mathrm{C}}(t,\omega_0) &= A_0\cos(\omega_0 t) = A_{\mathrm{C}}\frac{\mathrm{e}^{\mathrm{i}\omega_0 t} + \mathrm{e}^{-\mathrm{i}\omega_0 t}}{2} \\ f_{\mathrm{S}}(t,\omega_0) &= A_0\sin(\omega_0 t) = A_{\mathrm{S}}\frac{\mathrm{e}^{\mathrm{i}\omega_0 t} - \mathrm{e}^{-\mathrm{i}\omega_0 t}}{2\mathrm{i}}\end{aligned} \tag{4.19}$$

Hence, in order to obtain the response $h_{\mathrm{C}}(y,t,\omega_0)$ for cosine type loads or the response $h_{\mathrm{S}}(y,t,\omega_0)$ for sine type loads, equation (4.18) must first be used to calculate $h(y,t,\omega_0)$ and afterwards, since $h(y,t,-\omega_0) = \overline{h(y,t,\omega_0)}$, the real or imaginary component must be retained according to the following

$$\begin{aligned}h_{\mathrm{C}}(y,t,\omega_0) &= \frac{h(y,t,\omega_0) + h(y,t,-\omega_0)}{2} = \mathrm{Re}\left[h(y,t,\omega_0)\right] \\ h_{\mathrm{S}}(y,t,\omega_0) &= \frac{h(y,t,\omega_0) - h(y,t,-\omega_0)}{2\mathrm{i}} = \mathrm{Im}\left[h(y,t,\omega_0)\right]\end{aligned} \tag{4.20}$$

Similarly to the case of constant moving loads, for oscillating moving loads no integral needs to be evaluated in order to obtain the space-frequency domain response. Instead, the response in that domain is obtained simply by evaluating the transfer function $\tilde{h}(k_y,\omega)$ for the

wavenumber-frequency pair $((\omega-\omega_0)/V,\omega)$. In addition, the response of points that move with the same speed as the load is given by

$$h\left(y=Vt+y_0-y_{\mathrm{P}},t\right)=\frac{A_0}{2\pi V}\mathrm{e}^{\mathrm{i}\omega_0\left(t-\frac{y_{\mathrm{P}}}{V}\right)}\int_{-\infty}^{+\infty}\tilde{h}\left(\frac{\omega-\omega_0}{V},\omega\right)\mathrm{e}^{\mathrm{i}\omega\frac{y_{\mathrm{P}}}{V}}\mathrm{d}\omega \tag{4.21}$$

in which $y_{\mathrm{P}}=Vt+y_0-y$ is the distance between the moving point and the source. The previous equation clearly shows that the response fields move together with the load and oscillate with frequency ω_0.

Beam on a Kelvin foundation subjected to a cosine type moving load

For a load $f(t)=A_0\cos(\omega_0 t)$, the beam displacements are calculated with

$$u_{\mathrm{C}}\left(y,t,\omega_0\right)=\mathrm{Re}\left[u\left(y,t,\omega_0\right)\right] \tag{4.22}$$

in which

$$u\left(y,t,\omega_0\right)=\frac{A_0V^3}{2\pi}\mathrm{e}^{\mathrm{i}\omega_0\frac{y-y_0}{V}}\int_{-\infty}^{+\infty}\frac{\mathrm{e}^{\mathrm{i}\omega\left(t-\frac{y-y_0}{V}\right)}}{EI\left(\omega-\omega_0\right)^4+kV^4+\mathrm{i}\omega cV^4-\omega^2mV^4}\mathrm{d}\omega \tag{4.23}$$

Since the integrand in (4.23) is a regular expression and since it is bounded in the complex plane, the integral can be evaluated by means of contour integration, resulting in

$$u\left(y,t,\omega_0\right)=\mathrm{i}\frac{A_0V^3}{EI}\mathrm{e}^{\mathrm{i}\omega_0\frac{y-y_0}{V}}\mathrm{sign}\left(t-\frac{y-y_0}{V}\right)\sum_{\mathrm{imag}\left(\omega_j\right)\left(t-\frac{y-y_0}{V}\right)>0}^{4}\left(\mathrm{e}^{\mathrm{i}\omega_j\left(t-\frac{y-y_0}{V}\right)}\prod_{\substack{k=1\\k\neq j}}^{4}\frac{1}{\left(\omega_j-\omega_k\right)}\right) \tag{4.24}$$

In the previous equation, the values ω_j represent the roots of the polynomial

$$EI\left(\omega_j-\omega_0\right)^4+kV^4+\mathrm{i}\omega_j cV^4-\omega_j^2mV^4=0 \tag{4.25}$$

Similarly to the case of constant moving loads, when damping is null, there is a velocity above which the polynomial (4.25) presents real roots. However, in this case, for low frequencies ω_0, the minimum velocity that yields real roots only yields two of the poles real, and so there is a second velocity above which all the roots are real. At these two critical velocities, two roots of (4.25) become real and with the same value (double roots), which results in the amplification of the displacements of the beam.

In Figure 4.4, the (logarithm of) maximum of the displacements u_{C} is plotted as a function of the excitation frequency ω_0 and load speed V for a beam on a Kelvin foundation with the same properties of the system described in section 4.2.2 (with $c=0$ Ns/m).

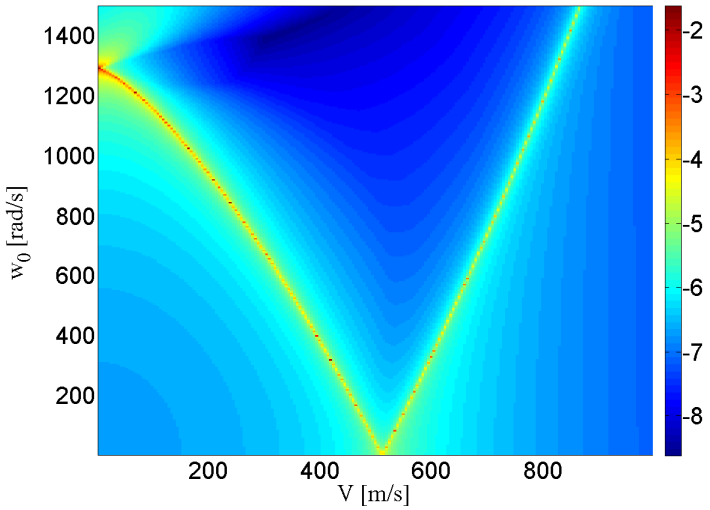

Figure 4.4: Logarithm of the beam maximum displacement as a function of the load speed V and excitation frequency ω_0 ($c = 0$ Ns/m)

For $\omega_0 = 0$, there is only one critical velocity which is calculated with (4.14). For, $\omega_0 \neq 0$, to determine the load speeds is cumbersome, but by rearranging equation (4.25) it can be concluded that these velocities correspond to the local real minima of

$$V = \sqrt[4]{\frac{(\omega - \omega_0)^4 EI}{\omega^2 m - k}}, \qquad |\omega| > \sqrt{\frac{k}{m}} \tag{4.26}$$

When $\omega_0 > \sqrt{k/m}$, there is only one critical velocity.

Next, the beam displacements are calculated considering the excitation frequency $\omega_0 = 100$ rad/s and considering the load speeds $V = 300$, $V = 500$ and $V = 700$ m/s. The properties of the beam and foundation are the same of the example of section 4.2.2, and it is assumed that the load crosses the cross-section $y = 0$ at the instant $t = 0$ ($y_0 = 0$). The results obtained with the time domain FEM procedure are not shown, but is was observed that the agreement between the FEM results and equations (4.22) and (4.23) is very good. The displacements at $t = 0$ are plotted in Figure 4.5.

For load speeds below the lower critical velocity (Figure 4.5a), the displacements evanesce with the distance to the source and the decay rate of the displacements depends on the proximity of the load speed to the critical velocity. For load speeds between the two critical velocities (Figure 4.5b), the displacements propagate both ahead ($y > 0$) and behind ($y < 0$) the load, being the wavelength of the displacements shorter ahead than behind. For load speeds greater than the highest critical velocity (Figure 4.5c), the displacements propagate mostly behind the load and the wavelengths are shorter ahead than behind. Note that there are two major wavelengths for each side of the response, a consequence of the existence of four distinct real roots in the polynomial (4.25) (for non-oscillating loads, the roots are paired up in groups of 2, $\pm\omega_1$ and $\pm\omega_2$, and so the two distinct wavelengths are not observed).

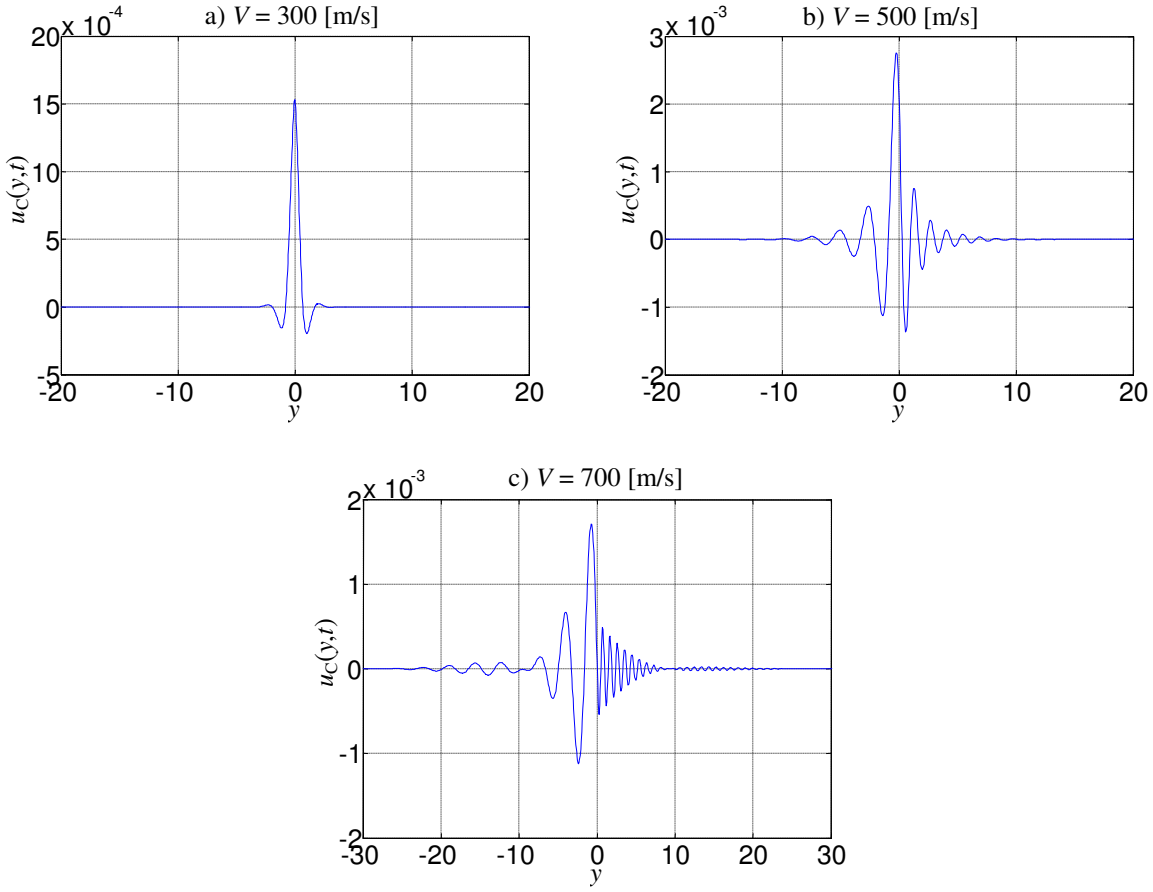

Figure 4.5: Beam displacements induced by harmonic moving loads

In Figure 4.6, the maximum displacements observed at the beam are plotted as a function of the load speed for the conditions referred to above (blue line) and for null damping (red line). The two critical velocities can be identified for the case of no damping, while for the case of damping, the critical velocities appear to merge into one. Such feature is observed for the damped case because the critical velocities are near each other and because the large amount of damping used not only reduces the maximum displacements as it also widens the "bell shaped response" associated with each velocity. If the damping is reduced or if the excitation frequency ω_0 is increased (and consequently the critical velocities are moved farther apart), then, even for the damped case, the two critical velocities can be noticed.

The example solved in this subsection considers cosine type loads. For sine type loads, the same conclusions can be drawn and the response of the structure is practically the same, being it simply shifted in time and in space. In the next subsection, structures for which the response fields cannot be determined analytically are studied.

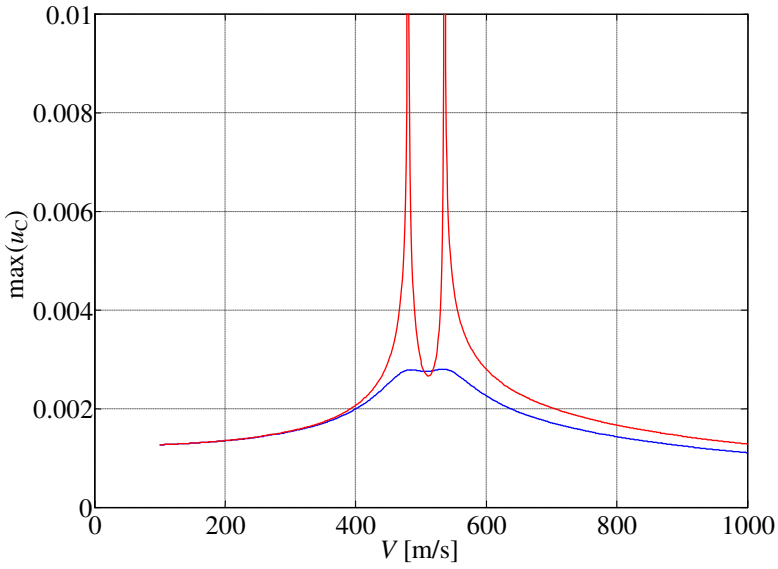

Figure 4.6: Beam maximum displacements as function of the load speed. Blue line – with damping; Red line – no damping

4.2.4 Examples

Next, equations (4.9) and (4.18)-(4.20) are used to calculate the response of longitudinally invariant structures of which the wavenumber transfer functions (and therefore the integrands of the mentioned equations) cannot be determined analytically.

The case study considered in this subsection consists in a flexible slab resting on the surface of a half-space (homogeneous or layered) that is subjected to a vertical load $f(t)$ that moves with speed V along the middle top alignment (point A), as exemplified in Figure 4.7 (it is assumed that the load crosses the section $y=0$ at $t=0$, i.e., $y_0=0$). The material properties of the slab are: density $\rho=2145\,\text{kg/m}^3$; Young's modulus $E=30\,\text{GPa}$; and Poisson's ratio $\nu=0.2$. The slab is modeled with 8 four-node volume elements with dimensions $0.25\times0.3\,\text{m}^2$ and the interface between the slab and the half-space is divided into 8 boundary elements of constant expansion.

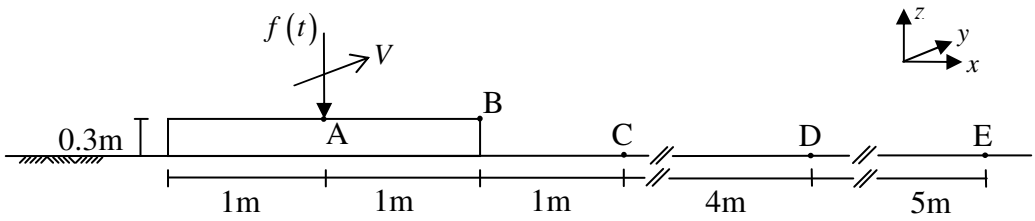

Figure 4.7: Slab resting on a half-space submitted to a moving load

Example 1 – Slab on a homogeneous half-space subjected to a constant moving load

In this first example, the slab is subjected to a constant moving load defined by $f(t)=1000\,\text{N}$ and the foundation, which consists in a homogeneous half-space, is given the following properties: density $\rho=1800\,\text{kg/m}^3$; shear modulus $G=0.1125\,\text{GPa}$; Poisson's ratio $\nu=0.25$

(the corresponding body wave velocities are $C_s = 250$ m/s and $C_p = 433$ m/s). A small amount of hysteretic damping $\xi_p = \xi_s = 0.02$ is considered, which renders complex wave velocities $\bar{C}_p = C_p\sqrt{1+\text{sign}(\omega)2i\xi_p}$ and $\bar{C}_s = C_s\sqrt{1+\text{sign}(\omega)2i\xi_s}$ (Dominguez, 1993).

For constant moving loads, the time domain response fields $h(y,t)$ are obtained through the evaluation of eq. (4.9), but since in this example the transfer functions $\tilde{h}(k_y,\omega_i)$ cannot be determined analytically, then the integral in (4.9) has to be evaluated numerically, being approximated with

$$h(y,t) \approx \frac{A_0\Delta\omega}{2\pi V}\sum_{i=-N_\omega}^{N_\omega}\tilde{h}(\omega_i/V,\omega_i)\,e^{i\omega_i\left(t-\frac{y-y_0}{V}\right)} \tag{4.27}$$

Due to the conjugate property $\tilde{h}(-k_y,-\omega_i) = \overline{\tilde{h}(k_y,\omega_i)}$, eq. (4.27) can be further simplified to

$$h(y,t) \approx \frac{A_0\,\Delta\omega}{\pi V}\sum_{i=1}^{N_\omega}\left(\text{Re}\left[\tilde{h}(\omega_i/V,\omega_i)\right]\cos\left(\omega_i\left(t-\frac{y-y_0}{V}\right)\right) - \text{Im}\left[\tilde{h}(\omega_i/V,\omega_i)\right]\sin\left(\omega_i\left(t-\frac{y-y_0}{V}\right)\right)\right) \tag{4.28}$$

In the following, equation (4.28) is used to calculate the time domain displacements at the cross-section $y = 0$ and for $V = 100$ m/s at point B, situated at the edge of the slab, and at points C, D and E, situated at the surface of the half-space. Two TLM models are tested: in the first model (TLM-1), the half-space is modeled with just one PML with parameters $\eta = 2$, $\Omega = 4$, $m = 2$ and $N = 10$ (see chapter 2); in the second model (TLM-2), the half-space is modeled with an elastic layer of thickness $H = 2$ m, divided into 40 quadratic thin-layers, and with a PML (same parameters as for model TLM-1). The displacements obtained with these TLM models are compared with the displacements obtained using a time domain methodology (TD) (dos Santos et al., 2010a; dos Santos et al., 2010b) and with the displacements obtained using eq. (4.28) together with the transfer functions $\tilde{h}(k_y,\omega_i)$ obtained from a 2.5D BEM-FEM procedure based on the stiffness matrices of Kausel and Roesset (1981) (SM). For the procedures based on eq. (4.28), 1500 frequencies with a step of 0.1 Hz are used. For the time domain procedure, a 100m long 3D model divided into 400 longitudinal sections and a time step of 0.002 s are used. Figure 4.8 plots the transverse displacements of the points B, C, D and E obtained with the four mentioned approaches, Figure 4.9 plots the longitudinal displacements and Figure 4.10 plots the vertical displacements.

From Figure 4.8, it can be observed that the four approaches yield significantly different transverse displacements: at the slab (Point B), the TLM-1, the TLM-2 and the SM results tend approximately to the same maximum value, but the shapes of the curves are different; still regarding point B, the TD solution differs both in shape and sign from the remaining solutions (a justification for this could not be found); at the surface of the half-space (points C, D and E), the results of the SM model tend the follow the TD results while the TLM-1 and the TLM-2 yield smaller displacements. Despite this fact, the passage of the load at the cross-section is noticed in all four approaches. As for the longitudinal and vertical displacements represented in Figure 4.9 and Figure 4.10, respectively, a better agreement is, in general, observed.

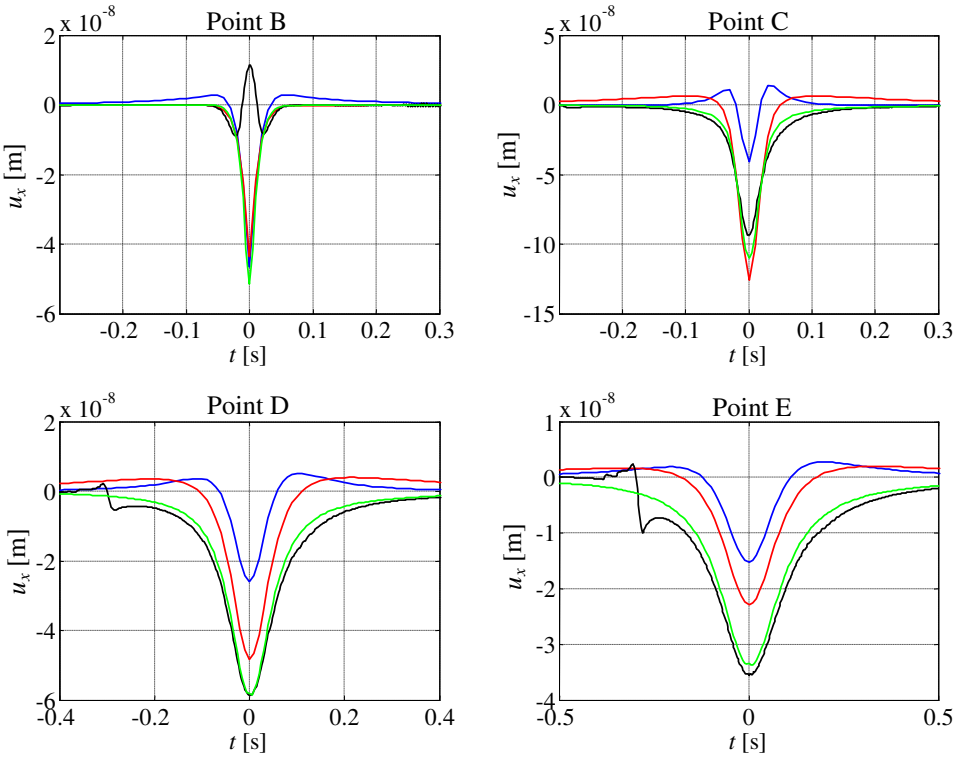

Figure 4.8: Transverse (x) displacements: blue = TLM-1; red = TLM-2; black = TD; green = SM

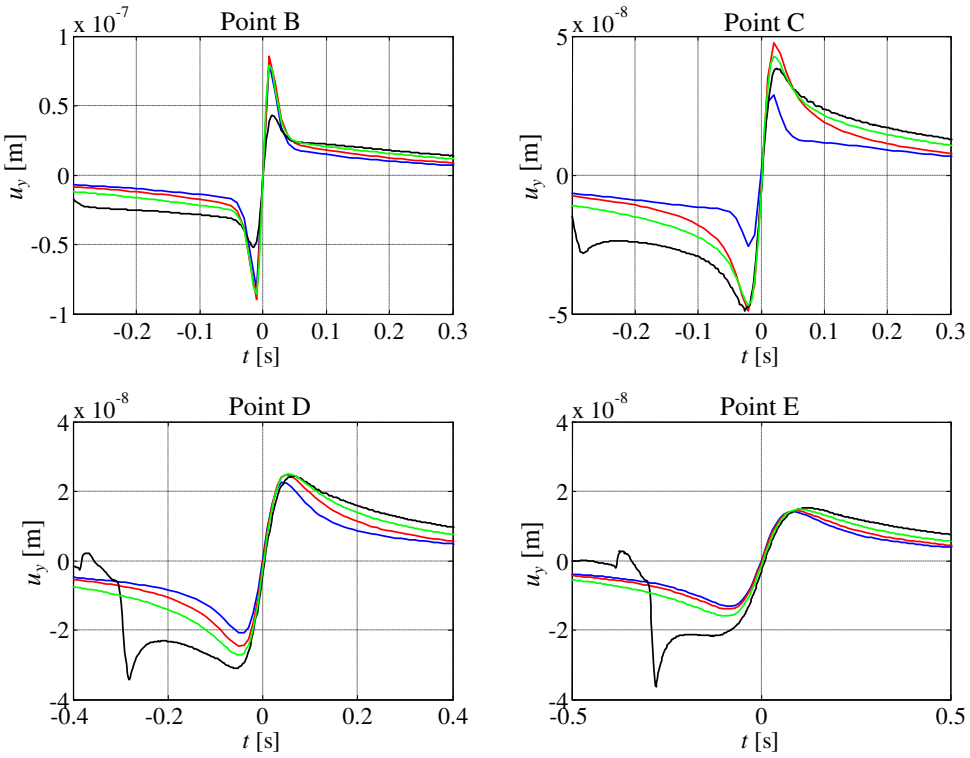

Figure 4.9: Longitudinal (y) displacements: blue = TLM-1; red = TLM-2; black = TD; green = SM

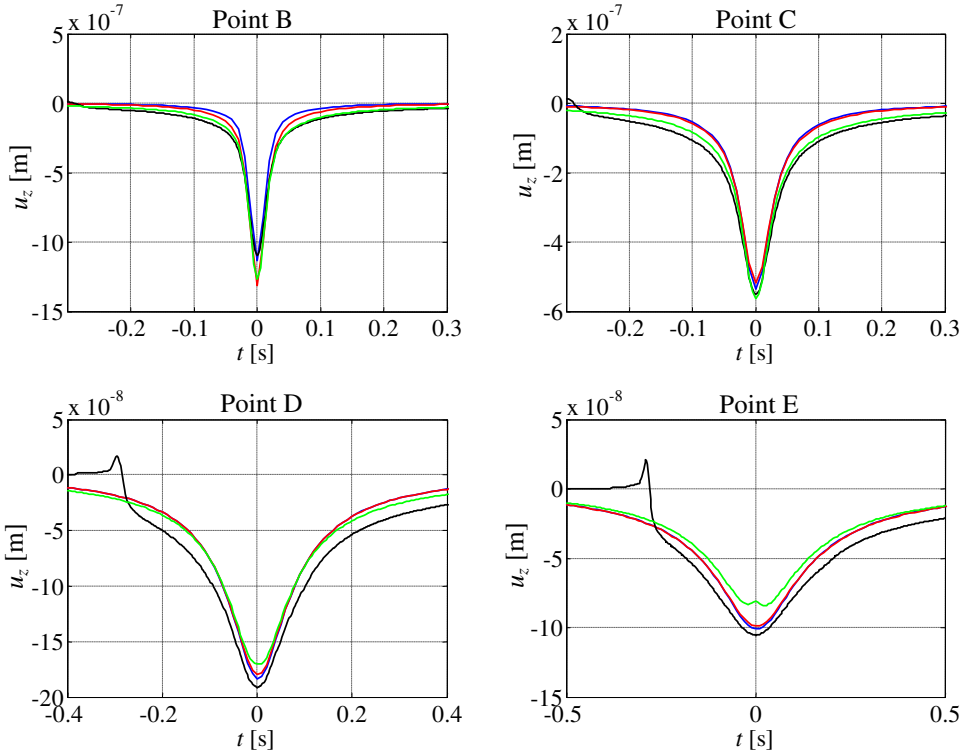

Figure 4.10: Vertical (z) displacements: blue = TLM-1; red = TLM-2; black = TD; green = SM

When comparing the TD results (black lines) with the remaining approaches, it is noticed that for the earlier moments ($t < 0.2$ s) the responses present very distinct behaviors. These differences are justified by the finite length of the 3D model used in the TD approach, a characteristic that violates the assumption of invariant cross-section considered in the 2.5D models. In this way, while in the TD approach the entrance of the load in the finite element model induces a transient phenomenon, in the 2.5D approaches, since it is assumed that the load travels from minus infinity to plus infinity, the phenomenon is not present. The transient phenomenon dissipates due to internal damping and therefore after some time its contribution is minimal. Apart from the transient phenomenon, the remaining differences may be justified by the longitudinal and temporal discretizations required by the TD approach: the TD and the SM approaches are based on the fundamental solutions obtained with the stiffness matrices and therefore, theoretically, they should yield the same values. This hypothesis has not been tested because to make the 3D mesh longer in the longitudinal direction and/or with thinner elements and smaller time-steps renders the calculation unfeasible (for the current 100 m long model, more than two days were required to calculate the passage of the load from one edge of the model to the other edge).

The differences between the results of the TLM-1, TLM-2, and SM approach can only be justified by differences in the transfer functions $\tilde{h}(k_y, \omega)$. Figure 4.11 compares the transfer functions $\tilde{u}_x(\omega/V, \omega)$ calculated with the three approaches at the four points and, as expected, they present discrepancies, which justify the distinct curves in Figure 4.8. Furthermore, when comparing the blue and red lines (TLM-1 and TLM-2) with the green line (SM), one realizes that the differences are concentrated in the lower frequency range ($\omega < 20$ rad/s $\rightarrow f < 3.2$ Hz),

which leads to the conclusion that these differences are caused by the inappropriate simulation of the infinite domain at the low frequency range. The comparison of the longitudinal and vertical responses is not shown here, but it was observed that the differences are smaller than for the transverse component, which justifies the better agreement obtained.

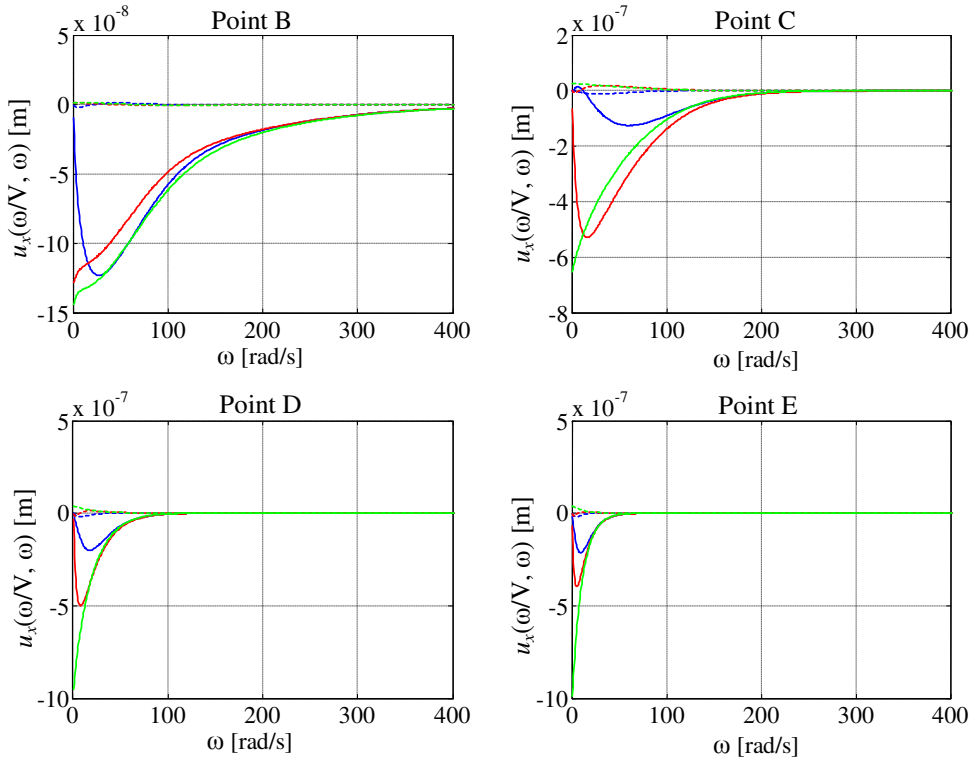

Figure 4.11: Transverse (x) displacements in the wavenumber-frequency domain: solid line = real part; dashed line = imaginary part; blue = TLM-1; red = TLM-2; green = SM

Note that for the low frequencies, the PML used to model the half-space is divided into thin-layers that are thicker than the widths of the slab and of the boundary elements (the PML and the thin-layers are made proportional to the shear wavelength) and so the boundary integrals calculated as explained in chapter 3 do not yield accurate results. Also, at low frequencies, when the waves, that are mostly evanescent, enter the PML, they propagate instead of evanesce, and that causes the waves to reflect at the bottom of the PML and return to the surface, which contaminates the results. This is also the reason why the TLM-2 model yields better results than the TLM-1 model: the TLM-2 model contains an elastic layer divided into thinner thin-layers where the waves evanesce before they reach the PML. A third TLM model in which the elastic part is made thicker (10 m divided into 100 quadratic thin-layers) has been tested and in this case the transfer functions $\tilde{u}_x(\omega/V,\omega)$ (and remaining components) approximate more closely the green line. Hence, the problem of simulating the half-spaces for low frequencies can be solved by using a sufficiently thick elastic thin-layer on top of the PML.

An alternative approach to overcome the above mentioned differences would be to replace the PML by the static half-space matrices derived by Kausel and Seale (1987), thus neglecting the mass of the half-space (in the very low frequency range, this simplification should not introduce significant errors). However, the terms derived in the mentioned work change the

structure of the TLM matrices and consequently the algorithms described in chapter 2 for the solution of the eigenvalue problems could not be applied. For this reason, since the differences in the results can be reduced by adding a thicker elastic layer, and since this problem is not observed for harmonic moving loads (as seen in the next example), the mentioned procedure has not been tested nor implemented.

Another study that can be performed with this example is the influence of the load speed on the response of the system. Figure 4.12 plots the maximum vertical displacement of point B obtained with TLM-2 as a function of the load speed V.

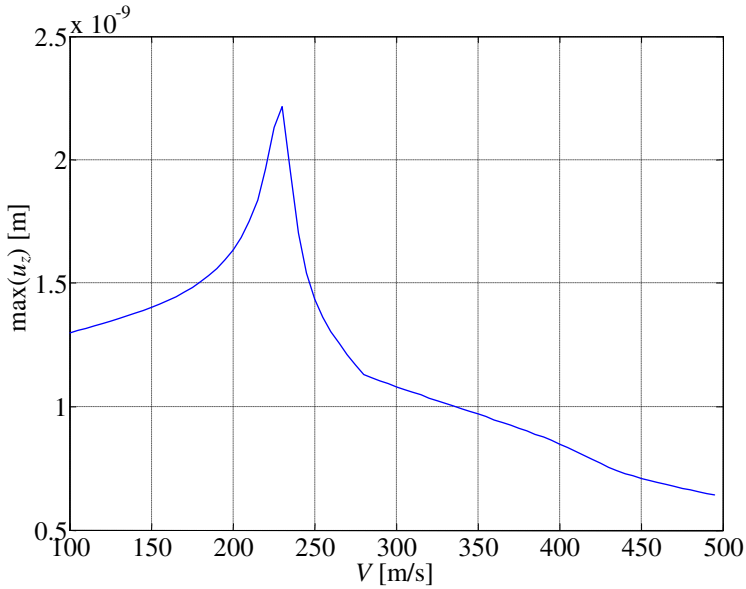

Figure 4.12: Maximum vertical displacement of point B as a function of the load speed V

Similarly to the case of a beam on a Kelvin foundation, there is a critical velocity V_{cr} at which the displacements of the slab are amplified. This velocity $V_{cr} \approx 230$ m/s corresponds to the Rayleigh wave speed of the half-space, which is in accordance with the conclusions obtained by other authors, (e.g., Dieterman and Metrikine, 1996; Metrikine and Popp, 2000).

Finally, the influence of the load speed V on the displacements at the surface of the half-space is analyzed. With that intention, a snapshot of the surface vertical displacements is represented in Figures 4.13-4.15 for $V = 100$ m/s (below the critical speed), $V = 300$ m/s (above the critical speed but below the pressure wave speed) and $V = 500$ m/s (above both the critical and pressure wave speeds), respectively.

From Figure 4.13, it can be seen that for load speeds below the critical velocity V_{cr}, the displacements are practically symmetric with respect to the load position. Also, at the surface of the half-space, the displacements evanesce with the radial distance to the load and are negative everywhere. This last feature is supported by Figure 4.10.

In Figure 4.14, it is observed that the displacements are no longer symmetric with respect to the loaded section: on the contrary, the wave-field forms a cone that moves with the load, which is a consequence of the load moving faster than the critical velocity V_{cr}. Ahead of the wave-front, the displacements are positive (upwards; red zones) while behind the wave-front the displacements are negative (downwards; blue and green zones).

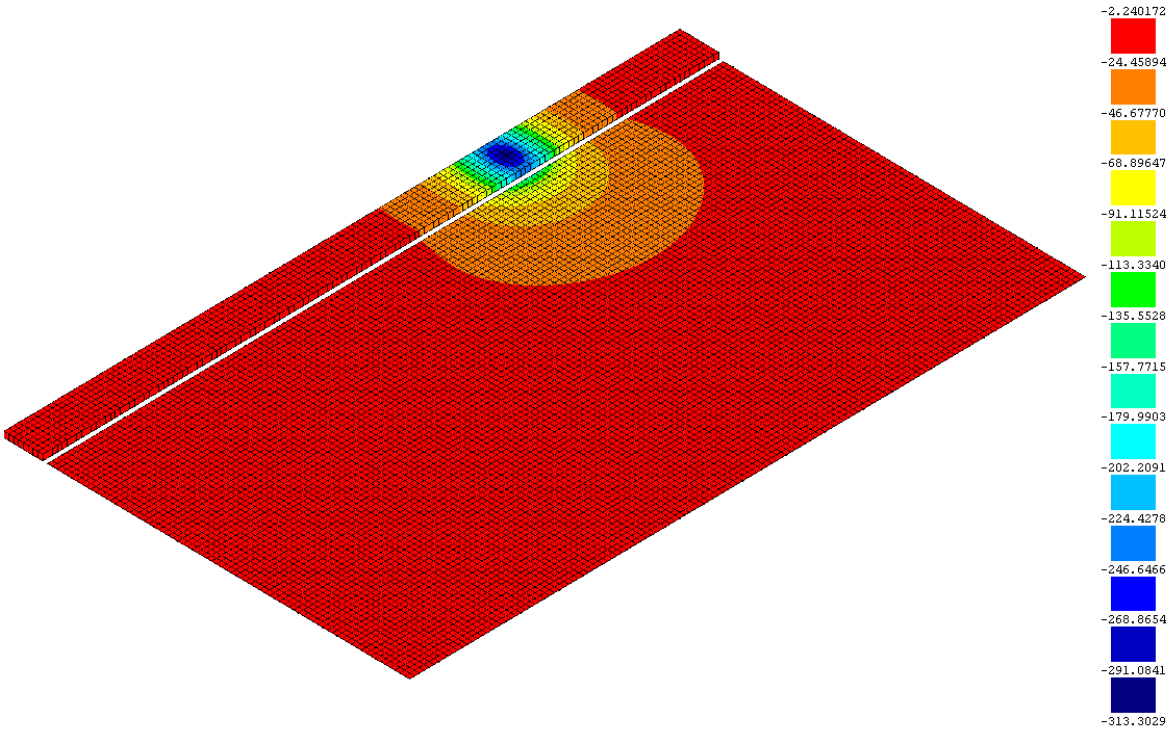

Figure 4.13: Vertical displacements for $V = 100$ m/s ($\omega_0 = 0$): the displacements are multiplied by the shear modulus of the half-space (values in N/m)

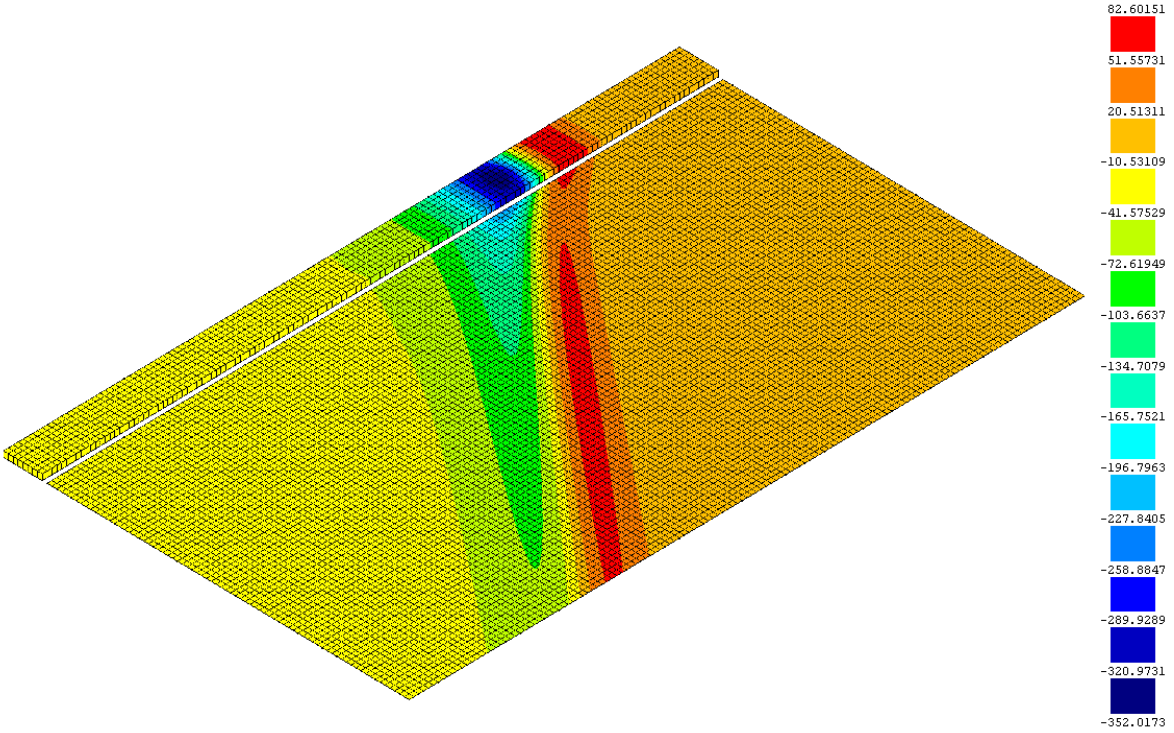

Figure 4.14: Vertical displacements for $V = 300$ m/s ($\omega_0 = 0$): the displacements are multiplied by the shear modulus of the half-space (values in N/m)

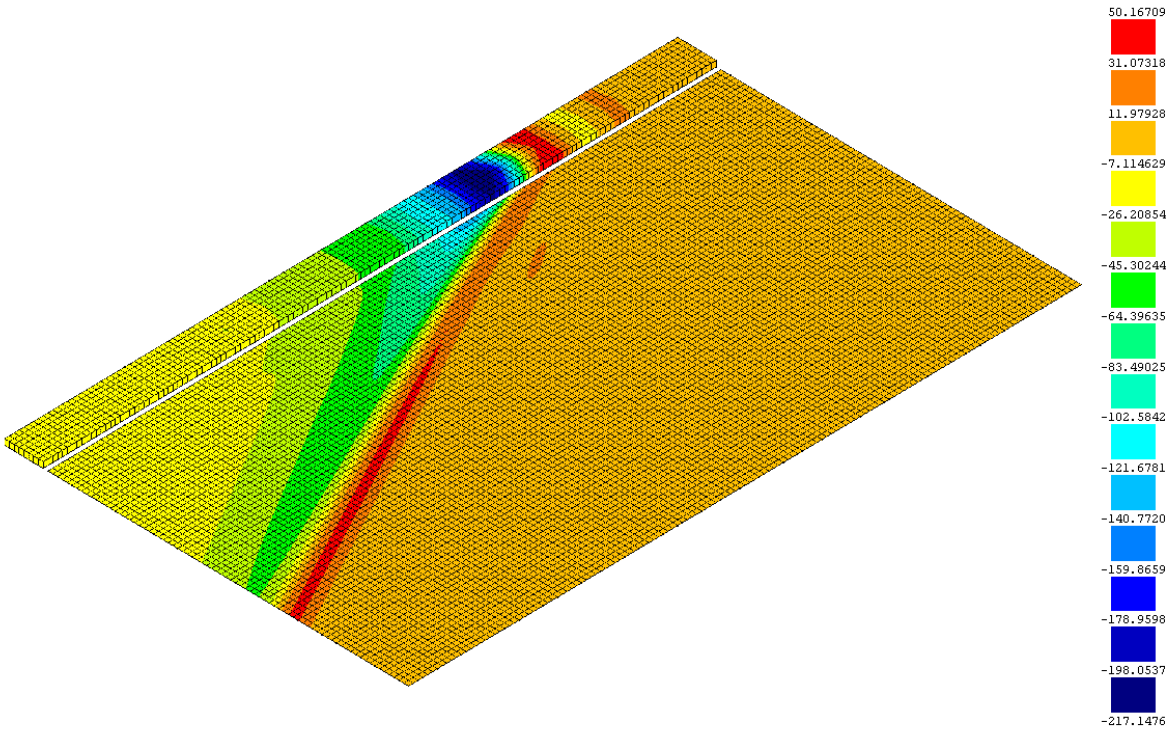

Figure 4.15: Vertical displacements for $V = 500$ m/s ($\omega_0 = 0$): the displacements are multiplied by the shear modulus of the half-space (values in N/m)

Figure 4.15 is very similar to Figure 4.14, being the main difference the angle of the cone, which is sharper because the load moves faster. Also, because in this case the load moves faster than the pressure wave ($V > C_P$), there is a second cone (or wave-front; not visible in the figure), not as sharp as the first, and ahead of which the amplitudes of the displacements are small (note that there are displacements ahead of this cone only because the waves at the slab are faster than the load speed; had the load been applied directly at the surface of the half-space, then no displacements would be observed ahead of the second cone).

The maximum downwards displacements of Figures 4.13-4.15 are in accordance with the maximum displacements plotted in Figure 4.12.

Example 2 – Slab on a homogeneous half-space subjected to a harmonic moving load

In this second example, the slab, which rests on a homogeneous half-space with the same properties as in the previous example, is subjected to a harmonic moving load of the type $f(t) = 1000\sin(\omega_0 t)$ (N).

For sinusoidal moving loads, the response fields in the time domain correspond to the imaginary component of equation (4.18), which in this example has to be calculated numerically given the fact that the transfer functions $\tilde{h}(k_y, \omega_i)$ cannot be determined analytically. For this reason, $h_S(y,t,\omega_0)$ is approximated with

$$h_S(y,t,\omega_0) \approx \frac{A_0\,\Delta\omega}{2\pi V}\,\mathrm{Im}\left[e^{i\omega_0\frac{y-y_0}{V}} \sum_{i=-N_\omega}^{N_\omega} \tilde{h}\left(\frac{\omega_i-\omega_0}{V},\omega\right) e^{i\omega_i\left(t-\frac{y-y_0}{V}\right)} \right] \tag{4.29}$$

which is equivalent to

$$h_S(y,t,\omega_0) \approx \frac{A_0\,\Delta\omega}{2\pi V}\,\mathrm{Im}\left[e^{i\omega_0\frac{y-y_0}{V}} \sum_{i=1}^{N_\omega} \left(\tilde{h}\left(\frac{\omega_i-\omega_0}{V},\omega_i\right) e^{i\omega_i\left(t-\frac{y-y_0}{V}\right)} + \overline{\tilde{h}\left(\frac{\omega_i+\omega_0}{V},\omega_i\right) e^{-i\omega_i\left(t-\frac{y-y_0}{V}\right)}} \right) \right] \tag{4.30}$$

Hence, for each sampled frequency ω_i, the transfer functions $\tilde{h}(k_y,\omega)$ must be calculated for the wavenumbers $k_1 = (\omega_i - \omega_0)/V$ and $k_2 = (\omega_i + \omega_0)/V$, which are then used in eq. (4.30).

Next, equation (4.30) is used to calculate the time domain displacements of points B, C, D and E (Figure 4.7) at the cross-section $y = 0$ and for $V = 100$ m/s and $\omega_0 = 40\pi$ rad/s (once again, it is assumed that the load crosses the section $y = 0$ at $t = 0$, i.e., $y_0 = 0$). The two TLM models described in Example 1 (TLM-1 and TLM-2) are used to simulate the half-space, and the results thus obtained are once again compared with the displacements obtained using the TD and the SM approaches. For the procedures based on eq. (4.30), 1500 frequencies with a step of 0.1 Hz are considered. For the time domain procedure, the same model and time steps considered in Example 1 are used. Figures 4.16-4.18 plot the transverse, longitudinal and vertical components of the displacements obtained with the four approaches.

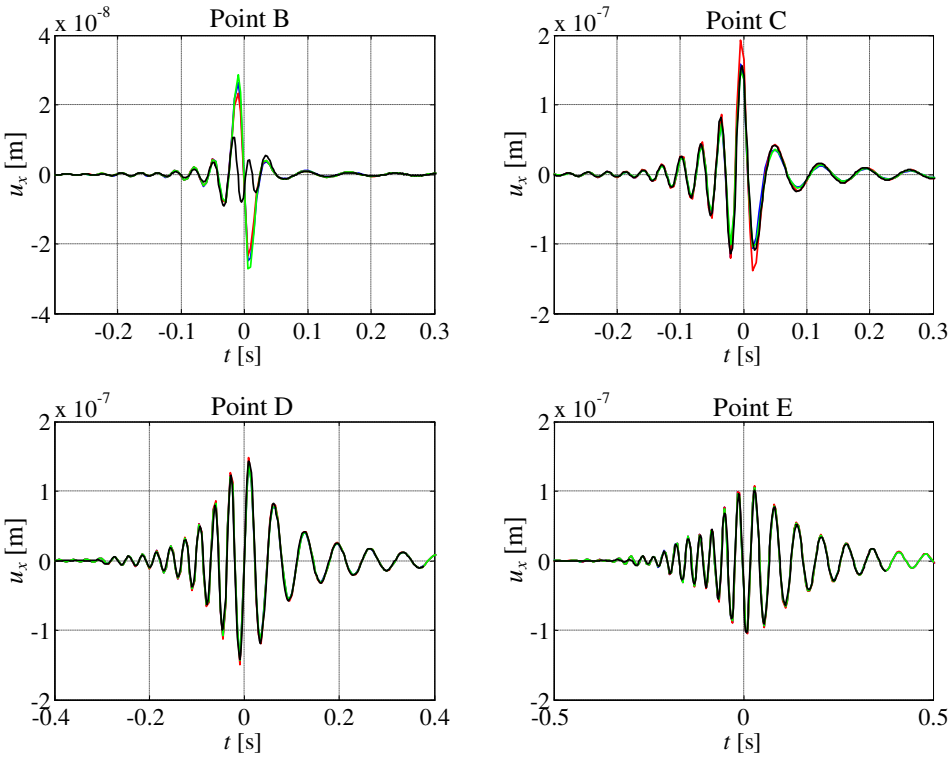

Figure 4.16: Transverse (x) displacements: blue = TLM-1; red = TLM-2; black = TD; green = SM

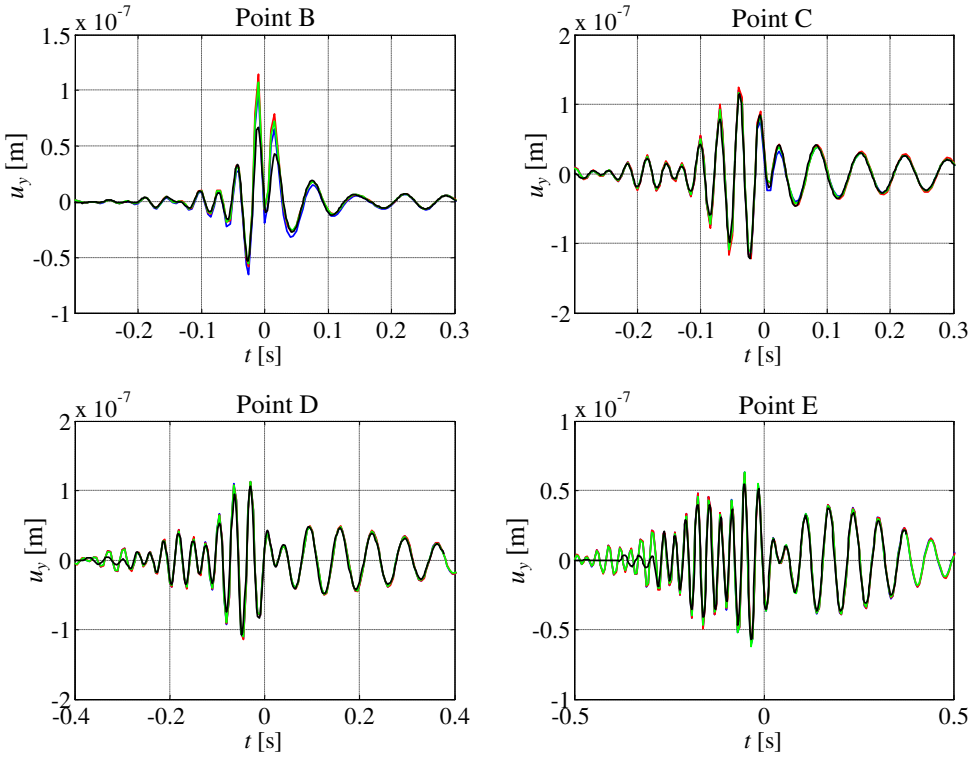

Figure 4.17: Longitudinal (y) displacements: blue = TLM-1; red = TLM-2; black = TD; green = SM

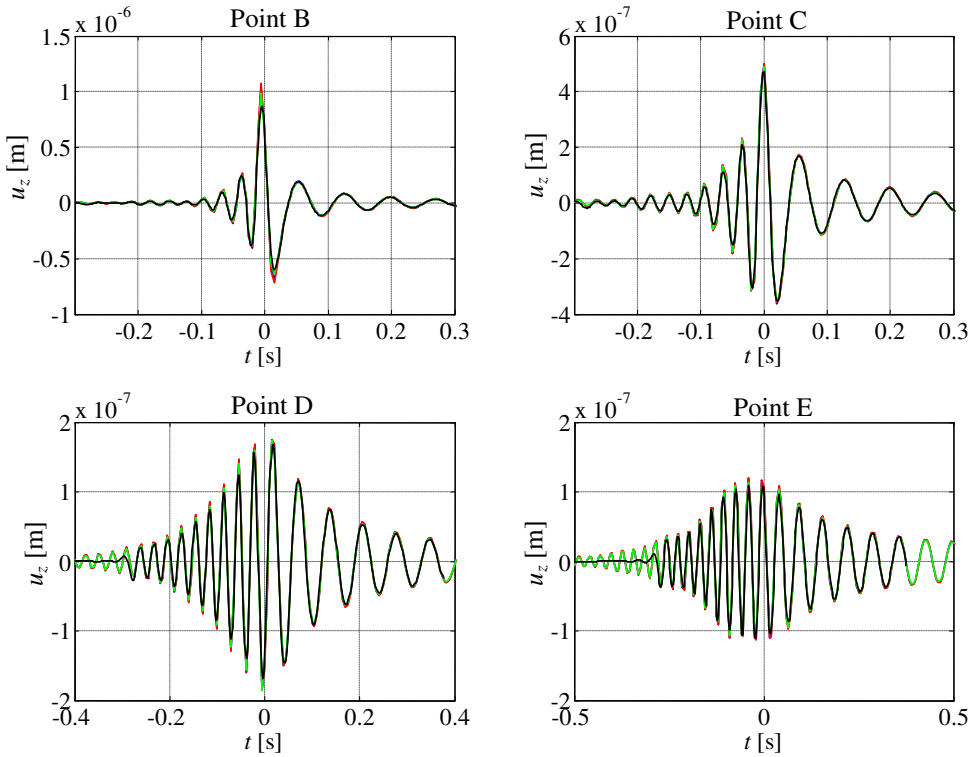

Figure 4.18: Vertical (z) displacements: blue = TLM-1; red = TLM-2; black = TD; green = SM

Except for the TD response of point B, a good agreement can be observed between the results of the four distinct approaches. The differences observed for the TD approach at point B can be justified by the longitudinal discretization, which is not fine enough to reproduce accurately the response near the loaded point (note that for large negative and positive times, i.e., when the load is far from the reference section $y = 0$, the agreement is good).

When comparing the results of examples 1 and 2, it can be observed that in general the agreement is better for the second example than for the first. The reason for this is that the time domain response in the second example is dominated by the radial frequencies $\omega_1 = \omega_0 V_R / (V_R - V)$ and $\omega_2 = \omega_0 V_R / (V_R + V)$, and not by the low frequencies, as in the first example. The mentioned radial frequencies correspond to the interceptions between the dispersion curves of the foundation (for a homogeneous half-space, the dispersion curve corresponds to $\omega = V_R k$, where V_R is the Rayleigh wave speed) and the integration paths of equation (4.18) ($\omega = \omega_0 + V k_y$ and $\omega = \omega_0 - V k_y$).

In opposition to what happens in example 1, for the oscillation frequency $\omega_0 = 40\pi$[rad/s] there is no critical load speed at which the displacements are amplified, and the reason for that is because the integrating paths $\omega = \omega_0 + V k_y$ and $\omega = \omega_0 - V k_y$, that intercept the dispersion curves at the frequencies $\omega_1 = \omega_0 V_R / (V_R - V)$ and $\omega_2 = \omega_0 V_R / (V_R + V)$, are never tangent to the mentioned curves (for $\omega_0 = 0$ and for $V = V_R$, the integrating path coincides with the dispersion line, i.e., are tangent everywhere, and that is the reason for the displacements to be amplified). This conclusion is in accordance with the work of Dieterman and Metrikine (1997) and is supported by Figure 4.19, which plots the maximum displacement observed at point B for different forcing frequencies ω_0 as a function of V, and where it can be observed that the displacements tend to decrease as V increases.

Taking into account the conclusions obtained in section 4.2.3 for a beam on a Kelvin foundation, it could be expected the existence of at least on critical velocity. However, in that case, the energy dissipates only along the longitudinal and vertical directions, while for the case of a slab on a half-space (a pure 3D case) the energy also dissipates along the transverse direction, thus changing completely the behavior of the system. This aspect supports the importance of 3D models in the simulation of vibration fields induced by moving loads.

Before proceeding to examples of layered domains, the influence of the load speed on the shape of the response of the system is evaluated with the aid of snapshots of the vertical displacements induced by loads moving at the speeds $V = 100$ m/s, $V = 300$ m/s and $V = 500$ m/s. The snapshots are represented in Figures 4.20-4.22.

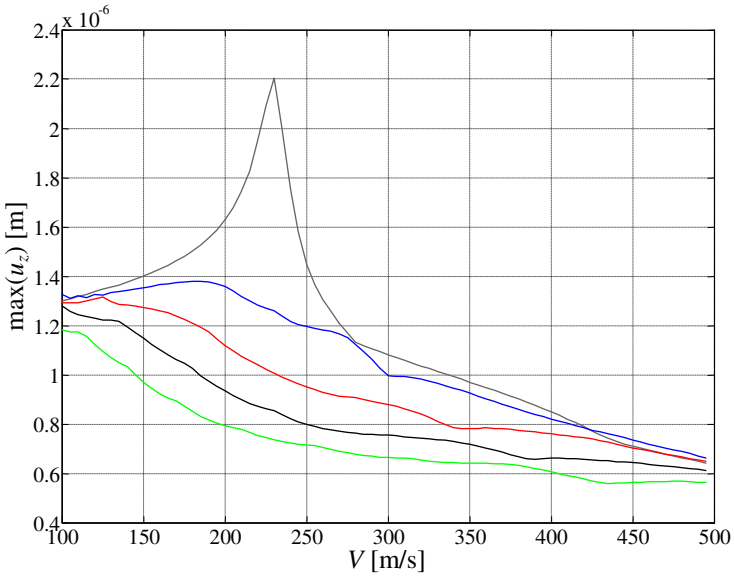

Figure 4.19: Maximum vertical displacement of point B as a function of the load speed V for: $\omega_0 = 0$ (gray); $\omega_0 = 10\pi$ rad/s (blue); $\omega_0 = 20\pi$ rad/s (red); $\omega_0 = 30\pi$ rad/s (black); and $\omega_0 = 40\pi$ rad/s (green)

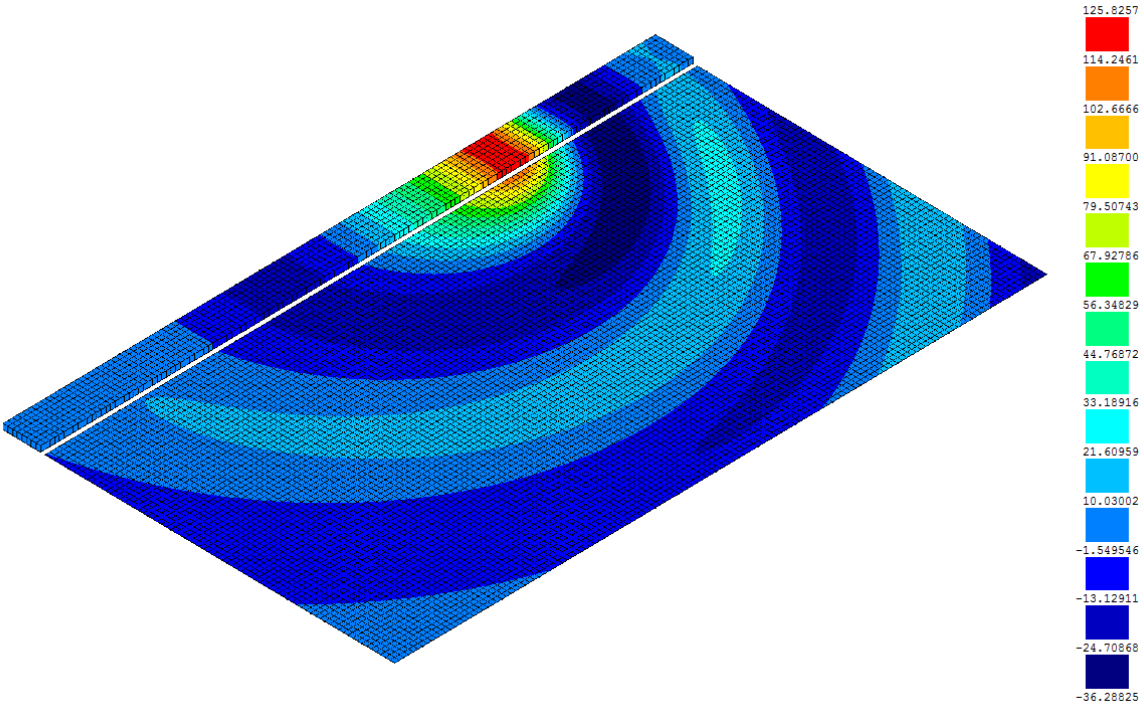

Figure 4.20: Vertical displacements for $V = 100$ m/s ($\omega_0 = 40\pi$ rad/s): the displacements are multiplied by the shear modulus of the half-space (values in N/m)

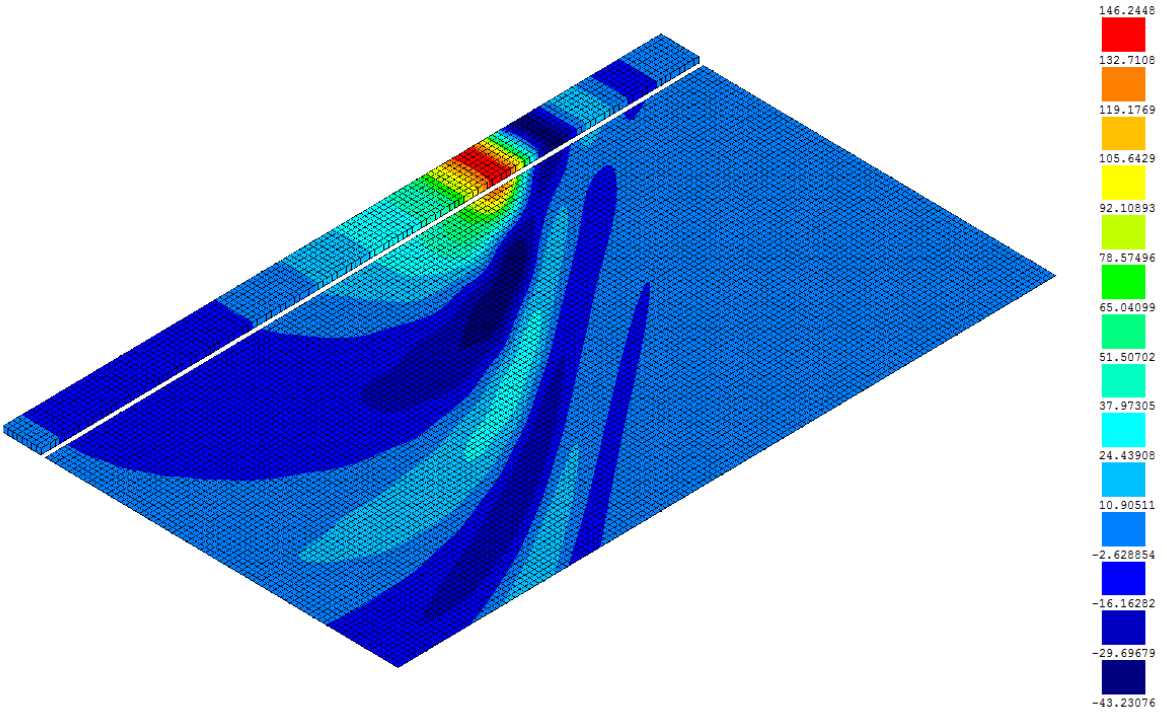

Figure 4.21: Vertical displacements for $V = 300$ m/s ($\omega_0 = 40\pi$ rad/s): the displacements are multiplied by the shear modulus of the half-space (values in N/m)

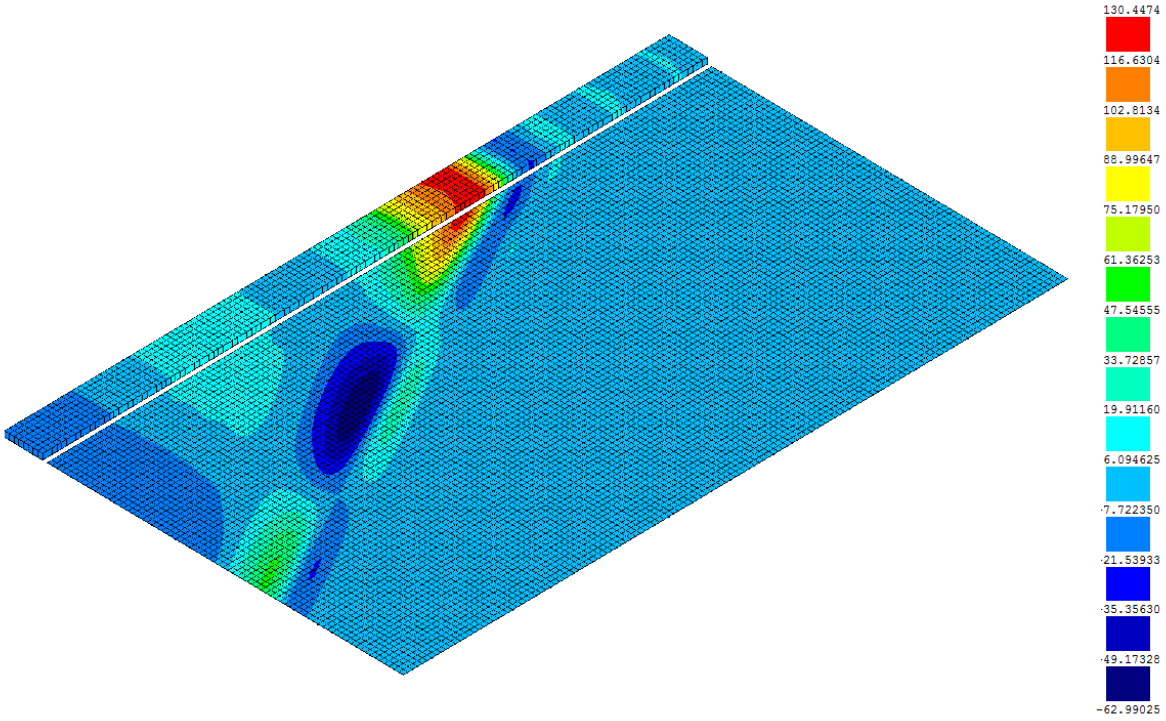

Figure 4.22: Vertical displacements for $V = 500$ m/s ($\omega_0 = 40\pi$ rad/s): the displacements are multiplied by the shear modulus of the half-space (values in N/m)

For $V = 100$ m/s (Figure 4.20) it can be observed that the waves propagate away from the load and that the wave-fronts present an elliptical shape, being the wavelengths ahead of the load shorter than the wavelengths behind the load. Such aspect is characteristic of waves induced by loads moving with speeds below the surface waves of the medium. Unlike the case of a constant moving load with the same speed (Figure 4.13), in this example the values of the displacements alternate between positive and negative, a consequence of the oscillatory nature of the load. Also, the reduction of displacements with the distance to the source is smaller, which emphasizes the importance of the dynamic loads in the calculation of wave-fields at remote positions.

For $V = 300$ m/s and for $V = 500$ m/s (Figure 4.21 and Figure 4.22, respectively) the wave-fronts form a cone, which is also observed for the case of constant moving loads, and that is a consequence of the load moving faster than the surface waves of the foundation. Similarly to constant loads, the cone is shaper for $V = 500$ m/s than for $V = 300$ m/s, and for $V = 500$ m/s there is a second cone that results from the fact that the load moves faster than the pressure wave of the foundation (this second cone cannot be noticed in Figure 4.22).

Example 3 – Critical speeds for layered foundations

The first two examples considered homogeneous foundations. In this example, the critical load speeds are calculated for different configurations of the foundation, namely: a) a stiffer layer on top of a softer half-space ($G_{\text{lay}} = 0.225$ GPa, $G_{\text{half}} = 0.1125$ GPa); b) a softer layer on top of a stiffer half-space ($G_{\text{lay}} = 0.05625$ GPa, $G_{\text{half}} = 0.1125$ GPa). The thickness of the upper layers is $H = 2$ m (divided into 40 quadratic thin-layers), and the material properties are the same of the homogeneous half-space used in examples 1 and 2 (except for the shear modulus, which is as indicated in the previous sentence).

According to Dieterman and Metrikine (1997), resonance occurs when the load speed equals the group velocity of the waves generated by the load, which in other words means that resonance takes place when the integrating path $\omega = \omega_0 + Vk_y$ or $\omega = -\omega_0 + Vk_y$ is tangent to a dispersion curve of the foundation.

The dispersion curves of a layered domain represent its free vibration modes and are defined by the curves $(k, \omega(k))$ that yield the system singular, i.e., undetermined. These curves are associated with the steady waves that are originated due to the existence of boundary conditions (such as free surface or interface between layers). These waves propagate horizontally with phase velocity $V_{\text{ph}} = \omega(k)/k$ and group velocity $V_{\text{gr}} = \partial\omega(k)/\partial k$.

For the case of a homogeneous full-space, there are no such steady waves because the only existent boundary condition is the radiation of waves to infinity. As for the case of a homogeneous half-space, the existence of a free surface originates the well-known Rayleigh wave, whose phase and group velocities are constant (Rayleigh wave speed). Under this scenario, the system is classified as non-dispersive. For the cases of layered systems, the number of existing waves and their phase velocity depend on the frequency being considered. The system is then said to be dispersive. The Love waves, which are observed in anti-plane systems consisting of a layer on a half-space, and the Stonely waves, which can exist at the interface between two adjacent layers for a certain range of frequencies, are examples of such dispersive waves (Erigen and Suhubi, 1975).

Besides being useful for the calculation of critical load speeds, the dispersion curves of a foundation can also be used to investigate some properties of the response of the layered domain, especially for remote positions where the evanescent waves are not noticed. For instance, for the case of non-moving harmonic loads with excitation frequency ω_0, the waviness of the response at remote positions is characterized by the wavelengths $2\pi/k_j$, being k_j the wavenumbers at which the line $\omega=\omega_0$ intercepts the dispersion curves. For moving loads, the dispersion curves indicate which frequencies dominate the response at the free-field, which correspond to the frequencies at which the lines $\omega=\omega_0+Vk_y$ and $\omega=-\omega_0+Vk_y$ intercept the dispersion curves.

Using the TLM, the dispersion curves are obtained through the calculation of the real modes k of the SH and SVP eigenvalue problems as a function of the frequency ω. However, when in the presence of PMLs to simulate half-spaces, the dispersion curves obtained with this method may not have any physical meaning, since the PML is not more than an artifact to simulate a half-space up to a certain distance. Alternatively, making use of the stiffness matrices of Kausel and Roesset (1981), the pairs $(k,\omega(k))$ are found by forcing the assembled stiffness matrices to become singular, or in other words, by forcing the determinant of the matrix to be null. This last procedure has been used in this work together with search techniques to calculate the dispersion curves of the layered system considered as foundations. The obtained curves are represented in Figure 4.23 together with the corresponding phase velocities V_{ph} and group velocities V_{gr}. Figure 4.23 also plots the expected critical load speeds that, according to Dieterman and Metrikine (1997), are calculated by

$$\omega_0=\left|\omega(k)-kV_{\text{gr}}(k)\right| \tag{4.31}$$

The first feature that can be observed in Figure 4.23 is that for layered half-spaces no wave propagates with phase velocity higher than the shear wave velocity of the half-space ($C_s=250$ m/s). That is so because for such waves to keep propagating, energy has to come from inside the half-space (otherwise the waves would propagate faster than it is admissible in the half-space), and that violates the radiation condition.

Due to the reason explained above, the inversely dispersive domain a) only presents one real pole, and that pole becomes complex for frequencies $\omega>52\pi$ (rad/s), which is approximately the frequency at which the phase velocity of the surface wave reaches the shear wave velocity of the half-space. In addition, the lowest critical load speed of this domain occurs for $\omega_0=0$ and equals the Rayleigh wave velocity of the half-space, as can be inferred from the last row of Figure 4.23. The highest admissible critical load speed is approximately $V_{\text{cr}}\approx 263$ m/s, which occurs for a excitation frequency $\omega_0\approx 2.7\pi$ rad/s. Above that excitation frequency, there are no critical load speeds.

As for the normally dispersive domain b), since the layer is softer than the half-space, there is a vast set of waves that can coexist at the interface between the layer and the half-space. Since one of the lower poles stabilizes at the phase velocity $V_{\text{ph}}\approx 162$ m/s (Rayleigh wave speed of the layer), for the frequency of excitation $\omega_0=0$, such velocity is one of the critical load speeds of the system. Nevertheless, that is not the minimal admissible critical load speed, as can be inferred from the last row of Figure 4.23: the lowest mode admits a critical speed of $V_{\text{cr}}\approx 142$ m/s that occurs for the excitation frequency $\omega_0\approx 17\pi$. In practice, this must be the

maximum speed for the vehicle to circulate without causing the resonance of the track-soil system.

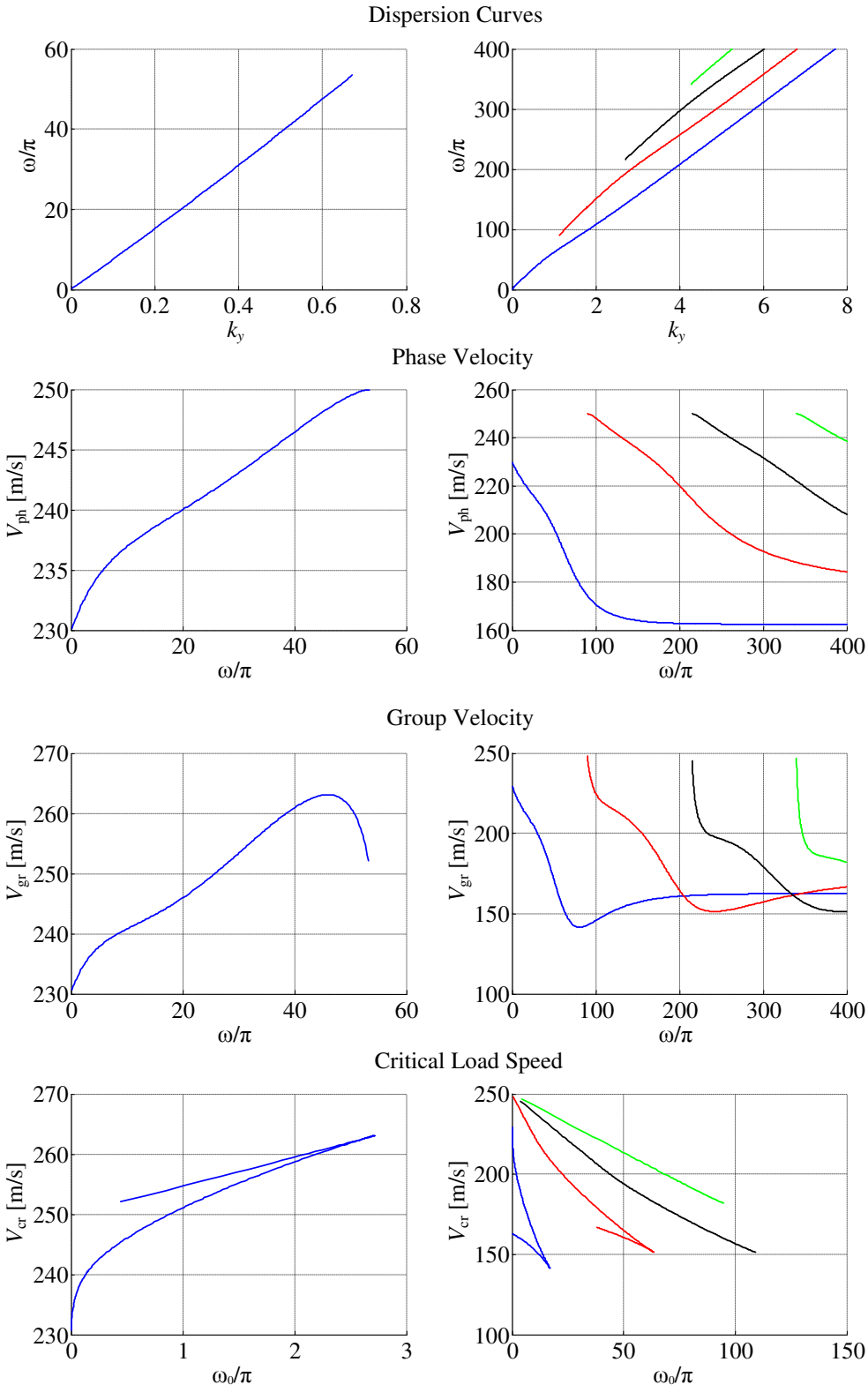

Figure 4.23: Dispersion curves, phase velocities, group velocities and expected critical load speeds for the layered domain a) (left) and for the layered domain b) (right)

Next, the critical load speeds are calculated using equations (4.28) and (4.30). With that intention, the maximum displacements of point B are calculated for a set of values of ω_0 and for the load speeds ranging from 80 to 480 m/s. The considered values of ω_0 are: $\omega_0 = 0$, $\omega_0 = \pi$ rad/s, $\omega_0 = 2\pi$ rad/s and $\omega_0 = 4\pi$ rad/s for the layered domain a); $\omega_0 = 0$, $\omega_0 = 10\pi$ rad/s, $\omega_0 = 15\pi$[rad/s] and $\omega_0 = 40\pi$ rad/s for the layered domain b). The results are shown in Figure 4.24.

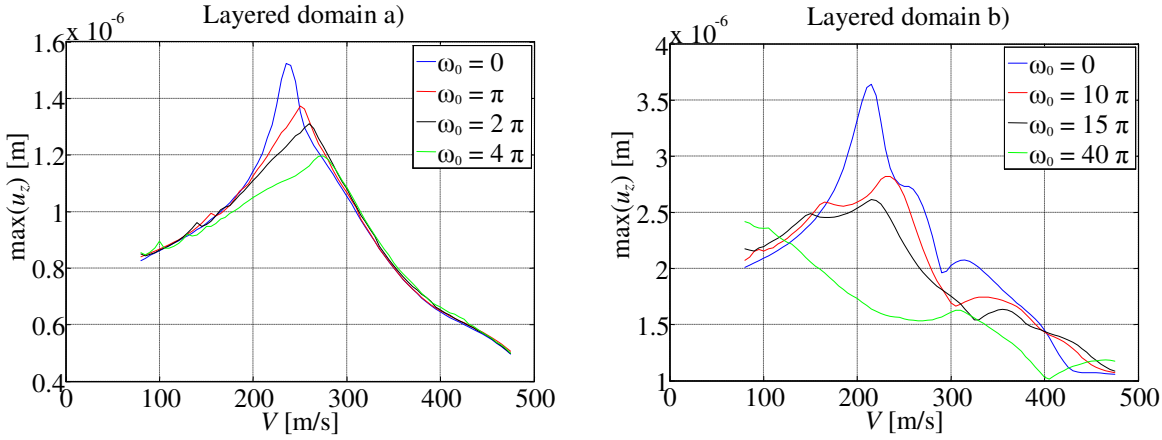

Figure 4.24: Maximum vertical displacement of point B as a function of the load speed V and excitation frequency ω_0 for the layered domain a) and layered domain b)

The analysis of the displacement envelope of the layered domain a) (left image of Figure 4.24) indicates that for $\omega_0 = 0$, $\omega_0 = \pi$ rad/s and $\omega_0 = 2\pi$ rad/s the critical load speeds are effectively those predicted in Figure 4.23. However, there is no evidence of the existence of the higher critical speed associated with the upper part of the blue line of Figure 4.23 (bottom left figure) for $\omega_0 = \pi$ rad/s and for $\omega_0 = 2\pi$ rad/s. Also, there is a peak at $V \approx 270$ m/s for $\omega_0 = 4\pi$ rad/s that according to Figure 4.23 does not correspond to a critical load speed.

As for the layered domain b), for the excitation frequencies $\omega_0 = 10\pi$ rad/s and $\omega_0 = 15\pi$ rad/s, the critical load speeds $V_{cr} \approx 160$ m/s and $V_{cr} \approx 150$ m/s associated with the upper part of the blue curve of Figure 4.23 (bottom right figure) can be identified in the right image of Figure 4.24. Nevertheless, the critical load speeds associated with the lower part of that curve cannot be distinguished. Also, for these excitation frequencies, the amplification is greatest for the critical load speeds associated with the red line (around 240 m/s). For $\omega_0 = 0$, it can be observed that the critical load speed associated with the upper part of the blue curve is slightly shifted to the left, being its value $V_{cr} \approx 215$ m/s instead of the expected 230 m/s. A local maximum can also be observed at the load speed $V = 250$ m/s, which corresponds to the group velocity with which the second and higher poles become real, and equals the shear wave-velocity of the half-space. Finally, for the excitation frequency $\omega_0 = 40\pi$ rad/s no critical load speed can be detected in Figure 4.24.

The differences between the critical load speeds calculated according to Dieterman and Metrikine (1997) and the critical speeds detected in Figure 4.24 can be justified by the presence of the slab, since the slab, which is not considered in the mentioned work, changes the behavior of the foundation, namely for the higher frequencies (Steenbergen and Metrikine,

2007) (note that when the integrating paths $\omega = \omega_0 + V_{cr}k$ and $\omega = -\omega_0 + V_{cr}k$ are tangent to the dispersion curves at low frequencies ω, the displacement envelope presents a local maximum for $V = V_{cr}$). Nonetheless, despite the differences, the critical load speeds calculated according to Dieterman and Metrikine (1997) can be very helpful to estimate the vehicle speeds that can cause the resonance of the track-soil system.

4.2.5 Conclusions

In this section, the equations used to calculate the response of invariant structures subjected to loads moving with constant speed are derived and discretized so that they can be used in cases in which the transfer functions cannot be determined in closed-form expressions. Important to retain is that in order to transform the transfer functions from the wavenumber-frequency domain to the space-frequency domain, no integral needs to be solved. Only if one attempts to obtain the space-time domain response it is needed to solve an integral.

Theoretical examples consisting of a beam on a Kelvin foundation are used to validate the equations and some conclusions concerning the critical load speeds are presented. Then, the example of a slab resting on the surface of a half-space is considered and the results obtained with the proposed methodology are compared with the results obtained with a time domain 3D FEM procedure. It is observed that the proposed procedure yields slightly different results for moving loads with constant magnitude (mostly due to the incorrect simulation of the half-space at very low frequencies) and that it yields excellent results for oscillating moving loads. This dynamic component of the load is crucial for a correct prediction of the vibrations at remote positions.

The influence of the speed of the load on the response of the slab-foundation system is also investigated, and it is concluded that while for foundations consisting of homogeneous half-spaces there is a critical load speed that coincides with the Rayleigh wave velocity of the half-space (but only if the load magnitude is constant in time), for foundations consisting of layered half-spaces the critical load speeds depend on the stratification of the domain (in the sense that it defines the dispersion curves) and on the frequency of the moving load. Hence, both the stratification of the foundation and the dynamic component of the loads are important aspects to consider in the calculation of the response of structures subjected to moving loads or vehicles.

4.3 Moving vehicles

4.3.1 Introduction

The forces that a moving vehicle transmits to the supporting structure can be divided into two components: the quasi-static part, which corresponds to the weight that each contact point bears under static conditions; and the dynamic part, that results from the interaction between the two structures. In the railway case, despite the fact that in most cases the dynamic forces are less than 15% of the quasi-static component (Kruse and Popp, 2001; Katou et al., 2008), their consideration is of the greatest importance for the calculation of the response of the track-soil system, namely at remote positions (free-field). The calculation of the dynamic forces is addressed in the present section.

As mentioned in the introduction to this chapter, the dynamic response of the vehicle is caused, among other aspects, by longitudinal variations of the stiffness of the supporting structure and by geometric irregularities at the contact between the vehicle and the structure.

Other aspects that influence the dynamic behavior of the vehicle-track system are the geometry and the dynamic properties of the track and vehicle, and the travel speed of the vehicle. All these aspects must be considered when developing a numerical model for the solution of this problem.

In this work, since it is assumed that the track-soil system is invariant in the longitudinal direction, the variations of the stiffness cannot be considered and consequently the excitation due to the discrete sleeper support is not accounted for. It must be mentioned, however, that there are works in the literature in which the periodicity of the track-soil system is considered (Gupta et al., 2007; Gupta et al., 2008; Gupta et al., 2010). The geometric irregularities at the contact between the vehicle and the supporting structure (in the railway case, wheel-rail contact) are considered by means of a position dependent gap/irregularity profile. The irregularity profile may account for the unevenness of the track and for the imperfections of the wheels (Wu and Thompson, 2002).

Besides the assumption of invariance in the longitudinal direction, this work also assumes that the vehicle and the supporting structure are linear and that the contact between the two structures is also linear. These two assumptions, which are commonly used by other authors (Metrikine et al., 2005; Lombaert et al., 2006), allow the analyses to be performed in the frequency domain, which is very convenient, since the 2.5D BEM-FEM yields results in the wavenumber-frequency domain and their transformation to the space-frequency domain is straightforward.

Before proceeding to the description of the solution method, it must be mentioned that if the non-linear behavior of the vehicle or track is to be considered, or if the loss of contact between the wheels and the rail is to be studied, then frequency domain procedures lose their applicability and therefore time domain procedures must be used (Lane et al., 2007; Katou et al., 2008; Neves et al., 2012). Hybrid methods, in which the response of the track-soil system is first obtained in the 2.5D domain, then transformed to the space-time domain, and finally given as inputs to time domain procedures, can also be applied (Grundmann and Lenz, 2003; Müller et al., 2008). Nevertheless, the increase of complexity associated with these approaches is considerable and would force simplifications in other components of the system, namely in the boundary conditions of the track and length of the model.

In the next sub-sections, the procedure used to calculate the dynamic forces that the vehicle transmits to the supporting structure is explained and exemplified.

4.3.2 Vehicle – structure interaction

Consider a vehicle moving with constant speed V on top of an invariant structure, as represented in Figure 4.25a. The vehicle contacts with the structure through N_{CP} contact points which may or may not belong to the same longitudinal alignment (in the example shown in Figure 4.25, the contact points belong to two distinct horizontal alignments).

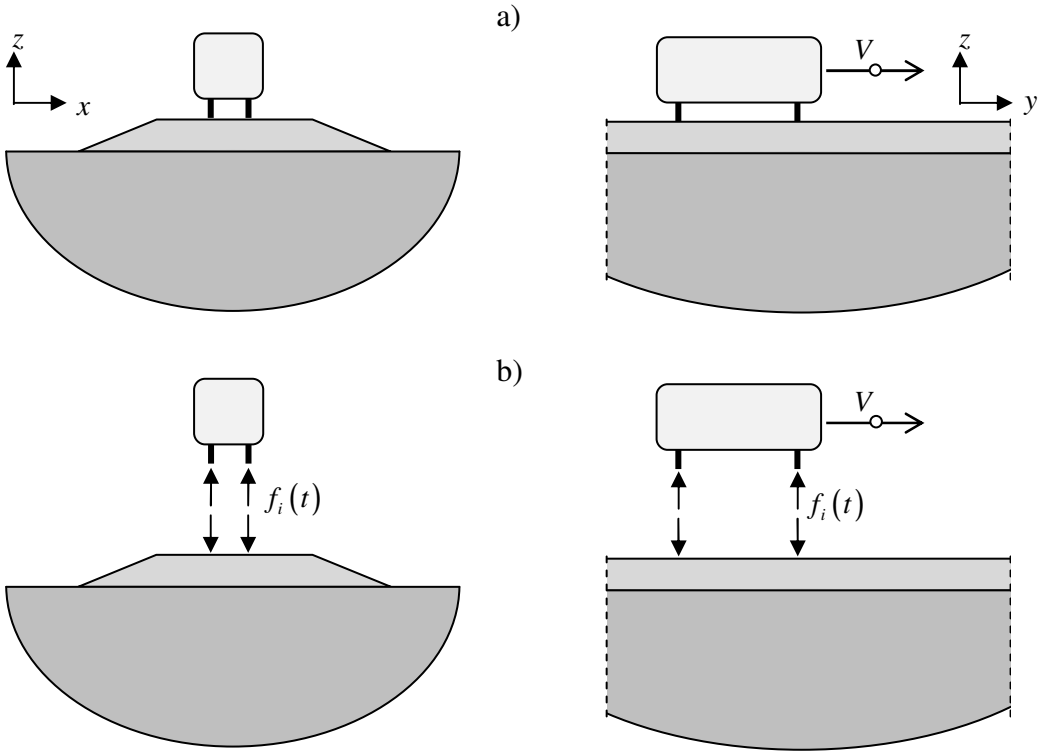

Figure 4.25: Vehicle-structure interaction – cross-section perspective (left) and longitudinal perspective (right): a) coupled system; b) substructuring method

The solution method for the vehicle-structure interaction consists in a substructuring technique (Figure 4.25b), in which the vehicle and the supporting structure are modeled independently and in which the equilibrium of forces and the compatibility of displacements is enforced between the N_{CP} contact points of the vehicle and the corresponding points of the supporting structure. The objective is to find the moving forces $f_i(t)$ $(i=1...N_{\mathrm{CP}})$ that the vehicle transmits to the supporting structure. Once the forces $f_i(t)$ are known, the response fields both of the vehicle and of the supporting structure can be calculated using the governing equations of each of the domains.

The compatibility of displacements is imposed through the condition

$$u_i^{\mathrm{v}}(t) = u_i^{\mathrm{s}}(y_{0i}+Vt,t) + \delta u_i(y_{0i}+Vt) \tag{4.32}$$

in which $u_i^{\mathrm{v}}(t)$ is the displacement of the i^{th} contact point of the vehicle, $u_i^{\mathrm{s}}(y_{0i}+Vt,t)$ is the displacement of the corresponding moving contact point of the supporting structure and $\delta u_i(y_{0i}+Vt)$ is the irregularity/gap experienced by the contact point. The quantities u_i^{s} and δu_i are defined in a fixed frame of reference, and so $y = y_{0i}+Vt$ represents the longitudinal position of the i^{th} contact point at the generic instant t, while y_{0i} represents the corresponding position at the instant $t=0$.

The displacements of the structure $u_i^{\mathrm{s}}(y_{0i}+Vt,t)$ result from the contribution of all N_{CP} contact points of the vehicle, and so they are calculated by the summation

$$u_i^{\mathrm{s}}\left(y_{0i}+Vt,t\right)=\sum_{j=1}^{N_{\mathrm{CP}}}u_{ij}^{\mathrm{s}}\left(y_{0i}+Vt,t\right)\Big|_{-f_j(t)\delta\left(y-y_{0j}+Vt\right)} \tag{4.33}$$

where $u_{ij}^{\mathrm{s}}\left(y_{0i}+Vt,t\right)\Big|_{-f_j(t)\delta\left(y-y_{0j}+Vt\right)}$ are the displacements that the force $-f_j\left(t\right)$ (force transmitted by the vehicle through the j^{th} contact point) induces at the moving contact point i. The negative sign is used to account for the equilibrium condition.

Since linear behavior and linear contact is assumed, eq. (4.32) can be transformed to the frequency domain, becoming

$$\tilde{u}_i^{\mathrm{v}}\left(\omega_0\right)=\tilde{u}_i^{\mathrm{s}}\left(y_{0i}+Vt,\omega_0\right)+\delta\tilde{u}_i\left(\omega_0\right) \tag{4.34}$$

with

$$\tilde{u}_i^{\mathrm{v}}\left(\omega_0\right)=\int_{-\infty}^{+\infty}u_i^{\mathrm{v}}\left(t\right)\mathrm{e}^{-\mathrm{i}\omega_0 t}\mathrm{d}t \tag{4.35}$$

$$\tilde{u}_i^{\mathrm{s}}\left(y_{0i}+Vt,\omega_0\right)=\int_{-\infty}^{+\infty}u_i^{\mathrm{s}}\left(y_{0i}+Vt,t\right)\mathrm{e}^{-\mathrm{i}\omega_0 t}\mathrm{d}t \tag{4.36}$$

$$\delta\tilde{u}_i\left(\omega_0\right)=\int_{-\infty}^{+\infty}\delta u_i\left(y_{0i}+Vt\right)\mathrm{e}^{-\mathrm{i}\omega_0 t}\mathrm{d}t \tag{4.37}$$

Some comments must be made about these three frequency domain variables. The variable $\tilde{u}_i^{\mathrm{s}}\left(y_{0i}+Vt,\omega_0\right)$ represents the frequency domain displacements of a point with longitudinal coordinates $y=y_{0i}+Vt$, i.e., a point that moves with the same speed as the set of loads. As mentioned in section 4.2.3 (equation (4.21)), the response field of points moving with the same speed as the load oscillate also with the same frequency as the load. Hence, accounting for (4.33) and (4.21), the integral (4.36) can be replaced with

$$\tilde{u}_i^{\mathrm{s}}\left(y_{0i}+Vt,\omega_0\right)=\sum_{j=1}^{N_{\mathrm{CP}}}-\tilde{f}_j\left(\omega_0\right)\overbrace{\frac{\mathrm{e}^{-\mathrm{i}\omega_0\frac{y_{0j}-y_{0i}}{V}}}{2\pi V}\int_{-\infty}^{+\infty}\tilde{u}_{ij}\left(\frac{\omega-\omega_0}{V},\omega\right)\mathrm{e}^{\mathrm{i}\omega\frac{y_{0j}-y_{0i}}{V}}\mathrm{d}\omega}^{\tilde{h}_{ij}} \tag{4.38}$$

where $\tilde{f}_j\left(\omega_0\right)$ is the frequency content of the load transmitted by the j^{th} contact point and calculated with

$$\tilde{f}_j\left(\omega_0\right)=\int_{-\infty}^{+\infty}f_j\left(t\right)\mathrm{e}^{-\mathrm{i}\omega_0 t}\mathrm{d}t \tag{4.39}$$

and where $\tilde{u}_{ij}\left(k_y,\omega\right)$ is the transfer function that relates the displacements of the alignment associated with the i^{th} contact point with the forces at the alignment associated with the j^{th} contact point. In this work, the referred to transfer function is calculated with the 2.5D BEM-FEM procedure explained in chapter 3.

On the other hand, the irregularity profile δu_i is a position dependent function, and so it is more convenient to define its Fourier transform in terms of the wavenumber k_y rather than the radial frequency ω_0. This leads to

$$\delta\overline{u}_i\left(k_y\right)=\int_{-\infty}^{+\infty}\delta u_i\left(y\right)\mathrm{e}^{\mathrm{i}k_y y}\mathrm{d}y \tag{4.40}$$

Hence, the Fourier transform (4.37) can be replaced with the more convenient expression

$$\delta\tilde{u}_i\left(\omega_0\right)=\frac{1}{V}\mathrm{e}^{\mathrm{i}\frac{\omega_0}{V}y_{0i}}\delta\overline{u}_i\left(-\frac{\omega_0}{V}\right) \tag{4.41}$$

Finally, the vehicle displacements $\tilde{u}_i^{\mathrm{v}}$ are obtained through the solution of the differential equations that governs its behavior. In this work, a FEM procedure is used to solve these equations (whether the elements are flexible or rigid), and so the displacements of the vehicle are obtained by solving the linear system

$$\begin{bmatrix}\tilde{\mathbf{K}}_{11} & \tilde{\mathbf{K}}_{12}\\ \tilde{\mathbf{K}}_{21} & \tilde{\mathbf{K}}_{22}\end{bmatrix}\begin{bmatrix}\tilde{\mathbf{u}}_1\\ \tilde{\mathbf{u}}_2\end{bmatrix}=\begin{bmatrix}\tilde{\mathbf{f}}_1\\ \mathbf{0}\end{bmatrix} \tag{4.42}$$

in which the index 1 refers to the degrees of freedom that contact with the structure, the index 2 refers to the remaining dofs, $\tilde{\mathbf{K}}_{mn}$ are the frequency domain matrices obtained with $\tilde{\mathbf{K}}_{mn}=\mathbf{K}_{mn}+\mathrm{i}\omega_0\mathbf{C}_{mn}-\omega_0^2\mathbf{M}_{mn}$ (being $\mathbf{K}_{mn}$, $\mathbf{C}_{mn}$ and $\mathbf{M}_{mn}$ the stiffness, damping and mass matrices of the vehicle model), and in which $\tilde{\mathbf{u}}_m$ is a vector containing the vehicle displacements and $\tilde{\mathbf{f}}_m$ is a vector containing the applied forces. The vector $\tilde{\mathbf{u}}_1$ collects the vehicle displacements $\tilde{u}_i^{\mathrm{v}}$ and the vector $\tilde{\mathbf{f}}_1$ collects the interaction forces $\tilde{f}_j\left(\omega_0\right)$. It is assumed that the remaining dofs are free of forces and therefore $\tilde{\mathbf{f}}_2=\mathbf{0}$.

System (4.42) can be condensed into

$$\left(\tilde{\mathbf{K}}_{11}-\tilde{\mathbf{K}}_{12}\tilde{\mathbf{K}}_{22}^{-1}\tilde{\mathbf{K}}_{21}\right)\tilde{\mathbf{u}}_1=\tilde{\mathbf{f}}_1 \tag{4.43}$$

and solved for $\tilde{\mathbf{u}}_1$, being thus obtained

$$\tilde{\mathbf{u}}_1=\tilde{\mathbf{F}}\tilde{\mathbf{f}}_1 \tag{4.44}$$

with

$$\tilde{\mathbf{F}}=\left(\tilde{\mathbf{K}}_{11}-\tilde{\mathbf{K}}_{12}\tilde{\mathbf{K}}_{22}^{-1}\tilde{\mathbf{K}}_{21}\right)^{-1} \tag{4.45}$$

By collecting all irregularities/gaps $\delta\tilde{u}_i\left(\omega_0\right)$ in the vector $\delta\tilde{\mathbf{u}}$ and all the coefficients $\tilde{h}_{ij}$ defined in equation (4.38) in matrix $\tilde{\mathbf{H}}$, the equality (4.34) can then be written as

$$\tilde{\mathbf{F}}\tilde{\mathbf{f}}_1=-\tilde{\mathbf{H}}\tilde{\mathbf{f}}_1+\delta\tilde{\mathbf{u}} \tag{4.46}$$

This equation can be solved for the interaction forces $\tilde{\mathbf{f}}_1$, yielding

$$\tilde{\mathbf{f}}_1=\left(\tilde{\mathbf{F}}+\tilde{\mathbf{H}}\right)^{-1}\delta\tilde{\mathbf{u}} \tag{4.47}$$

The irregularity/gap profiles $\delta u_i\left(y\right)$ are usually defined as combinations of trigonometric functions of the type sine and cosine, i.e.,

$$\delta u_i\left(y\right)=\sum_{l=1}^{N_{k_y}}A_{\mathrm{c},l}\cos\left(k_{yl}y\right)+A_{\mathrm{s},l}\sin\left(k_{yl}y\right) \tag{4.48}$$

Each harmonic k_{yl} is associated with a wavenumber content $\delta\tilde{u}_{i,l}\left(k_y\right)$ calculated with

$$\delta\overline{u}_{i,l}\left(k_y\right)=\pi\left(A_{\mathrm{c},l}+\mathrm{i}A_{\mathrm{s},l}\right)\delta\left(k_y-k_{y,l}\right)+\pi\left(A_{\mathrm{c},l}-\mathrm{i}A_{\mathrm{s},l}\right)\delta\left(k_y+k_{y,l}\right) \tag{4.49}$$

and with a corresponding frequency content $\delta\tilde{u}_{i,l}\left(\omega_0\right)$, which according to (4.41) is

$$\delta\tilde{u}_{i,l}\left(\omega_0\right)=\frac{\pi\left(A_{\mathrm{c},l}+\mathrm{i}A_{\mathrm{s},l}\right)}{V}\mathrm{e}^{\mathrm{i}\frac{\omega_0}{V}y_{0i}}\delta\left(-\frac{\omega_0}{V}-k_{y,l}\right)+\frac{\pi\left(A_{\mathrm{c},l}-\mathrm{i}A_{\mathrm{s},l}\right)}{V}\mathrm{e}^{\mathrm{i}\frac{\omega_0}{V}y_{0i}}\delta\left(-\frac{\omega_0}{V}+k_{y,l}\right) \tag{4.50}$$

The insertion of gap profiles of type (4.50) in equation (4.47) leads to interaction forces $\tilde{f}_{j,l}\left(\omega_0\right)$ of the form

$$\tilde{f}_{j,l}\left(\omega_0\right)=\left(B_{\mathrm{c},l}+\mathrm{i}B_{\mathrm{s},l}\right)\delta\left(-\frac{\omega_0}{V}-k_{y,l}\right)+\left(B_{\mathrm{c},l}-\mathrm{i}B_{\mathrm{s},l}\right)\delta\left(-\frac{\omega_0}{V}+k_{y,l}\right) \tag{4.51}$$

whose corresponding time domain functions are

$$f_{j,l}\left(t\right)=\frac{1}{2\pi}\int_{-\infty}^{+\infty}\tilde{f}_{j,l}\left(\omega_0\right)\mathrm{e}^{\mathrm{i}\omega_0 t}\mathrm{d}\omega_0=\frac{V}{\pi}\left[B_{\mathrm{c},l}\cos\left(k_{y,l}V\,t\right)+B_{\mathrm{s},l}\sin\left(k_{y,l}V\,t\right)\right] \tag{4.52}$$

The interaction forces are now known in terms of sines and cosines and they can be combined with equation (4.42) to obtain the response of the vehicle, or with the equations developed in section 4.2 to obtain the response of the supporting structure. [The factors V and π appear alternately in the denominator and numerator of equations (4.50) and (4.52), and therefore can be disregarded in the numerical implementation of the method.]

Before proceeding to the validation examples, notice that the equations derived above are not restricted to the vertical direction and therefore they can be used to study the transverse interaction as well. Nevertheless, in the railway case, under the assumptions of straight lines and constant movement, the transverse forces assume significant values only if there is a considerable misalignment of the rails in the horizontal direction, which is not likely to happen in high-speed lines, and therefore the horizontal interaction is not considered in this work. As for the interaction in the longitudinal direction, it is assumed that the vehicle moves with constant speed, which implies the resultant of forces in this direction to be null. Apart from the reactions of the supporting structure, it is assumed that no other force is applied at the vehicle, and so the reactions in the longitudinal direction must be null. For this reason, the interaction in the longitudinal direction cannot be considered. Hence, in this work, only the vertical interaction is considered, but since the contact points can belong to different alignments, three-dimensional modeling of the vehicle becomes possible, thus enabling the study of the rolling motion of the vehicle.

Next, two vehicle-structure interaction problems are solved with the equations derived in this section and the results are compared with the results obtained with a time domain 3D-FEM procedure. The first example consists of a point mass moving on top of a Winkler foundation, while the second example considers a multi-degree of freedom vehicle moving on top of a ballast track.

4.3.3 Point mass moving on top of a beam on a Kelvin foundation

Consider a mass M moving with speed V on top of an Euler beam with, flexural stiffness EI and unit mass m, that rests on a Kelvin foundation with stiffness k and damping c, as represented in Figure 4.26.

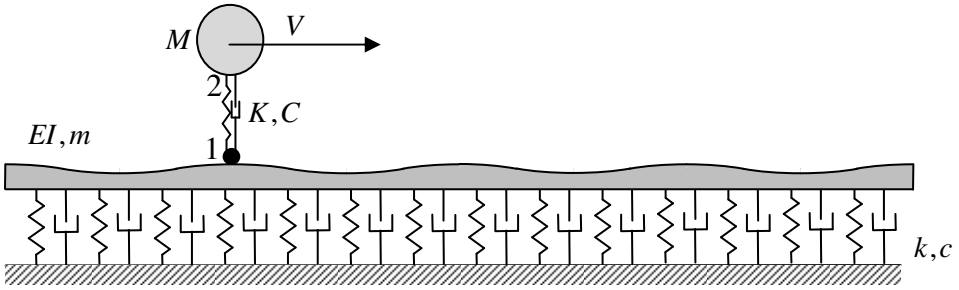

Figure 4.26: Point mass moving on top of a beam on a Kelvin foundation

The moving mass contacts with the supporting structure by means of a suspension system consisting of a spring with rigidity K and a dashpot with damping C. Consider also that the surface of the Euler beam is uneven and that the profile of the unevenness is described by the function $\delta u(y) = A_c \cos(k_y y) + A_s \sin(k_y y)$. The corresponding unevenness, as felt by contact point 1, has frequency content solely at the frequency $\omega_0 = k_y V$, and its value is

$$\delta\tilde{\mathbf{u}} = (A_c - \mathrm{i}A_s)\,\mathrm{e}^{\mathrm{i}\frac{\omega_0}{V}y_0} \tag{4.53}$$

(y_0 is the position of the point mass at the instant $t = 0$; the factors π and V are neglected.)

The vehicle responds also with frequency ω_0, and thus its dynamic stiffness matrix is

$$\tilde{\mathbf{K}} = \begin{bmatrix} K + \mathrm{i}\omega_0 C & -K - \mathrm{i}\omega_0 C \\ -K - \mathrm{i}\omega_0 C & K + \mathrm{i}\omega_0 C - \omega_0^2 M \end{bmatrix} \tag{4.54}$$

while its flexibility matrix $\tilde{\mathbf{F}}$ (in this case a scalar) is

$$\tilde{\mathbf{F}} = -\frac{K + \mathrm{i}\omega_0 C - \omega_0^2 M}{\omega_0^2 M\,(K + \mathrm{i}\omega_0 C)} \tag{4.55}$$

On the other hand, based on equation (4.24), the expression for $\tilde{h}_{ij}$ is

$$\tilde{h}_{ij} = \mathrm{i}\frac{V^3}{EI}\mathrm{e}^{-\mathrm{i}\omega_0\frac{y_{0j}-y_{0i}}{V}}\operatorname{sign}\left(\frac{y_{0j}-y_{0i}}{V}\right) \sum_{\operatorname{imag}\left(\omega_l\frac{y_{0j}-y_{0i}}{V}\right)>0}^{4} \left(\mathrm{e}^{\mathrm{i}\omega_j\frac{y_{0j}-y_{0i}}{V}} \prod_{\substack{k=1 \\ k\neq l}}^{4} \frac{1}{(\omega_l - \omega_k)}\right) \tag{4.56}$$

being the poles ω_k and ω_l the roots of the polynomial (4.25). Since there is only one contact point, matrix $\tilde{\mathbf{H}}$ is also a scalar. [Note: when $i = j$, the value $\tilde{h}_{ij}$ returned by eq. (4.56) is null, a consequence of the sign factor. The sign factor is associated with the complex half-plane used in contour integration, which in turn depends on the sign of the imaginary component of the term $\omega_l\frac{y_{0j}-y_{0i}}{V}$. When the imaginary part of this term is null (i.e., when $y_{0i} = y_{0j}$), the integrating functions do not vanish neither in the upper nor in the lower complex half-planes, and consequently contour integration can no longer be applied. Nevertheless, the function $\tilde{h}_{ij}$

must be continuous with the argument $y_{0j} - y_{0i}$, and so, when $y_{0i} = y_{0j}$, $\tilde{h}_{ij}$ can be evaluated with (4.56) by calculating its limit when $y_{0j} - y_{0i}$ tends to zero, either from the positive side or from the negative side.]

With the values of $\tilde{\mathbf{F}}$, $\tilde{\mathbf{H}}$, and $\delta\tilde{\mathbf{u}}$ known, equation (4.47) can be employed to obtain $\tilde{\mathbf{f}}$. To exemplify the procedure, the values indicated in Table 4.1 are given to the beam and foundation, point mass, and irregularity profile δu.

Table 4.1**:** Properties of track and Vehicle

Beam and foundation	Point mass	δu
$EI = 1.222\times10^{6}$ Pa	$M = 2003$ kg	$A_c = 0$
$m = 120.89$ kg/m	$K = 1.94\times10^{9}$ N/m	$A_s = 0.001$ m
$k = 200\times10^{6}$ N/m	$C = 0$ (no damping)	$k_y = 2\pi/2.4$ rad/m
$c = 30\times10^{3}$ Ns/m	$V = 200$ m/s	
(as in section 4.2)	$y_0 = 0$	

For the properties indicated above, the following values are obtained: $\omega_0 = 166.667\pi$ rad/s; $\tilde{\mathbf{F}} = -1.3056\times10^{-9}$ m/N; $\tilde{\mathbf{H}} = 8.2465\times10^{-9} - \mathrm{i}\times9.3581\times10^{-10}$ m/N; $\delta\tilde{\mathbf{u}} = -0.001\times\mathrm{i}$ m; $\tilde{\mathbf{f}} = 1.9078\times10^{4} - \mathrm{i}\times1.4150\times10^{5}$ N. The interaction force is then of the form $f(t) = 19.649\times10^{3} - 1.9078\times10^{4}\cos(166.667\pi\times t) - 1.4150\times10^{5}\sin(166.667\pi\times t)$, where the static term corresponds to the weight W of the SDOF ($W = Mg$, being $g = 9.81\,\mathrm{m/s^2}$ the gravity acceleration).

To validate these results, the example is solved with a time domain FEM approach in which the mass-beam interaction problem is solved according to the algorithm described in Neves et al. (2012). Figure 4.27 compares the obtained interaction forces $f(t)$ and the displacements of the beam at the section $y = 0$. As can be observed, the results agree perfectly, which validates the expressions developed in this section.

Similarly to the case of moving loads, the speeds V that lead to resonance of the mass-beam system can also be determined for a given irregularity profile δu. Figure 4.28 plots the maximum interaction force $f(t)$ and the maximum displacement of the beam for a range of speeds varying from 50 to 1000 m/s, considering both damped foundation and non-damped foundation.

The unique peak of the interaction force, which coincides with the first peak of the beam displacements, occurs at the speed $V \approx 100$ m/s and corresponds to the resonance of the moving mass-suspension system. For very stiff foundations, this resonance occurs at the speed $V = \sqrt{K/M}\,/k_y = 376$ m/s, i.e., at the speed for which the displacements prescribed at the contact point oscillate with the natural frequency of the mass-spring system ($\omega_{\mathrm{nat}} = \sqrt{K/M}$). However, in this case, due to the flexibility of the foundation, the resonance of the coupled

mass-beam structure is shifted to lower speeds. No other speed causes the resonance of the mass-spring system, as suggested in the left plot of Figure 4.28.

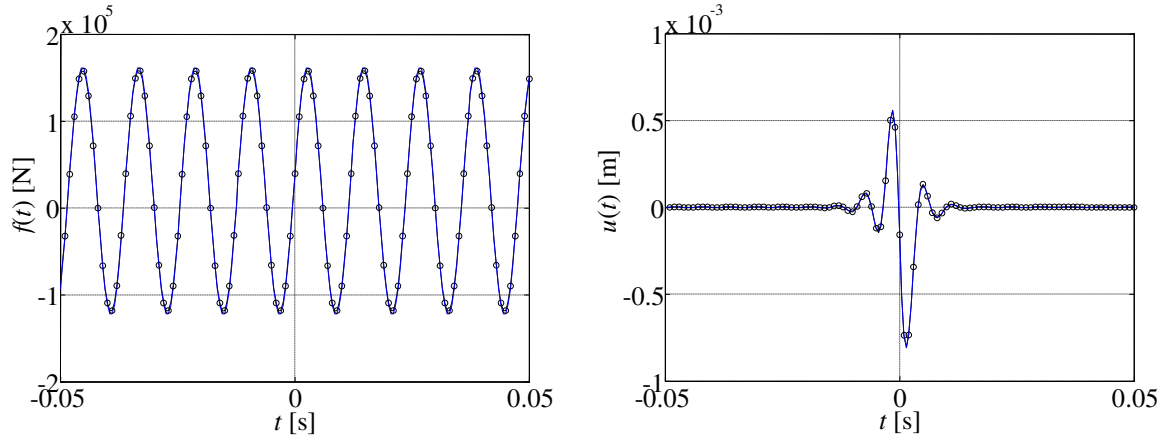

Figure 4.27: Interaction force $f(t)$ (left) and beam displacements $u(t)$ (right). Blue line – current work; black circles: time domain FEM

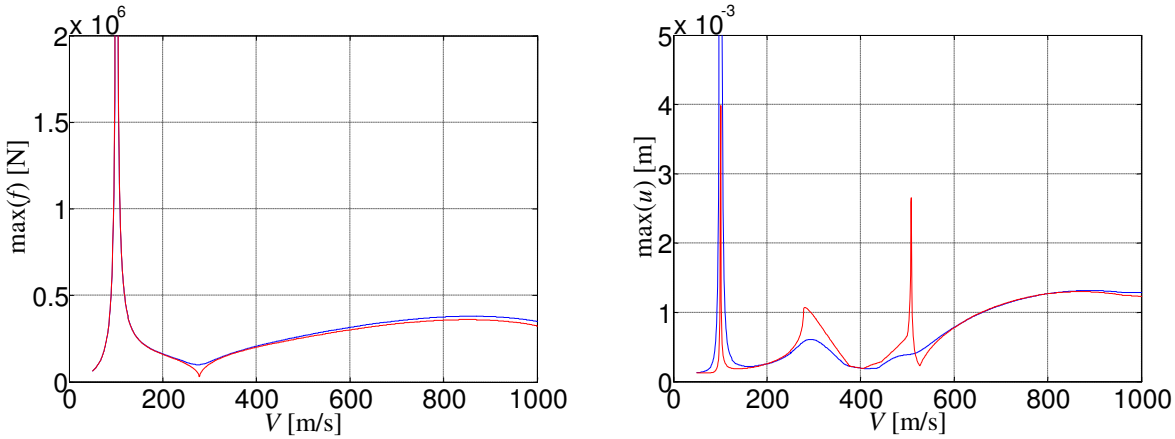

Figure 4.28: Interaction force $f(t)$ (left) and maximum beam displacement $u(t)$ (right). Blue line – $c = 30\times10^3$ Ns/m ; red line - $c = 0$ Ns/m

The second peak of the beam displacements occurs at the speed $V \approx 278$ m/s . This speed is the first speed at which the line $\omega_0 = k_y V$ intercepts the yellow region of Figure 4.4: the line $\omega_0 = k_y V$ relates the frequency of the interaction force with the speed of the point mass, while the yellow regions of Figure 4.4 correspond to the pairs (V, ω_0) that lead to amplification of the beam displacements; it is therefore expected that the response is amplified when the line crosses this region.

Finally, a third peak can be distinguished in the right plot of Figure 4.28 at the speed $V = 510$ m/s . This speed corresponds to the critical load speed of the beam (as defined in section 4.2), and the associated peak is observed because the interaction force $f(t)$ contains a static component that is independent of the moving speed. For the viscous foundation

($c = 30\times10^3$ Ns/m, blue line), this peak is strongly attenuated to the point that it can hardly be distinguished.

4.3.4 Multi-degree of freedom vehicle moving on top of a ballast track

The second example considered herein corresponds to a multi-degree of freedom vehicle moving on top of a ballast track (Figure 4.29). The track is composed of two UIC60 rails on top of a slab that rests on a ballast foundation, which lies on a rigid base (the rigid base is considered instead of a half-space in order to avoid the use of boundary elements in the time domain approach; also, since this example is used only for validation purposes, the slab is used instead of sleepers in order to make the 2.5D model and the time domain model geometrically the same). The rails and the slab are connected through rail pads.

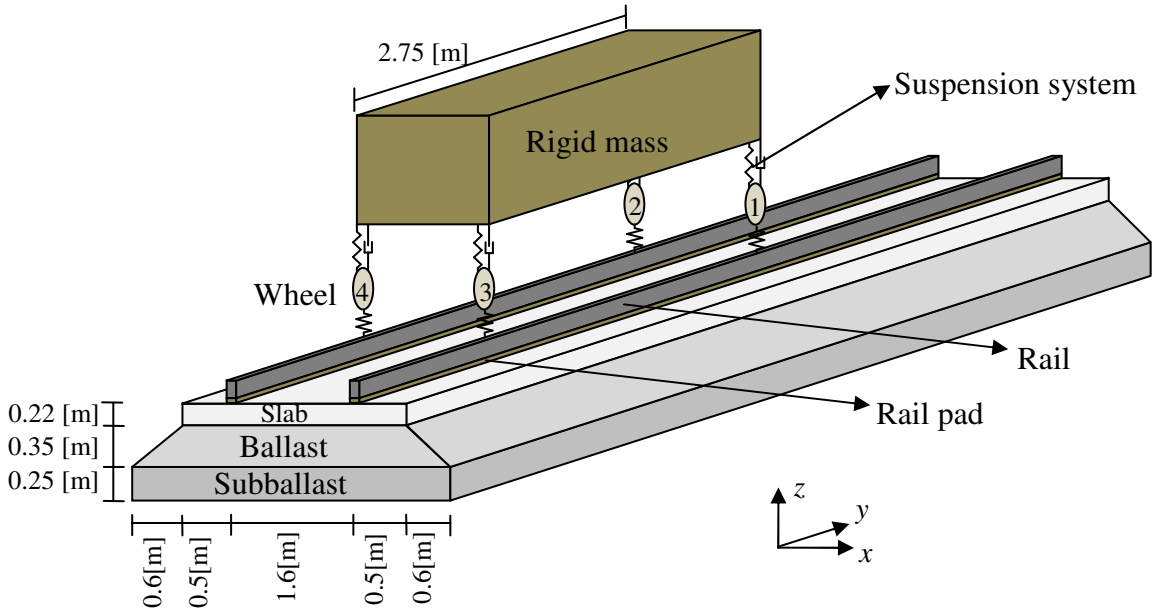

Figure 4.29: Multi-degree of freedom vehicle moving on top of a ballast track

The vehicle consists of a rigid mass with bouncing (u_z), pitching (θ_x) and rolling (θ_y) inertias, suspension systems, and wheels. Contact springs establish the connection between the vehicle and the rail.

The properties of the components of the problem are given in Table 4.2 (the properties of the ballast and subballast are taken from the work (Ribeiro et al., 2009), while the multi-degree of freedom vehicle corresponds to a bogie of an Alfa-Pendular train (Ribeiro et al., 2013)).

The main differences between this example and the example in subsection 4.3.3 reside in the transfer functions $\tilde{h}_{ij}$, which in this case cannot be determined analytically, being instead approximated by the summation

$$\tilde{h}_{ij} \approx \frac{\mathrm{e}^{-\mathrm{i}\omega_0\frac{y_{0j}-y_{0i}}{V}}}{2\pi V}\Delta\omega\sum_{i=1}^{N}\left[\tilde{u}_{ij}\left(\frac{\omega_i-\omega_0}{V},\omega_i\right)\mathrm{e}^{\mathrm{i}\omega_i\frac{y_{0j}-y_{0i}}{V}}+\overline{\tilde{u}_{ij}\left(\frac{\omega_i+\omega_0}{V},\omega_i\right)\mathrm{e}^{-\mathrm{i}\omega_i\frac{y_{0j}-y_{0i}}{V}}}\right] \tag{4.57}$$

and in the matrices $\tilde{\mathbf{F}}$ and $\tilde{\mathbf{H}}$ and the vectors $\delta\tilde{\mathbf{u}}$ and $\tilde{\mathbf{f}}$, which have dimension 4 instead of being scalars.

Table 4.2**:** Properties of track and vehicle

	Elastic modulus $E\,(\mathrm{Pa})$	Mass density $\rho\,(\mathrm{kg/m^3})$	Poisson ratio ν		
Ballast	70.0×10^6	1529	0.15		
Subballast	70.0×10^6	2090	0.30		
Slab	10.0×10^9	1200	0.16		
	Elastic modulus $E\,(\mathrm{Pa})$	Mass density $\rho\,(\mathrm{kg/m^3})$	Poisson ratio ν	Moment inertia $I_x\,(\mathrm{m^4})$	Area $A\,(\mathrm{m^2})$
Rail	210×10^9	7850	0.3	3.055×10^{-4}	7.686×10^{-3}
	Stiffness $k\,(\mathrm{N/m^2})$	Damping $c\,(\mathrm{N.s/m^2})$			
Rail pad	170×10^6	40×10^3			
	Mass $M\,(\mathrm{kg})$	Pitching inertia $M_x\,(\mathrm{kg.m^2})$	Rolling inertia $M_y\,(\mathrm{kg.m^2})$	Stiffness $K\,(\mathrm{N/m})$	Damping $C\,(\mathrm{N.s/m})$
Rigid mass	4930	2440	3615	---	---
Rigid wheel	840	---	---	---	---
Suspension	---	---	---	564×10^3	18×10^3
Contact spring	---	---	---	1.2×10^9	---

To excite the rolling motion of the vehicle, different irregularity profiles are given to each of the rails: the left rail is given an irregularity profile of the form $\delta u^{\text{left}} = -0.025\cos\left(\frac{2}{3}\pi y\right) - 0.01\sin\left(\frac{2}{3}\pi y\right) + 0.01\sin\left(\frac{2}{5}\pi y\right)$, while the irregularity profile associated with the right rail is of the form $\delta u^{\text{right}} = 0.02\sin\left(\frac{2}{3}\pi y\right) + 0.01\cos\left(\frac{2}{5}\pi y\right)$. The profiles are defined by the two wavelengths $\lambda_1 = 3\,\mathrm{m}$ and $\lambda_2 = 5\,\mathrm{m}$, whose corresponding wavenumbers are $k_{y1} = \frac{2}{3}\pi\ \mathrm{rad/m}$ and $k_{y2} = \frac{2}{5}\pi\ \mathrm{rad/m}$ (these profiles are not based on any real measurement).

Next, the interaction forces between the wheels and rails are calculated for a vehicle moving with speed $V = 80\ \mathrm{m/s}$. For the 2.5D FEM model, the cross-section is divided into 80 solid elements of 4 nodes (to simulate ballast, subballast and slab), two spring-dashpots couples (to simulate the rail pads) and two Euler beams (to simulate the rails). For the 3D time domain model, 400 slices with an equivalent cross section and thickness 0.25 m are used, satisfying a total length of 100 m. The results are plotted in Figure 4.30.

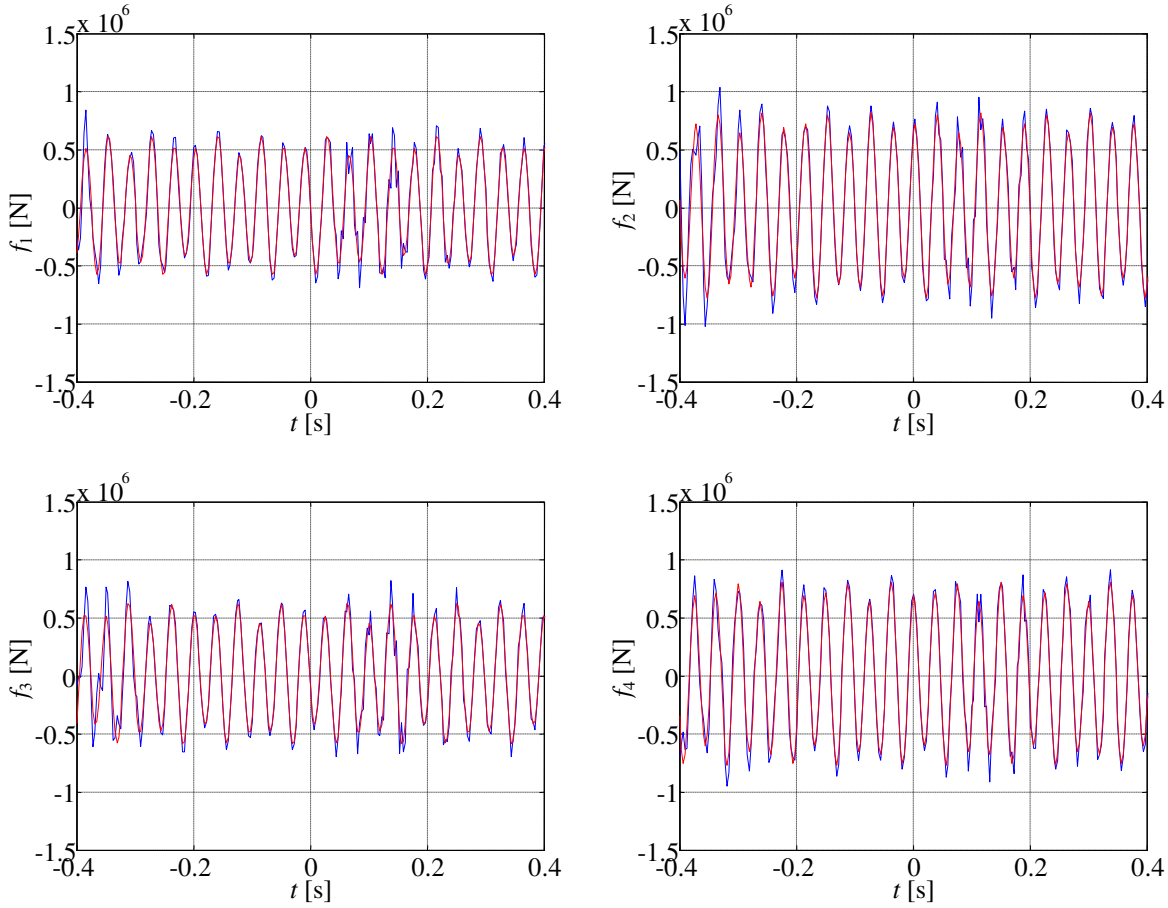

Figure 4.30: Interaction forces f_i: blue line = time domain approach; red line = 2.5D approach

It can be observed that the results obtained with the two approaches are identical, existing small differences at some local maxima or minima, but being the responses in perfect phase. Furthermore, Figure 4.30 confirms that the interaction forces are entirely defined by two frequencies, which in this example are $\omega_1 = k_{y1}V = \frac{160}{3}\pi$ rad/s and $\omega_2 = k_{y2}V = 32\pi$ rad/s.

The differences reported above can be justified by the longitudinal discretization of the domain, which is required for the 3D time-domain approach, and that violates the assumption of continuity and infinite length of the 2.5D model. While for the example of the Kelvin foundation treated in the previous section this "problem" can be easily solved by decreasing the discretization size and increasing the total length of the model used in the time-domain approach, for the current example doing so results in an excessive number of linear equations to be solved, and therefore in impracticable computational times. Nevertheless, given the good match between the two approaches, it can be concluded that the equations derived in this section yield good results also for structures with complex geometries and for vehicles contacting with the supporting structure at more than one contact point.

4.3.5 Conclusion

In this section, the equations needed to obtain the interaction forces between a supporting structure and a moving vehicle are derived and validated. The derivation of the equations is based on the following three assumptions: 1) both the supporting structure and the vehicle

behave linearly; 2) there is never loss of contact between the vehicle and the supporting structure; 3) the vehicle moves from minus infinity to plus infinity with constant speed. The first two assumptions allow the calculation to be performed in the frequency domain, as they are consistent with the principle of superposition of effects. The third assumption allows for the calculation to be cast in the wavenumber-frequency domain.

The equations here derived are used to determine the interaction forces between a moving mass and a beam on a Kelvin foundation, and the interaction forces between a multiple DOF vehicle and a ballast track that lies on a rigid base. In both cases, the forces obtained with the derived equations are compared with the forces obtained with a space-time domain procedure. A good agreement between the two approaches is observed, which validates the equations.

The example of the point mass moving on top of a beam on a Kelvin foundation is also used to calculate the critical velocities of the system. It is concluded that the critical speeds are related both to resonance of the mass-suspension system and to the critical load speeds of the supporting structure (discussed in section 4.2).

The calculation of the interaction forces (generation phase) is the last step described in this work, since the propagation stage (response of the supporting structure) and the reception stage (response of a nearby structure/building) have already been described in section 4.2 and sub-section 3.2.6, respectively. In the subsequent section, an illustrative example is solved in which the three phases are accounted for and linked.

4.4 Vibrations induced by a moving vehicle in a nearby structure

4.4.1 Introduction and general description of the example

In the previous chapters and sections it is discussed how to deal separately with the three stages of vibrations induced by moving vehicles: the generation stage is discussed in section 4.3; the propagation stage is discussed in section 4.2 (these first two stages rely on the transfer functions calculated with the 2.5D BEM-FEM procedure explained in chapter 3); and the reception stage is discussed in sub-section 3.2.6. In the present section, all the three stages are put together in an illustrative example used to explain how to link all the tools developed in this work.

In the example considered next, the response of a building due to a train passing in a nearby track is calculated. The soil corresponds to the layered domain b) described in "Example 3" of sub-section 4.2.4, the track corresponds to the supporting structure represented in Figure 4.29, and the vehicle corresponds to the X2000 train, whose geometries and properties can be found in Alves Costa (2011, p. 281) and are transcribed in Figure 4.31 and Table 4.3. Together with the train geometry, Figure 4.31 also presents the theoretical model used for each vehicle of the train: the vehicle model consists of 7 rigid bodies that represent the car-body, the bogies and the axles; the distinct bodies are connected through the primary and secondary suspension systems. Contact springs establish the connection between the axles and the rails (stiffness: 2.4×10^{9} N/m). The train moves at the speed $V = 60$ m/s.

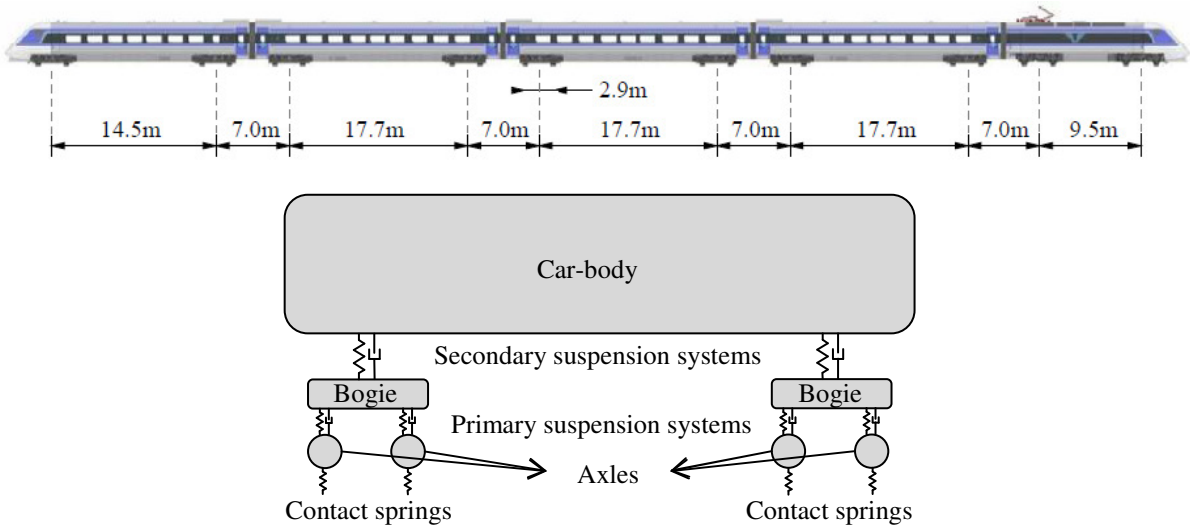

Figure 4.31: X2000 train – geometry and single vehicle model (Alves Costa, 2011)

Table 4.3**:** Properties of the vehicles of the X2000 train (Alves Costa, 2011)

		Leading vehicle	Middle vehicles	Rear vehicle
Car-body	Mass (kg)	48×10^3	31×10^3	35×10^3
	Bouncing inertia (kg.m^2)	760×10^3	1450×10^3	1100×10^3
Secondary suspensions	Stiffness (N/m)	1×10^6	0.8×10^6	0.9×10^6
	Damping (N.s/m)	70×10^3	60×10^3	60×10^3
Bogie	Mass (kg)	8.4×10^3	5.4×10^3	7.2×10^3
	Bouncing inertia (kg.m^2)	12×10^3	5.7×10^3	7.6×10^3
Primary suspensions	Stiffness (N/m)	2.4×10^6	1.8×10^6	2.0×10^6
	Damping (N.s/m)	80×10^3	60×10^3	60×10^3
Axles	Mass (kg)	2050	1300	1300

The same irregularity profile is considered for the left and right rails. This feature, together with the symmetry of the track, prevents the rolling motion of the vehicle, and therefore it is sufficient to consider a 2D model for the vehicle. The irregularity profile considered in this example is artificial, and is generated according to the function (Alves Costa, 2011)

$$\delta u(y)=\sum_{j=1}^{N_k} A_{cj}\cos\left(k_{yj}y\right)+A_{sj}\sin\left(k_{yj}y\right) \tag{4.58}$$

$$A_{cj}=A_j\cos\left(\theta_j\right) \qquad A_{sj}=A_j\sin\left(\theta_j\right) \qquad A_j=\sqrt{2S_r\left(k_{yj}\right)\Delta k_y} \tag{4.59}$$

where θ_j is a random variable with uniform distribution in the interval $]0,2\pi[$, S_r is the power spectral density function of the rail, and Δk_y is the increment in the longitudinal wavenumber. The function S_r used to define the irregularity profiles is also taken from Alves Costa (2011) and assumes the form

$$S_r\left(k_y\right)=1.36\times10^{-8}k_y^{-3.5} \tag{4.60}$$

The wavenumber sample contains $N_k=26$ equally spaced values ($\Delta k_y=0.3$ rad/m), being the first $k_{y1}=0.15$ rad/m (the corresponding maximum wavelength of the irregularity profile is approximately 42 m). Figure 4.32 plots the coefficients A_{cj} and A_{sj} and the corresponding irregularity profile $\delta u(y)$.

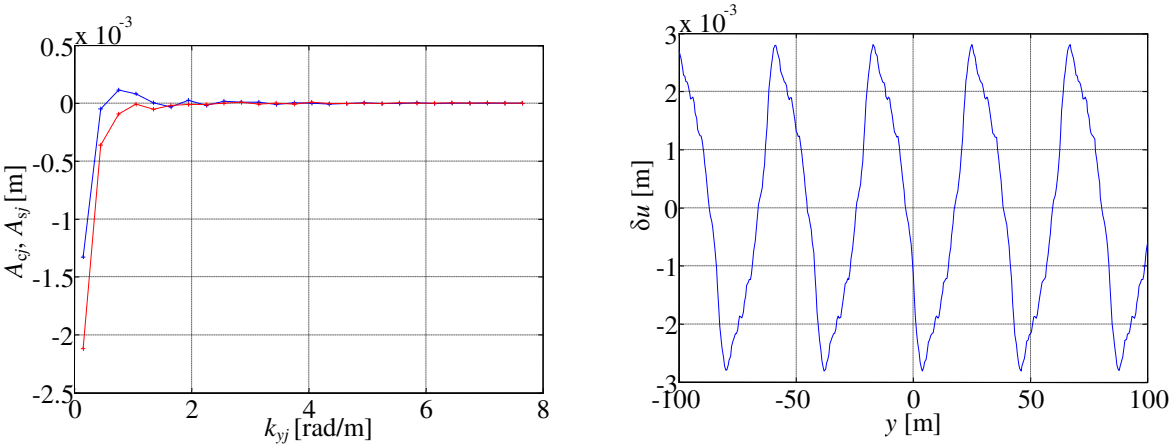

Figure 4.32: Left image = coefficients A_{cj} (blue) and A_{sj} (red); right image = irregularity profile $\delta u(y)$

The nearby structure consists of a two story building resting on the surface of the soil. Its geometry is indicated in Figure 4.33. The floors and roof are assumed rigid, and the footings are assumed rigid and massless. The total mass per unit surface (including self-weight and overweight loads) is $m_{floor}=2160\,\text{kg/m}^2$ for the floors and $m_{roof}=1080\,\text{kg/m}^2$ for the roof. The columns are made of concrete and their cross section is $0.40\times0.40\,\text{m}^2$. They are modeled with Euler beams and discretized as indicated in Figure 4.33. The dimensions of the footings are $1.5\times1.5\,\text{m}^2$, and each is divided into 25 square boundary elements of constant expansion. The distance between the center of the track and the closest column alignment is 20.0 m.

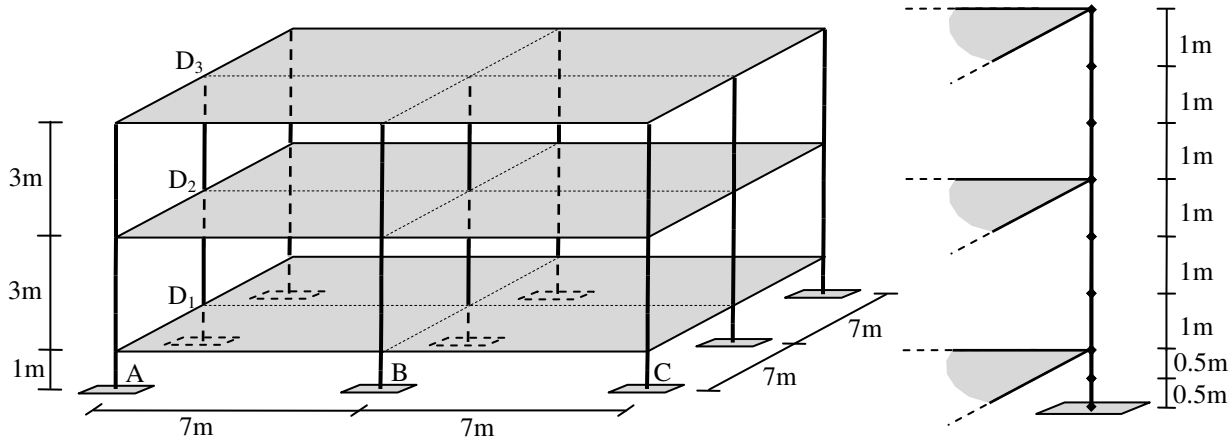

Figure 4.33: Geometry of the building and discretization of the columns

4.4.2 Step 1: eigenpairs of the soil (TLM)

The first step to solve this problem corresponds to the calculation of the vibration modes of the soil. With that objective, the TLM matrices indicated in Chapter 2 must be assembled and then used as inputs in the algorithms described in Table 2.7 and Table 2.8. The obtained eigenpairs are then used to calculate the transfer functions and boundary element matrices required for the three stages of the problem.

In this example, all integrals in $\mathrm{d}\omega$ are calculated numerically using a frequency sample consisting of 1500 frequencies, with frequency step $\Delta\omega = 0.2\pi$ rad/s ($\Delta f = 0.1$ hz) and initial frequency $\omega_1 = \Delta\omega/2$. The TLM modes must be calculated for this sample of frequencies.

4.4.3 Step 2: transfer functions

In the second step, the 2.5D BEM-FEM procedure described throughout sections 3.3 and 3.4 is used to calculate the transfer functions between sources at the rails and receivers at the rails, soil surface, and soil-building interaction surface. The eigenpairs calculated in step 1 are used here to calculate the 2.5D boundary element matrices of the soil.

Since the track and the irregularity profiles are symmetric, the transfer functions are calculated for a pair of vertical loads applied at the rails and with amplitude 0.5 N. Figure 4.34 plots the induced vertical displacements (transfer functions) of the rails and of receivers at the positions of columns A, B and C, for the wavenumber-frequency pairs $(k_y, \omega) = (\omega/V, \omega)$, $(k_y, \omega) = (\omega/V + k_{y10}, \omega)$ and $(k_y, \omega) = (\omega/V - k_{y10}, \omega)$ (the second and third pairs relate to the integration paths associated with the wavenumber $k_y = k_{y10}$ of the irregularity profile).

The first feature to be observed in Figure 4.34 is that the transfer functions for the pairs $(k_y, \omega) = (\omega/V + k_{y10}, \omega)$ (red line) are negligible when compared with those of the other pairs represented in the figure. Thus, the contribution of that branch for the final response is negligible.

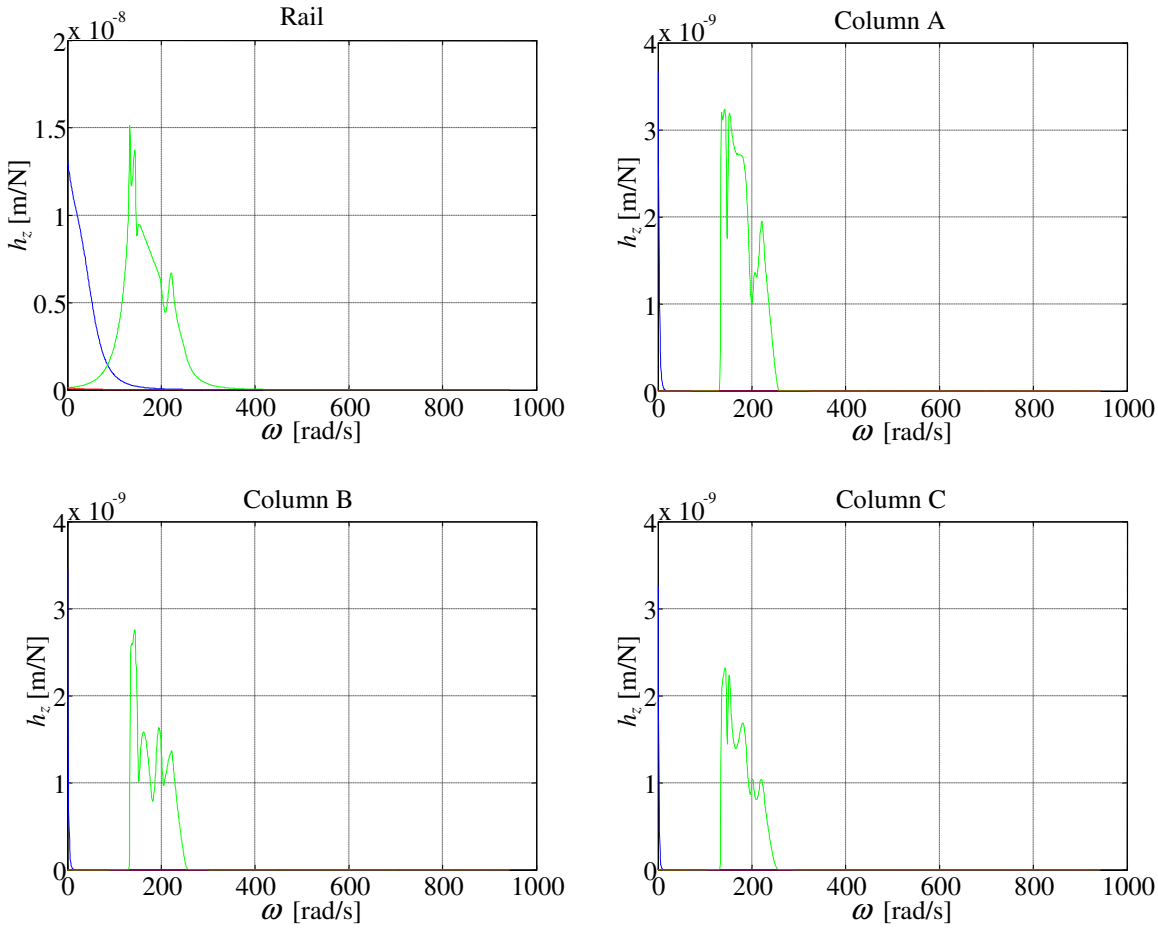

Figure 4.34: Transfer function at the rail and column: blue line - $k_y = \omega/V$; red line - $k_y = \omega/V + k_{y10}$; green line - $k_y = \omega/V - k_{y10}$

Regarding the path $(k_y, \omega) = (\omega/V, \omega)$ (blue line), it is observed that its contribution is limited to the lower frequencies, and that the contributing frequency range is narrower for receivers at the columns than for receivers at the rail. In fact, the farther a receiver is from the track, the narrower is the contributing frequency range.

As a last observation, the contribution of the path $(k_y, \omega) = (\omega/V - k_{y10}, \omega)$ (green line) is more expressive in the frequency interval $[130, 260]$ rad/s . This range limits the frequencies at which the referred to path intercepts the dispersion curves of Figure 4.23.

In general, the absolute value of the transfer functions decreases as the distance to the track increases.

4.4.4 Step 3: generation stage – dynamic forces

After calculating the transfer functions for receivers at the rails, these functions are used in conjunction with the irregularity profile and the FEM matrices of the vehicle in order to calculate the dynamic forces that the vehicle transmits to the track (procedure explained in section 4.3). Figure 4.35 plots the dynamic forces of the front and rear axles of the train.

As expected, since the front vehicle is heavier than the rear one, the interaction forces of the front axle are larger than the interaction forces of the rear axle. Also observed in the figure is that for both axles the interaction forces oscillate around 10% above and below the static force, as expected according to Kruse and Popp (2001) and Katou et al. (2008).

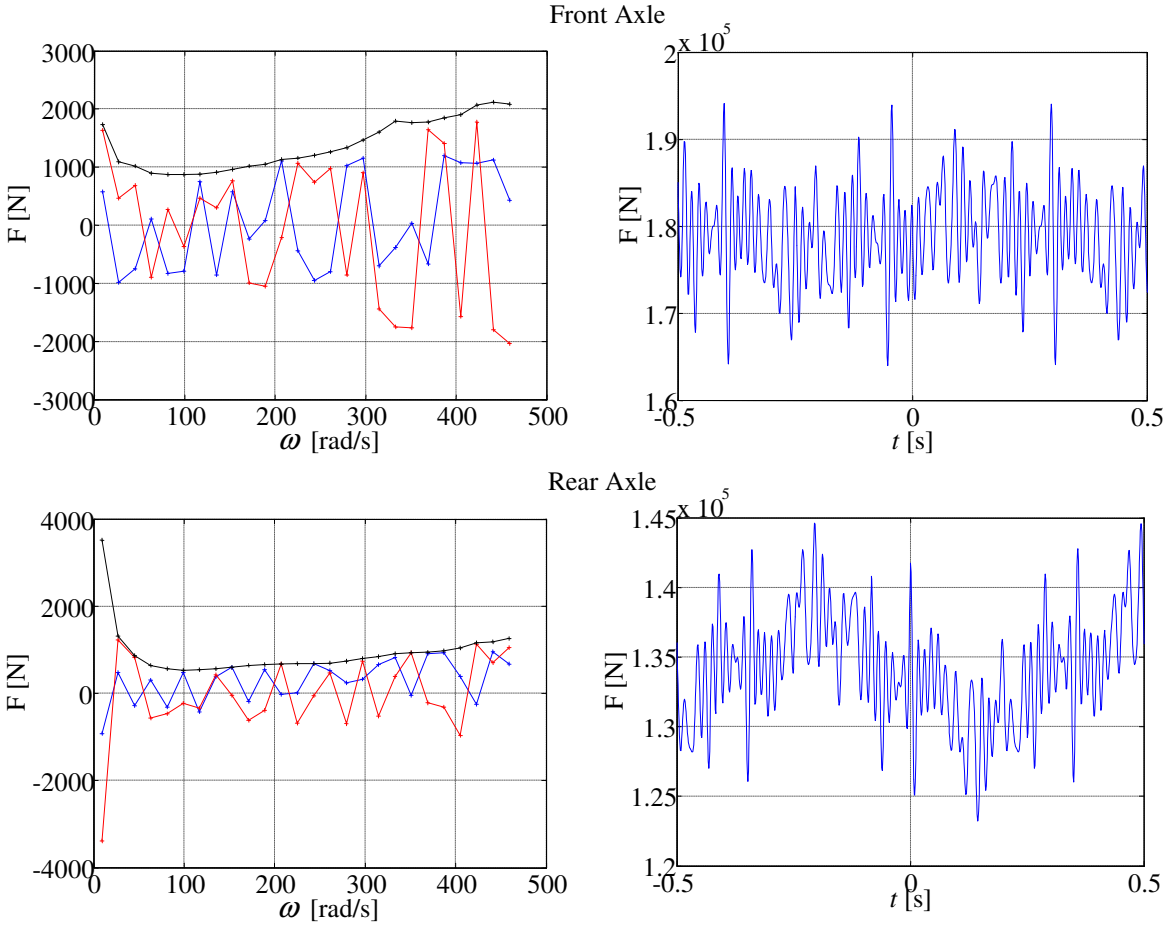

Figure 4.35: Interaction forces of front and rear axles. Left figures: cosine term A_c (blue), sine term A_s (red), and amplitude (black) of forces as a function of the frequency of oscillation. Right figures: time domain forces

4.4.5 Step 4: propagation stage – response of the supporting structure

After quantifying the dynamic forces, these forces and the transfer functions calculated in step 2 are used in the equations derived in section 4.2 in order to obtain the response of any point of the track-soil system. Hence, in this step, the frequency domain displacements of the boundary nodes of the discretized soil-building interaction surface are calculated, being for now the presence of the building neglected (weak coupling). These displacements serve as input for the last step, the reception stage, in which the response of the building is finally calculated.

In order to illustrate some results of this fourth step, the frequency and time domain displacements of the rails and of column A and the frequency and time domain velocities of column A are plotted in Figure 4.36. The results that are obtained when considering only the quasi-static component of the interaction forces are also plotted in the same figure.

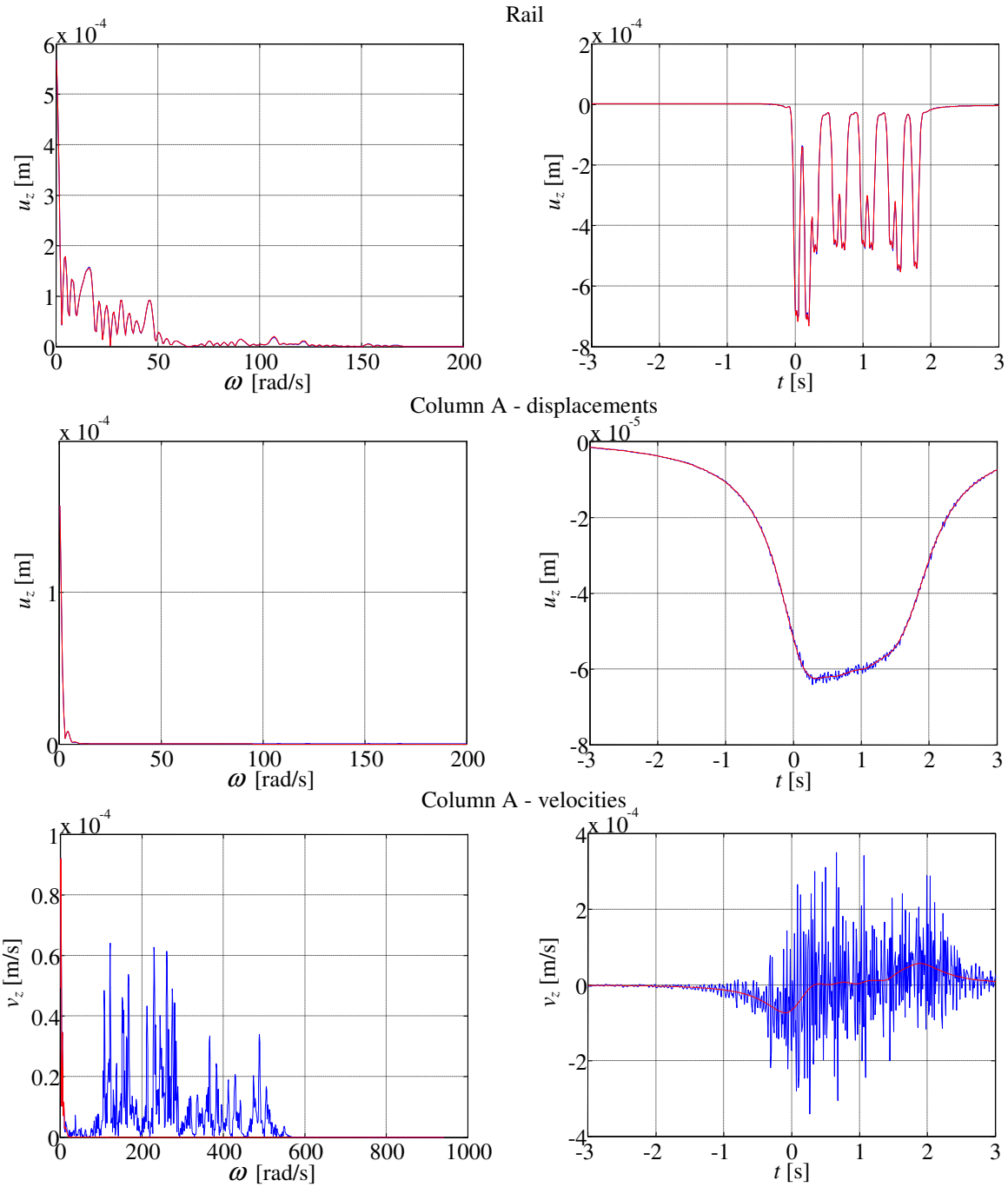

Figure 4.36: Displacements of rail and column A and velocities of column A: blue = quasi-static and dynamic forces; red = quasi-static forces only

In the first two rows of Figure 4.36, it is observed that the red line coincides with the blue line. This observation suggests that, at least up to the distance considered (approximately 20 m), the quasi-static component of the interaction forces is the major contributor to the displacements. Nonetheless, the rapid oscillations of the blue line (observed in the time domain displacements of column A) indicate that the dynamic component of the interaction forces has a greater contribution to the velocities than the quasi-static component. Such is

confirmed in the last row of Figure 4.36, and justifies why the dynamic component of the interaction forces have an important role in the vibrations at the far-field.

4.4.6 Step 5: reception stage – response of the building

In this last step, the response of the building due to an incoming wave-field is calculated using the 3D BEM-FEM procedure discussed in section 3.2. With that objective, the eigen modes calculated with the TLM in the first step are used in this step to calculate the boundary element matrices $\mathbf{U}$ and $\mathbf{P}$ of the soil-building interaction surface. The frequency domain displacements calculated in step 4 for receivers at the same surface are assembled in vector $\tilde{\mathbf{u}}^{\text{inc}}$ and used as indicated in subsection 3.2.6 to form the exterior forces $\mathbf{F}_{\text{BEM}}$. Knowing the matrices $\mathbf{U}$ and $\mathbf{P}$, the vector $\mathbf{F}_{\text{BEM}}$ and the FEM matrices of the building, one is ready to employ equations (3.26)-(3.31) and calculate the frequency domain displacements of the building.

Notice that in this example the building rests at the surface of the soil and therefore $\tilde{\mathbf{u}}^{\text{inc}}$ corresponds to the incident displacements as calculated in step 4. If the structure was buried or partially buried, then the incident stresses would also contribute to $\tilde{\mathbf{u}}^{\text{inc}}$, as suggested in equations (3.35)-(3.36).

In the ensuing, the responses of the floors and roof are calculated. The responses are calculated at the intersections between the slabs and the mid column of the alignment closest to the track, whose points are denoted with D_i in Figure 4.33. Figure 4.37 plots the frequency and time domains displacements while Figure 4.38 plots the frequency and time domains velocities. The response of point D_1 is represented in blue, of point D_2 in red and of point D_3 in black. The responses of points D_i are accompanied with the incident displacements and velocities at footing A, represented in green.

The transverse and longitudinal displacements represented in Figure 4.37 are in phase and tend to increase as the receiver is placed higher in the structure, which leads to the conclusion that the horizontal response of the building is dominated by the first horizontal mode. The natural frequency of this mode is $\omega = 15\,\text{rad/s}$ and, around that frequency, the horizontal responses present a peak that is not observed in the incident displacements field. [In the time domain plots, the oscillations at earlier and later times are consequence of the low damping of the building and of the large frequency step (0.1 Hz) used in the inverse Fourier transform. Such would not be observed if the frequency step was made smaller or if damping was considered]

The vertical displacements are independent of the floor level and match almost perfectly the incident vertical displacements. It can thus be concluded that the building responds vertically as a rigid body.

In general, the smoothness of the structure displacements, when compared with the incident displacements, suggest that the higher frequencies are filtered by the building. The frequency content of the velocities represented in Figure 4.38 confirms so: approximately at the frequency $\omega = 65\,\text{rad/s}$, the building velocities reduce to less than 10% of the value of the incident velocities; at the frequency $\omega = 300\,\text{rad/s}$, the building velocities almost vanish, while the incident velocities vanish only at the frequency $\omega = 570\,\text{rad/s}$. These features lead to lower peaks and smoother oscillations in the time history of the velocities.

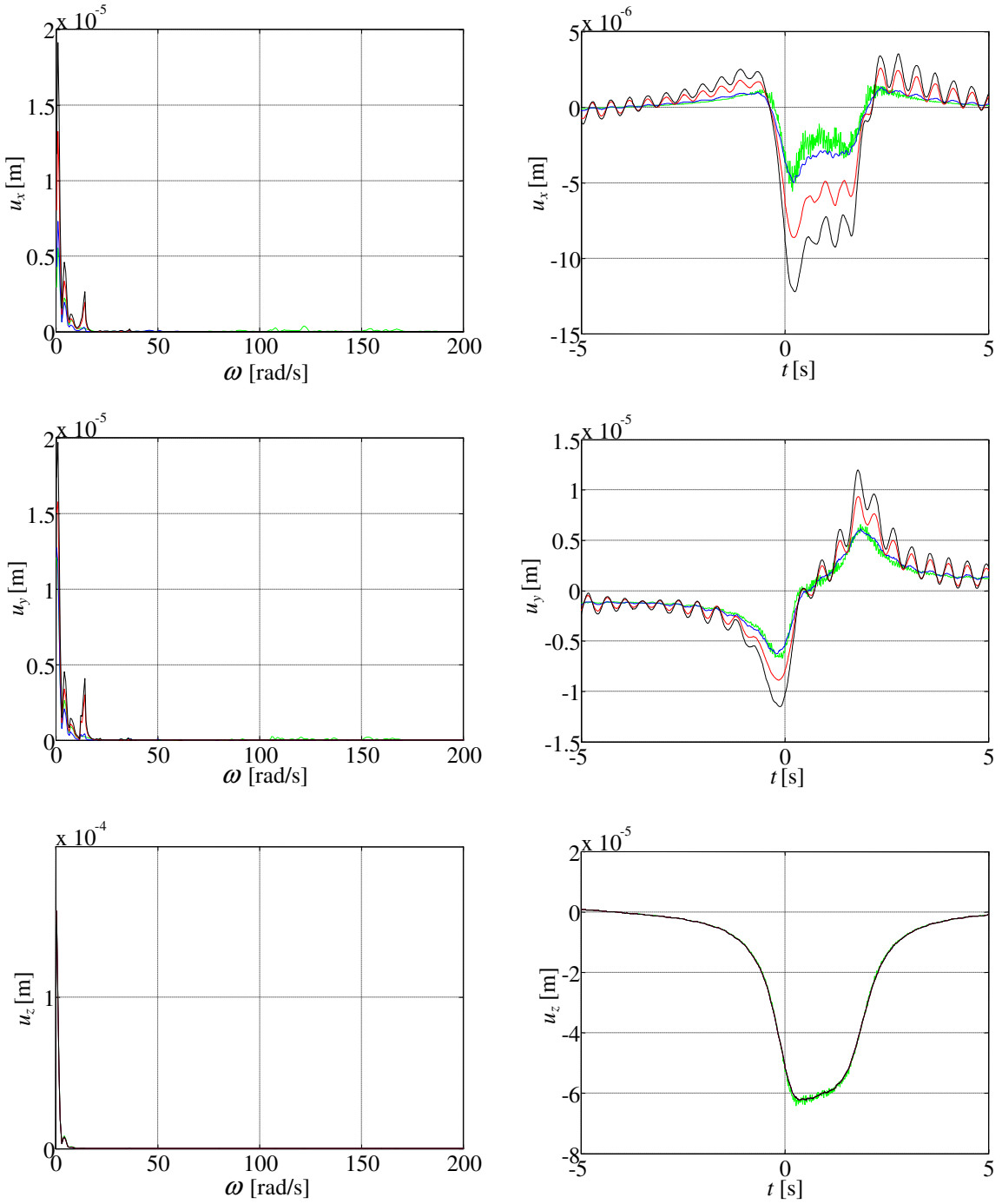

Figure 4.37: Transverse, longitudinal and vertical displacements of points D_1 (blue), D_2 (red), D_3 (black) and incident displacements at point A (green): left = frequency domain; right = time domain

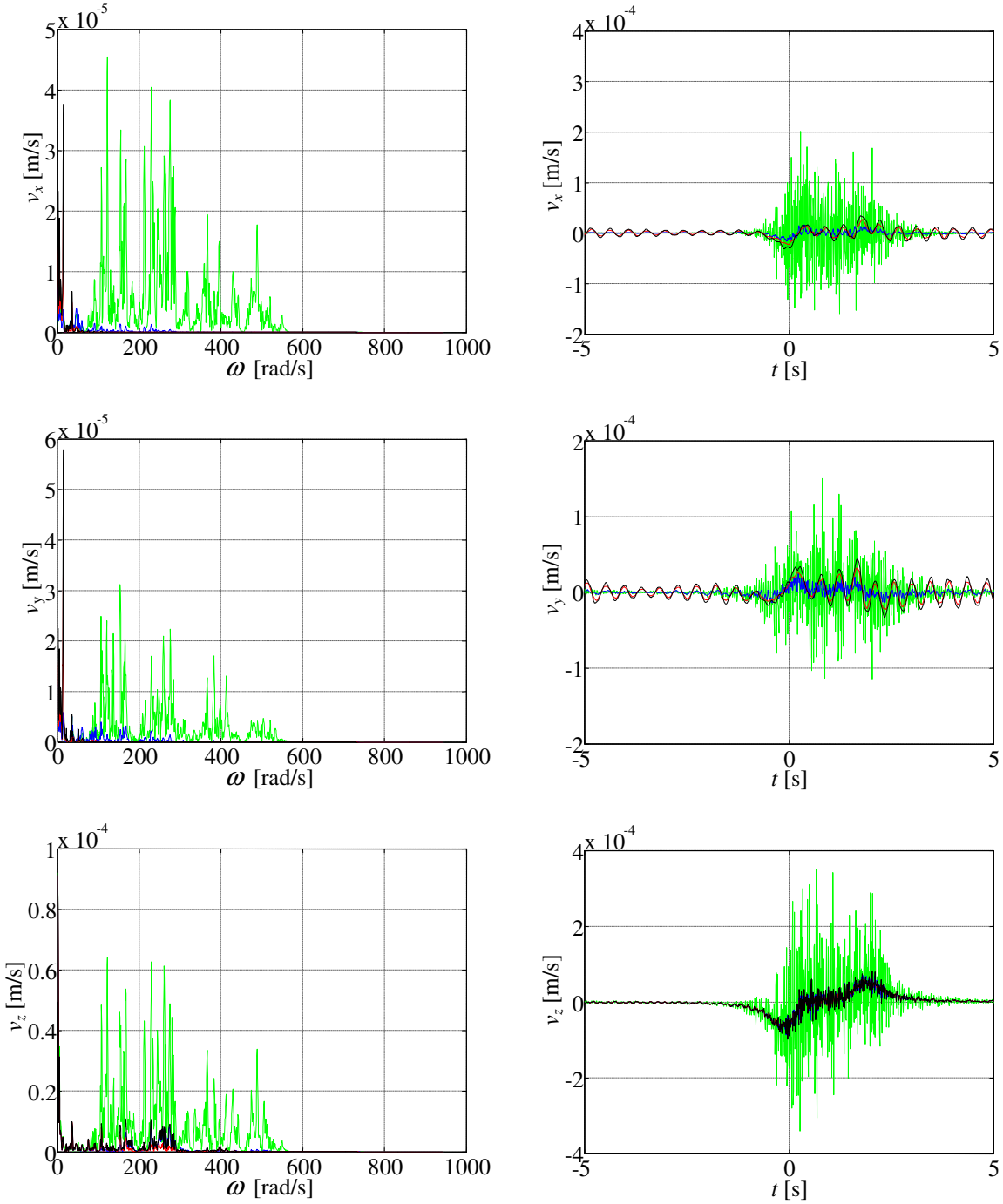

Figure 4.38: Transverse, longitudinal and vertical velocities of points D_1 (blue), D_2 (red), D_3 (black) and incident velocities at point A (green): left = frequency domain; right = time domain

4.5 Conclusions

In this chapter, the problems of moving loads and of moving vehicles are addressed, being the expressions for the former given in section 4.2 and the expression for the latter given in section 4.3. Furthermore, in section 4.4, all procedures addressed in this work are linked by means of an example in which the generation, propagation and reception stages are considered.

Concerning section 4.2, after the derivation of the equations for moving loads, these are validated through the comparison of the results thus obtained with the results obtained with a time domain procedure. The derived expressions are also used to investigate the critical load speeds of the different systems, namely: i) beam on a Kelvin foundation; ii) slab on a layered foundation. It is seen that the two systems present different features and therefore the former, which is a simpler two-dimensional model, cannot reproduce accurately the behavior of the second, which is a more complex three-dimensional model. Also, it is concluded that the stratification of the layered foundation influences the response fields and the critical load speeds, and therefore to consider homogeneous foundations may yield incoherencies in the results.

Concerning section 4.3, in which the interaction between an invariant structure and a moving vehicle is addressed, after the derivation of the expressions, these are validated through the comparison of the dynamic forces thus obtained with the dynamic forces obtained with a time domain procedure. The critical speed of a point mass moving on top of a beam on a Kelvin foundation is also studied and it is concluded that the critical speed is related to the resonance of the mass-spring system and to the critical load speeds of the foundation.

The example in section 4.4 links all the procedures explained in this work and therefore makes the connection between the three stages of the studied problem: the generation stage, in which the vehicle interacts with the track inducing on it a moving force field; the propagation stage, in which the vibrations propagate through the track and foundation; the reception stage, in which the vibrations reach the building and cause it to respond dynamically. The following characteristics are observed:

i) the dynamic forces correspond to approximately 10% of the total interaction force;

ii) the contribution of the dynamic forces can be neglected in the calculation of the track response;

iii) the displacements of the soil at remote positions are dominated by the static component of the interaction forces; however, the dynamic component dominates the velocities;

iv) the horizontal response of the building increases with the floor level and is dominated by the first mode of the building, which is activated long before the train reaches the proximity of the building;

v) the considered building filters the incident vibrations above the frequency $\omega = 65$ rad/s .

The mentioned observation are specific of the problem that was solved in this chapter, and should not be generalized.

5. Reduction of vibrations by means of trenches

5.1 Introduction

The prediction and mitigation of vibrations induced by moving vehicles has been a concern to engineers for the past decades, as can be confirmed by the publications on the subject, which go back to the 19th century (South, 1863). In fact, vibrations induced by traffic, including railway transportation, are responsible for the annoyance of inhabitants surrounding the transport infrastructures and, in the most severe situations, may induce damage, at least in an aesthetic point of view, in sensitive structures such as old heritage buildings.

The relevance of the above mentioned concern justified several studies on the topic in order to reach a deeper understanding of the problem and of its mitigation, but despite all the progress that has been made in recent years, there are still some gaps that deserve deeper studies, mainly in what concerns the comprehension and efficiency of mitigation measures. Nowadays, this topic is being object of attention by the political instances, as indicated by the currently running projects RIVAS (http://www.rivas-project.eu/) and CARGOVIBES (http://www.cargovibes.eu/), both subsidized by the European Commission and whose objective is to propose mitigation measures to obtain more sustainable and environmental friendly railway infrastructures.

The countermeasures for vibrations induced by railway traffic can be classified by the location where they are applied: i) at the source; ii) at the propagation path; iii) at the receiver. Mitigation at the source may involve, among other options, changing the properties of the trains (suspension system, masses, etc.), changing the type of the track (ballast track versus slab-track) and its resiliency (using rail pads, under-sleeper pads and/or ballast mats), and improving the rolling conditions of the vehicle (i.e., to reduce the defects of the wheels and the vertical roughness and unevenness of the rail) (Hemsworth, 2000). This last option appears to be the most efficient strategy because the improvement of the rolling quality of the vehicle results in the reduction of the dynamic forces transmitted by the vehicle to the track, and, consequently, in the reduction of the vibrations felt at large distances from the track (Nelson, 1996). Nevertheless, due to the high cost of the wheel truing/rail grinding, it becomes economically unsustainable to rely only on this approach. Regarding the modification of the resiliency of the track, the main purpose is to achieve a considerable attenuation of vibration levels at high frequencies (Alves Costa et al., 2012b; Bongini et al., 2011). However, the introduction of these elements on the track is also accompanied by the amplification of energy transmitted to the ground at the low frequency range, which may amplify the response of nearby buildings at their lower natural frequencies (Alves Costa et al., 2012b; Alves Costa et al., 2013).

On the other hand, mitigation at the receiver (a structure to be shielded from vibrations) involves the application of elastic materials at the foundations, so that the whole building is isolated, or at certain floors/compartments, in order to separate them from the rest of the building. Fiala proposes different approaches based on this idea (Fiala et al., 2007; Fiala et al., 2008). The drawback of this option is that it is only applicable, at least at a reasonable economical cost, to new buildings, since it involves drastic changes on the structural behavior

of existing constructions. The mitigation of vibrations induced by new railway lines generally demands solutions that do not imply modifications on existent buildings. Therefore, this kind of solution is excluded when it comes to these situations, where, on the other hand, the application of countermeasures at the propagation path may become more relevant.

The basic idea of the last type of countermeasures (at the propagation path) is to change the propagation of the waves through the soil, thus impeding the waves of reaching a building or, at least, reducing the amplitude of the incident vibrations. The most common strategies are: subgrade stiffening; WIBs (wave impeding block); trenches and rows of piles. Subgrade stiffening consists in stiffening the soil in the proximity of the track, usually through jetgrouting or soil mixing techniques, which results in the reduction of the vibrations that are induced in the ground (Ahmad and Al-Hussaini, 1991; Celebi and Göktepe, 2012). In turn, WIBs may be constructed beneath the track (active isolation) with the intention of replicating a rigid base, resulting in the decrease of the cut-off frequency of the foundation and in the attenuation of vibrations below this frequency, or under the building (passive isolation), with the purpose of deflecting waves that are about to impinge the building (Celebi and Göktepe, 2012). Trenches and rows of piles are used to reflect surface waves (Hung and Yang, 2001) and, like WIBs, can be bored or driven near the track (active isolation) or near the building that is going to be shielded (passive isolation). Their efficiency largely depends on the depth, and so, for moderate dimensions, they are merely suitable for reducing the vibrations at medium and high frequency ranges.

Several studies that focus on the reduction of vibrations through the use of trenches have been published before. The studied scenarios can be divided, according to the nature of the source, into mitigation of vibrations induced by standing loads, and mitigation of vibrations induced by moving loads. The difference between standing sources and moving sources resides in the vibration field that is induced in the ground: while in the former case the ground responds with the same frequency as the excitation, for moving loads the ground responds in a range of frequencies that depends on the speed of the source and on its frequency content, i.e., the Doppler effect becomes relevant. In the case of vibrations induced by railway traffic, an extra complexity arises since the frequency content of the moving source is characterized by the interaction between the track and the train.

Studies that consider standing sources can be found in several references. These works comprise experimental studies (Ahmad and Al-Hussaini, 1991; Alzawi and Hesham El Naggar, 2010; Celebi et al., 2009; Klein et al., 1997; Murillo et al., 2009) and parametric investigations (Ahmad et al., 1996; Beskos et al., 1986; Dasgupta et al., 1990; Hung and Ni, 2012; Leung et al., 1990; Shrivastava and Kameswara Rao, 2002; Yang and Hung, 1997). Some works consider plane strain conditions (Beskos et al., 1986; Hung and Ni, 2012; Leung et al., 1990; Yang and Hung, 1997) while others consider three-dimensional sources (Ahmad et al., 1996; Dasgupta et al., 1990; Shrivastava and Kameswara Rao, 2002): some analyze trenches placed near the source (Ahmad et al., 1996; Yang and Hung, 1997) while others consider trenches constructed near the receiver (Hung and Ni, 2012): very few consider non-linear behavior of materials (Celebi et al., 2009; Celebi and Kirtel, 2012; Hung and Ni, 2012). Tools such as the BEM and/or the FEM have been used, with formulations both in the time domain as in the frequency domain.

The mentioned works indicate the following aspects as those that significantly influence the efficiency of trenches:

- trench dimensions (depth and width): for open trenches only the depth plays a role, while for in-filled trenches both dimensions matter;
- properties of the in-fill material: open trenches perform better than in-filled trenches but their application in practical situations is complex due to the need of support of the trench walls; for in-filled trenches, in-fill materials that are more flexible than the ground tend to perform better than stiffer in-fill materials;
- properties and stratification of the soil: wave propagation in the soil depends on the stratification, and consequently so does the behavior of trenches; nevertheless, the stratification of the soil can be neglected if the lower layers are softer than the upper layers.

Additionally, it is also concluded that plane strain (2D) analyses are not suitable for the study of point sources (3D case). Contradictory statements are proffered concerning the best position of the trench: for example, in (Adam and von Estorff, 2005; Celebi et al., 2009) it is stated that the best position of the trench is near the receiver (passive isolation) while in (Celebi and Kirtel, 2012) it is determined that trenches near the source (active isolation) may perform better.

Few references can be found regarding studies in which the moving nature of the source is taken into consideration (case of interest for this chapter). The vast majority of them corresponds to numerical investigations, being (Dijckmans et al., 2013) the only reference that was found concerning experimental investigations on trenches under moving loads. Thereby, numerical works based on 3D formulations are found in (Andersen and Nielsen, 2005; Pflanz et al., 2002) while 2.5D formulations can be found in (Cao et al., 2012; Hung et al., 2004; Karlstrom and Bostrom, 2007). From a computational point of view, 2.5D formulations are considered more efficient, since they enable the simulation of three-dimensional problems based on series of simpler 2D problems. The disadvantage is that 2.5D models are limited to scenarios in which the longitudinal section of the problem is fairly constant and no variations of the stiffness are observed in that direction. These limitations are not perceived in 3D formulations; however, this type of models requires more computational resources. Nevertheless, the assumption of a constant cross-section is valid for the problem under study and, therefore, 2.5D analyses can be applied.

The common conclusions of the works concerning moving sources are that trenches perform better for moving loads with high frequency contents and that, apart from constant moving loads, open trenches perform better than in-filled trenches, being the performance of trenches filled with stiffer materials better than those filled with more flexible materials. Regarding this last conclusion, it is important to be aware that the forces that a train transmits to the track contain both quasi-static and dynamic components, which makes impossible to predict which type of trench shall perform better. Also, this last conclusion contradicts the conclusions reported for standing loads, and, therefore, emphasizes the need for numerical models that consider the moving nature of the load.

Of the works contemplating moving loads, references (Andersen and Nielsen, 2005; Hung et al., 2004) consider oscillating moving loads, references (Cao et al., 2012; Karlstrom and Bostrom, 2007) consider constant moving loads, reference (Pflanz et al., 2002) assumes a simplified law for the amplitude of the sources, and reference (Dijckmans et al., 2013) simulates the moving excitation by means of a finite number of standing point sources distributed along the longitudinal direction. No work was found in which the frequency content of the source is defined based on the vertical interaction between the train and the

track. As seen in chapter 4, this interaction has direct influence on the vibration field induced in the ground. For this reason, in this work, the circulation of the train and its interaction with the track are taken into account in the assessment and discussion of different trench solutions.

This chapter is organized as follows: section 2 contains a comprehensive study on the parameters that most influence the reduction achieved by trenches; section 3 investigates the efficiency of different trench solutions for the mitigation of vibrations induced by the passage of trains in an existing line (near Carregado, Portugal); section 4 evaluates the influence of such measure on a nearby building; finally, section 5 summarizes the main conclusions of the chapter.

5.2 Parameters influencing the efficiency of trenches

5.2.1 Introduction

In order to obtain a more comprehensive insight about the influence of the parameters with more relevance to the efficiency of trenches, a parametric study is presented. The study is similar to the studies presented in some of the works mentioned in section 5.1.

The problem to be considered is depicted in Figure 5.1: a homogenous half-space is submitted to a harmonic vertical point source and the response of the surface of the half-space is computed before and after the excavation of a trench with width w and depth d at the distance l from a point source. Plane strain conditions are assumed (unless otherwise stated), which means that in the parametric study the longitudinal wavenumber k_y is assumed to be null. The material properties of the soil are defined by the variables G_{Soil} (shear modulus), ρ_{Soil} (material density), ν_{Soil} (Poisson's ratio) and ξ_{Soil} (hysteretic damping), while the material properties of the in-fill material are defined by the variables G_{Mat}, ρ_{Mat}, ν_{Mat} and ξ_{Mat}.

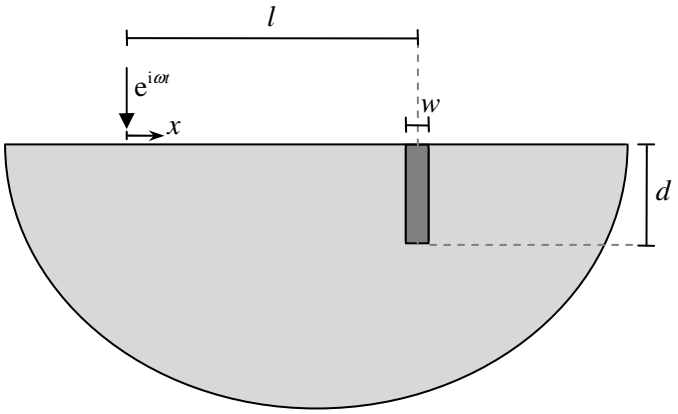

Figure 5.1: Trench in a half-space

To analyze the problem with the 2.5D BEM-FEM procedure, the trench limits are simulated with boundary elements of linear expansion, while the in-fill material is simulated with finite elements. The dimensions of the boundary elements and of the finite elements are such that 20 elements per Rayleigh wavelength are used. The fundamental solutions to be used in the BEM are calculated with TLM models such that for each boundary element there are two thin-layers of quadratic expansion. Additionally, for the TLM models, an elastic layer with

thickness λ_R is placed between the lower surface of the trench and the lower PML simulating the lower half-space.

The parameters to be studied are the trench depth d, the trench width w, the trench position l, the stiffness and density of the in-fill material, and the Poisson's coefficient of the soil. The influence of stratification and of modeling strategy (2D versus 3D) is considered afterwards.

In order to avoid dependency on the excitation frequency ω, all dimensions are made proportional to the Rayleigh wavelength $\lambda_R = 2\pi C_R/\omega$, in which C_R is the Rayleigh wave speed of the half-space. The Rayleigh wave speed can be approximated by the expression

$$C_R = \sqrt{G_{Soil}/\rho_{Soil}}\left(0.874+\left(0.197-\left(0.056+0.0276\nu_{Soil}\right)\nu_{Soil}\right)\nu_{Soil}\right) \tag{5.1}$$

Unless otherwise stated, the following values are assumed: $d=\lambda_R$, $w=0.2\lambda_R$, $l=5\lambda_R$, $\rho_{Mat}=\rho_{Soil}$, $\nu_{Soil}=0.25$, $\nu_{Mat}=0.3$, $\xi_{Soil}=\xi_{Mat}=0.03$. For each parameter investigated, three scenarios are considered for the in-fill material: $G_{Mat}=0$ (open trench), $G_{Mat}=0.2G_{Soil}$ (softer material) and $G_{Mat}=10G_{Soil}$ (stiffer material). For each scenario, the efficiency of the trench is evaluated through the position dependent ratio A_r

$$A_r(x)=\left|\frac{u_z^{\text{Trench}}(x)}{u_z^{\text{No trench}}(x)}\right| \tag{5.2}$$

in which u_z^{Trench} represents the vertical displacement at the surface of the soil after the construction of the trench, $u_z^{\text{No trench}}$ represents the vertical displacement at the surface of the soil before the construction of the trench, and in which x is the transverse distance to the point source (the smaller the ratio $A_r(x)$, the better the isolation). The average ratio $\bar{A}_r$, calculated with

$$\bar{A}_r=\frac{1}{L}\int_0^L A_r(x+l)\,\mathrm{d}x \tag{5.3}$$

may also provide important information and therefore is also represented. L represents the maximum distance of interest after the trench.

In the next sub-section, a validation example is shown. The parametric study starts in sub-section 5.2.3.

5.2.2 Validation example

The suitability of the 2.5D BEM-FEM procedure for the simulation of trenches is assessed prior to its utilization in the corresponding parametric study. With this purpose, the reduction achieved by an open trench is computed and compared with the results published in the literature and with the results obtained by means of a FEM approach. The validation problem consists of a trench with depth $d=1.0\lambda_R$ and width $w=0.1\lambda_R$, placed at the distance $l=5\lambda_R$ from a massless rigid footing with width $b=0.5\lambda_R$. The footing is perfectly bonded to the underlying homogeneous half-space and is submitted to a prescribed uniform vertical displacement. Figure 5.2 shows the ratios A_r obtained in this work (blue curve), the ratios A_r obtained by Yang and Hung (1997) (red curve), and the ratios A_r obtained with a 2D FEM approach (black curve). For the 2D FEM approach, an elastic region with width $11\lambda_R$ and

depth $2\lambda_R$ is modeled with 4 noded quadrilateral elements and such that there are 40 finite elements per Rayleigh wavelength. The elastic region is augmented with the PMLs defined in the work of Kausel and Barbosa (2011) in order to absorb the outgoing waves.

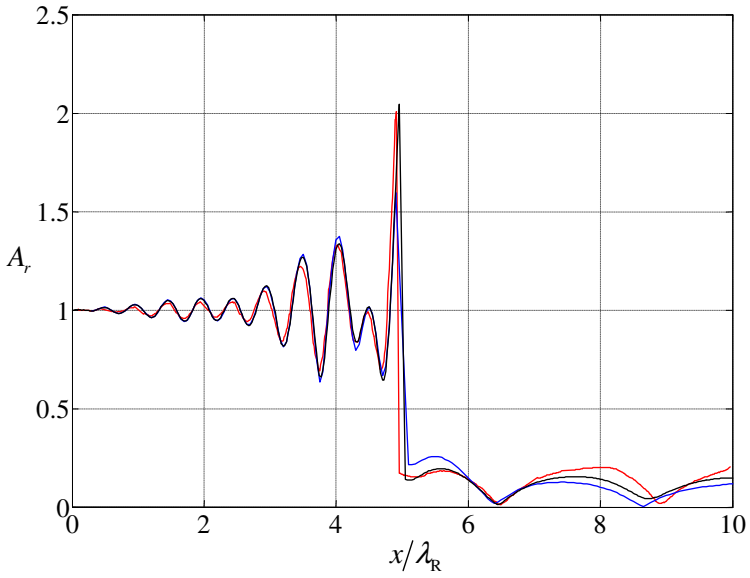

Figure 5.2: Reduction ratios A_r for an open trench: blue line = 2.5D-BEM FEM; red line = Yang and Hung (1997) ; black line = 2D FEM-PML

Some differences can be observed between the three curves, but the trends are the same and the deviations of the curves are relatively small. Thus, it can be concluded that the 2.5D BEM-FEM procedure is adequate for this parametric study and that the discretization used for the boundary elements is fine enough. It must be added, however, that the differences observed between the distinct curves, and namely after the trench (for $x/\lambda_R > 5$), can be justified by the dispersion associated with the discretization. The recalculation of the blue and black curves assuming 80 boundary elements per Rayleigh wavelength (for the blue curve) and assuming 80 finite elements per Rayleigh wavelength (for the black curve) leads to practically coincident results.

5.2.3 Influence of the trench depth

According to the literature, one of the parameters that significantly influence the efficiency of trenches is the depth. The influence of this parameter for the three trench solutions (open trench, trench filled with soft material and trench filled with stiff material) is represented in Figure 5.3 through the representation of the ratios A_r and their average $\overline{A_r}$ ($L = 25\lambda_R$) as a function of the trench depth. A maximum depth of $d = 3\lambda_R$ is assumed.

For the case of an open trench (Figure 5.3a), the efficiency of the trench appears to increase with its depth. However, above $d = \lambda_R$, increasing the depth does not seem to result in a considerable change of the trench efficiency, namely for $x < 30\lambda_R$. For $x > 30\lambda_R$, the ratio A_r oscillates around one, which means that there are zones where the response is amplified. These amplification zones are justified by horizontal shifts of the local minima due to the presence of the trench. Nevertheless, at these distances the response is so small that these amplifications have no practical consequence.

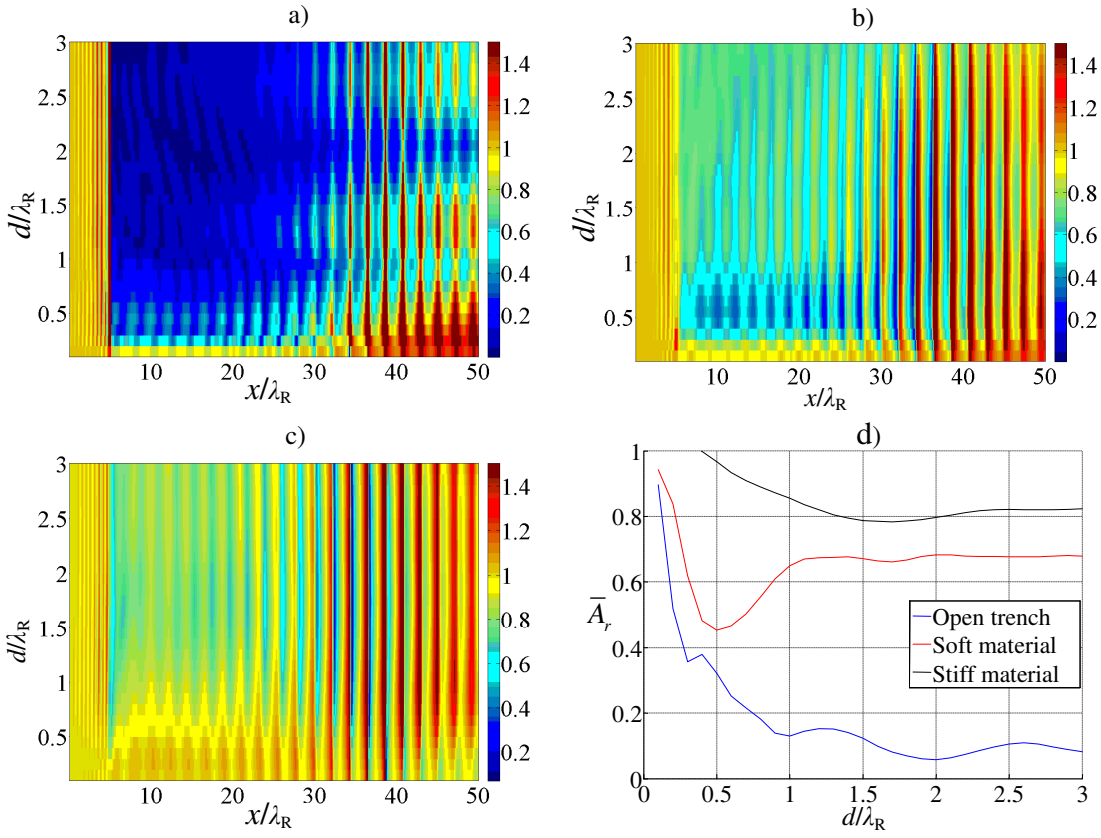

Figure 5.3: Ratio A_r as a function of the trench depth: a) open trench; b) trench filled with soft material; c) trench filled with stiff material; d) average ratio $\bar{A}_r$

For the case of a trench filled with a soft material (Figure 5.3b), the ratios A_r tend to decrease with the trench depth, reaching the minimum average value $\bar{A}_r$ at the depth $d = 0.5\lambda_R$. Above this depth, the ratios A_r start to increase, and when the trench depth $d = \lambda_R$ is reached, the ratios A_r remain approximately constant. Therefore, for this case the best efficiency seems to be achieved when the depth of the trench is one half of the Rayleigh wavelength. A deeper trench may result in a reduction of displacements of 30% instead of 50%.

Finally, for the case of a trench filled with a stiff material (Figure 5.3c), the best efficiency is obtained for the trench depth $d = 1.5\lambda_R$, but the average reduction is of only 20%. Immediately after the trench ($5\lambda_R < x < 6.5\lambda_R$) the reduction can reach up to 50%, but it decays as the distance to the source and trench increases.

In all these cases, the displacements before the trench ($x < l$) are amplified.

5.2.4 Influence of the trench width

The other dimension that also influences the trench performance is its width. The influence of this parameter is evaluated next through the calculation of the ratios A_r and $\bar{A}_r$ for a trench width varying from $0.1\lambda_R$ to $2\lambda_R$. Figure 5.4 shows the obtained results.

[A real trench is not likely to be wider than 1.5m. In this way, for a soil with Rayleigh wave speed $C_R = 120$ m/s (for example), the width $w = 0.5\lambda_R$ is achieved only for frequencies above

40 Hz. Thus, for the purpose of train induced vibrations, only the results considering small trench widths (say $w < 0.5\lambda_R$) are of interest.]

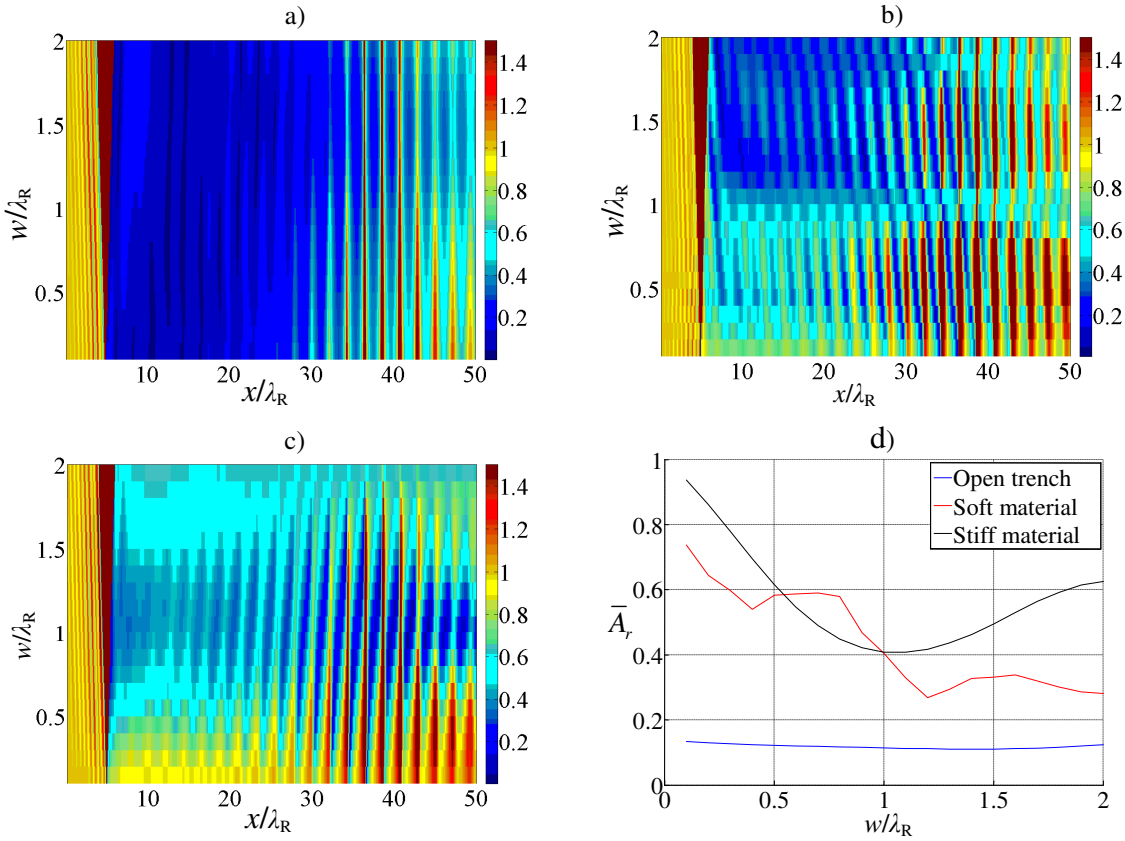

Figure 5.4: Ratio A_r as a function of the trench width: a) open trench; b) trench filled with soft material; c) trench filled with stiff material; d) average ratio $\bar{A}_r$

For the open trench, its width does not have much influence on the efficiency, at least up to the distance $x = 30\lambda_R$. For greater distances, increasing the width seems to enlarge the shielded zone (the darker blue area in Figure 5.4a extends farther as w increases). This tendency is not observed in the average ratio $\bar{A}_r$ because $L = 25\lambda_R$.

For the in-filled trenches, the increase of the trench width leads, in general, to an increase of the trench performance. The optimal trench width is $w = 1.2\lambda_R$ for the soft material and $w = \lambda_R$ for the stiff material. However, these values are not attainable for the frequencies excited by trains, and so it is concluded that for realistic values, to increase the trench width is always beneficial.

5.2.5 Influence of the trench position

With the aim of studying the influence of the trench position, the distance l between the point source and the trench assumes values between $l = 0.5\lambda_R$ and $l = 10\lambda_R$ and the ratios A_r and $\bar{A}_r$ are accordingly calculated. The results are represented in Figure 5.5.

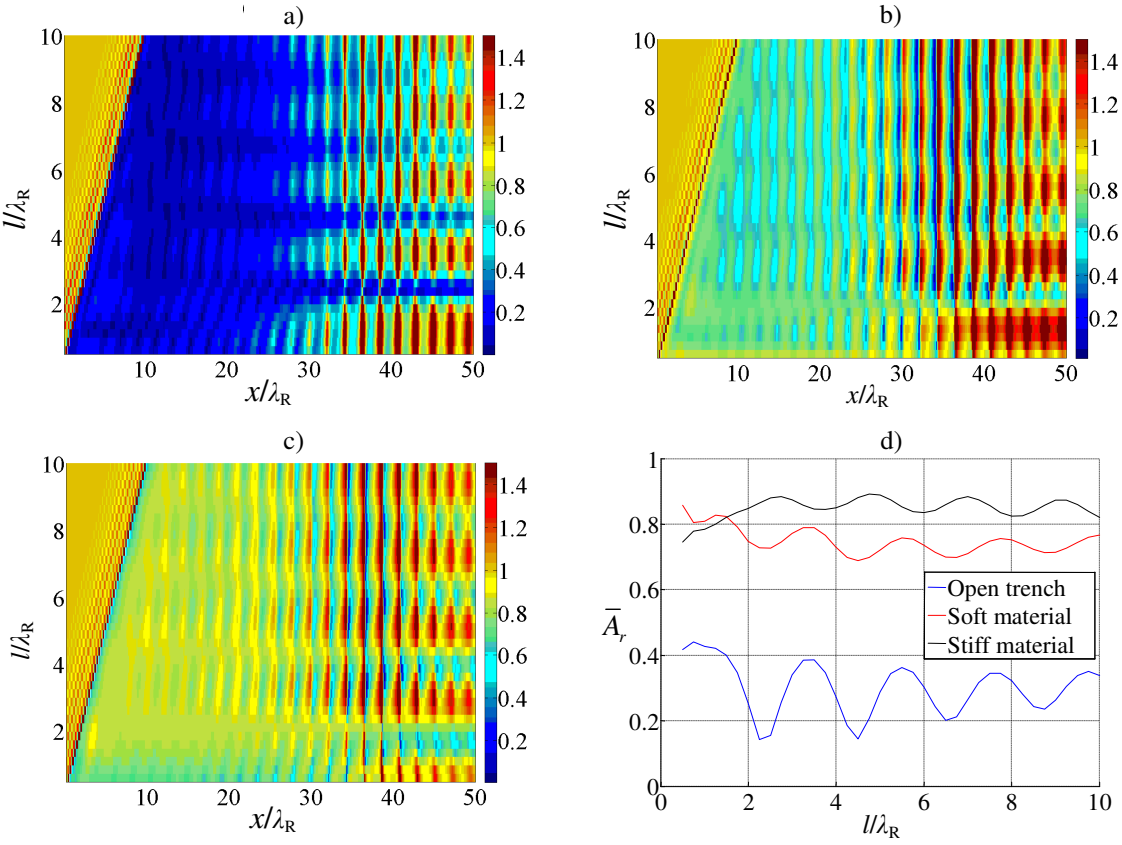

Figure 5.5: Ratio A_r as a function of the trench position: a) open trench; b) trench filled with soft material; c) trench filled with stiff material; d) average ratio $\bar{A}_r$

The results in Figure 5.5a-c suggest that the attenuation of the response after the trench ($x > l$) is almost independent of the trench position: vertical stripes can be identified in the colored plots, which sustain this conclusion. The average ratio $\bar{A}_r$ shows a similar trend: for the open trench, $\bar{A}_r$ oscillates around the value $\bar{A}_r = 0.3$, being the maximum deviation equal to 0.1; for the trench filled with the soft material, the mean value is $\bar{A}_r = 0.75$ and the maximum deviations are around 0.05; for the trench filled with the stiff material, the mean value is $\bar{A}_r = 0.85$, and the maximum deviations are also around 0.05.

5.2.6 Influence of the stiffness of the in-fill material

The present and the following sub-sections investigate the influence of the mechanical properties of the in-fill material: the stiffness is considered first, and the material density is considered second. The Poisson's ratio is not studied in this work, but it has been shown that its influence on the behavior of in-filled trenches is negligible (Yang and Hung, 1997).

The influence of the stiffness of the in-fill material is analyzed by varying the shear modulus from $G_{Mat} = 0.1 G_{Soil}$ to $G_{Mat} = 10 G_{Soil}$. Figure 5.6 shows the corresponding ratios A_r and $\bar{A}_r$.

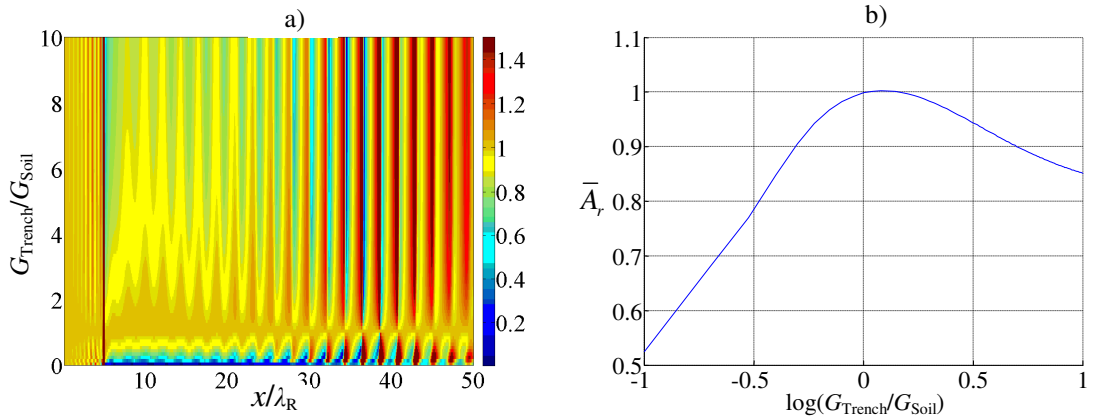

Figure 5.6: a) Ratio A_r as a function of the stiffness of the in-fill material; b) average ratio $\bar{A}_r$

It can be clearly observed from Figure 5.6b that softer in-fill materials perform better than stiffer in-fill materials. Furthermore, for softer in-fill materials, the isolation efficiency improves with the decrease of the stiffness, while for stiffer materials, the isolation efficiency improves with the increase of the stiffness.

5.2.7 Influence of density of in-fill material

The second property of the in-fill material to be studied is the density. With that aim, the ratios A_r and $\bar{A}_r$ are calculated for densities ρ_{Mat} varying between $\rho_{Mat}=0$ and $\rho_{Mat}=10\rho_{Soil}$. Again, the scenarios of stiff in-fill material ($G_{Mat}=10G_{Soil}$) and of soft in-fill material ($G_{Mat}=0.2G_{Soil}$) are considered. The open trench scenario is not applicable in this study. Figure 5.7 shows the corresponding results.

The main conclusion that can be inferred from the results shown in Figure 5.7 is that the density of the in-fill material considerably influences the behavior of trenches. While for soft in-fill materials a lighter material is beneficial, for stiffer materials it is convenient to have high densities. For the two stiffness scenarios studied, the density has more influence on the behavior of the stiff material than on the behavior of the soft material.

5.2.8 Influence of the Poisson's ratio of the soil

Since the soil is assumed homogeneous and since the trench dimensions are made proportional to the Rayleigh wavelength λ_R, then the unique parameter of the soil that may influence the behavior of the trench is the Poisson's ratio. The influence of this parameter is investigated next through the calculation of the ratios A_r and $\bar{A}_r$, which are represented in Figure 5.8.

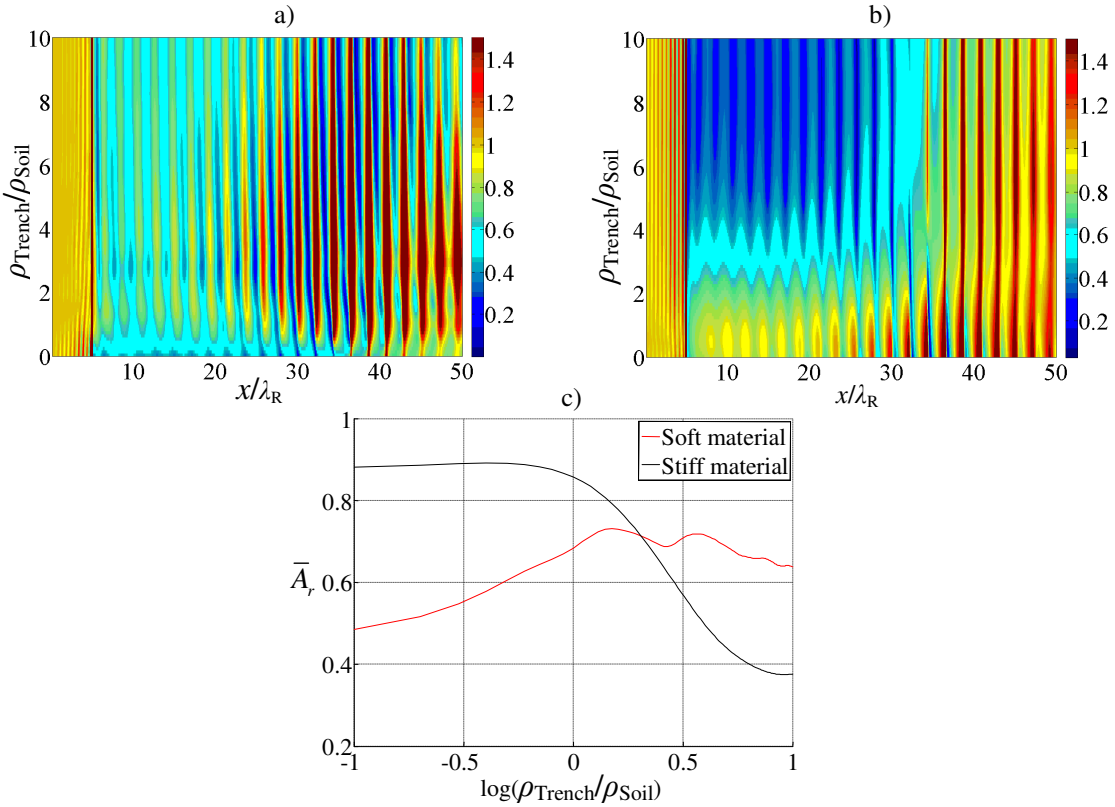

Figure 5.7: Ratio A_r as a function of the density of the in-fill material: a) trench filled with soft material; b) trench filled with stiff material; c) average ratio $\bar{A}_r$

For all three cases, the trend is that the average ratio $\bar{A}_r$ increases (slightly) with the increase of the Poisson's ratio. The explanation for this can be found in the ratio λ_P/λ_R (λ_P represents the wavelength of the P wave). This ratio increases with the increase of the Poisson's ratio and thus, for high values of this parameter, the dimensions of the trench become small when compared to the P wave. As a consequence, the reflection of P waves becomes negligible.

The decrease of efficiency of the trenches due to higher Poisson's ratios is more obvious away from the trench than in its proximity.

5.2.9 Influence of the ground stratification

In general, the ground conditions do not correspond to homogeneous half-spaces, and therefore soil stratification may need to be considered. In order to understand if disregarding the soil stratification may affect the predictions, in this section the homogeneous half-space is replaced by a layer on top of a half-space. The material properties of the layer and underlying half-space are indicated in the general description (sub-section 5.2.1), except for the shear modulus of the half-space, which assumes values between $G_{Half} = 0.1G_{Layer}$ and $G_{Half} = 5G_{Layer}$. The thickness of the layer is $H = \lambda_R$. Figure 5.9 shows the ratios A_r and $\bar{A}_r$ for this new scenario.

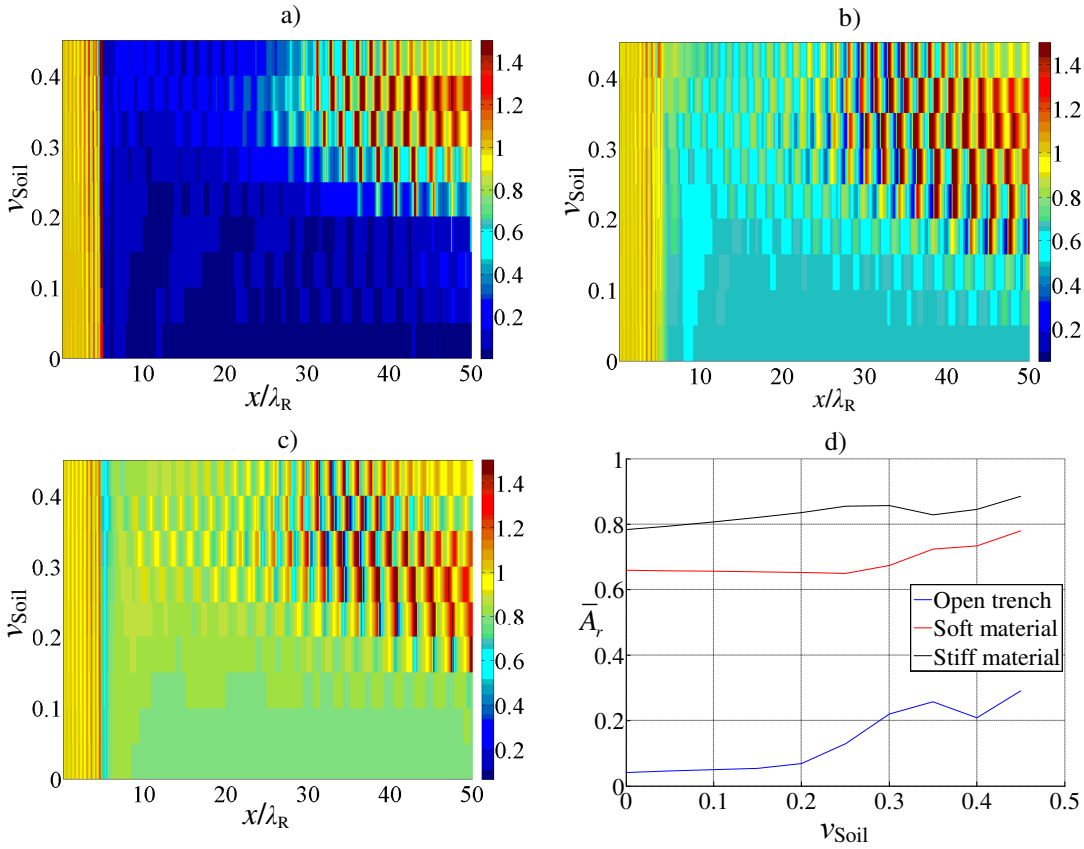

Figure 5.8: Ratio A_r as a function of the Poisson's ratio of the soil: a) open trench; b) trench filled with soft material; c) trench filled with stiff material; d) average ratio $\bar{A}_r$

It can be seen in Figure 5.9 that the stratification of the ground considerably changes the behavior of the trenches, namely when the lower half-space is stiffer than the upper layer. The influence of stratification is more noticeable for the open trench than for the in-filled trenches.

5.2.10 Influence of the modeling strategy

The modeling strategy is studied next to assess whether the simulations under plane-strain conditions are valid to infer about the behavior of trenches when acted upon by standing point loads (three-dimensional excitation). Figure 5.10 plots the ratio A_r as function of the longitudinal (y) and transverse (x) coordinates for a point source applied at the origin $(x, y) = (0,0)$.

For the open trench and for the trench filled with a soft material, the ratio A_r after the trench is approximately symmetric with respect to the loaded point. In opposition, for the stiff trench, one can notice the existence of a yellowish triangular region inside which the displacements are not attenuated. This shadow region is a consequence of the high bending stiffness of the trench, being the angle of these triangular shaped shadow zones dependent on the excitation frequency, on the Rayleigh wave speed of the soil, and on the bending dispersion of the trench. Expressions for this angle can be found in Coulier et al. (2013b). This feature indicates that for standing harmonic solicitations, the best orientation of a stiff trench is not perpendicularly to the line that connects source and receiver, but instead at a certain angle.

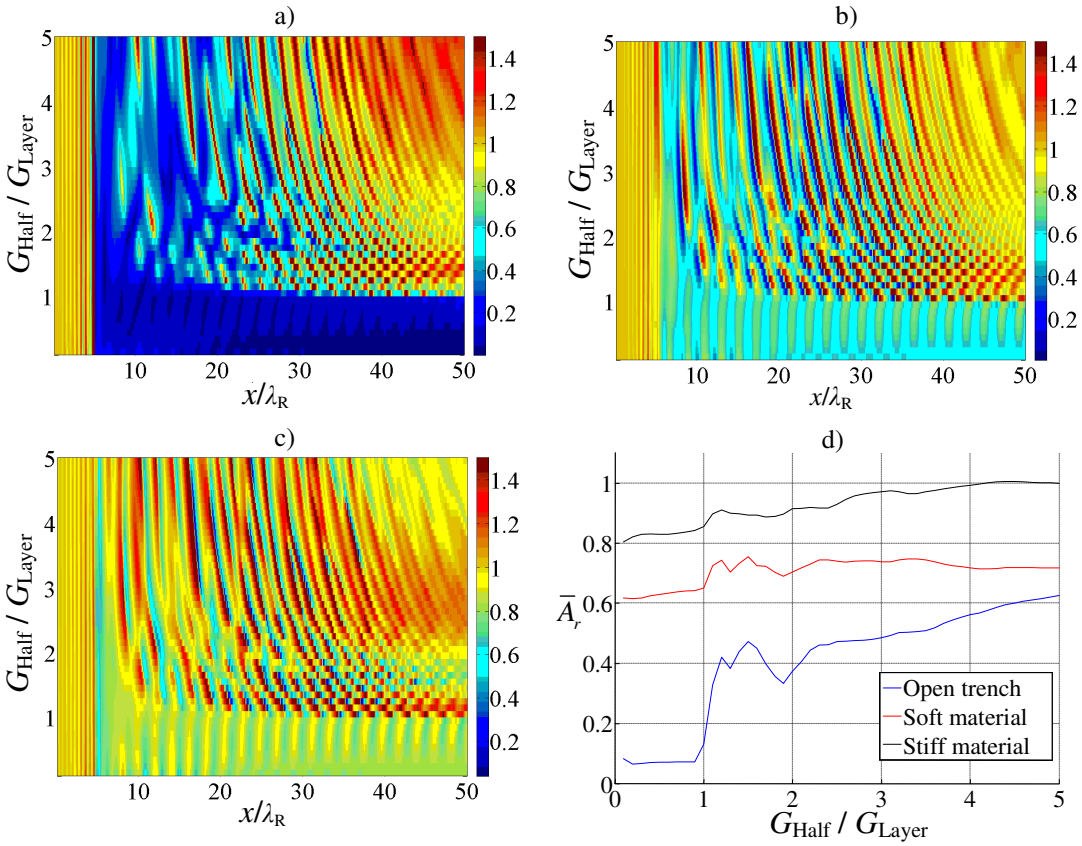

Figure 5.9: Ratio A_r as a function of the stiffness of the lower half-space: a) open trench; b) trench filled with soft material; c) trench filled with stiff material; d) average ratio $\bar{A}_r$

The average ratio $\bar{A}_r$ has been computed for the central alignment $y=0$, and it has been found that this ratio is very similar to the 2D ratio (results not shown here). In this way, for open trenches and trenches filled with soft materials, since the ratio A_r is almost symmetric with respect to the loaded point, 2D simulation can be used to estimate the reduction maps plotted in Figure 5.10a,b. For stiff in-fill materials, such is not possible due to the presence of the shadow zones. Thus, at least for the case of stiff in-fill materials, 3D simulations are necessary.

5.2.11 Conclusions

In this section, a parametric study was performed to evaluate the influence of some variables on the reduction of vibrations achieved by trenches. The following conclusions are drawn:

1. Increasing the depth of the trench has in general a beneficial effect, but above the value $d=\lambda_R$, increasing the depth does not improve significantly the efficiency of the trench. In the case of the trench filled with a soft material, the optimal value for the trench depth is one half of the Rayleigh wavelength.
2. For the case of open trenches, the trench width has no significance. For in-filled trenches, to enlarge the width reveals to be beneficial.

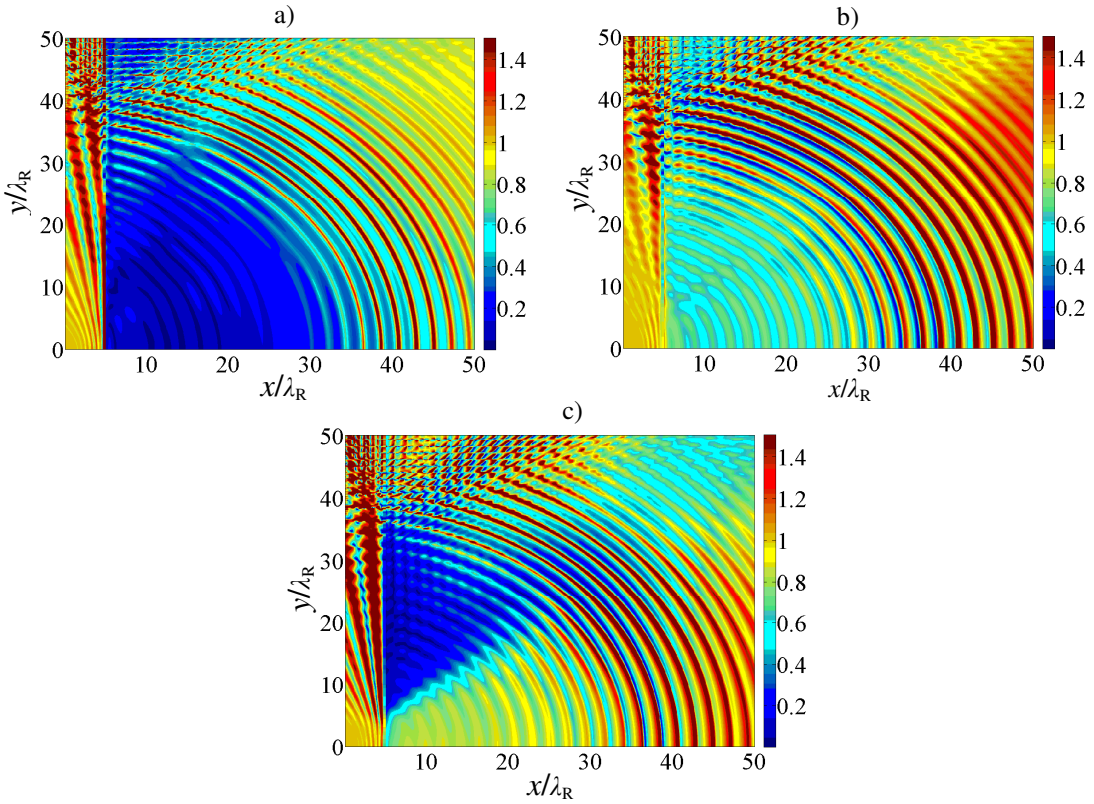

Figure 5.10: Ratio A_r for a 3D loading scenario: a) open trench; b) trench filled with soft material; c) trench filled with stiff material

3. The trench position does not influence much its efficiency.
4. Open trenches perform better than in-filled trenches, and within in-filled trenches, materials softer than the soil tend to perform better than materials stiffer than the soil. Trenches filled with soft materials perform better if the in-fill material is made softer, while trenches filled with stiff materials perform better is the in-fill material is made stiffer.
5. The density of the material also influences the trench performance. The trend is that as the in-fill material is made heavier, the reduction provided by the trench increases. This parameter has more influence in the case of a stiff material than in the case of a soft material.
6. The greater the Poisson's ratio of the soil, the worse the efficiency of the trench is. This parameter has more influence on open trenches than on in-filled trenches.
7. To consider the ground stratification changes considerably the performance of the trench.
8. For open trenches and trenches filled with a soft material, 2D simulations may provide good information about the reduction achieved with trenches when acted upon by point loads. The same is not valid for trenches filled with stiff materials. For this last situation, the best position of trenches is obliquely to the line that links source and receiver.

The conclusions obtained in this study are the same as those of the studies referred to in 5.1. However, it must be mentioned that each parameter is being studied independently of the others, and so, if more than one parameter varies in each study, then different conclusions may be reached.

As last comment, it must be restated that these investigations concern standing line loads. In the case of moving loads, the response of the ground is characterized by a wide frequency band and so the dimensionless study becomes impossible, turning the problem much more complex. This issue is addressed in the next sections, in which trenches are used as mitigation measures for the vibrations induced during the passage of a train.

5.3 Trenches for the mitigation of train induced vibrations

5.3.1 Introduction

In this section, distinct trench solutions are analyzed and compared in the context of vibrations induced by railway traffic. This problem differs from the problem of vibrations induced by fixed stationary loads in the fact that the motion induced by moving loads is characterized by a wide range of frequencies, while the response induced by stationary loads has the same frequency as the load.

The problem to be analyzed is schematized in Figure 5.11: a train runs on a surface track, next to which a trench is constructed in order to scatter the impinging waves and thus reduce the vibrations after the trench. For the study, the train is considered as a set of moving harmonic loads whose amplitudes result from the solution of the train-track interaction problem described in chapter 4, the track and the interior of the trenches are simulated with finite elements, and the ground is simulated with boundary elements.

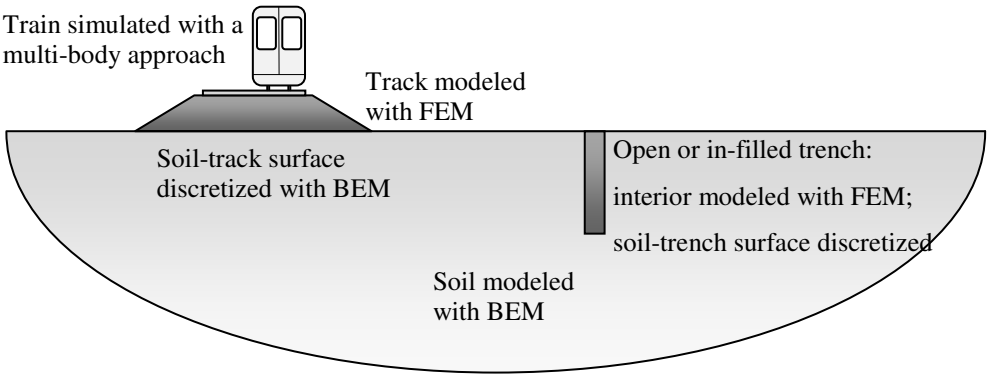

Figure 5.11: Schematization of the problem

The main objective of this section is the comparison between different trench solutions in the reduction of vibrations induced by railway traffic. For this purpose, the geometry and material properties of an existing and operational line are considered, being the scenario chosen for the analyses a stretch of the Portuguese railway network, near the town of Carregado. The reason for this option is the fact that the local conditions at this line have been obtained after some experimental campaigns that have been carried out with that intent. The reader is referred to Alves Costa et al. (2012a) for more details on these experimental campaigns.

The following paragraphs describe the soil conditions, track geometry and properties, rolling material properties and trench solutions assumed in the analyses.

Local soil conditions and TLM model for the soil

The local properties of the ground have been determined experimentally through cross-hole tests, CPT tests, and SASW tests, having the experiments revealed that it consists of several layers of clay with distinct wave velocities (Alves Costa et al., 2012a). In the following analyses, the soil model is assumed to be simpler than the conditions obtained experimentally, being the model composed by two elastic layers on top of a half-space, whose properties are indicated in Table 5.1.

Table 5.1: Soil stratification and properties

Layer	Thickness H [m]	Density ρ [kg/m3]	P wave speed C_P [m/s]	S wave speed C_S [m/s]	Hysteretic damping $\xi_P = \xi_S$
1	6	1900	1250	150	0.03
2	6	1900	1500	230	0.03
3	∞	1900	1600	310	0.03

For the TLM model, the layers one and two are divided into quadratic thin-layers with 0.10 m of thickness, while the lower half-space is simulated through the use of PMLs (Barbosa et al., 2012).

Figure 5.12 shows the dispersion curves and the corresponding phase velocities for the considered soil profile. The maximum phase velocity corresponds to the shear wave speed of the lower half-space, while the minimum phase velocity corresponds to the Rayleigh wave speed of the top layer (approximately 143 m/s).

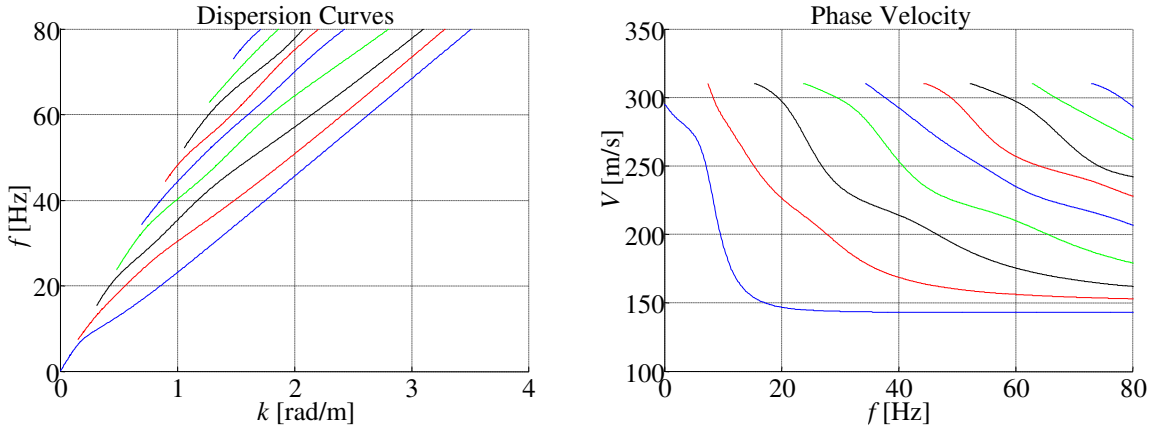

Figure 5.12: Dispersion curves (left) and corresponding phase velocities (right) of the soil.

Properties of the track and corresponding numerical model

The line at Carregado corresponds to a double ballast track, with a straight alignment, and is composed of UCI60 rails, Vossloh rail pads, concrete sleepers (spaced 0.60 m), and ballast and subballast layers. Despite the fact of being a double track, the numerical model used in the following analyses corresponds to a single track, whose geometry and FEM mesh are represented in Figure 5.13. As previously shown in Alves Costa et al. (2012a), the use of a single line model to simulate a double track is accurate enough. The elastic and dynamic properties of each component of the track are indicated in Table 5.2.

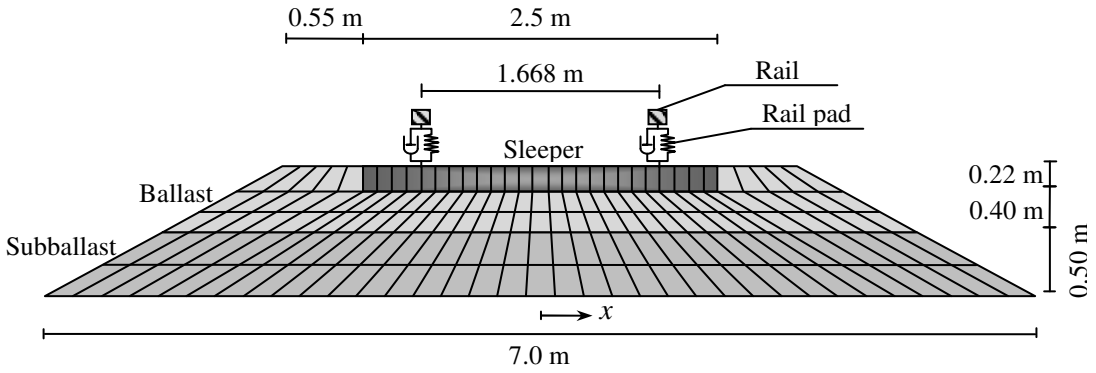

Figure 5.13: FEM model of the track

Table 5.2: Properties of the components of the track

Rails UIC60 (modeled with Euler beams)			
Young's Modulus E [Pa]	Mass Density ρ [kg/m^3]	Section Area A [m^2]	Section Inertia I_V [m^4]
200×10^9	7850.0	7.687×10^{-3}	7.860×10^{-6}

Rail Pads			
Vertical Stiffness K_V [kN/mm]		Vertical Damping C_V [kNs/mm]	
Real: 600	Model*: 1000	Real: 22.5	Model*: 37.5

Sleepers						
	Mass [kg/m]		E [Pa]		Dimensions [m^3]	
Real	300		30×10^9		$2.5\times0.6\times0.22$	
	ρ [kg/m^3]	E_{xz} [Pa]	ν_{xz}	E_y [Pa]	ν_y	ν_{xyz}	$\xi_P=\xi_S$
Model**	1850.0	20×10^9	0.2	97×10^6	0.1	0.04	0.01

Ballast			
E [Pa]	ρ [kg/m^3]	ν	$\xi_P=\xi_S$
97×10^6	1591.0	0.12	0.061

Subballast			
E [Pa]	ρ [kg/m^3]	ν	$\xi_P=\xi_S$
212×10^6	1913.0	0.3	0.054

* The rail pads are modeled with distributed line springs along the longitudinal direction

** The sleepers are modeled with anisotropic materials, as explained in chapter 3

Another important aspect related to the track is its unevenness, which is responsible for the generation of the dynamic train-track interaction forces. The unevenness at Carregado has been measured with a EMI recording car, capable of measuring the unevenness profiles of rails for the range of wavelengths between 0.4 and 25 m. With the power spectral density (PSD) of the measured unevenness profile, artificial profiles with 40 wavelengths ranging from 0.75 m to 30 m have been generated. These profiles are based on the expressions suggested in the norm ISO8680 (1995) and are such that their PSD approximate these of the measured profile. Figure 5.14 represents the PSD of the measured and artificial profiles, and the longitudinal variation of one possible random profile generated with the expressions of ISO8608. The same unevenness profile is assumed for both rails.

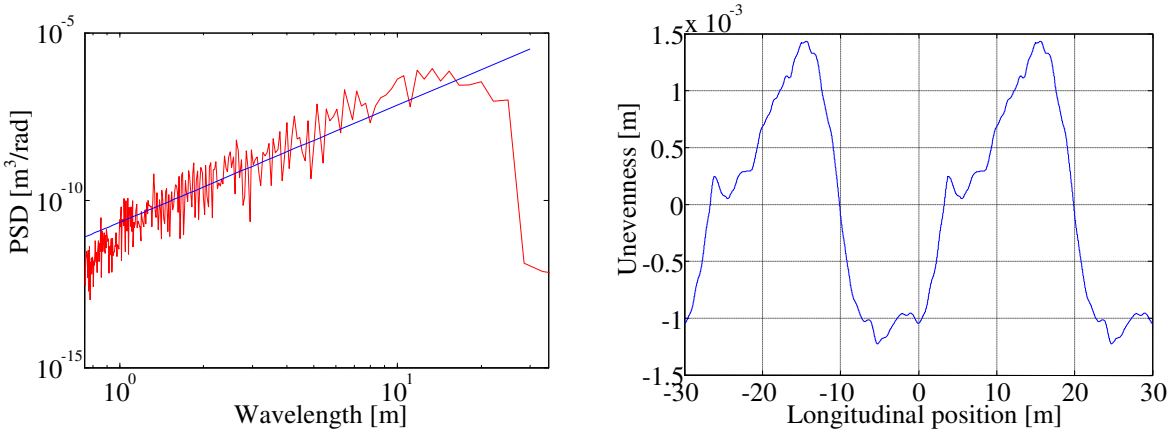

Figure 5.14: PSD of the unevenness (left: red = measured; blue = approximated) and random unevenness profile (right)

Rolling stock and numerical model

The trains that circulate in the Northern line near Carregado (Portugal) comprise commuter trains, with speeds of approximately 130 km/h, Inter Cities trains, which can travel up to 200 km/h, Alfa Pendular trains, which are the fastest trains operating in Portugal, with speeds up to 220 km/h, and in some cases, freight trains, which travel with speeds below 100 km/h. The train considered in this work is the Alfa Pendular.

The Alfa Pendular is a high-speed train composed of six vehicles, fulfilling a total length of 158.9 m. Each vehicle is composed of the car-body, two bogies and four axles. The car-body is linked to the bogies at its extremities through the secondary suspension system, and the bogies are connected to a pair of axles through the primary suspension system. In the following analyses each vehicle of the train is modeled as a two dimensional multi rigid-body system in which the axles, the bogies and the car-body are considered as rigid masses, and in which the suspension systems that connect these components are simulated by means of springs and dashpots. All displacements not contained in the vertical-longitudinal plane are neglected. The contact stiffness is accounted for by means of springs between the wheels and the rails, that simulate the Hertzian contact (Wu and Thompson, 2002). The geometry of the train is represented in Figure 5.15 and the 2D model of each vehicle is represented in Figure 4.31. The dynamic properties assumed for the different components of the train are given in Table 5.3.

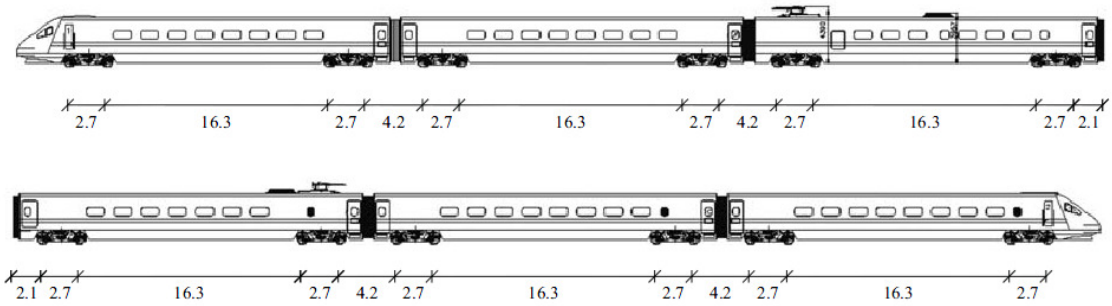

Figure 5.15: Geometry of the Alfa Pendular train

Table 5.3: Dynamic properties of the train

Vehicle	Car body		Front bogie		Rear bogie		Axles			
							FF	FR	RF	RR
	M [kg]	I_x [kg.m^2]	M [kg]	I_x [kg.m^2]	M [kg]	I_x [kg.m^2]	M [kg]	M [kg]	M [kg]	M [kg]
1	32901	2083600	4932	5150	4823	5150	1538	1884	1884	1538
2	32901		4823	5090	4823	5090	1538	1884	1884	1538
3	33124		4712	5000	4712	5000	1538	1538	1538	1538
4	33524		4712	5000	4712	5000	1538	1538	1538	1538
5	35710		4823	5090	4823	5090	1538	1884	1884	1538
6	33201		4823	5150	4932	5150	1538	1884	1884	1538

Primary suspension systems		Secondary suspension systems		Contact springs
K [N/m]	C [Ns/m]	K [N/m]	C [Ns/m]	K [N/m]
3420000	3600	1320000	3600	2.4×10^{12}

M = mass; I_x = momentum of inertia; K = stiffness; C = damping

Trench solutions and numerical models

The mitigation solutions analyzed in this work are materialized with trenches constructed 7.5m away from the central line of the track. The trenches are 0.40 m wide and two depths are considered: 3 m and 6 m. The trenches are open or in-filled with concrete or geofoam. The elastic and dynamic properties of these in-fill materials are listed in Table 5.4.

From a practical standpoint, the open trench is not a viable solution as it requires some type of supporting system in order to avoid its walls to collapse. Nevertheless, this solution is taken into consideration for comparison purposes. As for geofoam, it consists in an expandable polystyrene material with low density which provides flexibility in the design and easiness in its practical implementation. It has been investigated as a possible in-fill material for trenches by Alzawi and Hesham El Naggar (2009, 2010; 2011). The concrete filled trenches can be materialized through buried concrete walls and have also been investigated in several experimental and numerical studies (e.g., Celebi et al., 2009).

Table 5.4: Properties of the in-fill materials

Concrete			
E [Pa] (Young's modulus)	ρ [kg/m^3] (Mass density)	ν (Poisson's ratio)	$\xi_P = \xi_S$ (hysteretic damping)
30×10^9	2300.0	0.2	0.01
Geofoam			
E [Pa]	ρ [kg/m^3]	ν	$\xi_P = \xi_S$
13.3×10^6	61.0	0.0	0.01

The behavior of the trenches is simulated with quadrilateral finite elements with 4 nodes and with dimensions 0.20×0.20 m^2. The interface between the soil and the trench border is simulated by boundary elements of constant expansion in such a way that there is one boundary element per face of the finite element mesh in contact with the soil (the same rule applies for the interface between the track and the soil).

5.3.2 2D analyses – influence of the track

Before moving into the case of vibrations induced by traffic, the case of line loads ($k_y = 0$) is addressed so that some features of the numerical modeling may be inferred. The impact resulting from the exclusion of the track from the mathematical model, in what regards the predicted soil response and the predicted trench efficiency, is investigated. For that purpose, two scenarios are considered: a first scenario in which the track is included and loads of the type $F(t) = 0.5\mathrm{e}^{\mathrm{i}\omega t}$ are applied at each rail; and a second scenario in which the track is excluded and therefore a load of the type $F(t) = \mathrm{e}^{\mathrm{i}\omega t}$ is applied directly at the ground surface at the position $x = 0$ (central alignment of the track).

The differences in the ground surface responses are investigated first, and to this end, the vertical displacements are calculated as functions of the excitation frequency ω and of the transverse distance x. The results are depicted in Figure 5.16, where the variables u_z^{Track} and $u_z^{\text{No track}}$ correspond to the displacements in the presence and in the absence of the track, respectively. In order to facilitate the interpretation of the differences between the two scenarios, the ratios $u_z^{\text{No track}} / u_z^{\text{Track}}$ are also depicted. No trench is considered at this point.

Figure 5.16 confirms that the exclusion of the track from the mathematical model considerably alters the predicted ground response. As can be observed, the displacements are two orders of magnitude higher for frequencies above 40 Hz when the track is excluded. There is no significant difference for frequencies below 20 Hz.

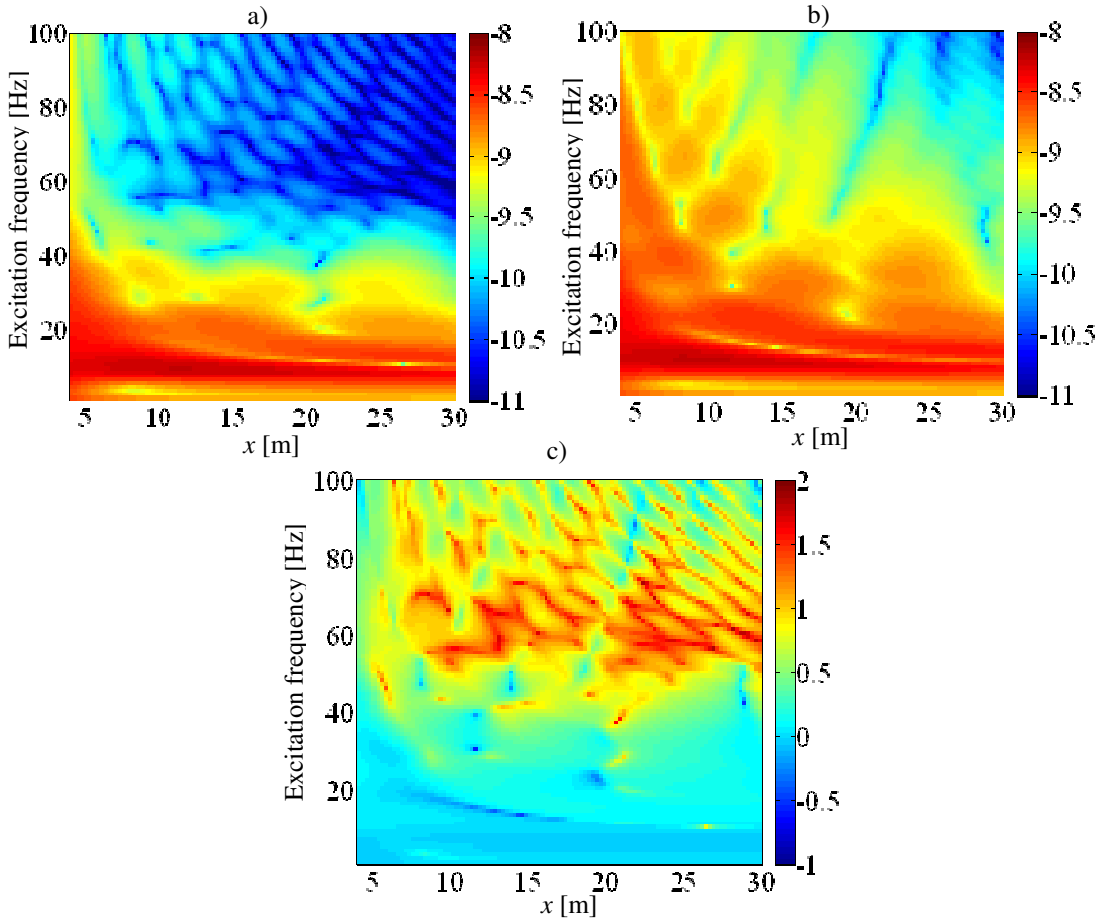

Figure 5.16: Displacements at the ground: a) $\log_{10}\left(u_z^{\text{Track}}\right)$; b) $\log_{10}\left(u_z^{\text{No track}}\right)$; c) $\log_{10}\left(u_z^{\text{No track}}/u_z^{\text{Track}}\right)$

The difference observed for frequencies above 40 Hz can be explained by the forces that are transmitted to the ground: firstly, the total transmitted force is not the same for the two scenarios (Figure 5.17a); secondly, in the first scenario, the transmitted force is distributed along the track-soil interface (Figure 5.17b), while in the second the force is concentrated at a single point. Therefore, as the force transmitted by the track is greater than the applied force, it could be expected that the predicted displacements were greater when the track was considered. However, since the load is distributed along the train-track interface, the near field displacements are smaller. For remote positions, the effect of the load distribution disappears and the predicted ground displacements are greater when the track is taken into account. This can be observed in Figure 5.17c, where the ground displacements are depicted for $x > 30$ m and for the excitation frequency 80 Hz, with and without the track.

The discrepancy between the two scenarios reveals that when the track is disregarded the predicted response of the near field is over-estimated, which can lead to an incorrect conclusion about the need for mitigation measures.

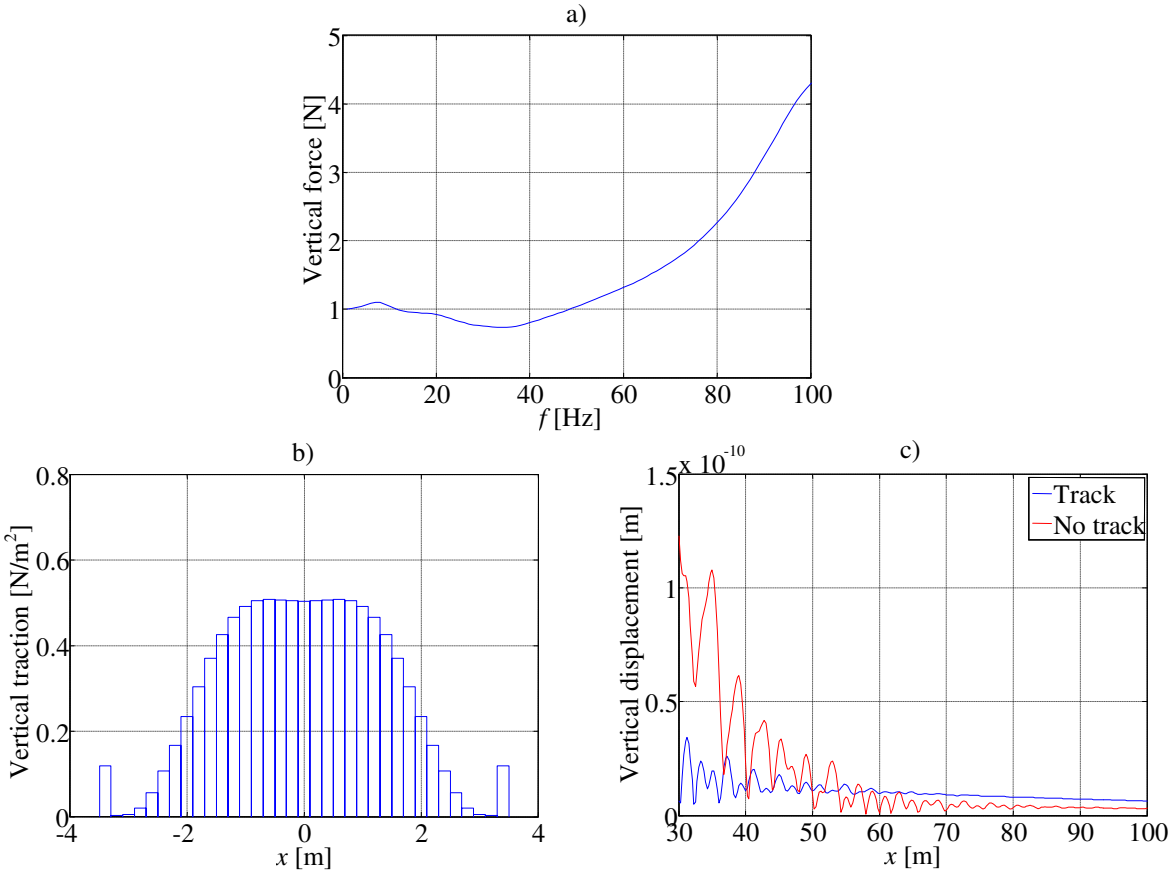

Figure 5.17: a) Resultant of the vertical forces between track and soil; b) distribution of tractions at the track-soil interface for f = 80 Hz; c) displacements at the ground surface for f = 80 Hz.

The importance of the track for the correct estimation of the efficiency of trenches is examined next. With that aim, the ratio A_r, defined in equation (5.2), is calculated as a function of the excitation frequency ω and of the transverse distance x for the two scenarios (with and without track). Figure 5.18 presents the results obtained for the trench solutions with 3 [m] of depth.

The comparison between the left and right columns of Figure 5.18 reveals differences in the estimated reduction levels: firstly, higher reduction levels are obtained when the track is not accounted for; secondly, there is a band near the frequency 60 Hz that causes the displacements after the trench to be amplified, if the track is included, which does not occur if the forces are applied directly to the ground. In general, the estimated reduction is higher in situations in which the track is disregarded, and lower when the track is considered. For this reason, the track exclusion may lead to under designed protective measures.

The differences reported in this sub-section point out the need for the inclusion of the track in the numerical model, as it is observed that considering simpler models in which the track is disregarded may result in over-estimated attenuation levels and, consequently, in inappropriate designs of trenches. On the other hand, neglecting the track results in over-estimations of the induced level of vibrations, which may lead to an incorrect judgment about the need for mitigation measures.

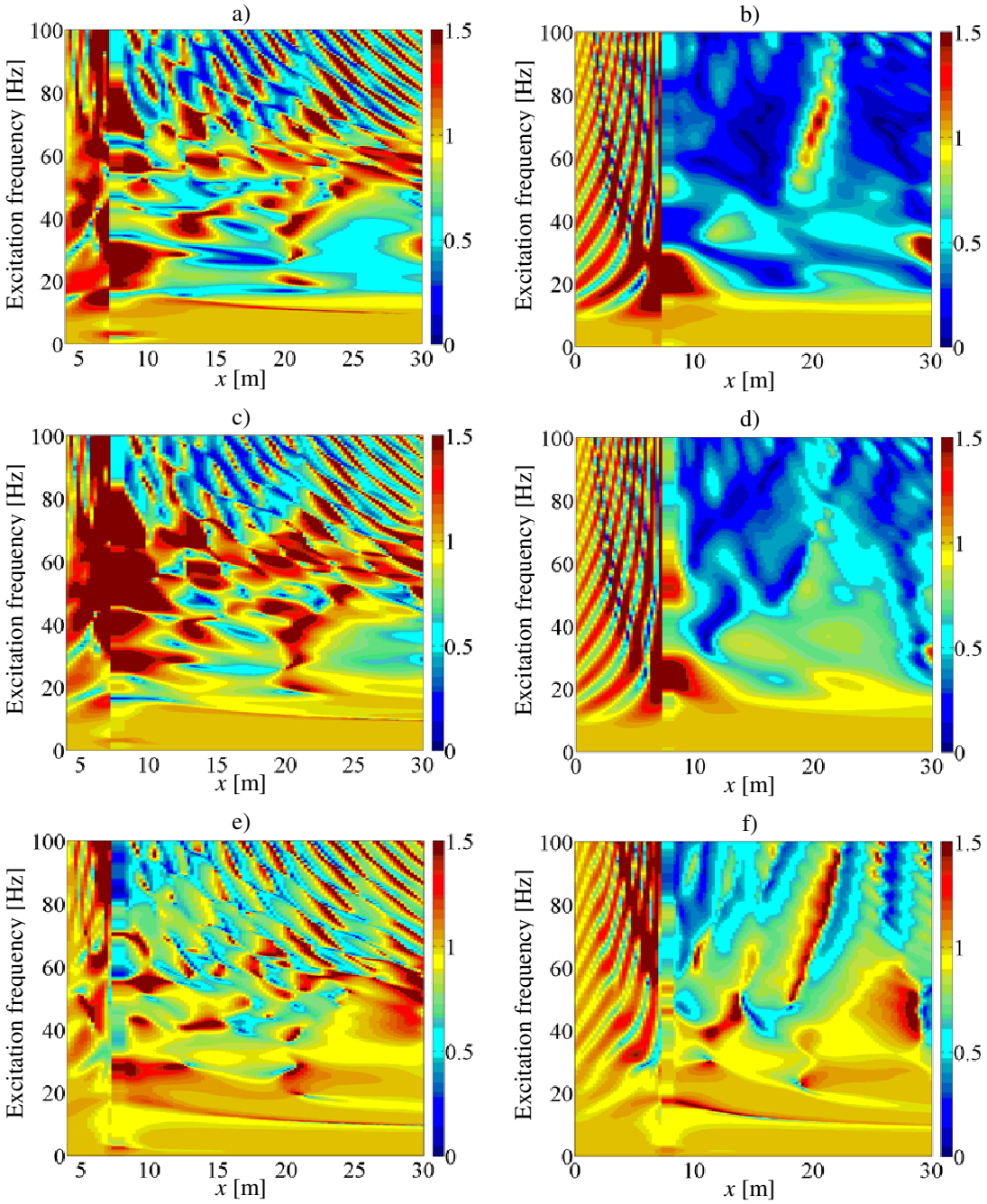

Figure 5.18: Ratios A_r for: a) open trench with track; b) open trench without track; c) geofoam trench with track; d) geofoam trench without track; e) concrete trench with track; f) concrete trench without track

A common feature of the two scenarios is the amplification of displacements before the trench, which is a consequence of the reflection of waves at the trench. It is therefore important to examine if this amplification effect may influence the train-track interaction, potentially causing an amplification of the interaction forces and resulting in the cancellation of the beneficial effects associated with the construction of trenches. This issue is addressed in the next sub-section, together with the evaluation and comparison of the efficiency of the distinct trench solutions.

5.3.3 3D analyses – vibrations induced by the Alfa Pendular train

In this sub-section, the vibrations induced by an Alfa Pendular train travelling at the speed $V = 60$ m/s are analyzed. Contrarily to the analyses reported in 5.3.2, the present study demands for the development of a 3D solution with train-track interaction. The dynamic interaction between the train and the track is taken into account through the formulation presented in chapter 4, for which the irregularity profile shown in Figure 5.14 is used.

This sub-section is divided into three topics: in the first topic, the influence of the trenches on the train-track interaction is discussed; in the second, the different trench solutions are compared; in the last topic, the behavior of the trenches along the longitudinal coordinate is assessed.

Influence of the trenches in the train-track interaction

As described in sub-section 5.3.2, the construction of trenches causes the amplification of displacements in the ground surface located between the track and the trench. At a first glance, this amplification may seem inconsequent, as the main objective is the attenuation of vibrations after the trench and not before it. However, since the vibrations are reflected at the trench and then come back towards the track, a deeper thought leads to the question: "Will the reflections interfere in the train-track interaction phenomenon, causing the increase of the dynamic forces and the cancellation of the beneficial effects of the trench?" This question is investigated next, through the comparison of the dynamic forces of the first wheel set for the mitigated and non mitigated situations. These forces and the relative deviations with respect to the non-mitigated scenario are overlapped in Figure 5.19 for the different trench solutions under analysis.

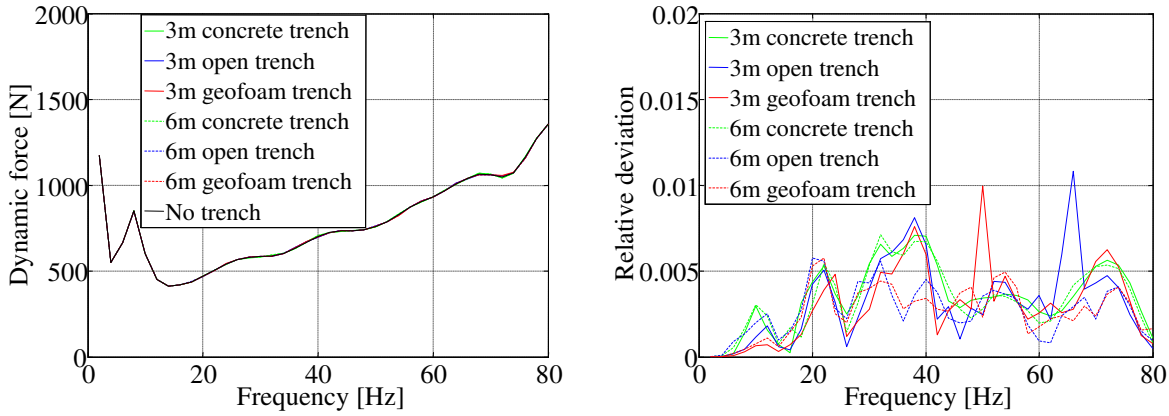

Figure 5.19: Dynamic forces (left) and relative deviations (right) of first wheel set

The maximum deviation of the magnitude of the dynamic forces is 1%, so it is concluded that the trenches do not affect the train-track interaction mechanism, at least for the track-trench distance considered in the present analysis. Though it could be expected that the waves that are reflected and that return to the track had more influence on the train-track interaction, the opposite happens, and the reason for that can only be another reflection of waves when they reach back the track-soil interface. This aspect can be used in the benefit of the simulations, since, according to the conclusions, the train-track interaction problem needs to be solved only for the non-mitigated scenario, enabling the use of the obtained results in the remaining situations.

The efficiency of trenches

The efficiency of distinct trench solutions is now compared. The trench solutions are compared based on the insertion loss (*IL*) and on the running root means square (*RRMS*) of the vertical velocity induced by the passage of the train. Three receivers are considered, being all of them placed after the trench, namely at the transverse positions $x_1 = 10$ m, $x_2 = 15$ m, and $x_3 = 20$ m ($x = 0$ corresponds to the central alignment of the track). The longitudinal position of all receivers is $y = 0$.

The insertion loss $IL(x, y, \omega)$ for a point with coordinates (x, y) is calculated with

$$IL(\omega) = 20\log_{10}\left|\frac{u_z^{\text{NoTrench}}(\omega)}{u_z^{\text{Trench}}(\omega)}\right| \tag{5.4}$$

and the *RRMS* for the same point is calculated with

$$RRMS(x, y, t) = \frac{\sqrt{\int_{t-\Delta t/2}^{t+\Delta t/2} v_z^2(x, y, \tau)\,\mathrm{d}\tau}}{\Delta t} \tag{5.5}$$

where $v_z(x, y, t)$ is the vertical velocity in the time domain. The insertion losses and *RRMS*s for the three receivers are represented in Figure 5.20 (in one-third-octave bands) and in Figure 5.21, respectively. For the calculation of the *RRMS*, the time window $\Delta t = 0.125$ s is used, as indicated in the norm DIN4150-2 (1999).

The *IL* curves depicted in Figure 5.20 show that above the frequency 10 Hz, the displacements are attenuated for all trench solutions and all receivers considered. For this frequency, the phase velocity of the Rayleigh wave is approximately 180 m/s (Figure 5.12) and the associated wavelength is 18 m, so even though the depth of the shallower trench is only 1/6 of the Rayleigh wavelength, it is concluded that the 3 m deep trenches are able to reduce the vibrations. This feature could not be inferred from the 2D analyses (Figure 5.18), thus highlighting the relevance of 3D analyses for the understanding of the problem.

Also based on the *IL* plots, it can be observed that the 6 m trenches tend to perform better than the 3 m trenches, as expected, and that no general trend can be distinguished in what concerns the influence of the distance between receivers and trench. As for the ranking of the in-fill material in terms of the performance of the trench, it is concluded that concrete trenches come first, empty trenches come second, though very close to the concrete trenches, and geofoam trenches come last, way below the other two. This ranking differs from the results of the 2D analyses (Figure 5.18), for which open trenches come first, geofoam trenches come second and concrete trenches get last place.

The *RRMS* plots can also provide information about the efficiency of the trenches. As observed in Figure 5.21, all trenches indeed succeed in reducing the velocities at all receivers, but with different levels of attenuation: as concluded from the *IL* plots, the concrete and open trenches provide very similar reduction levels (apart from the first receiver, for which the concrete trenches outperform the open trenches), while the geofoam trenches yield smaller attenuation levels. Additional information that can be perceived from Figure 5.21 is that geofoam trenches perform worse when the receiver is placed farther from the trench, while no significant difference is noticed regarding open and concrete trenches.

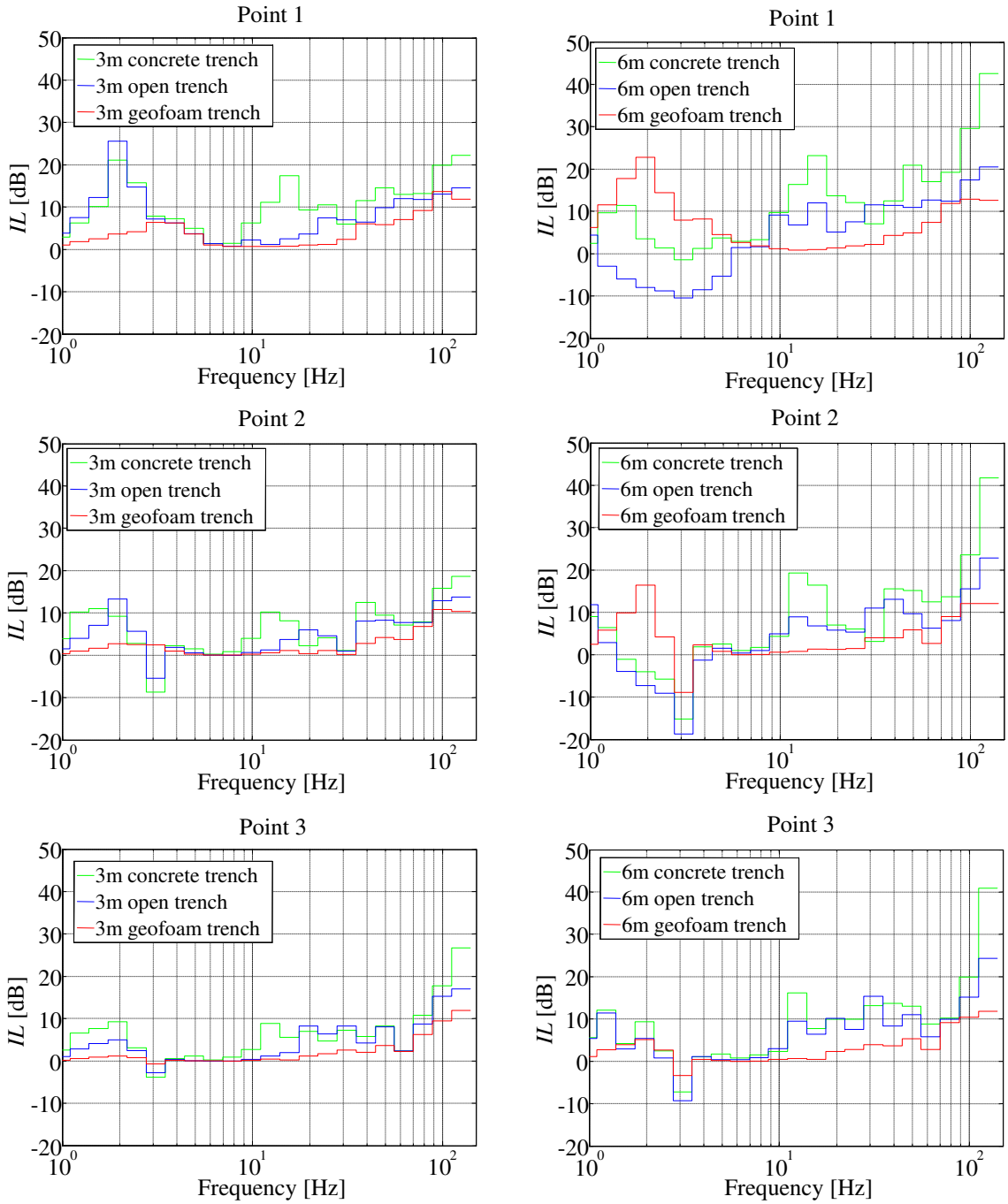

Figure 5.20: Insertion losses for distinct trench solutions and receivers

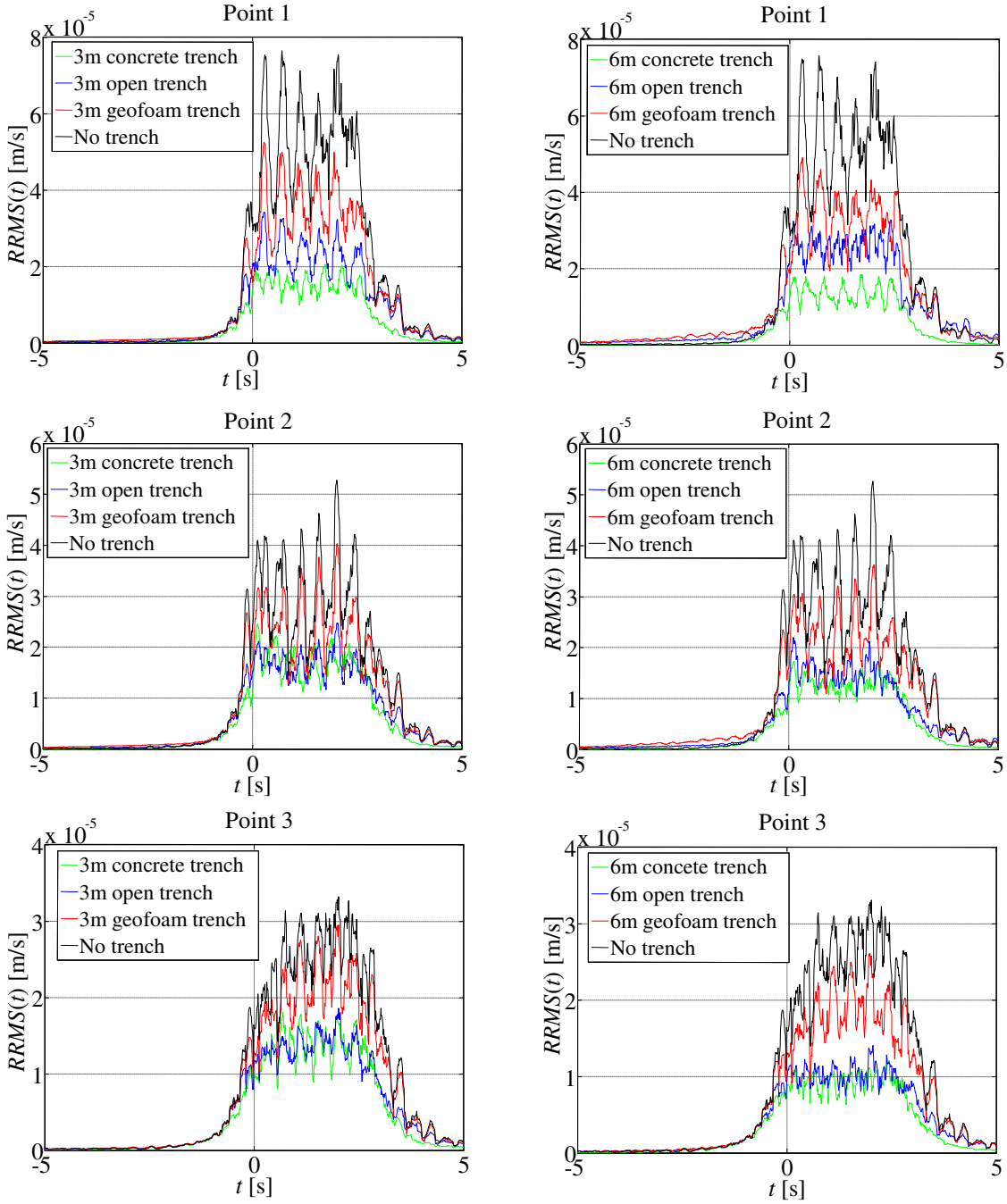

Figure 5.21: *RRMS* for distinct trench solutions and receivers

The reason why the concrete trenches outperform the geofoam trenches when acted upon by moving loads (as opposed to what happens in the 2D simulations) is related to their high bending stiffness. As explained in some works (Coulier et al., 2013a; Coulier et al., 2013b; Dijckmans et al., 2013), the transmission of plane waves in the soil with a longitudinal wavelength smaller than the longitudinal bending wavelength of the barrier is hindered. In other words, when the longitudinal wavelength λ_y of a propagating wave is smaller than the free bending wavelength in the barrier λ_{yB}, but not shorter than the Rayleigh wavelength of the soil λ_R, then the waves are reflected at the barrier due to its bending stiffness (waves

travelling with longitudinal wavelength smaller than the Rayleigh wavelength are evanescent in the transverse direction and therefore the barrier is ineffective for those cases). In plane strain conditions, the wavelength is infinite and so the bending stiffness has no influence, but in 3D conditions, waves can propagate in all directions and so surface waves that propagate with an angle θ such that $\sin\theta > \frac{\lambda_R}{\lambda_{yB}}$ are reflected by the trench. As a result, for standing point sources, there is a triangular zone delimited by the critical angle $\theta_{cr} = \sin^{-1}\frac{\lambda_R}{\lambda_{yB}}$, inside which the reduction of vibrations is not as significant as outside the mentioned zone. For the case of moving harmonic loads, the generated waves propagate with angles $\theta = \sin^{-1}\frac{k_R V}{\omega - \omega_0}$, and therefore the waves that impinge the barrier with an angle higher than θ_{cr} are also reflected.

The wavenumbers of the free longitudinal bending waves $k_{yB} = \frac{2\pi}{\lambda_{yB}}$ for the 3 m concrete and 3 m foam trenches (vertical bending, transverse bending and torsion), and the Rayleigh wavenumbers of the soil are represented in Figure 5.22. Superimposed is the line $k_y = \left|\frac{\omega - \omega_0}{V}\right|$ for $\omega_0 = 80\pi$ rad/s (this line corresponds to the integration path for a moving load with speed V and oscillation frequency $f_0 = 40$ Hz). As can be observed, the portion of transversely propagating waves ($k_y < k_R$) that reach the barrier with angles greater than the critical angle θ_{cr} ($k_y > k_{yB}$) is greater for the concrete trench than for the geofoam trench. Furthermore, for the geofoam trench, the transverse bending stiffness and the torsional stiffness of the barrier contribute for the reflection of waves only above the frequency $f = 60$ Hz. These aspects justify the considerable increase of performance of the concrete trenches and explain why they outperform the geofoam trenches. In general, the reflecting property expressed in the last paragraph also supports the idea that 2D simulations are not sufficient to predict with enough accuracy the abatement of vibrations induced by moving loads, since the obtained results will tend to underestimate the actual reduction.

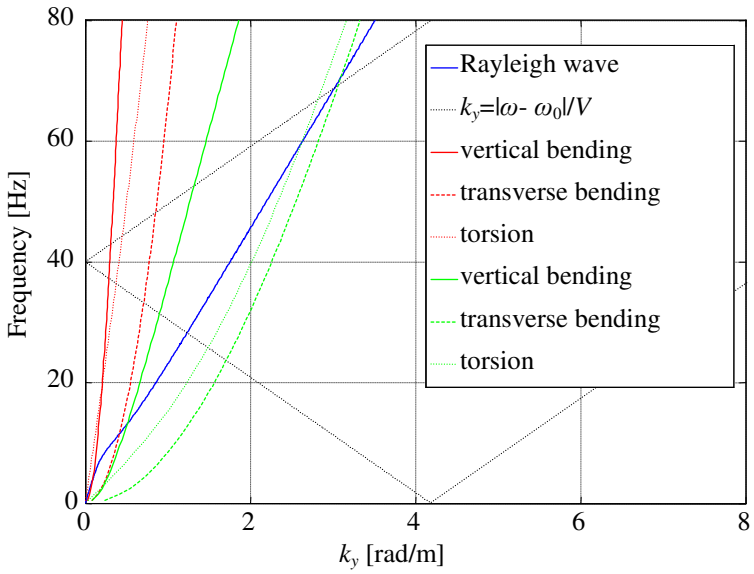

Figure 5.22: Rayleigh wavenumber (blue) and free bending wavenumber of 3 m concrete trench (red) and 3 m geofoam trench (green)

Behavior of trenches for various longitudinal positions

The insertion losses shown in Figure 5.20 concern receivers at the longitudinal position $y=0$. For other longitudinal positions, since the amplitudes of the moving forces are the same, with or without a trench, it could be expected that the ratios between the responses of the two scenarios were the same, and thus that the insertion losses for $y=0$ were representative of the problem. However, a deeper examination of the expression that yields the displacements induced by a set of moving forces with multiple frequencies reveals the opposite. This expression is derived from eq. (4.18) and assumes the form

$$u(x,y,\omega)=\frac{1}{V}\sum_{i=1}^{N_{\omega_0}}\sum_{j=1}^{N_{y_0}}P_j(\omega_{0i})\tilde{u}\left(x,\frac{\omega-\omega_{0i}}{V},\omega\right)\mathrm{e}^{\mathrm{i}\frac{\omega_{0i}-\omega}{V}(y-y_{0j})} \tag{5.6}$$

in which N_{ω_0} is the number of oscillation frequencies, N_{y_0} is the number of moving forces, $P_j(\omega_{0i})$ is the amplitude of the j^{th} force for the i^{th} oscillation frequency, ω_{0i} is the i^{th} oscillation frequency, y_{0j} is the longitudinal position of the j^{th} force at $t=0$, (x,y) are the coordinates of some point, and $\tilde{u}\left(x,\frac{\omega-\omega_{0i}}{V},\omega\right)$ is the 2.5D transfer function. Thus, the ratio A_r defined in equation (5.2) becomes

$$A_r(x,y,\omega)=\frac{\left|\sum_{i=1}^{N_{\omega_0}}\sum_{j=1}^{N_{y_0}}P_j(\omega_{0i})\tilde{u}_{\text{Trench}}\left(x,\frac{\omega-\omega_{0i}}{V},\omega\right)\mathrm{e}^{\mathrm{i}\frac{\omega_{0i}-\omega}{V}(y-y_{0j})}\right|}{\left|\sum_{i=1}^{N_{\omega_0}}\sum_{j=1}^{N_{y_0}}P_j(\omega_{0i})\tilde{u}_{\text{NoTrench}}\left(x,\frac{\omega-\omega_{0i}}{V},\omega\right)\mathrm{e}^{\mathrm{i}\frac{\omega_{0i}-\omega}{V}(y-y_{0j})}\right|} \tag{5.7}$$

and, in order for this ratio to be location independent, the following condition is necessary

$$\frac{\tilde{u}_{\text{Trench}}\left(x,\frac{\omega-\omega_{0i}}{V},\omega\right)}{\tilde{u}_{\text{NoTrench}}\left(x,\frac{\omega-\omega_{0i}}{V},\omega\right)}=\text{constant},\qquad i=1...N_{\omega_0} \tag{5.8}$$

The previous statement can be fulfilled only if $N_{\omega_0}=1$, and that leads to the conclusion that within the same transverse alignment and for multiple excitation frequencies, the ratio A_r in equation (5.7) and the insertion losses defined in eq. (5.4) change with the longitudinal coordinate y.

To assess the variation of the insertion losses, these values are calculated for 100 receivers placed at the alignment $x=15$ m and spread between the longitudinal positions $y=-30$ m and $y=30$ m. The results are plotted in Figure 5.23.

It is demonstrated that within each frequency band the maximum variation can reach 10 dB, which is a considerable value. Nevertheless, above the frequency 10 Hz, all trench solutions offer an attenuation of vibrations for the great majority of longitudinal positions (with very few exceptions).

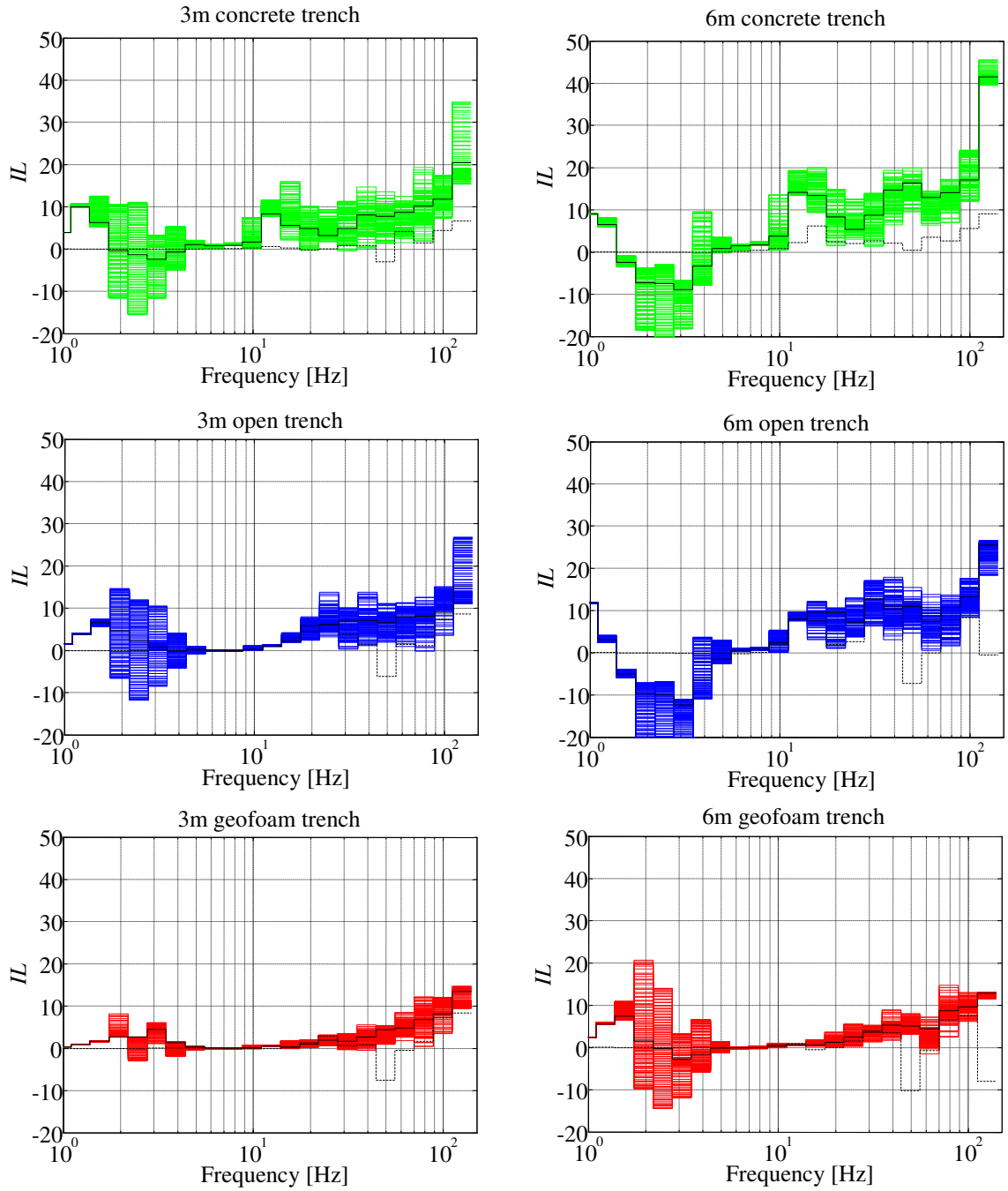

Figure 5.23: Insertion losses for receivers placed at $x = 15$ [m] and $-30 < y < 30$ [m]. The black solid line represents the IL' curves for the maximum responses (defined in eq. 5.9). The dashed black line illustrates the *IL* assuming plane strain conditions

For a given longitudinal position, the insertion loss varies between the maximum and the minimum values of the "insertion envelope". Thus, for design purposes, considering only the lower limit of the envelope yields over protective measures, while considering merely the upper limit yields very relaxed conditions. Therefore, it is recommended to consider a curve that passes through an intermediate value of both limits. A possible option is the curve calculated with the maximum responses, i.e.,

$$IL'(x,\omega) = 20\log_{10}\frac{\max\limits_{y}\left|u_z^{\text{NoTrench}}(x,y,\omega)\right|}{\max\limits_{y}\left|u_z^{\text{Trench}}(x,y,\omega)\right|} \tag{5.9}$$

For each frequency band, this curve considers the ratio of the response of points placed at different longitudinal positions. In this way, the value IL' cannot be considered as a reduction measure for a given point, but, instead, should be perceived as a reduction measure for the maximum response along a given alignment. The curves IL' for the $x = 15$ m alignment are represented in Figure 5.23 through solid black lines.

For comparison purposes, the *IL* lines for 2D line loads are also represented in Figure 5.23 (black dashed line). It is observed that for the concrete trenches, the 2D results underestimate their efficiency, even when compared with the lower limits of the envelope. As for the open and geofoam trenches, the 2D results run close to the lower limit of the envelope, but there are frequency bands where the 2D results predict amplification of displacements, a scenario that does not correspond to reality. This comparison corroborates that 2D results underestimate the efficiency of trenches and, therefore, plane strain conditions are not applicable for cases that include moving vehicles.

One interesting aspect that can be observed in Figures 5.20 and 5.23 is the amplification of the response below 5 Hz. The low frequency response of the soil is due to the quasi-static component of the interaction forces, and its effect evanesces with the distance (i.e., mainly evanescent waves contribute to the response of the ground in the low frequency range). Since the trench is placed at a small distance from the track, the evanescent waves still reach the trench with a considerable amount of energy, and so their interaction with the trench produces new waves that reach further than what they would if no heterogeneity was encountered. That is in fact the reason why amplifications are greater for 6 m trenches than for 3 m trenches (the energy of evanescent waves is distributed with the depth and, therefore, the deeper the trench, the greater the energy that "collides" with it), and why amplifications are larger for concrete and open trenches than for geofoam trenches (the material contrast in the first two is greater). In any case, these amplifications are inconsequent because the contribution of this low frequency content for the response of the ground surface is negligible when compared to the contribution of the medium and high ranges. This situation is represented in Figure 5.24, which plots the frequency content of the vertical velocities evaluated at the 100 receivers mentioned in the first paragraph of this sub-section for the non-mitigated scenario and for the 3 m and 6 m concrete trenches.

5.3.4 Conclusions

In section 5.3, the efficiency of distinct trench solutions is investigated numerically with the aid of the 2.5D BEM-FEM approach. The investigations comprise 2D simulations ($k_y = 0$), carried out to assess the need for the inclusion of the track in the numerical models, and 3D simulations of moving vehicles, performed to compare and rate the trench solutions and to investigate some features of the problem, namely the influence of the trenches in the train-track interaction phenomenon and the efficiency of trenches along the longitudinal direction.

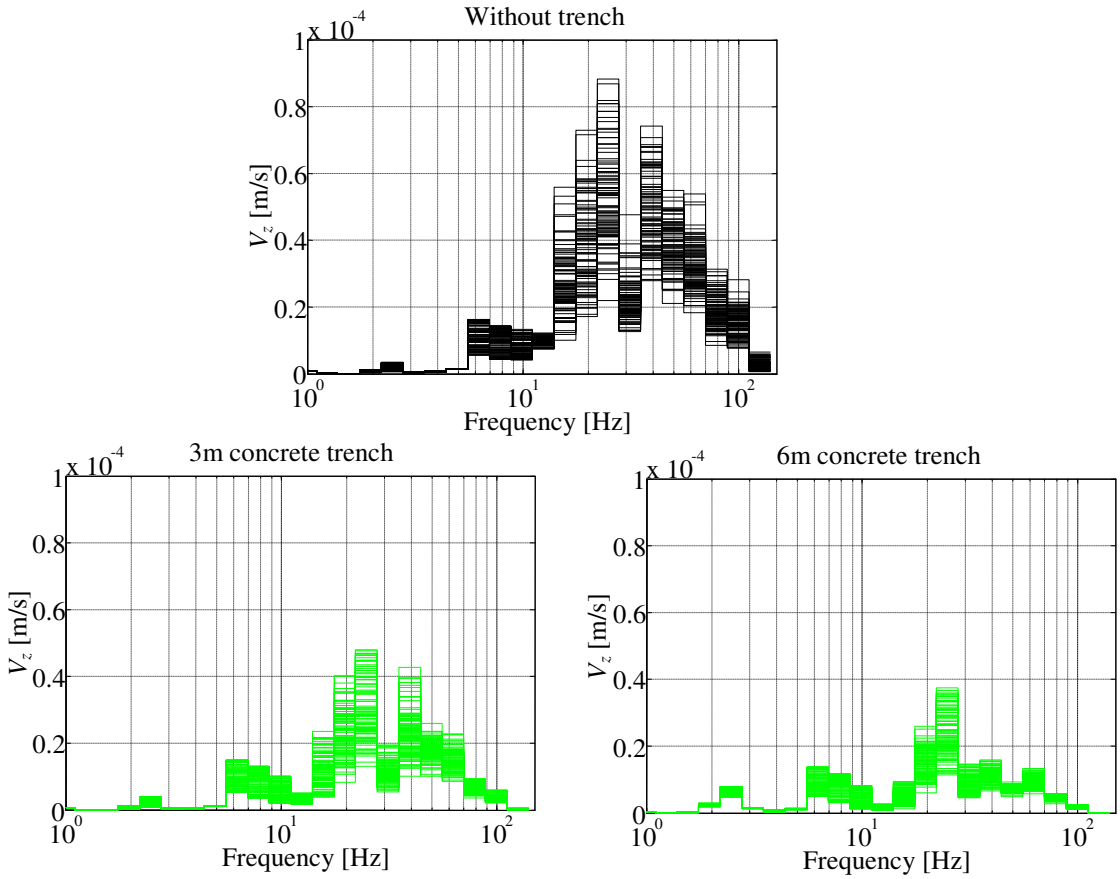

Figure 5.24: Frequency content of the vertical velocities for receivers placed at transverse position $x = 15$ m and longitudinal position $-30 < y < 30$ m

The following conclusions are achieved throughout this section:

1. Neglecting the track leads to higher vibration levels in the soil surface (at least for short and medium distances) and to lower efficiency of trenches. Thus, its inclusion in the numerical model is necessary to assess the need for mitigation measures and to estimate the efficiency of the abatement solutions more accurately.
2. The presence of the trench does not influence the train-track interaction phenomenon. This conclusion is important because it permits to calculate the train-track interaction forces for the non-mitigated scenario and to use these forces in the evaluation of trench like measures.
3. The behavior of trenches when acted upon by moving loads is very different from their behavior when acted upon by 2D line loads. In fact, 2D simulations tend to underestimate the efficiency of trenches, and that is more pronounced for concrete trenches than for geofoam trenches.
4. Ranking the in-fill materials according to the efficiency of the trench, from the 2D simulations open trenches are placed first, geofoam trenches second, and concrete trenches in last place, while from the 3D simulations concrete trenches and open trenches come together in the first place, and geofoam trenches are placed last, clearly below the other two.

5. In the studied example, within the same longitudinal alignment the insertion losses may vary up to 10 dB, which is a considerable value. Thus, for design purposes, to consider only the lower limit of the envelope leads to over protective measures, while to consider merely the upper limit yields relaxed conditions. Therefore, it is recommended to consider the insertion loss curve based on the maximum responses of the alignment.

5.4 Effect of trenches on a nearby structure

5.4.1 General description of the building

The response of a structure due to the passage of the Alfa train is now analyzed. The objective is to assess the efficiency of the trench solutions in reducing the vibration levels inside a building situated near a railway track.

The target structure consists in a two story building whose geometry is represented in Figure 4.33. It is composed of vertical columns with cross section 0.4×0.4 m^2, horizontal beams with 0.4 m of width and 0.5 m of height, and slabs with 0.3 m of thickness. The structure considered in this example differs from the structure considered in chapter 4 in two aspects: firstly, the slabs are flexible; secondly, the slabs are supported on beams and not directly on the columns.

The material considered for all components of the structure is concrete, being its properties given in Table 5.4. A distributed mass of 200 kg/m^2 is added to the floors and a mass of 100 kg/m^2 is added to the roof-top. The footings are assumed massless and rigid, with dimensions 1.5×1.5 m^2. The distance from the nearest side of the building to the central alignment of the track is 20 m.

In terms of the numerical model, columns and beams are simulated with 2 noded Euler beams, and the slabs are simulated with the 4 noded shell elements (the finite element model is created in ANSYS — www.ansys.com — being the corresponding matrices exported and used in the implemented procedure). The maximum size of the elements is 0.5 m. Each rigid footing is divided into 25 equally sized square boundary elements (0.3 m of side). The FEM mesh used in the numerical model is represented in Figure 5.25.

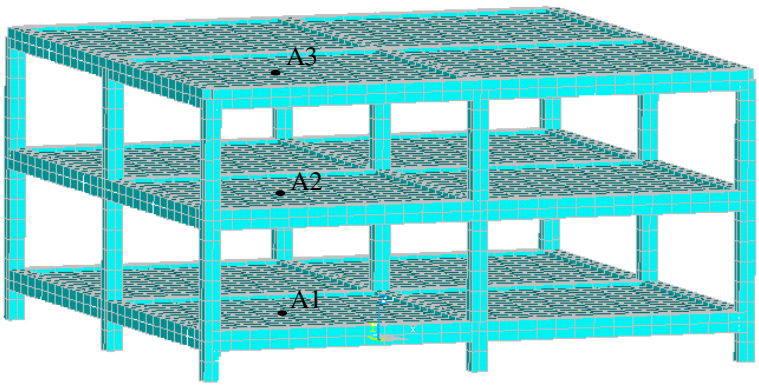

Figure 5.25: Finite element mesh of the building (generated with ANSYS)

5.4.2 Natural frequencies of the building

When a structure is subjected to incident wave-fields (seismic waves, or, as in the problem at hand, vehicle induced vibrations), it is expected that the structural response be amplified at its natural frequencies.

The natural frequencies of a structure depend on its geometry, on the material properties (elastic constants and density), and on the boundary conditions. For the structure represented in Figure 5.25, assuming that it rests on a stiff foundation, the natural frequencies ω_j correspond to the solutions of

$$\det\left(\mathbf{K}-\omega_j^2\mathbf{M}\right)=0 \tag{5.10}$$

in which $\mathbf{K}$ and $\mathbf{M}$ are the stiffness and mass matrices of the structure. There are as many natural frequencies ω_j as the number of rows and columns in $\mathbf{K}$ and $\mathbf{M}$ (approximately 16000 for this example), and all of them are real. The lowest 100 natural frequencies are depicted in the histogram of Figure 5.26, and the mode shapes associated with the natural frequencies below 20 Hz are represented in Appendix 5.1. Since the structure is symmetric, some natural frequencies ω_j are repeated, namely those associated with floor drifting and those associated with the bending of the slabs. The repeated frequencies are indicated in Appendix 5.1 together with the mode shapes.

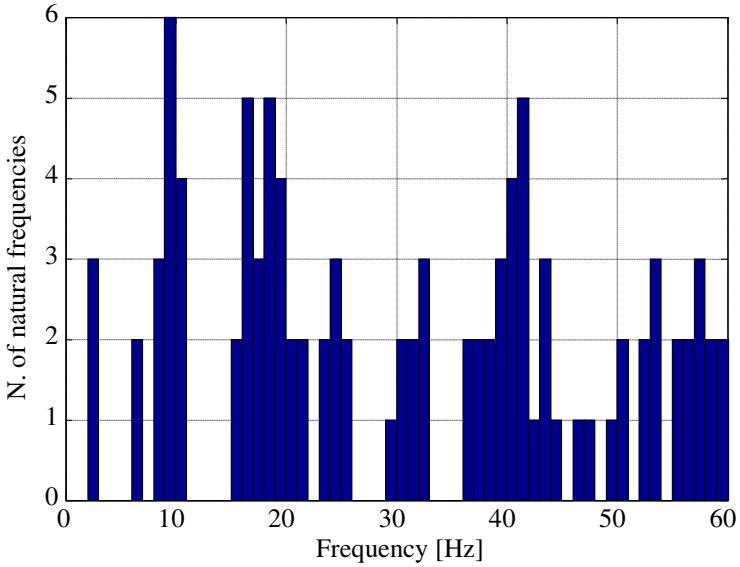

Figure 5.26: Number of natural frequencies per frequency interval (intervals of 1 Hz)

If more realistic boundary conditions are assumed, i.e., if the structure is considered to be resting on the soil (and if this is modeled with boundary elements), then the natural frequencies ω_j correspond to the solutions of

$$\det\left(\mathbf{K}+\mathbf{K}_{\mathrm{BEM}}(\omega_j)-\omega_j^2\mathbf{M}\right)=0 \tag{5.11}$$

in which $\mathbf{K}_{\mathrm{BEM}}(\omega)$ is the frequency dependent stiffness matrix of the soil, calculated as explained in chapter 3. Contrarily to the solutions of (5.10), since the soil absorbs waves and therefore introduces damping to the system, the natural frequencies ω_j of (5.11) are complex.

Nevertheless, some frequencies have small imaginary components and thus the structure can still resonate if excited near these frequencies.

Only the almost real solutions ω_j are of interest to the current analysis. These solutions can be found by exciting the structure in a wide range of frequencies and then observing at which frequencies the response is amplified. In this way, to find the natural frequencies, the structure is loaded in points A1, A2 and A3 (indicated in Figure 5.25) and the displacements of the same points are calculated. The loads are applied both in the horizontal (x) and vertical (z) directions, and the displacements are calculated in the direction of the loads. The obtained responses are represented in Figure 5.27, together with analogous results for the case of the rigid foundation.

The results presented in Figure 5.27 show that the presence of the soil (blue curves) cancels some of the natural frequencies of the rigidly supported structure (red curves). Furthermore, the amplification of the response near the natural frequencies appears to be smaller when the soil is considered, which can be justified by the damping introduced in the system due to the radiation of waves into the soil.

Figure 5.26 and Figure 5.27 show that there is a set of natural frequencies that lies in the frequency range below 10 Hz, which according to the conclusions of section 5.3, is the frequency range at which the trench solutions are ineffective. It can therefore be concluded that amplification problems may arise below the frequency 10 Hz. This issue is investigated in the following sub-sections.

5.4.3 Building response for the non-mitigated case

Before evaluating the reduction achieved by the trench solutions, the building response is first investigated considering the non-mitigated scenario. Figure 5.28 shows the horizontal and vertical components of the displacements of points A1, A2 and A3 that are induced by the passage of the Alfa Pendular train. The displacements are represented in one-third-octave bands, and for comparison purposes, the incident displacements at the central footing are also represented.

Figure 5.28a-b reveals amplification of the horizontal displacements u_x and u_y in the frequency intervals 2-3 Hz and 6-8 Hz. These frequencies correspond to the lower natural frequencies of the building, and are associated with translations of the slabs and rotation about their vertical axis (see Appendix 5.1). Above the frequency 10 Hz, the horizontal vibrations are almost completely filtered by the building, namely for the points A2 and A3.

Observe that for the frequency intervals 2-3 Hz and 6-8 Hz, the values of the displacements are consistent with the modal shapes of the associated natural frequencies: at the frequencies 2-3 Hz the horizontal displacements are greater at A3 than at A2, which in turn are greater than at A1 (first, second and third modal shapes); at the frequencies 6-8 Hz the displacements are greater at A2 than at the other two points (fourth, fifth and sixth modal shapes). Observe also that there is an amplification around the frequency 20 Hz, which is felt only at point A1. This amplification is justified by the natural frequency f = 18.069 Hz, whose associated modal shape corresponds to horizontal translations of the first floor.

In what concerns the displacements in the vertical direction (Figure 5.28c), amplifications occur in the frequency interval 6-30 Hz. This interval is explained by the bending motion of the slabs, whose corresponding modal shapes are associated with natural frequencies above 8 Hz. Moreover, in the frequency interval between 10 and 15 Hz the amplifications are

interrupted, coinciding this interval with the range where no natural frequency is observed (Figure 5.26 and Appendix 5.1: natural frequencies jump from 11 Hz to 15.7 Hz).

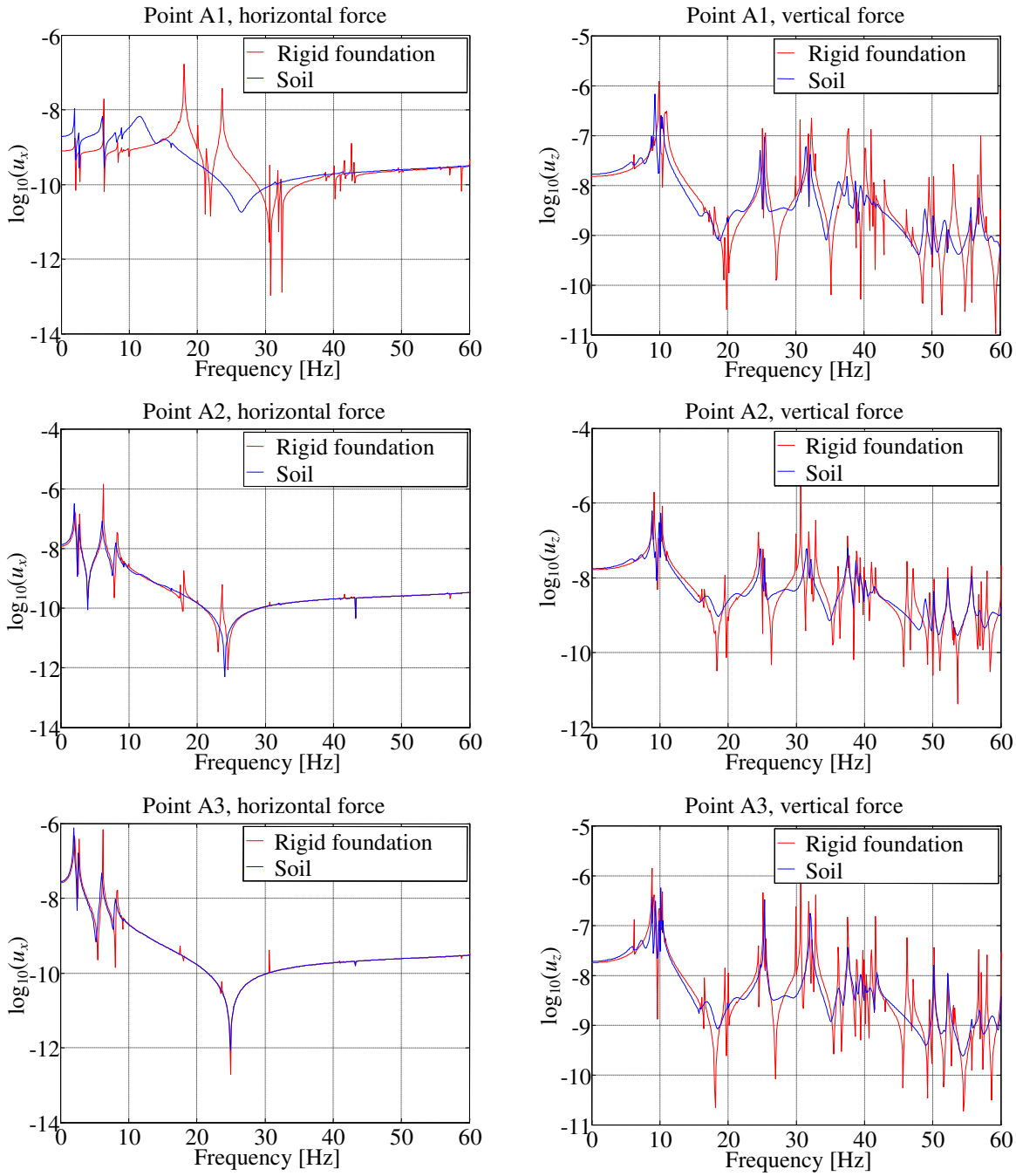

Figure 5.27: Displacements of points A1, A2 and A3 due to horizontal and vertical loads applied at the same points

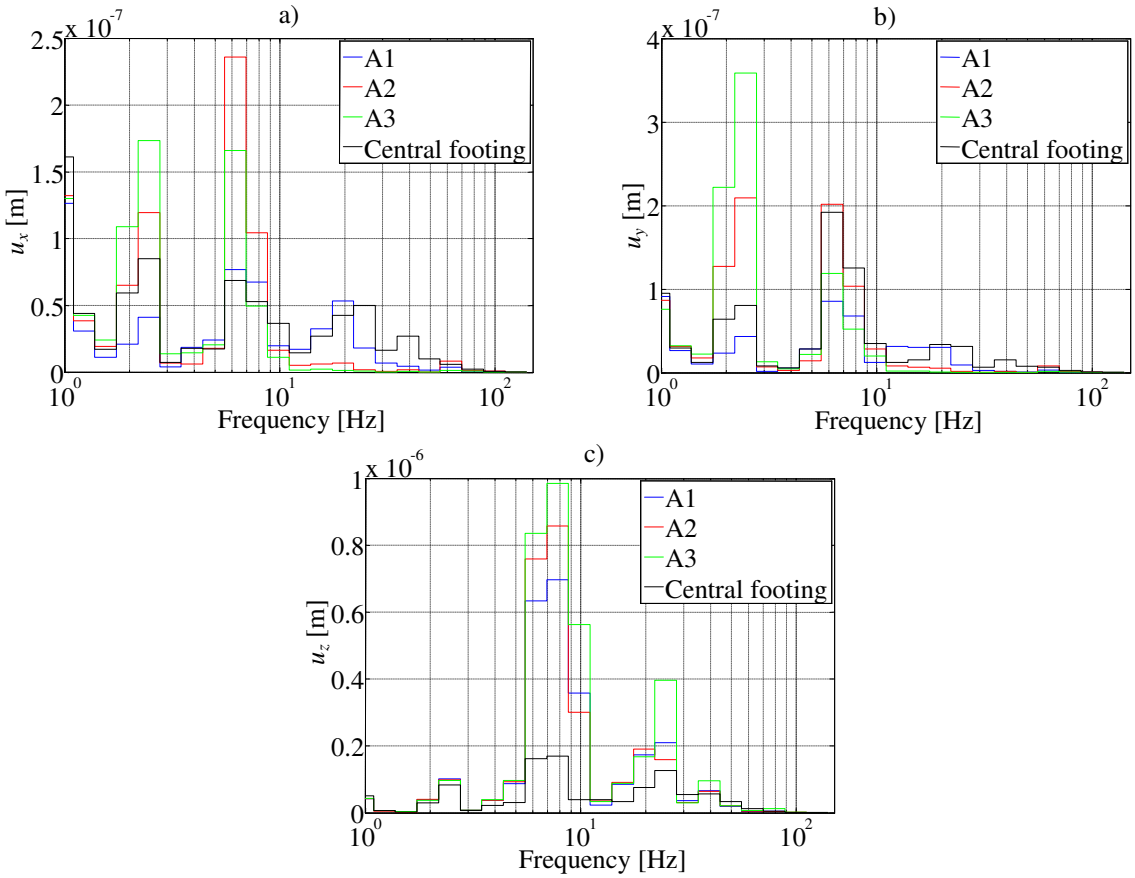

Figure 5.28: Displacements of points A1, A2 and A3 and incident displacements at the central footing: a) horizontal x displacements; b) horizontal y displacements; c) vertical z displacements

5.4.4 Reduction achieved by trenches

The reduction of vibrations in the building due to the six trench solutions described in section 5.3 is now studied. For that, the insertion losses defined by equation (5.4) are calculated for point A2 and represented in Figure 5.29 (for the horizontal directions, the insertion losses are calculated using the horizontal displacement in place of the vertical displacement; the results for points A1 and A3 are very similar and are not shown here).

Starting with the analysis of the horizontal vibrations, it can be observed that trenches lead to moderate amplifications in the frequency range below 4 Hz, have practically no influence on the frequency interval 4-10 Hz, and reduce the vibrations above 10 Hz. It has been seen in sub-section 5.4.3 that the horizontal response of the building is dominated by the lower natural frequencies, which are below 10 Hz. It can therefore be concluded that if there are problems associated with horizontal vibrations, the trenches will be ineffective, potentially causing amplifications instead of attenuation. Furthermore, for frequencies above 10 Hz the building filters the horizontal vibrations, and therefore the effect of the trench is irrelevant.

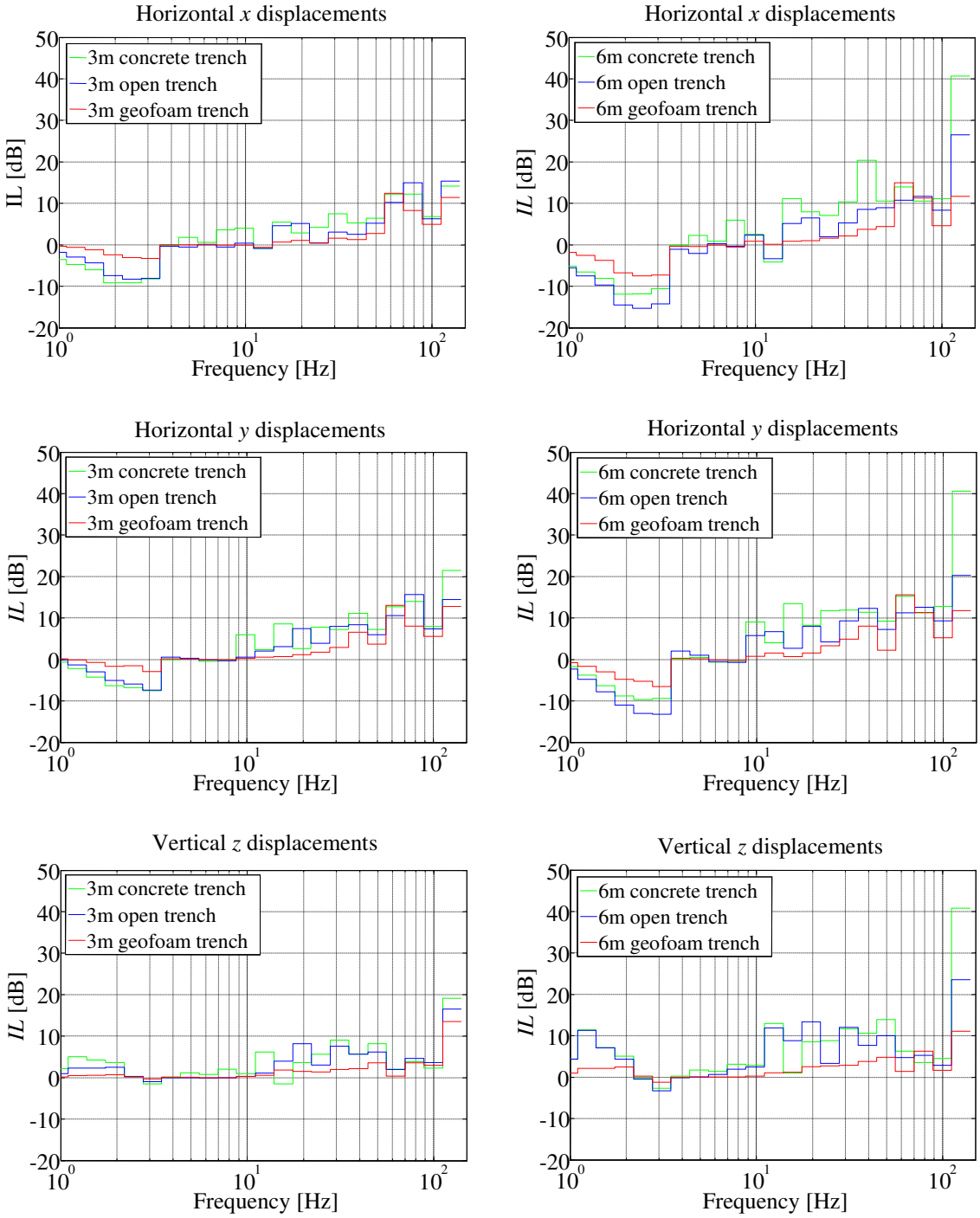

Figure 5.29: Insertion losses for point A2

Concerning the effect of trenches on the vertical vibrations, in Figure 5.29 it can be observed that below the frequency $f = 10$ Hz the reduction is negligible, thus failing to reduce the vibrations at the lowest natural frequencies associated with the bending motion of the slabs (at these frequencies, an amplification of the vertical vibrations in the building is observed). Moreover, above the frequency $f = 10$ Hz, the insertion losses are very modest (below 10 dB, which is equivalent to a reduction to one third of the original value). It can also be observed

that the 6m deep trenches perform better than the 3m deep trenches. Overall, it is concluded that trenches may have a beneficial effect.

As a final note concerning this topic, the insertion losses calculated for the building are quite similar to the insertion losses calculated for the ground response at the position of the building (incident wavefield). For instance, if the two plots at the bottom of Figure 5.29 are compared with the insertion losses of Point 3 represented in Figure 5.20, it can be observed that they are quite similar. The insertion losses for the horizontal response of the ground are not shown in this work, but similar conclusions can be obtained for that direction.

5.5 Conclusions

In this chapter, the methods described throughout chapters 2-4 are employed in the analysis of vibrations induced by trains and in the assessment of trench-like mitigation solutions. Chapter 5 starts with a parametric study of trenches, then the behavior of distinct trench solutions is investigated, and finally the effect of the trenches on the vibrations inside a building is assessed.

Based on the parametric study, it is concluded that the behavior of trenches depends on several parameters such as its dimensions, stiffness and density of the in-fill material, and properties and stratification of the soil. Each parameter is investigated separately, and so different conclusions can be obtained if different default scenarios are assumed. In any case, the efficiency of trenches largely depends on their depth and width, being the trenches ineffective when these dimensions are much smaller than the characteristic wavelength (Rayleigh wave) of the soil. For this reason, trenches are effective only in the medium and high frequency ranges.

Concerning the mitigation of the vibrations induced by the Alfa Pendular train, some aspects are studied, namely the need for the inclusion of the track in the numerical model, the impact of the trenches in the train-track interaction phenomenon, and the variability of the reduction of vibrations provided by trenches along the longitudinal position. It is concluded that the track must be included in the numerical model, that trenches do not change significantly the train-track interaction forces, and that the relative reduction may vary up to 10 dB within the same longitudinal alignment. It is also observed that concrete and open trenches present similar reduction levels, while geofoam trenches do not perform as well as the other two (this ranking order differs from the 2D ranking).

In section 5.4 the response of a building induced by the passage of an Alfa train is evaluated. It is observed that some amplifications occur at the natural frequencies of the structure, being the amplification of the horizontal response associated with the floor-shifting modes and the amplification of the vertical response associated with the slab-bending modes. Since the lower natural frequencies of the building are in the low frequency range (below 10 Hz), the trench solutions are ineffective in neutralizing these amplifications, possibly aggravating the horizontal response. Nevertheless, if problems are detected above 10 Hz, then the trench solutions may provide some protection. The reduction achieved inside the building resembles the reduction obtained for the soil surface at the location of the building. For this reason, the response of the building needs to be calculated only for the non-mitigated scenario.

As a final comment, it must be stressed that the results reported in section 5.3 and 5.4 concern the line near Carregado. The reductions obtained in different scenarios or at different train speeds may not necessarily be equivalent to the results reported here. Further studies are

required to contribute to the development of rules of thumb for the design of this type of mitigation measures.

6. Conclusions and recommendations for further research

6.1 Conclusions

The work described in this dissertation addresses the problem of vibrations induced by trains in the surrounding environment. All stages relevant to the problem are considered, namely the generation stage, in which the train interacts with the track-ground system, the propagation stage, in which the vibrations propagate through the track and ground, and the reception stage, in which the mentioned vibrations reach the building and induce its dynamic response. Mitigation at the propagation stage using trenches is also addressed.

The major focus of the work is on the development and implementation of numerical tools for the simulation of the three stages of the problem. The selected numerical approaches are described throughout chapters 2-4. In chapter 5, the derived tools are used to analyze trench like mitigation solutions.

Numerical approaches have to fulfill several requirements in order to provide reliable predictions, namely:

1. Moving nature of the source – while standing harmonic loads induce harmonic responses, moving loads induce transient responses characterized by a wide range of frequencies. Therefore, simplistic models in which moving loads are replaced by standing loads are not sufficient;
2. Train-track interaction – if the interaction is disregarded, then the moving forces remain constant in time (quasi-static components) and the induced response evanesces with the distance to the track. In order to obtain the response at remote positions, the dynamic components must also be accounted for. These components result from the solution of a train-track interaction problem;
3. Adequate soil model – soil connects the track with nearby buildings, and therefore its consideration is of great importance. The propagation of waves in the soil is affected by heterogeneities found along the propagation path. If these heterogeneities are neglected, the obtained results may be inaccurate;
4. Mitigation measures – in order to assess the efficiency of mitigation measures, they must be considered in numerical models, whether these measures are applied at the source, at the propagation path, or at the receiver.

The above mentioned requirements can be fulfilled through the use of three-dimensional finite element models, where the components of train, track, soil and building can be simulated with a suitable type of element and constitutive behavior (eventually nonlinear). However, the use of 3D FEM to solve soil-structure interaction problems (such as track-ground and building-ground interaction) leads to extremely large systems of equations whose solution is time consuming. For this reason, and in order to simplify the problem, some assumptions are made, namely the consideration of:

1. Linear behavior of the material and linear contact between train and track – this assumption enables the analysis to be performed in the frequency domain;
2. Constant cross section of the track – this assumption allows the problem to be analyzed in the wavenumber-frequency domain (2.5D domain). In other words, the 3D problem is reduced to a series of smaller 2D problems, which are faster to solve;
3. Constant speed of the train – the 2.5D models are exact in the simulation of loads (constant or oscillating) moving at constant speed;
4. Horizontally stratified soil –this assumption is commonly used in the literature, and allows the soil to be simulated with the boundary element method and with the thin-layer method, a combination that results in a very efficient strategy;
5. Weak coupling between the nearby building and the track – or in other words, waves that propagate from the track to a nearby building are accounted for, but waves that are reflected by the building and return to the track are neglected. This assumption allows the solution of the problem in two distinct phases: a first phase in which the generation and propagation stages are accounted for and in which the presence of the building is disregarded; a second phase in which the response fields calculated in the first phase are prescribed at the building, thus obtaining its response.

Based on the above mentioned requirements and assumptions, the following strategies are followed:

- Generation stage (train-track interaction): the train is simulated with a 3D multi-rigid-body approach, while the stiffness matrices for the track-ground system are obtained with the 2.5D transfer functions of that system (see the next point). The equilibrium and compatibility equations are formulated in a moving frame of reference and solved in the frequency domain. This procedure yields the dynamic interaction forces between train and track;
- Propagation stage: a 2.5D BEM-FEM approach is used to solve the soil-track interaction problem. The track is modeled with finite elements while the track-ground interface is modeled with boundary elements. Heterogeneities in the soil, such as trenches, are modeled with the same strategy. The interaction forces calculated in the generation stage are used as inputs in the 2.5D BEM-FEM, and the response of the ground at any position, including the positions of the nearby building, is calculated. The presence of the building is neglected at this point;
- Reception stage: a 3D BEM-FEM approach is used to solve the soil-structure interaction problem. The response fields calculated in the previous stage are transformed to the 3D space and used as inputs in the 3D BEM-FEM model, whose solution provides the response of the building.

The fundamental solutions used to nurture the BEM (both 2.5D BEM and 3D BEM) are calculated with the thin-layer method (TLM). This aspect represents the main difference between the methodology used in this work and the strategies followed by other authors.

The TLM is described in chapter 2, where expressions for the 2.5D fundamental solutions are derived, and where perfectly matched layers (PMLs) are coupled with the TLM in order to simulate half-spaces. All the developments are validated through the calculation of the fundamental solutions of full-spaces and a posteriori comparison with analytical solutions. It is concluded that the TLM is in fact an efficient option for the calculation of fundamental

solutions of layered half-spaces. It is also concluded that the coupled TLM+PML scheme is significantly more efficient than the paraxial boundaries (PB) approach, which prior to this work was the favorite procedure to model half-spaces with the TLM.

The coupled BEM-FEM strategy is used to solve soil-structure interaction problems. The soil, of unbounded geometry, is modeled with boundary elements, while the structure (track or nearby building), of bounded and complex geometry, is modeled with finite elements. The advantages of the coupled BEM-FEM approach are the reduction of the number of degrees of freedom needed to model the domain (and in particular, the soil), and the consideration of the radiation of waves to infinity. The main disadvantage resides in the need for the calculation of the BEM matrices, which is usually time consuming.

The coupled BEM-FEM approaches are described in chapter 3. There, for the case of the 2.5D BEM, it is explained how to use the TLM to calculate the boundary element coefficients without resorting to spatial integrations, and thus avoiding the complications associated with the singularities of the fundamental solutions.

When compared with similar approaches, the main drawback of the 2.5D BEM-TLM strategy is the time needed for the calculation of the eigenmodes, which becomes large when the fundamental solutions are needed at deep positions. Nevertheless, for each soil profile, the eigenmodes only need to be calculated once for each frequency. They can thereafter be used to analyze different configurations of tracks, buildings and countermeasures.

The train-track interaction problem involves the coupling between a moving discrete structure and an invariant structure. While the moving vehicle is simulated in the 3D domain, the underlying structure (track-ground system) is formulated in the 2.5D domain, and so the coupling between the two structures is not straightforward. This issue is addressed in chapter 4, where the expressions for the dynamic interaction forces and the transformation of the 2.5D results to the 3D space domain are described. The link between the distinct procedures and stages is exemplified also in chapter 4.

It is convenient to point out that the 2.5D BEM-FEM procedure, the TLM, and the train-track interaction solution procedure have been implemented in the finite element software FEMIX (http://www.alvaroazevedo.com/femix/). The software is structured in such a way that the user only needs to provide information about the soil profile and respective TLM model, finite element model of track and mitigation measures, boundary element model for soil-structure interfaces, vehicle model (multiple rigid body model), irregularity profiles, and frequencies of interest. The program then proceeds to complete all necessary operations and returns the outputs requested by the user, both in the time domain and in the frequency domain. The user does not need to provide a transverse wavenumber sample for the transformation of the fundamental solutions from the (k_x, k_y, ω) domain to the (x, k_y, ω) domain, since that transformation is accomplished internally by the TLM. The program is generic enough to account for surface lines or tunnels, stratification of the soil and obstacles in the propagation path (e.g., trenches).

The 3D BEM-FEM procedure has not been implemented in the FEMIX software, but a MATLAB module has been written with the purpose of calculating the response of a building due to an incoming wave field. The subroutine requires a binary file with the incident displacement field (this file is an output of FEMIX), and text files with the stiffness and mass matrices of the building. These matrices have to be written in the Harwell-Boeing format, as provided by ANSYS through the command HBMAT. This subroutine only handles structures resting on the surface of layered half-spaces.

In chapter 5, the above mentioned programs are used to study the efficiency of trenches as mitigation solutions. First a parametric study is performed and then the behavior of trenches under realistic conditions is investigated. The main conclusion of the parametric study is that the efficiency of a trench depends mostly on its dimensions, being the trench ineffective when its depth is much smaller than the characteristic wavelength of the soil (Rayleigh wave). For this reason, trenches are effective only in the medium and high frequency range.

In what concerns the use of trenches for the reduction of vibrations induced by trains, it is observed that excluding the track from the numerical model results in underestimations of the induced vibrations and overestimations of the efficiency of trenches. It is also observed that trenches do not affect significantly the train-track interaction forces (at least for the problem analyzed) and that concrete trenches and open trenches present similar reduction levels, while geofoam trenches perform worse than the other two.

An important observation regarding the modeling of mitigation solutions is that 2D models are not appropriate for the simulation of the trench behavior, namely when the system is acted upon by moving loads. The results in chapter 5 show that 2D simulations overestimated the efficiency of geofoam trenches and underestimated the efficiency of concrete trenches.

Regarding the reduction observed in nearby buildings, it is seen that trenches fail to diminish the amplifications at the low natural frequencies caused by the passage of trains. On the contrary, trenches are effective in reducing the vibrations at high frequencies (frequencies above 10 Hz for the case considered).

6.2 Recommendations for further research

Taking the FEMIX program and the MATLAB modules developed in the course of this thesis as framework for future investigations, the following studies are of great interest.

- Vibrations induced by underground trains: the examples presented in this thesis only consider surface lines. Nevertheless, trains running on tunnels are also a reality inside cities, and due to their close proximity to buildings, they may have a negative impact on inhabitants and equipments.
- Mitigation measures: in chapter 5 of this thesis, trenches are studied as measures for the abatement of vibrations induced by trains. Nevertheless, the conclusions obtained in that chapter refer to the particular problem there considered, and so the extension of the conclusions to different scenarios may be inappropriate. Thus, further studies are needed, and if possible, rules of thumb for their design should be attempted. Additionally, different mitigation solutions should be investigated. The developed programs are prepared to incorporate several mitigation solutions, whether they are applied at the source (e.g., suspension systems of the train, type of track, resilient materials in the track), at the propagation path (wave impeding blocks, for example), or at the target building (compartment isolation, for example). Studies on these measures can be found in the literature, but further studies are needed.

Additionally, improvements are required so that different studies become possible. For example, to solve each of the 6m deep trench problems described in chapter 5 takes a couple of days, which renders sensitive analyses impractical. In order to reduce the computation times, the following strategies are recommended.

- Reduced modal superposition: in the 2.5D BEM-FEM procedure, the step that is more time consuming is the calculation of the boundary element matrices. Their calculation

relies on a modal superposition, which in this work is performed combining all the vibration modes. It is known that vibration modes whose eigenvalues contain a large imaginary component are evanescent with the distance to the source, and therefore their contribution can be neglected when a collocation point and a boundary element are far from each other. To account for this feature may save some time in the computation of the boundary matrices.

- Parallel computing (GPU vs CPU): the objective is to reduce the computation time, which for more complex geometries (such as when discontinuities/heterogeneities are considered in the soil) may become excessively time consuming. In this work, GPU computation of the BEM matrices has been attempted, but the time reduction was not significant (CPU and GPU calculation took roughly the same time). The author believes that his implementation does not access the GPU memory in the most efficient way, and so he believes that better performances can be obtained.
- Parallel computing ("supercomputers"): the parallelization attempted in this work is performed in the calculation of the BEM matrices, but parallelization can be implemented at a higher level. Since the same type of problem needs to be solved for each wavenumber-frequency pair (k_y, ω), and since each of these 2.5D problems can be solved independently from the others, then the calculations can be distributed across different computers. If multiple computers or if supercomputers are available, then distributing the calculations across several processing units is expected to result in a considerable speed up.

Lastly, apart from the improvements associated with computation time, some of the limitations of the programs can be overcome so that new scenarios can be analyzed.

- Buried structures: the formulation of the 3D BEM-FEM procedure in chapter 3 is generic, but the method has been implemented only for structures resting at the surface. The reasons for this limitation are complications associated with the evaluation of the boundary integrals, which cannot be performed analytically. Furthermore, since the mesh is three dimensional, the time needed for the calculation of the BEM matrices may render the problem impracticable. A promising alternative for the calculation of the stiffness matrices of the soil is the use of finite elements coupled with perfectly matched layers (FEM+PML).
- Periodic geometries: in this thesis, it is assumed that the geometry is invariant in the longitudinal direction. There are, however, scenarios for which periodicity cannot be neglected, as for example, isolation of vibrations by means of rows of piles. In that example, the space between consecutive piles plays an important role in the efficiency of the measure, and therefore invariant models are revealed to be inadequate, being a more appropriate model one that accounts for the periodicity of the geometry.

Appendix I

Matrices $\mathbf{D}_{\alpha\beta}$ for cross-anisotropic materials

Based on the constitutive matrix $\mathbf{D}$ defined in equation (2.1), the matrices $\mathbf{D}_{\alpha\beta}$ in equation (2.13) are

$$\mathbf{D}_{xx}=\begin{bmatrix}\lambda+2G & 0 & 0\\ 0 & G & 0\\ 0 & 0 & G_t\end{bmatrix} \qquad \mathbf{D}_{xy}=\begin{bmatrix}0 & \lambda & 0\\ G & 0 & 0\\ 0 & 0 & 0\end{bmatrix} \qquad \mathbf{D}_{xz}=\begin{bmatrix}0 & 0 & \lambda_t\\ 0 & 0 & 0\\ G_t & 0 & 0\end{bmatrix}$$

$$\mathbf{D}_{yx}=\begin{bmatrix}0 & G & 0\\ \lambda & 0 & 0\\ 0 & 0 & 0\end{bmatrix} \qquad \mathbf{D}_{yy}=\begin{bmatrix}G & 0 & 0\\ 0 & \lambda+2G & 0\\ 0 & 0 & G_t\end{bmatrix} \qquad \mathbf{D}_{yz}=\begin{bmatrix}0 & 0 & 0\\ 0 & 0 & \lambda_t\\ 0 & G_t & 0\end{bmatrix}$$

$$\mathbf{D}_{zx}=\begin{bmatrix}0 & 0 & G_t\\ 0 & 0 & 0\\ \lambda_t & 0 & 0\end{bmatrix} \qquad \mathbf{D}_{zy}=\begin{bmatrix}0 & 0 & 0\\ 0 & 0 & G_t\\ 0 & \lambda_t & 0\end{bmatrix} \qquad \mathbf{D}_{zz}=\begin{bmatrix}G_t & 0 & 0\\ 0 & G_t & 0\\ 0 & 0 & D_t\end{bmatrix}$$

Thin-layer matrices for cross-anisotropic materials

Linear expansion

The shape functions for this case are

$$N_1=\zeta \qquad N_2=1-\zeta \qquad \zeta=z/h$$

where $z=0$ at the bottom surface of the thin-layer and $z=h$ at its top surface. The evaluation of equations (2.22) to (2.26) results in the following thin-layer matrices

$$\mathbf{M}=\frac{\rho h}{6}\begin{bmatrix}2\mathbf{I} & \mathbf{I}\\ \mathbf{I} & 2\mathbf{I}\end{bmatrix}$$

$$\mathbf{A}_{\alpha\alpha}=\frac{h}{6}\begin{bmatrix}2\mathbf{D}_{\alpha\alpha} & \mathbf{D}_{\alpha\alpha}\\ \mathbf{D}_{\alpha\alpha} & 2\mathbf{D}_{\alpha\alpha}\end{bmatrix} \qquad (\alpha=x,y)$$

$$\mathbf{A}_{xy}=\frac{h}{6}\begin{bmatrix}2\left(\mathbf{D}_{xy}+\mathbf{D}_{yx}\right) & \left(\mathbf{D}_{xy}+\mathbf{D}_{yx}\right)\\ \left(\mathbf{D}_{xy}+\mathbf{D}_{yx}\right) & 2\left(\mathbf{D}_{xy}+\mathbf{D}_{yx}\right)\end{bmatrix}$$

$$\mathbf{B}_{\alpha}=\frac{1}{2}\left(\begin{bmatrix}\mathbf{D}_{\alpha z} & -\mathbf{D}_{\alpha z}\\ \mathbf{D}_{\alpha z} & -\mathbf{D}_{\alpha z}\end{bmatrix}-\begin{bmatrix}\mathbf{D}_{z\alpha} & \mathbf{D}_{z\alpha}\\ -\mathbf{D}_{z\alpha} & -\mathbf{D}_{z\alpha}\end{bmatrix}\right) \qquad (\alpha=x,y)$$

$$\mathbf{G}=\frac{1}{h}\begin{bmatrix}\mathbf{D}_{zz} & -\mathbf{D}_{zz}\\ -\mathbf{D}_{zz} & \mathbf{D}_{zz}\end{bmatrix}$$

The elementary matrix $\tilde{\mathbf{B}}_{\alpha}$ is obtained by changing the sign of every third column of $\mathbf{B}_{\alpha}$.

Quadratic expansion

The shape functions are now

$$N_1 = \zeta(2\zeta - 1) \qquad N_2 = 4\zeta(1-\zeta) \qquad N_3 = (1-\zeta)(1-2\zeta) \qquad \zeta = z/h$$

where $z = 0$ at the bottom surface of the thin-layer and $z = h$ at its top surface. The evaluation of equations (2.22) to (2.26) results in the following elementary matrices

$$\mathbf{M} = \frac{\rho h}{30}\begin{bmatrix} 4\mathbf{I} & 2\mathbf{I} & -\mathbf{I} \\ 2\mathbf{I} & 16\mathbf{I} & 2\mathbf{I} \\ -\mathbf{I} & 2\mathbf{I} & 4\mathbf{I} \end{bmatrix}$$

$$\mathbf{A}_{\alpha\alpha} = \frac{h}{30}\begin{bmatrix} 4\mathbf{D}_{\alpha\alpha} & 2\mathbf{D}_{\alpha\alpha} & -\mathbf{D}_{\alpha\alpha} \\ 2\mathbf{D}_{\alpha\alpha} & 16\mathbf{D}_{\alpha\alpha} & 2\mathbf{D}_{\alpha\alpha} \\ -\mathbf{D}_{\alpha\alpha} & 2\mathbf{D}_{\alpha\alpha} & 4\mathbf{D}_{\alpha\alpha} \end{bmatrix} \quad (\alpha = x, y)$$

$$\mathbf{A}_{xy} = \frac{h}{30}\begin{bmatrix} 4(\mathbf{D}_{xy} + \mathbf{D}_{yx}) & 2(\mathbf{D}_{xy} + \mathbf{D}_{yx}) & -(\mathbf{D}_{xy} + \mathbf{D}_{yx}) \\ 2(\mathbf{D}_{xy} + \mathbf{D}_{yx}) & 16(\mathbf{D}_{xy} + \mathbf{D}_{yx}) & 2(\mathbf{D}_{xy} + \mathbf{D}_{yx}) \\ -(\mathbf{D}_{xy} + \mathbf{D}_{yx}) & 2(\mathbf{D}_{xy} + \mathbf{D}_{yx}) & 4(\mathbf{D}_{xy} + \mathbf{D}_{yx}) \end{bmatrix}$$

$$\mathbf{B}_{\alpha} = \frac{1}{6}\left(\begin{bmatrix} 3\mathbf{D}_{\alpha z} & -4\mathbf{D}_{\alpha z} & \mathbf{D}_{\alpha z} \\ 4\mathbf{D}_{\alpha z} & \mathbf{0} & -4\mathbf{D}_{\alpha z} \\ -\mathbf{D}_{\alpha z} & 4\mathbf{D}_{\alpha z} & -3\mathbf{D}_{\alpha z} \end{bmatrix} - \begin{bmatrix} 3\mathbf{D}_{z\alpha} & 4\mathbf{D}_{z\alpha} & -\mathbf{D}_{z\alpha} \\ -4\mathbf{D}_{z\alpha} & \mathbf{0} & 4\mathbf{D}_{z\alpha} \\ \mathbf{D}_{z\alpha} & -4\mathbf{D}_{z\alpha} & -3\mathbf{D}_{z\alpha} \end{bmatrix}\right) \quad (\alpha = x, y)$$

$$\mathbf{G} = \frac{1}{3h}\begin{bmatrix} 7\mathbf{D}_{zz} & -8\mathbf{D}_{zz} & \mathbf{D}_{zz} \\ -8\mathbf{D}_{zz} & 16\mathbf{D}_{zz} & -8\mathbf{D}_{zz} \\ \mathbf{D}_{zz} & -8\mathbf{D}_{zz} & 7\mathbf{D}_{zz} \end{bmatrix}$$

The elementary matrix $\tilde{\mathbf{B}}_{\alpha}$ is obtained by changing the sign of every third columns of $\mathbf{B}_{\alpha}$.

Appendix II

Evaluation of I_{4j} using contour integration

The Residue Theorem (Boas, 1983) states that the value of the contour integral for any contour in the complex plane depends only on the properties of a finite number of points contained inside the contour (the poles). Using mathematic representation, this theorem states that

$$\oint_C f(\xi)\, d\xi = 2\pi \mathrm{i} \sum_j \mathrm{Res}\, f(\xi_j) \tag{AII.1}$$

where ξ_j represents the j^{th} pole (inside the contour) of the single valued function $f(\xi)$, and $\mathrm{Res}\, f(\xi_j)$ represents the residue of the pole ξ_j. For a simple pole, the residue is calculated with

$$\mathrm{Res}\, f(\xi_j) = \lim_{\xi \to \xi_j} (\xi - \xi_j) f(\xi) \tag{AII.2}$$

Equation (AII.1) is valid for contour integrals in the anti-clockwise direction. For the clockwise direction, the right hand side is multiplied by -1.

The integral to be evaluated is

$$I_{4j} = \frac{1}{2\pi} \int_{-\infty}^{+\infty} \frac{k_y^2}{k^2 \left(k^2 - k_j^2\right)} \mathrm{e}^{-\mathrm{i} k_x x}\, dk_x, \qquad k^2 = k_x^2 + k_y^2 \tag{AII.3}$$

or equivalently,

$$I_{4j} = \frac{1}{2\pi} \int_{-\infty}^{+\infty} \frac{k_y^2}{\left(k_x^2 + k_y^2\right)\left[k_x^2 - \left(k_j^2 - k_y^2\right)\right]} \mathrm{e}^{-\mathrm{i} k_x x}\, dk_x \tag{AII.4}$$

For this case, the function $f(\xi)$ is

$$f(\xi) = \frac{1}{2\pi} \frac{k_y^2}{\left(\xi^2 + k_y^2\right)\left[\xi^2 - \left(k_j^2 - k_y^2\right)\right]} \mathrm{e}^{-\mathrm{i}\xi x} \tag{AII.5}$$

whose poles are (k_y is assumed to be real)

$$\left(\xi^2 + k_y^2\right)\left[\xi^2 - \left(k_j^2 - k_y^2\right)\right] = 0 \;\rightarrow\; \begin{cases} \xi_1 = \mathrm{i}\left|k_y\right| \\ \xi_2 = -\mathrm{i}\left|k_y\right| \\ \xi_3 = -\sqrt{k_j^2 - k_y^2} \\ \xi_4 = \sqrt{k_j^2 - k_y^2} \end{cases} \qquad \mathrm{Im}\left(\sqrt{k_j^2 - k_y^2}\right) < 0 \tag{AII.6}$$

The residues of the poles, as defined by equation (AII.2), are

$$\begin{aligned}
\operatorname{Res} f(\xi_1) &= \frac{\mathrm{i}}{4\pi}\operatorname{sign}(k_y)\frac{k_y}{k_j^2}\mathrm{e}^{|k_y|x} \\
\operatorname{Res} f(\xi_2) &= -\frac{\mathrm{i}}{4\pi}\operatorname{sign}(k_y)\frac{k_y}{k_j^2}\mathrm{e}^{-|k_y|x} \\
\operatorname{Res} f(\xi_3) &= -\frac{1}{4\pi}\frac{k_y^2}{k_j^2\sqrt{k_j^2-k_y^2}}\mathrm{e}^{\mathrm{i}\sqrt{k_j^2-k_y^2}x} \\
\operatorname{Res} f(\xi_4) &= \frac{1}{4\pi}\frac{k_y^2}{k_j^2\sqrt{k_j^2-k_y^2}}\mathrm{e}^{-\mathrm{i}\sqrt{k_j^2-k_y^2}x}
\end{aligned} \tag{AII.6}$$

In order to evaluate the integral (AII.4) using contour integration, the contours shown in Figure AII.1 are used.

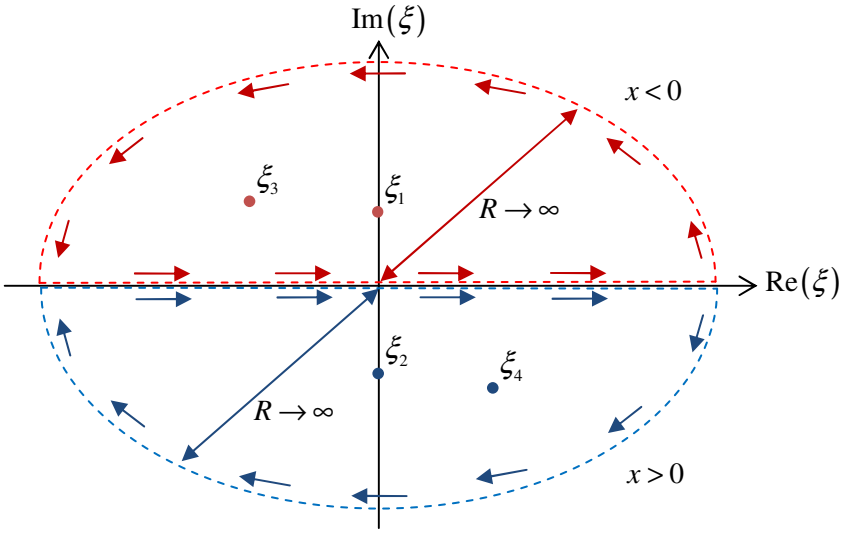

Figure AII.1: Contours for the evaluation of I_{4j}

The red contour must be considered when x is smaller than zero, while the blue contour must be considered when x is greater than zero. These conditions guarantee that the function $f(\xi)$ vanishes in the semi-circumferences of infinite radius, which means that only the integrals on the real axis are non-zero.

Equations (AII.1) and (AII.2) are used to evaluate the contour integral, yielding

$$\oint_C f(\xi)\,d\xi = 2\pi\mathrm{i}\sum_j \operatorname{Res} f(\xi_j) = \begin{cases} -2\pi\mathrm{i}\left(\operatorname{Res} f(\xi_2) + \operatorname{Res} f(\xi_4)\right), & x > 0 \\ 2\pi\mathrm{i}\left(\operatorname{Res} f(\xi_1) + \operatorname{Res} f(\xi_3)\right), & x < 0 \end{cases} \tag{AII.7}$$

Replacing the residues with the expressions (AII.6) leads to

$$\oint_C f(\xi)\,d\xi = \begin{cases} -2\pi\mathrm{i}\left(-\dfrac{\mathrm{i}}{4\pi}\,\mathrm{sign}\left(k_y\right)\dfrac{k_y}{k_j^2}\,\mathrm{e}^{-|k_y|x} + \dfrac{1}{4\pi}\dfrac{k_y^2}{k_j^2\sqrt{k_j^2-k_y^2}}\,\mathrm{e}^{-\mathrm{i}\sqrt{k_j^2-k_y^2}\,x} \right), & x>0 \\ 2\pi\mathrm{i}\left(\dfrac{\mathrm{i}}{4\pi}\,\mathrm{sign}\left(k_y\right)\dfrac{k_y}{k_j^2}\,\mathrm{e}^{|k_y|x} - \dfrac{1}{4\pi}\dfrac{k_y^2}{k_j^2\sqrt{k_j^2-k_y^2}}\,\mathrm{e}^{\mathrm{i}\sqrt{k_j^2-k_y^2}\,x} \right), & x<0 \end{cases} \tag{AII.8}$$

After some simplifications, equation (AII.8) becomes

$$I_{4j} = \oint_C f(\xi)\,d\xi = \left(-\frac{1}{2}\,\mathrm{sign}\left(k_y\right)\frac{k_y}{k_j^2}\,\mathrm{e}^{-|k_y x|} - \frac{\mathrm{i}}{2}\frac{k_y^2}{k_j^2\sqrt{k_j^2-k_y^2}}\,\mathrm{e}^{-\mathrm{i}\sqrt{k_j^2-k_y^2}\,|x|} \right) \tag{AII.9}$$

which is equivalent to the expression indicated in Table 2.3.

Appendix III

$\tilde{\mathbf{p}}_{\mathrm{I}}$ *as a function of* $\tilde{\mathbf{u}}_{\mathrm{I}}^{\mathrm{B}}$ *and* $\tilde{\mathbf{p}}_{\mathrm{II}}$

Consider the system of equations (3.22)

$$\begin{bmatrix} \mathbf{P}_{\mathrm{I,I}}+\mathbf{I} & \mathbf{P}_{\mathrm{I,II}} \\ \mathbf{P}_{\mathrm{II,I}} & \mathbf{P}_{\mathrm{II,II}}+\mathbf{I} \end{bmatrix} \begin{bmatrix} \tilde{\mathbf{u}}_{\mathrm{I}}^{\mathrm{B}} \\ \tilde{\mathbf{u}}_{\mathrm{II}}^{\mathrm{B}} \end{bmatrix} = \begin{bmatrix} \mathbf{U}_{\mathrm{I,I}} & \mathbf{U}_{\mathrm{I,II}} \\ \mathbf{U}_{\mathrm{II,I}} & \mathbf{U}_{\mathrm{II,II}} \end{bmatrix} \begin{bmatrix} \tilde{\mathbf{p}}_{\mathrm{I}} \\ \tilde{\mathbf{p}}_{\mathrm{II}} \end{bmatrix}$$

After solving the first row for $\tilde{\mathbf{p}}_{\mathrm{I}}$ and the second row for $\tilde{\mathbf{u}}_{\mathrm{II}}^{\mathrm{B}}$, one obtains

$$\begin{cases} \mathbf{U}_{\mathrm{I,I}}\tilde{\mathbf{p}}_{\mathrm{I}} = \left(\mathbf{P}_{\mathrm{I,I}}+\mathbf{I}\right)\tilde{\mathbf{u}}_{\mathrm{I}}^{\mathrm{B}} + \mathbf{P}_{\mathrm{I,II}}\tilde{\mathbf{u}}_{\mathrm{II}}^{\mathrm{B}} - \mathbf{U}_{\mathrm{I,II}}\tilde{\mathbf{p}}_{\mathrm{II}} \\ \tilde{\mathbf{u}}_{\mathrm{II}}^{\mathrm{B}} = \left(\mathbf{P}_{\mathrm{II,II}}+\mathbf{I}\right)^{-1}\left(\mathbf{U}_{\mathrm{II,II}}\tilde{\mathbf{p}}_{\mathrm{II}} + \mathbf{U}_{\mathrm{II,I}}\tilde{\mathbf{p}}_{\mathrm{I}} - \mathbf{P}_{\mathrm{II,I}}\tilde{\mathbf{u}}_{\mathrm{I}}^{\mathrm{B}}\right) \end{cases}$$

Substituting $\tilde{\mathbf{u}}_{\mathrm{II}}^{\mathrm{B}}$, defined in the second equation, into the first, yields

$$\mathbf{U}_{\mathrm{I,I}}\tilde{\mathbf{p}}_{\mathrm{I}} = \left(\mathbf{P}_{\mathrm{I,I}}+\mathbf{I}\right)\tilde{\mathbf{u}}_{\mathrm{I}}^{\mathrm{B}} + \mathbf{P}_{\mathrm{I,II}}\left(\mathbf{P}_{\mathrm{II,II}}+\mathbf{I}\right)^{-1}\left(\mathbf{U}_{\mathrm{II,II}}\tilde{\mathbf{p}}_{\mathrm{II}} + \mathbf{U}_{\mathrm{II,I}}\tilde{\mathbf{p}}_{\mathrm{I}} - \mathbf{P}_{\mathrm{II,I}}\tilde{\mathbf{u}}_{\mathrm{I}}^{\mathrm{B}}\right) - \mathbf{U}_{\mathrm{I,II}}\tilde{\mathbf{p}}_{\mathrm{II}}$$

and after some simplifications, $\tilde{\mathbf{p}}_{\mathrm{I}}$ can be obtained with

$$\mathbf{U}_{\mathrm{I,I}}\tilde{\mathbf{p}}_{\mathrm{I}} = \left[\left(\mathbf{P}_{\mathrm{I,I}}+\mathbf{I}\right) - \mathbf{P}_{\mathrm{I,II}}\left(\mathbf{P}_{\mathrm{II,II}}+\mathbf{I}\right)^{-1}\mathbf{P}_{\mathrm{II,I}}\right]\tilde{\mathbf{u}}_{\mathrm{I}}^{\mathrm{B}} + \left[\mathbf{P}_{\mathrm{I,II}}\left(\mathbf{P}_{\mathrm{II,II}}+\mathbf{I}\right)^{-1}\mathbf{U}_{\mathrm{II,I}}\right]\tilde{\mathbf{p}}_{\mathrm{I}} + \left[\mathbf{P}_{\mathrm{I,II}}\left(\mathbf{P}_{\mathrm{II,II}}+\mathbf{I}\right)^{-1}\mathbf{U}_{\mathrm{II,II}} - \mathbf{U}_{\mathrm{I,II}}\right]\tilde{\mathbf{p}}_{\mathrm{II}}$$

$$\left[\mathbf{U}_{\mathrm{I,I}} - \mathbf{P}_{\mathrm{I,II}}\left(\mathbf{P}_{\mathrm{II,II}}+\mathbf{I}\right)^{-1}\mathbf{U}_{\mathrm{II,I}}\right]\tilde{\mathbf{p}}_{\mathrm{I}} = \left[\left(\mathbf{P}_{\mathrm{I,I}}+\mathbf{I}\right) - \mathbf{P}_{\mathrm{I,II}}\left(\mathbf{P}_{\mathrm{II,II}}+\mathbf{I}\right)^{-1}\mathbf{P}_{\mathrm{II,I}}\right]\tilde{\mathbf{u}}_{\mathrm{I}}^{\mathrm{B}} + \left[\mathbf{P}_{\mathrm{I,II}}\left(\mathbf{P}_{\mathrm{II,II}}+\mathbf{I}\right)^{-1}\mathbf{U}_{\mathrm{II,II}} - \mathbf{U}_{\mathrm{I,II}}\right]\tilde{\mathbf{p}}_{\mathrm{II}}$$

$$\tilde{\mathbf{p}}_{\mathrm{I}} = \left[\mathbf{U}_{\mathrm{I,I}} - \mathbf{P}_{\mathrm{I,II}}\left(\mathbf{P}_{\mathrm{II,II}}+\mathbf{I}\right)^{-1}\mathbf{U}_{\mathrm{II,I}}\right]^{-1}\left[\left(\mathbf{P}_{\mathrm{I,I}}+\mathbf{I}\right) - \mathbf{P}_{\mathrm{I,II}}\left(\mathbf{P}_{\mathrm{II,II}}+\mathbf{I}\right)^{-1}\mathbf{P}_{\mathrm{II,I}}\right]\tilde{\mathbf{u}}_{\mathrm{I}}^{\mathrm{B}} + \left[\mathbf{U}_{\mathrm{I,I}} - \mathbf{P}_{\mathrm{I,II}}\left(\mathbf{P}_{\mathrm{II,II}}+\mathbf{I}\right)^{-1}\mathbf{U}_{\mathrm{II,I}}\right]^{-1}\left[\mathbf{P}_{\mathrm{I,II}}\left(\mathbf{P}_{\mathrm{II,II}}+\mathbf{I}\right)^{-1}\mathbf{U}_{\mathrm{II,II}} - \mathbf{U}_{\mathrm{I,II}}\right]\tilde{\mathbf{p}}_{\mathrm{II}}$$

Appendix IV

Displacements induced by disk loads

Knowing the eigenvectors of the SVP and SH problems (Chapter 2), the displacements in the space domain can be calculated with an appropriate combination of the eigen modes. The 2D displacements can be calculated with the equations found in (Kausel, 1981), for the 2.5D displacements (mixed domain) see Chapter 2 or (Barbosa and Kausel, 2012) and for the 3D cylindrical displacements (due to a point load) see (Kausel, 1999). As for the displacements induced by disk loads, the corresponding equations can be found in (Kausel and Peek, 1982), being transcribed below. In the superscripts, *m* represents the depth of the receiver and *n* the depth of the load. In the subscripts, *r* corresponds to the radial direction and *z* to the vertical direction. The first subscript of u indicates the direction of the displacement, and the second corresponds to the direction of the load. The parameter ρ is the radial distance between the receiver and the center of the disk load, *R* is the radius of the disk load (Figure AIV.1), *q* is the applied pressure, $J_n(X)$ is the Bessel function of first kind and n^{th} order, and $H_n^{(2)}(X)$ is the second Hankel function of n^{th} order.

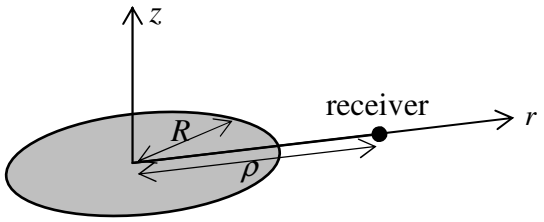

Figure AIV.1: Definition of directions z and r

$$u_{rr}^{mn}(\rho) = qR\left(\sum_{j=1}^{N_{\text{SVP}}} \frac{\partial I_3\left(\rho,R,k_{j,\text{SVP}}\right)}{\partial\rho}\phi_{jx}^m\phi_{jx}^n + \sum_{j=1}^{N_{\text{SH}}} I_3\left(\rho,R,k_{j,\text{SH}}\right)\phi_{jy}^m\phi_{jy}^n\right)$$

$$u_{rz}^{mn}(\rho) = -qR\sum_{j=1}^{N_{\text{SVP}}} I_3\left(\rho,R,k_{j,\text{SVP}}\right)k_{j,\text{SVP}}\phi_{jx}^m\phi_{jz}^n$$

$$u_{zr}^{mn}(\rho) = qR\sum_{j=1}^{N_{\text{SVP}}} I_3\left(\rho,R,k_{j,\text{SVP}}\right)k_{j,\text{SVP}}\phi_{jz}^m\phi_{jx}^n$$

$$u_{zz}^{mn}(\rho) = qR\sum_{j=1}^{N_{\text{SVP}}} I_1\left(\rho,R,k_{j,\text{SVP}}\right)k_{j,\text{SVP}}\phi_{jz}^m\phi_{jz}^n$$

$$I_1(\rho,R,k) = \begin{cases} \dfrac{\pi}{2ik}J_0(k\rho)H_1^{(2)}(kR) - \dfrac{1}{Rk^2} & 0<\rho<R \\ \dfrac{\pi}{2ik}J_1(kR)H_0^{(2)}(k\rho) & \rho>R \end{cases}$$

$$I_3(\rho,R,k)=\begin{cases}\dfrac{\pi}{2\mathrm{i}k^2}J_1(k\rho)H_1^{(2)}(kR)-\dfrac{\rho}{2Rk^2} & 0<\rho<R\\ \dfrac{\pi}{2\mathrm{i}k^2}J_1(kR)H_0^{(2)}(k\rho)-\dfrac{R}{2\rho k^2} & \rho>R\end{cases}$$

$$\frac{\partial I_3(\rho,R,k)}{\partial\rho}=\frac{1}{\rho}I_3(\rho,R,k)-I_1(\rho,R,k)$$

Appendix V

Vibration modes of the building

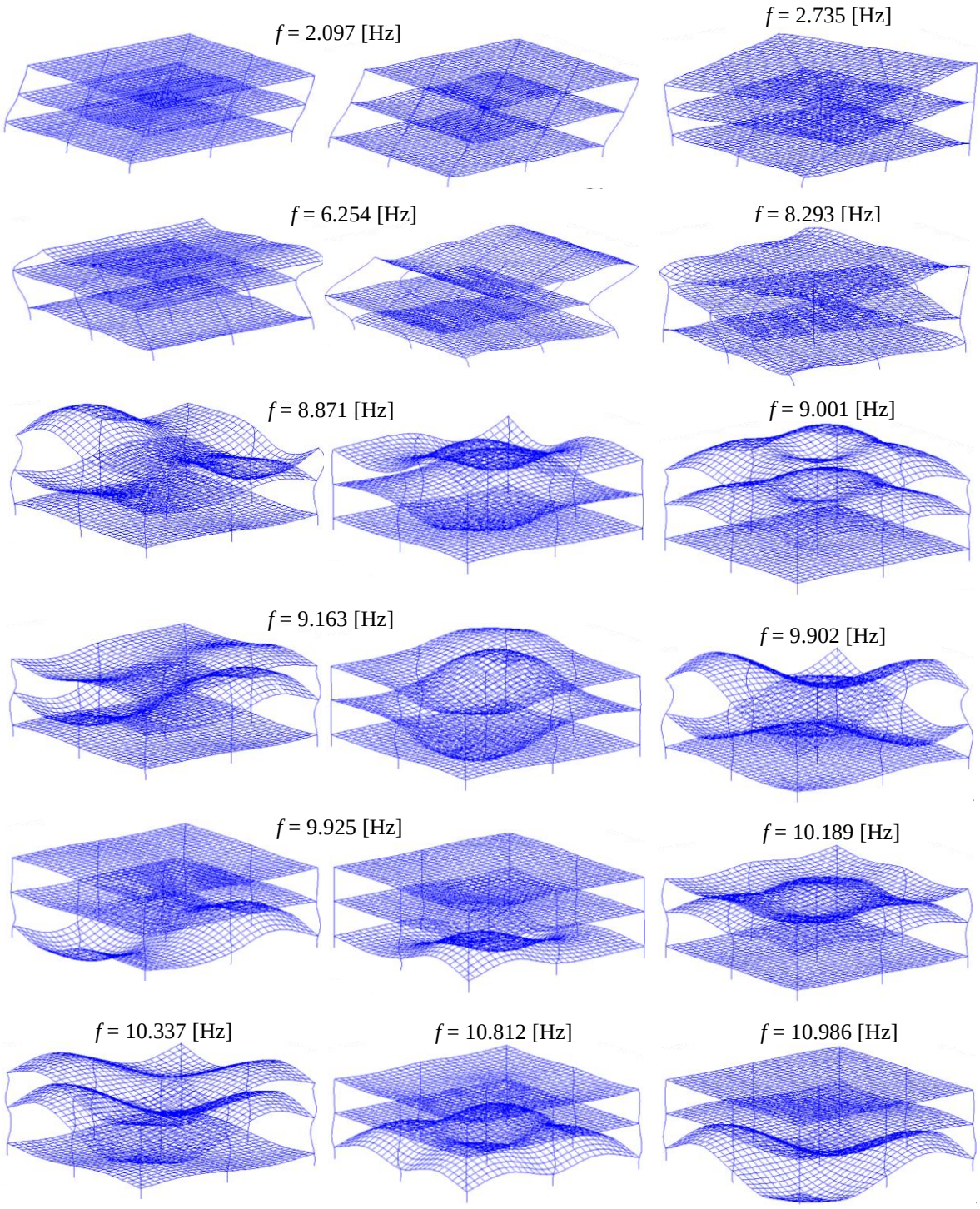

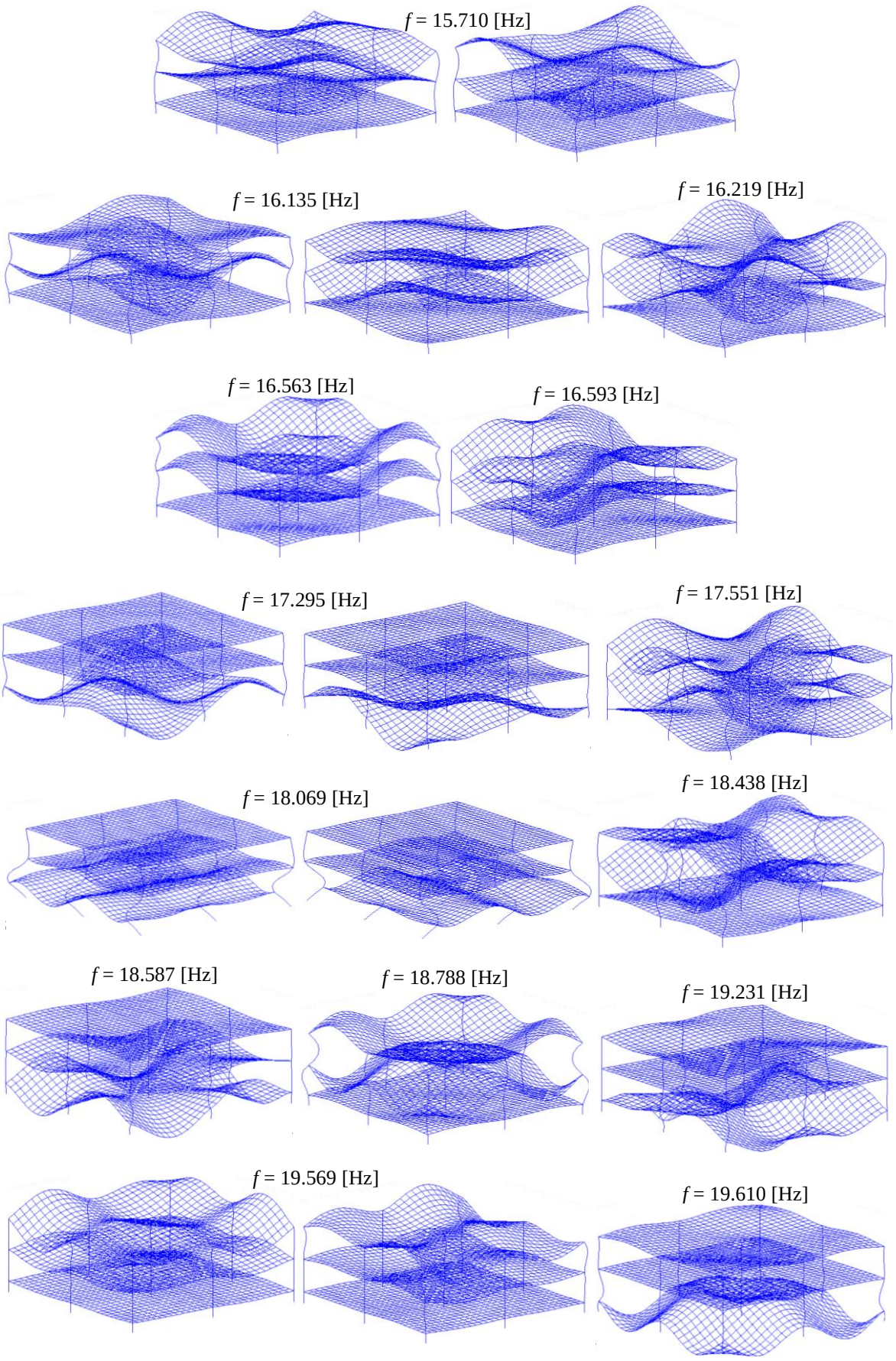
f = 15.710 [Hz]
f = 16.135 [Hz]
f = 16.219 [Hz]
f = 16.563 [Hz]
f = 16.593 [Hz]
f = 17.295 [Hz]
f = 17.551 [Hz]
f = 18.069 [Hz]
f = 18.438 [Hz]
f = 18.587 [Hz]
f = 18.788 [Hz]
f = 19.231 [Hz]
f = 19.569 [Hz]
f = 19.610 [Hz]

References

Achenbach, J. D. (1973). Wave propagation in elastic solids. Amsterdam, The Netherlands, Elsevier.

Adam, M. and O. von Estorff (2005). Reduction of train-induced building vibrations by using open and filled trenches. Computers & Structures 83(1): 11-24.

Ahmad, S. and T. Al-Hussaini (1991). Simplified design for vibration screening by open and in-filled trenches: Calcul simplifié d'écrans contre les vibrations, par tranchées ouvertes ou remplies. Journal of geotechnical engineering 117(1): 67-88.

Ahmad, S., T. Al-Hussaini and K. Fishman (1996). Investigation on Active Isolation of Machine Foundations by Open Trenches. Journal of Geotechnical Engineering 122(6): 454-461.

Al-Hunaidi, O. and J. Rainer (1991a). Remedial measures for traffic-induced vibrations at a residential site. Part 1: Field tests. Canadian Acoustics/Acoustique Canadienne 19(1): 3-13.

Al-Hunaidi, O. and J. Rainer (1991b). Remedial measures for traffic-induced vibrations at a residential site. Part 2: FEM simulations. Canadian Acoustics/Acoustique Canadienne 19(2): 11-20.

Al-Hunaidi, O., J. Rainer and M. Tremblay (1996). Control of traffic-induced vibration in buildings using vehicle suspension systems. Soil Dynamics and Earthquake Engineering 15(4): 245-254.

Al-Hunaidi, O. and M. Tremblay (1997). Traffic induced building vibrations in Montréal. Canadian Journal of Civil Engineering 24(5): 736-753.

Alves Costa, P. (2011). Vibrações do sistema via-maciço induzidas por tráfego ferroviário. Modelação numérica e validação experimental. Civil Engineering Department. Porto, FEUP, PhD Thesis.

Alves Costa, P., R. Calçada and A. Cardoso (2012a). Track–ground vibrations induced by railway traffic: In-situ measurements and validation of a 2.5D FEM-BEM model. Soil Dynamics and Earthquake Engineering 32: 111-128.

Alves Costa, P., R. Calçada and A. S. Cardoso (2012b). Influence of train dynamic modelling strategy on the prediction of track-ground vibrations induced by railway traffic. Proceedings of the Institution of Mechanical Engineers, Part F: Journal of Rail and Rapid Transit 226(4): 434-450.

Alves Costa, P., R. Calçada and A. Silva Cardoso (2012c). Ballast mats for the reduction of railway traffic vibrations. Numerical study. Soil Dynamics and Earthquake Engineering 42(0): 137-150.

Alves Costa, P., R. Calçada and A. Silva Cardoso (2013). Vibrations induced by Railway traffic: prediction, measurement and mitigation. Traffic induced enviromental vibrations and control: theory and application. R. Calçada and H. Xia, Nova: 48-89.

Alves Costa, P., R. Calçada, A. Silva Cardoso and A. Bodare (2010). Influence of soil non-linearity on the dynamic response of high-speed railway tracks. Soil Dynamics and Earthquake Engineering 30(4): 221-235.

Alzawi, A. and M. Hesham El Naggar (2009). Vibration Scattering Using GeoFoam Material as Vibration Wave Barriers. 62nd Canadian Geotechnical Conference, Halifax, Canada.

Alzawi, A. and M. Hesham El Naggar (2010). Full scale experimental study on vibration scattering using open and in-filled (GeoFoam) wave barriers. Soil Dynamics and Earthquake Engineering 31(3): 306-317.

Alzawi, A. and M. Hesham El Naggar (2011). Numerical investigations on vibration screening by in-filled geofoam trenches. Pan-Am CGS Geotechnical Conference.

Andersen, L. and S. R. K. Nielsen (2005). Reduction of ground vibration by means of barriers or soil improvement along a railway track. Soil Dynamics and Earthquake Engineering 25(7-10): 701-716.

Andersen, L. and S. r. R. K. Nielsen (2003). Vibrations of a track caused by variation of the foundation stiffness. Probabilistic Engineering Mechanics 18(2): 171-184.

Apsel, R. J. and J. E. Luco (1983). On the Green's functions for a layered half-space. Part II. Bulletin of the Seismological Society of America 73(4): 931.

Auersch, L. (1994). Wave propagation in layered soils: theoretical solution in wavenumber domain and experimental results of hammer and railway traffic excitation. Journal of Sound and Vibration 173(2): 233-264.

Auersch, L. (2005). The excitation of ground vibration by rail traffic: theory of vehicle-track-soil interaction and measurements on high-speed lines. Journal of Sound and Vibration 284(1-2): 103-132.

Bahrekazemi, M. (2004). Train-induced ground vibration and its prediction. Division of Soil and Rock Mechanics Dept. of Civil and Architectural Engineering. Stockholm, Royal Institute of Technology, PhD Thesis.

Barbosa, J. and E. Kausel (2012). The thin-layer method in a cross-anisotropic 3D space. International journal for numerical methods in engineering 89(5): 537-560.

Barbosa, J., J. Park and E. Kausel (2012). Perfectly matched layers in the thin layer method. Computer methods in applied mechanics and engineering 217-220(0): 262-274.

Basu, U. (2009). Explicit finite element perfectly matched layer for transient three dimensional elastic waves. International journal for numerical methods in engineering 77(2): 151-176.

Basu, U. and A. K. Chopra (2003). Perfectly matched layers for time-harmonic elastodynamics of unbounded domains: theory and finite-element implementation. Computer methods in applied mechanics and engineering 192(11-12): 1337-1375.

Basu, U. and A. K. Chopra (2004). Perfectly matched layers for transient elastodynamics of unbounded domains. International journal for numerical methods in engineering 59(8): 1039-1074.

Berenger, J. P. (1994). A perfectly matched layer for the absorption of electromagnetic waves. Journal of computational physics 114(2): 185-200.

Beskos, D., B. Dasgupta and I. Vardoulakis (1986). Vibration isolation using open or filled trenches. Computational mechanics 1(1): 43-63.

Bienstman, P. and R. Baets (2002). Advanced boundary conditions for eigenmode expansion models. Optical and quantum electronics 34(5): 523-540.

Bienstman, P., H. Derudder, R. Baets, F. Olyslager and D. De Zutter (2001). Analysis of cylindrical waveguide discontinuities using vectorial eigenmodes and perfectly matched layers. Microwave Theory and Techniques, IEEE Transactions on 49(2): 349-354.

Biot, M. (1956a). Theory of propagation of elastic waves in a fluid-saturated porous solid. II. Higher frequency range. J. Acoust. Soc. Am 28(2): 179-191.

Biot, M. A. (1956b). Theory of propagation of elastic waves in a fluid-saturated porous solid. I. Low-frequency range. J. Acoust. Soc. Am 28(2): 168-178.

Boas, M. L. (1983). Mathematical methods in the physical sciences. New York, U.S.A., John Wiley & Sons, Inc.

Bode, C., R. Hirschauer and S. A. Savidis (2002). Soil-structure interaction in the time domain using halfspace Green's functions. Soil Dynamics and Earthquake Engineering 22(4): 283-295.

Bongini, E., G. Lombaert, S. François and G. Degrande (2011). A parametric study of the impact of mitigation measures on ground borne vibration due to railway traffic. th International Conference on Structural Dynamics EURODYN 2011.

Brebbia, C. and J. Dominguez (1992). Boundary elements: an introductory course. Southampton, U.K., McGraw-Hill.

Cao, Z., Y. Cai, A. Boström and J. Zheng (2012). Semi-analytical analysis of the isolation to moving-load induced ground vibrations by trenches on a poroelastic half-space. Journal of Sound and Vibration 331(4): 947-961.

Celebi, E., S. Firat, G. Beyhan, I. Cankaya, I. Vural and O. Kirtel (2009). Field experiments on wave propagation and vibration isolation by using wave barriers. Soil Dynamics and Earthquake Engineering 29(5): 824-833.

Celebi, E. and F. Göktepe (2012). Non-linear 2-D FE analysis for the assessment of isolation performance of wave impeding barrier in reductin of railway-induced surface waves. Constructions and Building MAterials 36: 1-13.

Celebi, E. and O. Kirtel (2012). Non-linear 2-D FE modeling for prediction of screening performance of thin-walled trench barriers in mitigation of train-induced ground vibrations. Construction and Building Materials 42(0): 122-131.

Celebi, E. and G. Schmid (2005). Investigation of ground vibrations induced by moving loads. Engineering structures 27(14): 1981-1998.

Cerrolaza, M. and E. Alarcon (1989). A bi cubic transformation for the numerical evaluation of the Cauchy principal value integrals in boundary methods. International journal for numerical methods in engineering 28(5): 987-999.

Chao, C. C. (1960). Dynamical response of an elastic half-space to tangential surface loadings. Journal of Applied Mechanics 27(3): 559-567.

Chebli, H., R. Othman and D. Clouteau (2006). Response of periodic structures due to moving loads. Comptes Rendus Mécanique 334(6): 347-352.

Chew, W. C. and W. H. Weedon (1994). A 3D perfectly matched medium from modified Maxwell's equations with stretched coordinates. Microwave and optical technology letters 7(13): 599-604.

Chua, K., K. Lo and T. Balendra (1995). Building response due to subway train traffic. Journal of geotechnical engineering 121: 747.

Clouteau, D., M. Arnst, T. Al-Hussaini and G. Degrande (2005). Freefield vibrations due to dynamic loading on a tunnel embedded in a stratified medium. Journal of Sound and Vibration 283(1-2): 173-199.

Clouteau, D., G. Degrande and G. Lombaert (2001). Numerical modelling of traffic induced vibrations. Meccanica 36(4): 401-420.

Coulier, P., S. François, G. Degrande and G. Lombaert (2013a). A numerical study of subgrade stiffening as a mitigation measure for railway induced vibrtions through 2.5D FE-FE models. 4th nternational Conference on Computational MEthods in Structural Dynamics and Earthquake Engineering. Kos Island, Greece.

Coulier, P., S. François, G. Degrande and G. Lombaert (2013b). Subgrade stiffening next to the track as a wave impeding barrier for railway induced vibrations. Soil Dynamics and Earthquake Engineering 48: 119-131.

Cui, F. and C. Chew (2000). The effectiveness of floating slab track system--Part I. Receptance methods. Applied Acoustics 61(4): 441-453.

Dasgupta, B., D. Beskos and I. Vardoulakis (1990). Vibration isolation using open or filled trenches Part 2: 3-D homogeneous soil. Computational mechanics 6(2): 129-142.

Dawn, T. (1983). Ground vibrations from heavy freight trains. Journal of Sound and Vibration 87(2): 351-356.

Dawn, T. and C. Stanworth (1979). Ground vibrations from passing trains. Journal of Sound and Vibration 66(3): 355-362.

De Barros, F. and J. Luco (1994). Response of a layered viscoelastic half-space to a moving point load. Wave Motion 19(2): 189-210.

De Hoop, A. (1960). A modification of Cagniard's method for solving seismic pulse problems. Applied Scientific Research, Section B 8(1): 349-356.

Degrande, G., M. Schevenels, P. Chatterjee, W. Van de Velde, P. Holscher, V. Hopman, A. Wang and N. Dadkah (2006). Vibrations due to a test train at variable speeds in a deep bored tunnel embedded in London clay. Journal of Sound and Vibration 293(3-5): 626-644.

Degrande, G. and L. Schillemans (2001). Free field vibrations during the passage of a Thalys high-speed train at variable speed. Journal of Sound and Vibration 247(1): 131-144.

Derudder, H., F. Olyslager, D. De Zutter and S. Van den Berghe (2001). Efficient mode-matching analysis of discontinuities in finite planar substrates using perfectly matched layers. Antennas and Propagation, IEEE Transactions on 49(2): 185-195.

Dieterman, H. and A. Metrikine (1996). The equivalent stiffness of a half-space interacting with a beam. Critical velocities of a moving load along the beam. European Journal of Mechanics, A/Solids 15(1): 67-90.

Dieterman, H. and A. Metrikine (1997). Critical velocities of a harmonic load moving uniformly along an elastic layer. Journal of applied mechanics 64: 596.

Dijckmans, A., A. Ekblad, A. Smekal, G. Degrande and G. Lombaert (2013). A sheet piling wall as a wave barrier for train induced vibrations. 4th nternational Conference on Computational MEthods in Structural Dynamics and Earthquake Engineering. Kos Island, Greece.

DIN4150-2 (1999). Deutsches Institut für Normung - DIN 4150-2 - Structural vibrations, Part 2: Human exposure to vibration in buildings.

Dominguez, J. (1993). Boundary elements in dynamics. Southampton, U.K., Elsevier.

dos Santos, N. C. (2013). Vibrações induzidas por tráfego na via e na envolvente de linhas ferroviárias: modelação numérica 3D e validação experimental. Civil Engineering Department. Porto, Faculty of Engineering of University of Porto, PhD thesis.

dos Santos, N. C., J. Barbosa, R. Calçada, A. Azevedo and R. Delgado (2010a). A 3D time domain formulation for the analysis of train induced vibrations. International conference on noise and vibration engineering. Leuven, Belgium.

dos Santos, N. C., J. Barbosa, R. Calçada, A. Azevedo and R. Delgado (2010b). Implementation of a three-dimensional time domain formulation for the prediction of vehicle induced vibrations. Tenth International Conference on Computational Structures Technology. Valencia, Spain.

Ekevid, T. and N. E. Wiberg (2002). Wave propagation related to high-speed train:: A scaled boundary FE-approach for unbounded domains. Computer methods in applied mechanics and engineering 191(36): 3947-3964.

Erigen, A. and E. Suhubi (1975). Elastodynamics Vol. 2. linear theory. New York (USA), San Francisco (USA) and London (UK), Academic Press.

Ewing, W. M., W. S. Jardetzky, F. Press and A. Beiser (1957). Elastic waves in layered media. Physics Today 10: 27.

Fiala, P., G. Degrande and F. Augusztinovicz (2007). Numerical modelling of ground-borne noise and vibration in buildings due to surface rail traffic. Journal of Sound and Vibration 301(3-5): 718-738.

Fiala, P., S. Gupta, G. Degrande and F. Augustinovicz (2008). A parametric study on countermeausreus to mitigate sub-way traffic induced vibration and noise in buildings. International Conference on Noise and Vibration Engineering, Leuven, Belgium.

Forrest, J. and H. Hunt (2006a). Ground vibration generated by trains in underground tunnels. Journal of Sound and Vibration 294(4-5): 706-736.

Forrest, J. and H. Hunt (2006b). A three-dimensional tunnel model for calculation of train-induced ground vibration. Journal of Sound and Vibration 294(4-5): 678-705.

François, S. (2008). Nonlinear modelling of the response of structures due to ground vibrations. Leuven, Katholike Univeriteit Leuven, Ph. D. Thesis.

François, S., H. R. Masoumi and G. Degrande (2006). An iterative coupled boundary-finite element method for the dynamic response of structures. III European Conference on Computational Mechanics Solids, Structures and Coupled Problems in Engineering, Lisbon, Portugal.

François, S., M. Schevenels, P. Galvín, G. Lombaert and G. Degrande (2010). A 2.5 D coupled FE-BE methodology for the dynamic interaction between longitudinally invariant structures and a layered halfspace. Computer methods in applied mechanics and engineering 199(23-24): 1536-1548.

Galvín, P. (2007). Análisis numérico y experimental de las vibraciones ocasionadas por el paso de trenes de alta velocidad en el suelo y en estructuras cercanas a la vía, Universidad de Sevilla, Spain, Ph. D. Thesis.

Galvín, P., S. François, M. Schevenels, E. Bongini, G. Degrande and G. Lombaert (2010). A 2.5D coupled FE-BE model for the prediction of railway induced vibrations. Soil Dynamics and Earthquake Engineering 30(12): 1500-1512.

Gavric, L. (1995). Computation of propagative waves in free rail using a finite element technique. Journal of Sound and Vibration 185(3): 531-543.

Gedney, S. D. (1996). An anisotropic perfectly matched layer-absorbing medium for the truncation of FDTD lattices. Antennas and Propagation, IEEE Transactions on 44(12): 1630-1639.

Godinho, L., P. Amado-Mendes, A. Pereira and D. Soares Jr (2013). A coupled MFS-FEM model for 2-D dynamic soil-structure interaction in the frequency domain. Computers & Structures 129: 74-85.

Godinho, L., P. A. Mendes, J. Ramis, W. Cardenas and J. Carbajo (2012). A Numerical MFS Model for Computational Analysis of Acoustic Horns. Acta Acustica united with Acustica 98(6): 916-927.

Godinho, L., P. A. Mendes, A. Tadeu, A. Cadena-Isaza, C. Smerzini, F. Sanchez-Sesma, R. Madec and D. Komatitsch (2009). Numerical simulation of ground rotations along 2D topographical profiles under the incidence of elastic plane waves. Bulletin of the Seismological Society of America 99(2B): 1147-1161.

Godinho, L. and D. Soares Jr (2013). Frequency domain analysis of interacting acoustic-elastodynamic models taking into account optimized iterative coupling of different numerical methods. Engineering Analysis with Boundary Elements 37(7): 1074-1088.

Grootenhuis, P. (1977). Floating track slab isolation for railways. Journal of Sound Vibration 51: 443-448.

Grundmann, H. and S. Lenz (2003). Nonlinear interaction between a moving SDOF system and a Timoshenko beam/halfspace support. Archive of Applied Mechanics 72(11-12): 830-842.

Guiggiani, M. and A. Gigante (1990). A general algorithm for multidimensional Cauchy principal value integrals in the boundary element method. Journal of applied mechanics 57: 906.

Gupta, S., M. Hussein, G. Degrande, H. Hunt and D. Clouteau (2007). A comparison of two numerical models for the prediction of vibrations from underground railway traffic. Soil Dynamics and Earthquake Engineering 27(7): 608-624.

Gupta, S., W. Liu, G. Degrande, G. Lombaert and W. Liu (2008). Prediction of vibrations induced by underground railway traffic in Beijing. Journal of Sound and Vibration 310(3): 608-630.

Gupta, S., H. Van den Berghe, G. Lombaert and G. Degrande (2010). Numerical modelling of vibrations from a Thalys high speed train in the Groene Hart tunnel. Soil Dynamics and Earthquake Engineering 30(3): 82-97.

Gutowski, T. and C. Dym (1976). Propagation of ground vibration: a review. Journal of Sound and Vibration 49(2): 179-193.

Hall, L. (2000). Simulations and Analyses of Train-induced Ground Vibrations: A Comparative Study of Two-and Three-dimensional Calculations with Actual Measurements, Royal Institute of Technology, Division of Soil & Rock Mechanics, PhD Thesis.

Hall, L. (2003). Simulations and analyses of train-induced ground vibrations in finite element models. Soil Dynamics and Earthquake Engineering 23(5): 403-413.

Hanazato, T., K. Ugai, M. Mori and R. Sakaguchi (1991). Three-dimensional analysis of traffic-induced ground vibrations. Journal of geotechnical engineering 117(8): 1133-1151.

Harari, I. and U. Albocher (2006). Studies of FE/PML for exterior problems of time-harmonic elastic waves. Computer methods in applied mechanics and engineering 195(29-32): 3854-3879.

Haskell, N. A. (1953). The dispersion of surface waves on multilayered media. Bulletin of the Seismological Society of America 43(1): 17.

Hemsworth, B. (2000). Reducing groundborne vibrations: state-of-the-art study. Journal of Sound and Vibration 231(3): 703-709.

Hildebrand, R. (2004). Effect of soil stabilization on audible band railway ground vibration. Soil Dynamics and Earthquake Engineering 24(5): 411-424.

Hubert, W., K. Friedrich, G. Pflanz and G. Schmid (2001). Frequency–and Time-domain BEM Analysis of Rigid Track on a Half-Space with Vibration Barriers. Meccanica 36(4): 421-436.

Hugonin, J. P. and P. Lalanne (2005). Perfectly matched layers as nonlinear coordinate transforms: a generalized formalization. JOSA A 22(9): 1844-1849.

Hung, C.-C. and S.-H. Ni (2012). The horizontal amplitude screening effects of a rectangular strip in-filled trench. Journal of the Chinese Institute of Engineers 36(7): 932-940.

Hung, H., Y. Yang and D. Chang (2004). Wave barriers for reduction of train-induced vibrations in soils. Journal of geotechnical and geoenvironmental engineering 130: 1283-1291.

Hung, H. H. and Y. B. Yang (2001). A review of researches on ground-borne vibrations with emphasis on those induced by trains. Proc. Nat. Sci. Council Part A: Phys. Sci. & Eng 25(1): 1-16.

Hussein, M. and H. Hunt (2007). A numerical model for calculating vibration from a railway tunnel embedded in a full-space. Journal of Sound and Vibration 305(3): 401-431.

Hussein, M., H. Hunt, L. Rikse, S. Gupta, G. Degrande, J. Talbot, S. François and M. Schevenels (2008). Using the PiP model for fast calculation of vibration from a railway tunnel in a multi-layered half-space. Noise and Vibration Mitigation for Rail Transportation Systems: 136-142.

Hwu, W. and D. Kirk (2009). Programming massively parallel processors. Waltham, U.S.A., Elsevier.

ISO8680 (1995). ISO8680, Mechanical vibration - Road surface profiles.

Johnson, S. G. (2008) Notes on perfectly matched layers (PMLs). Lecture notes, Massachusetts Institute of Technology, downloadable from: <http://math.mit.edu/~stevenj/18.369/pml.pdf>.

Jones, C. and J. Block (1996). Prediction of ground vibration from freight trains. Journal of Sound and Vibration 193(1): 205-213.

Jones, C., X. Sheng and M. Petyt (2000). Simulations of ground vibration from a moving harmonic load on a railway track. Journal of Sound and Vibration 231(3): 739-751.

Jones, S. (2010). Ground vibration from underground railways: how simplifying assumptions limit prediction accuracy, University of Cambridge, PhD Thesis.

Jones, S. and H. Hunt (2011). Effect of Inclined Soil Layers on Surface Vibration from Underground Railways Using the Thin-Layer Method. Journal of engineering mechanics 137(12): 887-900.

Jones, S. and H. Hunt (2012). Predicting surface vibration from underground railways through inhomogeneous soil. Journal of Sound and Vibration 331(9): 2055-2069.

Ju, S. H. (2002). Finite element analyses of wave propagations due to a high speed train across bridges. International journal for numerical methods in engineering 54(9): 1391-1408.

Ju, S. H. (2004). Three-dimensional analyses of wave barriers for reduction of train-induced vibrations. Journal of geotechnical and geoenvironmental engineering 130(7): 740-748.

Karlstrom, A. (2006). An analytical model for ground vibrations from accelerating trains. Journal of Sound and Vibration 293(3-5): 587-598.

Karlstrom, A. and A. Bostrom (2006). An analytical model for train-induced ground vibrations from railways. Journal of Sound and Vibration 292(1-2): 221-241.

Karlstrom, A. and A. Bostrom (2007). Efficiency of trenches along railways for trains moving at sub- or supersonic speeds. Soil Dynamics and Earthquake Engineering 27(7): 625-641.

Katou, M., T. Matsuoka, O. Yoshioka, Y. Sanada and T. Miyoshi (2008). Numerical simulation study of ground vibrations using forces from wheels of a running high-speed train. Journal of Sound and Vibration 318(4): 830-849.

Kausel, E. (1981). An explicit solution for the Green functions for dynamic loads in layered media.M. Department of Civil Engineering.

Kausel, E. (1986). Wave propagation in anisotropic layered media. International journal for numerical methods in engineering 23(8): 1567-1578.

Kausel, E. (1988). Local transmitting boundaries. Journal of engineering mechanics 114(6): 1011-1027.

Kausel, E. (1992). Physical interpretation and stability of paraxial boundary conditions. Bulletin of the Seismological Society of America 82(2): 898.

Kausel, E. (1994). Thin layer method: Formulation in the time domain. International journal for numerical methods in engineering 37(6): 927-941.

Kausel, E. (1999). Dynamic point sources in laminated media via the thin-layer method. International journal of solids and structures 36(31): 4725-4742.

Kausel, E. (2004). Accurate stresses in the thin layer method. International journal for numerical methods in engineering 61(3): 360-379.

Kausel, E. (2006). Fundamental solutions in elastodynamics: a compendium. Cambridge, U.K., Cambridge University Press.

Kausel, E. (2010). Early history of soil-structure interaction. Soil Dynamics and Earthquake Engineering 30(9): 822-832.

Kausel, E. (2012). Lamb's problem at its simplest. Proceedings of the Royal Society of London A: Mathematical, Physical and Engineering Science.

Kausel, E. and J. Barbosa (2011). PMLs: A direct approach. International journal for numerical methods in engineering 90(3): 343-352.

Kausel, E. and R. Peek (1982a). Boundary integral method for stratified soilsMassachusetts Institute of Technology, Department of Civil Engineering.

Kausel, E. and R. Peek (1982b). Dynamic loads in the interior of a layered stratum: an explicit solution. Bulletin of the Seismological Society of America 72(5): 1459.

Kausel, E. and J. Roesset (1981). Stiffness matrices for layered soils. Bulletin of the Seismological Society of America 71(6): 1743.

Kausel, E. and S. Seale (1987). Static loads in layered halfspaces. Journal of applied mechanics 54: 403.

Klein, R., H. Antes and D. Le Houedec (1997). Efficient 3D modelling of vibration isolation by open trenches. Computers & Structures 64(1-4): 809-817.

Kogut, J., G. Degrande, W. Haegeman and L. Karl (2003). In situ vibration measurements on the high speed track L2 Brussels-Koln. IABSE REPORTS 87: 286.

Komatitsch, D. and R. Martin (2007). An unsplit convolutional perfectly matched layer improved at grazing incidence for the seismic wave equation. Geophysics 72(5): SM155-SM167.

Kressner, D. (2005). Numerical methods for general and structured eigenvalue problems. Berlin, Germany, Springer.

Kruse, H. and K. Popp (2001). A modular algorithm for linear, periodic train-track models. Archive of Applied Mechanics 71(6-7): 473-486.

Krylov, V. (1994). On the theory of railway-induced ground vibrations. Le Journal de Physique IV 4(C5).

Krylov, V. and C. Ferguson (1994). Calculation of low-frequency ground vibrations from railway trains. Applied Acoustics 42(3): 199-213.

Krylov, V. V. (1995). Generation of ground vibrations by superfast trains. Applied Acoustics 44(2): 149-164.

Kucukcoban, S. and L. Kallivokas (2010). Mixed perfectly-matched-layers for direct transient analysis in 2D elastic heterogeneous media. Computer methods in applied mechanics and engineering 200(1): 57-76.

Kurzweil, L. (1979). Ground-borne noise and vibration from underground rail systems. Journal of Sound and Vibration 66(3): 363-370.

Lai, C. G., A. Callerio, E. Faccioli, V. Morelli and P. Romani (2005). Prediction of railway-induced ground vibrations in tunnels. Journal of vibration and acoustics 127: 503.

Lamb, H. (1904). On the propagation of tremors over the surface of an elastic solid. Philosophical Transactions of the Royal Society of London. Series A, Containing Papers of a Mathematical or Physical Character 203(359-371): 1.

Lane, H. k., T. r. Ekevid, P. Kettil, C. Y. Ching and N.-E. Wiberg (2007). Vehicle-track-underground modeling of rail induced wave propagation. Computers & structures 85(15): 1215-1229.

Leung, K. L., D. E. Beskos and I. G. Vardoulakis (1990). Vibration isolation using open or filled trenches. Computational Mechanics 7(2): 137-148.

Lombaert, G. (2001). Development and experimental validation of a numerical model for the free field vibrations induced by road traffic. Leuven, Katholieke Universiteit Leuven, PhD Thesis.

Lombaert, G. and G. Degrande (2001). Experimental validation of a numerical prediction model for free field traffic induced vibrations by in situ experiments. Soil Dynamics and Earthquake Engineering 21(6): 485-497.

Lombaert, G. and G. Degrande (2003). The experimental validation of a numerical model for the prediction of the vibrations in the free field produced by road traffic. Journal of Sound and Vibration 262(2): 309-331.

Lombaert, G. and G. Degrande (2009). Ground-borne vibration due to static and dynamic axle loads of InterCity and high-speed trains. Journal of Sound and Vibration 319(3-5): 1036-1066.

Lombaert, G., G. Degrande and D. Clouteau (2000). Numerical modelling of free field traffic-induced vibrations. Soil Dynamics and Earthquake Engineering 19(7): 473-488.

Lombaert, G., G. Degrande and D. Clouteau (2001). The influence of the soil stratification on free field traffic-induced vibrations. Archive of Applied Mechanics 71(10): 661-678.

Lombaert, G., G. Degrande, J. Kogut and S. Francois (2006a). The experimental validation of a numerical model for the prediction of railway induced vibrations. Journal of Sound and Vibration 297(3-5): 512-535.

Lombaert, G., G. Degrande, B. Vanhauwere, B. Vandeborght and S. Francois (2006b). The control of ground-borne vibrations from railway traffic by means of continuous floating slabs. Journal of Sound and Vibration 297(3-5): 946-961.

Luco, J. E. and R. J. Apsel (1983). On the Green's functions for a layered half-space. Part I. Bulletin of the Seismological Society of America 73(4): 909-929.

Lysmer, J. (1970). Lumped mass method for Rayleigh waves. Bulletin of the Seismological Society of America 60(1): 89.

Lysmer, J., F. Ostadan and C. Chin, C. (1999). SASSI-2000, User Manual, Revision 1, A System for Analysis of Soil-Structure InteractionUniversity of California.

Lysmer, J. and G. Waas (1972). Shear waves in plane infinite structures. Journal of engineering mechanics 98(1): 85-105.

Madshus, C., B. Bessason and L. Hårvik (1996). Prediction model for low frequency vibration from high speed railways on soft ground. Journal of Sound and Vibration 193(1): 195-203.

Madshus, C. and A. Kaynia (2000). High-speed railway lines on soft ground: dynamic behaviour at critical train speed. Journal of Sound and Vibration 231(3): 689-701.

Mantic, V. (1993). A new formula for the C-matrix in the Somigliana identity. Journal of Elasticity 33(3): 191-201.

Melke, J. (1988). Noise and vibration from underground railway lines: proposals for a prediction procedure. Journal of Sound and Vibration 120(2): 391-406.

Melke, J. and S. Kramer (1983). Diagnostic methods in the control of railway noise and vibration. Journal of Sound and Vibration 87(2): 377-386.

Metrikine, A. and K. Popp (2000). Steady-state vibrations of an elastic beam on a visco-elastic layer under moving load. Archive of Applied Mechanics 70(6): 399-408.

Metrikine, A., S. Verichev and J. Blaauwendraad (2005). Stability of a two-mass oscillator moving on a beam supported by a visco-elastic half-space. International journal of solids and structures 42(3): 1187-1207.

Mooney, H. M. (1974). Some numerical solutions for Lamb's problem. Bulletin of the Seismological Society of America 64(2): 473.

Müller, K., H. Grundmann and S. Lenz (2008). Nonlinear interaction between a moving vehicle and a plate elastically mounted on a tunnel. Journal of Sound and Vibration 310(3): 558-586.

Murillo, C., L. Thorel and B. Caicedo (2009). Ground vibration isolation with geofoam barriers: Centrifuge modeling. Geotextiles and Geomembranes 27(6): 423-434.

Nelson, J. (1996). Recent developments in ground-borne noise and vibration control. Journal of Sound and Vibration 193(1): 367-376.

Neves, S., A. Azevedo and R. Calçada (2012). A direct method for analyzing the vertical vehicle-structure interaction. Engineering structures 34: 414-420.

O'Brien, J. and D. Rizos (2005). A 3D BEM-FEM methodology for simulation of high speed train induced vibrations. Soil Dynamics and Earthquake Engineering 25(4): 289-301.

Park, J. (2002). Wave motion in finite and infinite media using the Thin-Layer Method. Civil and Environment Engineering Department. Cambridge, Massachusetts Institue of Technology, PhD Thesis.

Park, J. and E. Kausel (2004a). Impulse response of elastic half-space in the wave number–time domain. Journal of engineering mechanics 130: 1211.

Park, J. and E. Kausel (2004b). Numerical dispersion in the thin-layer method. Computers & structures 82(7-8): 607-625.

Pekeris, C. (1955). The seismic surface pulse. Proceedings of the national academy of sciences of the United States of America 41(7): 469.

Pflanz, G., K. Hashimoto and N. Chouw (2002). Reduction of structural vibrations induced by a moving load. Journal of Applied Mechanics 5: 555-563.

Picoux, B. and D. Le Houedec (2005). Diagnosis and prediction of vibration from railway trains. Soil Dynamics and Earthquake Engineering 25(12): 905-921.

Rayleigh, L. (1885). On waves propagated along the plane surface of an elastic solid. Proceedings of the London Mathematical Society 1(1): 4.

Ribeiro, C. A., T. Dahlberg, R. Calçada and R. Delgado (2009). Dynamic analysis of transition zones on high speed railway lines by explicit analysis methods. 2nd International Conference on Computational Methods in Structural Dynamics & Earthquake Engineering Rhodes, Greece.

Ribeiro, D., R. Calçada, R. Delgado, M. Brehm and V. Zabel (2013). Finite-element model calibration of a railway vehicle based on experimental modal parameters. Vehicle System Dynamics 51(6): 821-856.

Rieckh, G., W. Kreuzer, H. Waubke and P. Balazs (2012). A 2.5D-Fourier-BEM model for vibrations in a tunnel running through layered anisotropic soil. Engineering Analysis with Boundary Elements 36(6): 960-967.

Rogier, H. and D. De Zutter (2001). Berenger and leaky modes in microstrip substrates terminated by a perfectly matched layer. Microwave Theory and Techniques, IEEE Transactions on 49(4): 712-715.

Saad, Y. (1992). Numerical methods for large eigenvalue problems. Manchester, U.K., SIAM.

Seale, S. H. and E. Kausel (1989). Point Loads in Cross Anisotropic, Layered Halfspaces. Journal of engineering mechanics 115: 509.

Sheng, X., C. Jones and M. Petyt (1999a). Ground vibration generated by a harmonic load acting on a railway track. Journal of Sound and Vibration 225(1): 3-28.

Sheng, X., C. Jones and M. Petyt (1999b). Ground vibration generated by a load moving along a railway track. Journal of Sound and Vibration 228(1): 129-156.

Sheng, X., C. Jones and D. Thompson (2003). A comparison of a theoretical model for quasi-statically and dynamically induced environmental vibration from trains with measurements. Journal of Sound and Vibration 267(3): 621-635.

Sheng, X., C. Jones and D. Thompson (2004). A theoretical study on the influence of the track on train-induced ground vibration. Journal of Sound and Vibration 272(3-5): 909-936.

Sheng, X., C. Jones and D. Thompson (2005). Responses of infinite periodic structures to moving or stationary harmonic loads. Journal of Sound and Vibration 282(1-2): 125-149.

Sheng, X., C. Jones and D. Thompson (2006). Prediction of ground vibration from trains using the wavenumber finite and boundary element methods. Journal of Sound and Vibration 293(3-5): 575-586.

Shrivastava, R. K. and N. S. V. Kameswara Rao (2002). Response of soil media due to impulse loads and isolation using trenches. Soil Dynamics and Earthquake Engineering 22(8): 695-702.

Soares, D., L. Godinho, A. Pereira and C. Dors (2012). Frequency domain analysis of acoustic wave propagation in heterogeneous media considering iterative coupling procedures between the method of fundamental solutions and Kansa's method. International journal for numerical methods in engineering 89(7): 914-938.

South, J. (1863). Experiments, Made at Watford, on the Vibrations Occasioned by Railway Trains Passing through a Tunnel. Proceedings of the Royal Society of London 13: 65-83.

Steenbergen, M. J. M. M. and A. V. Metrikine (2007). The effect of the interface conditions on the dynamic response of a beam on a half-space to a moving load. European Journal of Mechanics-A/Solids 26(1): 33-54.

Sutherland, H. B. (1950). A study of vibrations produced in structures by heavy vehicles. Proceedings of the Thirtieth Annual Meeting of the Highway Research Board 30: 406-419.

Tadeu, A. and J. António (2001). 2.5 D Green's functions for elastodynamic problems in layered acoustic and elastic formations. Computer Modeling in Engineering and Sciences 2(4): 477-496.

Tadeu, A. and J. António (2002). Green's functions for 2.5 D elastodynamic problems in a free solid layer formation. Engineering structures 24(4): 491-499.

Tadeu, A., J. António and L. Godinho (2001). Green's function for two-and-a-half dimensional elastodynamic problems in a half-space. Computational mechanics 27(6): 484-491.

Tadeu, A. J. B. and E. Kausel (2000). Green's functions for two-and-a-half-dimensional elastodynamic problems. Journal of engineering mechanics 126: 1093.

Takemiya, H. (2003). Simulation of track-ground vibrations due to a high-speed train: the case of X-2000 at Ledsgard. Journal of Sound and Vibration 261(3): 503-526.

Talman, J. D. (1978). Numerical Fourier and Bessel transforms in logarithmic variables. Journal of computational physics 29(1): 35-48.

Taniguchi, E. and S. Okada (1981). Reduction of ground vibrations by improving soft ground. Soil and Foundations 21(2): 99-113.

Tassoulas, J. L. and E. Kausel (1981). Elements for the numerical analysis of wave motion in layered media. NASA STI/Recon Technical Report N 82: 15292.

Teixeira, F. L. and W. C. Chew (1998). General closed-form PML constitutive tensors to match arbitrary bianisotropic and dispersive linear media. Microwave and Guided Wave Letters, IEEE 8(6): 223-225.

Thompson, D. (2008). Railway noise and vibration: mechanisms, modelling and means of control. Oxford, UK, Elsevier.

Thomson, W. T. (1950). Transmission of elastic waves through a stratified solid medium. Journal of Applied Physics 21(2): 89-93.

Verhas, H. (1979). Prediction of the propagation of train-induced ground vibration. Journal of Sound and Vibration 66(3): 371-376.

Vostroukhov, A. and A. Metrikine (2003). Periodically supported beam on a visco-elastic layer as a model for dynamic analysis of a high-speed railway track. International journal of solids and structures 40(21): 5723-5752.

Waas, G. (1972). Linear two-dimensional analysis of soil dynamics problems in semi-infinite layered media. Berkeley, University of California, PhD Thesis.

Wilson, G., H. Saurenman and J. Nelson (1983). Control of ground-borne noise and vibration. Journal of Sound and Vibration 87(2): 339-350.

Wolf, J. P. (2003). The scaled boundary finite element method, John Wiley & Sons Inc.

Wong, H. and J. Luco (1978). Dynamic response of rectangular foundations to obliquely incident seismic waves. Earthquake Engineering & Structural Dynamics 6(1): 3-16.

Wu, T. and D. Thompson (2002). A hybrid model for the noise generation due to railway wheel flats. Journal of Sound and Vibration 251(1): 115-139.

Xia, H., N. Zhang and Y. Cao (2005a). Experimental study of train-induced vibrations of environments and buildings. Journal of Sound and Vibration 280(3-5): 1017-1029.

Xia, H., N. Zhang and R. Gao (2005b). Experimental analysis of railway bridge under high-speed trains. Journal of Sound Vibration 282: 517-528.

Yang, Y., H. Hung and D. Chang (2003). Train-induced wave propagation in layered soils using finite/infinite element simulation. Soil Dynamics and Earthquake Engineering 23(4): 263-278.

Yang, Y. B. and H. H. Hung (1997). A parametric study of wave barriers for reduction of train induced vibrations. International journal for numerical methods in engineering 40(20): 3729-3747.

Yang, Y. B. and H. H. Hung (2001). A 2.5 D finite/infinite element approach for modelling visco elastic bodies subjected to moving loads. International journal for numerical methods in engineering 51(11): 1317-1336.